

Sustainability footprints and mechanical performance in multi-principal element alloys

Théo Langlois

▶ **To cite this version:**

Théo Langlois. Sustainability footprints and mechanical performance in multi-principal element alloys. Materials. INSA de Lyon; Deakin university (Geelong, Australie), 2025. English. ⟨NNT : 2025ISAL0036⟩. ⟨tel-05384152⟩

HAL Id: tel-05384152

https://theses.hal.science/tel-05384152v1

Submitted on 26 Nov 2025

HAL is a multi-disciplinary open access archive for the deposit and dissemination of scientific research documents, whether they are published or not. The documents may come from teaching and research institutions in France or abroad, or from public or private research centers.

L'archive ouverte pluridisciplinaire **HAL**, est destinée au dépôt et à la diffusion de documents scientifiques de niveau recherche, publiés ou non, émanant des établissements d'enseignement et de recherche français ou étrangers, des laboratoires publics ou privés.



HAL Authorization

N°d'ordre NNT : 2025ISAL0036

THESE de DOCTORAT DE L'INSA LYON,
Membre de l'UNIVERSITE DE LYON

Délivré en partenariat international avec
Institute for Frontier Materials (Deakin University)

Ecole Doctorale N° 34
Matériaux de Lyon

Spécialité de doctorat : Matériaux

Soutenue publiquement le 02/04/2025, par :
LANGLOIS Théo

SUSTAINABILITY FOOTPRINTS AND MECHANICAL PERFORMANCE IN MULTI-PRINCIPAL ELEMENT ALLOYS

Devant le jury composé de :

Mme. PEREZ PRADO, Maria Teresa	Professeur	IMDEA	Rapporteur
M. GODET, Stéphane	Professeur	ULB	Rapporteur
Mme. FRACZKIEWIECZ, Anna	Professeur	MINES Saint-Etienne	Examinatrice
M. TANCRET, Franck	Professeur	Univ Nantes	Président
M. BARNETT, Matthew	Professeur	Deakin University	Directeur de thèse
M. FABIJANIC, Daniel	Associate Professor	Deakin University	Co-directeur
M. FABREGUE, Damien	Professeur	INSA Lyon	Co-directeur
M. BOULNAT, Xavier	Maître de conférences	INSA Lyon	Co-directeur
M. GORSSE, Stéphane	Professeur	INP Bordeaux	Invité
Mme. VARVENNE, Céline	Chargée de recherche	INSA Lyon	Invitée
M. DORIN, Thomas	Associate Professor	Deakin University	Invité

Thèse accessible à l'adresse : https://theses.insa-lyon.fr/publication/2025ISAL0036/these.pdf © [T. Langlois], [2025], INSA Lyon, tous droits réservés

SUSTAINABILITY FOOTPRINTS AND MECHANICAL PERFORMANCE IN MULTI-PRINCIPAL ELEMENT ALLOYS

Deakin University



Théo Langlois

IFM PhD Student

Submitted in fulfilment of the requirements for the degree of Doctor of Philosophy

Principal Supervisor: Matthew Barnett

Associate Supervisor/s: Daniel Fabijanic

External Supervisor/s:

Xavier Boulnat

Damien Fabrègue

Stephane Gorsse

Submitted to Institute for Frontier Materials, Deakin University



Thèse accessible à l'adresse : https://theses.insa-lyon.fr/publication/2025ISAL0036/these.pdf © [T. Langlois], [2025], INSA Lyon, tous droits réservés

Département FEDORA – INSA Lyon - Ecoles Doctorales

SIGLE	ECOLE DOCTORALE	NOM ET COORDONNEES DU RESPONSABLE
ED 206 CHIMIE	**CHIMIE DE LYON** **https://www.edchimie-lyon.fr** Sec. : Renée EL MELHEM Bât. Blaise PASCAL, 3e étage secretariat@edchimie-lyon.fr	**M. Stéphane DANIELE** C2P2-CPE LYON-UMR 5265 Bâtiment F308, BP 2077 43 Boulevard du 11 novembre 1918 69616 Villeurbanne directeur@edchimie-lyon.fr
ED 341 E2M2	**ÉVOLUTION, ÉCOSYSTÈME, MICROBIOLOGIE, MODÉLISATION** **http://e2m2.universite-lyon.fr** Sec. : Bénédicte LANZA Bât. Atrium, UCB Lyon 1 Tél : 04.72.44.83.62 secretariat.e2m2@univ-lyon1.fr	**Mme Sandrine CHARLES** Université Claude Bernard Lyon 1 UFR Biosciences Bâtiment Mendel 43, boulevard du 11 Novembre 1918 69622 Villeurbanne CEDEX e2m2.codir@listes.univ-lyon1.fr
ED 205 EDISS	**INTERDISCIPLINAIRE SCIENCES-SANTÉ** **http://ediss.universite-lyon.fr** Sec. : Bénédicte LANZA Bât. Atrium, UCB Lyon 1 Tél : 04.72.44.83.62 secretariat.ediss@univ-lyon1.fr	**Mme Sylvie RICARD-BLUM** Laboratoire ICBMS - UMR 5246 CNRS - Université Lyon 1 Bâtiment Raulin - 2ème étage Nord 43 Boulevard du 11 novembre 1918 69622 Villeurbanne Cedex Tél : +33(0)4 72 44 82 32 sylvie.ricard-blum@univ-lyon1.fr
ED 34 EDML	**MATÉRIAUX DE LYON** **http://ed34.universite-lyon.fr** Sec. : Yann DE ORDENANA Tél : 04.72.18.62.44 yann.de-ordenana@ec-lyon.fr	**M. Stéphane BENAYOUN** Ecole Centrale de Lyon Laboratoire LTDS 36 avenue Guy de Collongue 69134 Ecully CEDEX Tél : 04.72.18.64.37 stephane.benayoun@ec-lyon.fr
ED 160 EEA	**ÉLECTRONIQUE, ÉLECTROTECHNIQUE, AUTOMATIQUE** **https://edeea.universite-lyon.fr** Sec. : Philomène TRECOURT Bâtiment Direction INSA Lyon Tél : 04.72.43.71.70 secretariat.edeea@insa-lyon.fr	**M. Philippe DELACHARTRE** INSA LYON Laboratoire CREATIS Bâtiment Blaise Pascal, 7 avenue Jean Capelle 69621 Villeurbanne CEDEX Tél : 04.72.43.88.63 philippe.delachartre@insa-lyon.fr
ED 512 INFOMATHS	**INFORMATIQUE ET MATHÉMATIQUES** **http://edinfomaths.universite-lyon.fr** Sec. : Renée EL MELHEM Bât. Blaise PASCAL, 3e étage Tél : 04.72.43.80.46 infomaths@univ-lyon1.fr	**M. Hamamache KHEDDOUCI** Université Claude Bernard Lyon 1 Bât. Nautibus 43, Boulevard du 11 novembre 1918 69 622 Villeurbanne Cedex France Tél : 04.72.44.83.69 direction.infomaths@listes.univ-lyon1.fr
ED 162 MEGA	**MÉCANIQUE, ÉNERGÉTIQUE, GÉNIE CIVIL, ACOUSTIQUE** **http://edmega.universite-lyon.fr** Sec. : Philomène TRECOURT Tél : 04.72.43.71.70 Bâtiment Direction INSA Lyon mega@insa-lyon.fr	**M. Etienne PARIZET** INSA Lyon Laboratoire LVA Bâtiment St. Exupéry 25 bis av. Jean Capelle 69621 Villeurbanne CEDEX etienne.parizet@insa-lyon.fr
ED 483 ScSo	**ScSo**[1] **https://edsciencessociales.universite-lyon.fr** Sec. : Mélina FAVETON Tél : 04.78.69.77.79 melina.faveton@univ-lyon2.fr	**M. Bruno MILLY** (INSA : J.Y. TOUSSAINT) Univ. Lyon 2 Campus Berges du Rhône 18, quai Claude Bernard 69365 LYON CEDEX 07 Bureau BEL 319 bruno.milly@univ-lyon2.fr

[1] ScSo : Histoire, Géographie, Aménagement, Urbanisme, Archéologie, Science politique, Sociologie, Anthropologie

Thèse accessible à l'adresse : https://theses.insa-lyon.fr/publication/2025ISAL0036/these.pdf © [T. Langlois], [2025], INSA Lyon, tous droits réservés

Acknowledgements

The DEAKIN UNIVERSITY and the INSTITUTE FOR FRONTIER MATERIALS are acknowledged for their financial support. Part of the research was undertaken on the X-ray Powder beamline at the Australian Synchrotron, part of ANSTO.

I express my sincere gratitude to the Chairperson for the great honour of presiding over my thesis defence, as well as to the examiners, reviewers and panel present during the defence. I also want to acknowledge Professor A. Fraczkiewicz, Professor P.A. Geslin, Professor T. Dorin and Professor R. Marceau for their support and guidance during the oral examinations at the first and second-year benchmarks of my thesis.

I am deeply grateful to my supervisors Matthew Barnett and Daniel Fabijanic at the Institute for Frontier Materials. I would also like to thank my supervisors Damien Fabrègue and Xavier Boulnat at MATEIS, as well as my supervisor Stéphane Gorsse at the Institut de la Matière Condensée de Bordeaux. Matthew, you encouraged me to approach every result with a critical eye. Daniel, your insights were invaluable. Damien, your help greatly facilitated the progress of this thesis. Xavier, your extensive knowledge, from material elaboration to characterisation, was an undeniable support. Stéphane, your approach of this thesis was very inspiring to me.

I would like to thank the Institute for Frontier Material for providing me with advanced equipment and materials. Alireza, Charline, Daniel Grasser, Jithin and Ziyu,; your support was so deeply appreciated. I also want to thank Professor Hossein Beladi for his time and dedication to the EBSD analysis. Daniel Jiang, Steven, John, Leticia, Beau and Raju, your assistance was also highly valuable to my project.

I would like to acknowledge the Laboratoire MATEIS at INSA Lyon and extend a warm thank you to all the people I had the opportunity to meet and work with there. Thierry, Sandrine and Delphine, I am so grateful for your support while I was finishing the last experimental parts. A special thanks to Ian and Maureen, my colleagues and housemates in this cotutelle between France and Australia.

Thank you to my friends in France and Australia, with warmer thanks to my Australian family and my French family.

Thèse accessible à l'adresse : https://theses.insa-lyon.fr/publication/2025ISAL0036/these.pdf © [T. Langlois], [2025], INSA Lyon, tous droits réservés

Abstract

In the current context of ecological transition, driven by the concerns regarding pollution, global warming and consumption of critical resources among others, there is an urgent need to shift towards greener sources of energy and materials. The critical role of metals in the ecological transition is increasingly evident. Over the current decade, the demand for lithium, nickel, and other strategic metals is expected to increase drastically. This surge in demand introduces new environmental, economic, and societal challenges. In various industrial sectors, medium-entropy alloys (MEAs) and high-entropy alloys (HEAs), composed of multiple metals in approximately equal proportions, present promising alternatives. Some HEAs are notable for their excellent mechanical properties, which remain stable despite compositional changes. Hence, those alloys offer a potential pathway to mitigate the reliance on critical materials. Among the most robust HEAs are the Cantor alloy (CoCrFeMnNi) and the ternary CrCoNi. These specific HEAs exhibit great resistance to wear and corrosion, as well as excellent mechanical properties such as high strength, ductility. The later properties are further improved at cryogenic temperatures. Among other potential industrial applications of HEAs, the storage and transportation of hydrogen highlights the importance of these materials in supporting the shift towards hydrogen as a greener energy source in the ecological transition. However, the use of cobalt in many HEAs raises concerns due to its environmental, economic and social impacts.

This works aims to develop new MEAs focused on sustainability while maintaining their mechanical performance. In this this thesis, we investigate new HEA compositions around the CrCoNi base with significantly reduced content of cobalt. Alongside the addition of other specific elements (C, N, W) from previous publications, we demonstrate here that the addition of silicon to our new compositions reduces drastically the sustainable impact of our materials while maintaining outstanding mechanical performance.

For this work, we have implemented a three-steps method for developing new HEA compositions. The first two layers involve a rapid screening of numerous potential compositions, followed by a more detailed evaluation and development of the most promising ones identified in the previous stages. We developed a rapid alloying process to enable fast and multiscale prediction, manufacturing, microstructural, and mechanical characterisation of a wide range of HEAs. We call this process “Fast Alloying” (FA). It is very powerful to explore a wide range of new HEA compositions efficiently while minimising resource consumption.

Thèse accessible à l'adresse : https://theses.insa-lyon.fr/publication/2025ISAL0036/these.pdf © [T. Langlois], [2025], INSA Lyon, tous droits réservés

This fast method involves the use of prediction models, correlation models with machine learning (ML), simultaneous manufacturing of multiple alloy compositions (up to 30 per day) via arc furnace, simultaneous thermal treatments, and rapid microstructural characterisation techniques. These techniques include X-ray diffraction (XRD) for phase analysis and stacking fault energy (SFE) measurement, scanning electron microscopy (SEM) imaging, energy-dispersive X-ray spectroscopy (EDS) analysis, and electron backscatter diffraction (EBSD) analysis. Additionally, rapid mechanical testing is performed via plastometry and compression.

The more advanced method involves manufacturing of 4 compositions by arc furnace, thermomechanical treatments (homogenisation, cold rolling and annealing), microstructural analysis (XRD, GDOES, EDS, EBSD) and mechanical testing (hardness, plastometry, tensile tests at room and cryogenic temperatures).

Our findings underline the potential for sustainable development of new materials by reducing the use of critical elements like cobalt and optimising alloy compositions through rapid then advanced manufacturing techniques. The use of tough and more sustainable alloys for hydrogen storage would thus have a double positive impact on the environment.

Keywords

Medium-Entropy Alloys, High-Entropy Alloys, Single-FCC alloys, Fast-Alloying, Arc-Furnace Melting, Mechanical properties, Cryogenic properties, Strengthening models, Stacking Fault Energy, X-ray Diffraction, SEM, EBSD, Sustainability, Sustainable Competitiveness, Material Databases.

Thèse accessible à l'adresse : https://theses.insa-lyon.fr/publication/2025ISAL0036/these.pdf © [T. Langlois], [2025], INSA Lyon, tous droits réservés

List of scientific communications

Publications in peer-reviewed journals

[A] S. Gorsse, T. Langlois, M.R. Barnett, Considering sustainability when searching for new high entropy alloys, Sustainable Materials and Technologies, 2024, Vol. 40

[B] S. Gorsse, T. Langlois, M.R. Barnett, Commercial, Environmental and Societal Implications of High Entropy Alloys, Ni-Based Alloys, and Steels, Scientific Data (Accepted)

Presentations in conferences

1. T. Langlois, S. Gorsse, X. Boulnat, D. Fabrègue, M.R Barnett, D. Fabijanic, *Prediction tool of the sustainable performance for a wide range of metals*, Technical Webinar on Strategies for carbon footprint reduction and its impact on steel industry technologies, Fives Keods, September 2022, INSA Lyon, France

2. S. Gorsse, T. Langlois, M.R. Barnett, Teaching responsible alloy design. Poster presented at: 12th International Materials Education Symposium (IMES), Clare College, April 2023, Cambridge, UK

3. S. Gorsse, T. Langlois, M.R. Barnett, *Societal impact-informed & artificial intelligence-guided design strategies of high entropy alloys*, THERMEC'2023, International Conference on Processing & Manufacturing of advanced Materials, Graz University of Technology, Jul 2023, Vienne, Austria

4. T. Langlois, M.R. Barnett, S. Gorsse, X. Boulnat, D. Fabrègue, *Prise en compte de la durabilité dans le design des alliages à haute entropie*, Journées annuelles 2024 SF2M, Nov. 2024, Paris, France

Thèse accessible à l'adresse : https://theses.insa-lyon.fr/publication/2025ISAL0036/these.pdf © [T. Langlois], [2025], INSA Lyon, tous droits réservés

Symbols and abbreviations

Symbol	Unit	Meaning
γ_{usf}, γ_{isf}, γ_{utf}, γ_{esf}	$mJ.m^{-2}$	Unstable stacking fault Intrinsic stacking fault Unstable twinning fault Extrinsic stacking fault
ΔH_{mix}	kJ	Enthalpy of mixing
$\Delta G_m^{fcc\text{-}hcp}$	mJ/mol	Molar Gibbs free energy
ΔL	mm	Gauge mark displacement
ΔS_{mix}	$kJ.K^{-1}$	Entropy of mixing
$\Delta\sigma_{s\text{-}h}$	MPa	strain hardening of a material under plastic deformation
$\sigma_{\rho i}$	MPa	Initial dislocation density contribution to yield strength
σ_{gb}	MPa	Grain boundary contribution to yield strength
σ_{ppt}	MPa	Precipitate contribution to yield strength
σ_{ss}	MPa	Solid Solution contribution to yield strength
δ	Ø	Atomic size difference
ε_E	Ø	Engineering strain
ε_f	Ø	Tensile ductility (strain to failure)
ε_T	Ø	True strain
$\Gamma^{fcc/hcp}$	$mJ.m^{-2}$	interfacial energy between FCC/HCP phases
μ or G	GPa	Shear modulus
$\overline{\mu}$	GPa	Average Shear modulus
ν	Ø	Poisson's ratio
$\overline{\nu}$	Ø	Average Poisson's ratio
ρ	$mol.m^{-2}$	Molar surface density
σ_c	MPa	Compressive strength
σ_E	MPa	Engineering stress
σ_{flow}	MPa	Flow stress
σ_{fr}	MPa	Frictional stress
σ_T	MPa	True stress
σ_{uts}	MPa	Ultimate tensile strength
σ_{ys}	MPa	Yield strength
τ_{cr}	MPa	Critical Stress for twinning

Thèse accessible à l'adresse : https://theses.insa-lyon.fr/publication/2025ISAL0036/these.pdf © [T. Langlois], [2025], INSA Lyon, tous droits réservés

τ_y	MPa	Critical resolved shear stress
τ_{y0}	MPa	Critical resolved shear stress at 0 K
A	Ø	Zener anisotropy correction
A_C	J	Impact Energy
A_0	Ø	Pre-exponential constant in the Arrhenius law for grain recrystallisation
a	Å	Lattice parameter
a_{FCC}	Å	Lattice parameter of the FCC phase
a_σ , c_σ	Å	Lattice parameter of the sigma phase
$\overline{AR}$	Ø	Aspect ratio
B	mm	Specimen thickness
b	Å	Burger's vector
CFP	$eqCO_2/kg$	Carbon Footprint (amount of $eqCO_2$ to get 1kg of a material)
C_{ij}	GPa	Elastic stiffness coefficient
c_i	mol/mol	Atomic fraction of element i
D	µm	Grain size diameter
$\overline{D}$	µm	Average grain size diameter
$d\sigma/d\varepsilon$	MPa	Strain-hardening rate
F	N	Applied force
EE	kJ/kg	Embodied Energy: Energy amount to get 1kg of a material
E_S	J/mm^2	Material's impact toughness or specific energy
$eqCO_2$	kg/kg	Heat absorbed by any greenhouse gas as a multiple of the heat that would be absorbed by the same mass of CO_2
G_{111}	GPa	Shear modulus along the (111) plane
K	$MPa\sqrt{m}$	Stress intensity factor, value at the crack tip
k	J/K	Boltzmann Constant
L	mm	Specimen length
N_A	mol^{-1}	Avogadro's constant
P°	Pa	Pressure of gas
Q	$kJ.mol^{-1}$	Activation energy for grain growth
$\overline{R}$	$J.K^{-1}.mol^{-1}$	Gas constant
$\overline{r}$	µm	Average atomic radius
r_i	µm	Atomic radius of component i
S	mm^2	Cross-sectional area of the specimen
SDQ	$kJ.mol^{-1}$	Self-Diffusion activation energy
SFE	$mJ.m^{-2}$	General Stacking Fault Energy
T_m	K	Melting temperature

Thèse accessible à l'adresse : https://theses.insa-lyon.fr/publication/2025ISAL0036/these.pdf © [T. Langlois], [2025], INSA Lyon, tous droits réservés

$\overline{VEC}$	Ø	Average valence electron concentration of the alloy
W	mm	Specimen width
w_i	kg/kg	Mass fraction of an element i

Abbreviation	**Meaning**
AC	As-Cast State
AH	As-Homogenised State
BC	Band Contrast
BCC	Base-Cubic Centred crystallography
CALPHAD	CALculation of PHAse Diagram methodology
Cantor Alloy	Metal alloy made of Co Cr Fe Mn Ni
CFP	Carbon Footprint
C-HEA	Cantor Alloy and Cantor Subset HEAs
Co33	$Cr_{33}Co_{33}Ni_{33}$ (atomic %)
Co33*	$Cr_{33}Co_{33}Ni_{33}$ with Iron contamination
Co33Si6	$(Cr_{33}Co_{33}Ni_{33})_{94}Si_6$ (atomic %)
Co33Si6*	$(Cr_{33}Co_{33}Ni_{33})_{94}Si_6$ with Iron contamination
Co10	$Cr_{45}Co_{10}Ni_{45}$ (atomic %)
Co10*	$Cr_{45}Co_{10}Ni_{45}$ with Iron contamination
Co10Si6	$(Cr_{45}Co_{10}Ni_{45})_{94}Si_6$ (atomic %)
Co10Si6*	$(Cr_{45}Co_{10}Ni_{45})_{94}Si_6$ with Iron contamination
CrCoNi	Chromium Cobalt Nickel alloy
CrCoNiSi	Chromium Cobalt Nickel Silicon alloy
CRM	Critical Raw Material
CVN	Charpy V-Notch impact specimen/test
DFT	Density Functional Theory
DLMD	Direct Laser Metal Deposition
DPI	Die Penetrant Inspection
DRC	Democratic Republic of Congo
EBSD	Electron Back-Scattered Diffraction
ECCI	Electron Channelling Contrast Imaging
Eco_FP	Average value of the rescaled economic footprints
Eco_score	Average economic score (10 – Eco_FP)
EDM	Electrical Discharge Machining
EDS, EDX	Energy-dispersive X-ray spectroscopy
EE	Embodied Energy

Thèse accessible à l'adresse : https://theses.insa-lyon.fr/publication/2025ISAL0036/these.pdf © [T. Langlois], [2025], INSA Lyon, tous droits réservés

EM	Electron Microscopy
Env_FP	Average value of the rescaled environmental footprints
Env_score	Average environmental score (10 – Env_FP)
FA	Fast-Alloying method
FE-SEM	Field Emission Scanning Electron Microscopy
FCC	Face-Cubic Centred crystallography
GDOES	Glow Discharge and Optical Emission Spectrometry
GOS	Grain Orientation Spread
HE	Hydrogen Embrittlement
HEA	High-Entropy Alloy (5 or more principal elements)
HE-BMG	High-Entropy Bulk Metallic Glass
HSR	Head-Shoulder-Rupture regions of tensile specimens
HV	Hardness Vickers
I_{eco}	Ecologic indicator
I_{env}	Environmental indicator
I_{soc}	Social indicator
KAM	Kernel Average Misorientation
LCA	Life Cycle Assessment
LT	Low Temperature
MBIP	Micro-Band Induced plasticity
MEA	Medium Entropy Alloy (2-4 principal elements)
ML	Machine Learning
MPEA	Multi-Principal Element Alloy
ND	Normal direction of rolling (axis coincident to the working force during rolling)
OM	Optical Microscopy
PIP	Profilometry-based Indentation Plastometry
RT	Room Temperature
RD	Rolling Direction
RX	Recrystallisation, Recrystallised
SC	Sustainable Competitiveness
SEM	Scanning Electron Microscopy
SE2	Secondary Imaging with Scanning Electron Microscope
SFE	Stacking Fault Energy
SFP	Stacking Fault Probability
SHR	Strain Hardening Rate
Soc_FP	Average value of the rescaled societal footprints
Soc_score	Average societal score (10 – Soc_FP)
Sust_FP	Average value of all the rescaled footprints
Sust_score	Average sustainable score (10 – Sust _FP)

Thèse accessible à l'adresse : https://theses.insa-lyon.fr/publication/2025ISAL0036/these.pdf © [T. Langlois], [2025], INSA Lyon, tous droits réservés

TA	Tensile Axis
TB	Twin Boundary
TD	Transverse Direction of rolling (axis normal to ND and RD)
TDB	Tensile Dog-Bone shape specimen
TRIP	Transformation induced plasticity
TWIP	Twinning induced plasticity
UTS	Ultimate Tensile Strength
VEC	Valence Electron Concentration
WU	Water Usage
YS	Yield Strength

Thèse accessible à l'adresse : https://theses.insa-lyon.fr/publication/2025ISAL0036/these.pdf © [T. Langlois], [2025], INSA Lyon, tous droits réservés

List of equations

(1.1)	$\Delta S_{mix} = -R \sum_i c_i \cdot ln\,(c_i)$ $1R \leq \Delta S_{mix} < 1.5\,R \rightarrow MEA$ $\Delta S_{mix} \geq 1.5\,R \rightarrow HEA$
(1.2)	$\frac{\overline{T_m}\,\Delta S_{mix}}{\lvert\Delta H_{mix}\rvert} \geq 1.1$
(1.3)	$\delta = \sqrt{\sum_{i=1}^{N} c_i \left(1 - \frac{r_i}{\bar{r}}\right)^2} \leq 6.6\%$
(1.4)	$\begin{cases} \overline{VEC} = \sum_{i=1}^{N} c_i (VEC)_i \\ VEC \geq 8 \rightarrow FCC \\ 6.7 \leq VEC < 8 \rightarrow FCC - BCC\ mixture \\ VEC < 6.7 \rightarrow BCC \end{cases}$
(1.5)	$\sigma_{flow} = \sigma_{ys} + \Delta\sigma_{s-h}$
(1.6)	$\sigma_{ys} = \sigma_{fr} + \sigma_{ss} + \sigma_{ppt} + \sigma_{\rho i} + \sigma_{gb}$
(1.7)	$\sigma_{ys} = \sigma_{fr} + \sigma_{ss} + \sigma_{gb}$
(1.8)	$\tau_{y0} = 0.051 \cdot \alpha^{-\frac{1}{3}} \cdot \bar{\mu} \left(\frac{1+\bar{\nu}}{1-\bar{\nu}}\right)^{\frac{4}{3}} f_\tau(w_c) \left[\frac{\sum_n c_n \Delta V_n^2}{b^6}\right]^{2/3}$
(1.9)	$\Delta E_b = 0.274 \cdot \alpha^{\frac{1}{3}} \cdot \bar{\mu} \cdot b^3 \left(\frac{1+\bar{\nu}}{1-\bar{\nu}}\right)^{\frac{2}{3}} f_{\Delta E}(w_c) \left[\frac{\sum_n c_n \Delta V_n^2}{b^6}\right]^{1/3}$
(1.10)	$\tau_y(T, \dot{\varepsilon}) = \tau_{y0} \left(1 - \left(\frac{k_b T}{\Delta E_b} \cdot \ln \frac{\dot{\varepsilon}_0}{\dot{\varepsilon}}\right)^{\frac{2}{3}}\right)$
(1.11)	$\sigma_y(T, \dot{\varepsilon}) = 3.06 \cdot \tau_y(T, \dot{\varepsilon})$
(1.12)	$\Delta V_i = V_i^{FCC} - \sum_i c_i\, V_i^{FCC}$

Thèse accessible à l'adresse : https://theses.insa-lyon.fr/publication/2025ISAL0036/these.pdf © [T. Langlois], [2025], INSA Lyon, tous droits réservés

(1.13)	$V_{binary} = c_i V_i^{FCC} + (1 - c_i) V_{Ni}$
(1.14)	$\begin{cases} \Delta\sigma_{ss} \propto \left(\sum_i c_i \Delta\bar{V}_i^{\,2} \right)^{\frac{1}{2}} \\ \sum_i c_i \Delta\bar{V}_i^{\,2} = 9\bar{V}^2 \left(\frac{\sum_i c_i r_i^2}{\bar{r}^2} - 1 \right) = 9\bar{V}^2 \delta^2 \end{cases}$
(1.15)	$\Delta\sigma_{s-h} = \Delta\sigma_{\rho} + \Delta\sigma_{SF} + \Delta\sigma_{twin}$
(1.16)	$\gamma_{ISF} = 2\,\rho\,\Delta G_m^{fcc \to hcp} + 2\,\Gamma^{fcc/hcp}$
(1.17)	$\rho = \frac{4}{\sqrt{3\,a_{(FCC)}^2}} \frac{1}{N_A}$
(1.18)	$\gamma_{ISF} = 248 - 835X_{Cr} - 323X_{Co} + 682X_{Cr}^2 - 39X_{Co}^2 + 777X_{Cr}X_{Co}$
(1.19)	$G_{111} = \frac{C_{11} - C_{12} + C_{44}}{3}$
(3.1)	$\mu_i = \frac{E_i}{2(1 + \nu_i)}$
(3.2)	$b_i = \frac{(4V_i^{FCC})^{1/3}}{\sqrt{2}}$
(3.3)	$A_{[E]} = \sum_{i=1}^{118} w_i * E_i$
(3.4)	$A_{[C]} = \sum_{i=1}^{118} w_i * \left(\sum_{j=1}^{180} f_{i,j} * C_j \right)$
(3.5)	$SR\,(alloy) = 1 - \prod_i (1 - SR_{(i)})$
(3.6)	$n\,\lambda = 2\,d\,sin\theta$
(3.7)	$HV = 0.1891 \frac{F}{d^2}$

Thèse accessible à l'adresse : https://theses.insa-lyon.fr/publication/2025ISAL0036/these.pdf © [T. Langlois], [2025], INSA Lyon, tous droits réservés

(3.8)	$\sigma = \sigma_S - (\sigma_S - \sigma_Y) \exp\left(\frac{\varepsilon}{\varepsilon_0}\right)$
(3.9)	$\bar{x} = \frac{\Sigma x_i}{n}$
(3.10)	$\sigma = \sqrt{\frac{\Sigma (x_i - \bar{x})^2}{n-1}}$
(3.11)	$\sigma_{\bar{x}} = \frac{\sigma}{\sqrt{n}}$
(3.12)	$\sigma = \sigma_S - (\sigma_S - \sigma_Y)\, exp\left(\frac{\varepsilon}{\varepsilon_0}\right)$
(3.13)	$\bar{x} = \frac{\Sigma\left(\frac{x_i}{\sigma_i^2}\right)}{\Sigma\left(\frac{1}{\sigma_i^2}\right)}$
(3.14)	$\sigma_{\bar{x}} = \sqrt{\frac{1}{\Sigma\left(\frac{1}{\sigma_i^2}\right)}}$
(3.15)	$S_0 = \frac{\pi \cdot {D_0}^2}{4}$
(3.16)	$\sigma_E = \frac{F}{S_0}$
(3.17)	$\varepsilon_E = \frac{\Delta L}{L_0}$
(3.18)	$\sigma_T = \sigma_E(1 - \varepsilon_E)$, in compressive deformation
(3.19)	$\varepsilon_T = -\ln(1 - \varepsilon_E)$, in compressive deformation
(3.20)	$SHR = \frac{d\sigma_T}{d\varepsilon_T}$
(3.21)	$\sigma_T = \sigma_E(1 + \varepsilon_E)$, in tensile deformation

Thèse accessible à l'adresse : https://theses.insa-lyon.fr/publication/2025ISAL0036/these.pdf © [T. Langlois], [2025], INSA Lyon, tous droits réservés

(3.22)	$\varepsilon_T = \ln(1+\varepsilon_E)$, in tensile deformation
(3.23)	$E_s = \frac{A_c}{B \times (W - 0.2)}$
(4.1)	$SFE\ (mJ/m^2) = 29.243 \cdot Co + 28.601 \cdot Cr + 32.015 \cdot Ni - 2977.431$
(4.2)	$Overall_{score} = \left(\frac{\frac{Eco_{score} + Env_{score} + Soc_{Score}}{3} + \frac{SS_{score} + SFE_{score}}{2}}{2} \right)$

Thèse accessible à l'adresse : https://theses.insa-lyon.fr/publication/2025ISAL0036/these.pdf © [T. Langlois], [2025], INSA Lyon, tous droits réservés

Contents

Introduction ---- **4**

Industrial and environmental context ... 4

Motivation ... 5

1 State-of-the-art ---- **6**

1.1 Multi-Principal Element Alloys ... 7

1.1.1 General principles and interest ... 7

1.1.2 Mechanical properties ... 10

1.1.3 Unexplored regions of C-MPEAS ... 23

1.2 Societal implications of metal alloys ... 30

1.2.1 General principles of material selection ... 30

1.2.2 Challenges of critical raw materials ... 32

1.2.3 Ethical and societal aspects of materials ... 34

1.2.4 Sustainability footprints of Cobalt ... 36

1.3 Concluding remarks ... 39

2 Research questions and outline ---- **40**

2.1 Research questions ... 40

2.2 Outline ... 41

3 Numerical and experimental methods ---- **43**

3.1 Adopted approach ... 44

3.2 Numerical methods: principle, data and tools ... 46

3.2.1 CALPHAD model ... 47

3.2.2 Solid Solution Strengthening model ... 50

3.2.3 Stacking Fault Energy Prediction models ... 54

3.2.4 Modelling the sustainable competitiveness of materials ... 58

Thèse accessible à l'adresse : https://theses.insa-lyon.fr/publication/2025ISAL0036/these.pdf © [T. Langlois], [2025], INSA Lyon, tous droits réservés

3.3 Experimental methods 67
3.3.1 Choice of raw materials 67
3.3.2 Manufacturing Methods 70
3.3.3 Thermomechanical treatments 75
3.3.4 Metallography: Sample preparation 77
3.3.5 Specimen machining 81
3.3.6 Chemical characterisation methods 84
3.3.7 Microstructural characterisation methods 88
3.3.8 Mechanical testing methods 98
3.4 Summary 109
4 Material predictions and explorations 110
4.1 FCC phase stability in C-MPEAs 111
4.2 Mechanical performance of C-MPEAs 120
4.2.1 Prediction of Solid solution strengthening in C-MPEAs 121
4.2.2 Prediction of deformation mechanisms in C-MPEAs 129
4.3 Sustainable competitiveness of metal alloys and C-MPEAs 133
4.3.1 Elemental scores 133
4.3.2 Sustainability scores for different classes of alloys 137
4.3.3 Sustainability properties of Cantor subsystems. 141
4.3.4 Co-Cr-Ni-Si subsystems 145
4.4 Multi-objective optimisation 148
5 Experimental investigations 152
5.1 Alloy processing 154
5.1.1 Manufacturing observations 154
5.1.2 Thermomechanical treatments 156
5.2 Chemical analysis 160
5.2.1 Raw materials purity and oxides 160

Thèse accessible à l'adresse : https://theses.insa-lyon.fr/publication/2025ISAL0036/these.pdf © [T. Langlois], [2025], INSA Lyon, tous droits réservés

5.2.2 Experimental compositions 163
5.2.3 Chemical gradient and segregation 167
5.3 Compression specimens 175
5.3.1 Reference-state microstructure 175
5.3.2 Mechanical properties 180
5.3.3 Postmortem microstructural observations 185
5.4 Impact loading specimens 187
5.4.1 Reference-state microstructure 187
5.4.2 Mechanical properties 192
5.4.3 Postmortem microstructural observations 194
5.5 Tensile specimens 198
5.5.1 Reference-state microstructure 198
5.5.2 Mechanical properties 200
5.5.3 Postmortem microstructural observations 206
5.6 Effect of composition and temperature 219
5.7 Concluding remarks 221
6 Discussion and conclusion ----- 222
6.1 Comprehensive discussion 222
6.1.1 Validation of the material's properties 223
6.1.2 Industrial-scale considerations 226
6.2 Conclusion 228
Appendix ----- 230
Appendix of Chapter 3 230
Appendix of Chapter 4 235
Appendix of Chapter 5 240
Bibliography ----- 255

Thèse accessible à l'adresse : https://theses.insa-lyon.fr/publication/2025ISAL0036/these.pdf © [T. Langlois], [2025], INSA Lyon, tous droits réservés

Introduction

Industrial and environmental context

The role of metals has constantly increased since the beginning of the 20th century, especially during the two industrial revolutions. From this time onwards, metallic components have been utilised in various fields, including transportation systems and energy infrastructure, such as gas pipelines and nuclear storage tanks. In recent years, their increased use is a factor of environmental disruption. Climate change is perceived in many ways, like greenhouse gas pollution, energy shortages but also with respect to resource scarcity. On this last point, the metals and mining sector is a crucial part of the energy transition, as demand for metal resources is expected to increase significantly in the coming 30 years [1]. Regarding metals and materials in general, a trade-off between material performance and sustainability needs to be found. In addition to material performance and cost, recyclability, energy intensity, and business ethics are important considerations in the development of new materials. To that extent, Medium Entropy Alloys (MEAs) and High Entropy Alloys (HEAs) are potential solutions to tackle the environmental challenges. HEAs are a relatively new class of alloy systems that contain a higher number of elements than traditional alloys. They have been investigated because of their potential for outstanding mechanical properties and relatively stable properties for different chemical compositions, offering a potential pathway for reduced use of critical materials. Nevertheless, there are not much work to date regarding the societal impact of HEAs. Because of their feature stability, it could be possible to adjust the chemical composition of HEAs to obtain better sustainable properties while maintaining good mechanical features.

Based on the designed use for which they are intended, each material has various functional properties. Materials have structural features, like dimensions, weight, and density. They also have mechanical properties. In case of metals, strength and ductility are two key mechanical parameters. In the automotive sector for instance, some parts of the cars are designed to withstand high loads without deforming to protect the passengers, while some others are very ductile to absorb crash impacts. The working temperature of a material is another functional criterion varying with the different applications. In the case of hydrogen transportation, metals are in contact with a cryogenic gas. While for nuclear applications, metals are working at very high temperatures. Therefore, until recently, products were designed based on functional

Thèse accessible à l'adresse : https://theses.insa-lyon.fr/publication/2025ISAL0036/these.pdf © [T. Langlois], [2025], INSA Lyon, tous droits réservés

specifications without considering the sustainability of the materials they contain. Indeed, sustainability is a relatively new scope for material design. Thanks to the growing awareness of climate change in the past 20 years, some environmental initiatives have emerged like removing lead from the houses and from the new materials, using thorium instead of Uranium, etc.... Environmental properties of materials such as the carbon footprint, the embodied energy or the toxicity can't be neglected anymore. Hence, economic, ethical, and environmental performances of materials are a rising aspect of a material design [1].

Motivation

The benchmark material that we selected is an equimolar CoCrNi. This ternary alloy is attractive for several reasons. First, due to its outstanding mechanical properties especially at cryogenic temperatures revealed in the literature (ductility, toughness, and resistance to fracture) [2], this material is interesting for hydrogen storage applications (related to the climate and energy transition). Second, the presence of Cobalt in alloy production has a negative impact on the environment, on human health and it is expensive. With this scope, MEAs and HEAs show promise for structural applications where high strength and toughness are required [3], [4]. HEAs also received significant attention as potential materials for hydrogen storage due to their outstanding properties at cryogenic temperatures [5]. The use of metals for hydrogen storage and transportation can help to reduce the dependence on fossil fuels and promote the use of clean, renewable energy sources. The present thesis explores the extent to which attractive structural performance in HEAs can be combined with reduced societal footprints. This requires in development of methods for incorporating societal impact on alloy design and of methods to rapidly predict and validate performance for a wide range of compositions.

Thèse accessible à l'adresse : https://theses.insa-lyon.fr/publication/2025ISAL0036/these.pdf © [T. Langlois], [2025], INSA Lyon, tous droits réservés

1 State-of-the-art

Contents

1.1 Multi-Principal Element Alloys ---------- 7

1.1.1 General principles and interest ---------- 7

1.1.2 Mechanical properties ---------- 10

1.1.3 Unexplored regions of C-MPEAS ---------- 23

1.2 Societal implications of metal alloys ---------- 30

1.2.1 General principles of material selection ---------- 30

1.2.2 Challenges of critical raw materials ---------- 32

1.2.3 Ethical and societal aspects of materials ---------- 34

1.2.4 Sustainability footprints of Cobalt ---------- 36

1.3 Concluding remarks ---------- 39

Thèse accessible à l'adresse : https://theses.insa-lyon.fr/publication/2025ISAL0036/these.pdf © [T. Langlois], [2025], INSA Lyon, tous droits réservés

1.1 Multi-Principal Element Alloys

In the early 1980s, Brian Cantor and his team from the United Kingdom began exploring the possibility of creating a metallic material based on a multicomponent alloy, also known as a multi-principal element alloy (MPEA) [6]. Notably, systems containing large Co-Cr-Ni proportions, such as IN-100 and Elgiloy, had already been studied and published in the 1970s. This type of alloy, which consists of at least three principal elements mixed in an equimolar or near-equimolar fraction, was later referred to as a High Entropy Alloy (HEA). The term "HEA" was first used in 1995 by Professor Jien-Wei Yeh of National Tsing Hua University in Taiwan [7]. Interest in these alloys surged in the early 2000s, after the publication of research by two groups of scientists [7].

1.1.1 General principles and interest

Conventional alloys are based on a single main element such as iron, aluminium, or nickel. The MPEAs are metal alloys with at least 3 principal elements, mixed in an equimolar or near-equimolar fraction, typically between 5% and 35% [6]. They are classified into two subclasses: the medium entropy alloys (MEAs) constituted by all the materials with 3 or 4 principal elements and the HEAs for materials with at least 5 principal elements. Expanded definitions of MPEAs only consider alloys that form solid solutions [8] or with a criterion on the mixing entropy of the alloy ΔS_{mix} [7], given in *Equation (1.1)*.

$$\begin{gathered} \Delta S_{mix} = -R \sum_i c_i \cdot ln\,(c_i) \\ 1R \leq \Delta S_{mix} < 1.5\,R \rightarrow MEA \\ \Delta S_{mix} \geq 1.5\,R \rightarrow HEA \end{gathered} \qquad (1.1)$$

c_i is the atomic fraction of element i and R denotes the gas constant.

For example, the mixing entropy of the equimolar CoCrFeMnNi Cantor alloy is 1.61R, the equimolar CrCoNi alloy has a mixing entropy of 1.10R. Austenitic stainless steels like AISI-316 and AISI-304 have averaged mixing entropies of 1.05R and 0.88R, respectively.

The booming interest in HEAs relies on their potential to achieve attractive combinations of properties. Among other attributes, some HEAs are reported to have high fracture toughness, good yield strength (σ_{ys}) and significant resistance to corrosion

Thèse accessible à l'adresse : https://theses.insa-lyon.fr/publication/2025ISAL0036/these.pdf © [T. Langlois], [2025], INSA Lyon, tous droits réservés

[4]. According to Yeh and Cantor, the promising properties of HEA are related to their high configurational entropy. Multi-phase microstructures are more prone to the formation of brittle intermetallic phases [9], while high entropy of mixing favours the stabilisation of solid solution. Moreover, this high mix of elements is supposed to promote a sluggish diffusion effect, favouring nanoprecipitation instead of second phases [7], [8].

However, most MPEAs are multi-phased in the experimental reports. This is related to the "confusion principle" [10]: the more elements involved, the lower the probability of forming a stable crystal structure [10]. Based on this principle, it has been suggested that HEAs should only incorporate alloys that form solid solutions, because second phases or intermetallic compounds reduce the entropy.

A commonly studied single-phased HEA is the quinary system based on the following transition metals: Iron, Nickel, Cobalt, Chromium and Manganese. This alloy is also known as Cantor Alloy CoCrFeMnNi. For convenience, the term C-MPEA is used to refer to any subset of the Cantor alloy (see *Figure 1.1*).

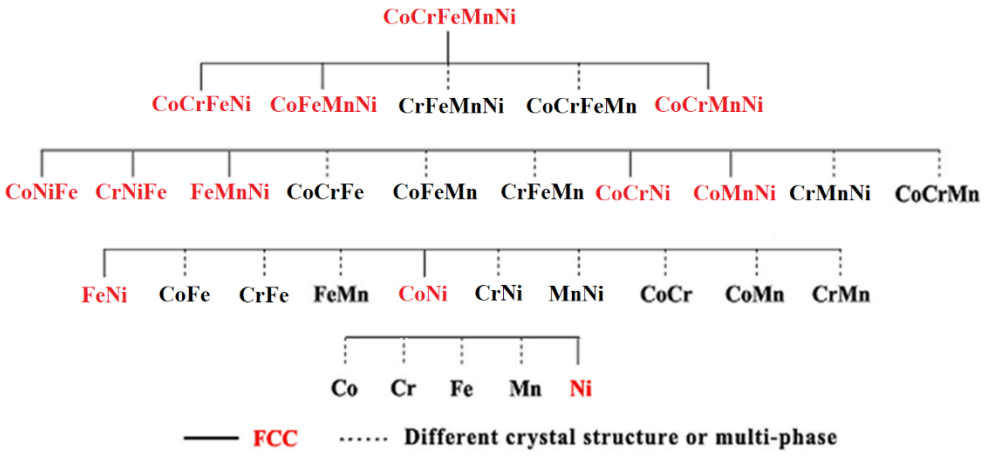


Figure 1.1. Crystal structure in the Cantor Alloy system and its subsets [11].

Alongside their single-phase structure, the other interesting aspect of austenitic C-MPEAs is their ability to maintain consistent mechanical values despite the presence of impurities or changes in composition. To refer to this ability, the term flexibility will be used. Research literature reveals that FCC C-MPEAs, when experimentally produced, maintain good mechanical properties despite a wide range of compositions [3]. Indeed, for a set of 30 compositions with a CoCrFeNi base, several mechanical features like the ductility, yield strength, etc... are constrained within a narrow range

Thèse accessible à l'adresse : https://theses.insa-lyon.fr/publication/2025ISAL0036/these.pdf © [T. Langlois], [2025], INSA Lyon, tous droits réservés

of values. For instance, *Table 1.1* illustrates the estimated yield strength (σ_{ys}) values that are ranging around a mean value of 215 MPa with a maximum variation of 60 MPa [3].

Table 1.1. Experimental compositions (σ_{YS} estimated from hardness using YS = 2HV-85 MPa) [3].

Composition (at.%)	Hardness (HV 5)	Estimated yield strength σ_{ys}(MPa)	XRD phase identification
Fe10Ni51Co7Cr32	163±3	241	fcc
Fe12Ni40Co18Cr30	162±3	239	fcc
Fe18Ni40Co12Cr30	151±2	217	fcc
Fe15Ni39Co16Cr30	162±5	239	fcc
Fe25Ni35Co10Cr30	147±2	209	fcc
Fe11Ni24Co37Cr28	172±4	259	fcc
Fe10Ni37Co25Cr28	164±3	273	fcc
Fe14Ni41Co17Cr28	156±3	269	fcc
Fe20Ni23Co32Cr25	154±2	223	fcc
Fe11Ni33Co31Cr25	162±4	239	fcc
Fe25Ni25Co25Cr25	146±3	207	fcc
Fe23Ni29Co23Cr25	159±3	233	fcc
Fe30Ni26Co19Cr25	154±2	223	fcc
Fe11Ni25Co44Cr20	155±5	225	fcc
Fe15Ni47Co18Cr20	151±5	217	fcc
Fe45Ni23Co12Cr20	131±4	177	fcc
Fe25Ni19Co41Cr15	145±3	205	fcc
Fe15Ni33Co37Cr15	145±3	205	fcc
Fe17Ni39Co29Cr15	150±3	215	fcc
Fe42Ni22Co21Cr15	139±5	193	fcc
Fe27Ni29Co34Cr10	130±5	175	fcc
Fe32Ni26Co32Cr10	126±4	167	fcc
Fe33Ni30Co27Cr10	127±5	169	fcc
Fe5Ni58Co27Cr10	142±2	199	fcc
Fe30Ni37Co23Cr10	134±3	183	fcc
Fe30Ni22Co43Cr5	122±3	159	fcc
Fe35Ni25Co35Cr5	132±6	179	fcc
Fe23Ni41Co31Cr5	133±3	181	fcc
Fe45Ni27Co23Cr5	130±4	175	fcc

These properties underline the potential of C-MPEAs in various applications, where maintaining consistent mechanical performance across different compositions is critical.

Thèse accessible à l'adresse : https://theses.insa-lyon.fr/publication/2025ISAL0036/these.pdf © [T. Langlois], [2025], INSA Lyon, tous droits réservés

1.1.2 Mechanical properties

Diverse compositions of HEA have been analysed in terms of microstructure (phase stability, grain size) and mechanical properties (elastic and thermal properties, deformation mechanics). According to experimental data, C-MPEAs exhibit outstanding properties including good work-hardening and a good strength-ductility balance (see *Figure 1.2*) [2]. C-MPEAs also show improved mechanical properties at low temperatures as shown in *Figure 1.3* , with CrCoNi alloy exhibiting the most promising mechanical performance [10]. These latest properties make C-MPEAs good candidates for industrial applications at low temperature [12, 13, 14]. Additionally, most HEAs are well-known for their good resistance to corrosion and oxidation, even under elevated temperature conditions [15].

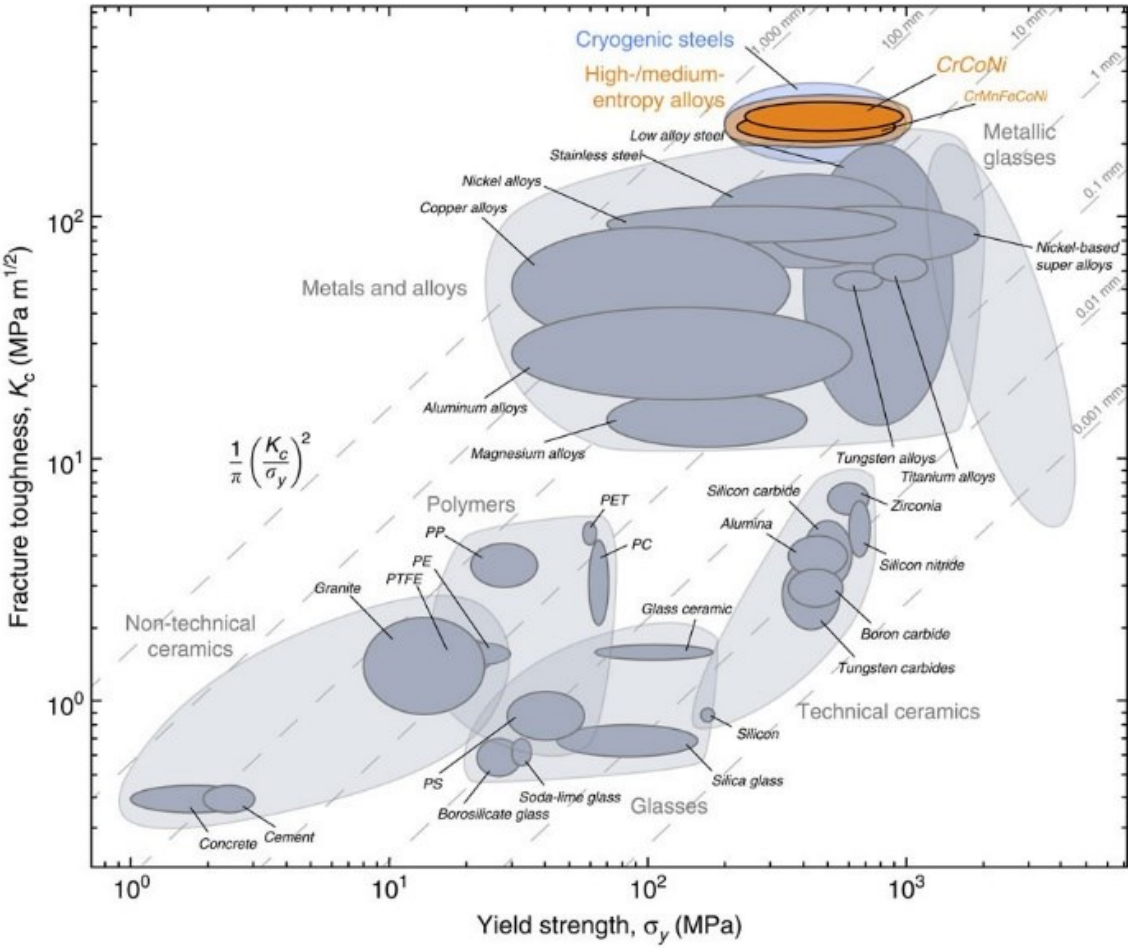


Figure 1.2. Outstanding strength-toughness performance at room temperature of C-MPEAs highlighted in orange [2].

Thèse accessible à l'adresse : https://theses.insa-lyon.fr/publication/2025ISAL0036/these.pdf © [T. Langlois], [2025], INSA Lyon, tous droits réservés

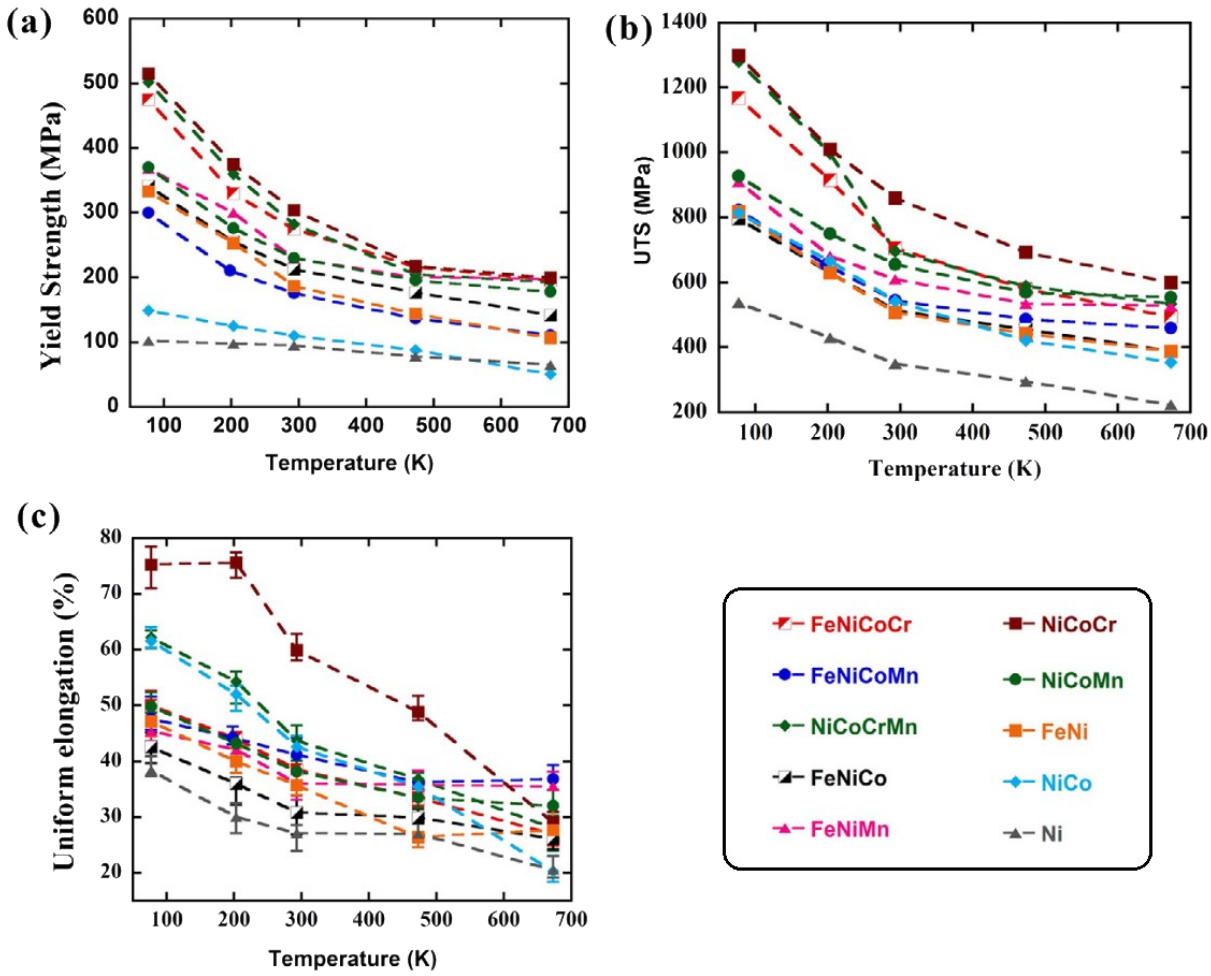


Figure 1.3. Improved mechanical properties of High-Entropy Alloys at low temperature [11].

The microstructure of a solid material refers to the arrangement of atoms. Single-phase alloys are those that have a single and uniform microstructure. Single-phase C-MPEAs are often FCC or BCC. The functional properties of the alloy, both desired or unwanted for different applications, depend on the obtained microstructure. To predict the microstructure of an alloy, researchers have developed certain rules or guidelines. The following equations give absolute preconditions to form solid solution: outside these ranges, C-MPEAs are always multi-phased. Inside these ranges, most C-MPEAs are single phase, but multi-phased structures can still be observed. *Equation (1.2)* relates to configurational thermodynamic parameters [14], while *Equation (1.3)* refers to the mean square atomic difference (δ) between elements, also known as misfit parameter [10].

$$\frac{\overline{T_m}\,\Delta S_{mix}}{|\Delta H_{mix}|} \geq 1.1 \qquad (1.2)$$

Thèse accessible à l'adresse : https://theses.insa-lyon.fr/publication/2025ISAL0036/these.pdf © [T. Langlois], [2025], INSA Lyon, tous droits réservés

$$\delta = \sqrt{\sum_{i=1}^{N} c_i \left(1 - \frac{r_i}{\bar{r}}\right)^2} \leq 6.6\% \quad (1.3)$$

With $\overline{T_m}$ being the concentration weighted average melting point of the elements of the alloy, ΔS_{mix} and ΔH_{mix} represent the entropy and enthalpy of mixing. c_i and r_i are the atomic fraction and radius of component i, and $\bar{r} = \sum c_i r_i$ the average atomic radius. In addition, *Equation (1.4)*, related to the valence electron concentration (VEC), can separately predict FCC and BCC solid solutions [16]:

$$\begin{cases} \overline{VEC} = \sum_{i=1}^{N} c_i (VEC)_i \\ VEC \geq 8 \rightarrow FCC \\ 6.7 \leq VEC < 8 \rightarrow FCC - BCC\ mixture \\ VEC < 6.7 \rightarrow BCC \end{cases} \quad (1.4)$$

To this extent, it is worth mentioning that Ni and Co are elements that tend to stabilise the γ-FCC phase, while Cr tends to stabilise the α-BCC phase with respect to their elemental VECs [16]. For the rest of this study, austenitic single-phased C-MPEAs are the focus of our attention. Indeed, there is a ductile-to-brittle transition temperature in many BCC alloys [17], [18], including in BCC-MPEAs [19], [20]. In addition, the prediction models used in this thesis are solely valid for FCC single phased alloys (see Chapter 3).

In pursuit of developing tougher alloys, various strategies can be employed to tailor the strengthening mechanisms of MPEAs. The material's flow stress (σ_{flow}) is commonly described as the combination of two contributions [21]: the elastic component, whose threshold is represented by the yield stress (σ_{ys}) and the plastic component, which accounts for strain-hardening ($\Delta\sigma_{s\text{-}h}$) under plastic deformation. Thus, a general expression for the flow stress can be written as displayed in *Equation (1.5)* [21].

$$\sigma_{flow} = \sigma_{ys} + \Delta\sigma_{s-h} \quad (1.5)$$

Depending on the processing route, the yield stress of a material results from different contributing factors. These include the frictional stress (σ_{fr}), which accounts

Thèse accessible à l'adresse : https://theses.insa-lyon.fr/publication/2025ISAL0036/these.pdf © [T. Langlois], [2025], INSA Lyon, tous droits réservés

for the intrinsic lattice resistance to dislocation motion, as well as the contribution of solid solution (σ_{ss}), precipitates (σ_{ppt}), the initial dislocation density ($\sigma_{\rho i}$) and the Hall-Petch effect (σ_{gb}) such as:

$$\sigma_{ys} = \sigma_{fr} + \sigma_{ss} + \sigma_{ppt} + \sigma_{\rho i} + \sigma_{gb} \quad (1.6)$$

In the present work, *Equation (1.6)* can be simplified, as we focus on single-phase alloys, thereby eliminating the contribution from precipitates (σ_{ppt}). The manufacturing routes adopted in this thesis involve fully recrystallised heat-treatments, making the initial dislocation density negligible, so $\sigma_{\rho i}$ can also be omitted. The simplified expression is shown in *Equation (1.7)*:

$$\sigma_{ys} = \sigma_{fr} + \sigma_{ss} + \sigma_{gb} \quad (1.7)$$

In alloy design, solid solution strengthening (σ_{ss}) is a key mechanism contributing significantly to the overall yield strength of a material [22], [23]. Several theoretical models have been developed to predict σ_{ss} in HEAs, including the works of Labusch [24], Senkov et al. [25], Toda-Caraballo et al. [26], Varvenne et al. [5], and Walbrühl et al. [27]. Complementary strengthening models for BCC solid solutions have been developed [28], but they fall outside our target for tough alloys [19].

In this work, we focus on the Varvenne et al. model, which provides σ_{ss} predictions that are close to the experimental values for near-equiatomic FCC alloys [5], [29], as shown in *Figure 1.4*. In this model, the choice of alloying elements plays a major role in the overall yield strength of the material. It calculates the interaction energy between a dislocation and a solute atom. Dislocations are defects or imperfection in the crystal structure of a material. The energy involved in this interaction can affect the material's yield strength, which is a measure of its resistance to plastic deformation. Ultimately, the reduced theory only considers the elastic contribution to the energy involved in the solute/dislocation interactions. The associated model provides a way to calculate the critical resolved shear stress (τ_y). The combined expression primarily considers the influence of size mismatch (ΔV_n), the activation energy required for dislocation motion (ΔE_b), and the Peierls stress at absolute zero (τ_{y0}), as described in the following *Equations (1.8)* and *(1.9)* [5].

$$\tau_{y0} = 0.051 \cdot \alpha^{-\frac{1}{3}} \cdot \bar{\mu} \left(\frac{1+\bar{\nu}}{1-\bar{\nu}}\right)^{\frac{4}{3}} f_\tau(w_c) \left[\frac{\sum_n c_n \Delta V_n^2}{b^6}\right]^{2/3} \quad (1.8)$$

Thèse accessible à l'adresse : https://theses.insa-lyon.fr/publication/2025ISAL0036/these.pdf © [T. Langlois], [2025], INSA Lyon, tous droits réservés

$$\Delta E_b = 0.274 \cdot \alpha^{\frac{1}{3}} \cdot \bar{\mu} \cdot b^3 \left(\frac{1+\bar{\nu}}{1-\bar{\nu}}\right)^{\frac{2}{3}} f_{\Delta E}(w_c) \left[\frac{\sum_n c_n \Delta V_n^2}{b^6}\right]^{1/3} \quad (1.9)$$

where α is a proportionality constant related to the line tension of the dislocation, representing the energy per unit length of the dislocation line. In this model, its value is rescaled to 0.123 at room temperature and divided by two at 77 K. The f_τ and $f_{\Delta E}$ functions are dimensionless core coefficients, with values of 0.35 and 5.7 respectively. $\bar{\mu}$, $\bar{\nu}$ and b are respectively the averaged values (molar-weighted with a Vegard's law) of shear modulus, Poisson's ratio and Burger vector of the alloy. c_i is the atomic fraction of component i, ΔV_i the average misfit volume of solute i, explained in *Equation (1.10)*.

k_b is the Boltzmann constant and the strain rates $\dot{\varepsilon}$ and $\dot{\varepsilon}_0$ are set to 10^{-3} s^{-1} and 10^4 s^{-1}, respectively. *Figure 1.4* shows the predicted σ_{ss} values obtained by Varvenne [5], compared to the experimental values after subtraction of the Hall-Petch contribution (σ_{gb}) to strength [11], [21], for several C-MPEAs.

$$\Delta V_i = V_i^{FCC} - \sum_i c_i V_i^{FCC} \quad (1.10)$$

$$V_{binary} = c_i V_i^{FCC} + (1 - c_i) V_{Ni} \quad (1.11)$$

Here V_i^{FCC} is the apparent FCC volume of component i, which is extrapolated from the volumes of single-phase FCC binary solutions between Ni and component i, as detailed in *Equation (1.11)* [5]. The use of Vegard's law in this context implies that we consider FCC volumes for elements that are not naturally FCC at room temperature, such as cobalt, chromium, and silicon, which are HCP, BCC, and diamond cubic structures, respectively.

This shear stress model incorporates the effects of strain rate and temperature (see *Equation (1.12)*), which can be translated into yield strength using the Taylor factor of 3.06 (see *Equation (1.13)*).

$$\tau_y(T, \dot{\varepsilon}) = \tau_{y0} \left(1 - \left(\frac{k_b T}{\Delta E_b} \cdot ln \frac{\dot{\varepsilon}_0}{\dot{\varepsilon}}\right)^{\frac{2}{3}}\right) \quad (1.12)$$

$$\sigma_y(T, \dot{\varepsilon}) = 3.06 \cdot \tau_y(T, \dot{\varepsilon}) \quad (1.13)$$

Thèse accessible à l'adresse : https://theses.insa-lyon.fr/publication/2025ISAL0036/these.pdf © [T. Langlois], [2025], INSA Lyon, tous droits réservés

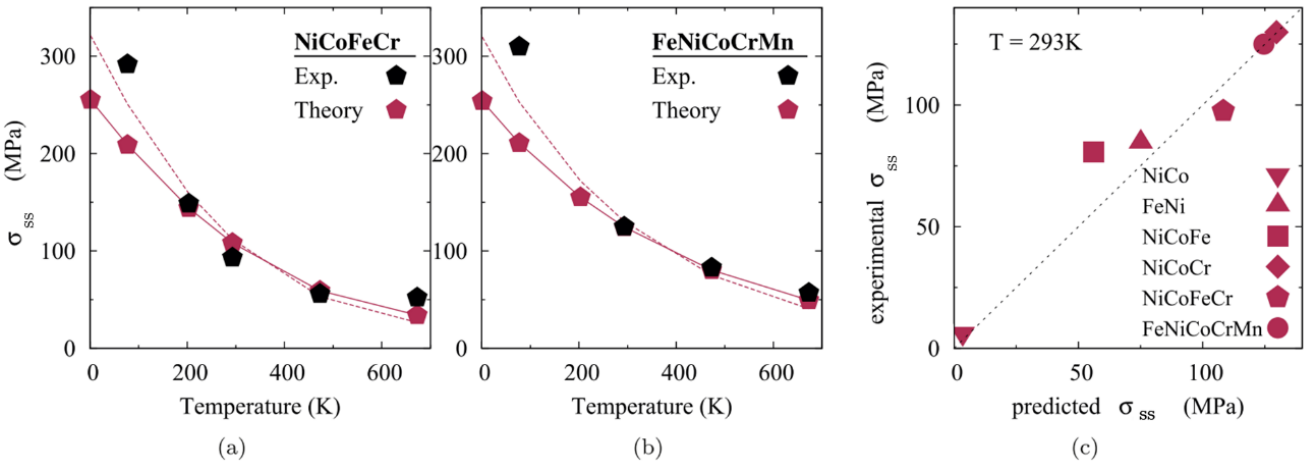


Figure 1.4. (a, b) σ_{ss} evolution with temperature for NiCoFeCr and FeNiCoCrMn alloy ($\dot{\varepsilon}$ =$10^{-3}s^{-1}$). (c) Experimental vs predicted σ_{ss} at room temperature for several C-MPEAs (updated from [5])

According to this model [5], a larger solute misfit parameter δ leads to increased yield strength (*Equation (1.14)*).

$$\begin{cases} \Delta\sigma_{ss} \propto \left(\sum_i c_i \Delta\bar{V}_i^2\right)^{\frac{1}{2}} \\ \sum_i c_i \Delta\bar{V}_i^2 = 9\bar{V}^2\left(\frac{\sum_i c_i r_i^2}{\bar{r}^2} - 1\right) = 9\bar{V}^2\delta^2 \end{cases} \quad (1.14)$$

where c_i and r_i are the atomic fraction and radius of component i. $\bar{V}$ is the average atomic volume of the alloy. $\Delta\bar{V}_i$ the average misfit volume of solute i. δ is the mean square atomic difference. Hence, a larger δ tends to achieve higher strength. Indeed, increased lattice misfit hinders dislocation mobility.

However, it is important to note that this strengthening model only considers the elastic contributions to evaluate the yield strength and is only valid if the dislocation width d exceeds 6.5b, depends on elastic constants, and neglects the solute/stacking fault interaction contribution and the grain size contribution. This model is highly dependent on the atomic radii and shear modulus values used. Additional work has been performed on this model, using more refined set of atomic radii [30], or refined elastic constants [31], to obtain more accurate predictions over a larger range of compositions. As a result, this model can be used to obtain first approximations of yield strength values, and can be improved by physical models, computer-aided searching and machine learning.

Thèse accessible à l'adresse : https://theses.insa-lyon.fr/publication/2025ISAL0036/these.pdf © [T. Langlois], [2025], INSA Lyon, tous droits réservés

After yielding, the material deforms plastically. Under plastic deformation the increase in flow stress ($\Delta\sigma_{s\text{-}h}$) is the result of several potential contributions acting as obstacles to dislocation movement, introduced by the following *Equation (1.15))* [32]

$$\Delta\sigma_{s-h} = \Delta\sigma_{\rho} + \Delta\sigma_{SF} + \Delta\sigma_{twin} \quad (1.15)$$

where $\Delta\sigma_{\rho}$, $\Delta\sigma_{SF}$ and $\Delta\sigma_{twin}$ represent the dislocation density strengthening, the stacking fault contribution and the twin contribution, respectively [32]. The deformation mechanisms that occur during plastic deformation have a significant influence on the strength and ductility of the alloy. Key deformation mechanisms in C-MPEAs include dislocation-induced plasticity or microband-induced plasticity (MBIP), twinning-induced plasticity (TWIP) and transformation-induced plasticity (TRIP) [33].

Dislocation glide is a deformation mechanism that occurs in metals and alloys when a dislocation, or defects in the crystal structure, moves through the material under the influence of applied stress. Under plastic deformation, the increased dislocation density hinders the movement of other dislocations, leading to strain-hardening. Dislocation glide is the primary mechanism of plastic deformation in many metals and alloys and can lead to an increase in the material's work-hardening rate, or resistance to deformation.

Transformation-induced plasticity (TRIP) is a deformation mechanism that occurs when the material undergoes a transformation from FCC-austenite (γ) to an HCP-martensite (ε) under the influence of plastic stress. TRIP effect, resulting in a combination of soft and ductile γ-phase with a hard and brittle ε-phase can enhance the material's strength and is often observed in austenitic steels and other metals. However, large proportion of deformation-induced $\gamma \rightarrow \varepsilon$ transformation leads to premature failure with low ductility [34, 35, 36].

Twinning-induced plasticity (TWIP) is a deformation mechanism that occurs when the material undergoes twinning, or the formation of crystal structures with mirror symmetry. TWIP effect is commonly observed in FCC metals and can lead to an increase in material ductility [33].

Thèse accessible à l'adresse : https://theses.insa-lyon.fr/publication/2025ISAL0036/these.pdf © [T. Langlois], [2025], INSA Lyon, tous droits réservés

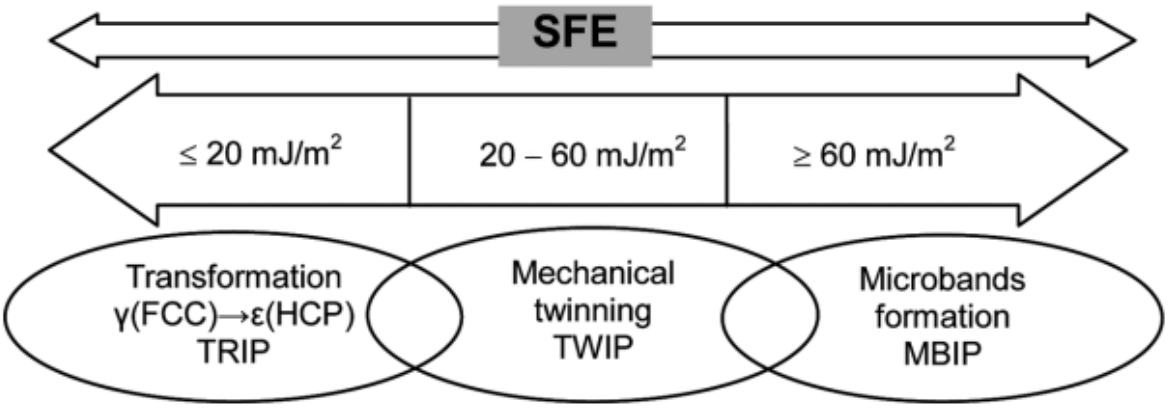


Figure 1.5. SFE ranges and corresponding deformation mode [37].

The latter three deformation mechanisms and many others are significantly related to the stacking fault of the material. Stacking Fault Energy (SFE) is the energy associated with an irregularity in a crystal structure known as a stacking fault. This irregularity occurs when the normal sequence of atomic planes is disrupted. *Figure 1.5* illustrates how the SFE influences the main deformation mechanisms of an alloy [37]. In FCC metals, the SFE plays a key role to determine some mechanical properties, including the strain-hardening rate (SHR = $d\sigma/d\varepsilon$) and the critical stress for twinning (τ_{cr}). A thorough understanding of the SFE is essential for the design and optimisation of these materials. The SFE can be investigated using various energy barriers:

- Glide Stacking Fault (GSF) energy, which quantifies the ability of a dislocation in a crystal to glide onto an intersecting slip plane.
- Unstable Stacking Fault (USF) energy, which represents energy maxima or minima on the GSF energy surface.
- Intrinsic Stacking Fault (ISF) energy, which is the energy required to create a stacking fault within a single crystal.
- Extrinsic Stacking Fault (ESF) energy, which is the energy of a vacancy plane that creates a stacking fault.
- Unstable Twinning Fault (UTF) energy, which depicts the stability of twin structures without involving twin formation or nucleation dynamics.

Those barrier energies can be extracted from a generalised stacking fault energy surface (GSFE), which is a graphical representation of the energy required to create a stacking fault in a crystal as a function of the stacking fault width. This surface can be

Thèse accessible à l'adresse : https://theses.insa-lyon.fr/publication/2025ISAL0036/these.pdf © [T. Langlois], [2025], INSA Lyon, tous droits réservés

obtained from density functional theory (DFT) simulations [38]. These five deformation mechanisms are significantly related to the stacking fault of a material.

The main energy barrier associated with the SFE is the intrinsic stacking fault (ISF). For the remaining of the manuscript, SFE calculation or prediction are based on ISF measurements. This value can vary for different alloy classes, compositions, and deformation temperatures. In the case of C-MPEAS, most of the experimental compositions with a SFE between 15 and 25 mJ/m^2 are likely to promote twinning when the material is deformed [39]. Several experimental techniques can be used to measure ISF of a material, including X-ray diffraction (XRD), transmission electron microscopy (TEM), and other observation techniques [40] [41]. However, these techniques can be challenging and time-consuming, requiring specialised equipment and sample preparation. As a result, the amount of experimental data that is available for the SFE of different materials is relatively limited.

To overcome these limitations and obtain more data, several SFE prediction models for FCC alloys have been developed. A thermodynamical model proposed by Olson and Cohen [42] is illustrated in *Equation (1.16))*. It is based on equations with molar Gibbs energies ($\Delta G_m^{fcc \rightarrow hcp}$), based on elemental molar Gibbs energies according to the flowchart mentioned in the literature [43]. It provides reasonably accurate estimations of SFE for CrCoNi alloys, compared to experimental data [44]. Additionally, an empirical model developed by Bertoli et al. [45] incorporates experimental data from approximately 40 different CrCoNi compositions, giving SFE predictions with a coefficient of determination R^2 of 98%, as illustrated in *Figure 1.6* and *Equation (1.18)*. Finally, a model based on Density Functional Theory (DFT) calculation has been developed by Khan et al. [39]. It gives accurate SFE predictions in Co-Cr-Fe-Mn-Ni-V subsystems.

$$SFE = 2\,\rho\,\Delta G_m^{fcc \rightarrow hcp} + 2\,\Gamma^{fcc/hcp} \qquad (1.16)$$

Where $\Delta G_m^{fcc\text{-}hcp}$ is the molar Gibbs free energy related to the austenitic to martensitic phase transformation (in mJ/mol) [43] and $\Gamma^{fcc/hcp}$ is the fitted interfacial energy between two FCC/HCP phases (in mJ/m^2). ρ is the molar surface density (in mol/m^2), function of the Avogadro's constant N_A and the lattice parameter of the FCC alloy $a_{(FCC)}$, as expressed in *(1.17)*:

$$\rho = \frac{4}{\sqrt{3\,a_{(FCC)}^2}} \frac{1}{N_A} \qquad (1.17)$$

Thèse accessible à l'adresse : https://theses.insa-lyon.fr/publication/2025ISAL0036/these.pdf © [T. Langlois], [2025], INSA Lyon, tous droits réservés

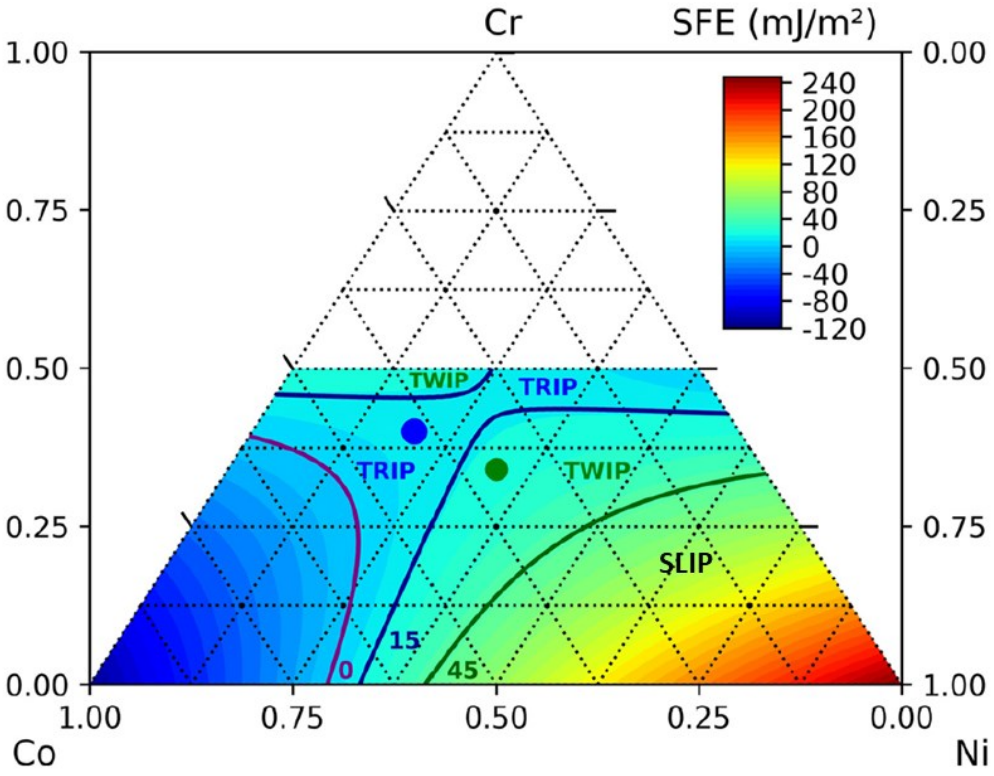


Figure 1.6. SFE values in CrCoNi alloys, calculated using *Equation (1.18)*. The SFE limits proposed by [45] for Slip deformation (>45 mJ/m²), TWIP (15<SFE<45 mJ/m²) and TRIP (<15 mJ/m²) are represented by the coloured contour lines.

$$SFE = 248 - 835X_{Cr} - 323X_{Co} + 682X_{Cr}^2 - 39X_{Co}^2 + 777X_{Cr}X_{Co} \qquad (1.18)$$

Computer-assisted methods, such as molecular dynamics simulations, can provide more accurate value for SFE of a wide range of materials. In the study by Khan et al. [39], SFE of approximately 500 different HEA compositions has been calculated from first principle using density functional theory (DFT). The obtained dataset includes information on a wide range of HEA compositions and offers relatively accurate SFE values compared to a limited number of experimental measurements.

SFE values are highly useful for predicting the prolonged strain-hardening rate θ_0 of many austenitic metals, that corresponds to the more or less pronounced plateaus where $d\sigma/d\varepsilon$ is constant after the yield point. Alloys with higher SFE tend to have lower prolonged θ_0 because dislocations are more easily activated in these materials. *Figure 1.7* illustrates this correlation between SFE and the prolonged θ_0 of medium to high Mn-steels [46]. Other alloy classes show similar results [47].

Thèse accessible à l'adresse : https://theses.insa-lyon.fr/publication/2025ISAL0036/these.pdf © [T. Langlois], [2025], INSA Lyon, tous droits réservés

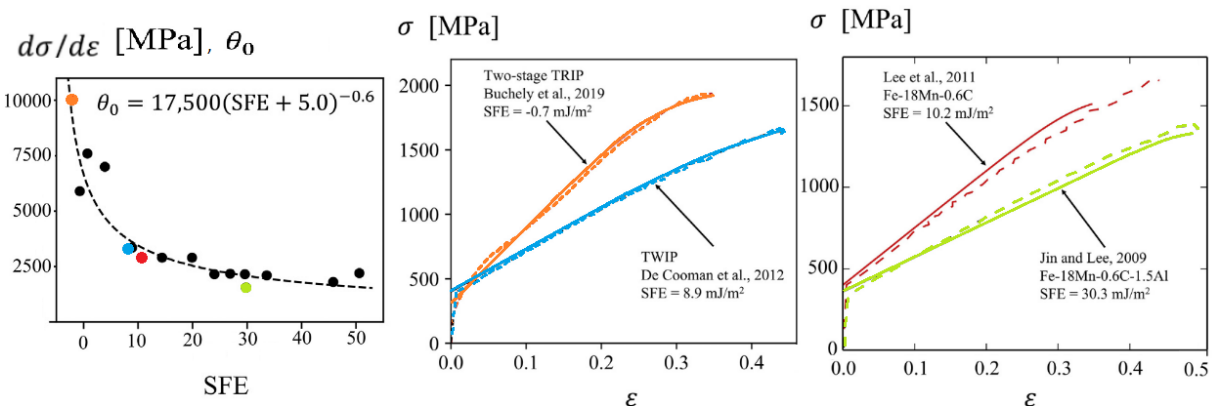


Figure 1.7. Relation between intrinsic stacking fault energy (ISF) and strain-hardening rate (adapted from [46]).

However, deformation twinning has been observed in some alloys with higher γ_{ISF} values. For instance, Iridium metal deforms by twinning, while its γ_{ISF} value is 480mJ/m^2. Therefore, other studies [48], [49] have introduced a stronger correlation for twinning with another computed stacking fault energy barrier known as unstable twinning fault energy γ_{UTF}. *Figure 1.8* shows the strong correlation between the critical stress for twinning nucleation (τ_{cr}) and γ_{UTF} while there is no consistent relationship with γ_{ISF} values.

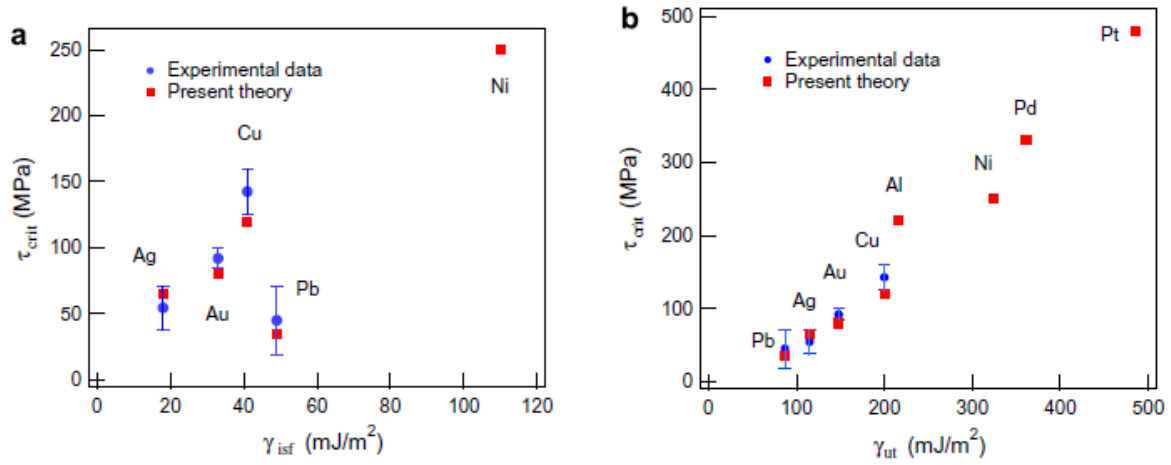


Figure 1.8. Twinning Stress evolution with a) ISF (non-monotonic) and b) UTF (monotonic) [48].

This publication suggests that τ_{cr} is not entirely dependent on ISF, as often assumed in classical models [33], [39]. More specifically, in FCC lattices, dislocation motion introduces a multi-layered fault. γ_{ISF} represents the energy related to the passage of a partial dislocation on the first layer of stacking fault. There is a greater correlation of the twinning stress with the unstable twinning fault energy γ_{UTF} because this energy barrier incorporates the twin boundary formation and twin boundary migration at the same time [49]. The value of γ_{UTF} can be derived from the material's

Thèse accessible à l'adresse : https://theses.insa-lyon.fr/publication/2025ISAL0036/these.pdf © [T. Langlois], [2025], INSA Lyon, tous droits réservés

elastic parameters, the Burger vector b and the shear modulus along the (111) plane G_{111}, as depicted in *Figure 1.9* [49].

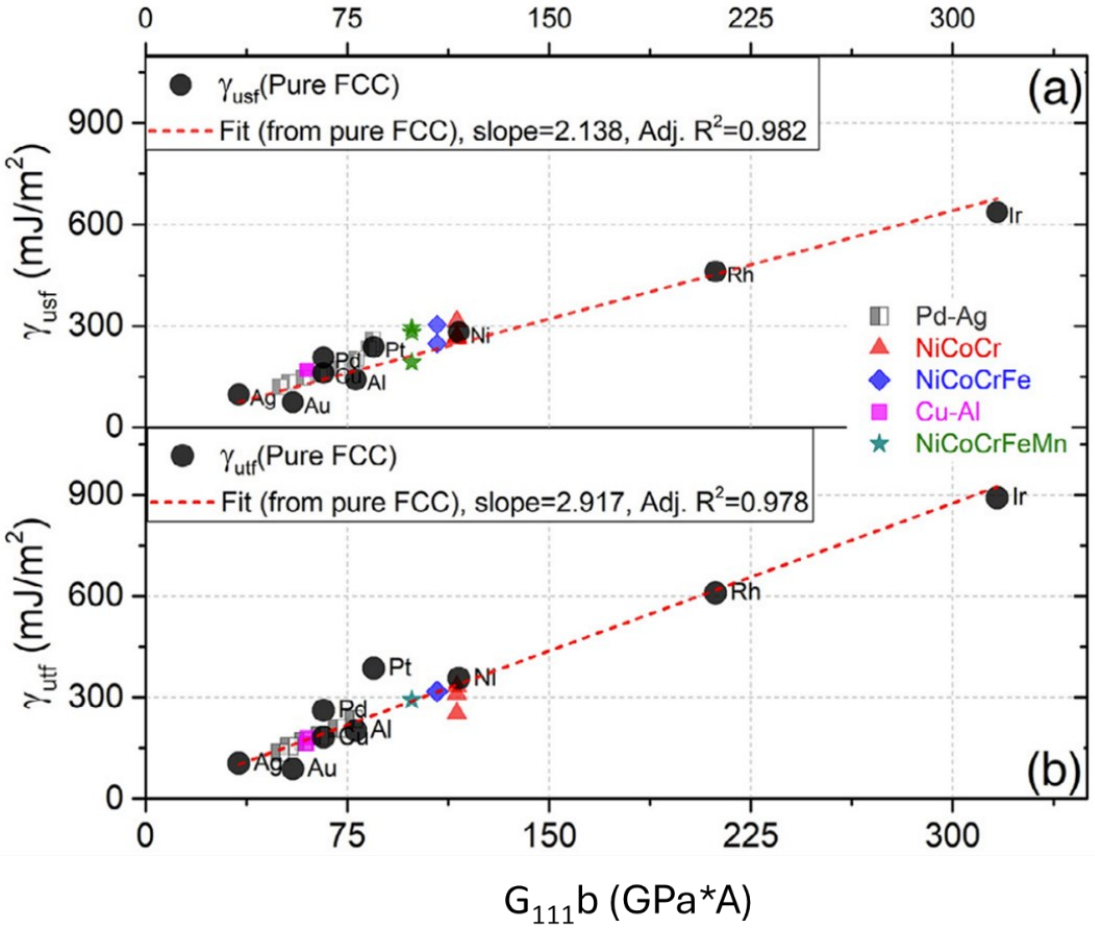


Figure 1.9. Correlation between γ_{USF}, γ_{UTF}, and $\mu_{slip}b$ for various pure elements and FCC alloys (adapted from [49])

The shear modulus G111 can be extrapolated from the material's elastic moduli C_{ij} with *Equation (1.19)*:

$$G_{111} = \frac{C_{11} - C_{12} + C_{44}}{3} \qquad (1.19)$$

By combining solid solution strengthening, ISF and UTF data on deformation mechanisms, such as work-hardening and critical stress for twinning, it is possible to

Thèse accessible à l'adresse : https://theses.insa-lyon.fr/publication/2025ISAL0036/these.pdf © [T. Langlois], [2025], INSA Lyon, tous droits réservés

predict the stress-strain behaviour of materials, as demonstrated in the case of this austenitic CrMnNi alloy [50] shown in *Figure 1.10*.

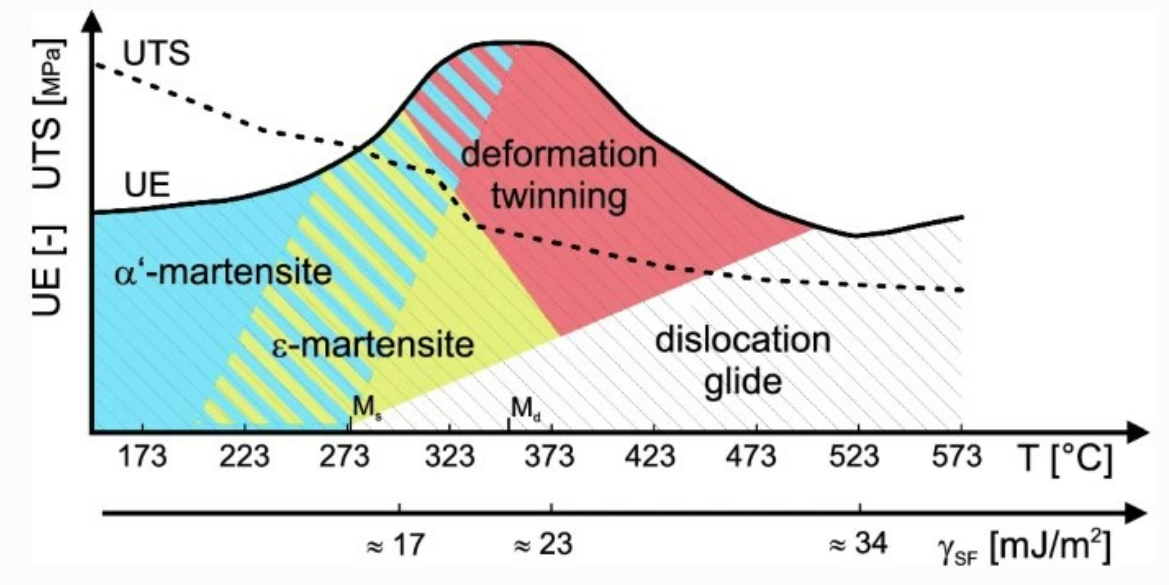


Figure 1.10. Uniform elongation and Tensile strength for different deformation mechanisms and the corresponding ISF (and Temperature) [50].

The main factors influencing the mechanical properties of C-MPEAs are also investigated in the literature [14-19]. These include the effect of temperature [5], [2], [51], the choice of alloying elements [5], doping elements and unwanted interstitials [15], [52], [53], and the influence of diffusion coefficients [54], [55].

Thèse accessible à l'adresse : https://theses.insa-lyon.fr/publication/2025ISAL0036/these.pdf © [T. Langlois], [2025], INSA Lyon, tous droits réservés

1.1.3 Unexplored regions of C-MPEAS

The systematic exploration of cobalt content variation in near-equimolar CrCoNi and their interaction with additional elements remain limited. While few additions of elements such as Al, W, Ti and Mo have been studied individually, there is no comprehensive exploration combining elemental additions with non-equimolar CrCoNi, especially Co-lean compositions. Moreover, there is still many unexplored regions of C-MPEAs combining non-equimolar matrices and substitutional elements such as silicon. Furthermore, studies investigating the temperature-dependant behaviour of such alloys, especially at cryogenic temperatures, are scarce. These gaps in literature highlight the need to explore Co-lean CrCoNi composition with addition of metalloids such as Silicon, to better understand their potential for balancing mechanical properties and sustainability.

Reduced cobalt content in CrCoNi ternary alloy:

Cobalt is a widely acknowledged as a powerful element for enhancing the mechanical properties of FCC C-MPEAs. Studies on Co-rich alloys in the $Co_x(CrNi)_{100-x}$ system (x=33, x=40 or x=50 at.%) [56] and (x=20, x=40, x=60 at.%) [36] reported exceptionally strong and ductile materials at room temperature with increasing cobalt content, as demonstrated by their tensile curves in *Figure 1.11* [56].

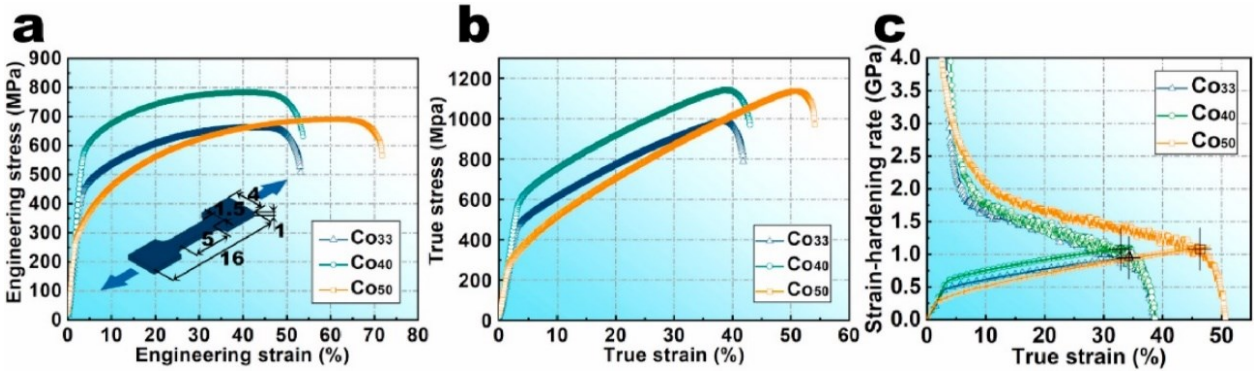


Figure 1.11. Tensile properties of Co33, Co40 and Co50 alloys with (a) Engineering stress-strain curves; (b) True stress-strain curves; (c) Strain-hardening rate curves [56].

An increase in both tensile elongation and tensile strength is observed in *Figure 1.11* b with rising Cobalt content from 33 to 40 at.%. A further increase to 50 at.% of cobalt maintains the alloy's tensile strength while also enhancing its ductility. For 60 at.% of cobalt, the high proportion of deformation-induced $\gamma \rightarrow \varepsilon$ led stress concentration at the γ/ε interface, resulting in premature failure.

Thèse accessible à l'adresse : https://theses.insa-lyon.fr/publication/2025ISAL0036/these.pdf © [T. Langlois], [2025], INSA Lyon, tous droits réservés

Cobalt content has minimal impact on the grain size of CrCoNi alloys. While a slight decrease in grain size was observed with increasing cobalt concentrations in [56], no significant variations were noted in other studies [36].

Importantly, Cobalt plays a crucial role in reducing the alloy Stacking Fault Energy (SFE) of Co-rich CrCoNi ternary alloys [56] and other C-MPEAs [57]. Predicted SFE values in the $Co_x(CrNi)_{100-x}$ alloys at room temperature are shown in *Figure 1.12* [36].

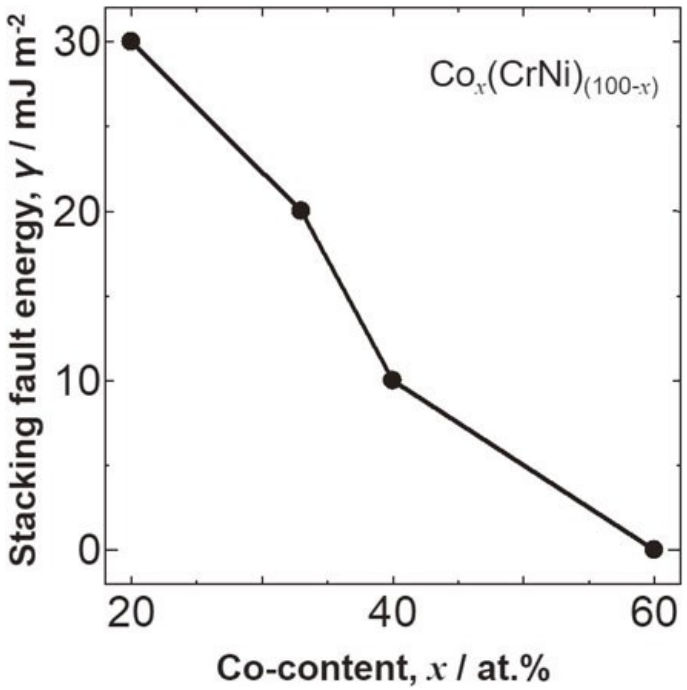


Figure 1.12. Predicted evolution of SFE values as a function of cobalt concentration in $Co_x(CrNi)_{100-x}$ alloys [36].

As discussed previously in *Figure 1.5*, low SFE values in FCC alloys promotes deformation mechanisms such as TWIP and TRIP. Experimental observations confirms that both effects are prominent in Co-rich MPEAs with low SFE. The fraction of deformations twins increases with higher cobalt content [56], and ε-martensitic transformation is observed in CrCoNi alloy containing 60 at.% of cobalt, as depicted in *Figure 1.13* [36].

Thèse accessible à l'adresse : https://theses.insa-lyon.fr/publication/2025ISAL0036/these.pdf © [T. Langlois], [2025], INSA Lyon, tous droits réservés

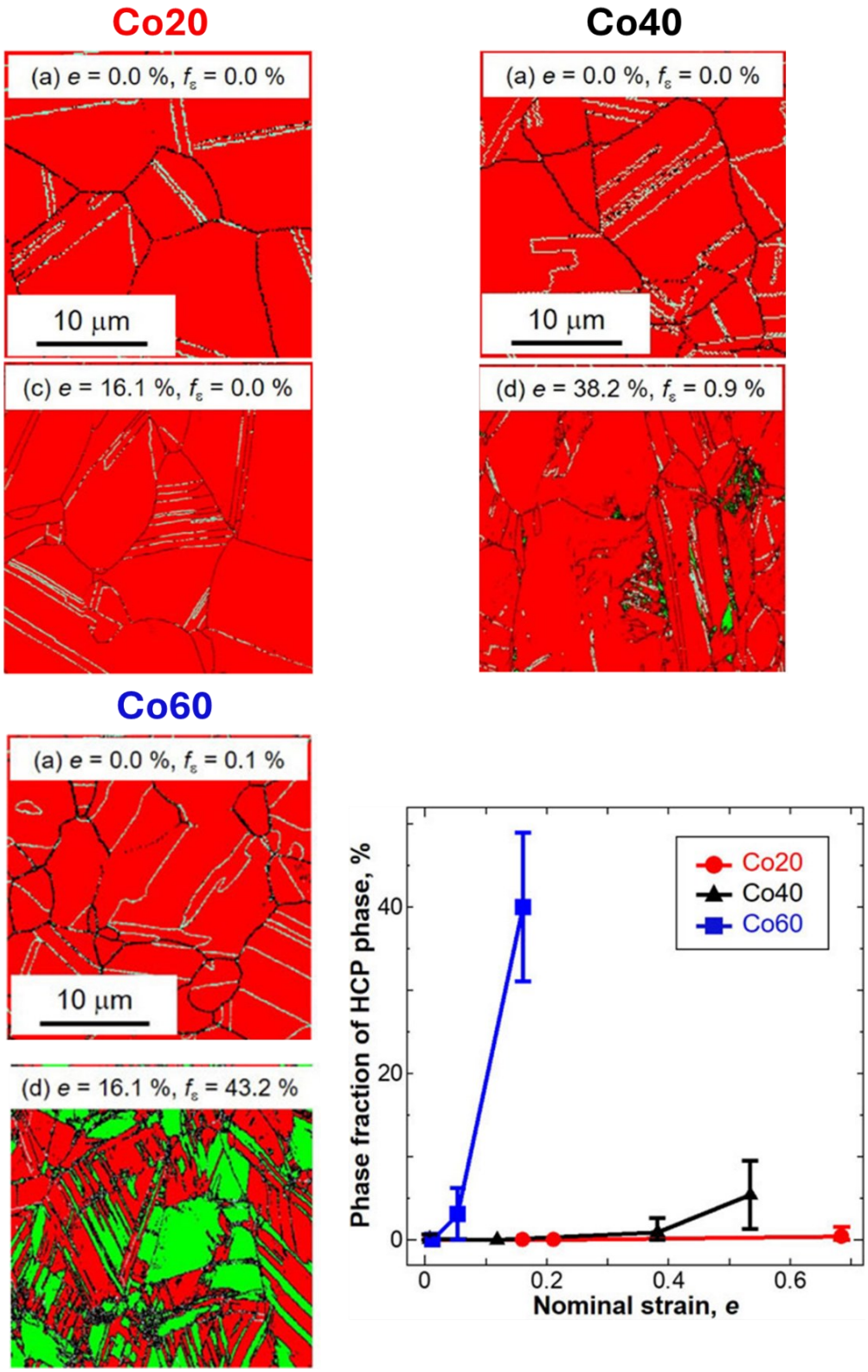


Figure 1.13. Microstructure evolution during tensile deformation for Co20, Co40 and Co60 alloys; corresponding fraction of martensite observed (reconstructed from [36]: EBSD maps of FCC phase in red and HCP phase in green, e is the elongation in %, f_ε is the surface percentage of HCP phase in the map, black boundaries are the high-angle grain boundaries and blue boundaries are twin boundaries.)

Thèse accessible à l'adresse : https://theses.insa-lyon.fr/publication/2025ISAL0036/these.pdf © [T. Langlois], [2025], INSA Lyon, tous droits réservés

In other FCC single-phased C-MPEAs, higher cobalt concentrations reduce the lattice parameter, increase dislocation density and lead to an earlier onset of deformation twinning. These phenomena significantly improve both strength and ductility of these alloys [57].

Despite these insights, studies on C-MPEAs with reduced cobalt content remain scarce. In addition, there is a lack of research on the mechanical response of Co-lean CrCoNi to low temperature environment, which could be promising or detrimental for potential hydrogen applications in C-MPEAs.

Improved strength-ductility synergy in Si-added C-MPEAS:

In recent years, there has been a growing interest in research and publication about silicon-containing C-MPEAS, as displayed in *Figure 1.14.* Traditionally used as addition in steel [58] or aluminium alloys [59] [60], recent research shows that silicon plays a crucial role in overcoming the traditional trade-off between strength and ductility.

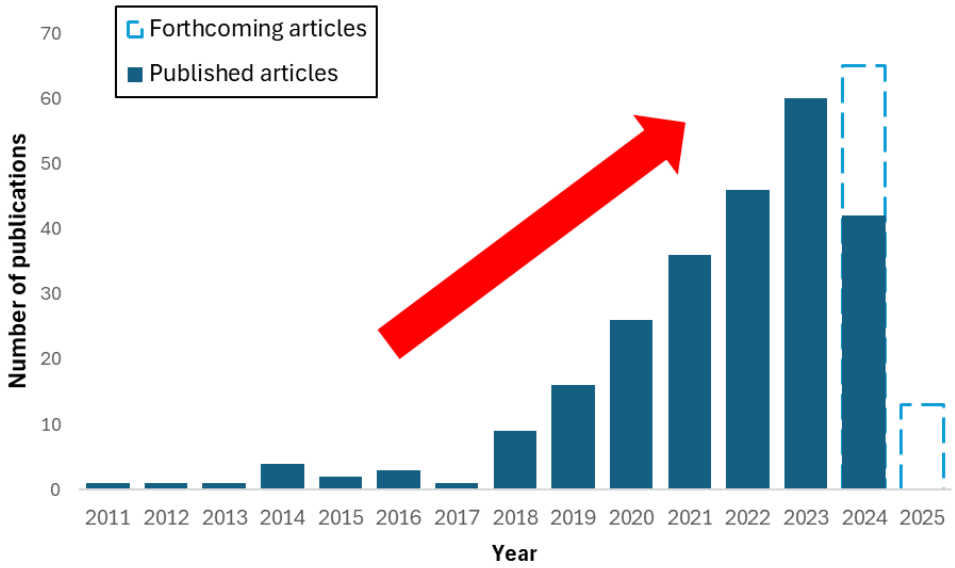


Figure 1.14. Number of Si-added HEAs publication based on Scopus data.

Among other metalloid elements like B, Ge, As, Sb, Te..., the addition of silicon to C-MPEAS is one of the most promising pathways to improving both strength and ductility, as shown in *Figure 1.15* [20]. Silicon and other metalloid elements are known to have a significantly smaller atomic size compared to transition metals, thus leading to stronger interstitial solid solution strengthening compared to substitutional solid

Thèse accessible à l'adresse : https://theses.insa-lyon.fr/publication/2025ISAL0036/these.pdf © [T. Langlois], [2025], INSA Lyon, tous droits réservés

solution [61]. Studies show that the addition of Silicon typically decreases the SFE of many C-MPEAs allowing for stronger strain-hardening too [20], [44], [62], [63]. Moreover, the increment of dislocation density under plastic deformation is larger in some Si-added HEAs compared to their non-Si counterparts [32].

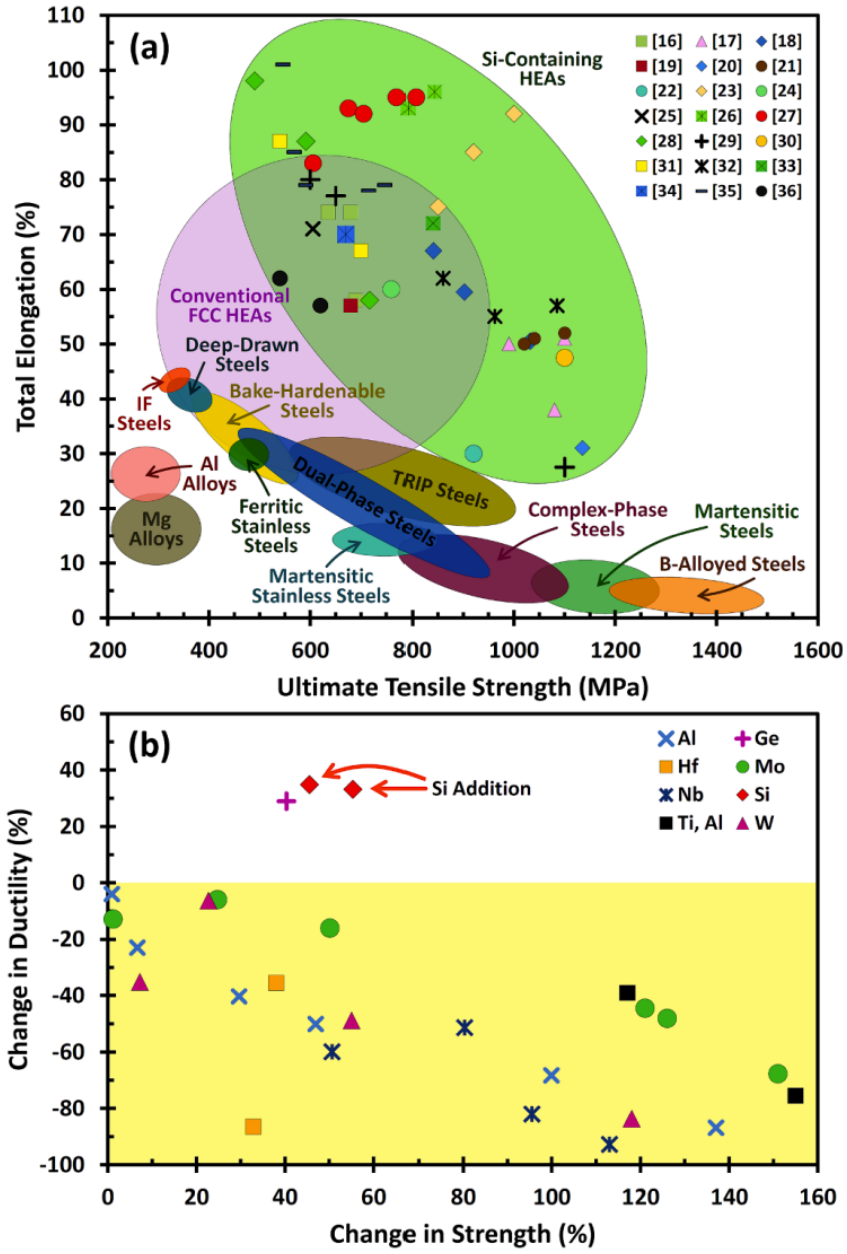


Figure 1.15. (a) Strength-ductility diagram for different classes of alloys, with Si-containing C-MPEAS in green. (b) Change in strength and ductility in C-MPEAS with the addition of different elements [20]. Si and Ge are the only additions that increase both strength and ductility.

In particular, the addition of silicon to ternary CrCoNi seems to have an outstanding influence on tensile properties of the alloys, as illustrated in *Figure 1.16* [44].

Thèse accessible à l'adresse : https://theses.insa-lyon.fr/publication/2025ISAL0036/these.pdf © [T. Langlois], [2025], INSA Lyon, tous droits réservés

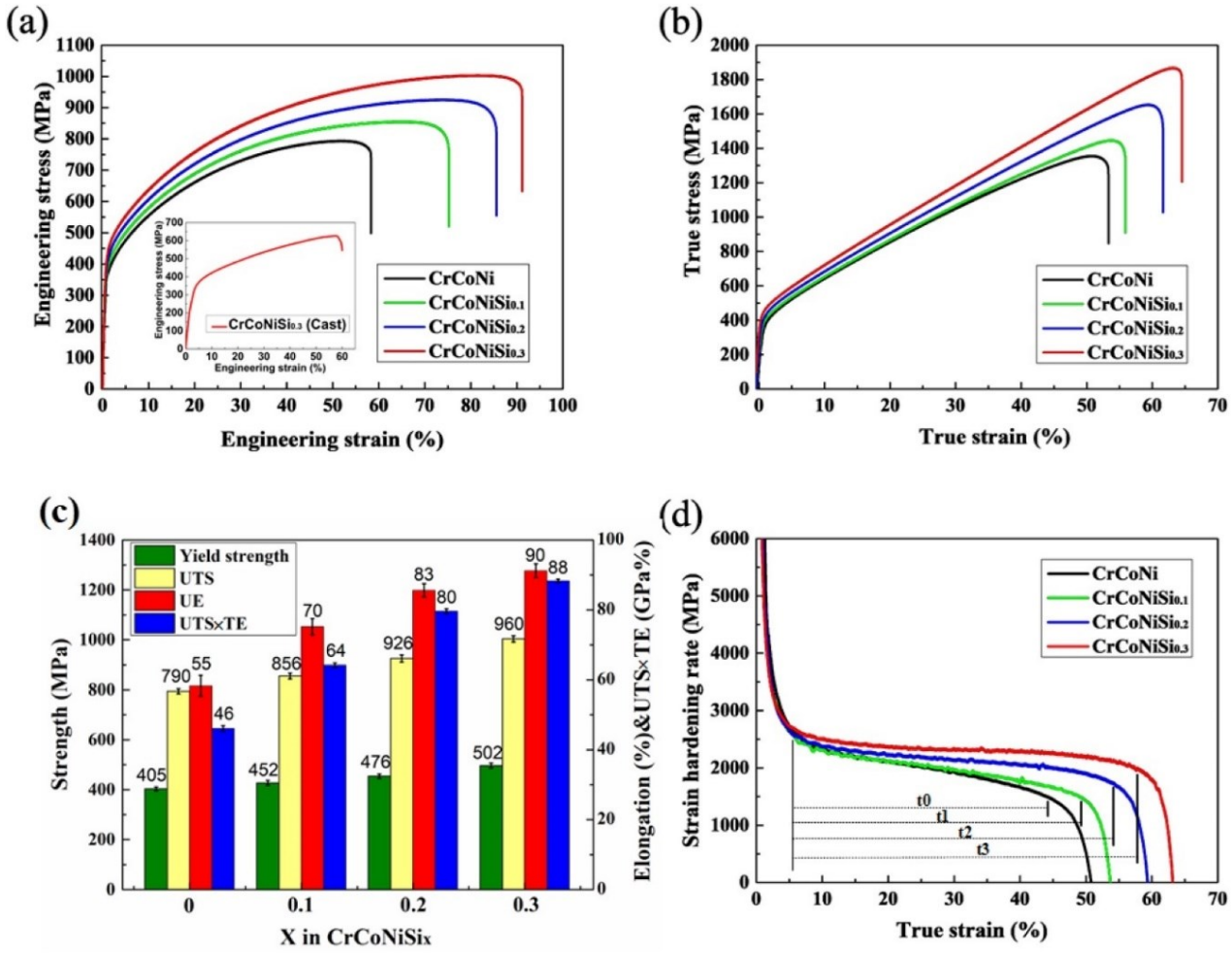


Figure 1.16. Silicon Addition to CrCoNi and mechanical improvements [44].

There is a significant improvement of the mechanical properties in the CrCoNi alloy with Silicon addition in proportion up to 9%. Yield strength is slightly increased, while the tensile strength and ductility are much improved, resulting in higher toughness as well.

However, the increasing amount of silicon can lead to the formation of secondary phases or intermetallics. These microstructures typically increase the strength of the material, but they are very brittle and can act as initiation site of failure [20]. For an equimolar CrCoNi, experimental results show that the addition of 9 at.% of silicon can lead to the formation of sigma-phase containing 36% of Cr, 26% of Co, 21% of Ni and 16% of Silicon using EDS analysis [64]. The sigma phase is a brittle, intermetallic phase with a tetragonal crystal structure. For this CrCoNi alloy with 9at.% of silicon, a CALPHAD calculation using TCHEA5 database from ThermoCalc predicts that sigma phase start forming for temperatures of 820°C and below. The tensile properties of this alloy are significantly decreased, as demonstrated in *Figure 1.17* [64].

Thèse accessible à l'adresse : https://theses.insa-lyon.fr/publication/2025ISAL0036/these.pdf © [T. Langlois], [2025], INSA Lyon, tous droits réservés

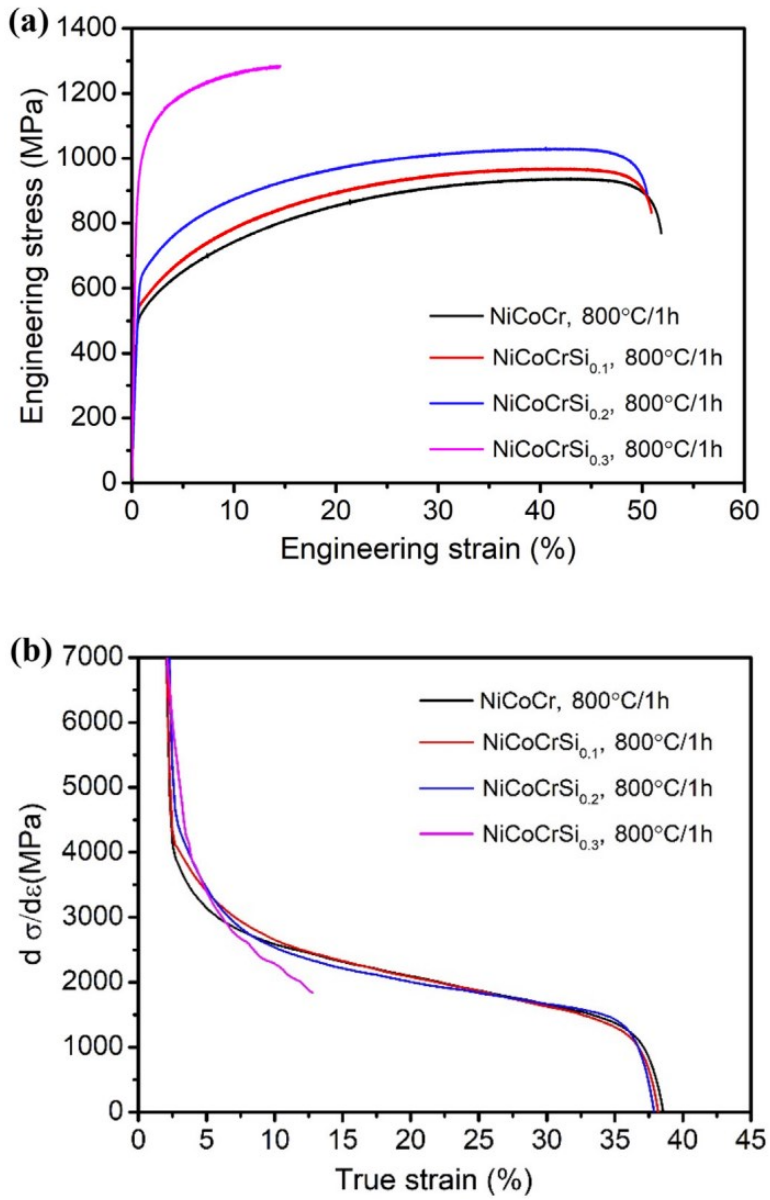


Figure 1.17. Experimental Stress-strain curves (a) and strain-hardening evolution (b) for different additions of Si to CrCoNi after annealing at 800°C [64].

In summary, the elaboration of new Si-containing C-MPEAS is a promising pathway for improved mechanical properties. Special care needs to be taken regarding the processing route and phase predictions to avoid formation of brittle compounds. The influence of silicon on non-equiatomic C-MPEAS could be the object of further research.

While the exploration of mechanical properties in C-MPEAS highlights their potential for advanced engineering applications, especially in extreme environmental conditions like hydrogen storage for the energy transition, it is equally important to consider the broader impact of these materials on sustainability, as many of these materials involve critical and rare elements.

Thèse accessible à l'adresse : https://theses.insa-lyon.fr/publication/2025ISAL0036/these.pdf © [T. Langlois], [2025], INSA Lyon, tous droits réservés

1.2 Societal implications of metal alloys

From the Stockholm Declaration in 1972 to the Paris agreement in 2021, and including Kyoto's protocol in 1997, there has been significant amount of climate warnings and actions in the last 50 years. Those discussions have addressed different aspects of climate change like global warming, gas emissions and resource consumption. In the present work, we are conducting research on the use of metals in applications related to the energy transition.

The shift towards greener energy sources is crucial for reducing greenhouse gas emissions and mitigating climate change. Hydrogen, as a clean and renewable energy carrier, presents a promising solution for achieving these goals. Produced through methods like water electrolysis powered by renewable electricity, hydrogen can be used in fuel cells for vehicles or to generate electricity for stationary systems. In addition to production, hydrogen storage and transportation raise significant challenges. Various methods are under investigation, including physical storage systems such as tanks, which require extremely robust materials like MPEAs. Additionally, other types of MPEAS are being explored for their hydrogen storage capacities. These alloys can serve as hydrogen carrier, reversibly storing and releasing hydrogen through hydrogenation and dehydrogenation [65], making them suitable for portable electronic devices, fuel cell vehicles, and stationary power systems. The use of metals and metal hydrides in hydrogen storage can enhance the efficiency and reduce the cost of hydrogen-based energy systems, making them more practical and accessible for widespread use.

However, the use of metals in the energy transition comes with a certain cost. Each alloy composition carries a societal impact, including factors such as Carbon footprint (CFP), water usage (WU), embodied energy (EE), mining workforce, etc....Thus, it is essential to gather comprehensive data on the various alloying elements and combined them to estimate the overall societal impact of an alloy [66].

1.2.1 General principles of material selection

M. Ashby made significant contributions to the field of material selection [67], particularly through methodologies like material selection charts, which are often used alongside tools such as Life Cycle Assessment (LCA) to evaluate the environmental impacts of products, processes, or materials. The choice of a material can be made on a wide range of sustainable properties of the raw elements that it contains. For instance,

Thèse accessible à l'adresse : https://theses.insa-lyon.fr/publication/2025ISAL0036/these.pdf © [T. Langlois], [2025], INSA Lyon, tous droits réservés

a material can be selected based on economic criteria such as material price, supply risks and concentration index. Otherwise, the material choice can also be related to its environmental features like carbon footprint (CFP), embodied energy (EE), toxicity. For example, *Figure 1.18* illustrates that higher strength mostly comes with higher CFP [67]. This is generally the case for most mechanical properties: better performance comes at a certain cost. Material selection often leads to compromise between mechanical and environmental properties, and such diagrams are useful to optimise different classes features at the same time (see the guideline for minimum Co_2 optimisation in *Figure 1.18*, for instance).

In this work, we use the terms "societal impact" and "societal implications" to refer to any environmental, ethical, sustainable, and economic aspects related to human activity that we address.

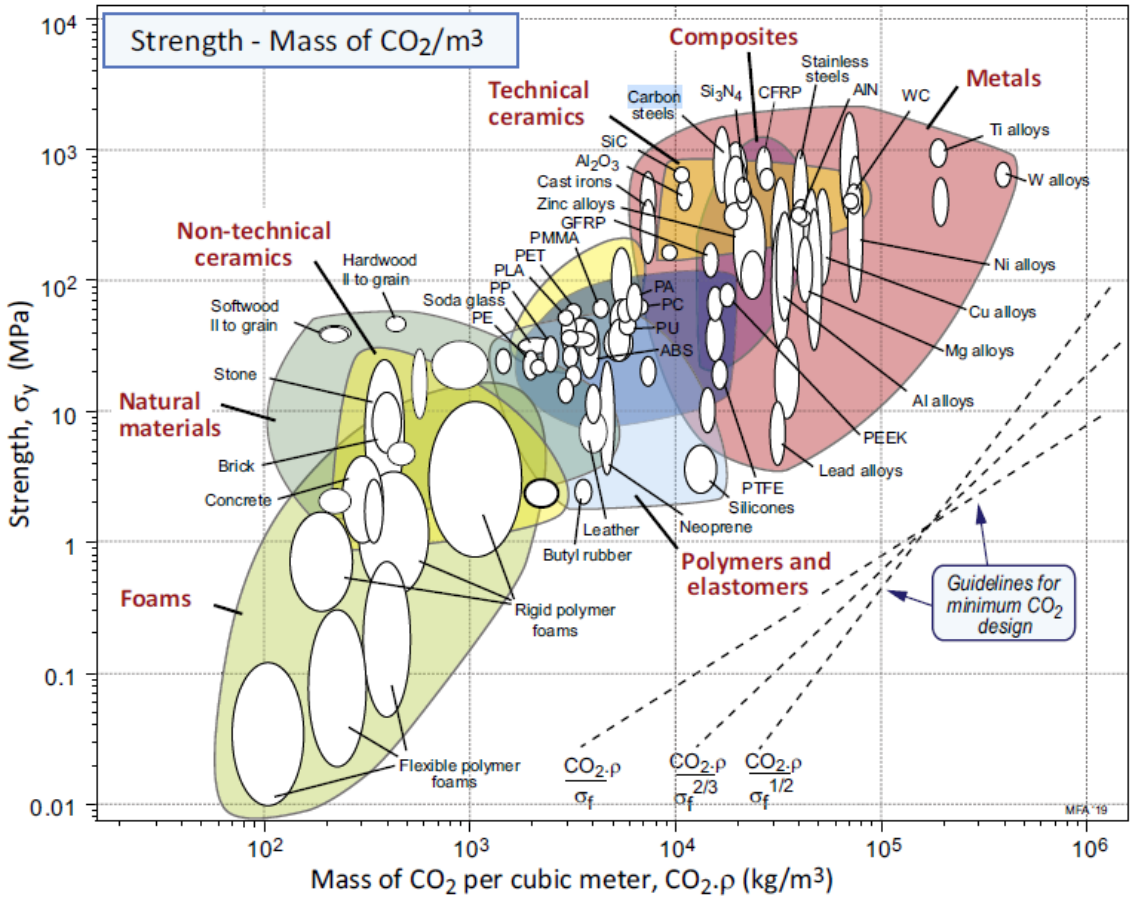


Figure 1.18. The Strength-Carbon footprint Ashby diagram [67].

Thèse accessible à l'adresse : https://theses.insa-lyon.fr/publication/2025ISAL0036/these.pdf © [T. Langlois], [2025], INSA Lyon, tous droits réservés

1.2.2 Challenges of critical raw materials

Material abundance in the Earth's crust or oceans is a concern. Naturally, the metal consumption in alloy production is high (*Figure 1.19-b*). Overuse of natural resources has led to the classification of many metals as Critical Raw Materials (CRM). In Europe, the critical aspect of an element is measured with the alloy critical index, described as a mean value of different economic factors such as supply risk and economic importance [1, 68]. The number of CRM is around 70 - though it may vary depending on European or US specifications – showing that most elements available on earth are critical (*Figure 1.19-a*). Amongst various CRM elements, strategic metals like aluminium, iron, manganese, chromium and nickel are critical.

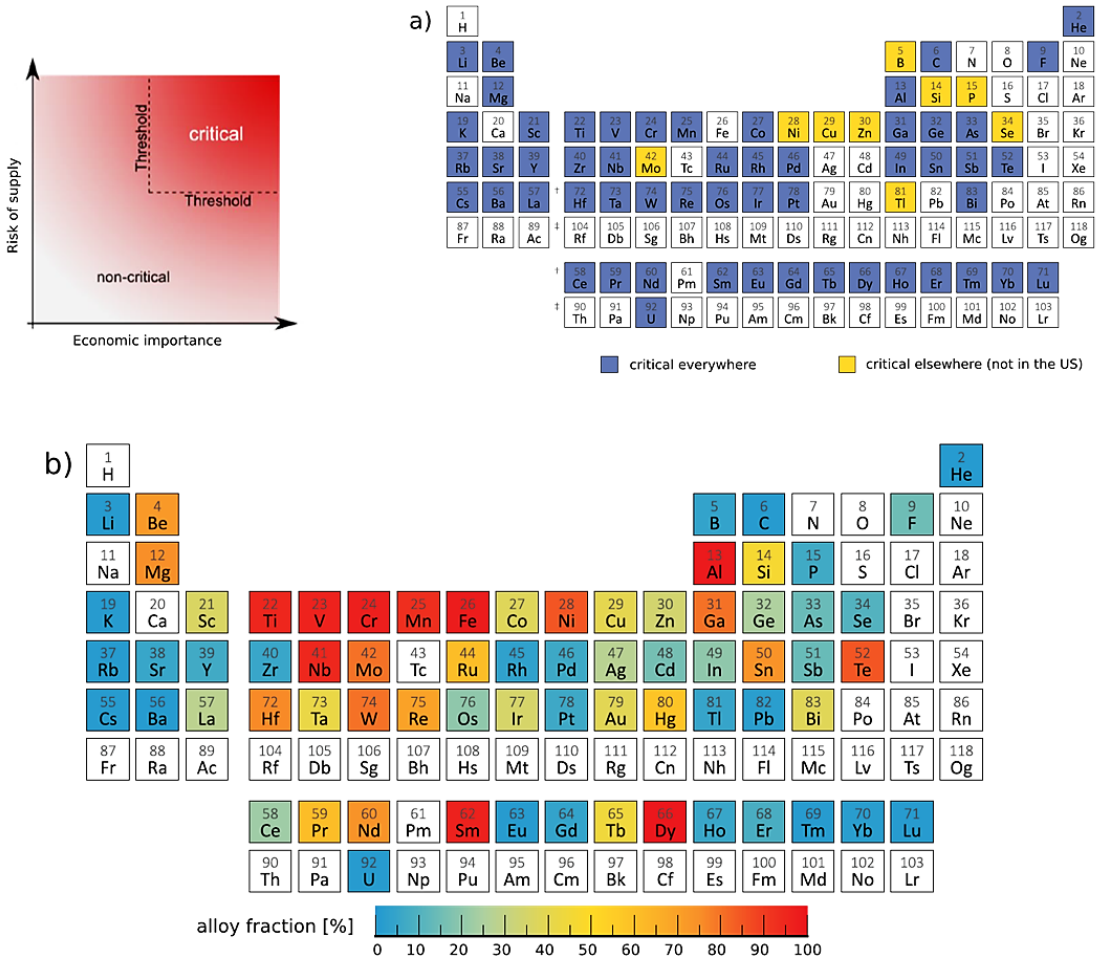


Figure 1.19. (a) Periodic table with CRM highlighted in colours. (b) Overall use of raw material as alloying elements [68].

Recycling materials and using scrap elements can help address the issue of criticality. *Figure 1.20* compares the embodied energy (EE) of primary resources versus recycled elements. Recycling requires 10 to 1000 times less energy than extracting

Thèse accessible à l'adresse : https://theses.insa-lyon.fr/publication/2025ISAL0036/these.pdf © [T. Langlois], [2025], INSA Lyon, tous droits réservés

primary resources [67]. However, there is a lack of comprehensive data on recycled materials, which often leads to their exclusion from material selection processes. Another gap in the literature relates to the sustainability of MPEAs in use. More research is needed on the long-term sustainability of MPEAs in real-world applications, including their potential for recyclability and reuse. Therefore, there is still work to do to provide more data on secondary resources. However, this topic has gained increasing interest in recent years, as depicted in *Figure 1.21*.

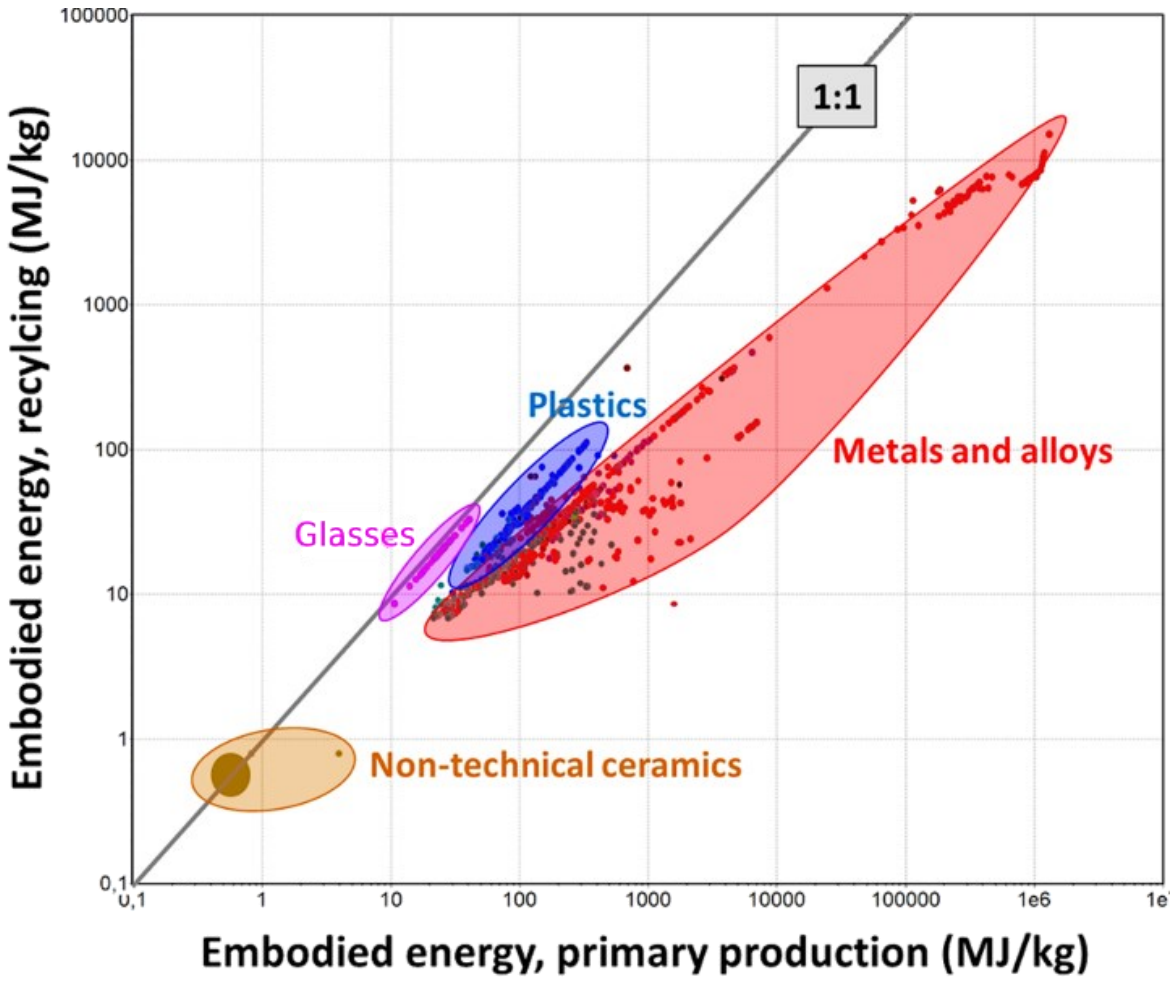


Figure 1.20. Embodied Energy of primary vs recycled materials [67].

Thèse accessible à l'adresse : https://theses.insa-lyon.fr/publication/2025ISAL0036/these.pdf © [T. Langlois], [2025], INSA Lyon, tous droits réservés

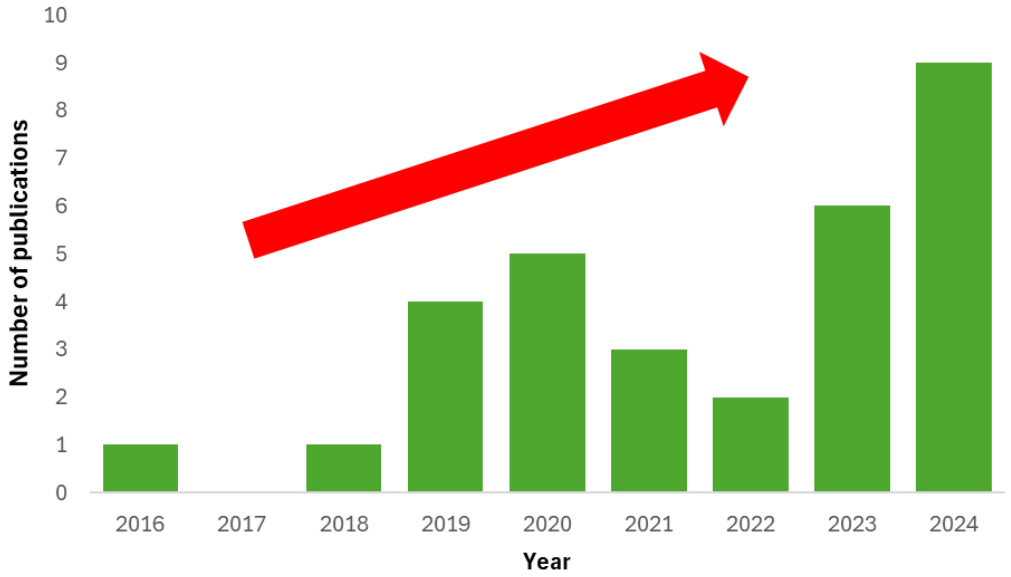


Figure 1.21. Number of publications about recycling in HEAs according to Scopus data.

Recent studies show that these recycled materials can achieve mechanical properties comparable to those of HEAs made from primary resources. For example, cobalt and nickel elements from e-waste materials have been successfully reused in HEAs [69].

1.2.3 Ethical and societal aspects of materials

Moreover, the ethical impact of material choice is often neglected. Country-specific data on where metals are extracted and where final products are used are rarely considered. Thankfully, this information is available in annual reports from organisations such as the European Commission [70]. Some data on materials and their main importing countries are also accessible online [71]. In terms of the ethical-social pillar of sustainable development, an example of ethical material selection would be prioritising the use of metals exported from countries with strong human rights record or high education levels. Additional sustainable scores for countries are also available on different publications: the sustainable thinktank Solability has created a very detailed database on sustainable criteria for countries [72]. This dataset is based on 131 measurable criteria grouped in different sub-classes: Natural Capital, Resource Efficiency & Intensity, Intellectual Capital, Governance Efficiency, and Social Cohesion. The following map (*Figure 1.22*) illustrates the overall country scores for societal implications.

Thèse accessible à l'adresse : https://theses.insa-lyon.fr/publication/2025ISAL0036/these.pdf © [T. Langlois], [2025], INSA Lyon, tous droits réservés

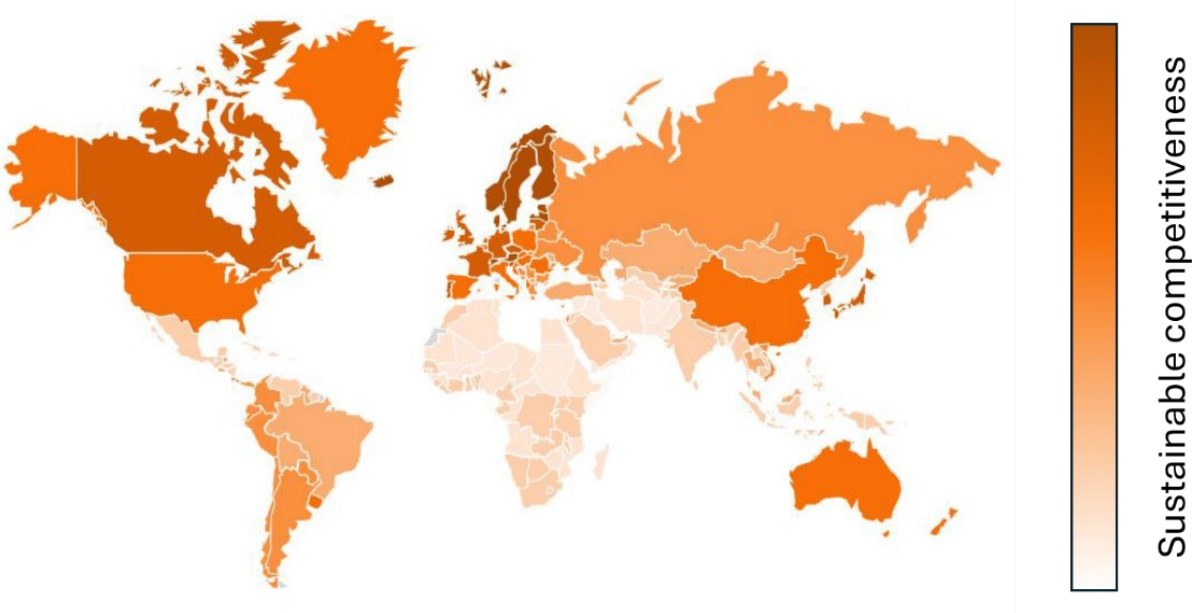


Figure 1.22. Sustainable Competitiveness score for countries in 2023 (redrawn from [72]).

Although data are available for assessing the societal impact of elements, such as elemental data, export and import flux, data on scrap metals; there is still no systematic integration of these data into alloy analysis. Indeed, there is a lack of studies that consider this dimension. There is a real opportunity to make progress in material selection by including these aspects.

This underlines the lack of connection between mechanical performance and societal aspect of alloys in the current literature. While some studies have demonstrated that MPEAs have the potential for improved mechanical properties compared to traditional alloys, it remains not clear to what extent these improvements come at the cost of increased sustainability impacts. Further research is needed to understand the trade-offs between sustainability and mechanical performance in MPEAs and to identify strategies for optimising both.

Thèse accessible à l'adresse : https://theses.insa-lyon.fr/publication/2025ISAL0036/these.pdf © [T. Langlois], [2025], INSA Lyon, tous droits réservés

1.2.4 Sustainability footprints of Cobalt

In the present work related to high performance and sustainability of MPEAs, the benchmark alloy is CrCoNi because of its superior toughness [2]. Numerous research studies have also highlighted the negative societal impact of Cobalt.

Over 60% of the world's cobalt supplies comes from mining sites in the Democratic Republic of Congo (DRC), as illustrated in *Figure 1.23* [73] and *Figure 1.24* [74]. 70% of cobalt's extraction in DRC is concentrated in southern provinces of Lualaba and Haut Katanga, also known as Katangese Cobalt-Copperbelt [75].

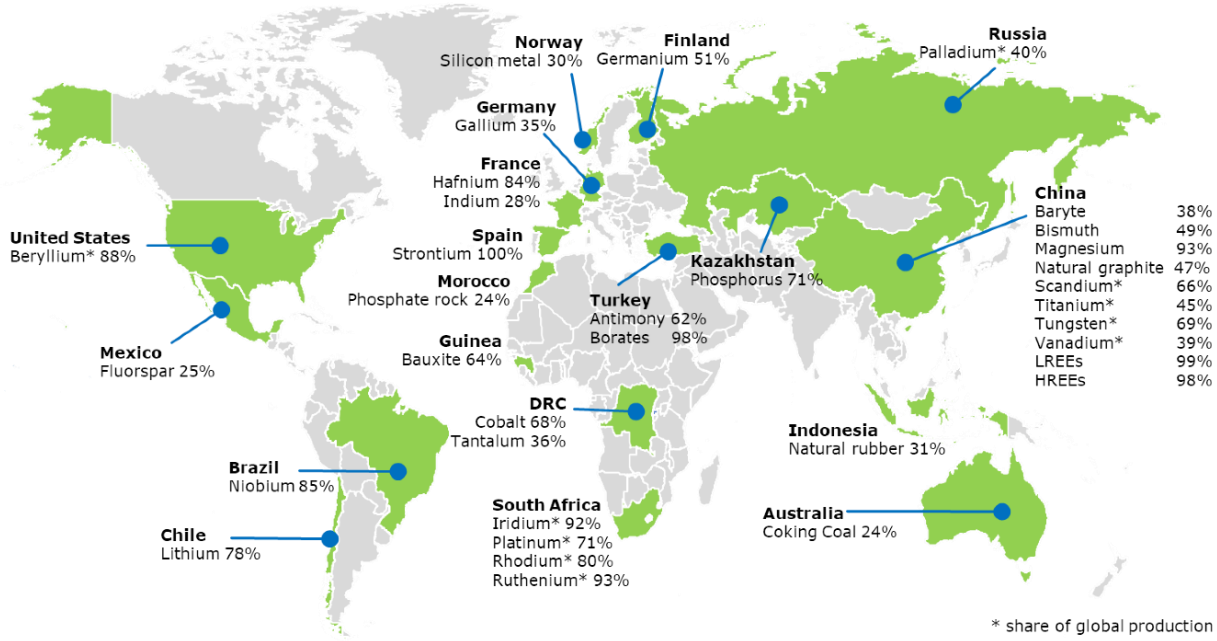


Figure 1.23. Main countries supplying critical raw materials to the EU [73].

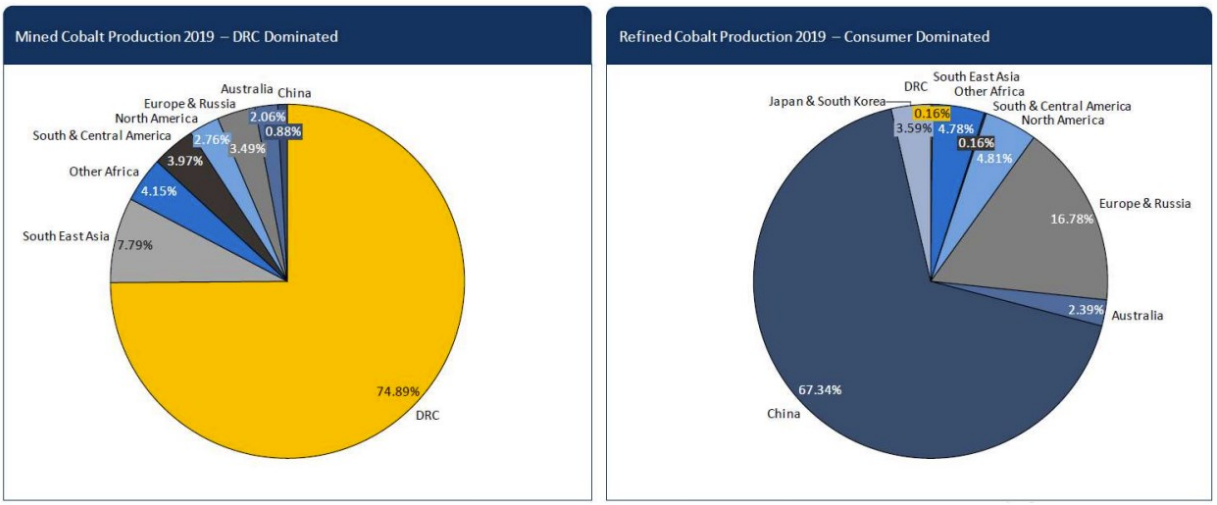


Figure 1.24. (left) Main regions for cobalt mining. (right) Main regions for refined cobalt [74].

Thèse accessible à l'adresse : https://theses.insa-lyon.fr/publication/2025ISAL0036/these.pdf © [T. Langlois], [2025], INSA Lyon, tous droits réservés

Driven by the demand for cobalt in electronic devices and electric-battery vehicles, the need for cobalt has tripled over the last decade and is expected to increase even more by 2035 [75]. This is also demonstrated by the evolution of refined cobalt, the end-user form of cobalt (*Figure 1.25*). For example, the manufacturing of most smartphone involves at least 10 grams of refined cobalt and most electric-vehicle battery requires 10 to 15 kilograms of it [75].

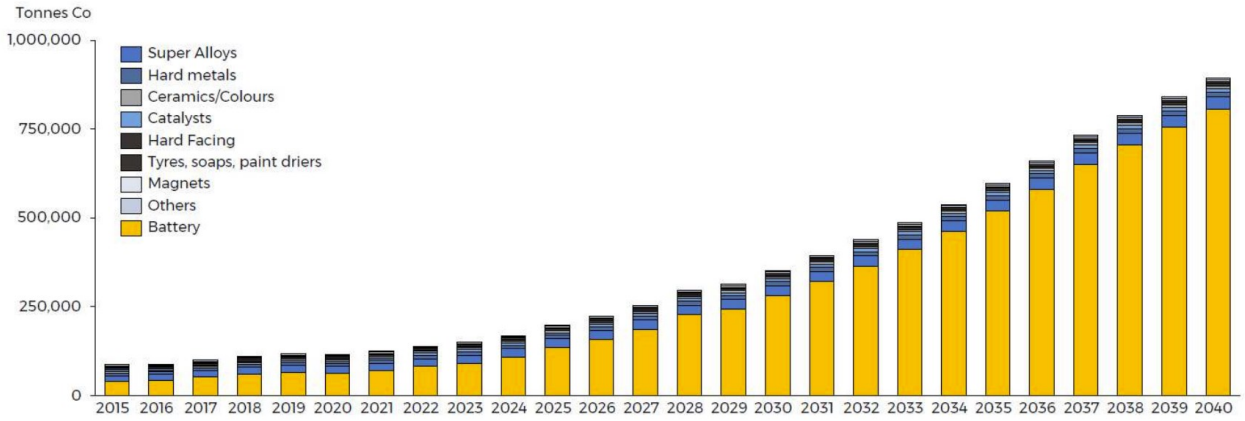


Figure 1.25. Evolution of the global demand of refined cobalt from 2015 to 2040 [74].

The near-monopoly from DRC on cobalt production, coupled with the increasing demand, creates a significant supply risk.

Second, cobalt extraction in the mining sector raises concern in terms of political instability and corruption. In addition, 8 of the 14 largest cobalt mining companies in the DRC are now China-owned, which influence the guidelines of cobalt mining in the country.

Finally, regarding human health, working condition and child labour, studies have shown elevated exposure levels to trace elements at mining sites of the town of Kolwezi, leading to oxidative DNA damages among the local population [76].

Thèse accessible à l'adresse : https://theses.insa-lyon.fr/publication/2025ISAL0036/these.pdf © [T. Langlois], [2025], INSA Lyon, tous droits réservés

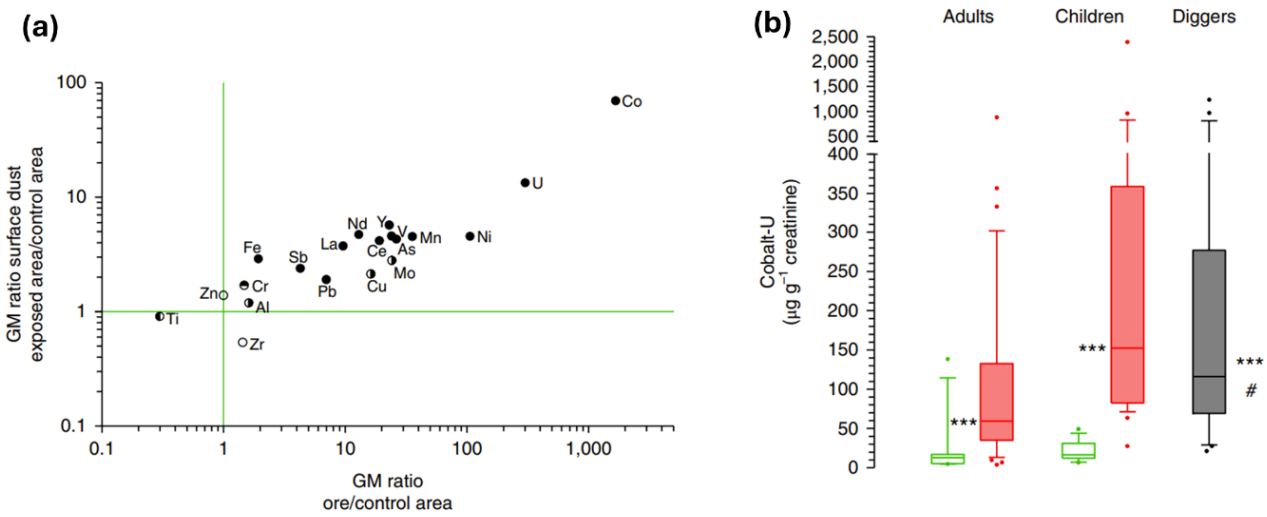


Figure 1.26. (a) Ratio of measured trace elements in ore, exposed areas (mines) and control areas (part of the town far from mining activities). (b) Concentration of Cobalt in urine and blood (residents in control areas in green, residents in exposed areas in red, mineworkers in grey) (redrawn from [76]).

As observed in *Figure 1.26*, the concentration of cobalt in exposed area is 70 times higher than in control area. Subsequently, urinary concentration of cobalt is almost 10 times for exposed children compared to control children, and 5 times higher in exposed adults. Additionally, a measure of 8-hydroxydeoxyguanosine in blood, an index reflecting oxidative DNA damage, showed the strong correlation between the concentration of cobalt and the DNA damage, especially in children results [76].

The exploration of sustainability in metals and C-MPEAs, particularly with cobalt, highlights the trade-offs between achieving high mechanical performance and minimising sustainability impacts. Methods such as Ashby plots and Life Cycle Assessment (LCA) offer valuable tools for evaluating the environmental and economic impacts of materials, and offering pathway for reducing their footprint. However, it is equally important to incorporate societal metrics into sustainability evaluations, ensuring that alloy design considers broader social and ethical implications.

Thèse accessible à l'adresse : https://theses.insa-lyon.fr/publication/2025ISAL0036/these.pdf © [T. Langlois], [2025], INSA Lyon, tous droits réservés

1.3 Concluding remarks

The investigation of Medium and High Entropy Alloys (MEAs and HEAs) reveals their significant potential for enhancing mechanical properties such as strength and ductility. These alloys, particularly those in the CrCoNi system, are promising candidate for energy transition technologies. While the path forward for MPEAs in high-performance applications is promising, it requires careful consideration of processing routes and alloy compositions to control the strengthening mechanisms and avoid the formation of brittle phases, especially with silicon addition.

Transitioning to the sustainable aspects of materials, our exploration focused on the societal impact of material selection. The focus on critical raw materials (CRMs), particularly cobalt, reveals significant challenges in sourcing materials that meet both mechanical performance and ethical standards. The sustainable cost of MPEAs containing cobalt cannot be overlooked. This highlights the need for systematic approach to material selection that incorporates sustainability metrics alongside traditional mechanical criteria. The potential for recycling and the use of secondary resources paves the way toward more sustainable material use, but gaps in data and research still need to be addressed.

Thèse accessible à l'adresse : https://theses.insa-lyon.fr/publication/2025ISAL0036/these.pdf © [T. Langlois], [2025], INSA Lyon, tous droits réservés

2 Research questions and outline

Contents

2.1 Research questions ---------- 40

2.2 Outline---------- 41

2.1 Research questions

Despite the recent surge in publications on MPEAs, a significant gap in literature remains in understanding their societal implications and how these considerations can guide future alloy development. The interplay between societal implications and mechanical performance, crucial for any structural application of MPEAs, is particularly underexplored. Existing research tends to focus on isolated aspect of materials, such as price, criticality, or carbon footprint, without considering multiple societal indicators. This presents an opportunity for a study that combines mechanical performance and societal implications of an alloy, especially in the case of C-MPEAs. By adopting a holistic approach that considers multiple indicators of sustainability and performance, such a study could provide valuable insights into the potential and limitations of MPEAs as sustainable material choices.

The thesis will address the following questions:

- How can a novel **sustainability scoring tool** be integrated into the design of C-MPEAs to guide more responsible material selection.
- How can mechanical performance predictions for C-MPEAs be coupled with sustainability metrics to enable a **multi-objective optimisation** strategy

Thèse accessible à l'adresse : https://theses.insa-lyon.fr/publication/2025ISAL0036/these.pdf © [T. Langlois], [2025], INSA Lyon, tous droits réservés

that balances high performance and low environmental impact? How do societal implications in material selection affect material performances and vice versa?

- What is the influence of varying **cobalt** content on the mechanical performance and microstructural evolution of MPEAs under cryogenic conditions, and how does it compare to room-temperature behaviour?
- How does **silicon** addition affect the mechanical properties and sustainability footprints of non-equiatomic Cr-Co-Ni-Si alloys, especially under cryogenic testing ?

2.2 Outline

The following is an overview of the content and objectives of each chapter.

First, a comprehensive review of the current literature knowledge regarding MPEAs has been provided, particularly focusing on their mechanical properties and the emerging importance of societal implications in material selection. The review identified significant gaps in the literature, especially the need for a holistic approach that integrates mechanical performance with sustainable implications of the alloys. This chapter paved the way for developing the research questions and associated guidelines.

Chapter 2 provides an overview of the thesis structure and briefly describes the content of each subsequent chapter. This roadmap ensures that the reader can easily follow the investigation process and see how each chapter contributed to addressing the identified gaps in the literature.

In the third chapter, the methodology chapter elaborates on the research questions and explain the adopted approach. It will detail the methods and techniques used to investigate the societal and mechanical properties of alloys, including prediction models and experimental procedures. The first subsections will outline the methods used to obtain microstructural, mechanical and sustainable predictions, respectively. Our holistic approach involves a prediction of stable FCC-phase, a model that evaluate the sustainable competitiveness of an alloy with different ecological, economical and ethical indicators, a model that predicts the solid solution strengthening and predictions

Thèse accessible à l'adresse : https://theses.insa-lyon.fr/publication/2025ISAL0036/these.pdf © [T. Langlois], [2025], INSA Lyon, tous droits réservés

of the SFE. Subsequently, we will introduce the materials and methods used experimentally.

In the fourth chapter, we detail the input datasets and results for our different predictions. We will evaluate the robustness of our mechanical predictions with existing experimental data. We will evaluate the sustainable scores of existing classes of metals. The chapter will explore the synergy between mechanical performance and sustainability, providing a thorough understanding of how they can inform alloy development. Finally, a framework will be proposed to identify compositions that offer a promising balance between performance and sustainability.

The fifth chapter will investigate both impacts of reducing cobalt and adding silicon on the mechanical properties of CrCoNi and CrCoNiSi alloys, under room and low-temperature conditions. The experimental section will include tensile tests, microstructural analysis, and fracture toughness measurements to determine how cobalt reduction affects the alloy's performance. Additionally, the results will be compared to existing literature to identify potential benefits and drawbacks of cobalt reduction in high-performance alloys.

In Chapter 6, the key findings are summarised to form a conclusion regarding the design of MPEAs, guided by mechanical and sustainability metrics. After discussing the modelling and experimental outcomes, this chapter investigates the broader implications of the results for industrial applications, and suggests potential avenues for future work to further refine the insights gained in this study.

Thèse accessible à l'adresse : https://theses.insa-lyon.fr/publication/2025ISAL0036/these.pdf © [T. Langlois], [2025], INSA Lyon, tous droits réservés

3 Numerical and experimental methods

Contents

3.1 Adopted approach ---------- 44

3.2 Numerical methods: principle, data and tools ---------- 46

3.2.1 CALPHAD model ---------- 47

3.2.2 Solid Solution Strengthening model ---------- 50

3.2.3 Stacking Fault Energy Prediction models ---------- 54

3.2.4 Modelling the sustainable competitiveness of materials ---------- 58

3.3 Experimental methods ---------- 67

3.3.1 Choice of raw materials ---------- 67

3.3.2 Manufacturing Methods ---------- 70

3.3.3 Thermomechanical treatments ---------- 75

3.3.4 Metallography: Sample preparation ---------- 77

3.3.5 Specimen machining ---------- 81

3.3.6 Chemical characterisation methods ---------- 84

3.3.7 Microstructural characterisation methods ---------- 88

3.3.8 Mechanical testing methods ---------- 98

3.4 Summary ---------- 109

Thèse accessible à l'adresse : https://theses.insa-lyon.fr/publication/2025ISAL0036/these.pdf © [T. Langlois], [2025], INSA Lyon, tous droits réservés

3.1 Adopted approach

To address the challenges of this thesis, we will investigate the potential trade-offs between mechanical and sustainable properties in the design and processing of a prototype MPEA containing chromium, cobalt and nickel. The methodology in this thesis is structured as a three-steps process covering both design and elaboration. The first step delves into alloy modelling and simulations. The second step involves a high-throughput exploration using the Fast-Alloying (FA) method, which allows for the rapid production and evaluation of numerous compositions in the form of compression cylinders. Finally, the third step involves advanced elaboration of the most promising compositions identified in the first two steps, with specimens prepared for Charpy impact and tensile tests. The adopted approach is summarised in *Figure 3.1.*

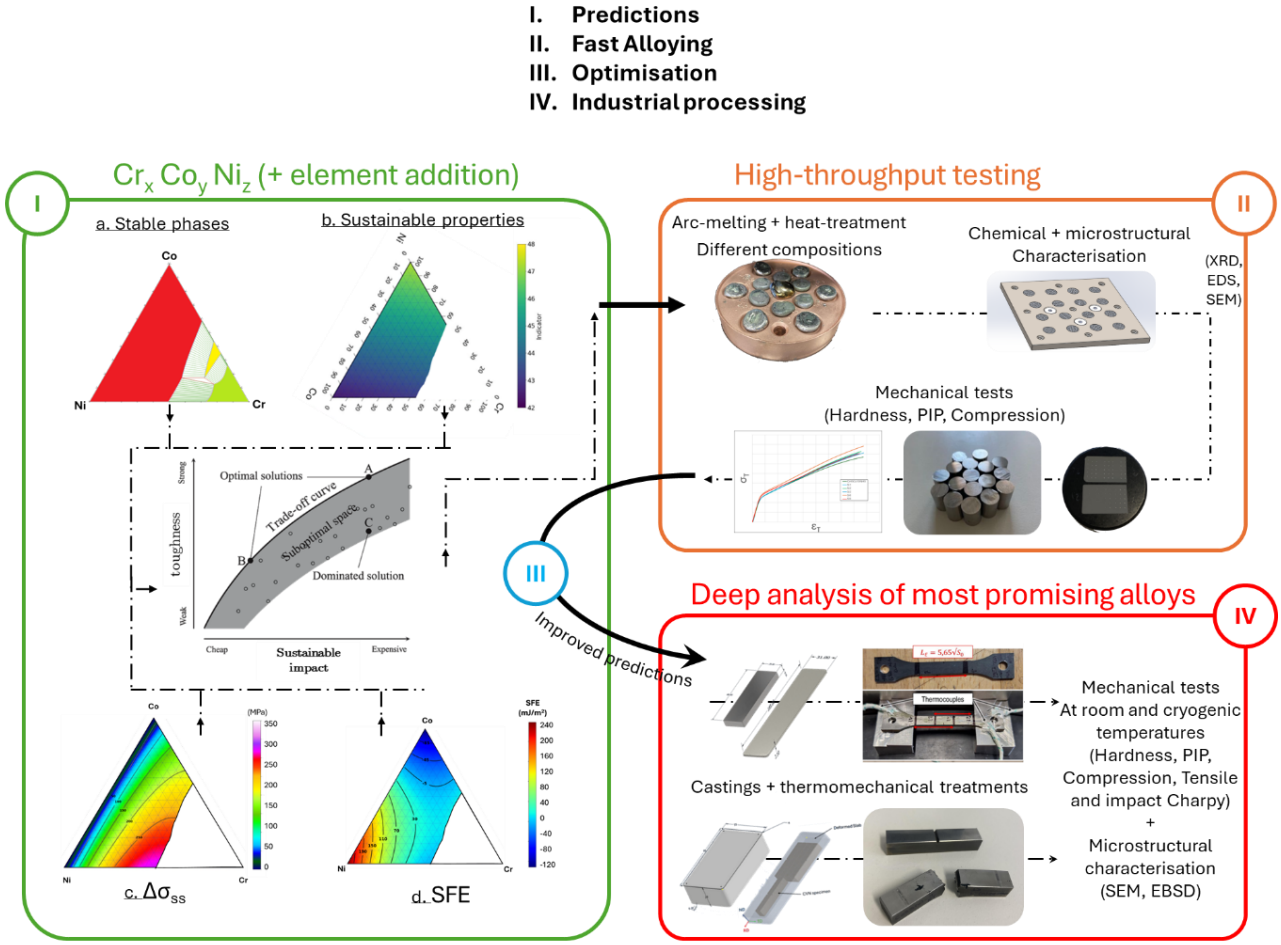


Figure 3.1. PhD Thesis general approach. Analysis of different MEAs and HEAs compositions with different exploration layers [5], [77].

Thèse accessible à l'adresse : https://theses.insa-lyon.fr/publication/2025ISAL0036/these.pdf © [T. Langlois], [2025], INSA Lyon, tous droits réservés

The first layer in our approach of the work involves various prediction models. A Calculation of Phase Diagram (CALPHAD) methodology is applied to predict the FCC single-phase regions. We developed a model that determines the sustainable impacts of pure elements and alloys based on their intrinsic properties and on their geographic origins. Finally, two empirical mechanical models are employed. They estimate the incremental σ_{ss} [5] and the SFE [77], respectively. With these different prediction models, we aim to identify the most interesting compositional regions, that meet our criteria for sustainability, mechanical performance and single-FCC structure.

Then, we apply our FA (Fast Alloy) process to analyse over 20 MPEAs compositions. The following properties of the produced homogenised specimens are determined: chemical composition and potential impurities, stable phases, SFE and microstructural morphology. The following mechanical properties are also evaluated: Hardness Vickers (HV5), estimations of $\sigma_{ys} - \sigma_{uts}$ with Profilometry-based Indentation Plastometry (PIP) and compressive strength σ_c.

The interactions between our prediction models and the FA results are predominant in this thesis, as shown in *Figure 3.1.* Indeed, modelling serves as a catalyst for new material development because it allows for a faster, larger, and more efficient exploration of the compositional space. Conversely, high-throughput manufacturing of new material compositions is useful for modelling because experimental results can be used to improve the developed models with the help of computer-assisted algorithms. Machine Learning is helping to navigate across complex spaces.

With this smart and sustainable approach, we can significantly reduce the resources used for this project. Compared to traditional elaboration, we have quantified a reduction in raw materials consumption by over 500%. This is explained in the technical description of the FA later in this chapter. Hence, with respect to the data of the first two layers, only the most promising compositions undergo the advanced elaboration process to optimise the mechanical properties.

The first part of the thesis, which focused on simulation work, took place in France between ICMCB in Bordeaux and MATEIS in Lyon. The second part, involving experimental work, has been conducted in Australia at IFM due to the availability of equipment and materials. The final part, involving final experiments, completing the analysis of the experimental results and their summarisation, was done at MATEIS in Lyon.

Thèse accessible à l'adresse : https://theses.insa-lyon.fr/publication/2025ISAL0036/these.pdf © [T. Langlois], [2025], INSA Lyon, tous droits réservés

3.2 Numerical methods: principle, data and tools

The four predictions models involved in this project are listed in *Table 3.1.* In this chapter, we introduce the framework and workflow of each model, including:

- Their **relevance** to this project and for the broader context.
- Their underlying **principles**, including equations and input parameters.
- Their **computational medium**, such as coding in python or MATLAB, and excel calculations.
- The **target materials** they are applied to.
- The **accuracy** of the predictions.
- The **output formats**, like graphs or figures to illustrate the results.

For each alloy composition, because the calculation methods for the different models are either based on mass unit or molar unit, we initially developed a conversion table from molar fraction to mass fraction and vice versa. This conversion table is available in *Figure 0.1* of the Appendix of Chapter 3.

Table 3.1. Symbols and units of the 4 predictions models.

Prediction model	Phase diagrams	Solid Solution Strengthening	Stacking Fault Energy	Sustainable Competitiveness
symbol / Abbreviation	CALPHAD	σ_{ss}	SFE	SC
base unit	1 mol *	1 mol	1 mol	1 kg

** the software used for CALPHAD predictions allows mass and molar calculations. We chose a molar unit for convenience.*

In addition, all our prediction models for alloys require input data on the elements. For clarity and convenience to our numerical models, we are classifying elemental data under different categories. Intrinsic data are properties inherent to the materials, typically being constant values. Extrinsic data vary with time and location. Mechanical, societal and general aspects of the materials are other subdivisions of the material properties. The following list gives a few examples for each category:

- **Intrinsic general properties (IGP),** like the density, atomic radii, etc.
- **Intrinsic mechanical properties (IMP),** like the elastic moduli, the Poisson ratio, etc.

Thèse accessible à l'adresse : https://theses.insa-lyon.fr/publication/2025ISAL0036/these.pdf © [T. Langlois], [2025], INSA Lyon, tous droits réservés

- **Intrinsic societal properties (ISP),** like material toxicity, carbon footprint.
- **Extrinsic societal properties (ESP),** like the material price, water usage.

For high-throughput exploration of alloys, the process can begin right from the initial stage by automating the retrieval of IGP and IMP data on pure elements and materials for our prediction models. A script has been written using Python 3.9 in the Jupyter Notebook 6.4 interface. The open-access databases of the *Material Project* [78] and *Citrination* [79] are used to manipulate extensive sets of data. *Matminer* [80] and *Pymatgen* [81] are the Python libraries used to communicate with these databases.

Special care was taken to extract data of the pure elements with the highest stability, using conditional selection in the *Matminer* library. The resulting output provides a nearly full dataset for over 100 chemical elements, with full data available for at least 70 elements. Missing data has been inferred by using a machine learning algorithm. With a KNN implementation process from *Scikit-Learn* python library [82], we have identified elemental properties with strongest correlation with the missing data and extrapolates the missing values.

3.2.1 CALPHAD model

The equations and prediction models associated with the two mechanical properties, such as σ_{ss} and SFE, are only valid in the FCC single-phase domain. Therefore, the first modelling tool we used for new material design is a thermodynamical CALPHAD model, which allows for the prediction of phase stability of materials based on their composition. This represents an optimisation of calculation time in our high-throughput exploration of alloys, limiting the research to FCC regions.

CALPHAD models are based on thermodynamic databases for known systems, also called assessed systems, which store data for the free enthalpy of various phases as a function of temperature, composition, and pressure. Under given conditions, the model uses these databases to identify the most stable phase or combination of phases that minimise the free enthalpy of the system [83]. Phase prediction of unknown systems is based on extrapolating data from the respective assessed binary or ternary subsystems. The accuracy of a CALPHAD model depends on the quality of its databases. Criteria for a database quality have been developed based on the fraction of fully assessed binary (FAB) and ternary (FAT) systems over the total number of systems [84]. Systems that are fully assessed account for a value of 1, while system assessed over an uncomplete range of composition and temperature, called tentatively

Thèse accessible à l'adresse : https://theses.insa-lyon.fr/publication/2025ISAL0036/these.pdf © [T. Langlois], [2025], INSA Lyon, tous droits réservés

assessed, account for 0.1. A database with a complete thermodynamic description has FAB and FAT values of 1.

The software used to perform CALPHAD predictions is ThermoCalc-2023b. We consistently selected a mole unit for phase prediction in ThermoCalc, based on the unit for our two mechanical models. ThermoCalc was coupled with the TCHEA5 database to predict phases on C-MPEAs. This database gathers experimental information for binary and ternary alloys within the following 26 elements given in alphabetic order of their symbol: Al, B, C, Co, Cr, Cu, Fe, Hf, Ir, Mn, Mo, N, Nb, Ni, Re, Rh, Ru, Si, Sn, Ta, Ti, V, W, Y, Zr, Zn. Within the 26 elements of the database, a total of 325 binary and 2600 ternary systems can be formed. A total of 310 binary systems have been fully assessed; 192 ternary system have been fully assessed while 309 ternary systems have been tentatively assessed. All the binary subsystems of Co-Cr-Ni system have been fully assessed. The system Co-Cr-Ni has been fully assessed itself. All the binary subsystem of Co-Cr-Ni-Si have been fully assessed. However, the Co-Cr-Si system has only been tentatively assessed, thus accounting for 0.1. *Table 3.2* provides the accuracy criteria of TCHEA5 and of the two systems that we are focusing on in the next part of the thesis.

Table 3.2. TCHEA5 database overall quality and for two subsystems.

System	FAB	FAT
TCHEA5	0.954	0.086
Co-Cr-Ni	1	1
Co-Cr-Ni-Si	1	0.775

Most of the binary systems in the TCHEA5 database have been assessed. However, only a small fraction of the 2600 possible ternary systems have been evaluated, resulting in an overall FAT of 0.086. When focusing on Co-Cr-Ni and Co-Cr-Ni-Si systems, the FAT values are significantly improved. It is commonly accepted that a system with a FAT of at least 0.6 is required to ensure accurate predictions [85].

The required inputs for a single CALPHAD calculation are chemical composition, temperature and pressure of the system. The phase predictions are performed in a quinary compositional space, consisting of the following transition metals: cobalt (Co), chromium (Cr), iron (Fe), manganese (Mn) and nickel (Ni). This compositional space represents the domain of C-MPEAs. Subsequently, phase predictions are performed with addition of silicon (Si) with a maximum content of 10 atomic percent. This limit is chosen because secondary phases like the sigma phase have been observed experimentally at similar Si content in Co-Cr-Ni and Cr-Fe-Mn-Ni alloys

Thèse accessible à l'adresse : https://theses.insa-lyon.fr/publication/2025ISAL0036/these.pdf © [T. Langlois], [2025], INSA Lyon, tous droits réservés

[64]. The sigma phase is a brittle, intermetallic phase with a tetragonal crystal structure, that can lead to significant loss of ductility and toughness even in very small quantity [64]. Phase prediction calculations have been performed on alloys containing 3 to 6 elements. Predictions have been made at atmospheric pressure and for temperatures varying from 1000 °C to 1200 °C, corresponding to the heat-treatment temperatures used experimentally in this project.

Depending on the number of elements involved in the phase predictions, results can be represented in various forms, as displayed in *Figure 3.2*. For a given set of composition, pressure and temperature, single-equilibrium calculations simply give the predicted stable phase(s). Ternary phase diagrams are useful to map the entire compositional space of a ternary alloy with predicted phases (*Figure 3.2*-a). For quaternary alloys, we generated exploded views of the tetrahedron walls (*Figure 3.2*-b) using TC-python. Pseudo-ternary diagrams are also quite convenient for quaternary alloys like ours, with constant levels of Silicon added to Co-Cr-Ni (*Figure 3.2*-c). For alloys with more than 4 elements, only single-equilibrium calculations are possible.

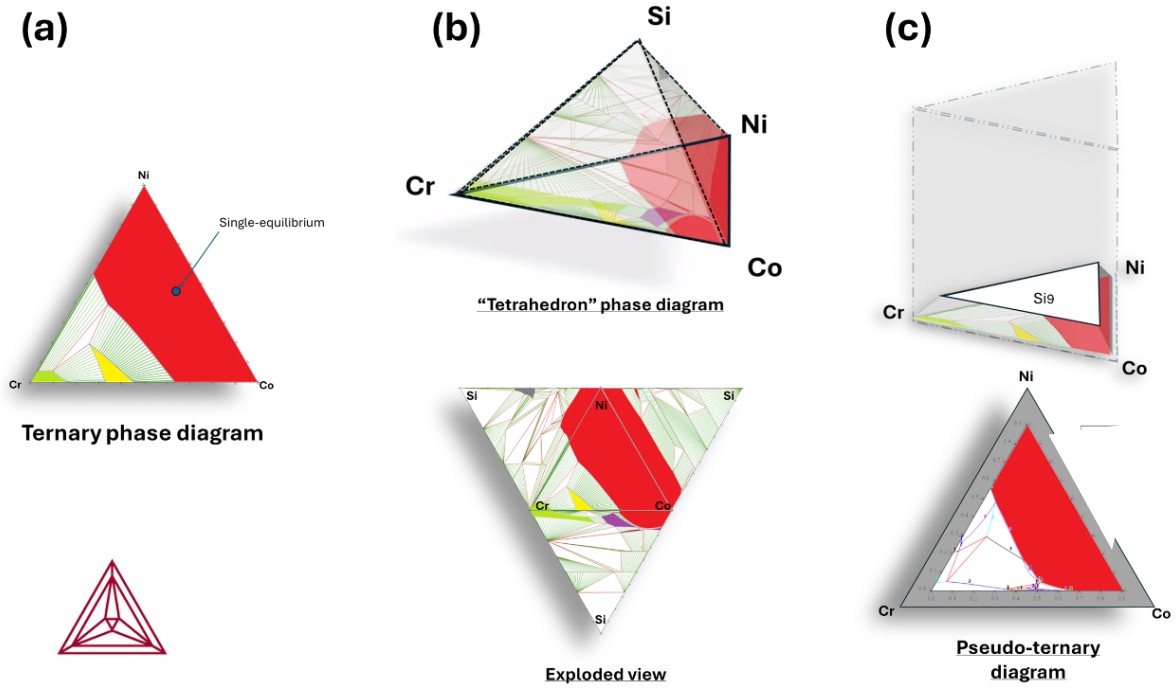


Figure 3.2. Different representations of phase prediction results based on ThermoCalc calculations.

Ternary diagrams and single-equilibrium calculations can be performed either using the graphical interface or console mode in ThermoCalc. However, in the context of a high-throughput methodology aimed at identifying properties of a large compositional space, performing individual calculation via the user interfaces is not feasible. For example, within the Cantor system, there are 10 different ternary subsystems, 5 quaternary subsystems and one quinary. With a 1% atomic step between

Thèse accessible à l'adresse : https://theses.insa-lyon.fr/publication/2025ISAL0036/these.pdf © [T. Langlois], [2025], INSA Lyon, tous droits réservés

each composition, there are 5,151 different equilibria in a ternary system, 176,851 in a quaternary system, and 4,598,126 in a quinary system. This totals 4,780,144 single-equilibrium systems to calculate. Given that each single-equilibrium calculation, including system definition, temperature, and pressure input, and the computational process, requires approximately 2 minutes, the total computation time would amount to approximately 9.56 million minutes, or approximately 6,639 days, if conducted manually. This underscores the impracticality of a manual approach for such a large dataset.

Fortunately, our high-throughput exploration can be automated using the TC-Python module from ThermoCalc. This module is a Python API that allows users to perform thermodynamic and phase equilibrium calculations using ThermoCalc databases within a Python programming environment. This approach is highly effective for automating complex analyses using scripts and batch processes. Our python codes for automating the detection of FCC single phase in Cantor domain and for pseudo-ternary diagrams are available in *Figure 0.2* and *Figure 0.3* of in the Appendix of Chapter 3. Calculations can be run overnight, reducing the overall time to less than 2 days.

In summary, we are using CALPHAD predictions to

- **Identify FCC single-phase regions** in Co-Cr-Fe-Mn-Ni-Si subsystems.
- Develop an **automated process** to evaluate all the potential FCC composition.
- Enhance the **exploration efficiency** for subsequent models and reduce calculation time.
- **Illustrate the results** with various diagrams.

3.2.2 Solid Solution Strengthening model

As explained in the motivation and in the literature review, it is crucial to optimise mechanical properties like yield strength without compromising ductility. Unlike most precipitation strengthening strategies which commonly enhance strength at the expense of ductility, solid solution in FCC alloys does not adversely affect the strain-hardening behaviour of materials. Therefore, our approach to optimise the yield strength of our C-MPEAs involves predicting σ_{ss} in subsystems of the Cantor alloy.

Thèse accessible à l'adresse : https://theses.insa-lyon.fr/publication/2025ISAL0036/these.pdf © [T. Langlois], [2025], INSA Lyon, tous droits réservés

Despite the existence of other models, we employ the model from Varvenne et al. in this work [5]. As demonstrated in the literature, this model provides a good approximation of σ_{ss} for equiatomic or near-equiatomic compositions, such as C-MPEAs [5]. However, it tends to overestimate σ_{ss} for conventional alloys like steels [29].

Since we focus on C-MPEAs and silicon additions, it is necessary to gather the required properties of the pure elements Co, Cr, Fe, Ni, Mn and Si. The Varvenne et al. model involves the following elastic properties in *Equations (1.8)* and *(1.9)* : Young's modulus (E), Shear modulus (μ) and Poisson's ratio (ν), as well as size parameters like the apparent FCC volume (V^{FCC}) and the Burger's vector (b) of individual elements. In isotropic materials, only two elastic constants are required to evaluate the third one, using *Equation (3.1)*. Burger's vector is evaluated for FCC-apparent system with *Equation (3.2)*.

$$\mu_i = \frac{E_i}{2(1+\nu_i)} \tag{3.1}$$

$$b_i = \frac{(4V_i^{FCC})^{1/3}}{\sqrt{2}} \tag{3.2}$$

To obtain these parameters, we use existing sets of constants for Co, Cr, Fe, Ni, Mn, and we introduce a new one with additional parameter for Si. The first set is the one used by Manescau et al. [29], where elastic constants are extracted from [86]. We implement a second set using our IGP and IMP data from the *MaterialProject*. In this set, the V^{FCC} are estimated from the lattice parameter (a) using the formula $V^{FCC} = a^3/4$. The third set is derived from updated size properties from Coury et al [30] combined with refined elastic parameters from Bracq et al. [31]. Data for silicon were collected from [87] and its apparent FCC volume was measured by X-ray Diffraction (XRD) with two FCC single-phase master alloys, $Ni_{96}Si_4$ and $Ni_{92}Si_8$, produced by Arc melting. *Table 3.3* summarises the values of the three datasets containing Co, Cr, Fe, Ni, Mn elements.

Thèse accessible à l'adresse : https://theses.insa-lyon.fr/publication/2025ISAL0036/these.pdf © [T. Langlois], [2025], INSA Lyon, tous droits réservés

Table 3.3. Different sets of constants for the prediction of solid solution strengthening. (Data reproduced from a: [29]; b: [78]; c: [30], [31])

Manescau Dataset [a]

Parameters	Co	Cr	Fe	Mn	Ni
E [Gpa]	231.7	275.4	127.8	177.6	194.3
μ [Gpa]	81.8	115	60.7	90	70.1
ν	0.416	0.197	0.053	-0.013	0.384
V^{FCC} [Å^3]	11.12	12.27	12.09	12.6	10.94

Dataset from TheMaterialProject [b]

Parameters	Co	Cr	Fe	Mn	Ni
E [Gpa]	270.9	332.8	195.4	193.4	245.1
μ [Gpa]	105	129	74	78	95
ν	0.29	0.29	0.32	0.24	0.29
V^{FCC} [Å^3]	11.07	12.01	11.7	12.2	10.94

Dataset from Coury and Bracq [c]

Parameters	Co	Cr	Fe	Mn	Ni
E [Gpa]	210.5	263.9	139.9	172.1	199.9
μ [Gpa]	81.4	103.5	51.7	81.5	76.3
ν	0.293	0.275	0.353	0.056	0.310
V^{FCC} [Å^3]	10.86	12.45	11.82	12.26	10.44

The other required inputs for this model are the chemical composition, the temperature and the strain rate for deformation $\dot{\varepsilon}$. The chemical compositions are given in mole fraction unit. In this work, we analyse systems from the comparison datasets [86], [30], [88] at room temperature and for a constant strain rate of $\dot{\varepsilon} = 10^{-3}\ s^{-1}$. Subsequently, we focus on the Co-Cr-Fe-Mn-Ni-Si compositional space, conducting calculations at constant strain rate of $\dot{\varepsilon} = 10^{-3}\ s^{-1}$, at room temperature and at 110 K, to evaluate the theoretical evolution of σ_{ss} during our cryogenic tensile tests.

The accuracy of the different sets is analysed by comparing predictions with experimental values for equiatomic compositions measured by Laplanche et al. [86], as well as a broader set of experimental values in C-MPEAs gathered by Coury et al. [30], and an extensive set of alloys from Borg et al [88]. This latter gathers data for over 500

Thèse accessible à l'adresse : https://theses.insa-lyon.fr/publication/2025ISAL0036/these.pdf © [T. Langlois], [2025], INSA Lyon, tous droits réservés

C-MPEAs compositions extracted from 265 publications between 2004 and 2019. Silicon data from the literature [87] and using our XRD data are added to most accurate dataset.

The implementation of this code is performed with python in Jupyter Notebook 6.4., using an open-access toolkit *pySSpredict* developed by Wen et al. [89]. The resulting data can be presented as a simple set of Activation Energy, Shear stress at 0K, Shear stress at current temperature and Solid solution strengthening {ΔE_b (in J); τ_{y0} (in MPa); τ_y (in MPa); σ_{ss} (in MPa)}, or as ternary diagrams for ternary and pseudo-ternary systems (*Figure 3.3-a*) using *MatPlotLib* and *Ternary* python libraries [90]. Additionally, the evolution of the mechanical properties and energy barriers with respect to the strain or temperature can also be visualised (*Figure 3.3-b*).

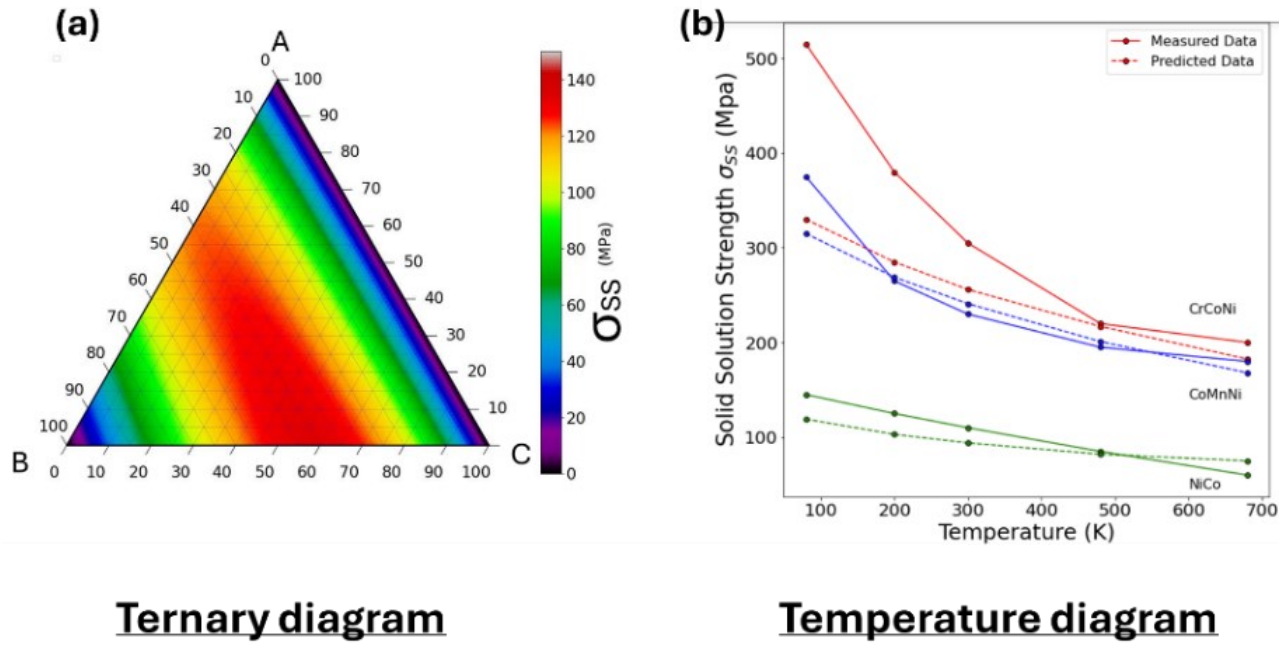


Figure 3.3. Possible representations for the solid solution strengthening predictions.

In summary, we are using σ_{ss} predictions to:

- **Validate the best set of parameters** by comparing σ_{ss} from prediction models and from industrial alloys.
- **Map the Co-Cr-Fe-Mn-Ni-Si** space in the identified FCC regions.
- **Evaluate the effect of cobalt and silicon** on yield strength values at room temperature and cryogenic temperature.

Thèse accessible à l'adresse : https://theses.insa-lyon.fr/publication/2025ISAL0036/these.pdf © [T. Langlois], [2025], INSA Lyon, tous droits réservés

3.2.3 Stacking Fault Energy Prediction models

As explained in the literature, assessing the SFE of a material is crucial for predicting the deformation mechanisms that are likely to occur. We have demonstrated that decreasing SFE values often lead to higher strain-hardening rates due to the activation of specific deformations mechanisms, such as TWIP and TRIP effect, which hinder dislocation movement.

We presented three approaches to estimate SFE values in the literature survey, these includes:

- An **empirical model**, predicting SFE in confined Co-Cr-Ni systems [77].
- A **thermodynamical model**, for Co-Cr-Ni-Si systems [44].
- A **DFT model**, for FCC Co-Cr-Fe-Mn-Ni-V subsystems [39].

Additionally, we discussed the correlation between the critical stress for twinning (τ_{cr}) and the unstable stacking fault (γ_{UTF}) [48]. Assuming that this correlation for pure elements is also valid for alloys, we can estimate τ_{cr} for specific systems with known elastic moduli (C_{ij}) and Burger's vector (b).

Figure 3.4 illustrates our applications of the three models. The empirical model, represented with *Equation (3.3),* gives SFE estimates with a coefficient of determination R^2 of 0.98 [77]. We apply this model in the FCC regions of Co-Cr-Ni subsystems with respect to the atomic fraction of the three elements.

Thèse accessible à l'adresse : https://theses.insa-lyon.fr/publication/2025ISAL0036/these.pdf © [T. Langlois], [2025], INSA Lyon, tous droits réservés

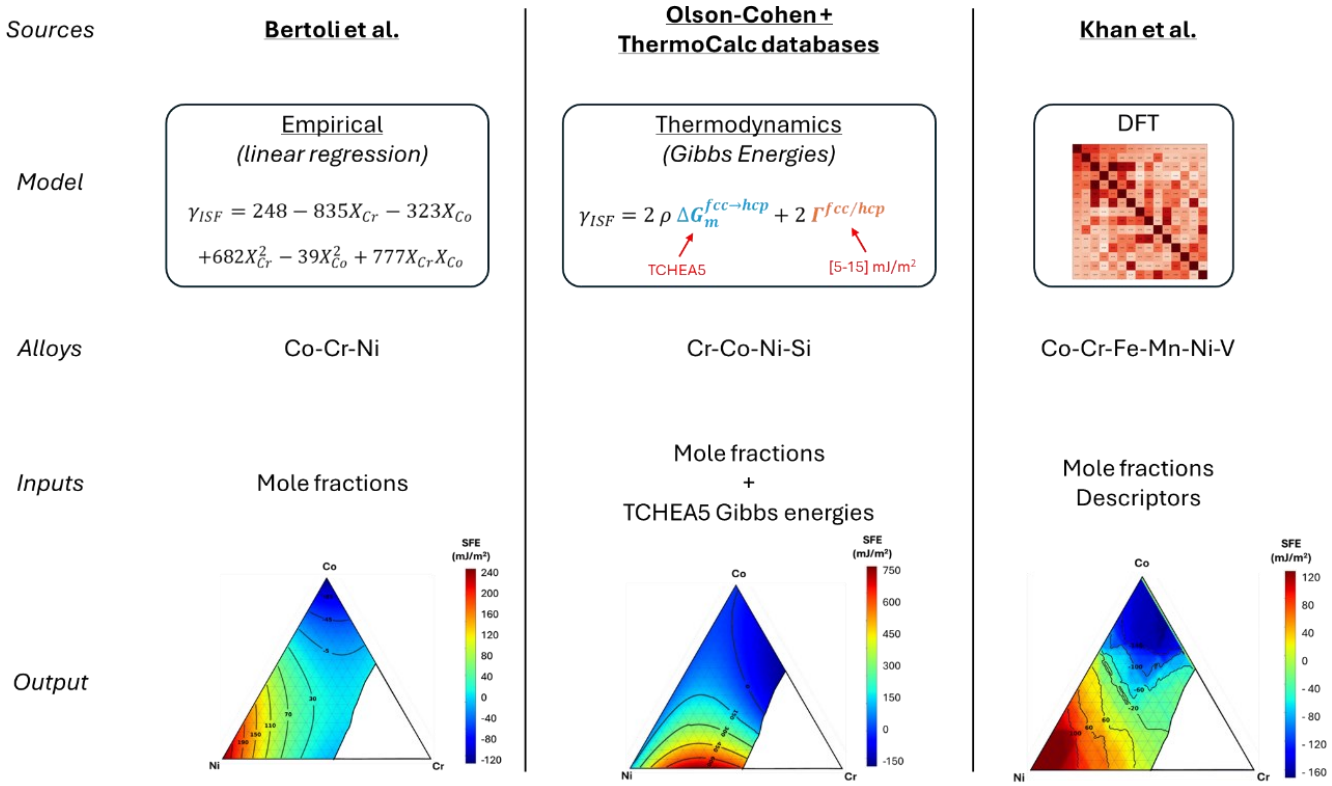


Figure 3.4. General principle of the three SFE predictions models.

$$SFE = 248 - 835X_{Cr} - 323X_{Co} + 682X_{Cr}^2 - 39X_{Co}^2 + 777X_{Cr}X_{Co} \qquad (3.3)$$

The thermodynamical model is based on the Olson-Cohen equation involving Gibbs Energies ($\Delta G_m^{fcc\text{-}hcp}$), obtained using the TCHEA5 database from ThermoCalc. As with phase predictions, the quality of SFE predictions depends on the experimental dataset. The values for the interfacial energy ($\Gamma^{fcc/hcp}$) are reported to range between 5 and 10 mJ/m^2 for FCC alloys, with this parameter being compositionally dependent. Therefore, this term is often used as an adjustment parameter to fit the experimental values. With the TCHEA5 database, predicted SFE values vary significantly from -175 mJ/m^2 to 765 mJ/m^2 and the use of constant values for $\Gamma^{fcc/hcp}$ can introduce an even larger uncertainty. The use of machine learning can significantly improve the accuracy of thermodynamic predictions [91]. We refined the DFT and thermodynamic datasets with GradientBoosting and RandomForrest machine learning algorithms [82]. The different parameters of the datasets are transformed into featurisers, allowing us to identify the best descriptors related to the SFE predictors, as depicted in *Figure 3.5* for the DFT dataset. The final descriptor set includes properties like elastic constants (C12, C'), elemental concentrations (Co, Fe, Ni), thermodynamic values, electronegativity, and specific heat capacity.

Thèse accessible à l'adresse : https://theses.insa-lyon.fr/publication/2025ISAL0036/these.pdf © [T. Langlois], [2025], INSA Lyon, tous droits réservés

With the DFT model, we identified the most influential descriptors using correlation matrix and feature importance scores. With these descriptors, SFE values for new set of compositions in Co-Cr-Ni subsystems are expected within a confident range of $\pm$ 4 mJ/m^2 [39].

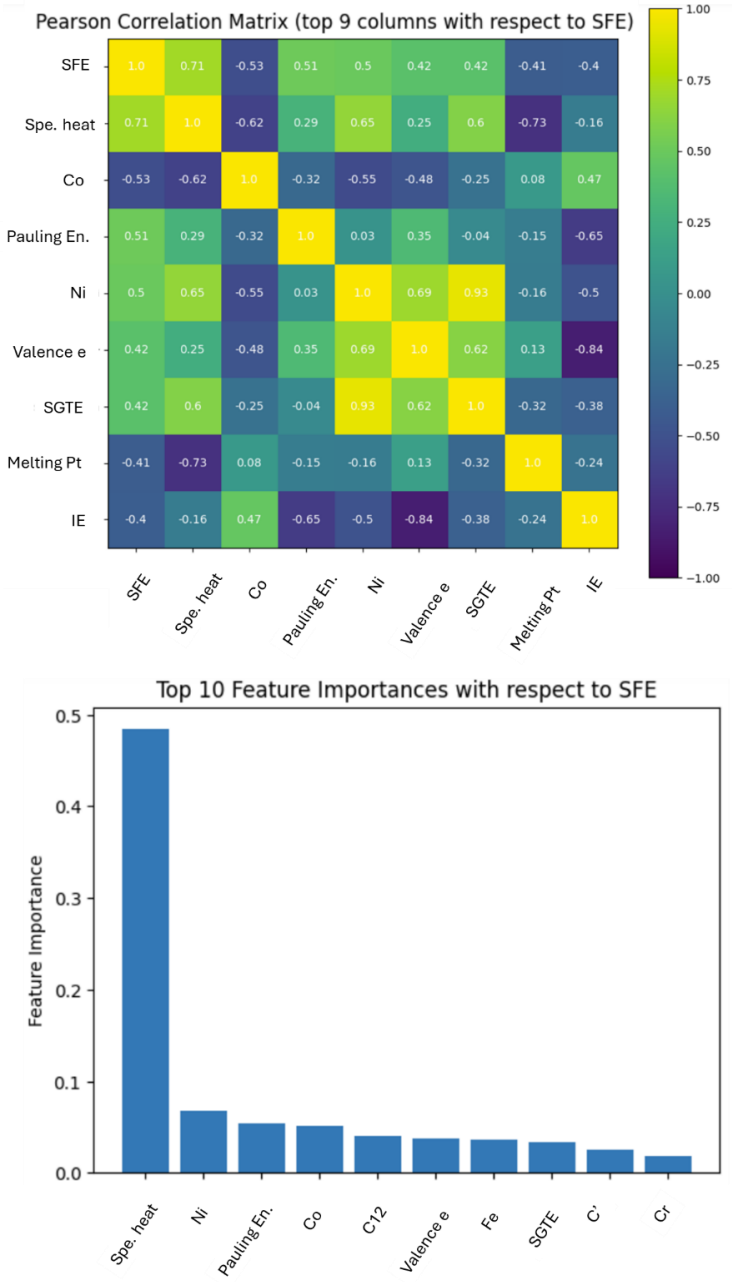


Figure 3.5. Correlated descriptors for SFE (DFT Dataset [39]) Pearson correlation matrix and feature importance diagram.

To evaluate the accuracy of the prediction models, we compiled experimental data from 144 entries and compared them with prediction for the same chemical compositions. Calculations are performed with a python Script on Jupyter Notebook

Thèse accessible à l'adresse : https://theses.insa-lyon.fr/publication/2025ISAL0036/these.pdf © [T. Langlois], [2025], INSA Lyon, tous droits réservés

6.4, with compositions expressed in mole fraction units. *MatPlotLib* and *Ternary* python libraries are used for ternary plots [90]. *SciPy* and *Scikit-learn* libraries are used for ML algorithms [82].

In line with our ambition for smart, high-throughput approach, we initially restricted our study to FCC-regions. Then, we restrict the exploration to FCC-regions with promising solid solution strengthening values, within Co-Cr-Ni-Si subsystems.

In summary, we are using SFE predictions models to:

- **Evaluate the accuracy** of the 3 predictions models compared to experimental values.
- **Map the SFE** values in FCC regions of Cantor Subsystems and predict the deformation mechanisms.
- Assess the **predicted effect of cobalt and silicon** on SFE values.

Thèse accessible à l'adresse : https://theses.insa-lyon.fr/publication/2025ISAL0036/these.pdf © [T. Langlois], [2025], INSA Lyon, tous droits réservés

3.2.4 Modelling the sustainable competitiveness of materials

Incorporating sustainable considerations into material selection and alloy design is crucial, but often underestimated in research. To prioritise sustainable impacts, we developed a counselling tool that estimates a wide range of commercial, environmental, and well-being implications. We believe that each of these considerations has the potential to play a critical factor in guiding future alloy development.

Our approach to defining the sustainable competitiveness of a material is based on the development of economic, environmental and societal criteria. These criteria consider both inherent properties of the material and characteristics of the regions where this material is extracted. We have organised data in matrices using Excel, categorised as follows:

- **Matrix [E]**: Data for pure **elements**.
- **Matrix [C]**: Data for **countries**.
- **Matrix [F]**: Material **flux** (stocks and markets).
- **Matrix [W]**: **Weight percentages** of alloying constituent of materials

First, we collected intrinsic data related to each pure element. These data points are independent of the locations where the materials are extracted or manufactured, and typically correspond to some of the IGP and ISP data from our MaterialProject dataset. The second type of data is country related, assuming that certain sustainable criteria for materials depends on the extraction location. However, all indicators remain global, and variation may occur in specific case. For instance, the price of a particular element might fluctuate based on the availability of an industrial by-products. *Table 3.4* presents a non-exhaustive list of the indexes considered in our sustainable alloy design approach.

Thèse accessible à l'adresse : https://theses.insa-lyon.fr/publication/2025ISAL0036/these.pdf © [T. Langlois], [2025], INSA Lyon, tous droits réservés

Table 3.4. Sample list of sustainable implications.

	Data for material	**Data for country**
Environmental criteria	Carbon footprint Embodied energy Recycling rate Substitutability Toxicity ...	GDP Employment School enrolment R&D ...
Economic criteria	Price Abundance Annual production Supply risk Material concentration ...	Biodiversity Agriculture Resource management (Material, energy, water, pollution) ...
Societal criteria	Safety and risks ...	HDI Healthcare system Governance ...

Abbreviations: GDP = Gross Domestic Product / R&D = Research and Development / HDI = Humand Development Index

Overall, we retrieved intrinsic data for 118 pure elements from various sources [92], [93], [94], [95], stored in matrix **[E]**. Sustainable data for 180 countries were sourced from the *Solability think-tank* [96], organised in matrix **[C]**. We collected data on the export flux of raw materials, to connect country-specific data with materials [97], [98], [94], [99], stored in matrix **[F]**. Finally, the weight fractions of industrial alloys and pure elements (viewed as alloys with a weight fraction of 100%) are stored in matrix **[W]**.

The comprehensive elemental data enabled us to identify correlations between various indicators, as illustrated in *Figure 3.6*. This analysis helped us extract key elemental indicators that we believe encompass the diverse economic, social and environmental implications of materials. These main indicators are presented in *Table 3.5*. Further details on our indicators are given in our publication [100].

Thèse accessible à l'adresse : https://theses.insa-lyon.fr/publication/2025ISAL0036/these.pdf © [T. Langlois], [2025], INSA Lyon, tous droits réservés

Table 3.5. Description of the 9 main indictors for sustainable implications.

Indicator	Name	Abbrev.	Description
Environment	Embodied Energy	EE	Total energy required for producing a metal from its ores, including extraction, production, and transportation.
	Water Usage	WU	Total amount of water consumed in the extraction and production processes of an alloy.
	Rock-to-Metal	RMR	Measure of the environmental impact of mining, indicating the amount of waste rock and ore mined to produce a unit of refined metal. A higher ratio signifies greater land disturbance and environmental degradation.
Economy	Material Price	MP	Cost of an alloying element in its pure form, used as a proxy for alloying costs, often representing the upper estimate since master alloys and recycled materials may be cheaper.
	Supply Risk	SR	Indicator reflecting the likelihood of supply disruptions due to geopolitical issues, export quotas, resource nationalism, and natural disasters, based on Graedel et al.
	Normalised Vulnerability to Supply Risk	NVSR	A measure of how critical an element is, adjusted by the logarithmic production volume to reflect its scarcity. This normalization considers the impact of additional demand relative to the existing supply, with greater recycling potential when larger quantities are already in circulation. For example, iron's vulnerability is high but has less economic impact per unit than a rarer element like neodymium with this normalisation.
Society	Human Health Damage	HHD	Measure of the impact of metals on human well-being, based on the ReCiPe endpoint methodology. It includes effects from climate change, ozone depletion, human toxicity, photochemical oxidant and particulate matter formation, and ionizing radiation.
	Child Labour	CL	Measure of the children percentage engaged in child labor. Higher values indicate a greater reliance on child labor, often associated with significant social costs, including the deprivation of education and the loss of childhood for the children involved. Sourced from UNICEF
	Corruption	COR	Indicator based on the "Control of corruption" metric from World Bank, which captures perceptions of the extent to which public power is used for private gain. Corruption is averaging the inverse of the latter metric score for extracting and mining countries.

Thèse accessible à l'adresse : https://theses.insa-lyon.fr/publication/2025ISAL0036/these.pdf © [T. Langlois], [2025], INSA Lyon, tous droits réservés

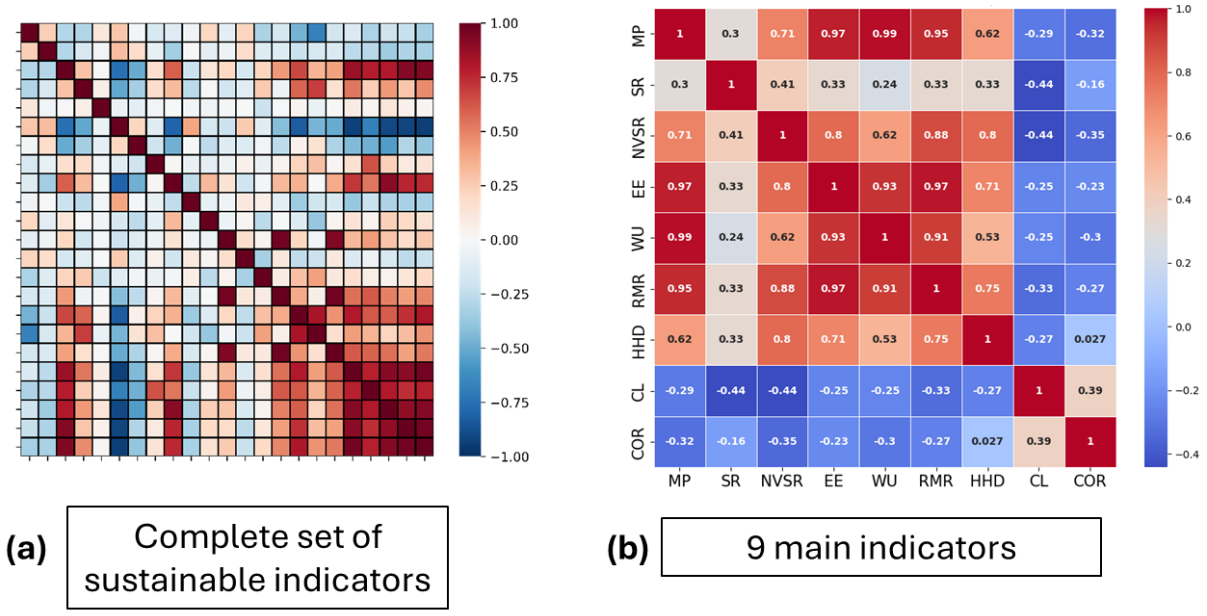


Figure 3.6. Correlation heatmaps with the sustainable indicators for elements. (a) Overall correlations (b) Correlation heatmap within the selected indicators (abbreviations are explained in *Table 3.5*).

Missing data for the selected criteria are shown in *Figure 3.7*. While some data gaps exist for the selected criteria, our dataset is nearly complete for 73 elements, including the most used metallic and post-transition elements. The correlation matrix in *Figure 3.6-a* is useful for inferring missing data using *Scikit-learn* python library for machine learning algorithms. Full datasets were finally rescaled from 0 to 100, where higher values represent more negative sustainability implications. This normalisation was performed using *RobustScaler* and *MinMaxScaler* from Scikit-learn, ensuring that the elemental data scores are appropriately balanced on the overall normalised scale.

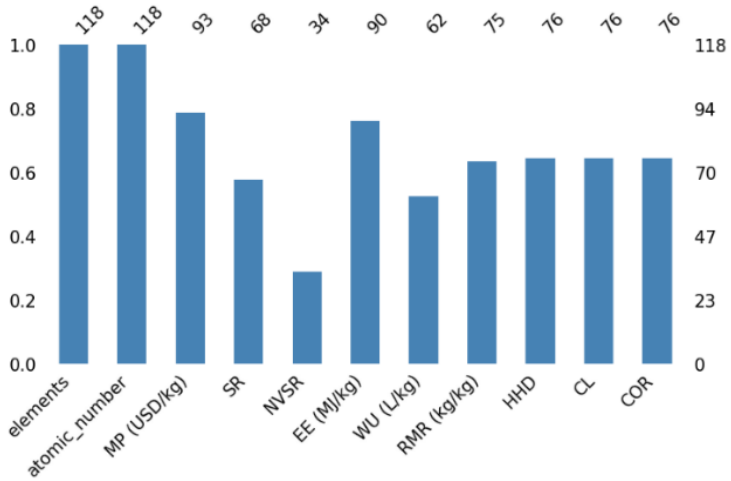


Figure 3.7. Missing data in the elemental dataset (The left vertical axis ranges from 0 to 1, where 1 denotes 100% completeness of data. The right vertical axis indicates absolute size of the dataset and ranges from 0 to 118, the latter value equals to the number of chemical elements).

Thèse accessible à l'adresse : https://theses.insa-lyon.fr/publication/2025ISAL0036/these.pdf © [T. Langlois], [2025], INSA Lyon, tous droits réservés

Excel was used both for storing the data and for performing calculations between the four matrices **[E]**, **[C]**, **[F]** and **[W]**. Given that flux and exchanges of materials are commonly measured in tonnes, it is convenient to use mass unit in this model. We implemented calculation rules to evaluate the sustainable scores for an alloy, weighted by the mass fraction of its constituent elements. The sustainable scores for alloys are stored in the matrix **[A]**. The calculation rules to obtain [A] are the following:

- For each indicator in [E] or [C], we have rescaled the data from 0 to 100 (best value to worst value). For instance, expensive materials have a low score regarding the "material price" index.
- $A_{[E]}$: Alloy value for any environmental, social or economic indicator of [E] can be obtained using *Equation (3.4)*.
- $A_{[C]}$: Alloy value for any environmental, social or economic indicator of [C] can be obtained using *Equation (3.5)* except for the Supply Risk indictor (SR) given by *Equation (3.6)*.

$$A_{[E]} = \sum_{i=1}^{118} w_i * E_i \tag{3.4}$$

$$A_{[C]} = \sum_{i=1}^{118} w_i * \left(\sum_{j=1}^{180} f_{i,j} * C_j \right) \tag{3.5}$$

$$SR\ (alloy) = 1 - \prod_i (1 - SR_{(i)}) \tag{3.6}$$

Where E_i is any elemental index and w_i is the mass fraction of the element i. C_j is any country index and $f_{i,j}$ the fraction of the element i produced in country j. The SR of an alloy depends on the constitutive elements that it is made of, they have their own $SR_{(i)}$. The higher the number of constitutive elements, the higher the risk of supply disruption. Therefore, we treat SR as a probability of disruption.

The calculation process can be visualised either from the perspective of individual indices or from the matrices, as represented in *Figure 3.12 a and Figure 3.12 b*. We create the matrices $[A]_{[E]}$ and $[A]_{[C]}$ that store the alloy sustainable score from elemental data and country data, respectively. Hence, $\mathbf{[A]_{[E]}} = \mathbf{[W]*[E]}$, $\mathbf{[A]_{[C]}} = \mathbf{[W]*[F]*[E]}$ and $\mathbf{[A]} = \mathbf{[A]_{[E]}} + \mathbf{[A]_{[C]}}$.

Thèse accessible à l'adresse : https://theses.insa-lyon.fr/publication/2025ISAL0036/these.pdf © [T. Langlois], [2025], INSA Lyon, tous droits réservés

In preparation for deploying our counselling tool online for the scientific community, we represented the data by raw materials, countries and alloys with suitable visuals using python codes in Jupyter Notebook 6.4.

We found it particularly useful to visualise elemental data in **[E]** using periodic tables using the *Periodic_ Trends* python script developed by A.S. Rosen [101]. We also used the *Dash* python library to create an interactive interface. This way, the user can compare different elements and browse the [E] dataset. As an example, *Figure 3.8.* illustrates the price of raw materials in a periodic table.

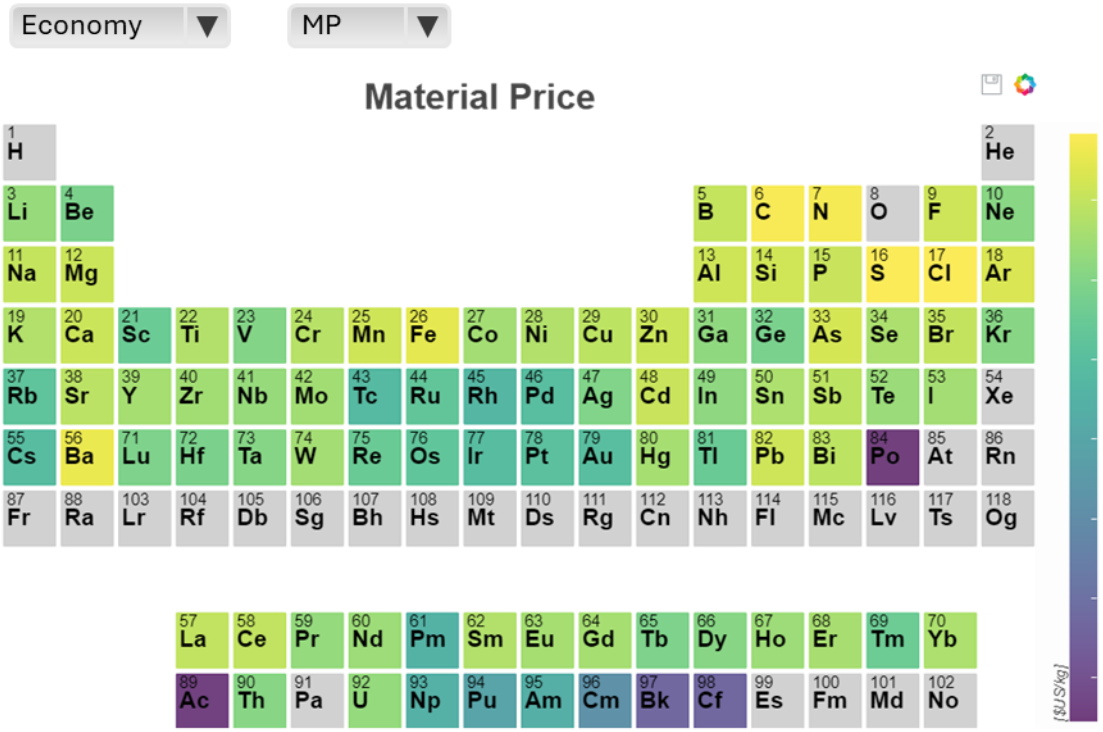


Figure 3.8. Periodic table for Material Price (US$/kg) (Elements in grey represent missing data that are subsequently infer by machine learning).

It is important to note that [E], [C], [F], [W] data are fluctuating throughout time. In this report, values are taken as for 2022. It would be necessary to update the databases for more recent or future analyses.

Similarly, representing Countries Data **[C]** with a world map is helpful for visualise important information. We implemented a python code that can dynamically display country criteria on an interactive world map, using *Dash* and *Plotly* python libraries, as illustrated in Figure 3.9 where the intellectual capital is shown.

Thèse accessible à l'adresse : https://theses.insa-lyon.fr/publication/2025ISAL0036/these.pdf © [T. Langlois], [2025], INSA Lyon, tous droits réservés

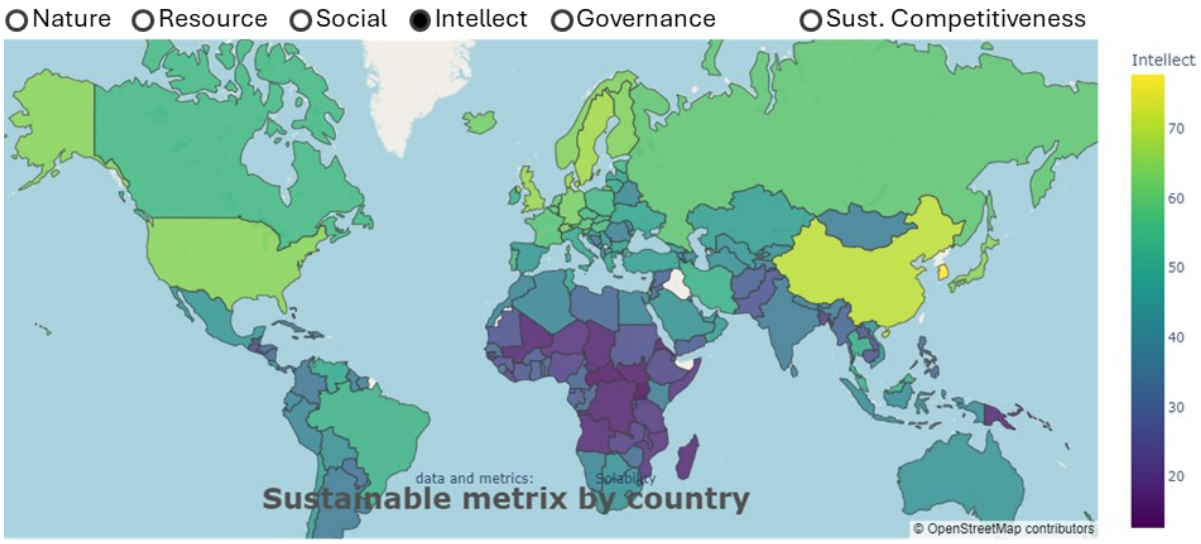


Figure 3.9. World map of the intellectual capital from matrix [C] (from Solability [96]).

For material origins and flux **[F]**, we implemented a python code to plot global market shares of raw materials and industrial alloys, as shown *Figure 3.10* and *Figure 3.11*, respectively. This allows users to trace the origin of resources required in materials.

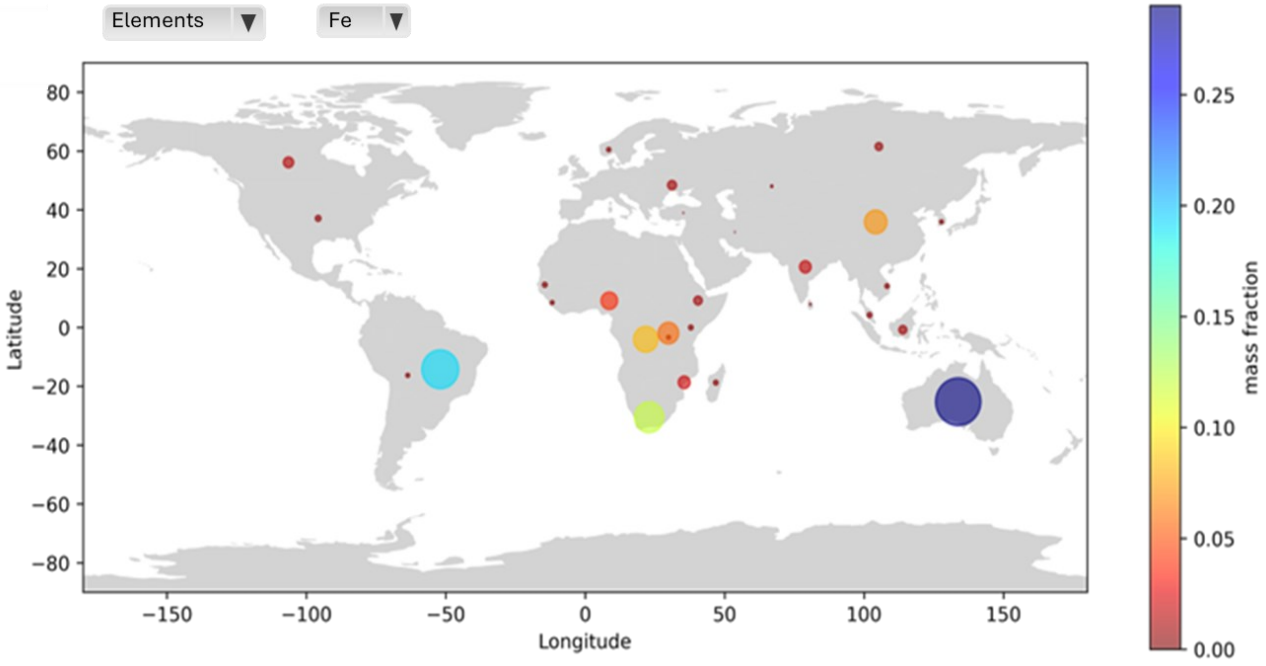


Figure 3.10. World map of the origins and flux of Iron from matrix [F].

Thèse accessible à l'adresse : https://theses.insa-lyon.fr/publication/2025ISAL0036/these.pdf © [T. Langlois], [2025], INSA Lyon, tous droits réservés

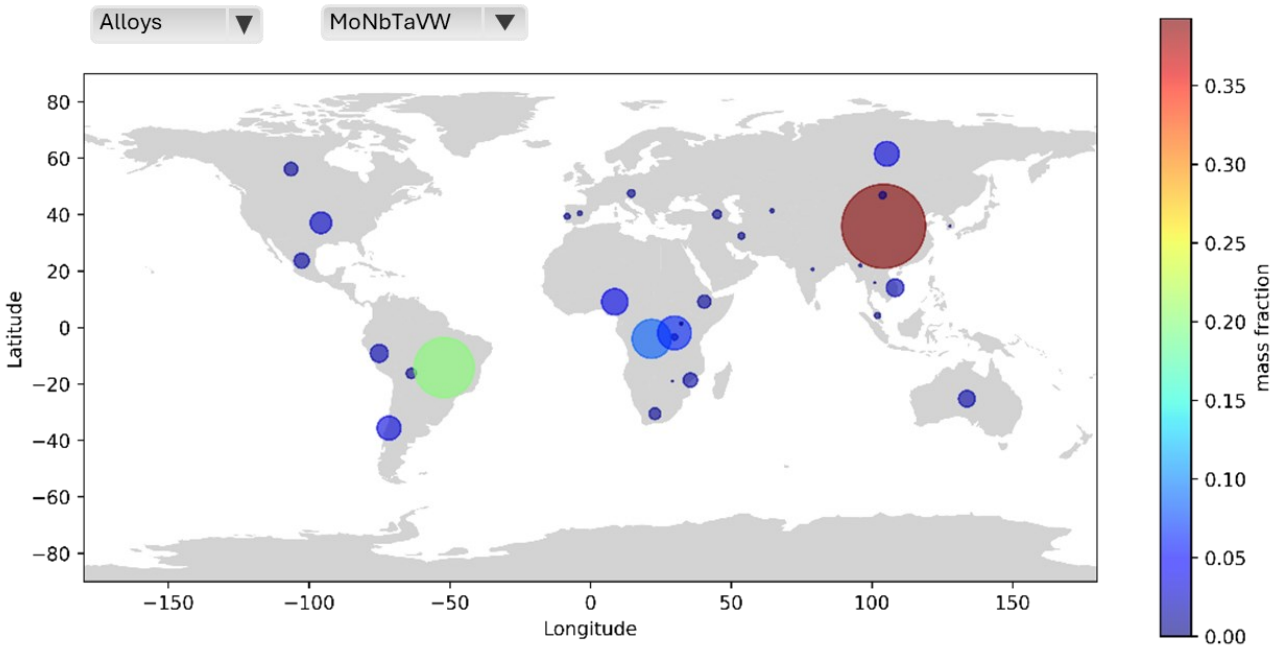


Figure 3.11. World map of the origins and flux of MoNbTaVW alloy from matrix [F].

[NB: colour scales are inverted between raw elements and alloys]

The obtained values in **[A]** vary significantly across materials, making them useful for differentiation and guiding focused research avenues. This sustainable dataset has been useful to perform calculations on different classes of metals using the database from Gorsse et al. [102] [103], and perform a mechanical-sustainable analysis on 340 MPEAs, Ni-superalloys and steels [104]. In this project, we focus the sustainable exploration on Cantor subsystems and on Co-Cr-Ni subsystem. The resulting data can be presented in various formats, such as box plots to compare different alloy classes or radar diagrams to assess the effect of individual alloy elements on the overall alloy score. The overall workflow for this sustainable model is illustrated in *Figure 3.12.* To discuss about the detrimental impact of a material or alloy, we often employ the term "footprint" of this material.

Thèse accessible à l'adresse : https://theses.insa-lyon.fr/publication/2025ISAL0036/these.pdf © [T. Langlois], [2025], INSA Lyon, tous droits réservés

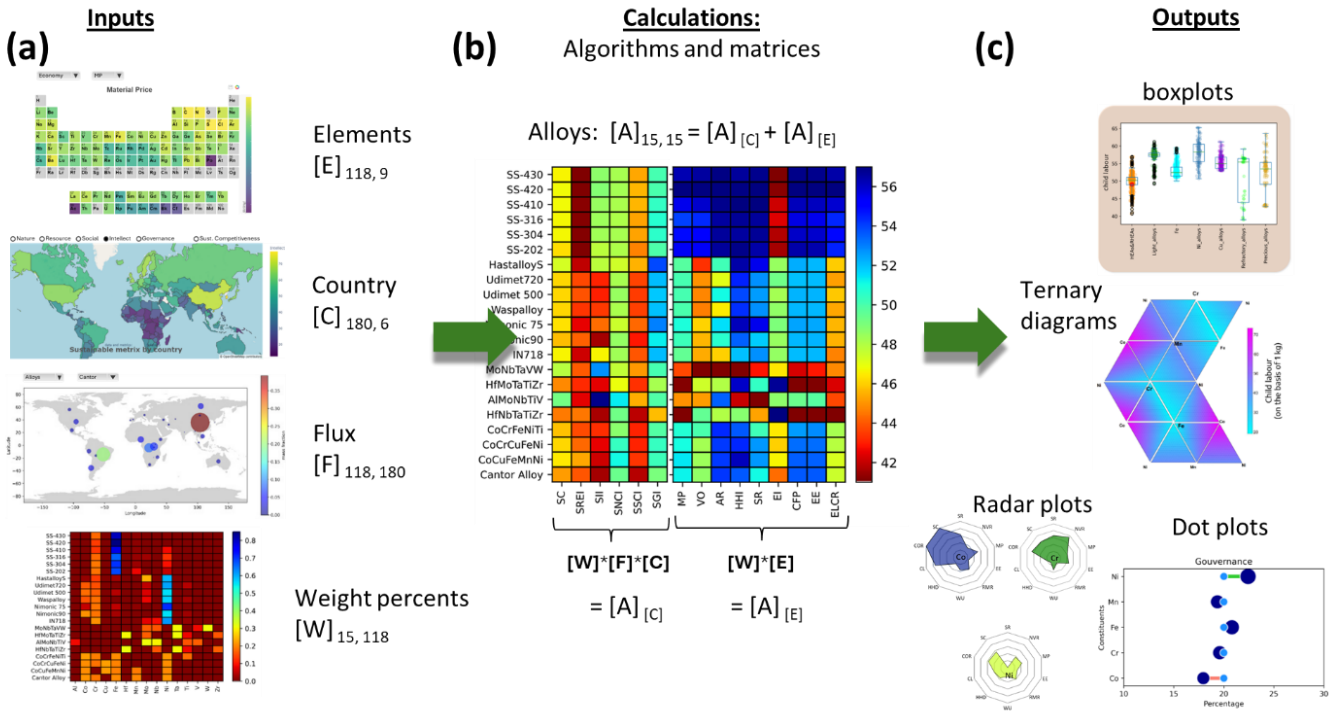


Figure 3.12. Workflow of the sustainable modelling.

In summary, using element data, country-specific data, flux and material compositions, we have developed a numerical model to evaluate the sustainable competitiveness of different materials. We aim to use this tool to:

- Compare the **sustainable competitiveness** of different classes of materials, including Ni-superalloys and MPEAs.
- Evaluate the **individual effect of elemental addition** in MPEAs.
- Cross-reference this numerical model with our mechanical prediction to assess the **mutual influence of sustainability and performance**.
- **Identify optimised compositions** in C-MPEAs that balance mechanical performance and sustainable competitiveness.

Thèse accessible à l'adresse : https://theses.insa-lyon.fr/publication/2025ISAL0036/these.pdf © [T. Langlois], [2025], INSA Lyon, tous droits réservés

3.3 Experimental methods

After predicting material properties with mechanical and sustainability considerations, this allowed us to identify the most promising systems with the best balance. The results of chemical analysis will be discussed in Chapter 5. In the current section, we introduce the different experimental methods used for the sample preparation, ranging from the organisation of raw materials to final microstructural characterisation, to assess their actual mechanical properties. The Fast Alloy (FA) process and the development of more advanced alloys involve similar and different experimental techniques, which we will also mention in this section.

To provide an overview, the main production process involves various casting techniques to produce small samples for the high-throughput exploration and larger samples for advanced elaboration. Thermal treatments were performed in furnaces, and mechanical treatments were conducted using rolling process. The metallographic methods employed in this project, involved cutting, mounting, grinding and polishing to prepare sample surfaces for microstructural characterisation or mechanical testing. SEM techniques were used to analyse the microstructure, assess grain size and examine homogeneity. Phase analysis using XRD was performed to verify single-phase FCC microstructures. Finally, various mechanical tests were conducted to evaluate mechanical properties of the materials such as hardness, yield strength, tensile strength, strain-hardening rate, compressive strength, stacking fault energy, and material toughness.

3.3.1 Choice of raw materials

As explained above, the choice of pure elements for the experimental part of this project is detailed in Chapter 3. Here, we will only mention the selected target compositions and the handling of raw materials.

Using our four predictive models, we aim to analyse the evolution of mechanical properties in the following Cantor subsystems (C-MPEAs):

- $\mathbf{(CrNi)_{100-x}Co_x}$ systems with x = {10, 20, 33, 40, 50}, to study the influence of cobalt. For simplicity, we refer to these systems as **Co10**, **Co20**, **Co33**, **Co40** and **Co50**, respectively.

Thèse accessible à l'adresse : https://theses.insa-lyon.fr/publication/2025ISAL0036/these.pdf © [T. Langlois], [2025], INSA Lyon, tous droits réservés

- $\mathbf{(Cr_{40}Co_{20}Ni_{40})_{100-x}Si_x}$ with x = {0, 3, 6, 9}, to examine the effect of silicon and compensate for the change in mechanical properties due to lower cobalt content. For simplicity, we refer to these systems as **Co20**, **Co20Si3**, **Co20Si6** and **Co20Si9**, respectively.

- $\mathbf{(Cr_{45}Co_{10}Ni_{45})_{100-x}Si_x}$ with x = {0, 3, 6, 9}, to examine the effect of silicon and compensate for the change in mechanical properties at the lowest cobalt content. For simplicity, we refer to these systems as **Co10**, **Co10Si3**, **Co10Si6** and **Co10Si9**, respectively.

The corresponding targeted chemical compositions, in atomic percentages, are given in *Table 3.6*.

Table 3.6. Selected compositions.

Alloy name	sample name	target composition (at%)			
		Cr	Ni	Co	Si
$Cr_{25}Co_{50}Ni_{25}$	Co50	25	50	25	0
$Cr_{30}Co_{40}Ni_{30}$	Co40	30	40	30	0
$Cr_{33}Co_{33}Ni_{33}$	Co33	33.33	33.33	33.33	0.0
$(Cr_{33}Co_{33}Ni_{33})Si_6$	Co33Si6	31.33	31.33	31.33	6.0
$Cr_{40}Co_{20}Ni_{40}$	Co20	40.0	40.0	20.0	0.0
$(Cr_{40}Co_{20}Ni_{40})Si_1$	Co20Si1	39.6	39.6	19.8	1.0
$(Cr_{40}Co_{20}Ni_{40})Si_2$	Co20Si2	39.2	39.2	19.6	2.0
$(Cr_{40}Co_{20}Ni_{40})Si_3$	Co20Si3	38.8	38.8	19.4	3.0
$(Cr_{40}Co_{20}Ni_{40})Si_6$	Co20Si6	37.6	37.6	18.8	6.0
$(Cr_{40}Co_{20}Ni_{40})Si_9$	Co20Si9	36.4	36.4	18.2	9.0
$Cr_{45}Co_{10}Ni_{45}$	Co10	45.0	45.0	10.0	0.0
$(Cr_{45}Co_{10}Ni_{45})Si_1$	Co10Si1	44.55	44.55	9.9	1.0
$(Cr_{45}Co_{10}Ni_{45})Si_2$	Co10Si2	44.1	44.1	9.8	2.0
$(Cr_{45}Co_{10}Ni_{45})Si_3$	Co10Si3	43.65	43.65	9.7	3.0
$(Cr_{45}Co_{10}Ni_{45})Si_6$	Co10Si6	42.3	42.3	9.4	6.0
$(Cr_{45}Co_{10}Ni_{45})Si_9$	Co10Si9	40.95	40.95	9.1	9.0

Raw materials used in this project are available at Deakin IFM. Bulk Co and Ni are purchased from Dickinson Metallurgical Supplies (Australia), Bulk Cr and Si from Cast Metal Services (Australia), and all material chips are purchased from the Shanghai Metal Corporation (China). Special care was taken in their preparation to minimise contamination risks and achieve the target compositions as closely as possible, using cleaned equipment and nitrile gloves at every step of preparation. Raw materials were

Thèse accessible à l'adresse : https://theses.insa-lyon.fr/publication/2025ISAL0036/these.pdf © [T. Langlois], [2025], INSA Lyon, tous droits réservés

available in bulk blocks or smaller chips (*Figure 3.13-a*), with respective purity levels displayed in *Table 3.7*. They were carefully hand-picked, avoiding parts with visible contamination. Their surfaces were ground with 240-grit silicon carbide abrasive discs (Hermes, Germany), as depicted in *Figure 3.13-b*. Subsequent cutting of the largest block was performed with an Accutom-100 equipped with a Cut-off Wheel 50A15 containing Al_2O_3 (Struers, Denmark) and crushing with a hydraulic press (HPT30P; Hare&Forbes Machineryhouse, Australia). They were cleaned in an ultrasonic bath with ethanol to remove any contamination. They were finally dried thoroughly and stored in a designated desiccator to remove any potential moisture and humidity.

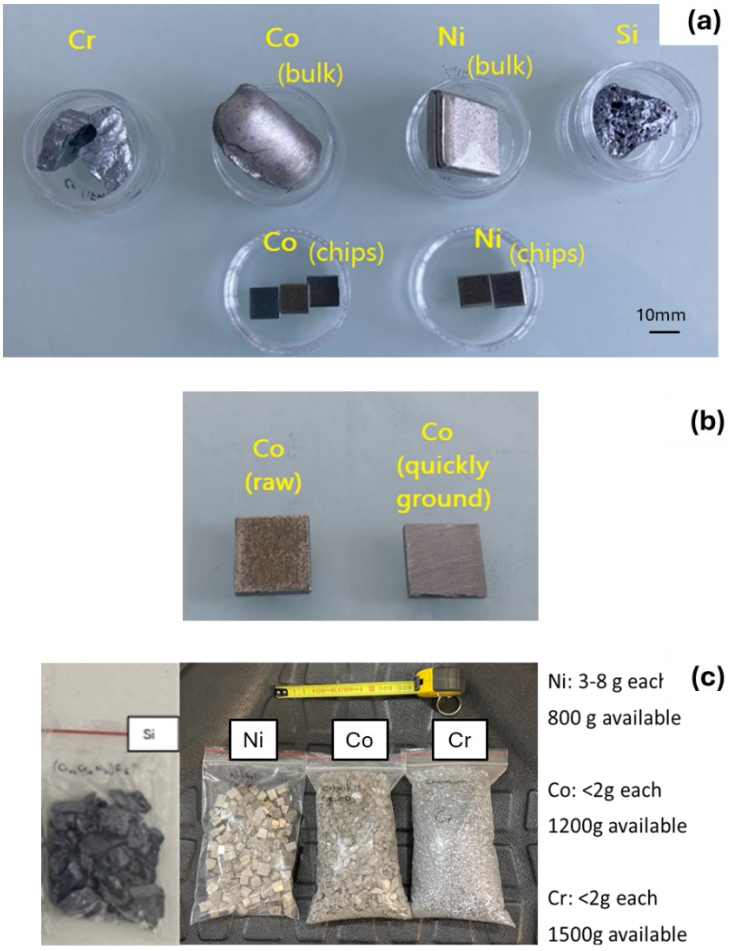


Figure 3.13. Raw materials at IFM: (a) Different shapes; (b) Grinding; (c) Prepared materials after cutting, crushing and cleaning.

Based on these atomic percentages, the desired masses of raw elements were calculated using our conversion table, documented in *Figure 0.1* in the Appendix of Chapter 3. These masses were measured from the prepared raw materials using a precision digital scale (50grams precision scale; TODO, Australia). The scale was calibrated prior to use to ensure an accuracy of 0.001 grams.

Thèse accessible à l'adresse : https://theses.insa-lyon.fr/publication/2025ISAL0036/these.pdf © [T. Langlois], [2025], INSA Lyon, tous droits réservés

Table 3.7. Purity of the raw materials used at Deakin IFM (Data provided by the suppliers. C, O, N and H concentrations in the raw materials are measured later in the manuscript).

Element	Type	Purity (wt.%)
Chromium	Bulk	99.1
Cobalt	Bulk	99.37
	Chip	99.99
Nickel	Bulk	99.8
	Chip	99.9
Silicon	Bulk	99.8

Raw materials were then ready for casting and stored in sealed bags. Shortly after weighing, they were transported to the manufacturing laboratory.

3.3.2 Manufacturing Methods

As outlined in the project motivation, the initial plan was to use the additive manufacturing for the FA process, with a gradient of composition to characterise a broader range of compositions. However, due to technical issues, the LENS machine designed for Laser Metal Deposition (LMD) manufacturing was under maintenance. As a result, we had to adopt alternative casting processes. The following manufacturing techniques were employed:

- Arc melting and casting of **small-sized** specimens, referred to as **Arc50**. These specimens were used for the Fast alloy (FA) method.
- Arc melting and casting of **medium-sized** ingots, referred to as **Arc200**. These ingots were subsequently thermomechanically treated to produce tensile dog-boned specimens (TDB) for tensile tests.
- Induction melting and casting of **large-sized** ingots, referred to as **Ind500**. These ingots underwent thermomechanical treatments to produce Charpy V-Notch specimens (CVN) for impact tests.

Table 3.8 lists the C-MPEA compositions manufactured by Arc 50 (FA compression), Arc200 (TDB) and Ind500 (CVN), respectively. Some samples were not tested due to manufacturing issues, which are discussed in the dedicated sections.

Thèse accessible à l'adresse : https://theses.insa-lyon.fr/publication/2025ISAL0036/these.pdf © [T. Langlois], [2025], INSA Lyon, tous droits réservés

Table 3.8. Synthesised compositions at Deakin IFM.

Alloy name	sample name	target composition (at%) Cr	Ni	Co	Si	Fast alloys compression	Advanced alloys tensile / impact test	
$Cr_{25}Co_{50}Ni_{25}$	**Co50**	25	50	25	0	■		
$Cr_{30}Co_{40}Ni_{30}$	**Co40**	30	40	30	0	■		
$Cr_{33}Co_{33}Ni_{33}$	**Co33**	33.33	33.33	33.33	0.0	■	■	■
$(Cr_{33}Co_{33}Ni_{33})Si_6$	**Co33Si6**	31.33	31.33	31.33	6.0	■	■	
$Cr_{40}Co_{20}Ni_{40}$	**Co20**	40.0	40.0	20.0	0.0	■		■
$(Cr_{40}Co_{20}Ni_{40})Si_1$	**Co20Si1**	39.6	39.6	19.8	1.0	■		
$(Cr_{40}Co_{20}Ni_{40})Si_2$	**Co20Si2**	39.2	39.2	19.6	2.0	■		
$(Cr_{40}Co_{20}Ni_{40})Si_3$	**Co20Si3**	38.8	38.8	19.4	3.0	■		
$(Cr_{40}Co_{20}Ni_{40})Si_6$	**Co20Si6**	37.6	37.6	18.8	6.0	■		
$(Cr_{40}Co_{20}Ni_{40})Si_9$	**Co20Si9**	36.4	36.4	18.2	9.0	■		
$Cr_{45}Co_{10}Ni_{45}$	**Co10**	45.0	45.0	10.0	0.0	■	■	■
$(Cr_{45}Co_{10}Ni_{45})Si_1$	**Co10Si1**	44.55	44.55	9.9	1.0	■		
$(Cr_{45}Co_{10}Ni_{45})Si_2$	**Co10Si2**	44.1	44.1	9.8	2.0	■		
$(Cr_{45}Co_{10}Ni_{45})Si_3$	**Co10Si3**	43.65	43.65	9.7	3.0	■		
$(Cr_{45}Co_{10}Ni_{45})Si_6$	**Co10Si6**	42.3	42.3	9.4	6.0	■	■	■
$(Cr_{45}Co_{10}Ni_{45})Si_9$	**Co10Si9**	40.95	40.95	9.1	9.0	■		■

Figure 3.14-a and *Figure 3.14-b* illustrate the principles of arc melting [105] and induction melting [106], respectively.

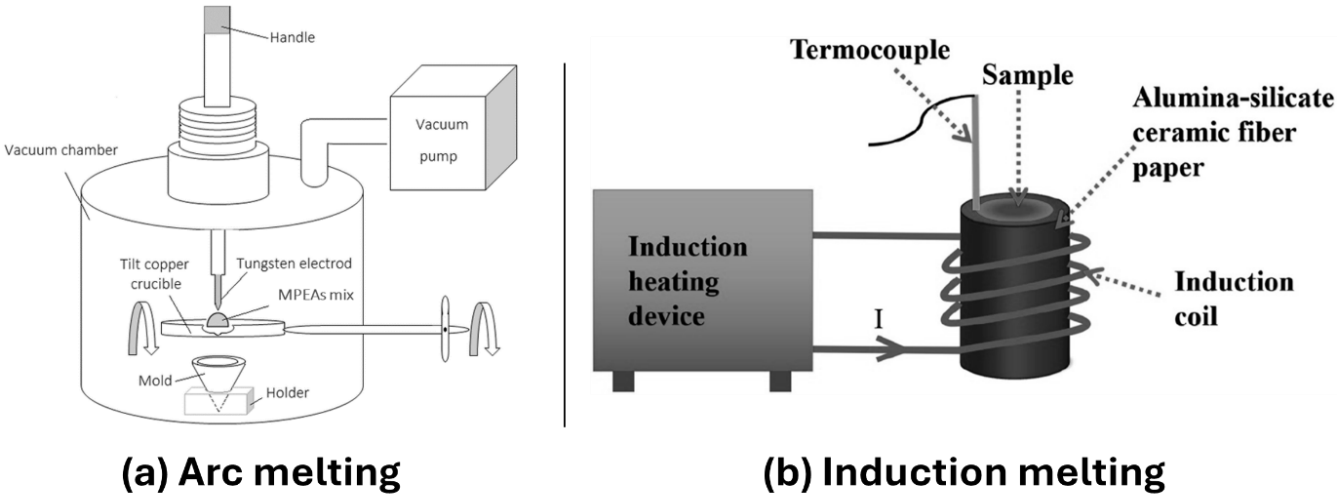


Figure 3.14. Descriptive diagrams of (a) Arc melting and (b) Induction melting (redrawn from [105] and [106]).

The manufacturing of **small-sized specimens (Arc50)** was performed within a vacuum arc melter with water-cooled copper crucible (Micro Vacuum Arc Melter; Arcast Inc, USA), optimised for the melting of 50 grams of raw materials. Argon was supplied to the melting chamber with compressed Argon Grade 4.7 bottle (Argon ≥ 99.997%). System checks were conducted, and the cleanliness of equipment is also verified. The Arc50 system is illustrated in *Figure 3.15*.

Thèse accessible à l'adresse : https://theses.insa-lyon.fr/publication/2025ISAL0036/these.pdf © [T. Langlois], [2025], INSA Lyon, tous droits réservés

12 to 15 grams of the prepared raw materials were placed into the melting area and mixed, with larger parts on top to prevent smaller parts from being ejected during melting. A piece of titanium was inserted in the centre of the copper crucible, acting as an oxygen getter. Once the chamber was closed, five purging cycles of the chamber environment were performed, alternating between Argon and vacuum. After purging, medium vacuum was applied to reach a pressure below 10^{-2} mbar.

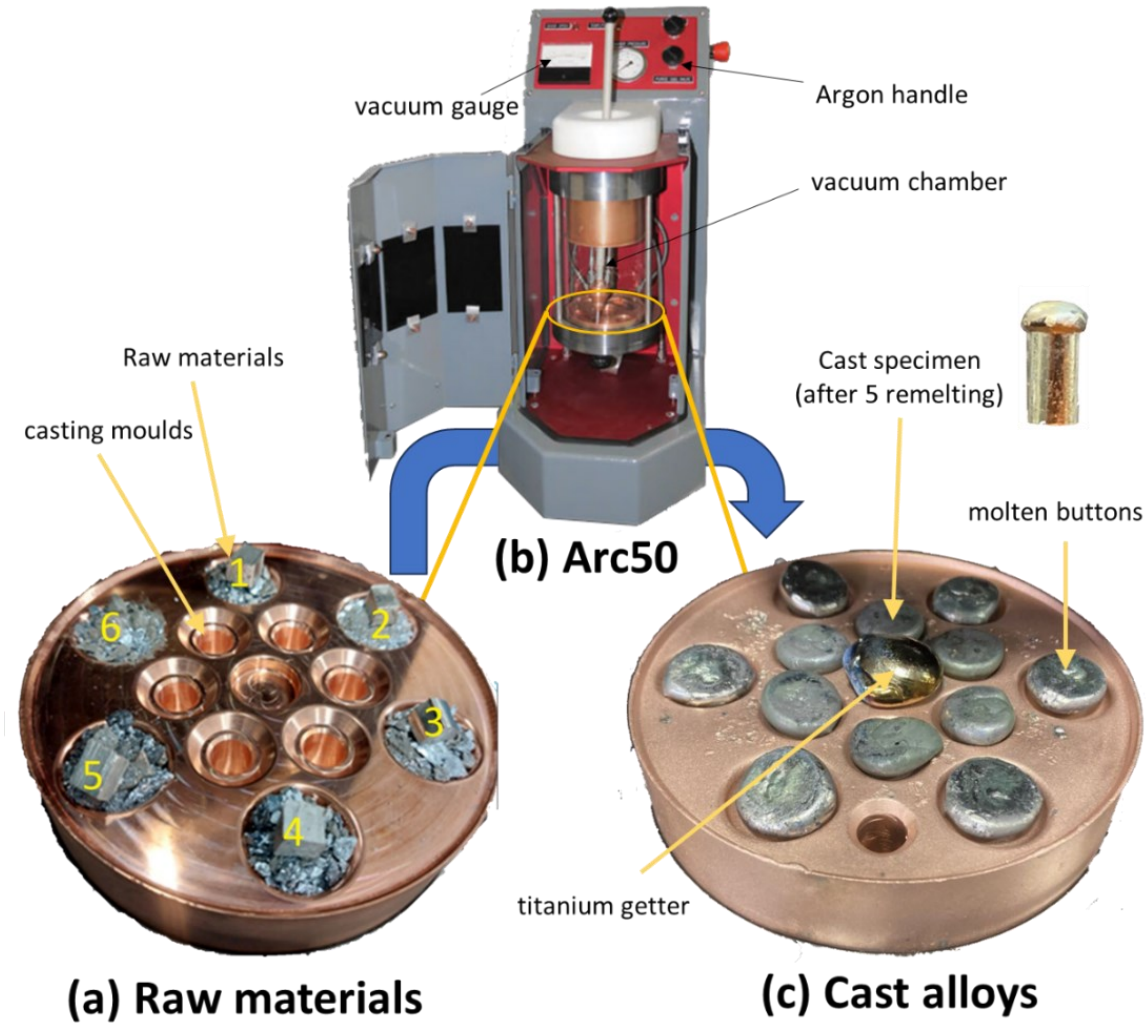


Figure 3.15. Arc50 melting and casting furnace equipped with a copper crucible.

The raw materials were subsequently melted with a tungsten electrode and the titanium getter absorbs stray gases in the chamber. The obtained buttons were flipped and re-melted at least five times to promote thorough mixing and are drop-cast into moulds to produce cylinders with a diameter of 10 mm and a length of 15 mm (*Figure 3.16*). Specimens with any visible defect like shrinkage or incomplete melting of raw pieces are re-melted.

Thèse accessible à l'adresse : https://theses.insa-lyon.fr/publication/2025ISAL0036/these.pdf © [T. Langlois], [2025], INSA Lyon, tous droits réservés



Figure 3.16. Geometry and dimensions of a cylinder specimen produced with Arc50.

The manufacturing of **medium-sized ingots (Arc200)** was performed in a water-cooled hemispherical copper crucible inside a furnace (Arc200 Furnace; Arcast inc., USA). The chamber was sealed and purged under Argon 4.7. 150 to 200 grams of pure materials are melted under a high vacuum of 10^{-5} mbar. An electromagnetic stirring system allowed for better mixing of the melted materials, which were flipped over and re-melted five times. The liquid mixture was then tilt-cast into specific rectangular moulds, whose dimensions are given in *Figure 3.17*.

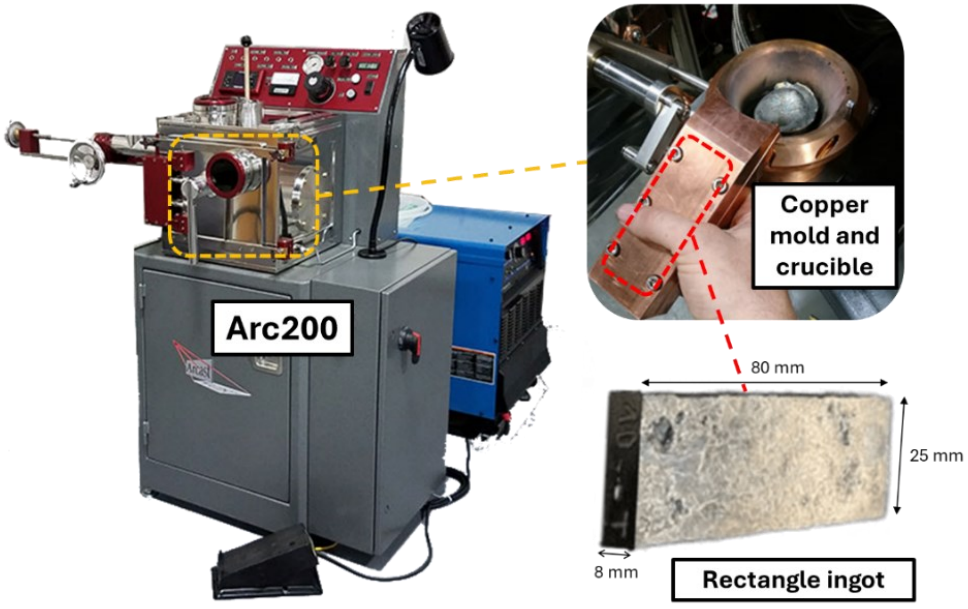


Figure 3.17. Arc200 melter equipped with copper mould and crucible.

For **larger ingots (Ind500)**, approximately 1500 grams of raw materials were mixed in an Al_2O_3 crucible and placed in an induction furnace (IND500 Furnace; Arcast inc., USA), as illustrated in *Figure 3.18*. The chamber was sealed and purged under Argon 4.7. The pure materials were melted under a high vacuum of $5x10^{-6}$ mbar. The melted materials were then tilt-casted into rectangular moulds, whose dimensions are shown in *Figure 3.18*.

Thèse accessible à l'adresse : https://theses.insa-lyon.fr/publication/2025ISAL0036/these.pdf © [T. Langlois], [2025], INSA Lyon, tous droits réservés

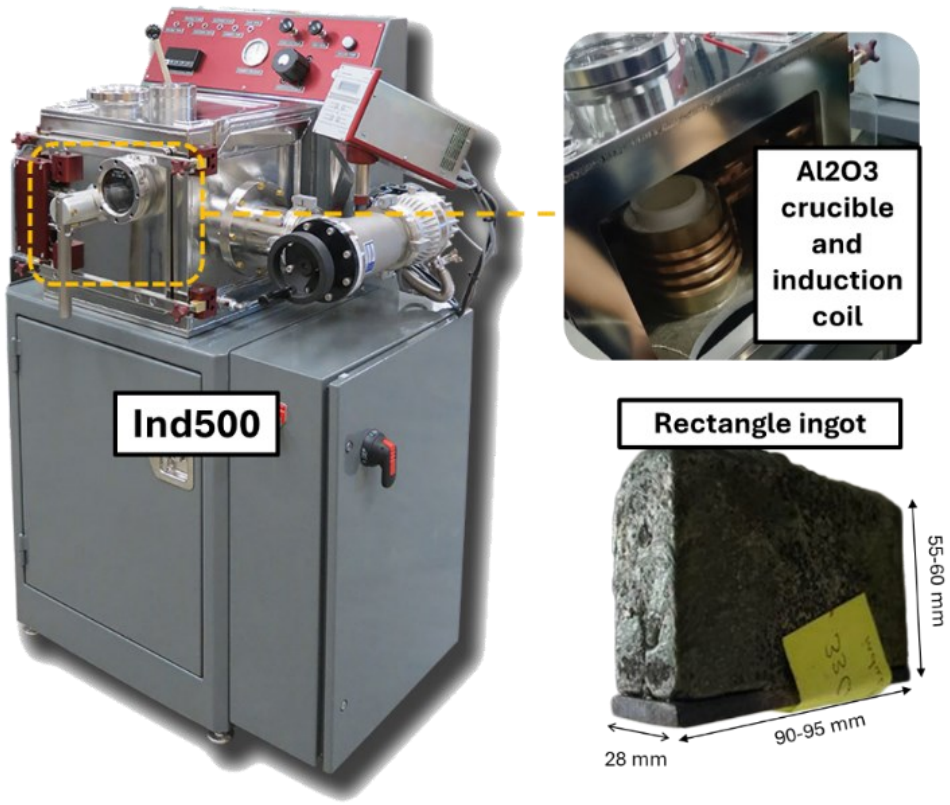


Figure 3.18. Ind500 melter, equipment and produced ingot.

Table 3.9 summarises the characteristics of each manufacturing system. Naturally, Arc50 was chosen for the high-throughput FA method. Six specimens can be produced simultaneously with less than 100 grams of raw materials, saving time and resources (material, equipment and energy). Arc200 and Ind500 require significantly more resources to produce a single composition. We estimated that Arc50 saves more than 500% of resources compare to Arc200 and Ind500. Arc200 was reserved for producing master alloys and machining TDB samples. Ind500 was reserved for producing larger ingots used for machining CVN samples.

Table 3.9. Characteristics of the different casting machines.

System	mass (g)	quantity	geometry	dimensions (mm) (LxWxT) or (LxDø)
Arc50	12-15	6	cylinder	15 x 10ø
Arc200	150-200	1	rectangle	80 x 25 x 8
Ind500	1500	1	rectangle	90 x 55 x 28

Thèse accessible à l'adresse : https://theses.insa-lyon.fr/publication/2025ISAL0036/these.pdf © [T. Langlois], [2025], INSA Lyon, tous droits réservés

After cleaning them with ethanol and a sandblasting machine, samples were ready for the next steps of elaboration and characterisation. At this stage, the microstructure is referred to as the As-Cast state (AC) of materials.

3.3.3 Thermomechanical treatments

The development of advanced alloys involves thermomechanical treatments, which are known to improve specific mechanical properties of the materials. In this project, the following heat treatments and mechanical treatments have been performed:

- **Homogenisation**: eliminating chemical segregation by holding materials at high temperatures to allow the diffusion of alloying elements, resulting in a more uniform composition and microstructure.
- **Hot rolling**: deformation of the material at high temperatures, typically above the recrystallisation temperature, to refine the grain size and enhance ductility.
- **Cold rolling**: deformation of the material at low temperatures to increase the strength through strain hardening.
- **Recrystallisation**: holding materials at sufficient temperatures to allow new, strain-free grains to form, restoring ductility and removing internal stresses.

Homogenisation treatments were performed in a Fluidised-Bed-Furnace (Ac500 Furnace: ALS Technologies Pty, Australia) filled with sand and under argon 4.7. The desired temperatures for homogenisation were determined using One-Axis CALPHAD calculation in ThermoCalc, to determine the present phases in the system (detailed in Chapter 4.1). Optimised homogenisation durations were established by evaluating chemical segregation for Arc50 and Arc200 geometries with EDS maps after different treatment times (see Chapter 5.1). The goal was to achieve minimal segregation without excessively long durations. Homogenisation times for Ind500 samples were based on literature [2]. A set of three thermocouple type S allows for checking the temperature at the bottom, middle and top parts of the furnace within a range of $\pm$ 3 °C. Once the target temperature was reached in the furnace, air was replaced by Argon 4.7, AC samples were placed in a metal basket made of Inconel and inside the furnace. Once the desired homogenisation time was completed, the basket was quickly removed from the furnace to apply a water quench to the samples, rapidly reducing the sample temperature to preserve the microstructure obtained in the homogenisation process. Great care was taken to prevent the development of a heat-

Thèse accessible à l'adresse : https://theses.insa-lyon.fr/publication/2025ISAL0036/these.pdf © [T. Langlois], [2025], INSA Lyon, tous droits réservés

affected layer around the samples by stirring the basket during the quenching process. After homogenisation, sample microstructure is referred to as As-Homogenised state (AH).

Ingots produced by Arc200 and Ind500 underwent further thermo-mechanical processing using rolling equipment. Ideally, cold rolling followed by an annealing treatment is preferred to enhance the material strength and subsequently restore its ductility. However, rolling pressure increases with the material's yield strength and dimensions (thickness and width) [107]. Materials deformed at room temperature experience strain hardening, which increases the yield stress, while prolonged high temperatures effectively mitigate strain hardening after deformation [108]. Given that the rolling equipment at Deakin is designed to sustain a maximum pressure of 1500 MPa, hot rolling was employed for large ingots produced by Ind500. In contrast, smaller ingots produced by Arc200 were cold rolled.

Hot rolling was performed on Ind500 ingots, reducing their thickness by approximately 60% to produce 10mm thick CVN specimens. This process was carried out according to standard procedures described in ASTM B947 (2020 [109]), using a two-rolling-mill machine (Dinkel, USA) with 350mm roll diameter. The thermal part of the treatment was performed in a gas furnace under Argon 4.7. Multi-pass rolling was organised to reduce the thickness by approximately 10% at each stage. The thickness was measured after every second pass using an electronic Vernier calliper (Series 500; Mitutoyo, Japan). Between each pass, ingots were returned to the furnace until the set temperature was reached again. After the last rolling, ingots were water quenched. These microstructures are referred as to Hot rolled (HR) state.

Cold rolling was employed for Arc200 ingots to obtain metals sheet for tensile testing specimen machining. The process was carried out according to standard procedures described in ASTM A1008 (2023 [110]), using the two-rolling-mills machine. An intermediate recrystallisation process was performed after 45% thickness reduction with the fluid bed furnace filled with sand and under Argon4.7. Less than 10% of the ingot's thickness was reduced at each pass to prevent catastrophic failure. Ingot thickness was measured after every pass with an electronic Vernier calliper (Absolute Digimatic Calliper Series 500, Mitutoyo, Japan). At the end of the cold rolling process, each ingot was recrystallised, and water quenched. Recrystallisation temperature and time were optimised based on Thermo-Calc predictions and experimental results from control samples. These microstructures are referred to as Annealed (ANN) state.

Thèse accessible à l'adresse : https://theses.insa-lyon.fr/publication/2025ISAL0036/these.pdf © [T. Langlois], [2025], INSA Lyon, tous droits réservés

3.3.4 Metallography: Sample preparation

Different metallographic processes have been employed to prepare samples for microscopic characterisation and mechanical testing.

Cutting was performed at Deakin IFM with an Accutom-100 (Struers, Denmark) and at Mateis with a Flexicut (Presi, France). Both systems, equipped with Al_2O_3 cut-off wheels designed for hard materials (range of 500-800 HV), are displayed in *Figure 3.19*. After cutting, each specimen was cleaned with ethanol and dried.

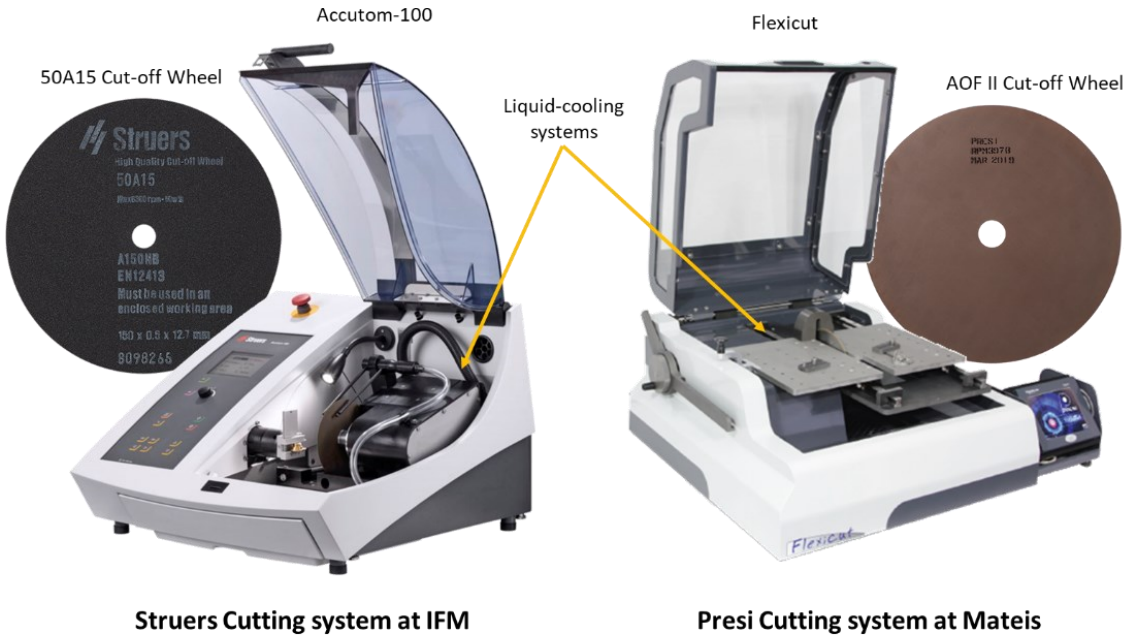


Figure 3.19. Cutting equipment at IFM (left) and Mateis (right).

Mounting samples in resin is essential for microscopic analyses and for indentation tests. This step was carried out at Deakin IFM with a CitoPress-30 (Struers, Denmark), shown in *Figure 3.20*. The embedding resin used is Polyfast (Cat. No. 40100037; Struers, Denmark). The ram, with a diameter of 30 mm, was cleaned with an Antistick product (Cat. No. 40300043, Struers, Denmark). Bulk specimens were deliberately positioned off-centre to facilitate EBSD observation procedures. 25ml of Polyfast were added on top of the specimen. Heating at a pressure of 250 bar was applied for 5.5 minutes, followed by a cooling of 3.5 minutes.

Thèse accessible à l'adresse : https://theses.insa-lyon.fr/publication/2025ISAL0036/these.pdf © [T. Langlois], [2025], INSA Lyon, tous droits réservés



Figure 3.20. Mounting equipment at Deakin IFM.

Grinding surfaces of bulk samples helps remove any oxide layers or scratches. This step was performed on mounted specimens with the grinding machine Rotopol-21 (Struers, Denmark), using a sequence of 240, 600 and 1200-grit silicon carbide abrasive discs, with a diameter of 250 mm (Hermes, Germany), as depicted in *Figure 3.21*. The sequence was performed at a rotation speed of 300 rpm with water. The 240-grit paper was used only to round the edges of the mounted sample surface and gently remove any resin or contaminants. Subsequent grinding was performed using 600-grit and 1200-grit discs. At each grit level, uniform pressure was applied across the entire surface, rotating the sample by 90 degrees to remove scratches from the previous grinding direction.

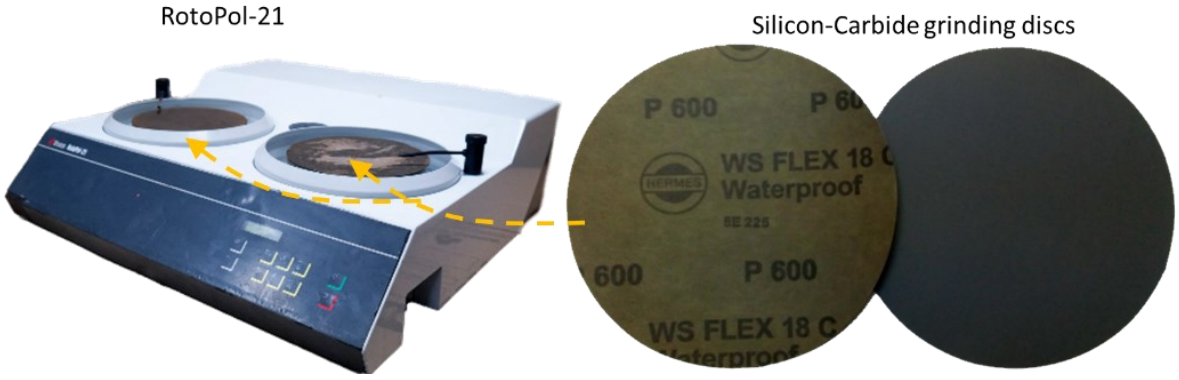


Figure 3.21. Grinding equipment at Deakin IFM.

A semi-automatic **polishing** process was performed with the Tegramin-25 (Struers, Denmark), equipped with a set of polishing pads and corresponding suspensions (MD-pads and DP-suspensive; Struers, Denmark). *Figure 3.22* shows the setup at Deakin IFM. These pads were reserved for this project, cleaned after use, and carefully stored in individual boxes. *Table 3.10* details the sequence that gives the best results for our alloys.

Thèse accessible à l'adresse : https://theses.insa-lyon.fr/publication/2025ISAL0036/these.pdf © [T. Langlois], [2025], INSA Lyon, tous droits réservés



Figure 3.22. Polishing system at Deakin IFM.

Table 3.10. 4-steps method for polishing C-MPEAs.

Polishing Pad	Suspension	Force [N]	Time [mm:ss]	rotation speed [rpm] platten		rotation speed [rpm] specimen holder
MD-Dac	DP-9µm-P	30	10:00	-150		150
MD-Mol	DP-3µm-P	30	12:30	150		150
MD-Nap	DP-1µm-P	30	10:00	-150		150
MD-Chem	OPS - nondry	30	1:30	150		150
	water	30	1:30			

Between each polishing step, the specimens undergo an ethanol ultrasonic cleaning for 10 minutes. After cleaning, the specimens are observed with a light-microscope Olympus DP-70 (Olympus Pty, Australia; shown in *Figure 3.23-a*) and Hirox RX-1 (Hirox Co Ltd, Japan; shown in *Figure 3.23*-b) to see the evolution of scratches size and quantity (*Figure 3.24*). If necessary, additional vibratory polishing steps are applied using VibroMet2 equipment (Buehler, USA) with OPS suspension.

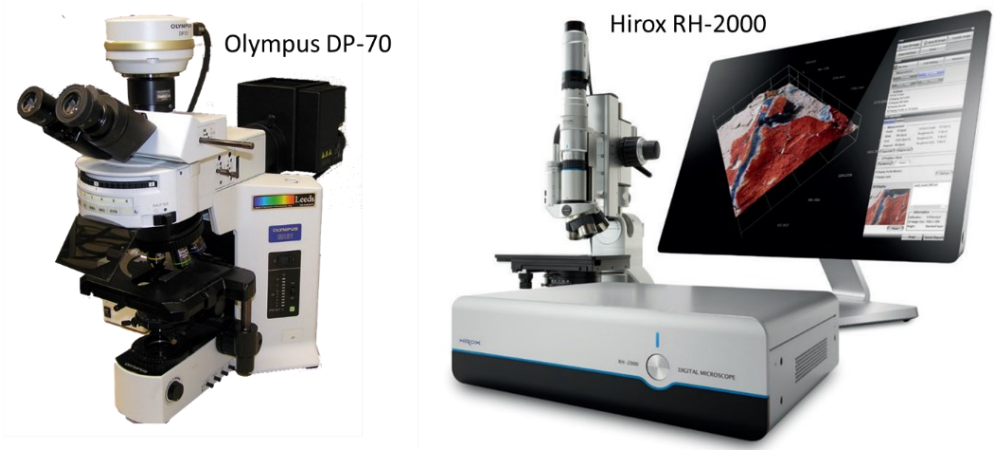


Figure 3.23. Optical microscopy equipment: (a) Olympus DP-70 used at Deakin; (b) Hirox RH-2000 used at Mateis.

Thèse accessible à l'adresse : https://theses.insa-lyon.fr/publication/2025ISAL0036/these.pdf © [T. Langlois], [2025], INSA Lyon, tous droits réservés

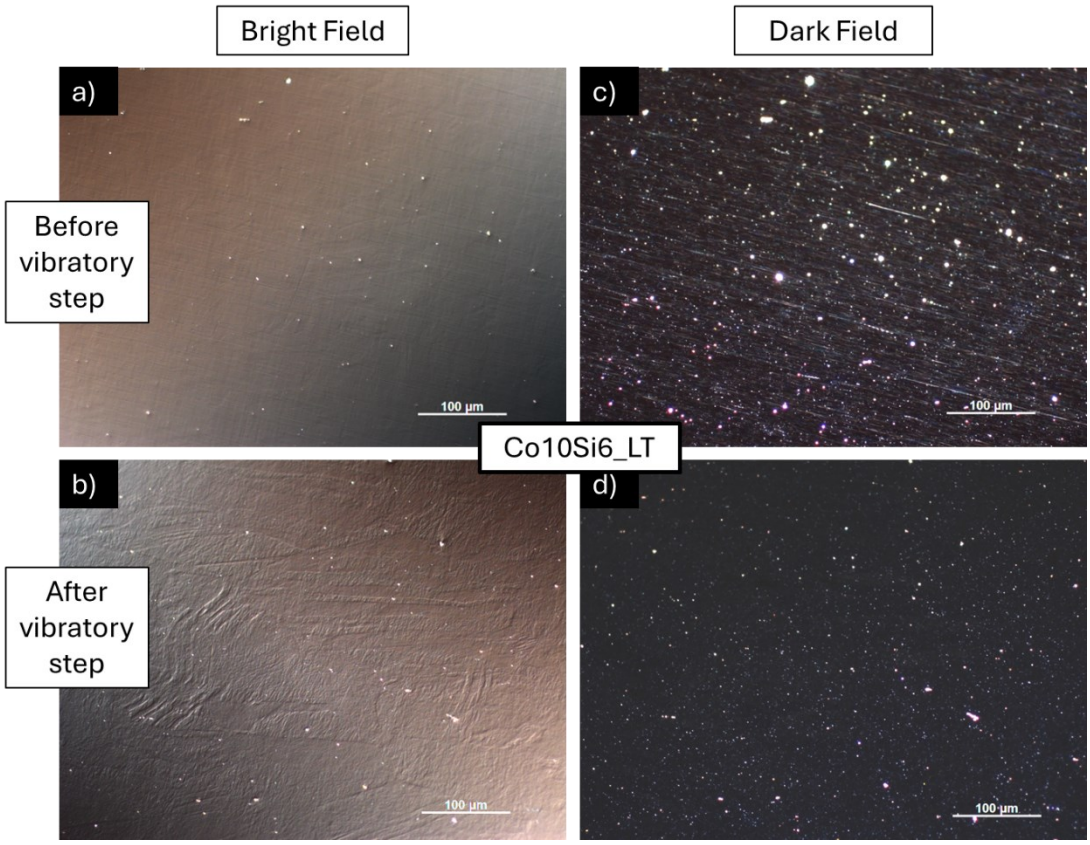


Figure 3.24. Quality of the surface with vibratory polishing in the case of the Co10Si6 alloy, observed with optical microscopy.

The polished specimens are stored in a desiccator designated for MPEAs, containing regenerated silica crystals to maintain low humidity levels. The regeneration of silica crystal is performed every 6 months, using aluminium trays inside a heating oven (Binder 9010-0082; SigmaAldrich, Germany) at 160°C for 48 hours (*Figure 3.25*).



Figure 3.25. Heating Oven and Silica Crystals.

Thèse accessible à l'adresse : https://theses.insa-lyon.fr/publication/2025ISAL0036/these.pdf © [T. Langlois], [2025], INSA Lyon, tous droits réservés

3.3.5 Specimen machining

Machining of TDB specimens

The cold rolled metal sheets produced by Arc200 were used to machine the TDB geometries using Wire Electrical Discharge Machining (EDM). This process was outsourced to Mecanium (INSA Lyon, France). The specimen geometry and dimension are displayed in *Figure 3.26* in line with specifications from ISO6892-1 (2019 [111]).

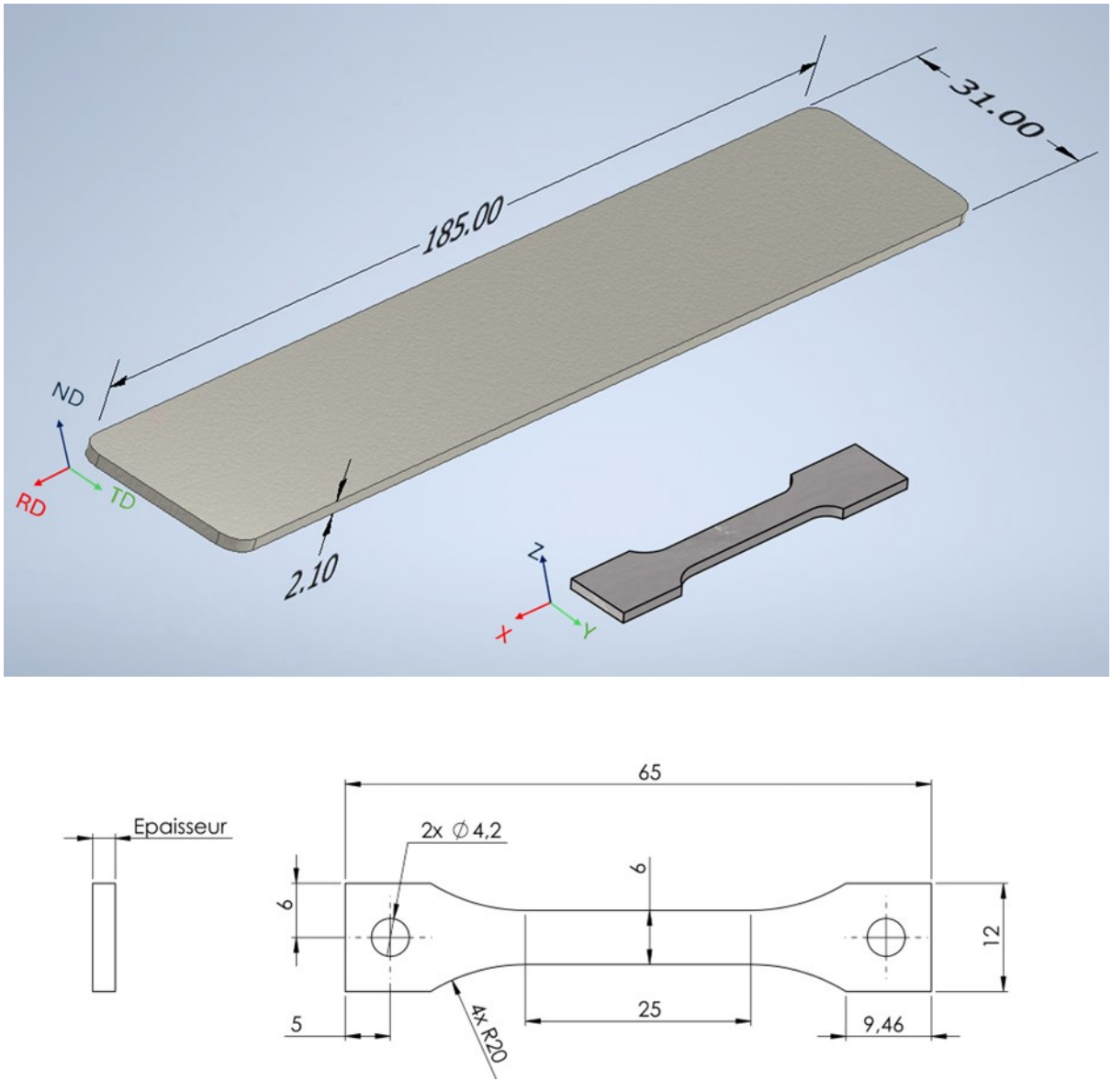


Figure 3.26. Schematics of TDB specimens cut from cold rolled sheets (dimensions in mm).

In rolling processes, the rolling direction (RD) is the axis along which the material is deformed during rolling, the normal direction (ND) is the axis aligned with the working force of the rolls, and the transverse direction (TD) is perpendicular to both RD and ND. The machining of TDB specimens ensures that the tensile axis (X) aligns with RD. Each specimen was labelled on both sides prior to testing.

Thèse accessible à l'adresse : https://theses.insa-lyon.fr/publication/2025ISAL0036/these.pdf © [T. Langlois], [2025], INSA Lyon, tous droits réservés

Machining of CVN specimens

The machining of CVN specimens for impact-toughness measurements was performed by NuTooling (Australia) using wire cutting techniques. The specimen dimensions, in line with standards from ASTM E23-23a (2024, [112]), are illustrated in *Figure 3.27*. Each specimen was labelled on both part prior to testing.

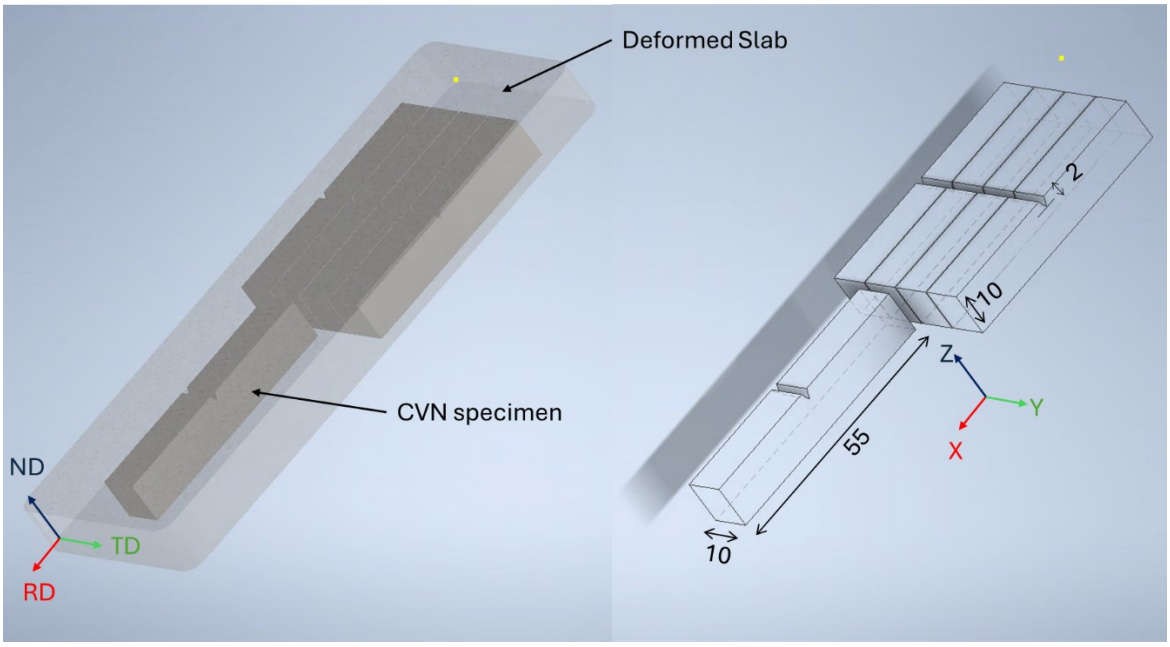


Figure 3.27. Schematic of CNV specimens cut from the hot rolled slabs.

The CVN specimens were cut along RD and the notch depth is machined along ND. Special care was taken to ensure that the specimens had no surface defects near the notch.

Powder-filing

The top parts of cylindrical samples produced by Arc50 in the AH state were kept for powder preparation. To analyse the microstructure via X-Ray diffraction (XRD), it was necessary to convert part of the alloy into powder. Powders are advantageous over bulk materials for XRD measurements as they represent a polycrystalline state, which is more indicative of the structural orientations. The random orientation of the crystallites in the powder reduces the likelihood of peak extinction and residual stress compared to bulk samples. Additionally, the powder state allows for the measurement of Stacking Fault Energy (SFE) [113, 114, 115, 116, 117].

Powder was separated from the bulk material through mechanical filing, as depicted in *Figure 3.28*. For consistent and repeatable powder preparation, mechanical filing was carried out using a Pin-On-Disk setup coupled with the UMT TriboLab

Thèse accessible à l'adresse : https://theses.insa-lyon.fr/publication/2025ISAL0036/these.pdf © [T. Langlois], [2025], INSA Lyon, tous droits réservés

platform (Bruker, USA), as shown in *Figure 3.28*. This setup involves fixing the specimen under a load-cell while the filing material rotates and collects the powder in an aluminium foil. Carbon-steel hand files with a hardness of 900 HV were used for the filing process. To prevent heating of the powder, the following parameters were employed: a load of 100 N was applied to the top part of the sample for 30 seconds, and the lower circular drive was rotated at 100 rpm. The specimen was then held still for 90 seconds. This cycle was repeated until approximately 100 milligrams of powder was obtained.

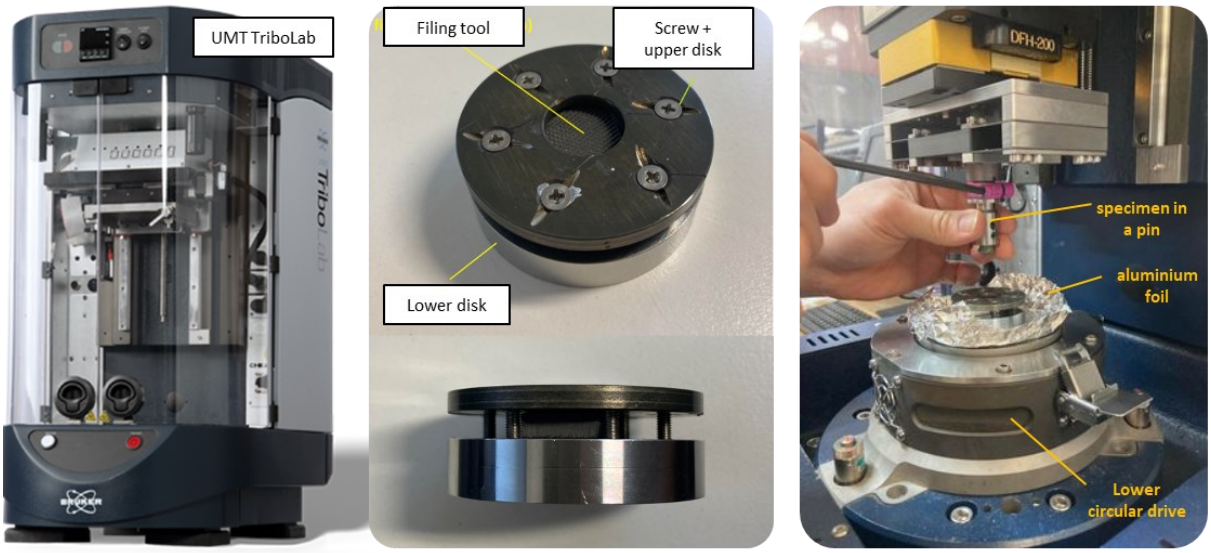


Figure 3.28. Mechanical filing process (UMT TriboLab, Bruker).

A mortar was used to further reduced the particle size of the obtained powders, which were sieved to below 75 µm. The powders resulting from mechanical filing, characterised by high plastic deformation, are referred to as the "cold-worked" (CW) powders. An annealing process is applied to half of the obtained powders, producing what is referred to as "annealed" (ANN) powders. This process is described in the following part.

To remove the high plastic deformation induced by the mechanical filing, the powders were heat-treated in the furnace B-VAC-1600 (Camco Furnace, USA) equipped with a high-vacuum turbo pump and connected to an Argon 4.7 bottle. The powders were placed in ceramic crucibles with a lid (Ceramic Oxide Fabricators, Australia). The setup is shown in *Figure 3.29*.

Thèse accessible à l'adresse : https://theses.insa-lyon.fr/publication/2025ISAL0036/these.pdf © [T. Langlois], [2025], INSA Lyon, tous droits réservés

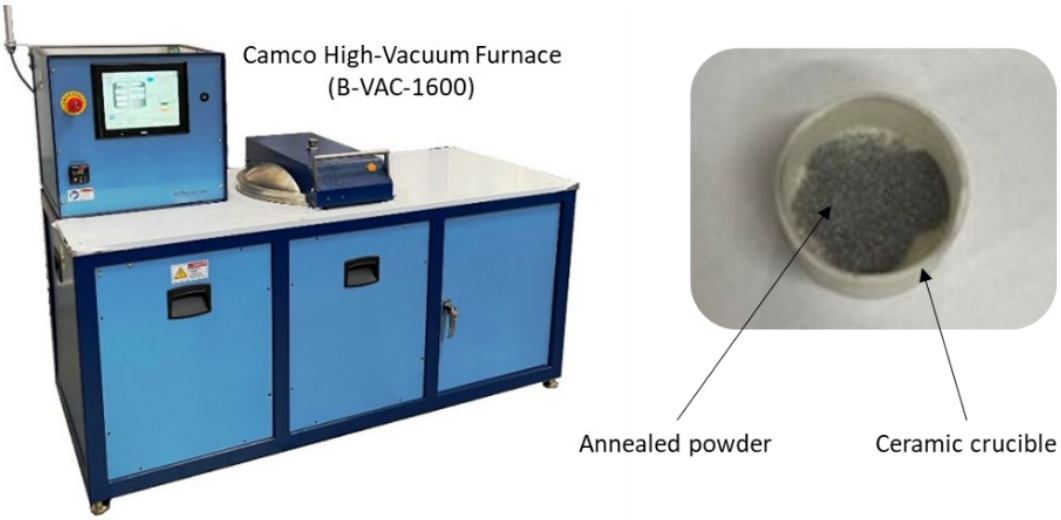


Figure 3.29. Annealing heat-treatment in high-vacuum furnace (Camco Furnace).

The furnace chamber was purged with argon for 15 minutes, and a high vacuum of 5.10^{-5} torr was applied for 1 hour. The temperature was then raised to the values predicted by Thermo-Calc for single-phased FCC within 20 minutes. The temperature was maintained for 3 hours to complete the annealing of powders. Rapid cooling was achieved by injecting argon into the chamber to prevent the formation of secondary phases (*Figure 0.5* in the Appendix of Chapter 3). The chemical composition of CW and ANN powders was verified with Energy Dispersive X-Ray spectroscopy (EDS) to ensure that no contamination occurred during mechanical filing or annealing.

3.3.6 Chemical characterisation methods

Chemical characterisation is essential to analyse the actual composition of the produced materials and compare them with the targeted values. Additionally, it helps in evaluating any contamination that may have occurred during various stages of production. The following chemical characterisation methods are employed:

- **Glow Discharge Optical Emission Spectroscopy (GDOES)**. This technique measures the mass fractions and trace elements (in ppm) in the material, making it suitable for both major and trace element detection, particularly for surface analysis.

- **Energy Dispersive Xray-Spectroscopy (EDS)**. This method measures the mass fractions in materials, typically as part of a Scanning Electron Microscope (SEM).

Thèse accessible à l'adresse : https://theses.insa-lyon.fr/publication/2025ISAL0036/these.pdf © [T. Langlois], [2025], INSA Lyon, tous droits réservés

- **ONH and CS elemental analysis (ONH-CS)**. This method assesses the presence of oxygen (O), nitrogen (N), and hydrogen (H), as well as carbon (C) and sulphur (S) in the material.

GDOES uses plasma to sputter atoms from the surface of a bulk sample. The emitted light is analysed to determine elemental composition by comparing the observed spectral lines with a known database. This method provides high accuracy in measuring elemental concentrations, especially in the near-surface regions of the material. For this project, we employed the GD-Profiler 2 (Horiba, Japan) at Deakin IFM, as displayed in *Figure 3.30*. We created a custom database for C-MPEAs, as the preloaded databases were not suitable for this class of alloys. To establish this database, five C-MPEA compositions were manufactured by Arc200 and analysed using Inductively Coupled Plasma Atomic Emission Spectroscopy (ICP-AES) at the Spectrometer Service (Melbourne, Australia). Certified compositions are documented in *Figure 0.4* in the Appendix of Chapter 3. New C-MPEAs are evaluated by comparing emitted spectral lines with data from this custom database and using interpolation algorithms.



Figure 3.30. GD-Profiler 2 and analysed areas on Arc200 samples.

EDS detects X-rays emitted from a sample when bombarded with an electron beam. The energy and intensity of these X-rays are characteristic of specific elements, allowing for qualitative and semi-quantitative analysis. EDS is particularly useful for identifying and mapping the distribution of elements within a sample. However, its

Thèse accessible à l'adresse : https://theses.insa-lyon.fr/publication/2025ISAL0036/these.pdf © [T. Langlois], [2025], INSA Lyon, tous droits réservés

accuracy for light elements such as carbon (C) and oxygen (O) may be limited due to the low energy of their X-ray emissions. In this project, EDS was conducted with a JEOL-7800F SEM at Deakin IFM, as displayed in *Figure 3.31*. The system was operated at a working distance of 15 mm and an electron beam current of 20 mA. The Aztec software (Oxford Instruments) was used for setup and data analysis. The EDS detector examines regions of interest for composition, element distributions and segregation within grains.

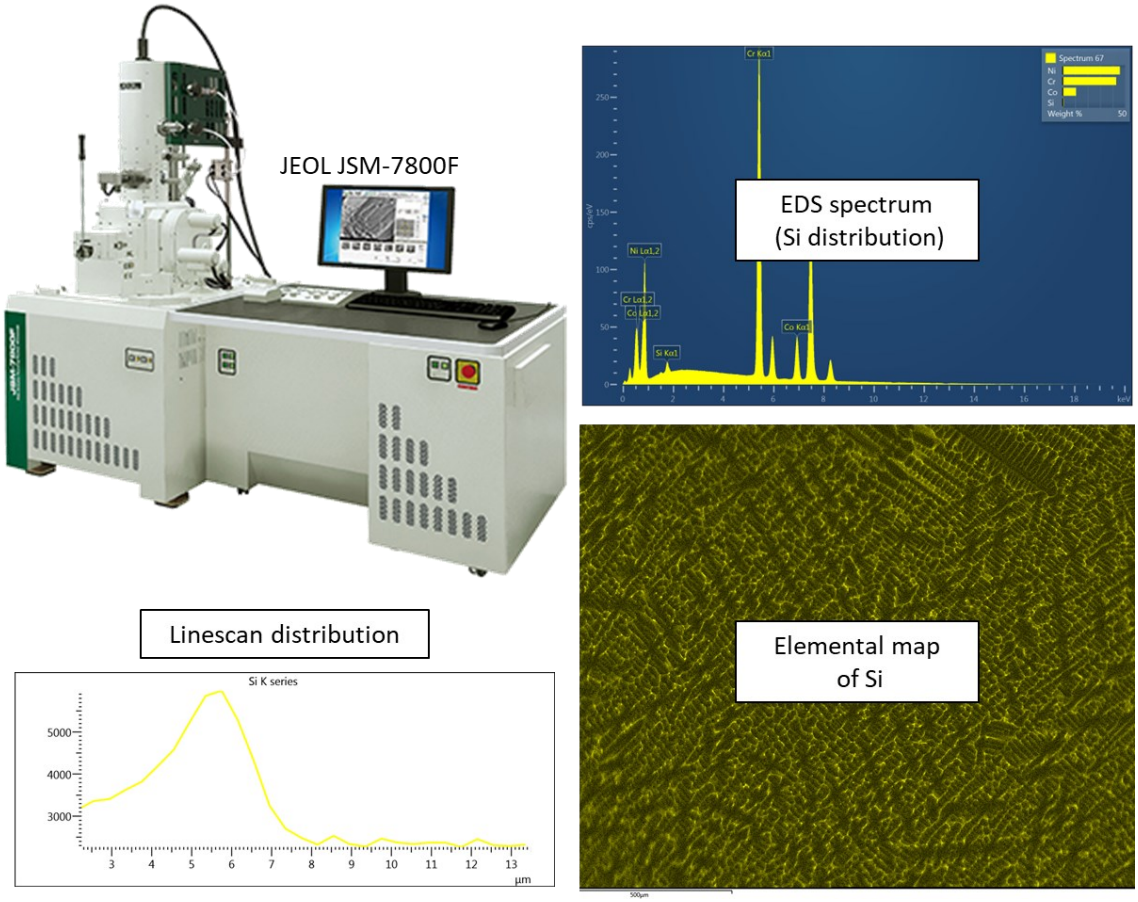


Figure 3.31. JEOL JSM-7800F and semi-quantitative analysis of a CrCoNiSi mounted sample.

ONH-CS analysis involves fusion and combustion processes, respectively. For ONH analysis, there is a reaction between the material, catalyst products, graphite crucible and inert argon, resulting in the release of gas. For CS analysis, the combustion happens between the material, catalyst products, a crucible in graphite and pure oxygen. The released gases are then passed through a series of filters for analysis against calibration standards. Accurate measurement of these elements is crucial as they can significantly influence material properties. The ONH 836 and CS 744 Elemental

Thèse accessible à l'adresse : https://theses.insa-lyon.fr/publication/2025ISAL0036/these.pdf © [T. Langlois], [2025], INSA Lyon, tous droits réservés

Analysers used at Mateis employ argon and oxygen with high purity (Alphagaz 1 grade 99.999%; Air Liquide, France). Both systems are displayed in *Figure 3.32*. ONH-CS measurements were at least conducted 3 times for each material composition and regular calibration with reference samples is performed to ensure accuracy.

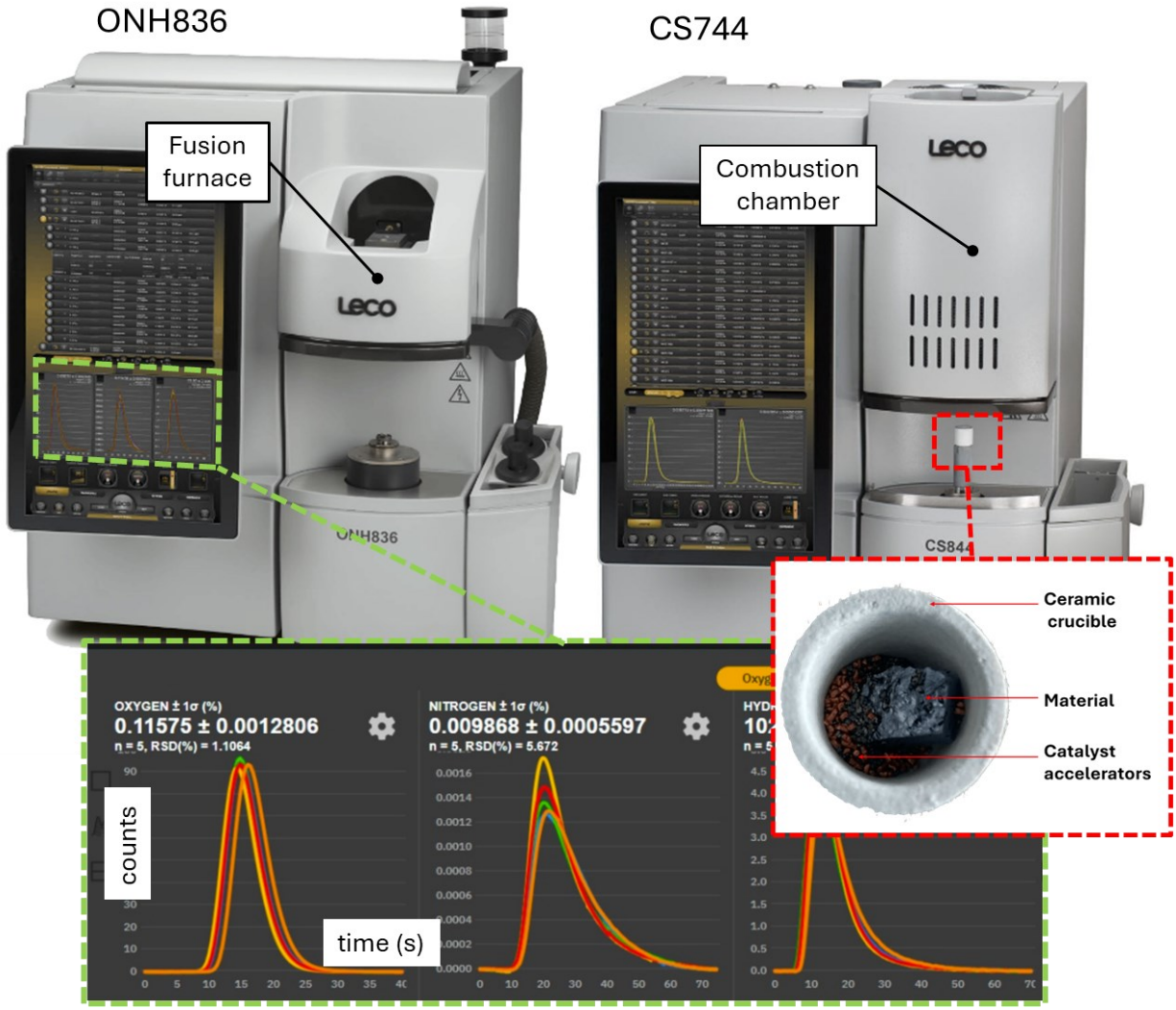


Figure 3.32. ONH836 and CS744 for elemental analysis at Mateis.

Thèse accessible à l'adresse : https://theses.insa-lyon.fr/publication/2025ISAL0036/these.pdf © [T. Langlois], [2025], INSA Lyon, tous droits réservés

3.3.7 Microstructural characterisation methods

In this PhD, various microstructural characterisation techniques are employed to assess material aspects that influence properties, including phases, segregation, grain size, defects (e.g. inclusion, cracks, porosities), etc. These properties are determined with the following techniques:

- **X-Ray diffraction (XRD)**. This technique determines the present phases lattice parameters and perform texture and stress analyses, useful for SFE measurements detailed in Chapter 5.3.1.
- **Scanning Electron Microscopy (SEM)**. This method analyses the material morphology, including grain size and defects.
- **Electron Back-Scattered Diffraction (EBSD)**. This technique allows for determination of the present phases, grain size distribution, identification of specific grain boundaries (annealing twins, deformed twins).

XRD operates on the principle of Bragg's law, reported in *Equation (3.7)*, where X-rays are diffracted by the crystal lattice planes at specific angles θ, allowing for phase identification and lattice parameter measurements. This technique was performed with an XPert PRO MRD (Malvern Panalytical, UK), shown in *Figure 3.33-a*. This instrument uses a copper X-ray source with wavelengths of λ_{cu}(Kα1) =1.540598 Å and λ_{cu}(Kα2) = 1.544426 Å. The system was employed with bulk or powder specimens. Powders were placed in an aluminium steel crucible covered with a Kapton tape to ensure a flat surface (*Figure 3.33-b*).

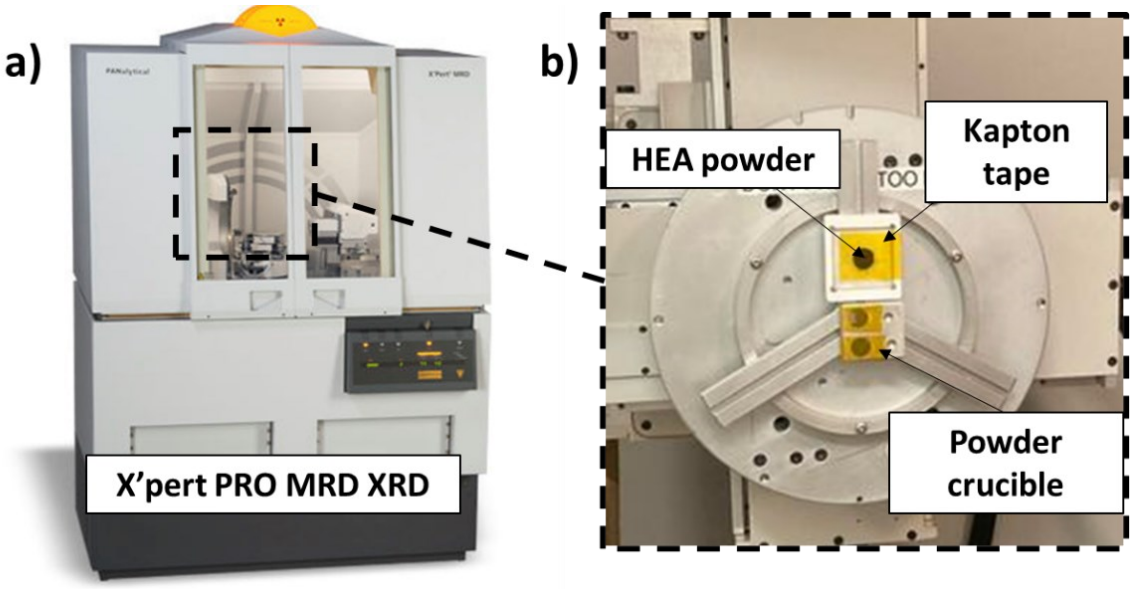


Figure 3.33. (a) X'Pert Pro MRD XRD instrument and (b) powder setup.

Thèse accessible à l'adresse : https://theses.insa-lyon.fr/publication/2025ISAL0036/these.pdf © [T. Langlois], [2025], INSA Lyon, tous droits réservés

$$n\,\lambda = 2\,d\,sin\theta \qquad (3.7)$$

Where n is the diffraction order, d the interatomic layer distance, λ is the wavelength of the copper source and θ is the angle between the X-ray beam and the crystal lattice planes.

Geometrical calibration was performed along the x, y, z translation axes and the omega rotation axis around the y-axis to ensure that XRD measurements only account for material contributions. The following parameters were set to collect line profiles of our HEA specimens: the instrument operated in Point Focus mode with an applied voltage and current of 40 kV and 40 mA. A beam size of 2 mm x 2 mm was used for bulk specimens, and 3 mm x 3 mm for powder specimens. For strain analysis performed with powders, a stress-free Nist-660a LaB6 calibration sample [118] was also acquired at the corresponding beam size. After geometrical calibration, a quick scan was performed on each sample with a 2θ range from 40° to 105°, targeting first five reflections of the FCC-phase, using a step size of 0.02° and 1 second per point. This was followed by a more detailed scan of the individual reflections, with a step size of 0.01° and 25 seconds per point.

The Stacking Fault Energy (SFE) of the materials was estimated by analysing the diffraction peak profiles obtained from XRD [113, 114, 115, 116, 117]. The working principle of this SFE measurement is illustrated in *Figure 3.34*. By comparing the peak positions (2ϑ) of deformed (CW) and annealed (ANN) powders, Stacking Fault Probability (α) of the material can be derived (Equation A in *Figure 3.34*). The lattice parameter (a_0) of the material is obtained from the stress-free peak reflections (ANN) using Bragg's law for FCC crystal (Equation B). K_{111} and ω_0 are material constants, whose product is equal to 6.6 in FCC alloys (Relation C [115]). Additionally, the Shear modulus in the (111) plane (G_{111}) and the Zener anisotropy (A) are functions of the material's elastic moduli (Equation D and E [114]), which have been experimentally determined for CrCoNi [119, 120] and CrCoNiSi alloys [64]. For cobalt-lean compositions, the materials properties, reported in *Table 0.1* in the Appendix of Chapter 3 were predicted using atomistic calculations by P.A. Geslin explained in [121], employing the machine learning potential for CrCoNi alloys provided in [122].

The remaining variables for SFE calculations (Equation F [113]) are obtained from peaks deconvolution, a methodology equivalent to the Warren-Averbach approach [113]. Individual peaks were fitted using a pseudo-Voigt function implemented in Topas software, allowing precise deconvolution of the stress-free Nist-660a LaB6 calibration sample , the annealed and deformed profiles. This procedure ensures that instrumental

Thèse accessible à l'adresse : https://theses.insa-lyon.fr/publication/2025ISAL0036/these.pdf © [T. Langlois], [2025], INSA Lyon, tous droits réservés

contributions are effectively removed from the peak profiles. The analysis focused on (111) and (222) reflections, from which parameters such as FWHM, peak position, and Pseudo-Voigt shape factor were extracted. These parameters were then used to calculate the microstrain ($\langle \varepsilon_{50}^2 \rangle_{111}$) in Matematica software [123].

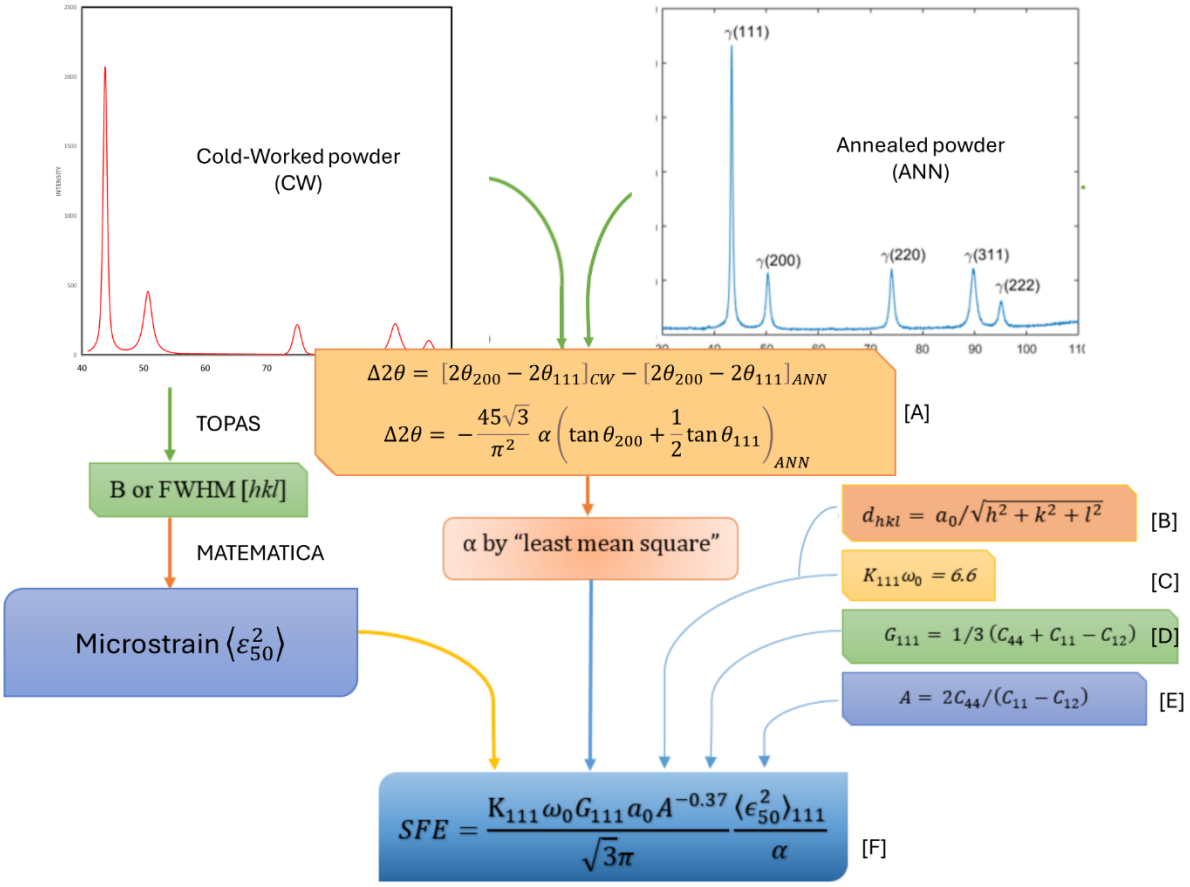


Figure 3.34. Schematic of the powder-XRD method for SFE measurement (adapted for this work from [117]). A: Schramm-Reed equation [114]; B: Bragg's Law in FCC systems; C: Material constant, equal to 6.6 in FCC alloys; D: Shear Modulus in the (111) plane as a function of elastic moduli; E: Zener Anisotropy as a function of elastic moduli [114]; F: Warren-Averbach Analysis [113].

Powder-XRD measurements were performed for all the composition with the X'Pert Pro MRD equipment at IFM, introduced just above. 4 compositions (Co33, Co33Si6, Co10 and Co10Si6) were also performed at the ANSTO Australian Synchrotron (main-in experiment) to obtain more precise results. The technical parameters for XRD acquisition with both equipment are given in *Table 3.11*.

Thèse accessible à l'adresse : https://theses.insa-lyon.fr/publication/2025ISAL0036/these.pdf © [T. Langlois], [2025], INSA Lyon, tous droits réservés

Table 3.11. XRD equipment specifications at Deakin and at the Australian Synchrotron.

Instrument	**MRD (Deakin IFM)**	**PD Beamline (ANSTO)**
Source	Copper: 8.05 keV	Bending magnet: 21 keV
Mode	Line Focus	Point Focus
Current	40 mA	200 mA
Voltage	40 kV	-
Beam size	1 mm x 1 mm	3 mm x 1 mm
Step size	0.02	0.1
Time per step	15 s	45 ms
Angular range	40 - 100	5 - 175

Measurement with the Powder-Diffraction (PD) beamline from Ansto provides more precise results since the instrumental contribution to peak broadening is less important. This instrumental contribution needs to be deducted when performing strain measurements. *Figure 3.35* shows the two XRD profiles acquired with both systems for a stress-free reference powder (Nist-660a LaB6) with much thinner peaks obtained with Ansto equipment. The corresponding Caglioti curves that express the peak broadening at higher angles [124] are illustrated in *Figure 3.36*.

Thèse accessible à l'adresse : https://theses.insa-lyon.fr/publication/2025ISAL0036/these.pdf © [T. Langlois], [2025], INSA Lyon, tous droits réservés

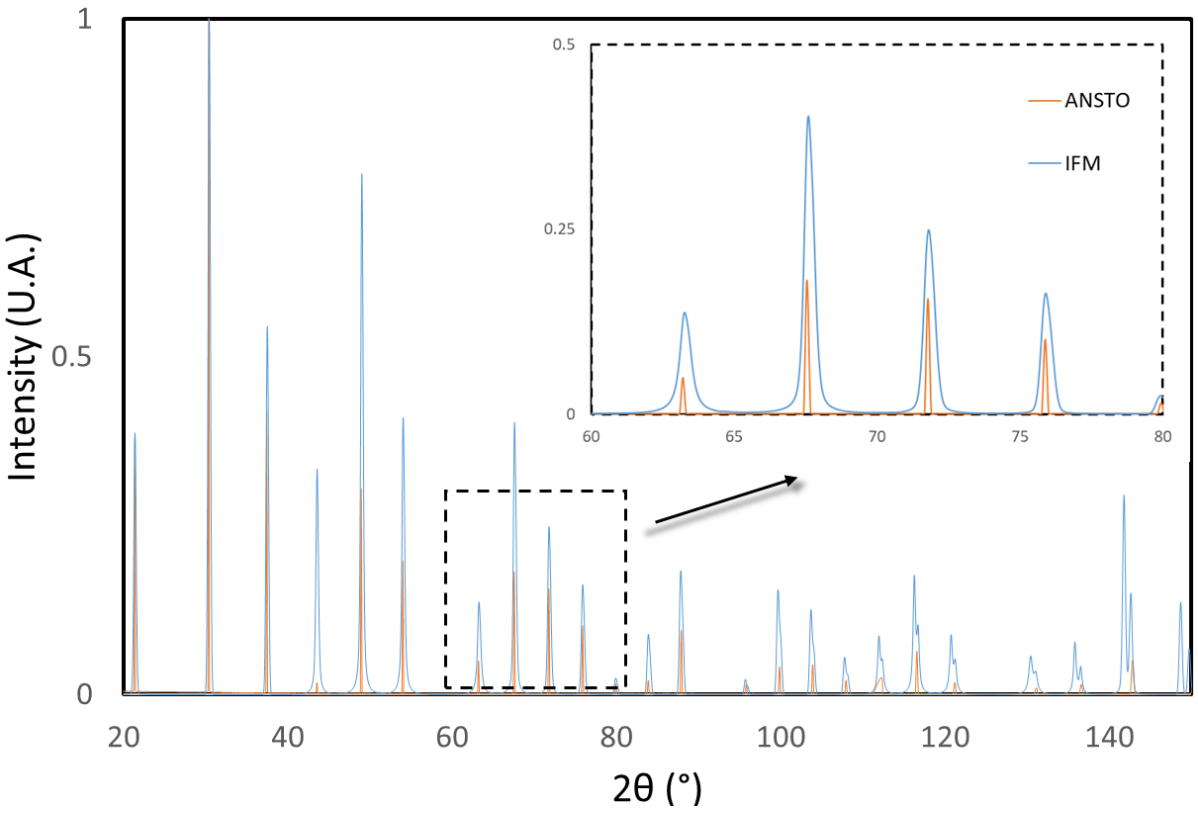


Figure 3.35. XRD profiles of a stress-free Nist 660a LaB6 powder [118] acquired with X'Pert Pro MRD equipment at IFM (blue curve) and PD Beamline at Ansto (orange curve).

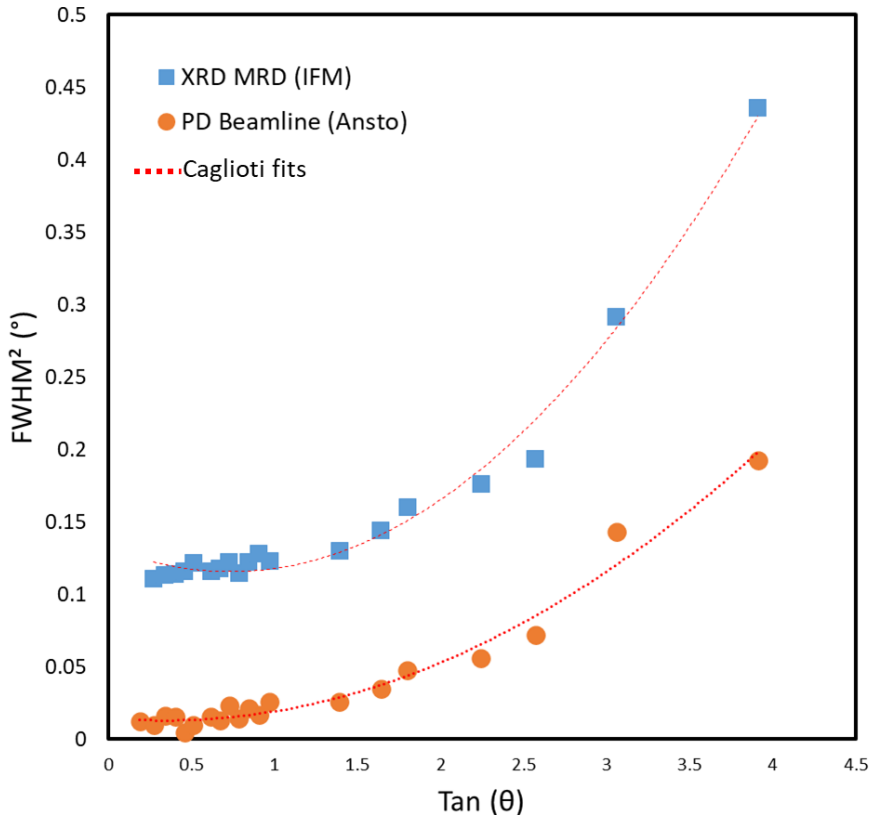


Figure 3.36. Caglioti Curves characterising the peak reflection broadening for the equipment at IFM (blue) and equipment at ANSTO (orange). FWHM is the full width at half maximum for each reflection at angle 2ϑ [124].

Thèse accessible à l'adresse : https://theses.insa-lyon.fr/publication/2025ISAL0036/these.pdf © [T. Langlois], [2025], INSA Lyon, tous droits réservés

In our study, microstructural analysis using electron microscopy (EM) were systematically applied to various regions of the sample (top, middle, bottom, outer, inner) to observe potential gradients in size or composition. For EM observation, polished sample surfaces were stored in a vacuum chamber with minimum presence of air and moisture to prevent oxidation and contamination. The storage chamber is illustrated in *Figure 3.37*.

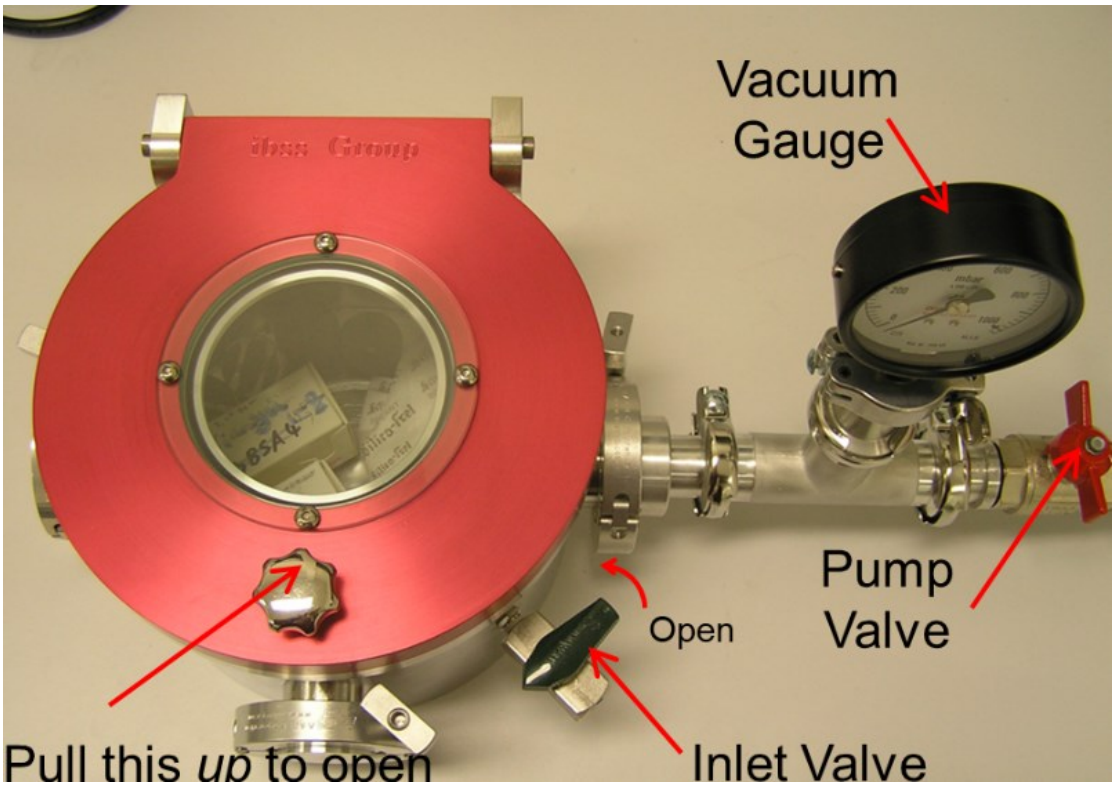


Figure 3.37. Vacuum chamber for specimens storage before SEM observations.

SEM operates by directing a beam of high energy electrons onto a sample's surface. The interaction between the electron beam and the sample generates various signals, including secondary electrons (SE2), backscattered electrons (BSE) and characteristic X-rays. These signals, collected by various detectors, are used to form images that reveals various characteristics of the materials. Two SEM systems were used based on availability: a Supra55VP (Carl Zeiss, Germany) and a JSM-7800F (JEOL, Japan). Both are equipped with SE2, BSE, EDS and EBSD detectors, offering a resolution up to 1.2 nm 0.8 nm, respectively. These systems are illustrated in *Figure 3.38*.

Thèse accessible à l'adresse : https://theses.insa-lyon.fr/publication/2025ISAL0036/these.pdf © [T. Langlois], [2025], INSA Lyon, tous droits réservés

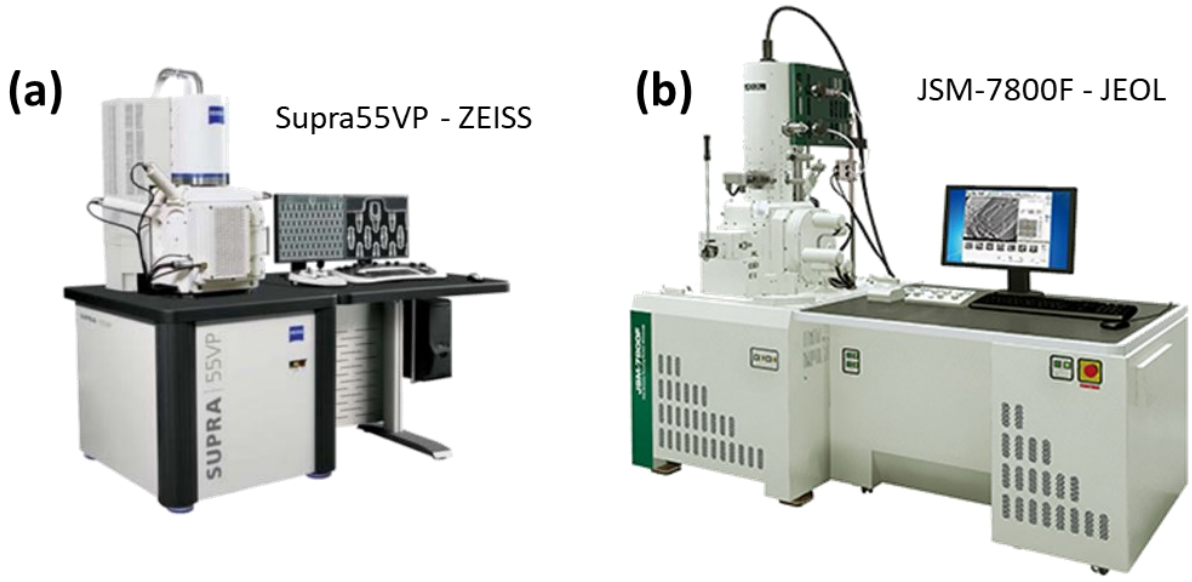


Figure 3.38. SEM systems: (a) Supra55VP used at Deakin and at Mateis; (b) JSM-7800F used at Deakin.

Despite differences in interfaces and characteristics, both SEMs were used with a similar standard procedure. They were operated at an acceleration voltage of 20 kV, with fine adjustments to current intensity or objective aperture based on the specific system. For low-magnification imaging, a working distance of 20 mm was applied to capture a broad view of the sample surface, useful for observing macroscopic features like secondary phases, casting morphology, or defects. Higher magnifications and shorter working distances were then used for detailed SE2 imaging to focus on potential oxide inclusions, as shown in *Figure 3.39*.

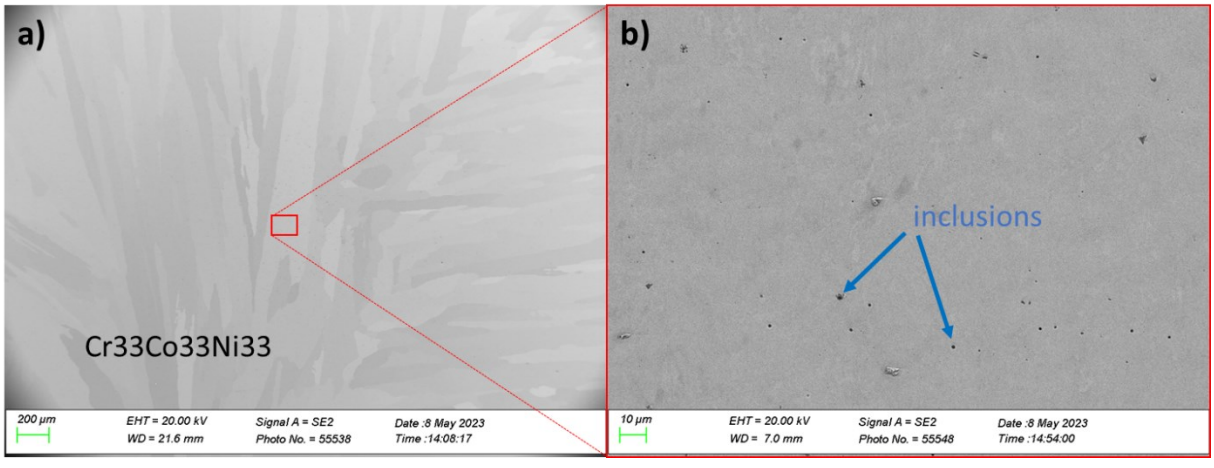


Figure 3.39. SEM SE2 Imaging (Supra55VP): (a) low magnification; (b) high magnification, inclusions are shown with blue arrows.

Additional ECCI (Electron Channelling Contrast Imaging) was performed using the SEM at Mateis on postmortem tensile specimens. Images were acquired using a

Thèse accessible à l'adresse : https://theses.insa-lyon.fr/publication/2025ISAL0036/these.pdf © [T. Langlois], [2025], INSA Lyon, tous droits réservés

BSE detector, at a working distance of 5 mm and an accelerating voltage of 10 kV. Depending on the crystal orientations, ECCI enables the detection of defects such as dislocations, stacking fault or deformation twins, as illustrated in *Figure 3.40*. This technique also provides crystallographic contrast, allowing differentiation between the FCC matrix and potential ε-martensitic transformation induced by deformation.

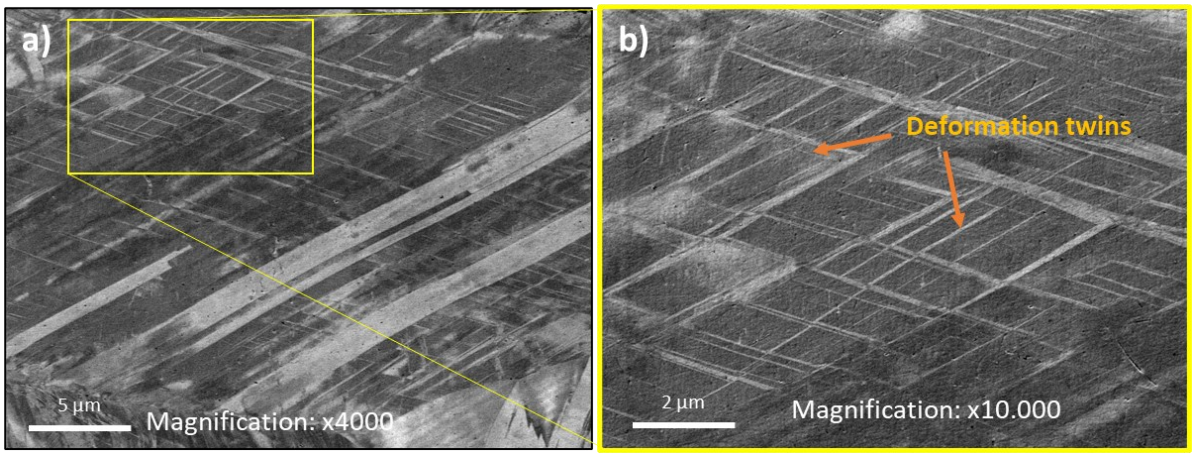


Figure 3.40. SEM ECCI Imaging (Supra5SVP) (a) high magnification of a deformed region in the Co10 tensile sample; (b) Very high magnification highlighting deformation twins in orange.

Electron Back-Scattered Diffraction (EBSD) is a technique that maps the crystallographic orientation of materials by analysing the pattern formed when electrons backscatter from the sample. For EBSD, a working distance of 10 mm, 20 kV voltage, and high current were used. Samples were tilted at 70 degrees, and dynamic focus was applied for EBSD detection. We indexed phases at five principal points before generating maps. EBSD data were collected using Aztec software (Oxford Instruments) to systematically analyse phase distribution, grain size, grain orientation and twin statistics across different regions of the CrCoNi and CrCoNiSi tensile samples. After EBSD acquisition, [.cpr] and [.ctf] files were exported from Aztec into MTEX, an opensource MATLAB toolbox for advanced crystallographic analysis. *Figure 3.41* summarises the MTEX analysis workflow.

Thèse accessible à l'adresse : https://theses.insa-lyon.fr/publication/2025ISAL0036/these.pdf © [T. Langlois], [2025], INSA Lyon, tous droits réservés

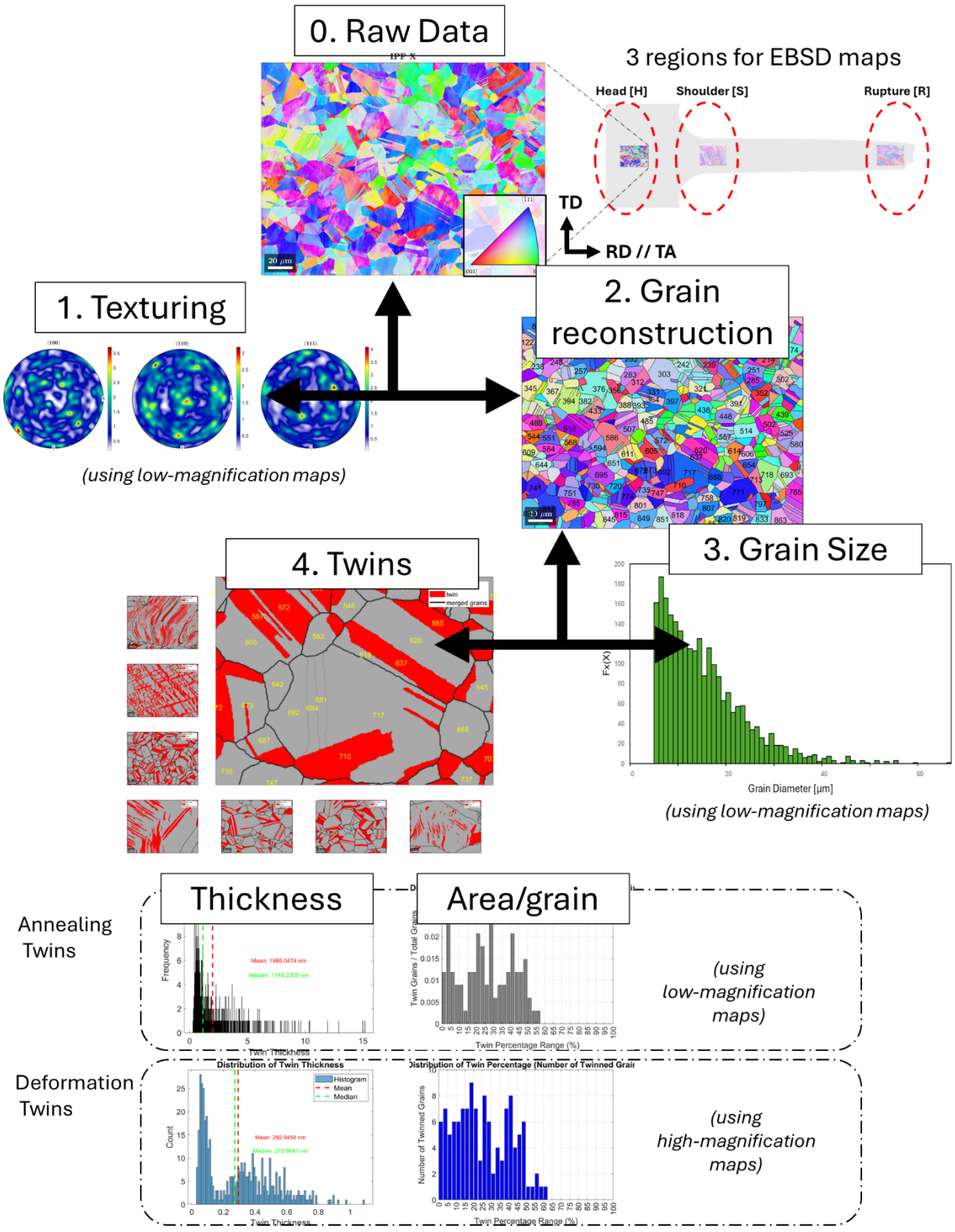


Figure 3.41. Schematic representation of the MTEX analysis workflow (systematic study in head, shoulder and near the rupture of each tensile specimen).

Phases were identified based on crystallographic data of austenite [44], ε-martensite [125] and sigma [126, 127] phases observed in Co-Cr-Ni-Si subsystems. This

Thèse accessible à l'adresse : https://theses.insa-lyon.fr/publication/2025ISAL0036/these.pdf © [T. Langlois], [2025], INSA Lyon, tous droits réservés

analysis also integrated our experimental XRD data. The crystallographic information files (CIFs), containing details such as space group, unit cell parameters and Wyckoff positions, were created using HKL Twist software and then imported into Aztec for phase indexing.

Grain size analysis was conducted on low-magnification EBSD maps using the Linear Intercept method, as detailed in ASTM E1382 (2023 [128]). Measurements were primarily obtained from undeformed microstructures prior to mechanical testing to support the interpretation of mechanical behaviour. The corresponding microstructures are presented in *Table 3.12*. For elongated grain structures, the analysis was performed following the guidelines of Annex-A1 of ASTM E1382. Grain size measurements were performed in microns, with map dimensions converted from pixels to microns based on the magnification of each EBSD map. Grain size was evaluated both with and without accounting for the contribution of detected annealing twins.

Table 3.12. Observed microstructures for grain size measurements corresponding to the geometries for the different mechanical tests.

Manufacturing equipment	**Specimen geometry**	**Mechanical test**	**Processed microstructure**	**General Observations**
Arc50	Cylinder	Compression test	As-Homogenised	Coarse and elongated grains structure
Ind500	Charpy V-Notch	Impact test	As-Rolled (hot-rolling and waterquench)	Medium-sized and homogeneous grain structure
Arc200	Dog-bone plate	Tensile test	As-Recrystallised (after cold-rolling)	Small and homogeneous grain structure

Grain texturing was measured on low-magnification EBSD maps and quantified using a texture index [129]. We considered original pixel orientations without applying continuous contouring. Results are represented through pole figures of the {100}, {110} and {111} crystallographic plane families, plotted in a reference system aligned with the tensile axis. This approach is essential to account for plastic deformation and orientation changes at high deformation levels. Grain reorientation was analysed by comparing microstructures from the undeformed state to those after the tensile breaking point.

Thèse accessible à l'adresse : https://theses.insa-lyon.fr/publication/2025ISAL0036/these.pdf © [T. Langlois], [2025], INSA Lyon, tous droits réservés

Statistics on **annealing twins and deformation twins** in tensile specimens have also been investigated with MTEX. Existing MATLAB scripts developed for other crystallographic systems [130, 131] were adapted for twin boundary identification and parent grain reconstruction in FCC alloys. Twins were identified as $\Sigma 3$ boundaries with $60°/<111>$ misorientations in FCC alloys. For annealing twins, statistics were obtained from undeformed sample regions using low-magnification EBSD maps. Deformation twin statistics were subsequently extracted from high-magnification EBSD maps in deformed regions by removing contributions from annealing twins.

Map dimensions were converted from pixel to micron for consistence across the low- and high-magnification data. Twin thickness distribution was calculated using the minor axis of an equivalent ellipse fitted to each identified twin. The percentage of twin area per grain was determined as the ratio of twin surface to total parent grain surface. To enable comparison across alloys, since each EBSD map is "randomly" located, twin thickness and twin area distributions were normalised by the total fraction of twinned surface within each map. A detailed version of our script for twin analysis in FCC alloys is available online [132].

3.3.8 Mechanical testing methods

In this PhD, various mechanical testing methods were conducted to analyse the synthesised C-MPEAs. These methods were used to assess key properties, including material toughness, strength, and ductility. The primary focus is on evaluating how these mechanical properties evolve with changes in chemical composition, microstructural state (such as as-cast (AC), as-homogenised (AH), hot rolled, or annealed), sample position, and temperature. The following testing methods were performed:

- **Hardness Vickers (HV)**: Measures the resistance to deformation of the material.
- **Profilometry-based Indentation Plastometry (PIP)**: Indentation technique used to estimate the yield strength and ultimate strength.
- **Compression testing**: Observes the stress-strain compressive behaviour of FA cylinders.
- **Tensile testing**: Measures yield strength, ultimate tensile strength and strain-hardening rate of the material under tensile deformation. This test is performed at two temperature, 110 K and 293 K, respectively.

Thèse accessible à l'adresse : https://theses.insa-lyon.fr/publication/2025ISAL0036/these.pdf © [T. Langlois], [2025], INSA Lyon, tous droits réservés

- **Impact-testing**: Measures impact toughness. This test is performed at two temperature, 77 K and 293 K, respectively.

HV tests were carried out using a DuraScan-20 (Struers, Denmark) at Deakin IFM and with a Wilson VH3300 (Buehler, USA). Both systems support various indentation methods, magnifications, and automated measurement sequences For Vickers Hardness (HV), a pyramidal indent is formed under a load F, with d as the average diagonal length. HV is calculated using *Equation (3.8)*. Calibration samples were tested to ensure the accuracy of system and loading parameters.

$$HV = 0.1891\frac{F}{d^2} \tag{3.8}$$

In this PhD, both systems were configured for HV measurements according to ASTM E92-17 (2023 [133]), applying a 5 kg load applied for 15 s. This method was used on Arc50, Arc200 and Ind500 samples to estimate their mechanical properties at various stages of thermomechanical treatment. At least 15 indents were performed on each sample to reduce measurement error. Hardness testing provides characteristic of materials, including a rough correlation with yield strength (YS) with YS ≈ 3 HV for many alloys [134], [135]; though this relationship may vary for C-MPEAs [136]. HV testing systems and calibration samples are illustrated in *Figure 3.42*.



Figure 3.42. Automated systems for HV5 measurements at Deakin IFM (Struers) and Mateis (Buehler).

Thèse accessible à l'adresse : https://theses.insa-lyon.fr/publication/2025ISAL0036/these.pdf © [T. Langlois], [2025], INSA Lyon, tous droits réservés

Given that single values are provided for each indent measurement, the hardness values are calculated using the arithmetic mean $\bar{x}$ and the standard error of the mean $\sigma_{\bar{x}}$. These statistics are calculated using *Equations (3.9), (3.10) and (3.11).*

$$\bar{x} = \frac{\Sigma x_i}{n} \tag{3.9}$$

$$\sigma = \sqrt{\frac{\Sigma (x_i - \bar{x})^2}{n-1}} \tag{3.10}$$

$$\sigma_{\bar{x}} = \frac{\sigma}{\sqrt{n}} \tag{3.11}$$

Where x_i represents each individual measurement, n is the number of measurements, and σ is the standard deviation quantifying the spread of data points around the mean. The standard error $\sigma_{\bar{x}}$ reflects the precision of the mean value.

PIP testing was conducted with a PLX-Benchtop (Plastometrex, UK). This technique was used on both Arc50 and Arc200 samples to estimate their mechanical properties (yield strength σ_y, ultimate tensile strength σ_{uts} and strain at UTS. This method involves indenting a flat, polished surface with a spherical tip under specific load and time conditions. The indent profile was analysed and compared with benchmark alloys using inverse finite element analysis in Corsica software [137], allowing for the estimation of tensile properties. System calibration includes load cell and profilometer calibration with certified samples. The PLX-Benchtop has a load cell resolution of 0.1 N and a profilometer resolution of 0.4 µm. The load cell measurement error at 8.5 kN, corresponding to the maximum applied force, is within 0.5% (±37.5 N), and the profile measurement error for a 200 µm indent is less than 1% (± 2 µm). For most materials, much smaller force and vertical displacement are needed.

The software fits the indent profile to tensile properties using the Voce expression *(Equation (3.12))*, a constitutive law describing the plastic deformation of materials [137].

$$\sigma = \sigma_S - (\sigma_S - \sigma_Y)\, exp\left(\frac{\varepsilon}{\varepsilon_0}\right) \tag{3.12}$$

where σ is the true stress, ε is the true strain, σ_y is the yield stress, σ_s is a saturation stress level and ε_0 is a material-specific strain constant that characterises the rate at which the flow stress approaches σ_s.

Thèse accessible à l'adresse : https://theses.insa-lyon.fr/publication/2025ISAL0036/these.pdf © [T. Langlois], [2025], INSA Lyon, tous droits réservés

At least 5 valid PIP measurements were performed for each composition. The estimations of yield stress (YS) and ultimate tensile stress (UTS) are presented with an individual error σ_i. Their mean value $\bar{x}$ and error $\sigma_{\bar{x}}$ are calculated using Inverse-variance weighting with *Equations (3.13)* and *(3.14)*:

$$\bar{x} = \frac{\Sigma\left(\frac{x_i}{\sigma_i^2}\right)}{\Sigma\left(\frac{1}{\sigma_i^2}\right)} \tag{3.13}$$

$$\sigma_{\bar{x}} = \sqrt{\frac{1}{\Sigma\left(\frac{1}{\sigma_i^2}\right)}} \tag{3.14}$$

The testing system and its working principle are illustrated in *Figure 3.43*.

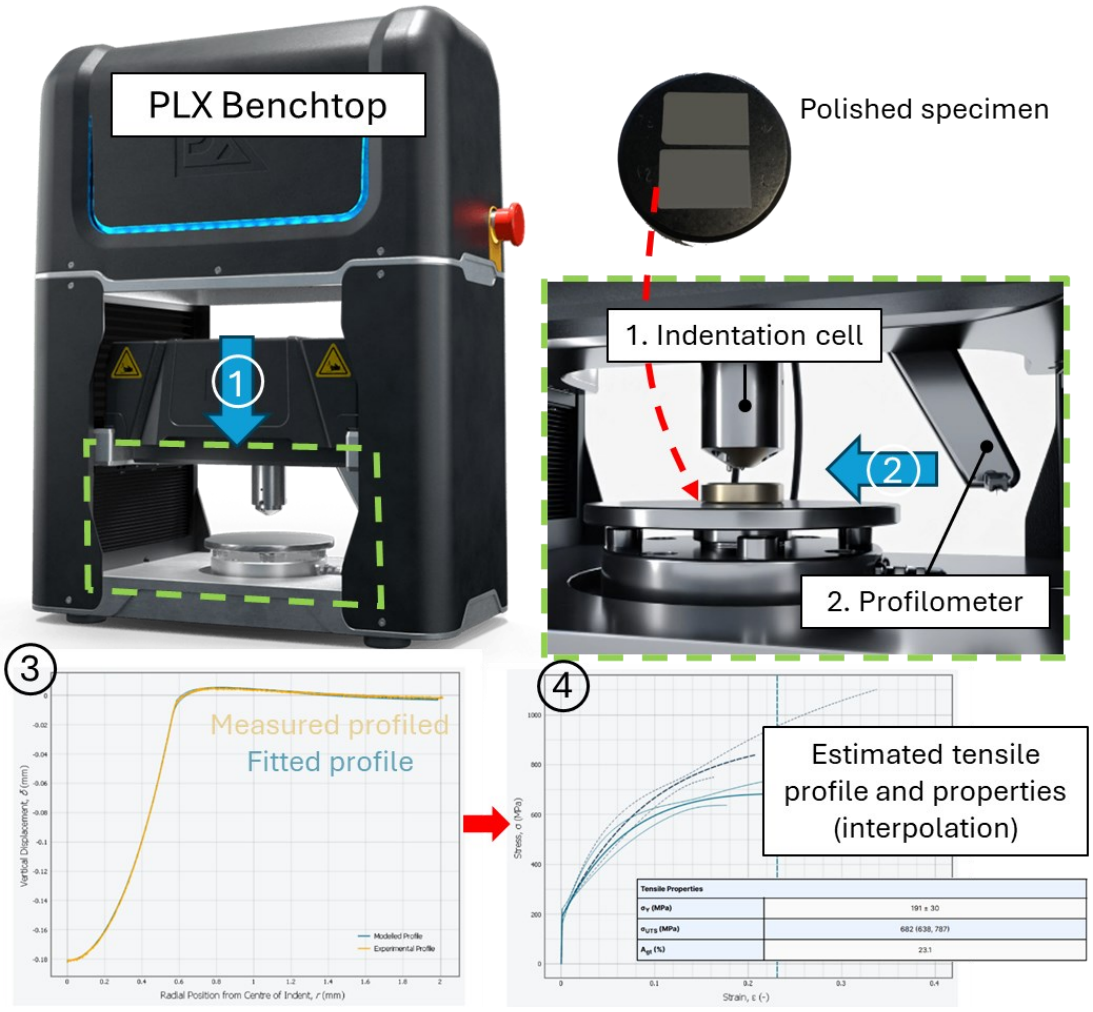


Figure 3.43. PLX-Benchtop for PIP measurements. (1) Overall view of the system; (2) Close-view of the indentation and profilometry tools; (3) Indent profile reading and fitting using FEM [137]; (4) Stress-Strain extrapolation using FEM fitting and Voce law [137].

Thèse accessible à l'adresse : https://theses.insa-lyon.fr/publication/2025ISAL0036/these.pdf © [T. Langlois], [2025], INSA Lyon, tous droits réservés

Compression testing was carried out on cylindrical FA specimens using a 8801 Servohydraulic system (Instron, USA), operated with a video extensometer and Bluehill 3 software at Deakin IFM. This machine is depicted in *Figure 3.44*. The procedure follows ASTM E9-19 standards (2019 [138]). An increasing load of 100 kN was applied to the specimen at a strain rate of $5x10^{-3}$ s^{-1}, with force and displacement recorded every 0.25 s.

Cylindrical samples were cleaned and wrapped with Teflon tape to minimise the barrelling effect caused by friction, as illustrated in *Figure 3.45*. The friction coefficient during compression was evaluated using MATLAB [139]. White marks on the sample indicate the initial length L_0, measured with the video extensometer, and the initial diameter D_0 was determined using a digital calliper. The initial cross-sectional area S_0 was calculated using *Equation (3.15)*. From the recorded load F and displacement ΔL, the engineering flow stress σ_E and engineering strain ε_E are calculated using *Equation (3.16)* and *Equation (3.17)*, respectively.

$$S_0 = \frac{\pi \cdot {D_0}^2}{4} \tag{3.15}$$

$$\sigma_E = \frac{F}{S_0} \tag{3.16}$$

$$\varepsilon_E = \frac{\Delta L}{L_0} \tag{3.17}$$

Because the cross-sectional area of the material changes during plastic deformation represented by the barrelling effect, true stress σ_T and true strain ε_T are used to more accurately describe the material's behaviour under compression. The relationships between engineering and true values under compression are provided *Equation (3.18)* and *Equation (3.19)*, and the strain-hardening rate (SHR) is determined using *Equation (3.20)*.

$$\sigma_T = \sigma_E(1 - \varepsilon_E) \tag{3.18}$$

$$\varepsilon_T = -ln\,(1 - \varepsilon_E) \tag{3.19}$$

$$SHR = \frac{d\sigma_T}{d\varepsilon_T} \tag{3.20}$$

Thèse accessible à l'adresse : https://theses.insa-lyon.fr/publication/2025ISAL0036/these.pdf © [T. Langlois], [2025], INSA Lyon, tous droits réservés

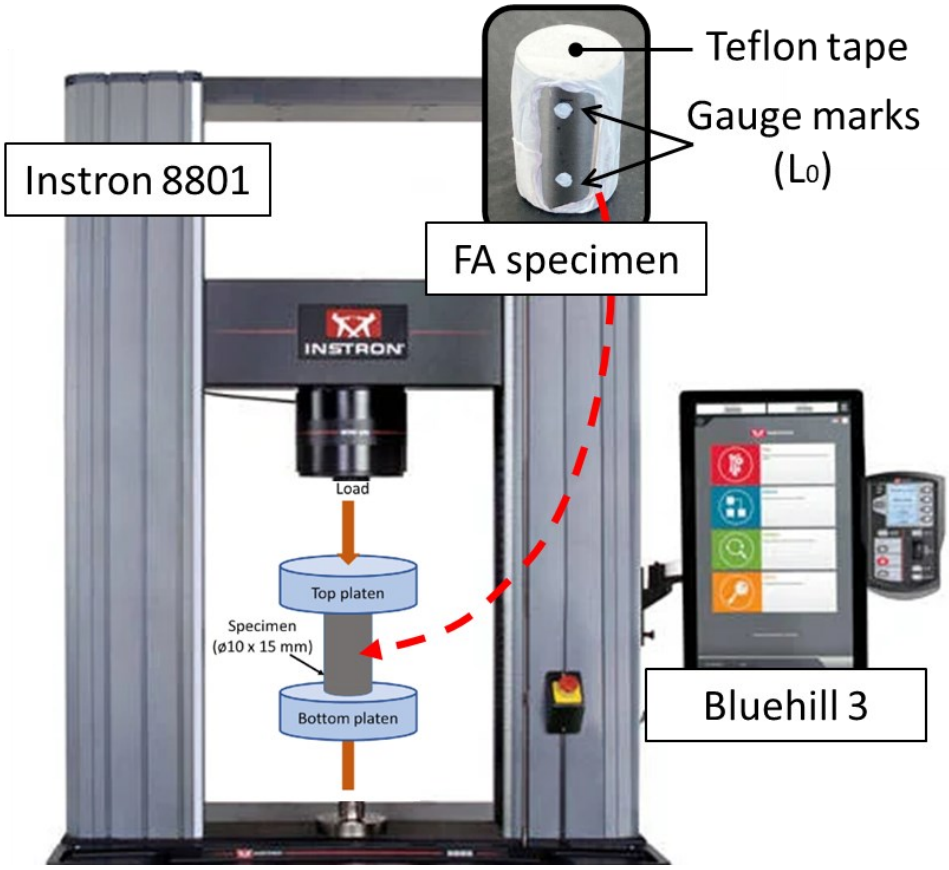


Figure 3.44. Instron 8801 system for compression measurement of FA specimens (cylinders produced by Arc50).

We used annealed Stainless Steel 304 as reference material to validate our compression setup. The compressive strain-stress curve of this reference material was compared to established literature values [140]. Subsequently, at least three replicates for each composition were tested, Yield Stress (YS) values were measured at 0.2% of plastic deformation using engineering stress and the strain hardening rate (SHR) was calculated using *Equation (3.20)*. Results are given with arithmetic and standard error.



Figure 3.45. Friction compensation with PTFE tape (SS304 reference compression specimen).

Thèse accessible à l'adresse : https://theses.insa-lyon.fr/publication/2025ISAL0036/these.pdf © [T. Langlois], [2025], INSA Lyon, tous droits réservés

Tensile tests were conducted on TDB specimens. Testing was performed with a traction bench 5967 (Instron, USA) for test at room temperature and Zmart.Pro (Zwick/Roell, Germany) at low temperatures. Technical details of both systems are given in *Table 3.13* and the setup at low temperature is illustrated in *Figure 3.46*.

Table 3.13. Characteristic of the two tensile systems used at ambient temperature and cryogenic temperature.

Tensile testing machine	**Test temperature**	**chamber**	**Gas**	**location**
5967	300 K	None	Air	INSA / MATEIS
Zmart.Pro	110 K	Influtherm Cryostat	Liquid N2 (99.999%)	INSA / MECANIUM

Tensile testing machine	**Standard**	**displacement mode**	**load cell**	**extenso. type**	**mag. lense**	**acquisition rate**
5967	ISO 6892-1	strain-controlled	30kN	AVE-1	x50	50 Hz
Zmart.Pro	ISO 6892-3	strain-controlled	100 kN	Limess (Video)	x 200	50 Hz

Tensile tests were conducted in line with standards for room temperature in ISO 6892-1 (2019 [111]), and low temperature in ISO 6892-3 (2015 [141]). Tests were conducted in strain-controlled mode. Thermocouples were employed to maintain the testing temperature at 110 ± 3 K. Annealed Stainless Steel AISI 304 serves as a reference material to validate the accuracy of the setups, with results compared against literature data at room temperature [142] and at low temperature [143], [144]. Duplicate and triplicate tests were performed at cryogenic and room temperature, respectively.

Thèse accessible à l'adresse : https://theses.insa-lyon.fr/publication/2025ISAL0036/these.pdf © [T. Langlois], [2025], INSA Lyon, tous droits réservés

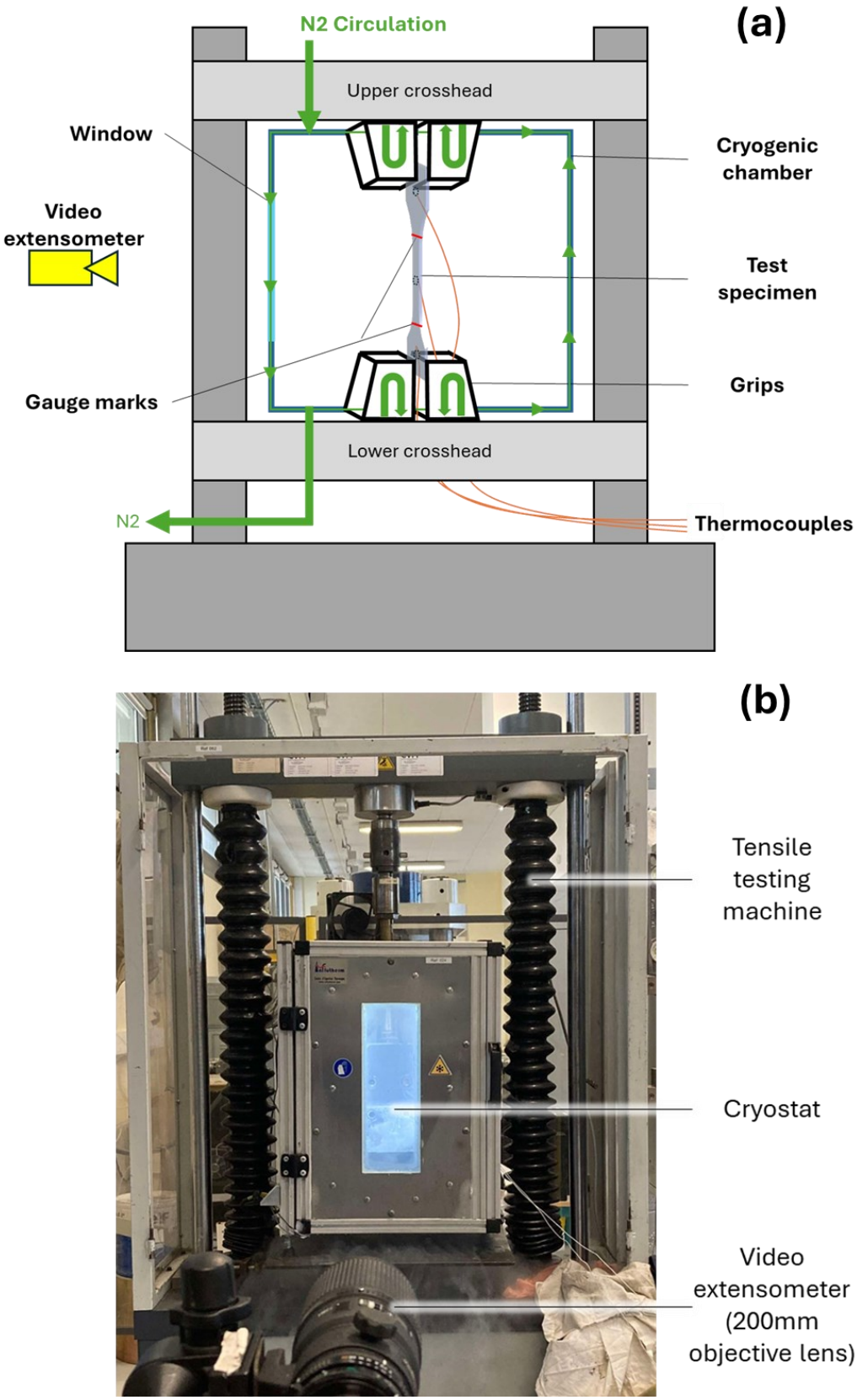


Figure 3.46. (a) Descriptive diagram and (b) Photography of the cryogenic setup for tensile testing with Zmart.Pro.

TDB specimens are marked in the reduced section as depicted in *Figure 3.47*.

Thèse accessible à l'adresse : https://theses.insa-lyon.fr/publication/2025ISAL0036/these.pdf © [T. Langlois], [2025], INSA Lyon, tous droits réservés

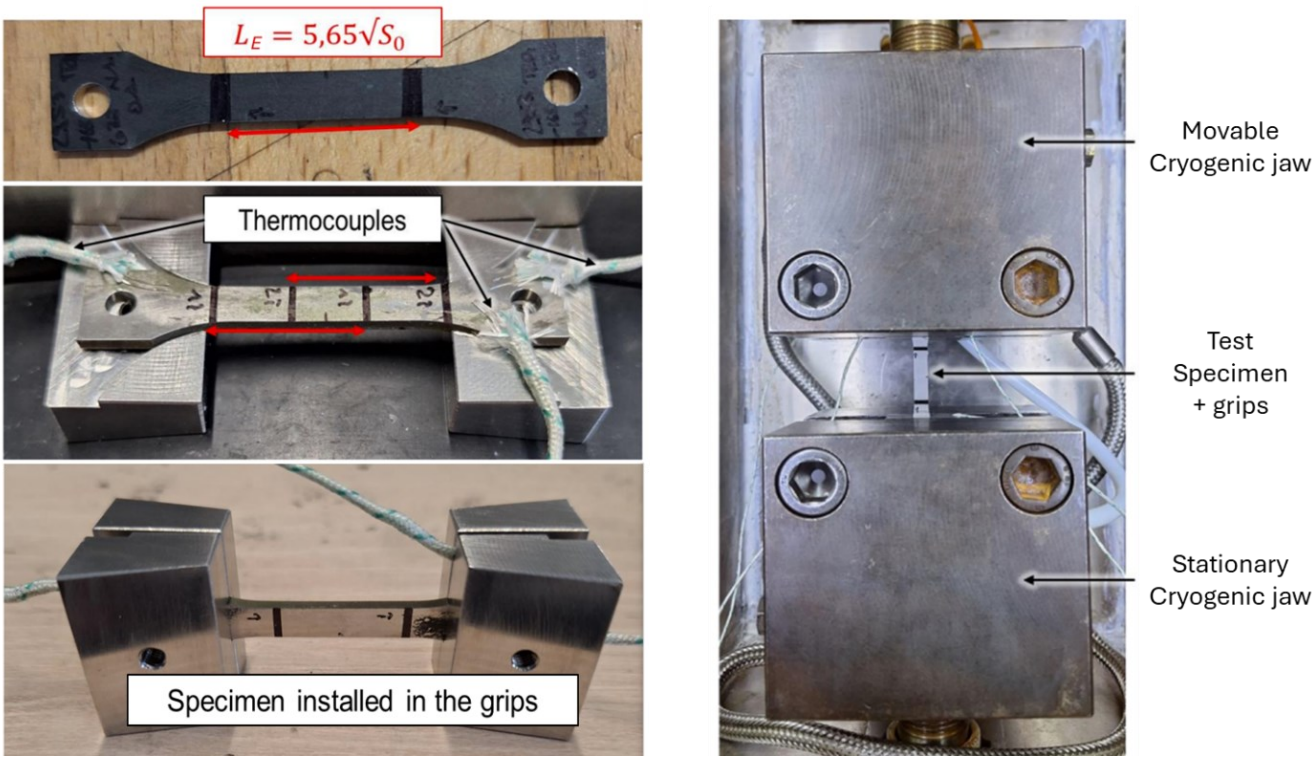


Figure 3.47. Thermocouple disposition for cryogenic tensile test.

With recorded load F and displacement ΔL, the engineering flow stress σ_E and engineering strain ε_E were calculated using *Equation (3.16)* and *Equation (3.17)*, respectively. *Equation (3.21)* and *Equation (3.22)* provide the relationship between engineering and true values of the material under tensile deformation.

$$\sigma_T = \sigma_E(1 + \varepsilon_E) \tag{3.21}$$

$$\varepsilon_T = ln\,(1 + \varepsilon_E) \tag{3.22}$$

The Yield Stress (YS) was measured at 0.2% of plastic deformation using engineering stress and strain. The uniform elongation ε_u (before necking), the elongation to rupture ε_f and the ultimate tensile stress (UTS) were also determined from engineering strain values. Finally, the strain hardening rate (SHR) was calculated using *Equation (3.20)*. Results are given with arithmetic and standard error.

Thèse accessible à l'adresse : https://theses.insa-lyon.fr/publication/2025ISAL0036/these.pdf © [T. Langlois], [2025], INSA Lyon, tous droits réservés

Impact testing was performed on CVN specimens from Ind500 ingots using a MPX Pendulum Impact (Instron, USA) with automated control via Fracta software. The system includes a motorised hammer lift, anvils and 8mm-striker inserts designed for CVN. The setup is depicted in *Figure 3.48*, with technical parameters aligned with ASTM E23 (2024, [112]), shown in *Figure 3.49*.

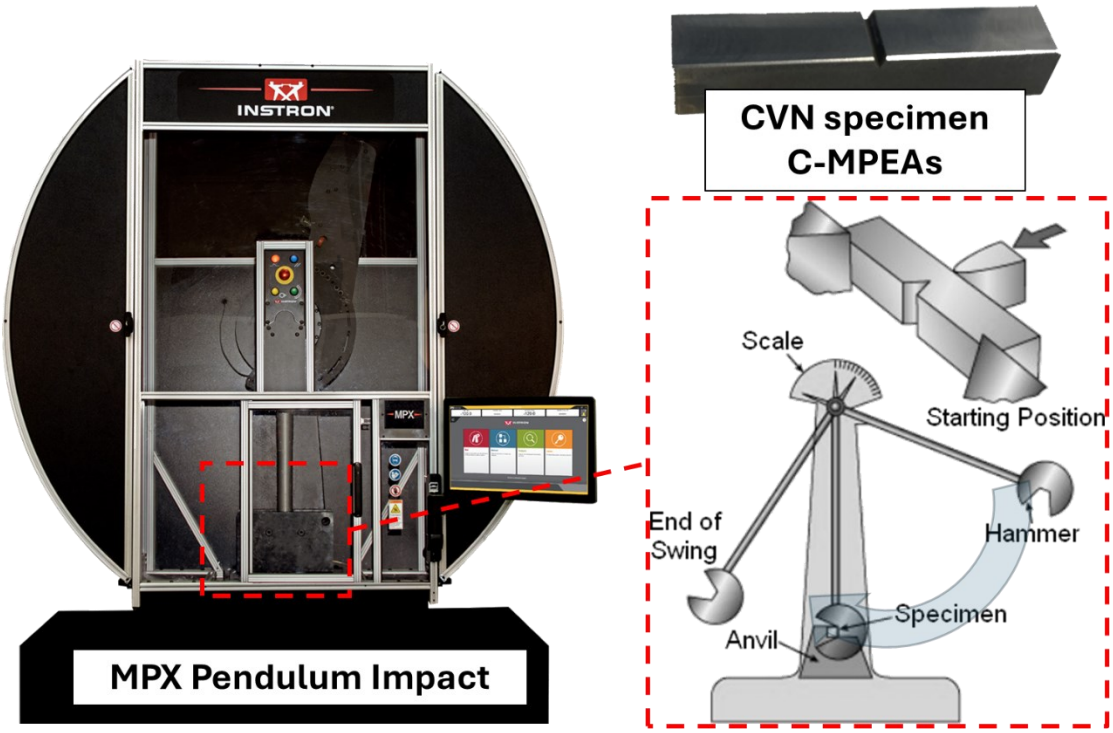


Figure 3.48. Impact-testing equipment and descriptive diagram (Green Mechanic, 2019).

During testing, the potential energy of the hammer is converted to kinetic energy upon impact. The impact energy A_c (in Joules) is calculated as the difference between the initial energy and the remaining energy after the specimen is struck, determined from the peak angle of the hammer post-impact. The material's impact toughness E_s in Joule/cm^2 is calculated using *Equation (3.23)*.

$$E_s = \frac{A_c}{B \times (W - 0.2)} \tag{3.23}$$

Where W is the specimen width (mm), and B is the thickness (mm).

Thèse accessible à l'adresse : https://theses.insa-lyon.fr/publication/2025ISAL0036/these.pdf © [T. Langlois], [2025], INSA Lyon, tous droits réservés

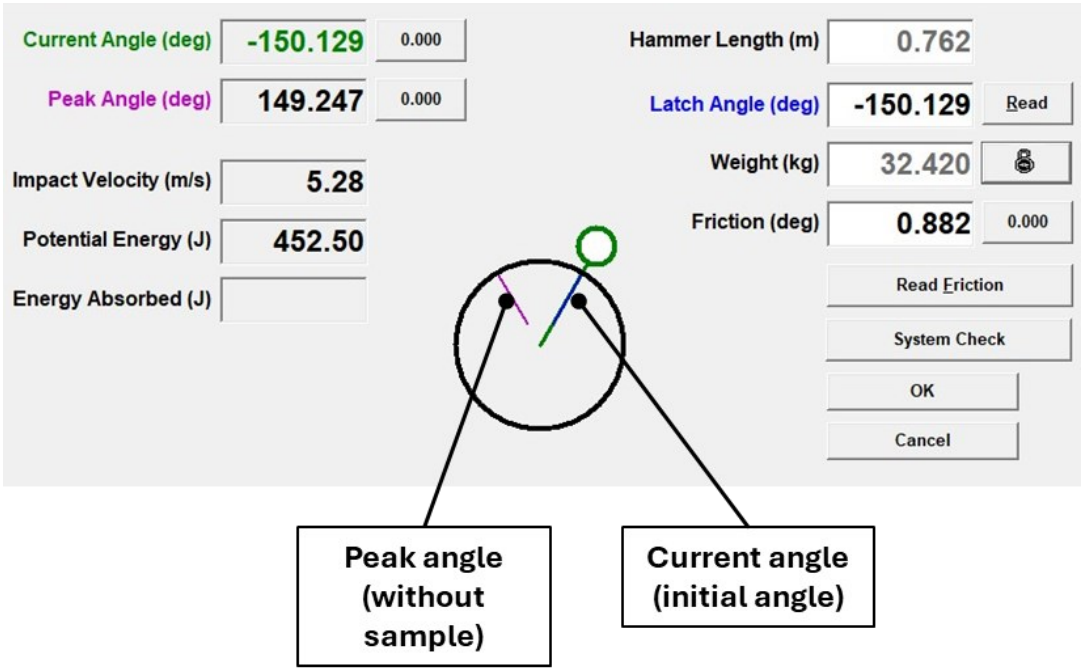


Figure 3.49. Technical parameters for Impact testing.

Stainless steel AISI 316L was used as standard reference material for test at room temperature and low temperature [145]. Measurements were performed on three replicates for each composition, and results are given with arithmetic and standard error. For low-temperature impact tests, specimens were cooled in an insulating dewar filled with liquid nitrogen (99.95 % at -196 °C; BOC, Australia). The temperature evolution on the specimen surface was monitored using thermocouples positioned at various locations, as depicted in *Figure 0.6* in the Appendix of Chapter 3. Testing was conducted within 5 seconds after removal from the dewar, in accordance with the recommended procedures in the ASTM E23 standard [112].

Thèse accessible à l'adresse : https://theses.insa-lyon.fr/publication/2025ISAL0036/these.pdf © [T. Langlois], [2025], INSA Lyon, tous droits réservés

3.4 Summary

Table 3.14 summarises the experimental methods employed for Fast Alloys (FA) and advanced alloys.

Table 3.14. Summary of the experimental methods for FA and advanced alloys.

Processing			
Manufacturing	**Arc50**	**Arc200**	**Ind500**
Geometry	Cylinder	Rectangle	Rectangle
Dimensions	L: 15 mm D: 10 mm	L: 80 mm W: 10 mm B: 8 mm	L: 95 mm W: 55 mm B: 28 mm
Homogenisation	0.5 h	1.5 h	3 h
Rolling	No	Cold	Hot
Machining	(Cylinders)	TDB	CVN
Composition			
GDOES	Yes	Yes	Yes
EDS	Yes	Yes	Yes
ONH/CS	Yes	Yes	Yes
Microstructural analysis (grain size and phase)			
XRD	Yes	Yes	Yes
powder-XRD	Yes	-	-
SE2/EBSD	Yes	Yes	Yes
Mechanical testings and analysis			
HV	HV5	HV5	HV5
PIP	Yes	Yes	Yes
Compression	Yes	-	-
Tensile	-	Yes	-
Impact	-	-	Yes
Post-mortem EBSD	Yes	Yes	Yes

Thèse accessible à l'adresse : https://theses.insa-lyon.fr/publication/2025ISAL0036/these.pdf © [T. Langlois], [2025], INSA Lyon, tous droits réservés

4 Material predictions and explorations

Contents

4.1 FCC phase stability in C-MPEAs ---------- 111

4.2 Mechanical performance of C-MPEAs ---------- 120

4.2.1 Prediction of Solid solution strengthening in C-MPEAs ---------- 121

4.2.2 Prediction of deformation mechanisms in C-MPEAs ---------- 129

4.3 Sustainable competitiveness of metal alloys and C-MPEAs ---------- 133

4.3.1 Elemental scores ---------- 133

4.3.2 Sustainability scores for different classes of alloys ---------- 137

4.3.3 Sustainability properties of Cantor subsystems. ---------- 141

4.3.4 Co-Cr-Ni-Si subsystems ---------- 145

4.4 Multi-objective optimisation ---------- 148

As explained in the methodology section, a key aspect of this thesis is to use existing models or develop new predictions for the mechanical and sustainable behaviour of HEAs, especially in the Co-Cr-Ni compositional space. Predictions of mechanical properties include phase stability, the contribution of solid solution to yield strength (σ_{SS}) and the stacking fault energy (SFE). Estimations of alloys sustainability are based on the 9 indicators that we developed [103]. The purpose of these models is to conduct a multi-objective optimisation to identify the most promising compositions in terms of both sustainability and mechanical performance trade-offs.

Stabilising single-phase FCC solid solution is essential for achieving the desired mechanical properties and the mechanical predictions are limited to single-phased FCC

Thèse accessible à l'adresse : https://theses.insa-lyon.fr/publication/2025ISAL0036/these.pdf © [T. Langlois], [2025], INSA Lyon, tous droits réservés

alloys. To efficiently explore the mechanical performance of FCC HEAs, it is necessary to apply the phase prediction layer first. In contrast, the sustainability prediction model can be applied to any metal and alloy.

4.1 FCC phase stability in C-MPEAs

The starting point of the exploration is the Cantor subsystem, containing Co-Cr-Fe-Mn-Ni elements. The use of ThermoCalc and TCHEA5 database is giving reliable results, as demonstrated in the numerical methods. The exploration of compositions starts on a broader scale with quinary systems and subsequently focuses on ternary Co-Cr-Ni systems. The effect of Si addition is visualised eventually.

Using the TC-Python module from ThermoCalc with TCHEA5, we estimated the stable phases from 900°C to 1100°C in quinary Co-Cr-Fe-Mn-Ni subsystems with an increment of 10 at.% between each composition. This range of temperature corresponds to experimental values applied in thermomechanical treatments for most MPEAs in the literature. *Figure 4.1* shows the results for 1770 compositions, with 436 systems having a single-phased FCC microstructure. Higher chromium and manganese contents promote the formation of multiphase microstructures. Indeed, Cr is a ferrite stabiliser and has a high VEC value, in accordance with prediction of FCC-BCC mixture (see *Equation 1.3* and *Figure 0.8* in Appendix of Chapter 4*)*. Mn is known as an austenitic stabiliser but forms a β-Mn microstructure between 700 and 1100°C. Therefore, high Mn content leads to multiphase microstructures.

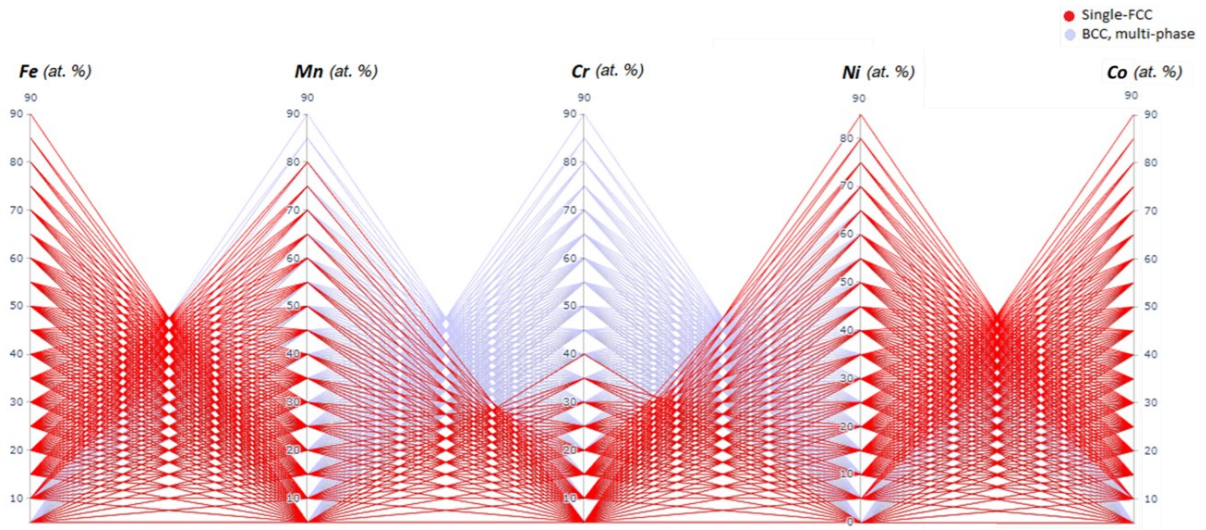


Figure 4.1. Parallel plot of Co-Cr-Fe-Mn-Ni subsystems (from binary to quinary alloys), with stable FCC single-phase shown in red, for a temperature between 900°C and 1100°C.

Thèse accessible à l'adresse : https://theses.insa-lyon.fr/publication/2025ISAL0036/these.pdf © [T. Langlois], [2025], INSA Lyon, tous droits réservés

The later observation suggests that chromium is the limiting element when designing C-MPEAs with FCC microstructures. When looking for the stable FCC phases in the Cantor subsystems, another approach consists in series of ternary maps, as displayed in *Figure 4.2*. This process was automated with a python script in TC-Python ThermoCalc, provided in *Figure 0.7* in the Appendix of Chapter 4. Calculations were performed with TCHEA5 database at 800°C, 1000°C and 1200°C to determine the optimal temperature for experimental heat-treatments.

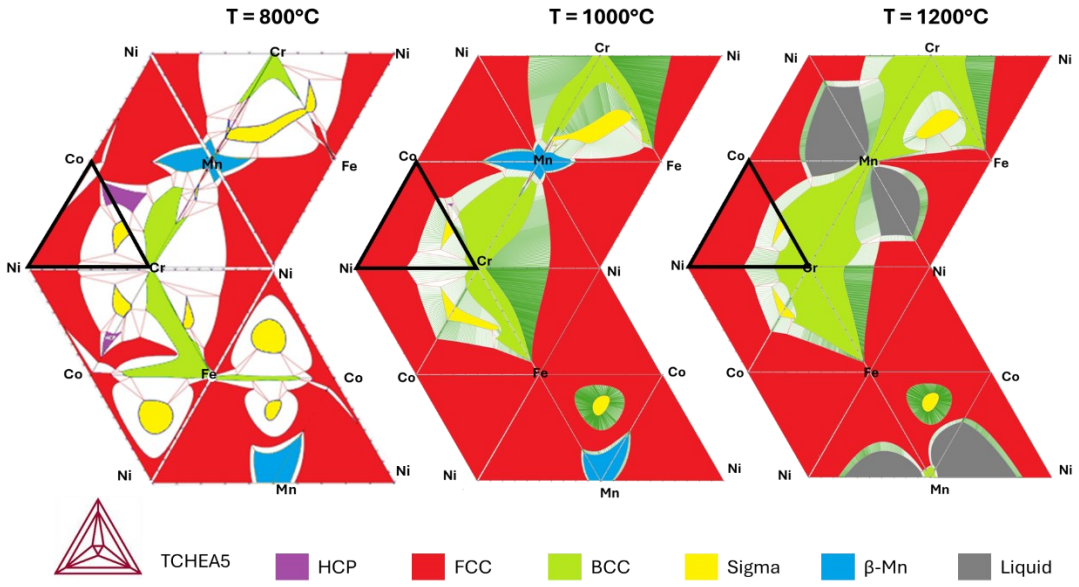


Figure 4.2. Ternary phase diagrams of the Co-Cr-Fe-Mn-Ni subsystem, generated with TCHEA5 at three different temperatures. The ternary space Co-Cr-Ni containing our benchmark alloy is represented with a black triangle.

As observed in the parallel plots, high concentrations of Cr and Mn tend to result in multiphase structures or non-FCC phases. Higher temperatures promote the stabilisation of FCC solid solutions (represented in red), because element solubility increases at elevated temperatures. However, these high temperatures also approach the formation of liquid phases, particularly in alloys with high Mn content, due to lower melting point of this element given in *Table 4.1* [78]. Therefore, the control of FCC-regions must account for both compositions and temperature considerations. These considerations are addressed in the specific cases of CrCoNi and CrCoNiSi alloys later in this section (see *Figure 4.8*), where the manufacturing robustness is discussed in terms of the temperature ranges suitable for heat treatments that avoid the formation of liquid or secondary phases while preserving the FCC single-phase solid solution.

Thèse accessible à l'adresse : https://theses.insa-lyon.fr/publication/2025ISAL0036/these.pdf © [T. Langlois], [2025], INSA Lyon, tous droits réservés

Table 4.1. Melting temperature of pure elements used in this study [78].

Element	Co	Cr	Fe	Mn	Ni	Si
Melting Temperature (°C)	1495	1907	1538	1246	1455	1414

Although phase predictions are performed at elevated temperatures relevant to heat-treatment processes, the metastability of microstructures upon water-quenching should be considered. Indeed, metastability plays an important role in deformation mechanisms, notably with phase transformation from FCC to BCC or HCP, varying the materials properties drastically.

Because we want to assess the influence of silicon addition on mechanical properties of the Cantor subsystems, we are exploring the compositions and temperatures that predict a single FCC phase when adding Silicon. Like the Co-Cr-Fe-Mn-Ni space, we are examining compositions and temperatures with varying silicon concentrations. Pseudo-ternary phase diagrams were generated using TC-Python and TCHEA5 database, with fixed silicon concentrations (Si = 0; 3; 6; 9 at.%) at 1200°C, as shown in *Figure 4.3*. With higher Si concentrations, BCC regions expand around Fe because Si is a ferritic stabiliser in steels. Silicon also promotes the formation of intermetallic phases and silicides with elements like Cr, which is detrimental to forming a single-phase FCC structure.

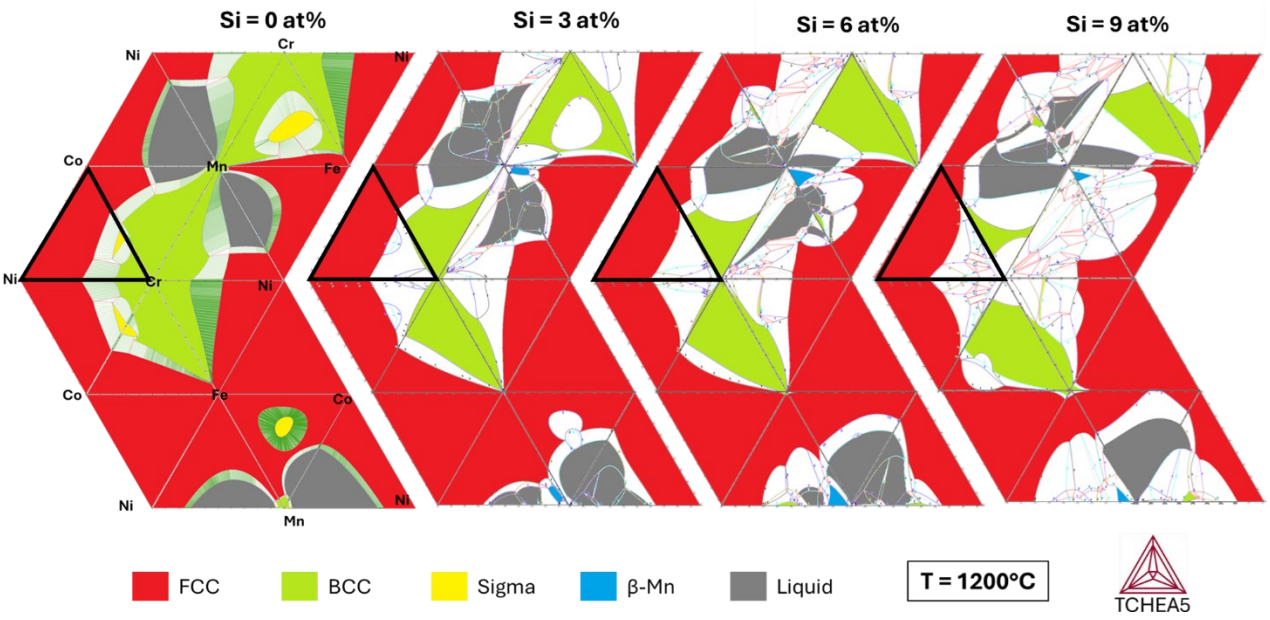


Figure 4.3. Pseudo-Ternary phase diagrams in the Cantor subsystem with Si additions.

Thèse accessible à l'adresse : https://theses.insa-lyon.fr/publication/2025ISAL0036/these.pdf © [T. Langlois], [2025], INSA Lyon, tous droits réservés

These predictions, consistent with experimental observations [64], confirm that silicon addition must be carefully controlled to avoid forming secondary phases. Focusing on Co-Cr-Ni and Co-Cr-Ni-Si systems, we estimated the stable phases in these systems using ThermoCalc. The tetrahedral representation, shown in *Figure 4.4*, allows phase estimation within the ternary subsystems, referred to as the tetrahedron walls. The single-phase FCC region, highlighted in red, is restricted to compositions between Co and Ni, with less than 50 at.% of Cr and very low silicon content.

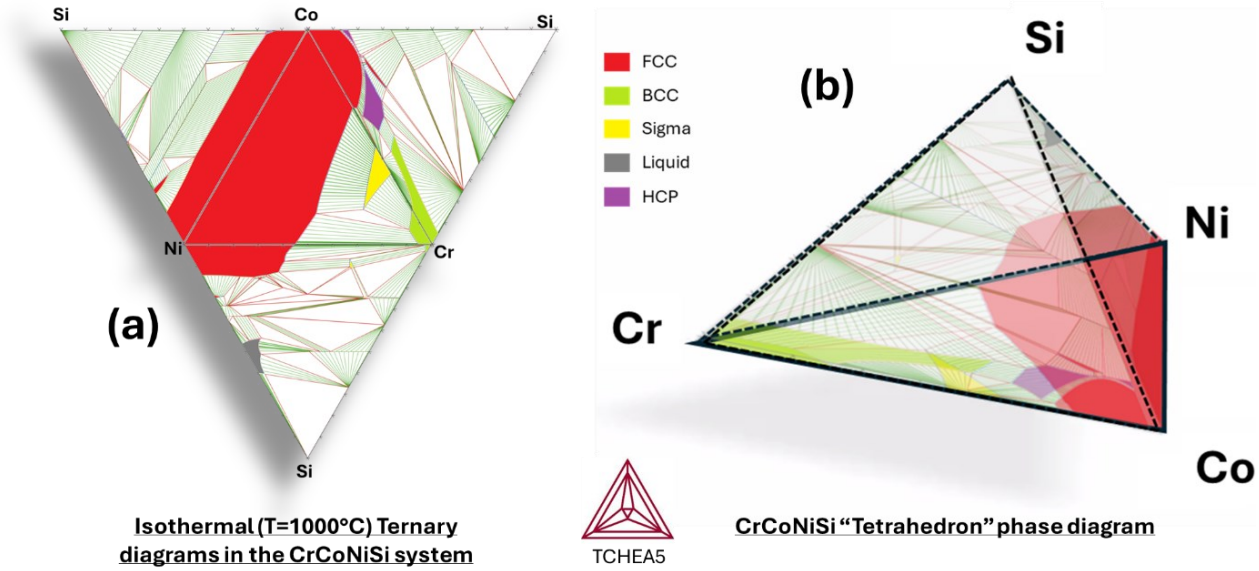


Figure 4.4. (a) Ternary phase diagrams of Co-Cr-Ni-Si system at 1000°C. (b) Tetrahedral view of Co-Cr-Ni-Si system at 1000°C.

For better visualisation of the phases present in Co-Cr-Ni-Si quaternary compositions, pseudo-ternary diagrams were also generated using scripts in ThermoCalc's console mode with TCHEA5 (*Figure 4.5* and *Figure 4.6*). These diagrams illustrate the core of the tetrahedron, with silicon concentrations of 3, 6 and 9 at.%.

Thèse accessible à l'adresse : https://theses.insa-lyon.fr/publication/2025ISAL0036/these.pdf © [T. Langlois], [2025], INSA Lyon, tous droits réservés

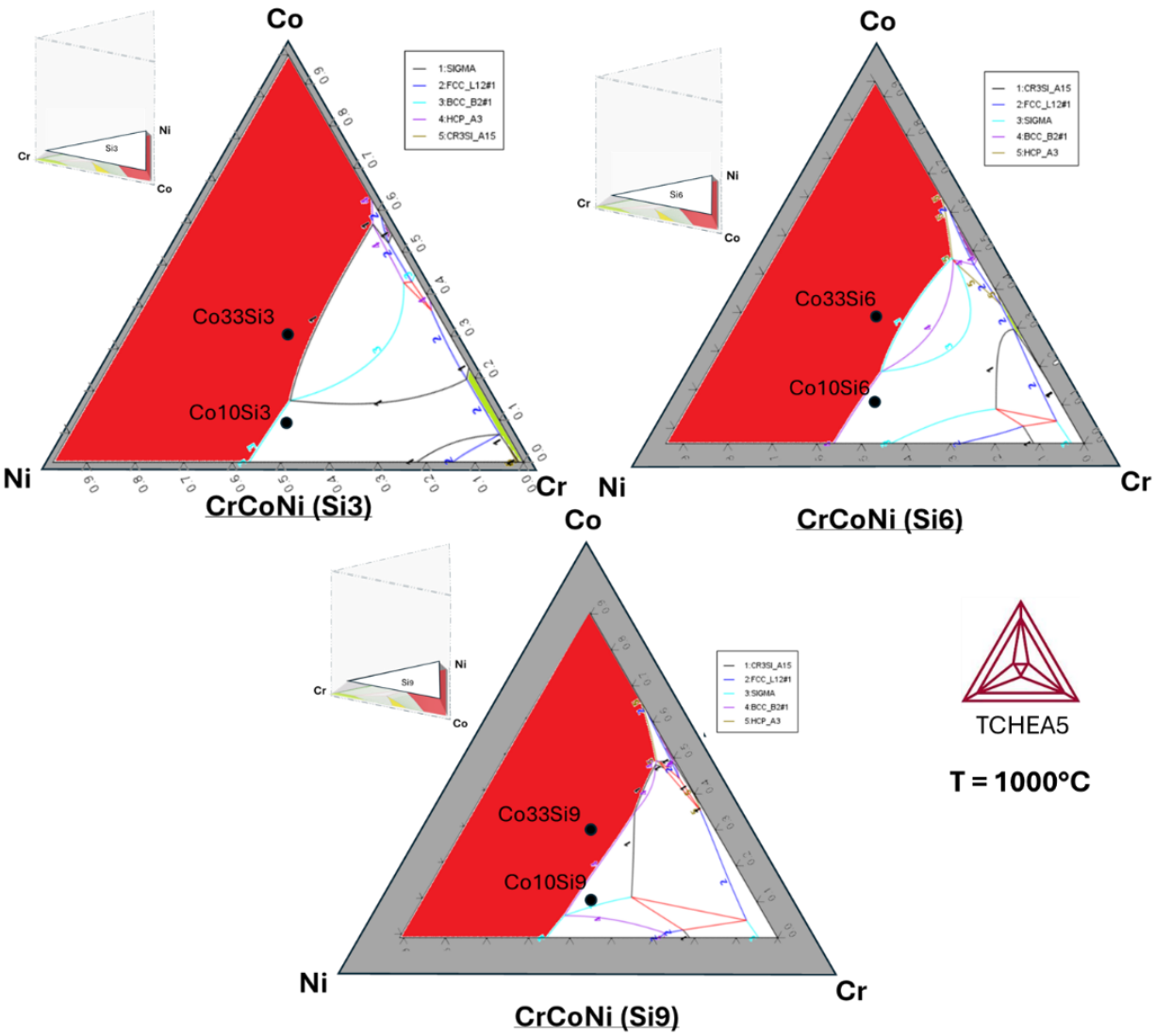


Figure 4.5. Pseudo-Ternary diagrams in Co-Cr-Ni-Si systems at 1000°C. Solid solution domains with FCC phase in red. Regions in white are complex multiphase domains.

At 1000°C, corresponding to the heat-treatment temperature of near equimolar C-MPEAS in previous studies [31, 44, 30, 146, 11, 21, 51], we can see that not all the desired compositions form a single-phase FCC microstructure, especially in cobalt-lean.

Thèse accessible à l'adresse : https://theses.insa-lyon.fr/publication/2025ISAL0036/these.pdf © [T. Langlois], [2025], INSA Lyon, tous droits réservés

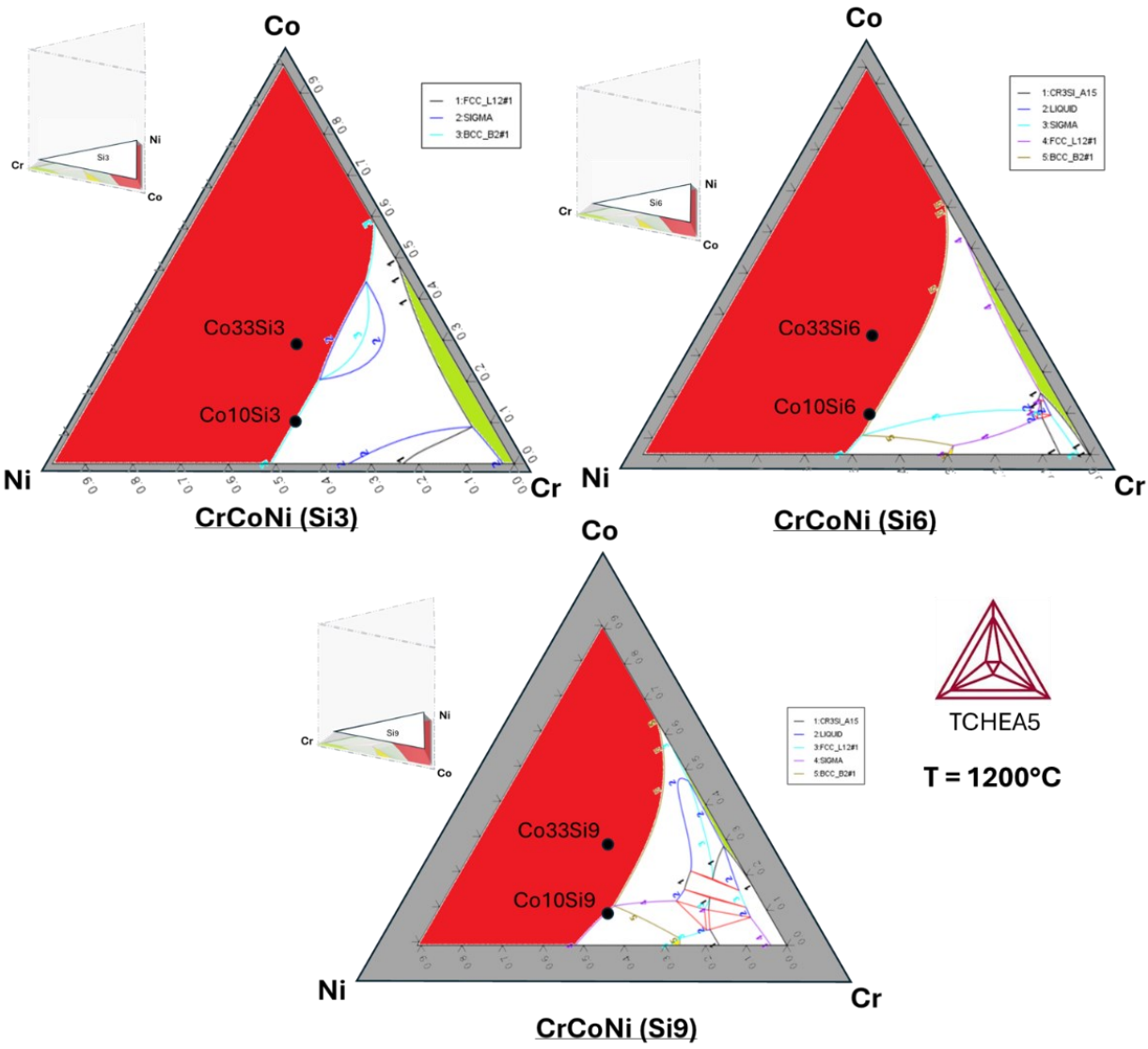


Figure 4.6. Pseudo-Ternary diagrams in Co-Cr-Ni-Si systems at 1200°C. Solid solution domains with FCC phase in red. Regions in white are complex multiphase domains.

At 1200°C, which corresponds to the experimental limitations of the furnace used in this project, higher temperatures stabilise the FCC single-phase regions. The compositions experimentally produced in this project are indicated with black dots in the figures.

To clearly visualise the influence of cobalt content, silicon content and temperature on the Co-Cr-Ni-Si systems, pseudo-binary phase diagrams with Si additions are generated with TC-Python (*Figure 4.7*).

Thèse accessible à l'adresse : https://theses.insa-lyon.fr/publication/2025ISAL0036/these.pdf © [T. Langlois], [2025], INSA Lyon, tous droits réservés

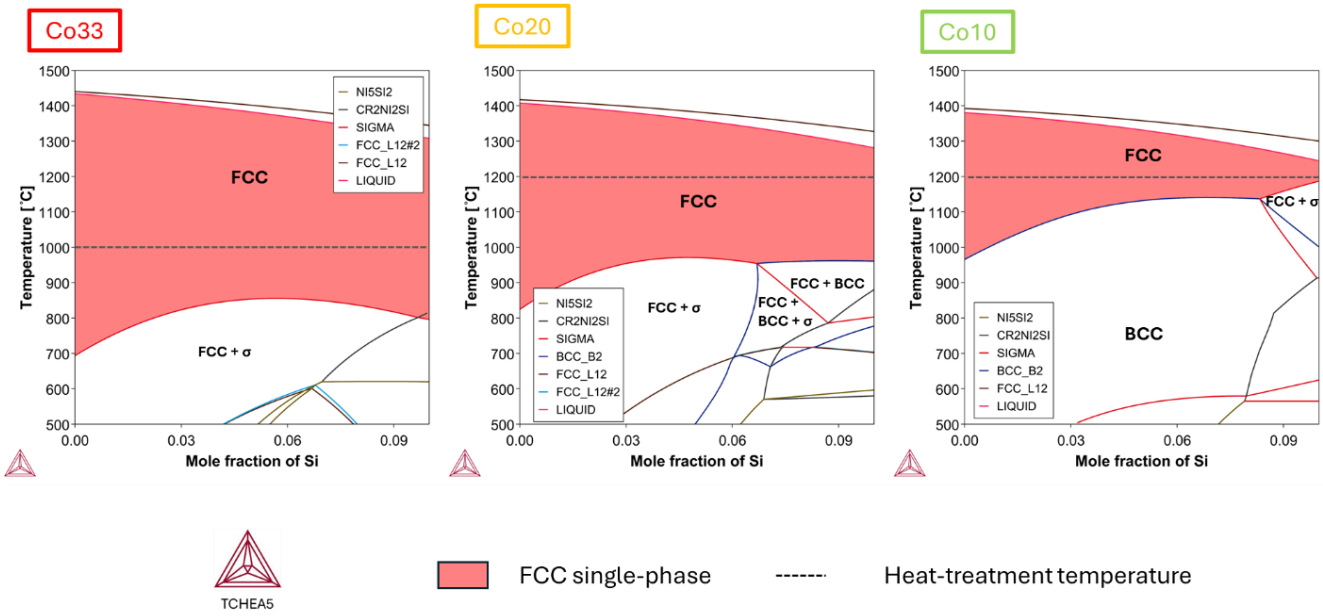
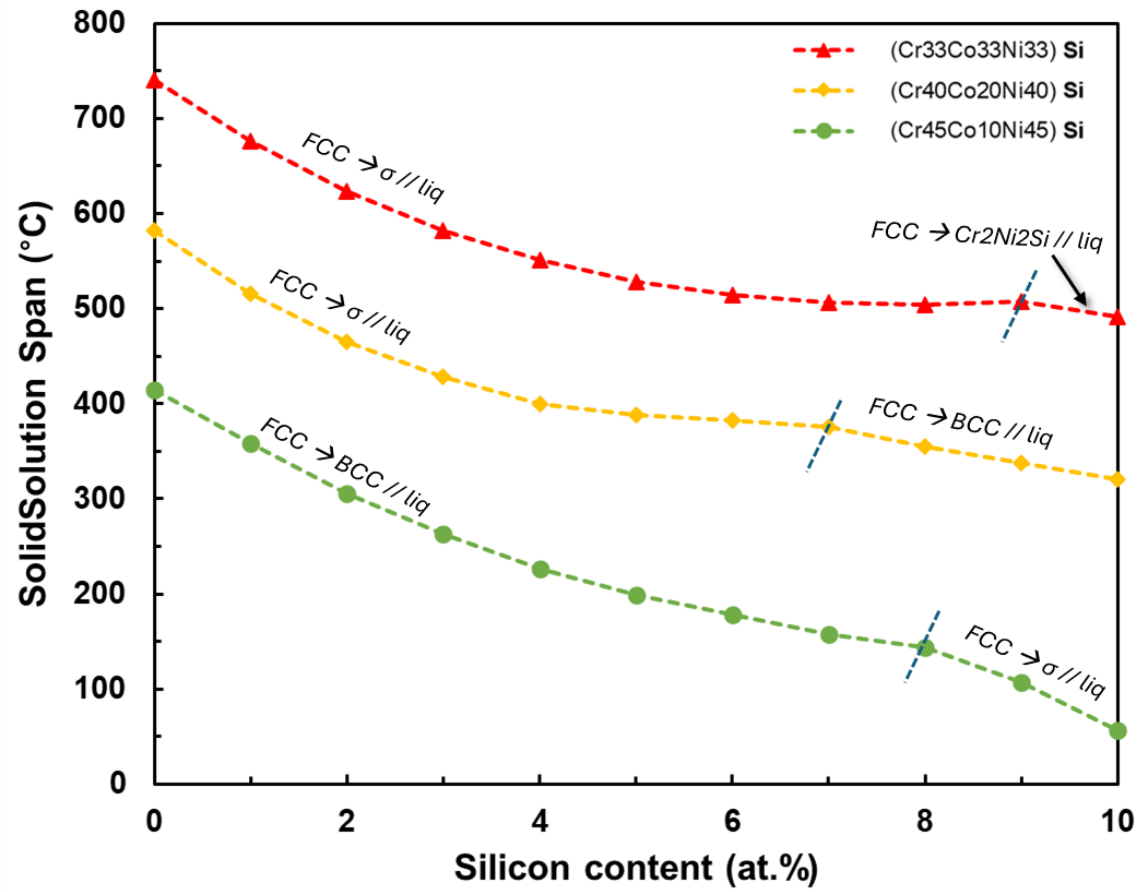


Figure 4.7. Pseudo-Binary phase diagrams in $(Cr_{33}Co_{33}Ni_{33})_{100-x}$-$Si_x$, $(Cr_{40}Co_{20}Ni_{40})_{100-x}$-$Si_x$ and $(Cr_{45}Co_{10}Ni_{45})_{100-x}$-$Si_x$.



Thèse accessible à l'adresse : https://theses.insa-lyon.fr/publication/2025ISAL0036/these.pdf © [T. Langlois], [2025], INSA Lyon, tous droits réservés

Figure 4.8. Influence of cobalt and silicon contents on the temperature range of the FCC domain in solid solution for CrCoNiSi alloys (the predicted secondary phases are indicated on each curve with respect to silicon content).

With decreasing Co content in the ternary base $Co_x(CrNi)_{100-x}$, the proportion of Cr increases, reducing the stability of the FCC microstructure. As depicted in *Figure 4.7*, the formation of a second phase like sigma-phase or BCC, can occur even at high temperatures, particularly in the Co10 alloy. The addition of silicon further narrows the FCC stability.

Although higher temperatures stabilise FCC structures, the proximity to the liquidus temperature restricts the thermal window for processing. The solid solution span, defined as the temperature range maintaining stable FCC microstructure [147], is plotted in *Figure 4.8* using TCHEA5 database. For a given silicon concentration in the studied alloy compositions, heat-treatment temperatures outside this range can lead to the formation of liquid phase, sigma phase, BCC phase or Cr_2Ni_2Si. The solid solution span is significantly reduced with decreasing cobalt content, and the addition of silicon further narrows this range, particularly in compositions with low cobalt content. Therefore, cobalt-lean compositions exhibit limited manufacturing robustness, as their reduced window for thermal treatment increases the risk of forming undesirable phases.

Thèse accessible à l'adresse : https://theses.insa-lyon.fr/publication/2025ISAL0036/these.pdf © [T. Langlois], [2025], INSA Lyon, tous droits réservés

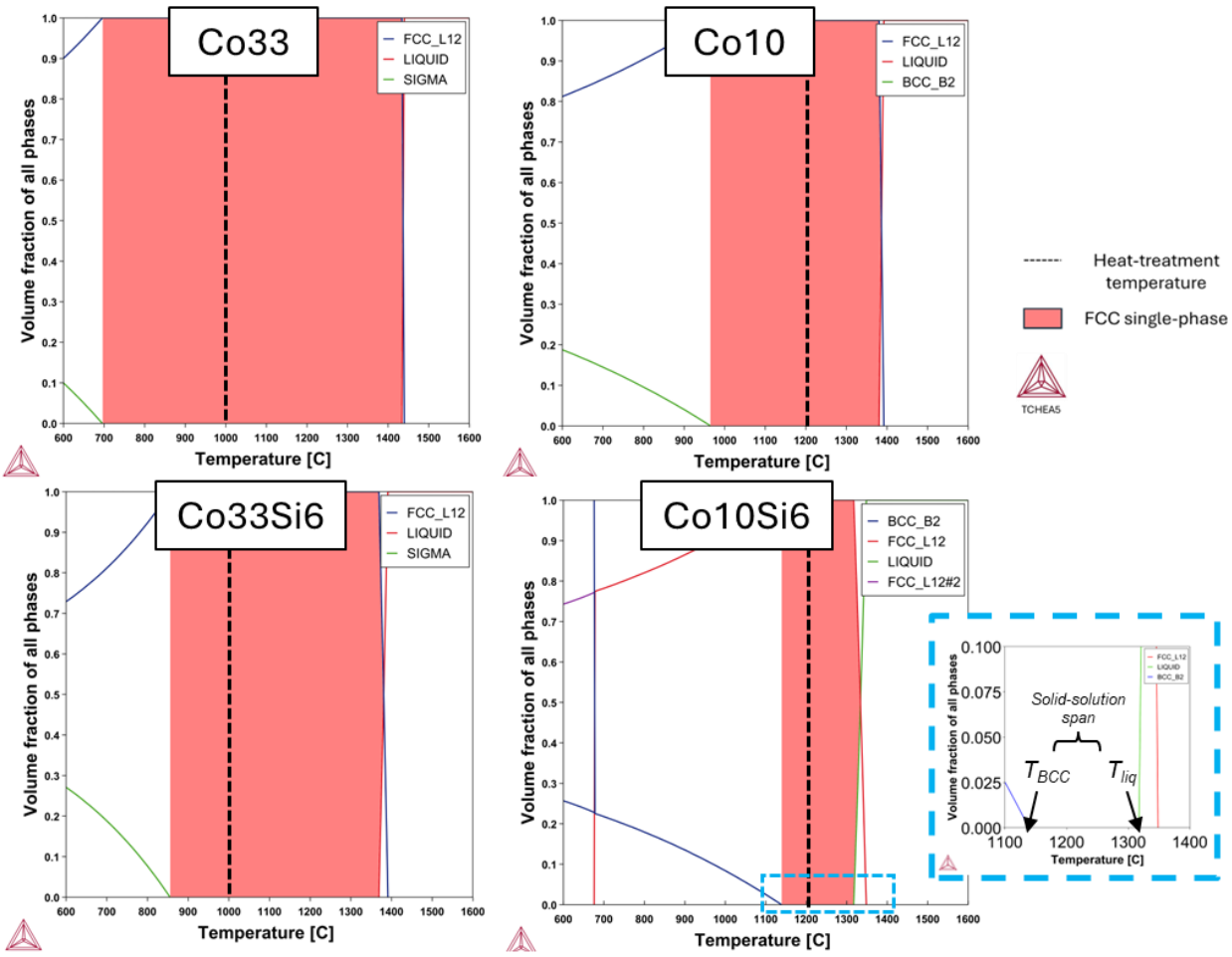


Figure 4.9. Temperature selection for homogenisation and annealing processes applied to cold rolled specimens for tensile tests.

Finally, temperature diagrams were calculated to determine the optimal heat-treatment temperatures that preserve the desired single-FCC microstructure (*Figure 4.9*). The complete set of temperature diagrams is available in *Figure 0.9* in the Appendix of Chapter 4.

In line with these phase predictions, and to optimise furnace consumption, *Table 4.2* summarises the selected temperature for heat-treatments (homogenisation and/or annealing) for all experimentally manufactured compositions.

Table 4.2. Selected temperatures for heat-treatments of different C-MPEA compositions.

Thèse accessible à l'adresse : https://theses.insa-lyon.fr/publication/2025ISAL0036/these.pdf © [T. Langlois], [2025], INSA Lyon, tous droits réservés

Alloy name	sample name	Heat-treatment temperature (°C)
$Cr_{25}Co_{50}Ni_{25}$	Co50	1000
$Cr_{30}Co_{40}Ni_{30}$	Co40	1000
$Cr_{33}Co_{33}Ni_{33}$	Co33	1000
$(Cr_{33}Co_{33}Ni_{33})Si_6$	Co33Si6	1000
$Cr_{40}Co_{20}Ni_{40}$	Co20	1200
$(Cr_{40}Co_{20}Ni_{40})Si_1$	Co20Si1	1200
$(Cr_{40}Co_{20}Ni_{40})Si_2$	Co20Si2	1200
$(Cr_{40}Co_{20}Ni_{40})Si_3$	Co20Si3	1200
$(Cr_{40}Co_{20}Ni_{40})Si_6$	Co20Si6	1200
$(Cr_{40}Co_{20}Ni_{40})Si_9$	Co20Si9	1200
$Cr_{45}Co_{10}Ni_{45}$	Co10	1200
$(Cr_{45}Co_{10}Ni_{45})Si_1$	Co10Si1	1200
$(Cr_{45}Co_{10}Ni_{45})Si_2$	Co10Si2	1200
$(Cr_{45}Co_{10}Ni_{45})Si_3$	Co10Si3	1200
$(Cr_{45}Co_{10}Ni_{45})Si_6$	Co10Si6	1200
$(Cr_{45}Co_{10}Ni_{45})Si_9$	Co10Si9	1200

In summary, this tool allows for:

- Assessing the **effect of elements** on the microstructure.
- Assessing the **effect of temperature** on the microstructure.
- Identifying C-MPEAs compositions that form **single-phase FCC structures**.
- Identifying **heat-treatments temperatures** for the selected experimental compositions.

4.2 Mechanical performance of C-MPEAs

The first layer of phase prediction allowed us to identify the single-phase FCC domains in the compositional space of C-MPEAs. It is necessary to restrict the calculations of our mechanical models to FCC domains. The second set of predictions

Thèse accessible à l'adresse : https://theses.insa-lyon.fr/publication/2025ISAL0036/these.pdf © [T. Langlois], [2025], INSA Lyon, tous droits réservés

involves mechanical models that estimate the contribution of solid solution to yield strength (σ_{SS}) and stacking fault energy (SFE). The estimation of SFE is important for understanding the deformation mechanisms. Alloys with low SFE are more likely to exhibit twinning or phase transformations during deformation, both enhancing the materials work-hardening. (toughness, UTS and A% using the Ashby maps or other maps) By applying these filters, we want to examine the influence of composition on yield strength and SFE, identifying promising regions with high σ_{SS} and low SFE.

4.2.1 Prediction of Solid solution strengthening in C-MPEAs

The Varvenne et al. model was used to estimate the contribution of solid solution to yield strengthening in the C-MPEA compositional space [5]. First, we evaluated the optimal set of inputs as described in the numerical methods, by comparing an experimental set of σ_{SS} values with the predicted values from the model. Results for the three input datasets applied to the Varvenne model are shown in

Table 4.4. The data from the MaterialProject gives the poorest results, as this dataset is not account for the apparent FCC volume in its raw data. This is a key limitation in our project of high-throughput data handling. The combination of size parameter from Coury et al. [30] and elastic parameters from Bracq et al. [31] provided the most accurate estimation of σ_{SS}. Refined data for silicon was added to this dataset, based on our experimental results for the binary Ni-Si master alloys produced by Arc200, and cross-checked with data from Kishore [87]. *Table 4.3* shows the complete set of inputs for the 6 elements used in this work, referred to as C-MPEAs+Si dataset.

Table 4.3. Complete set of inputs for the Varvenne model used in this work.

Parameters	Co	Cr	Fe	Mn	Ni	Si
E [Gpa]	210.5	263.9	139.9	172.1	199.9	209.9
μ [Gpa]	81.4	103.5	51.7	81.5	76.3	82.1
ν	0.293	0.275	0.353	0.056	0.310	0.280
V^{FCC} [Å^3]	10.86	12.45	11.82	12.26	10.44	10.23

Thèse accessible à l'adresse : https://theses.insa-lyon.fr/publication/2025ISAL0036/these.pdf © [T. Langlois], [2025], INSA Lyon, tous droits réservés

Table 4.4. Experimental vs Prediction of the Solid solution contribution to YS (σ_{SS}) for different input datasets.

σ_{ss} [MPa]	Experiment (*)	Prediction			Source (*)	
		Manescau Dataset	Material Project Dataset	C-MPEAs+Si Dataset		
$Ni_{50}Co_{50}$	18.7	-4.8	-4.4	13.3	[1]	Z.Wu, Acta.mat 81 (2014)
$Fe_{50}Ni_{50}$	94.7	48.5	53.6	107.6	[1]	Z.Wu, Acta.mat 81 (2014)
$Co_{33}Fe_{33}Ni_{33}$	116.7	60.2	46.8	92.9	[1]	Z.Wu, Acta.mat 81 (2014)
$Co_{33}Cr_{33}Ni_{33}$	218.0	150.8	125.4	247.7	[2]	.Yin, Nature Communications (202(
$Co_{33}Ni_{33}Mn_{33}$	138.8	145.9	119.6	135.5	[1]	Z.Wu, Acta.mat 81 (2014)
$Fe_{33}Ni_{33}Mn_{33}$	129.2	65.1	83.8	113.6	[1]	Z.Wu, Acta.mat 81 (2014)
$Co_{37.5}Cr_{25}Ni_{37.5}$	172.7	132.6	105.3	213.8	[3]	F.Coury, Scientif Reports 8 (2018)
$Co_{27.5}Cr_{45}Ni_{27.5}$	339.5	161.3	142.9	280.0	[3]	F.Coury, Scientif Reports 8 (2018)
$Co_{25}Cr_{25}Fe_{25}Ni_{25}$	160.7	95.4	96.8	186.6	[1]	Z.Wu, Acta.mat 81 (2014)
$Co_{25}Cr_{25}Mn_{25}Ni_{25}$	179.2	148.9	136.0	189.9	[1]	Z.Wu, Acta.mat 81 (2014)
$Co_{28.3}Cr_{33.3}Mn_{10}Ni_{28.3}$	250.1	159.2	139.2	233.4	[3]	F.Coury, Scientif Reports 8 (2018)
$Co_{31}Cr_{31}Ni_{31}Si_{6}$	260.0	157.0	318.2	280.7	[4]	S.Liu, J.allcom 844 (2020)
$Co_{20}Cr_{20}Fe_{20}Mn_{20}Ni_{20}$	146.3	97.5	105.8	152.0	[5]	G.Laplanche, Acta.mat 118 (2016)
RMSE		58.9	80.7	25.8		

Figure 4.10 compares the accuracy of the original inputs and of our refined dataset. The latter dataset produced the best results, especially with improved values of lattice misfit, with a RMSE of 25.79 MPa and a R^2 of 0.981.

Thèse accessible à l'adresse : https://theses.insa-lyon.fr/publication/2025ISAL0036/these.pdf © [T. Langlois], [2025], INSA Lyon, tous droits réservés

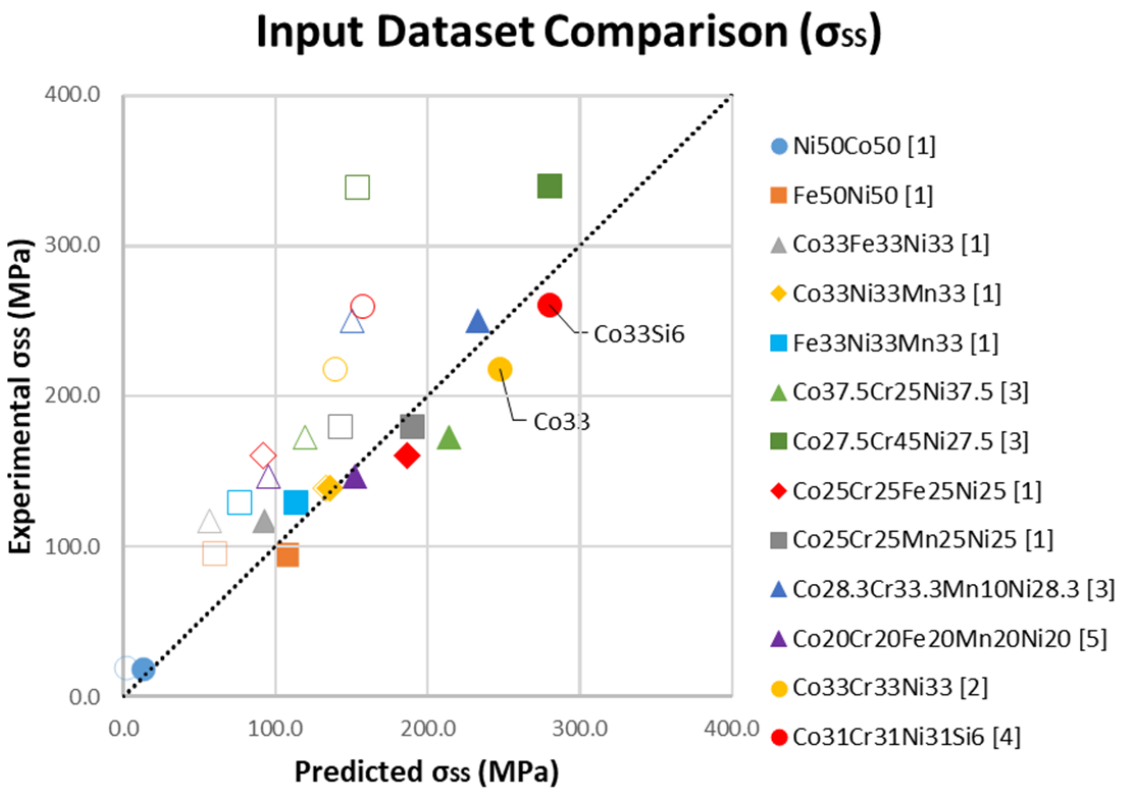


Figure 4.10. Quantitative comparison between predictions and experiments with Manescau. inputs (empty shapes) and C-MPEAs+Si inputs (full shapes).

We used this dataset to check the model's accuracy on a larger experimental dataset of HEAs, proposed by Borg et al. [88], containing 267 datapoints with complete information on yield strength at room temperature and grain size for about 100 compositions in the Co-Cr-Fe-Mn-Ni subsystems (*Figure 4.11*). After subtracting their Hall-Petch contribution to strength, the comparison of prediction and experimental points produced a RMSE of 22.8 MPa on this large dataset. Therefore, the refined input parameters result in accurate predictions.

Thèse accessible à l'adresse : https://theses.insa-lyon.fr/publication/2025ISAL0036/these.pdf © [T. Langlois], [2025], INSA Lyon, tous droits réservés

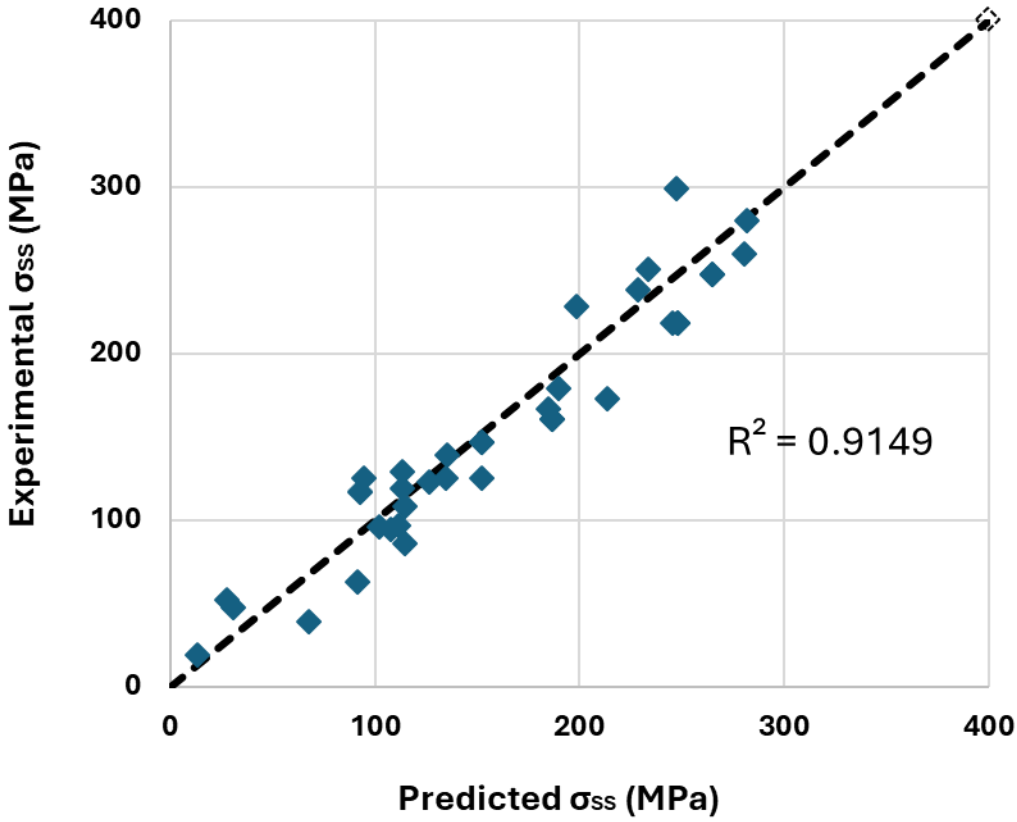


Figure 4.11. Quantitative comparison between predictions of σ_{SS} using the C-MPEAs+Si dataset and a larger experimental database from Borg et al. [88].

Subsequently, we applied the Varvenne model with our optimised inputs to the Cantor compositional space to assess the regions with the highest solid solution strengthening. As this model is valid within the FCC domain, we applied the CALPHAD filter, which isolates single-phase FCC region in this system, to evaluate their σ_{SS}. *Figure 4.12* shows σ_{SS} at room temperature in the ternary subsystems of Cantor, with coloured FCC domains for heat-treatments at 1200°C. Similar maps for different heat-treatment temperatures are provided in *Figure 0.10* in the Appendix of Chapter 4. Key σ_{SS} values for C-MPEAs are provided in *Table 4.5*.

Thèse accessible à l'adresse : https://theses.insa-lyon.fr/publication/2025ISAL0036/these.pdf © [T. Langlois], [2025], INSA Lyon, tous droits réservés

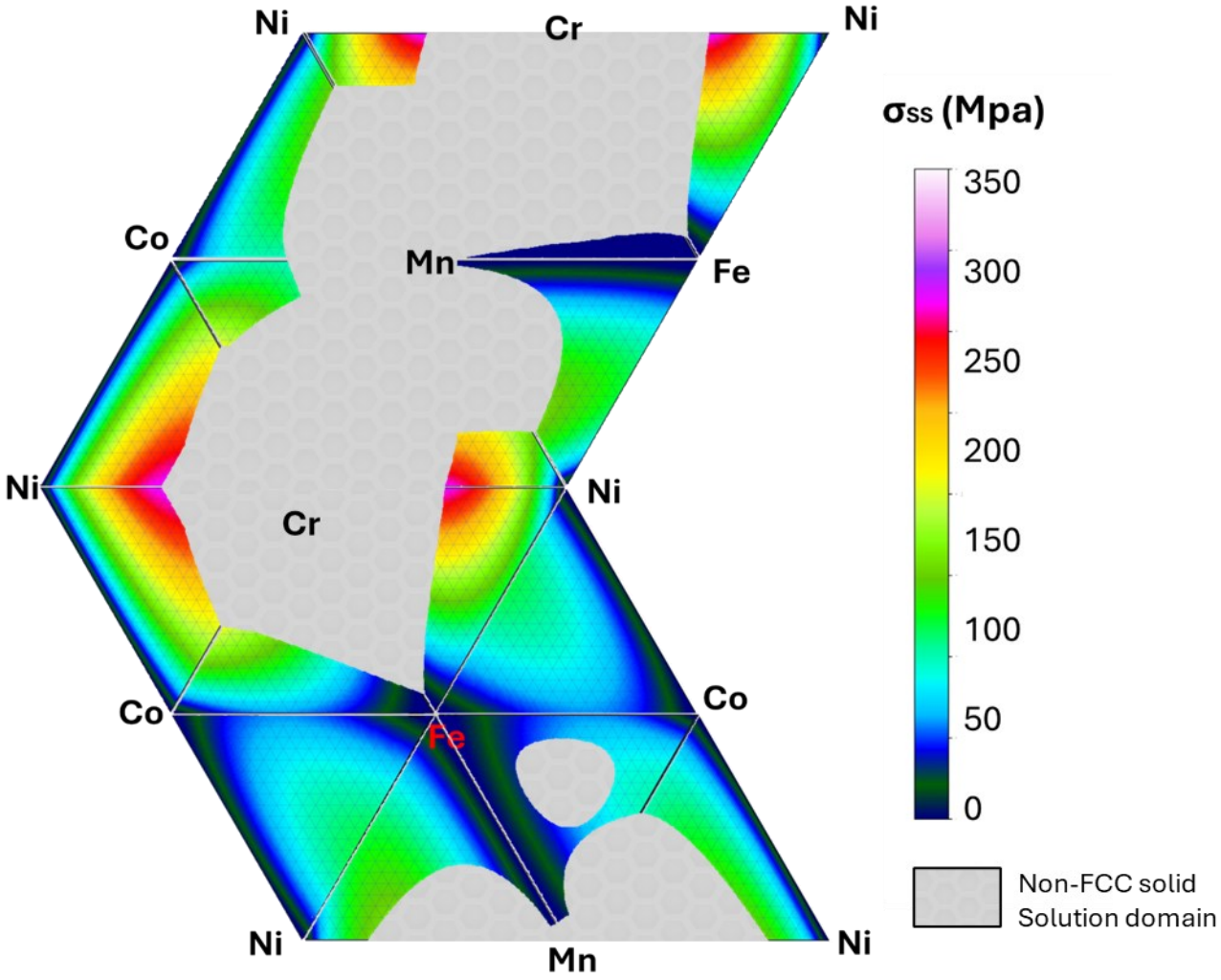


Figure 4.12. σ_{SS} map in the FCC regions of the Cantor compositional space (for a heat-treatment at 1200°C)

Table 4.5. Statistics for σ_{SS} and corresponding misfit parameter δ in the Cantor compositional space.

	Co (at.%)	**Cr** (at.%)	**Fe** (at.%)	**Mn** (at.%)	**Ni** (at.%)	ΔS_{mix}	σ_{SS} (MPa)	δ (%)
Max	0	45	0	0	55	0.81R	322	2.94
Min	0	14	71	15	0	0.82R	5	0.68
Cantor	20	20	20	20	20	1.61R	152	2.27
CrCoNi	33.33	33.33	0	0	33.33	1.10R	248	2.57

Thèse accessible à l'adresse : https://theses.insa-lyon.fr/publication/2025ISAL0036/these.pdf © [T. Langlois], [2025], INSA Lyon, tous droits réservés

We further investigated the contribution of the different elastic and geometric parameters used in the Varvenne et al. model (*Figure 4.13*). There is a clear correlation between the key misfit volume parameter $\sum c_n \Delta V_n^2$ and σ_{SS}, as outlined in *(1.14)* and shown in *Figure 4.14* (see also *Figure 0.11* in Appendix of Chapter 4, which illustrates the evolution of each input in the CrCoNi space). Focusing on the Co-Cr-Ni ternary space, we evaluated the individual effect of each element on the alloy's strength using isopleths. The misfit volume parameter is maximised in the Cr-Ni region. Therefore, this prediction indicates that lower cobalt concentration leads to higher σ_{SS} values, as depicted in *Figure 4.14*. Alloys with 33, 20 and 10 at.% of Cobalt are highlighted with marks.

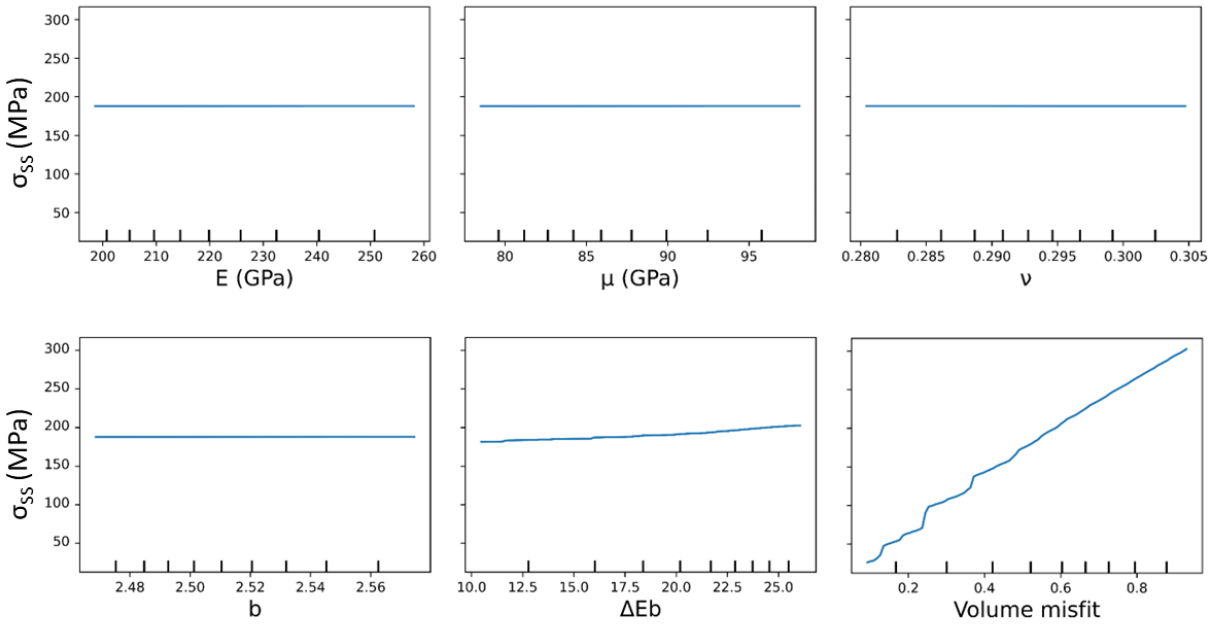


Figure 4.13. Partial dependence plots of σ_{SS} on the main parameters in Varvenne et al. model.

Thèse accessible à l'adresse : https://theses.insa-lyon.fr/publication/2025ISAL0036/these.pdf © [T. Langlois], [2025], INSA Lyon, tous droits réservés

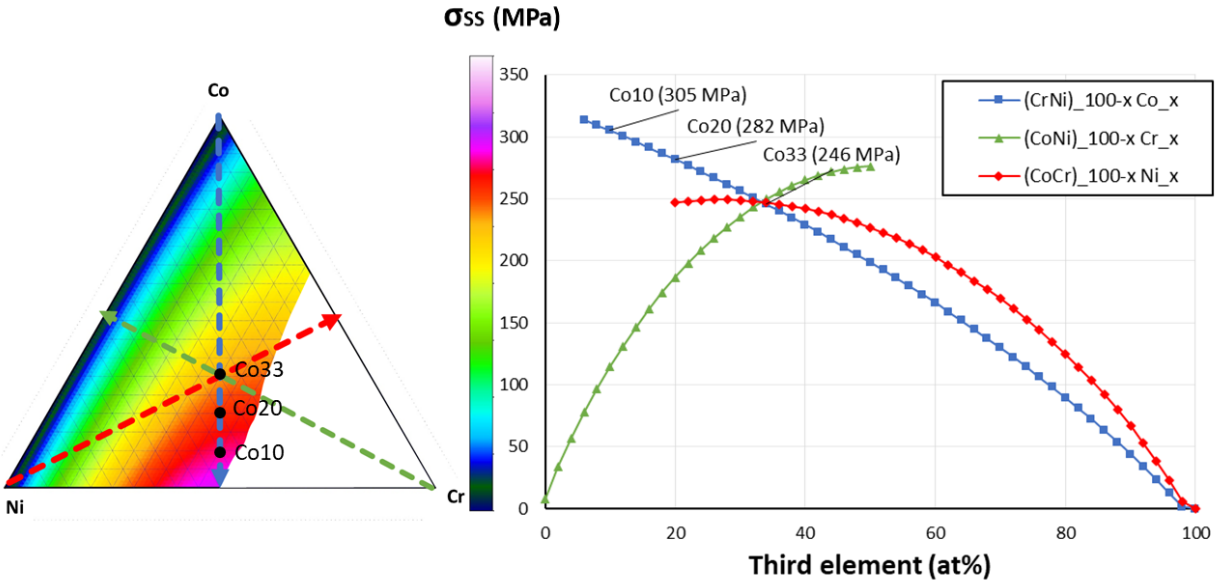


Figure 4.14. (left) Ternary diagram of σ_{SS} in FCC regions of the CrCoNi alloys. (right) Corresponding isopleths showing the effect of Co, Ni and Cr.

The highest σ_{SS} contributions are located in the Cr-Ni regions and lowest contributions found near the Cr-Fe-Mn regions (*Figure 4.12*), if we neglect compositions with very low mixing entropy. The maximum calculated value in the Cantor space is 322 MPa for $Cr_{45}Ni_{55}$ (at.%), where the lattice misfit is the highest. This result aligns with other models where the average lattice distortion is a key parameter [24], [148]. Experimental results showed that alloy compositions with large lattice distortions like $Cr_{46}Co_{10}Ni_{44}$ and $Co_{20}(CrNi)_{80}$ tend to exhibit higher strength values [148].

In our exploration of silicon addition, we also aimed to predict the effect of silicon in the Co-Cr-Ni ternary space. We measured σ_{SS} values in quaternary CrCoNiSi alloys with up to 9 at.% of silicon. Residual map representing the difference $\Delta\sigma_{SS}$ (given by the formula $\Delta\sigma_{SS} = \sigma_{SS}$ (x at.% of Si) - σ_{SS} (0 at.% of Si)) are shown in *Figure 4.15*. Highest σ_{SS} value of 356 MPa was calculated for $(Cr_{45}Ni_{55})_{91}Si_9$. The highest σ_{SS} values allow for fine tuning of the alloy properties to achieve a favourable balance between strength and ductility.

Thèse accessible à l'adresse : https://theses.insa-lyon.fr/publication/2025ISAL0036/these.pdf © [T. Langlois], [2025], INSA Lyon, tous droits réservés

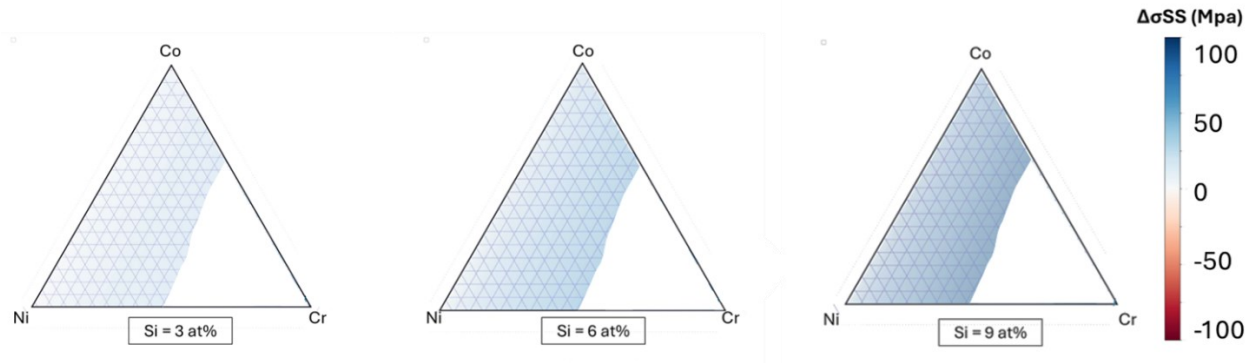


Figure 4.15. Residual pseudo-ternary maps of $\Delta\sigma SS$ in CrCoNi space with 3, 6 and 9 at.% of silicon, very slight increase of $\Delta\sigma SS$ with silicon content.

σ_{SS} predictions must be interpreted with caution. The simplified model considers only average size and elastic misfits, while complex structures like MPEAs may experience local size mismatch and local shear strain. In this context, the mean squared atomic displacement (MSAD), influenced by both size and elastic misfits, strongly correlates with yield strength [149], [121]. Moreover, the use of Vegard's law approximates the material's elastic and size properties, which may not accurately reflect the actual values of these parameters. For example, ab initio calculations have revealed substantial non-linearity in the elastic constants (c_{ij}) of Cr-Ni alloys (See *Table 0.1* in the appendix of Chapter 3 [150]), leading to non-linear behaviour in derived properties like Poisson's ratio (ν) and shear modulus (μ) when calculated using the Voigt averages. Additionally, at lower temperatures, this model tends to underpredict σ_{SS} and is very sensitive to the line tension parameter [146]. Therefore, we only applied the prediction at room temperature, where results are satisfying.

In summary, this tool allows for:

- **Good estimations** of σ_{SS} in Co-Cr-Fe-Mn-Ni-Si FCC regions at room temperature.
- Identification of **extremum values** to maximise the material's strength.
- Assessment of the **effect of individual raw elements** on strength.

Thèse accessible à l'adresse : https://theses.insa-lyon.fr/publication/2025ISAL0036/these.pdf © [T. Langlois], [2025], INSA Lyon, tous droits réservés

4.2.2 Prediction of deformation mechanisms in C-MPEAs

Accurate estimations of SFE are essential for identifying promising compositions with enhanced work-hardening and toughness properties. In this section, we compare the accuracy of three SFE prediction models and identify compositions in the Co-Cr-Ni space with low SFE values, which are beneficial for promoting TWIP and TRIP effects. These mechanisms can improve ductility, work-hardening, and toughness by enabling more complex deformation modes.

The empirical model by Bertoli et al. [77] was applied to estimate SFE in the CrCoNi compositional space. Experimental compositions used to fit this model are represented by black dots in *Figure 4.16-a*, while Co33, Co20 and Co10 alloys are represented by white symbols. TWIP and TRIP limits are depicted with coloured contour lines in *Figure 4.16-b*.

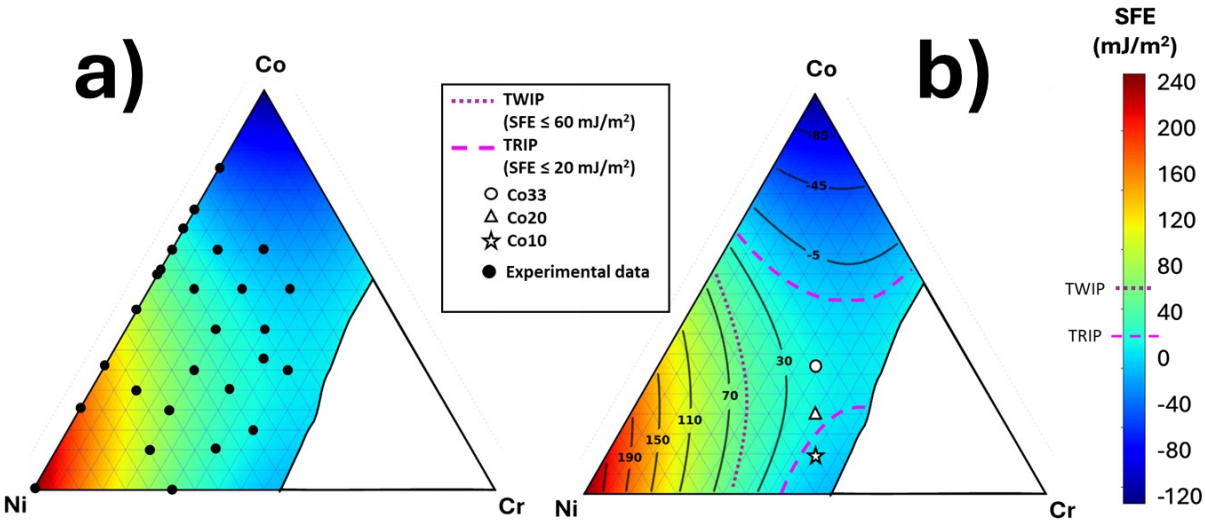


Figure 4.16. Ternary map of SFE prediction with empirical model from Bertoli et al [77].

Results from thermodynamic calculations with TCHEA5 database and machine learning calculations based on the DFT dataset are displayed in *Figure 4.17-a* and *Figure 4.17-b*, respectively.

Thèse accessible à l'adresse : https://theses.insa-lyon.fr/publication/2025ISAL0036/these.pdf © [T. Langlois], [2025], INSA Lyon, tous droits réservés

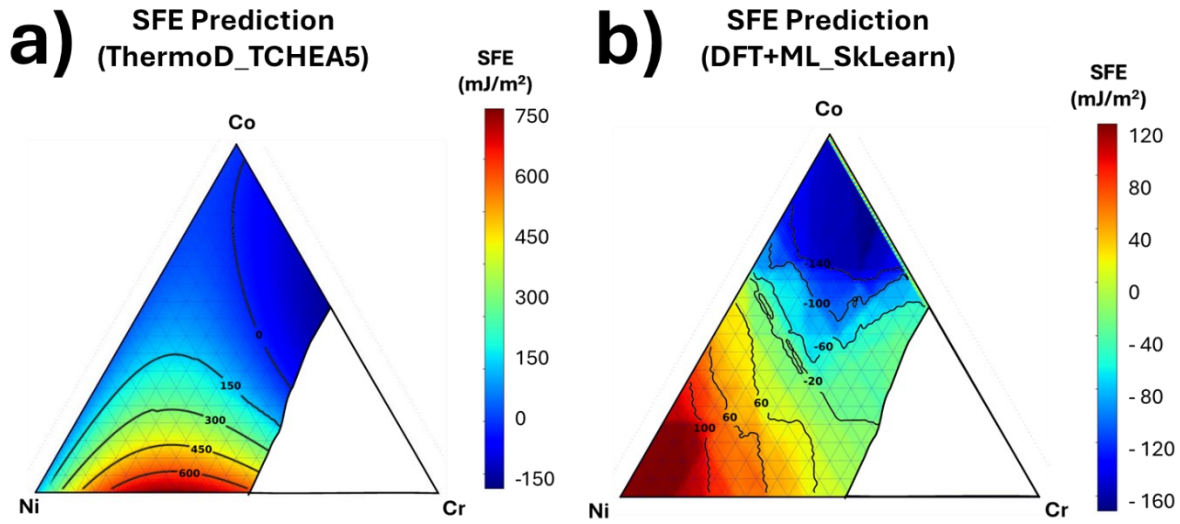


Figure 4.17. (a) SFE prediction with TCHEA5 database; (b) SFE prediction extrapolated from DFT calculations.

While all three prediction models show overall similar trend, such as higher SFE values near nickel-based alloys and lower values near cobalt, the ranges of SFE differ quite significantly between the models, with TWIP and TRIP regions varying substantially, especially in Cr-Ni regions with low cobalt. As a result, we need the most reliable model to accurately predict SFE within the Co-Cr-Ni compositional space, especially for Co30, Co20 and Co10 alloys. *Figure 4.18* illustrates that the empirical model provides the most accurate predictions with respect to the experimental dataset from Bertoli et al. [77]; while the DFT and TCHEA5 predictions models tends to underpredict SFE values for alloys that have high SFE and overpredict low SFE values.

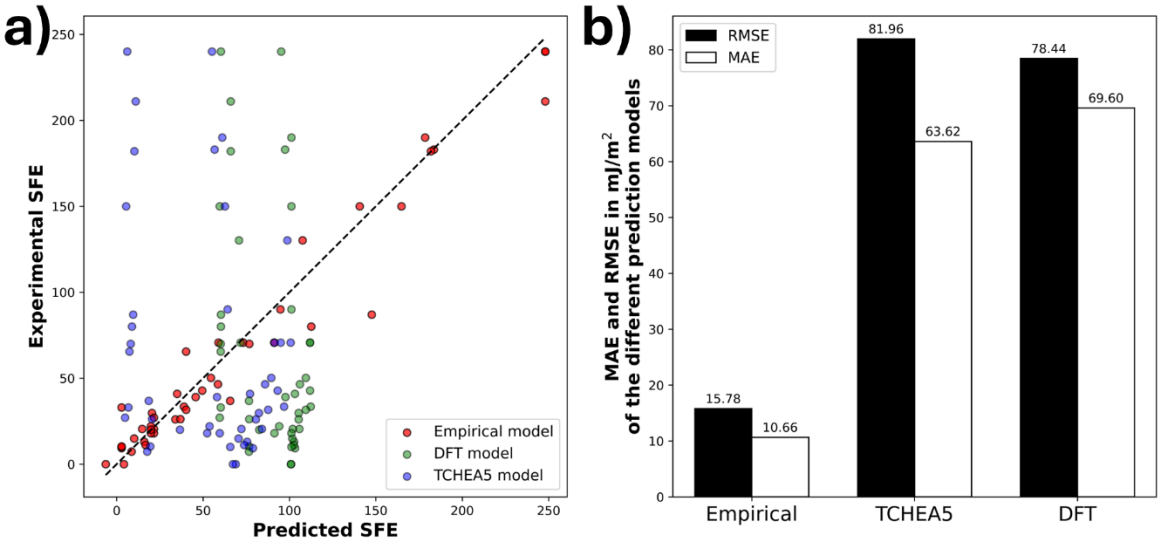


Figure 4.18. (a) Comparison of experimental (from [77], standard deviations are unknown) and predicted SFE across the three models; (b) Model accuracy with MAE and RMSE.

Thèse accessible à l'adresse : https://theses.insa-lyon.fr/publication/2025ISAL0036/these.pdf © [T. Langlois], [2025], INSA Lyon, tous droits réservés

For the remainder of this study, we estimate SFE using the empirical model based on its accurate predictions. Additionally, we developed a regression model using our expanded experimental dataset containing 165 alloys in the Co-Cr-Fe-Mn-Ni space, with a greater focus on low-cobalt regions compared to Bertoli et al [77], [36]. However, it is important to note that experimental SFE measurements can be influenced by various factors, including the microstructural effects such as grain size and short-range order (SRO) [77]; as well as the measurement temperature, technique and equipment accuracy [91], [151]. In previous studies, linear regression of experimental SFE dataset with random intercepts provided relatively accurate results despite the biases listed above [151]. We used a similar regression method with our experimental dataset. Outliers were removed from the datasets. With this method, the SFE in Co-Cr-Ni system is given by *Equation (4.1)*, where alloying elements are in at.%. Predicted SFE values are illustrated in *Figure 4.19.*

$$SFE\ (mJ/m^2) = 29.243 \cdot Co + 28.601 \cdot Cr + 32.015 \cdot Ni - 2977.431 \qquad (4.1)$$

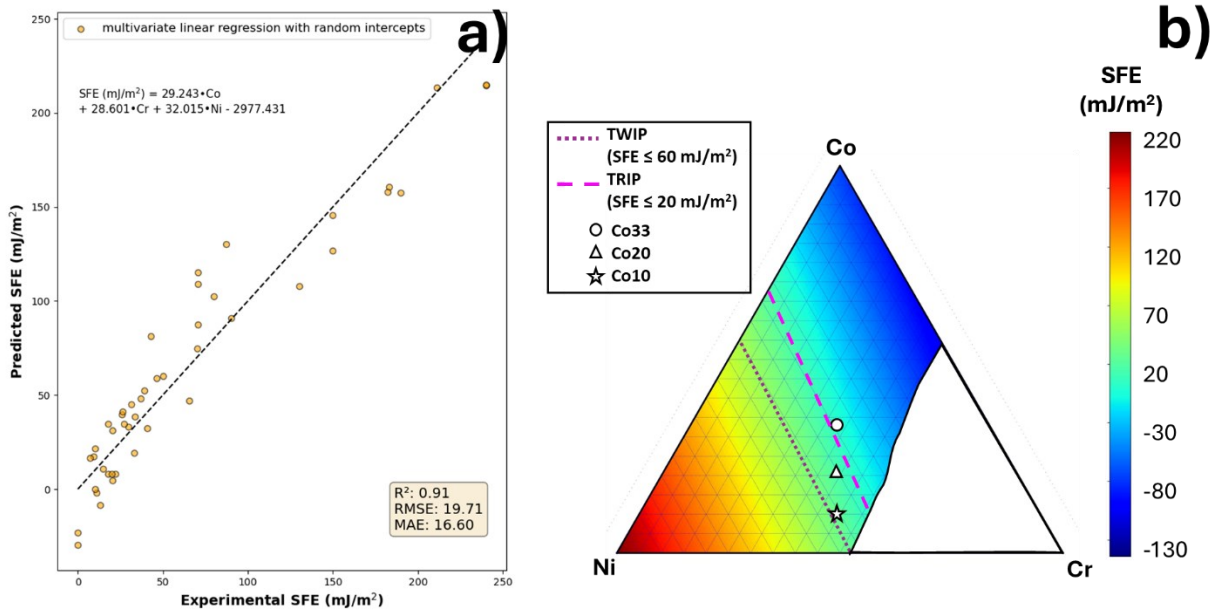


Figure 4.19. (a) Comparison of experimental and predicted SFE using Equation (4.1); (b) Corresponding map of predicted SFE in the Co-Cr-Ni space.

Unlike Bertoli's model, which uses a quadratic form that increases SFE at low cobalt contents, a linear relationship appears more accurate when considering

Thèse accessible à l'adresse : https://theses.insa-lyon.fr/publication/2025ISAL0036/these.pdf © [T. Langlois], [2025], INSA Lyon, tous droits réservés

experimental values for low cobalt compositions [152], [36]. *Table 4.6* summarises the predicted SFE for the ternary compositions that we manufactured experimentally.

Table 4.6. Predicted SFE for the manufactured ternary compositions.

Co (at%)	**Cr** (at%)	**Ni** (at%)	**Predicted SFE** (mJ/m^2)
10	45	45	42.72
20	40	40	32.07
33.33	33.33	33.33	17.57

As discussed in the literature, low SFE values significantly enhance strain-hardening rates [46]. Alloys with lower cobalt content generally exhibit higher SFE, which subsequently results in a decline ductility and toughness.

In summary, the chosen SFE prediction highlights:

- the **effect** of cobalt in reducing the SFE of Co-Cr-Ni alloys.
- The predicted **loss of ductility** for alloys with low cobalt content.

While the effect of silicon on SFE could not be included in our prediction model due to limited available data (see *Figure 1.14*), experimental results suggest that adding silicon to MPEAs can lead to renewed mechanical properties [20].

Thèse accessible à l'adresse : https://theses.insa-lyon.fr/publication/2025ISAL0036/these.pdf © [T. Langlois], [2025], INSA Lyon, tous droits réservés

4.3 Sustainable competitiveness of metal alloys and C-MPEAs

As mentioned in the literature review, sustainability has not been sufficiently considered in alloy and new material design. The use of raw materials with large environmental and societal footprints has significant consequences, not only for the planet due to resource criticality, but also for humans as their exploitation is often tied to poor working conditions, economic instability, corruption, and even conflict. Our goal is to highlight the critical impact of existing materials, especially metals, and to apply the sustainability toolbox we developed to design new materials with lower sustainability impact. First, we will present an overall picture of this model across many material classes. Then, we will analyse the results for several steels and nickel-based alloys. Finally, we are going to show the scores in the Co-Cr-Ni-Si compositional space.

4.3.1 Elemental scores

It is essential to first observe the impact of individual elements. In the case of conventional alloys, typically composed of one or two principal elements, the footprint of the base element largely influences the overall sustainability score. For MPEAs, a different approach is required to visualise the influence of each element when mixed in comparable proportions. *Figure 4.20* indicates the most used raw materials in the analysed datasets [1], [14], [27], represented in terms of mass fractions.

Thèse accessible à l'adresse : https://theses.insa-lyon.fr/publication/2025ISAL0036/these.pdf © [T. Langlois], [2025], INSA Lyon, tous droits réservés

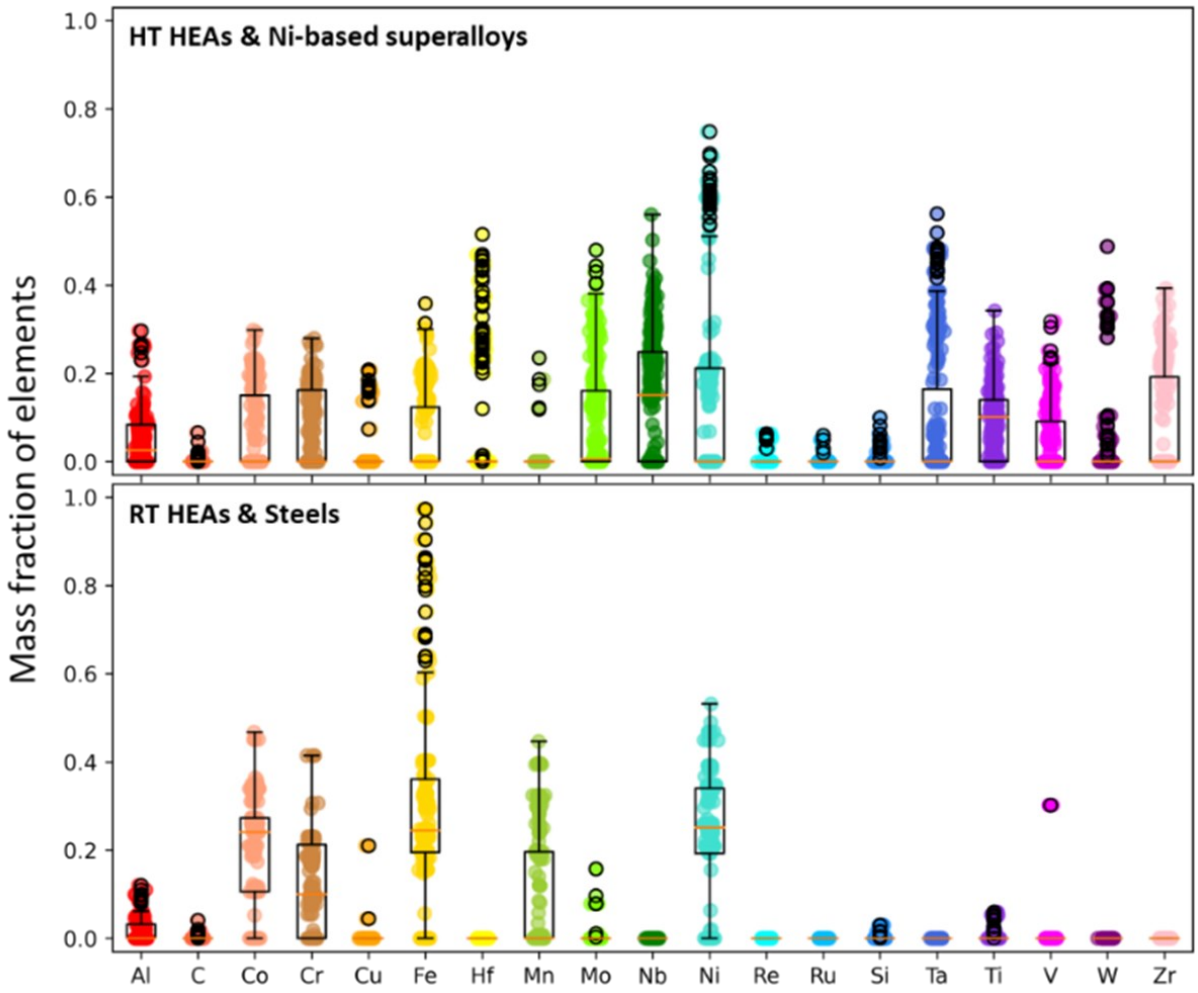


Figure 4.20. Boxplots illustrating the mass fraction distribution of alloying elements. The top panel presents data for Ni-based superalloys and high-temperature (HT) high-entropy alloys (HEAs), including BCC-type HEAs, refractory HEAs (RHEAs), BCC refractory complex concentrated alloys (RCCAs), and FCC high-entropy stabilised alloys (HESAs). The bottom panel displays data for steels and room-temperature (RT) HEAs, which focus on FCC-type HEAs [1].

Radar charts of the 9 sustainability indicators for these raw elements are plotted in *Figure 4.21*. As explained in the numerical methods, material descriptors were rescaled in "footprints" from 0 to 10, with higher values indicating a more detrimental impact. The values in the economic, environmental and societal categories were averaged into three footprints: the "economic footprint" (Eco_FP), "environmental footprint" (Env_FP) and "societal footprint" (Soc_FP), respectively. The overall "sustainability footprint" (Sust_FP) represents the average of these three categories, with the equal weight assigned to each.

Thèse accessible à l'adresse : https://theses.insa-lyon.fr/publication/2025ISAL0036/these.pdf © [T. Langlois], [2025], INSA Lyon, tous droits réservés

It is important to interpret the material footprints carefully, as they are based on primary source data at a specific time and do not account for every aspect of a material's impact. A key observation is that the footprints can vary widely from one metal to another, and their radar profile vary significantly, indicating weak correlation between the chosen indicators. *Figure 4.22* illustrates how the societal, economic, and environmental aspects of materials can have vastly different footprints. For instance, cobalt and zirconium (represented by dashed lines in the figure) exhibit distinct distributions: zirconium's footprint is primarily economic due to resource scarcity, while cobalt's footprint reflects its high societal impact, mainly related to sourcing from the Democratic Republic of the Congo (DRC).

Among the widely used element in alloys, iron stands out with one of the least impactful sustainability footprints. The primary exporters of iron are Australia, Brazil and Canada [28], all of which are developed nations with low societal footprints. Additionally, iron's abundance and favourable rock-to-metal ratio, coupled with centuries of mining optimisation, lead to a relatively low economic and environmental footprint.

In contrast, ruthenium, tantalum and cobalt have higher sustainability footprints for different reasons. As seen in the literature review, Cobalt is mainly produced in DRC explaining the large societal footprints. Ruthenium's environmental footprints are substantial due to the large energy requirements for ore extraction.

Because conventional alloys rely heavily on base elements, the addition of smaller quantities of elements with lower sustainability impacts has a minimal effect on the overall Sust_FP. Therefore, conventional alloys like steels are expected to have the lowest overall impact. Aluminium alloys, in comparison with copper- or nickel-based alloys, are also anticipated to have a lesser footprint. The case of MPEAs/HEAs is intriguing because they mix elements like iron, which has a low footprint, with elements like cobalt and chromium, whose Sust_FP is much higher. The next section will examine whether these predictions hold for conventional alloys assess the behaviour of MPEAs.

Thèse accessible à l'adresse : https://theses.insa-lyon.fr/publication/2025ISAL0036/these.pdf © [T. Langlois], [2025], INSA Lyon, tous droits réservés

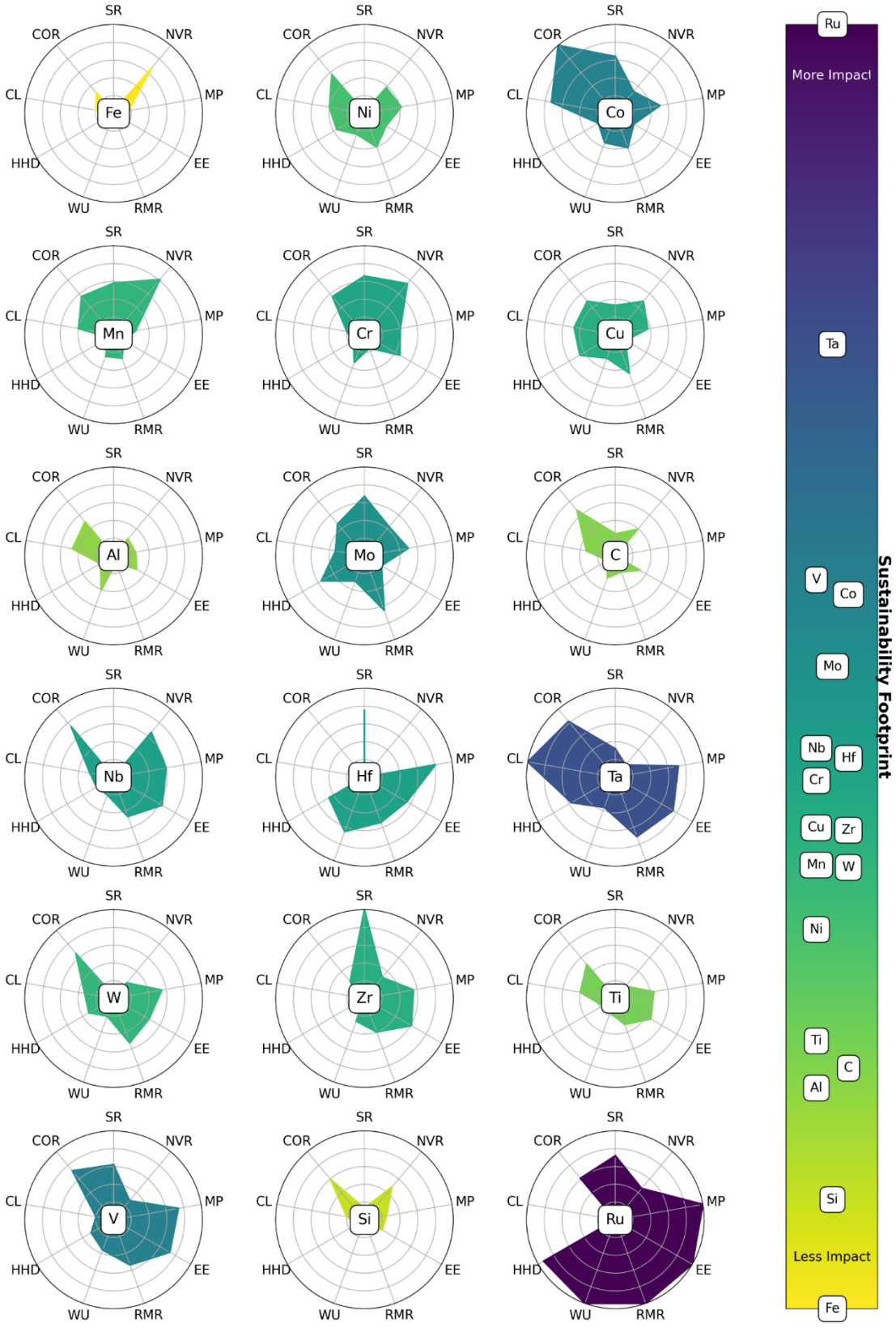


Figure 4.21. "Sustainability footprints" of the most mined and used elements in alloys (SR-supply risk, NVSR-normalised vulnerability to supply risk, MP-material price, EE-embodied energy, RMR-rock-to-metal ratio, WU-water usage, HHD-human health damage, CL-child labour, COR-Corruption)

Thèse accessible à l'adresse : https://theses.insa-lyon.fr/publication/2025ISAL0036/these.pdf © [T. Langlois], [2025], INSA Lyon, tous droits réservés

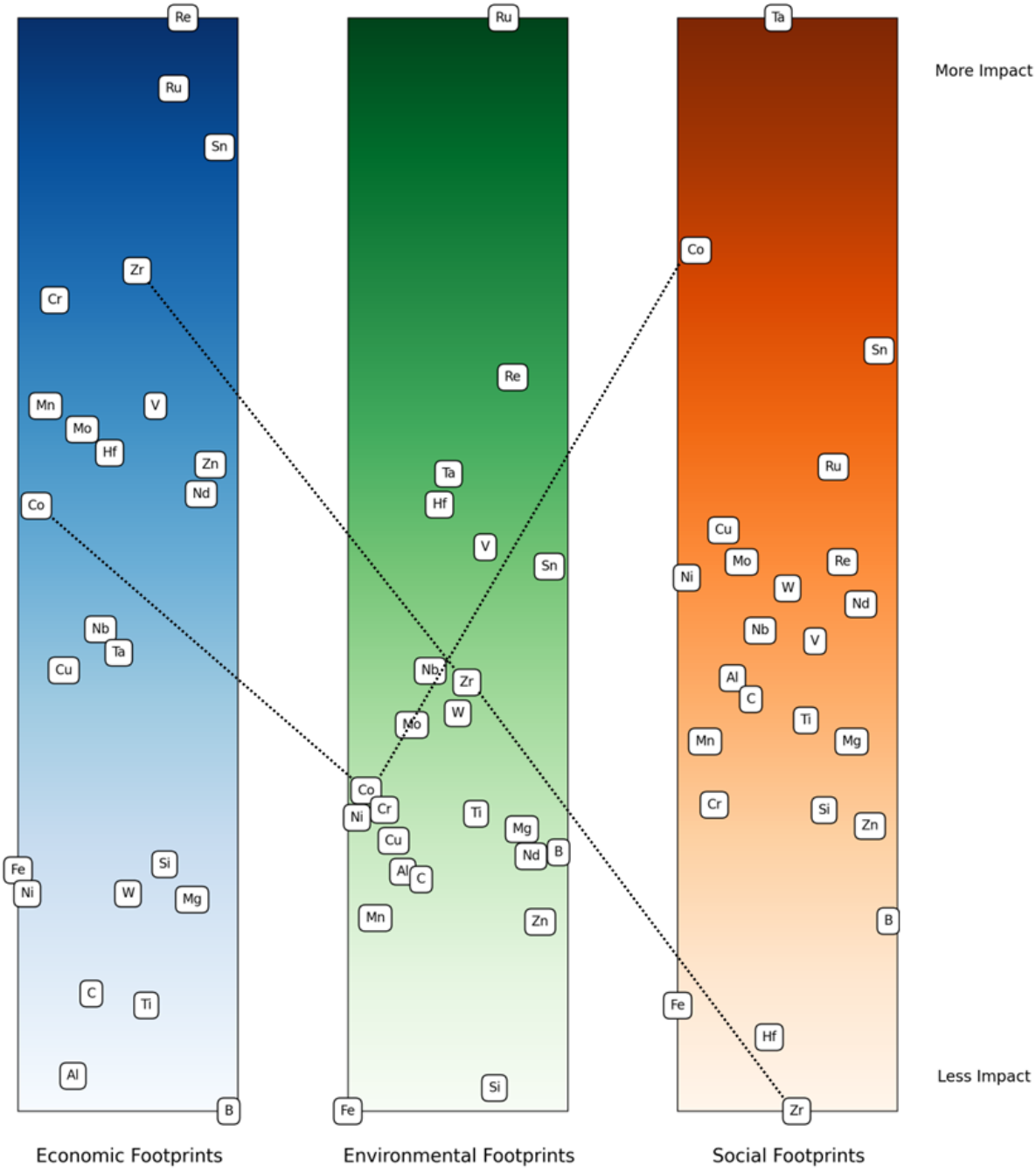


Figure 4.22. Average economic, environmental and societal footprints for the raw elements present in the datasets (score scale adapted to the materials with extremum values in Eco_FP, Env_FP and Soc_FP)

4.3.2 Sustainability scores for different classes of alloys

The preparation of a complete dataset for 73 elements made it possible to evaluate the sustainability footprints for a wide range of alloy classes. As mentioned in

Thèse accessible à l'adresse : https://theses.insa-lyon.fr/publication/2025ISAL0036/these.pdf © [T. Langlois], [2025], INSA Lyon, tous droits réservés

the numerical methods, the sustainability footprints for various conventional alloy [14, 27], Ni-superalloys, steels and MPEAs [1] were calculated using *Equation (3.3), Equation (3.4) and Equation (3.5).*

Boxplots in *Figure 4.23* illustrate the environmental, economic, and societal footprints for different alloy classes. The indicators chosen for this comparison are Material Price (economic), Embodied Energy (environmental), and Corruption (societal). Seven alloy classes are compared: MPEAs, aluminium-based light alloys, iron-based steels, nickel-based alloys, copper-based alloys, refractory alloys (Nb-Mo-Ta-W-Re subsystems), and precious metal alloys (gold, silver, platinum). Data were taken before rescaling to show the real disparities in footprints across different alloys.

Each boxplot represents the distribution of alloy footprints, with the edges of the box showing the first and third quartiles (25% and 75% of the population), the median (50%) indicated by a green line, and the whiskers showing the minimum and maximum values. Outliers are displayed as points outside the acceptable range, defined as 1.5 times the interquartile range. The red dot in the MPEAs distribution marks the value of the Cantor alloy.

As expected, conventional alloys exhibit a narrower range of sustainability footprints compared to MPEAs and precious alloys, primarily due to the dominant contribution of their main elements—iron, aluminium, nickel, and copper. For nickel-based alloys, the wider distribution of societal footprint is attributed to the varied alloying elements, which can include up to 12 wt.% tantalum, 6 wt.% rhenium, and 6 wt.% ruthenium. Even in small quantities, these elements significantly influence the alloy's sustainability footprint due to their high societal and environmental impacts.

Precious and refractory alloys show higher economic and environmental footprints due to the high energy and cost associated with their extraction. In contrast, MPEAs have the largest disparity of values for many sustainability criterions. The majority of MPEAs have a more detrimental impact compared to conventional alloys but the large distribution also indicates the great potential in changing the alloy composition to obtain better sustainability footprints.

Thèse accessible à l'adresse : https://theses.insa-lyon.fr/publication/2025ISAL0036/these.pdf © [T. Langlois], [2025], INSA Lyon, tous droits réservés

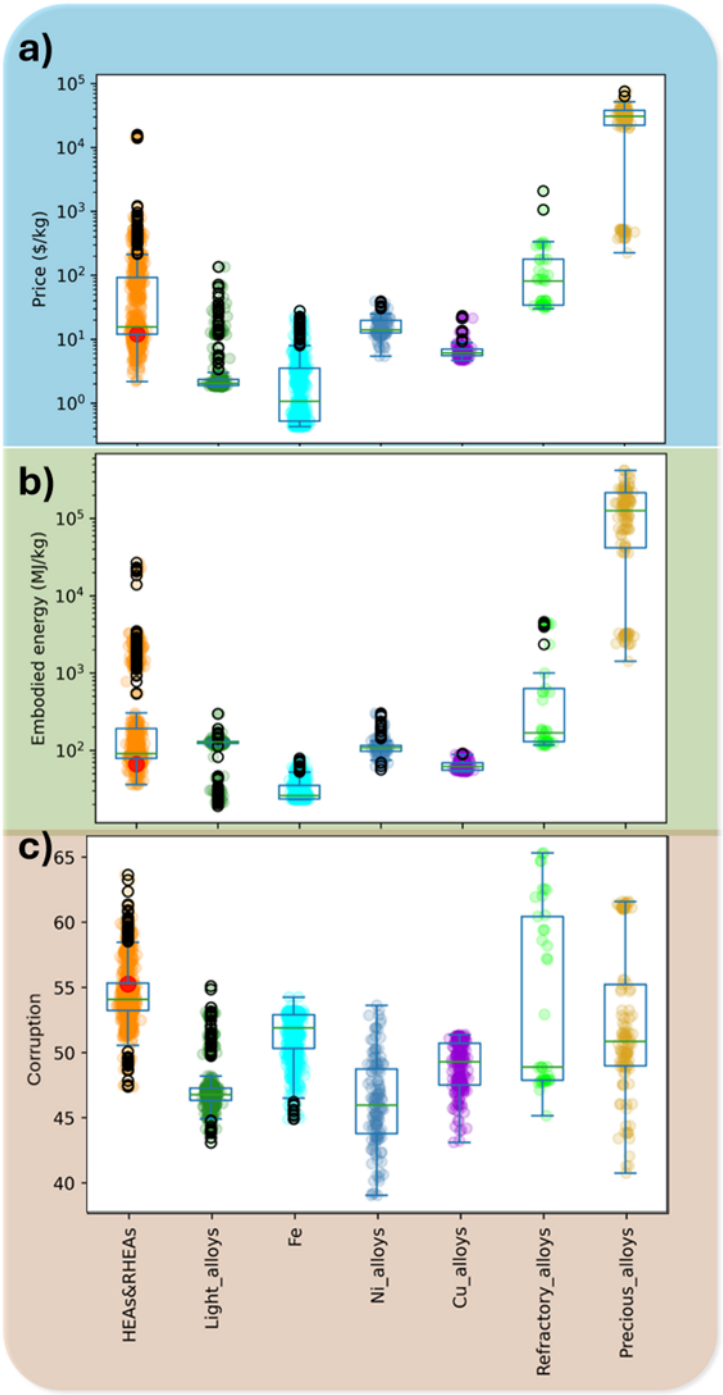


Figure 4.23. (a) Material Price; (b) Embodied Energy; (c) Corruption. 3 Sustainability indicators scoring different classes of alloys from economic, environmental, and societal perspectives.

We also used these experimental datasets to assess the "strength-to-environment" cost of a materials, for annealed steels and MPEAs. This metric is defined as the amount of embodied energy (in MJ/kg) required to enhance the material's strength by 1 MPa. Using experimental data, we plotted yield strength and tensile strength against

Thèse accessible à l'adresse : https://theses.insa-lyon.fr/publication/2025ISAL0036/these.pdf © [T. Langlois], [2025], INSA Lyon, tous droits réservés

the embodied energy of the alloy's constituent elements, weighted by their mass fractions. After eliminating dominated solutions (i.e., those with higher energy but lower strength), we calculated the minimum "strength-to-environment" costs, as shown in *Figure 4.24*.

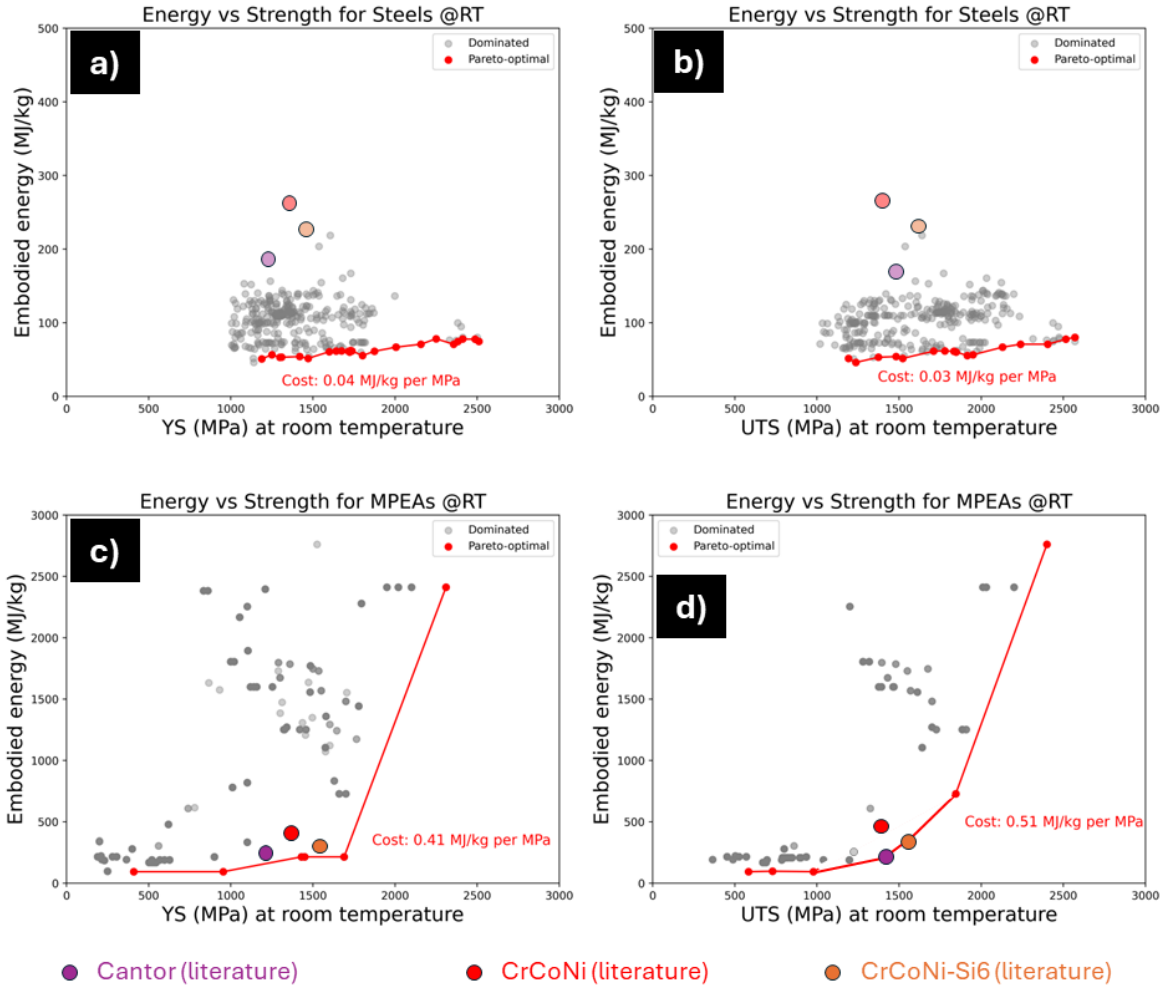


Figure 4.24. Plots of (a) Embodied Energy vs Yield strength of steels at room temperature, (b) Embodied Energy vs Tensile strength of steels at room temperature, (c) Embodied energy vs Yield strengths of FCC HEAs at room temperature, (d) Embodied energy vs Tensile strength of FCC HEAs at room temperature.

The results reveal that the "strength-to-environment" cost for MPEAs is approximately ten times higher than that for steels when achieving strength values above 2000 MPa. This substantial increase is primarily due to the inclusion of elements with a high sustainability impact, such as tantalum, niobium and hafnium, in large concentration in the alloy compositions. However, when restricting MPEA compositions to transition metals, this cost significantly drops to 0.14 MJ/kg per MPa, which is not too far from the steel's average value.

Thèse accessible à l'adresse : https://theses.insa-lyon.fr/publication/2025ISAL0036/these.pdf © [T. Langlois], [2025], INSA Lyon, tous droits réservés

4.3.3 Sustainability properties of Cantor subsystems.

Using the developed sustainability toolbox, it is possible to visualise the global distribution of the elements in the Cantor alloy, defined as the product of [W][G] matrices, illustrated in *Figure 4.25-a*. The primary sources of the elements Co, Cr, Fe, Mn, and Ni in Cantor alloys are South Africa (15.63 wt.%), the Democratic Republic of Congo (13.21 wt.%), and Australia (12.53 wt.%). These countries have very different sustainability scores, as illustrated in *Figure 4.25-b* [153], which contributes to the disparities observed in the sustainability indicators for MPEAs.

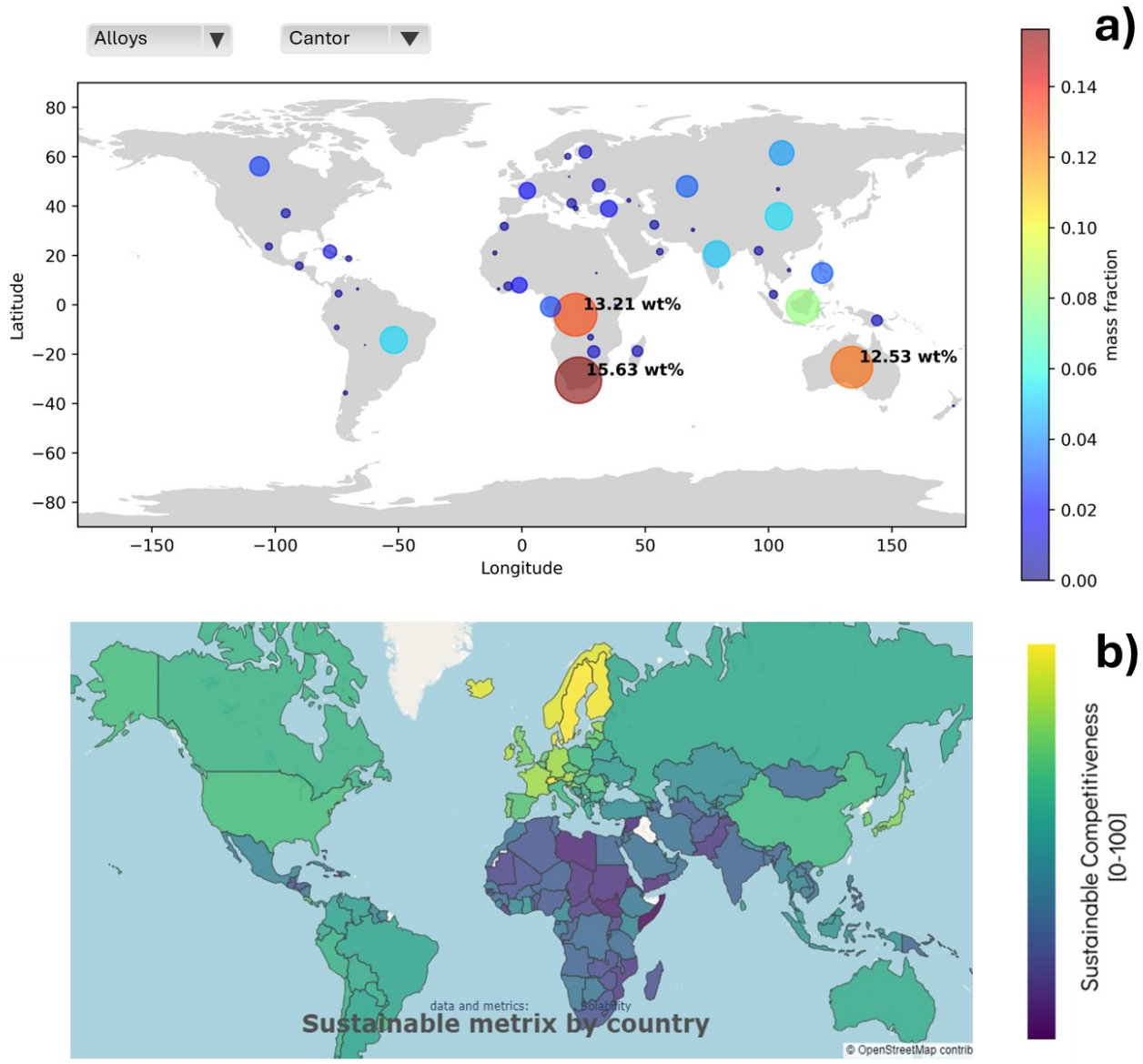


Figure 4.25. (a) Global composition breakdown of the Cantor alloy (CoCrFeMnNi), illustrating the worldwide distribution of its elemental constituents; (b) Sustainability competitiveness index (from Solability data [153]).

It is also important to examine how each element influences the sustainability footprint of the Cantor alloy. Even though the alloy contains equimolar amounts of

Thèse accessible à l'adresse : https://theses.insa-lyon.fr/publication/2025ISAL0036/these.pdf © [T. Langlois], [2025], INSA Lyon, tous droits réservés

each element, their contributions to the alloy's overall footprint differ significantly. *Figure 4.26* shows the individual contributions of each element to the economic, environmental, and societal indicators. The further apart the sky-blue and navy-blue dots are, the greater or lesser the impact of an element is on the alloy's footprint, with green lines indicating lesser impact and red lines indicating greater impact.

For instance, while chromium constitutes just over 20 wt.% of the alloy, it accounts for more than 45% of the total required energy to produce it. Meanwhile, iron and manganese contribute very little to the overall footprint. Cobalt, however, has a major negative influence on societal indicators, while its environmental and economic impact is also far from optimal. Chromium heavily influences the economic and environmental aspects of the alloy, while nickel shows a generally positive influence, except for its health damage and rock-to-metal ratio.

The diverse influences of Cantor elements underscore the complexity of designing a material composition that maximises sustainable performance in C-MPEAs. To better understand the influence of multiple elements simultaneously, ternary maps are particularly useful (*Figure 4.27*). These maps also help limit the exploration to FCC single-phase regions using our CALPHAD filter, and they can be further used to integrate other criteria like strength and stacking fault energy (see optimisation section).

Thèse accessible à l'adresse : https://theses.insa-lyon.fr/publication/2025ISAL0036/these.pdf © [T. Langlois], [2025], INSA Lyon, tous droits réservés

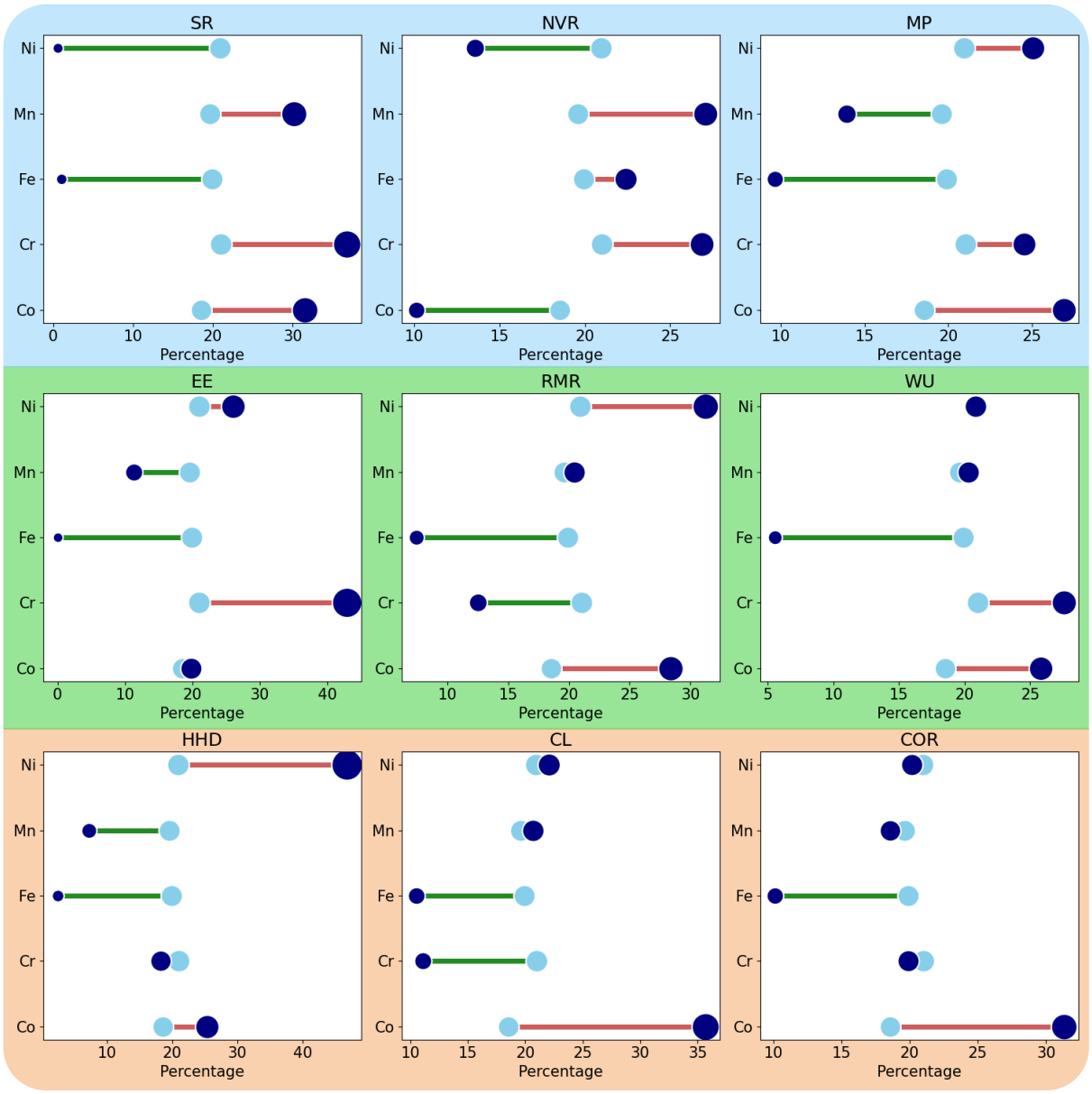


Figure 4.26. Dot plots illustrating the weighted contribution of each element compared to their actual mass fraction (navy and sky blue dots, respectively) for ecomomic, environmental and societal indicators (blue, green and orange, respectively).

Thèse accessible à l'adresse : https://theses.insa-lyon.fr/publication/2025ISAL0036/these.pdf © [T. Langlois], [2025], INSA Lyon, tous droits réservés

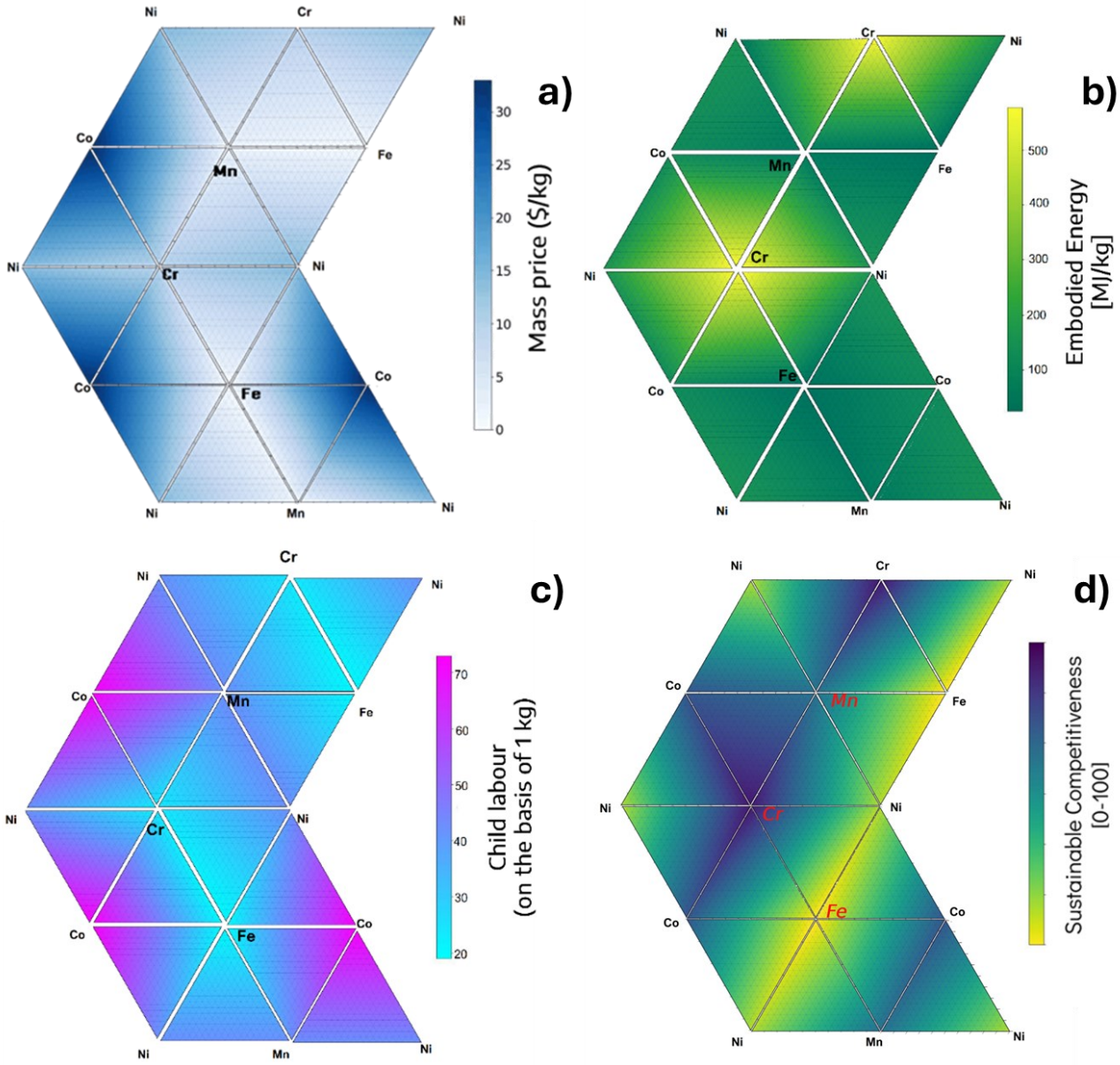


Figure 4.27. Four sustainability ternary maps showing evolution of (a) material price, (b) embodied energy, (c) child labour and (d) the overall sustainability footprint in Co-Cr-Fe-Mn-Ni systems.

These graphs emphasise cobalt's detrimental societal and economic footprint, as well as chromium's high embodied energy. Ternary alloy maps allow us to evaluate the mixed contributions of the elements to different sustainability indicators. For example, cobalt has the worst impact in terms of price and child labour. Then, the maps help deciding which direction is the less detrimental when moving away from cobalt The overall sustainability footprint map helps identify regions with lower impacts across multiple sustainability factors. From a sustainability-focused perspective, designing an alloy around the Fe-Mn-Ni regions shows potential for minimising sustainability footprints.

Thèse accessible à l'adresse : https://theses.insa-lyon.fr/publication/2025ISAL0036/these.pdf © [T. Langlois], [2025], INSA Lyon, tous droits réservés

4.3.4 Co-Cr-Ni-Si subsystems

As the CrCoNi alloy represents a benchmark material for analysis, it is essential to evaluate its sustainability footprints and assess how changes in composition impact these properties. Since we aim to study the mechanical effects of silicon, it is also important to investigate its influence on the sustainability footprints of new MPEAs.

As previously shown in *Figure 4.21*, cobalt and chromium exhibit relatively poor sustainability performances compared to other common raw materials, while nickel and silicon score more favourably. The overlay of the four element's sustainability footprints in *Figure 4.28* allows for a direct comparison of their respective footprints.

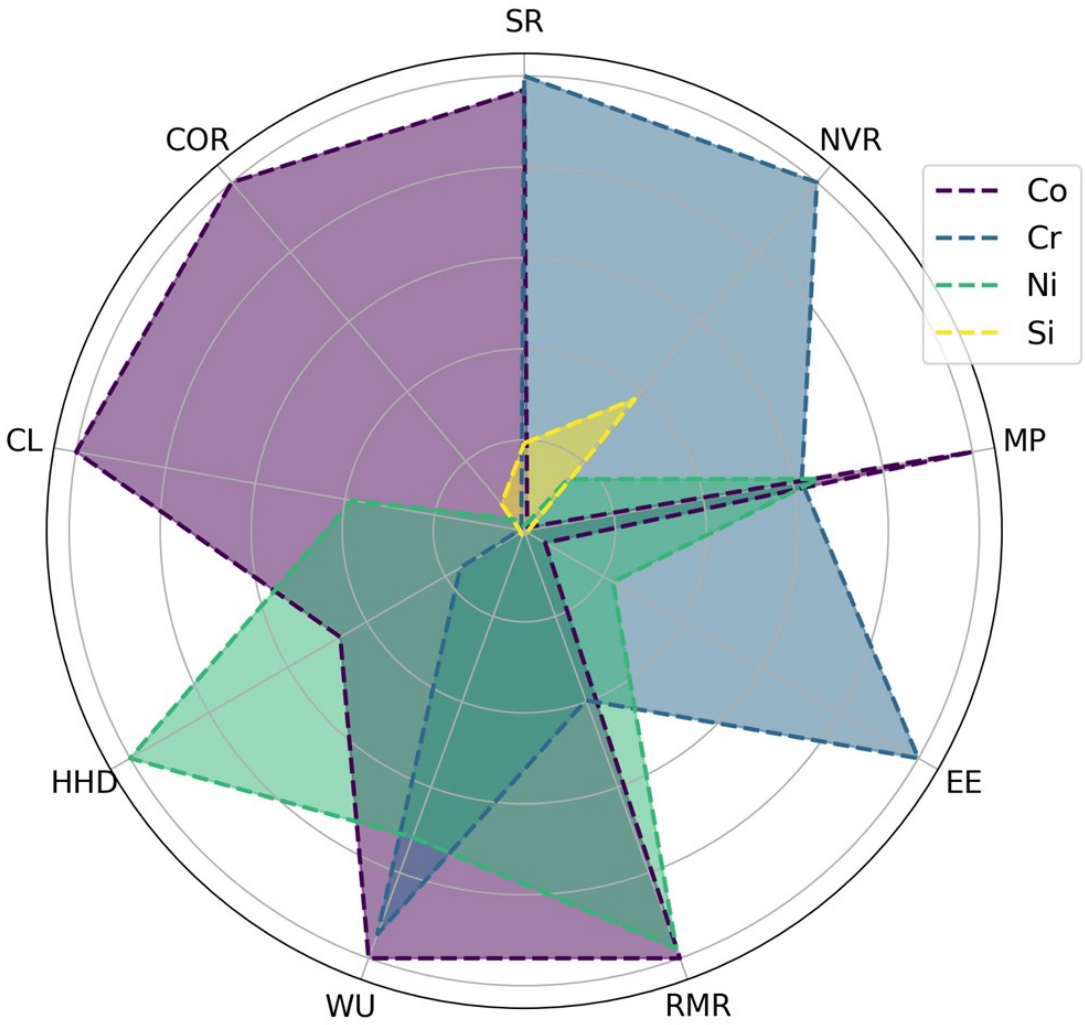


Figure 4.28. Radar chart of the 9 sustainability indicators for the four elements of interests (data has been rescaled to compare the elements among themselves; purple: cobalt, blue: chromium, green: nickel, yellow: silicium).

The shapes of the radar charts reveal that in a Co-Cr-Ni-Si system, societal footprints stem primarily from cobalt, while most economic impact are associated with

Thèse accessible à l'adresse : https://theses.insa-lyon.fr/publication/2025ISAL0036/these.pdf © [T. Langlois], [2025], INSA Lyon, tous droits réservés

chromium. Environmental impacts are not dominated by a single element, but nickel contributes significantly to health damage. Notably, silicon shows minimal impacts across all categories, making it an attractive element from a sustainability perspective. Nevertheless, literature indicates that high concentrations of silicon in MPEAs may lead to brittle phases formation, negatively affecting the alloy's mechanical performance.

To analyse the influence of compositional change in the Co-Cr-Ni-Si systems, we compare the sustainability radar chart of the equimolar Cantor alloy and equimolar CrCoNi ternary alloy (*Figure 4.29 a*). As cobalt, chromium and nickel content increases from 20 at.% to 33.33 at.%, while removing iron and manganese from the alloy, the larger footprint in the radar chart is expected, given that Co and Cr have higher sustainability footprints compared to Fe and Mn.

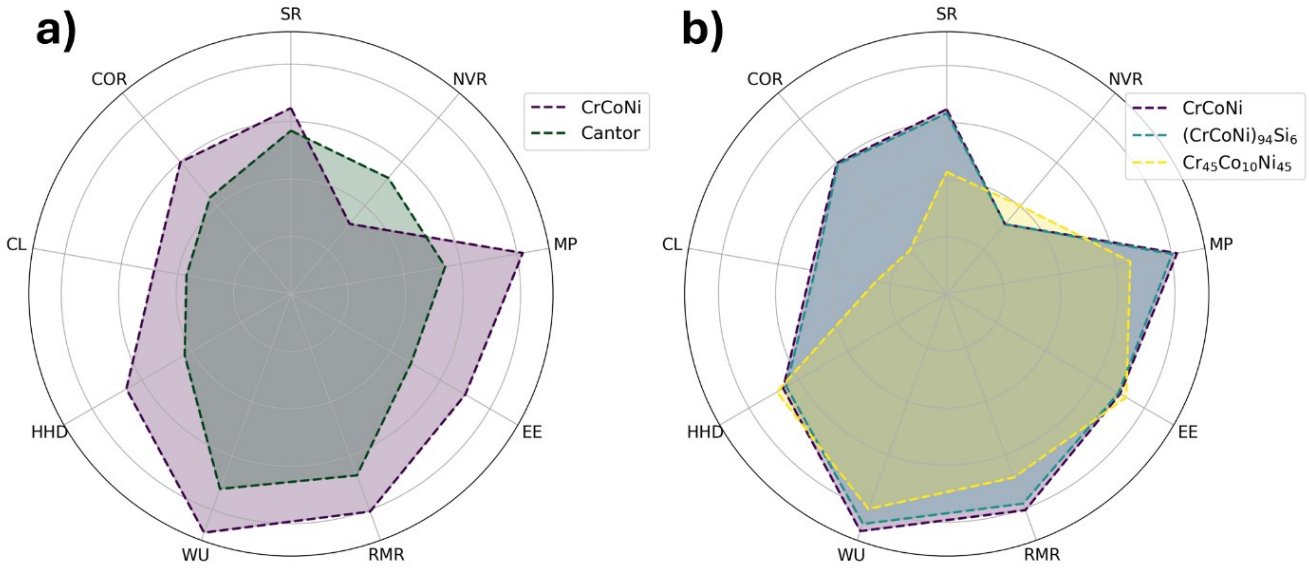


Figure 4.29. Radar charts illustrating the sustainability footprints of (a) Cantor alloy and CrCoNi alloy (b) Si-added CrCoNi and Co-reduced CrCoNi.

Next, we evaluated the effect of adding up to 6 at.% silicon to the equimolar CrCoNi and reducing cobalt content in the ternary alloy (*Figure 4.29 b*). The addition of silicon slightly improves the alloy's sustainability performance. Silicon's low-density results in a minor contribution to the overall footprint. Conversely, reducing cobalt content substantially alters the footprints, particularly in the societal aspects such as child labour and governance. Nonetheless, the required energy and health damage indicators remain unchanged, as lower cobalt content is offset by increased chromium and nickel. Therefore, identifying a greener composition within the Co-Cr-Ni-Si system

Thèse accessible à l'adresse : https://theses.insa-lyon.fr/publication/2025ISAL0036/these.pdf © [T. Langlois], [2025], INSA Lyon, tous droits réservés

is limited by several factors, including the definition of MPEAs (See *Equation (1.1)*), microstructural stability (to avoid secondary phases), and the trade-offs between different economic, environmental or societal impacts. From a holistic approach, the optimal sustainability composition is the one that minimises the radar chart area, or that minimises the overall sustainable competitiveness. Considering these constraints, the optimum composition is $Cr_{23}Co_8Ni_{63}Si_6$ with a relative Sust_FP of 4.94 out of 10, as shown in *Table 4.7*. This alloy reduces Sust_FP by 14.7 % compared to the equimolar CrCoNi.

Table 4.7. Relative average footprint in the CoCrNiSi systems (comparing only these elements with each other).

	Co	**Cr**	**Ni**	**Si**	**CrCoNi**	**$Cr_{23}Co_8Ni_{63}Si_6$**
Sust_FP [0-10]	7.22	5.71	4.60	0.78	5.79	4.94

In summary, this tool enables:

- Measuring the individual **footprints** of raw materials and their influence on the overall alloy score.
- Comparing **different classes of alloys**.
- Identifying the **contributions of Co-Cr-Ni and Si** in the sustainability footprints of MPEAs.
- Identifying **compositions** that **minimise the sustainability footprint** of alloys.

Thèse accessible à l'adresse : https://theses.insa-lyon.fr/publication/2025ISAL0036/these.pdf © [T. Langlois], [2025], INSA Lyon, tous droits réservés

4.4 Multi-objective optimisation

So far in this chapter, we have introduced several prediction models that assist our selection of compositions based on microstructure, mechanical performance and sustainability footprint. As mentioned in the motivation, our goal is to explore new C-MPEAs compositions where sustainability and mechanical performance have a great balance. To achieve this, we combine our different screening models and perform a multi-objective exploration.

From each screening prediction in the Co-Cr-Ni-Si systems, we first restricted the exploration to regions that satisfy the entropy criteria (see *Equation 1.1*) microstructure criteria (for FCC single phase alloys). We then identified regions that optimise σ_{SS}, SFE and sustainability footprints. As a reminder, we have the following observations in the choice of compositions:

- From the criterion on mixing entropy of MPEAs (see equation 1.1), the elemental concentration must be between 15 and 64 at.% for ternary alloys and 3.5 and 68 at.% for quaternary alloys.
- Based on CALPHAD predictions, a maximum of 6 at.% silicon can be added to ensure the stability of the single-phase FCC solid solution during heat-treatments.
- Based on CALPHAD predictions, a maximum of 48 at.% chromium can be included while maintaining the stability of a single-phase FCC with 6 at.% silicon.
- Solid solution strengthening is maximised in the Cr-Ni and Cr-Si regions.
- The lower SFE values are found in the cobalt-rich region.
- Economic footprints are minimised in the nickel-rich region.
- Environmental footprints are minimised in the nickel-rich region.
- Societal footprints are minimised at higher chromium content.
- Overall "sustainability footprints" are minimised in the nickel-rich region.

To select a composition, the performance in each category is associated with a score from 0 to 10. *Figure 4.30* represents four indicators, two for sustainability and

Thèse accessible à l'adresse : https://theses.insa-lyon.fr/publication/2025ISAL0036/these.pdf © [T. Langlois], [2025], INSA Lyon, tous droits réservés

two for mechanical performance, to illustrate an example of alloy exploration. No composition can lead to an optimisation of all the sustainability criterions at the same time. Achieving a balance between sustainability and mechanical performance is even more challenging. For example, compositions with high nickel content tend to be less expensive and have lower embodied energy, leading to favourable sustainability scores; however, their SFE and strength scores are considerably lower. Therefore, an optimisation tool is necessary to identify the best compromise among all criteria.

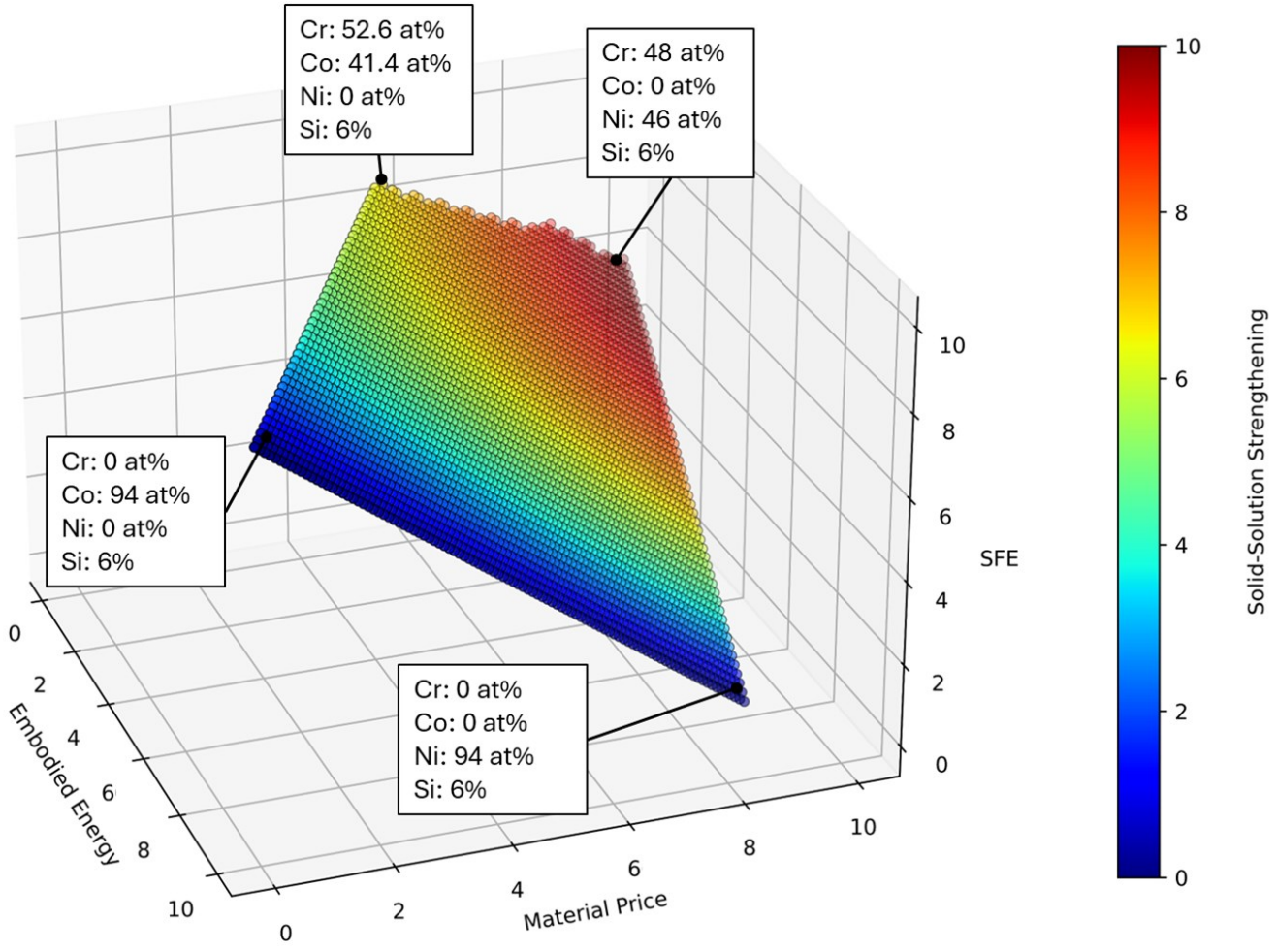


Figure 4.30. Scoring of Co-Cr-Ni-Si systems based on four properties (two sustainability criteria with Embodied Energy score and Material Price score; two mechanical criteria with SFE score and solid solution strengthening score).

Our primary motivation is to equally weigh sustainability and mechanical performance during composition exploration, as detailed in *Equation (4.2)*. This choice

Thèse accessible à l'adresse : https://theses.insa-lyon.fr/publication/2025ISAL0036/these.pdf © [T. Langlois], [2025], INSA Lyon, tous droits réservés

of equal weighting, while arbitrary, was selected as it provides a neutral and objective approach for balancing sustainability and mechanical performance without favouring any one criterion.

$$Overall_{score} = \left(\frac{\frac{Eco_{score} + Env_{score} + Soc_{Score}}{3} + \frac{SS_{score} + SFE_{score}}{2}}{2} \right) \quad (4.2)$$

Despite some correlations between the sustainability scores cannot be entirely avoided, they were developed to minimise their interdependence as described in the sustainability methods in Chapter 3.2.4. Similarly, SS_score and SFE_score exhibits correlated data as part of the strain-stress properties of materials, but low SFE materials promote twinning and or transformations effects that enhance both work-hardening and elongation. To this extent, combining these two mechanical scores allows to better capture the trade-offs between strength and ductility.

In *Table 4.8*, we present the scores of various compositions that optimise a single aspect of sustainability, including societal, environmental, and economic scores. The last composition listed represents the best compromise and overall average score.

Table 4.8. Cr-Co-Ni-Si compositions optimising different sustainability and mechanical criteria (a large value is desired).

		sustainable performance				mechanical performance		
Alloy	**Composition** (at%)	**Eco_score** [0-10]	**Env_score** [0-10]	**Soc_score** [0-10]	**Sust_score** [0-10]	**σ_{SS}_score** [0-10]	**SFE_score** [0-10]	**Total**
SolidSolution_best	$Cr_{47.1}Co_4Ni_{44.5}Si_6$	4.44	3.15	7.11	4.90	9.76	5.82	6.35
SFE_best	$Cr_{18.9}Co_{64.7}Ni_{10.4}Si_6$	3.59	3.24	3.74	3.52	4.90	7.29	4.81
Economy_best	$Cr_{12.9}Co_{15.5}Ni_{65.5}Si_6$	5.95	3.56	5.33	4.95	4.67	3.64	4.55
Environment_best	$Cr_{5.8}Co_{28.4}Ni_{59.8}Si_6$	5.87	3.59	4.66	4.71	2.78	3.49	3.92
Society_best	$Cr_{48}Co_{3.4}Ni_{42.6}Si_6$	4.45	3.15	7.13	4.91	9.72	6.22	6.44
Sustainability_best	$Cr_{23}Co_8Ni_{63}Si_6$	5.67	3.46	6.01	5.05	7.19	4.64	5.48
Benchmark	$Cr_{33}Co_{33}Ni_{33}$	4.04	3.06	5.53	4.21	6.99	6.43	5.46
Co10Si6	$Cr_{42.3}Co_{9.4}Ni_{42.3}Si_6$	4.46	3.18	6.73	4.79	9.27	6.38	6.31
Optimised_alloy	$Cr_{48}Co_{3.4}Ni_{42.6}Si_6$	4.45	3.15	7.13	4.91	9.72	6.22	6.44

Thèse accessible à l'adresse : https://theses.insa-lyon.fr/publication/2025ISAL0036/these.pdf © [T. Langlois], [2025], INSA Lyon, tous droits réservés

Experimentally, we selected the Co10Si6 alloy, with a composition of $Cr_{42.3}Co_{9.4}Ni_{42.3}Si_6$. This choice allows us to analyse the effects of cobalt and silicon without altering the Cr/Ni ratio, and the sustainability performance of this composition is very close to the optimum identified earlier.

In conclusion, we have successfully developed and applied a multi-scale method to explore new MPEA compositions, balancing between mechanical performance and sustainability. By integrating multi-objective screening models, we have shown that it is possible to achieve compositions with reduced environmental, economic, and societal impacts while maintaining mechanical integrity.

The selected alloy $Cr_{42.3}$ $Co_{9.4}$ $Ni_{42.3}$ Si_6 shows significant improvement in its overall sustainability, with an 11.1% reduction in footprint compared to the equimolar CrCoNi, without compromising its predicted mechanical performance. In the next chapters, we will focus on verifying these mechanical predictions through experimental testing, ensuring that this greener alloy composition meets the required performance standards in real-world applications.

Thèse accessible à l'adresse : https://theses.insa-lyon.fr/publication/2025ISAL0036/these.pdf © [T. Langlois], [2025], INSA Lyon, tous droits réservés

5 Experimental investigations

Contents

5.1 Alloy processing ---- 154

5.1.1 Manufacturing observations ---- 154

5.1.2 Thermomechanical treatments ---- 156

5.2 Chemical analysis ---- 160

5.2.1 Raw materials purity and oxides ---- 160

5.2.3 Chemical gradient and segregation ---- 167

5.3 Compression specimens ---- 175

5.3.1 Reference-state microstructure ---- 175

5.3.2 Mechanical properties ---- 180

5.3.3 Postmortem microstructural observations ---- 185

5.4 Impact loading specimens ---- 187

5.4.1 Reference-state microstructure ---- 187

5.4.2 Mechanical properties ---- 192

5.4.3 Postmortem microstructural observations ---- 194

5.5 Tensile specimens ---- 198

5.5.1 Reference-state microstructure ---- 198

5.5.2 Mechanical properties ---- 200

5.5.3 Postmortem microstructural observations ---- 206

5.6 Effect of composition and temperature ---- 219

5.7 Concluding remarks ---- 221

Thèse accessible à l'adresse : https://theses.insa-lyon.fr/publication/2025ISAL0036/these.pdf © [T. Langlois], [2025], INSA Lyon, tous droits réservés

In consideration of current environmental challenges, sustainability must be prioritised alongside mechanical performance when designing new alloys. Our analysis of the raw material's footprints revealed the significant environmental, societal, and economic impact of cobalt. Therefore, there is an urge to reduce cobalt content in future alloys.

In contrast, silicon is a promising alternative to cobalt due to its significantly lower sustainable footprints. Moreover, studies cited in the literature review indicate that silicon addition can enhance the mechanical properties of many C-MPEAs by improving the strength-ductility trade-off.

With these insights, we have conceptualised an optimised alloy that aim to balance sustainability and mechanical performance. To validate our predictions, we must systematically evaluate the effects of compositional changes. Specifically, we aim to assess the impact of reducing cobalt content in Cr-Co-Ni systems and subsequently analyse the effect of silicon addition in Cr-Co-Ni-Si systems.

Consequently, the objectives in this chapter are as follow:

- Evaluate the influence of cobalt reduction on the microstructure and mechanical properties of a $Co_x(CrNi)_{100-x}$ alloys at both room and low temperatures.
- Evaluate the influence of silicon addition on the microstructure and mechanical properties of a Co-Cr-Ni-Si alloys with different cobalt concentrations, at both room and low temperatures.
- Assess the accuracy of our prediction models for mechanical properties.
- Evaluate the sustainability scores and mechanical performance of our target system, Co10Si6.

Thèse accessible à l'adresse : https://theses.insa-lyon.fr/publication/2025ISAL0036/these.pdf © [T. Langlois], [2025], INSA Lyon, tous droits réservés

5.1 Alloy processing

This section provides detailed information about the experimental processing of CrCoNi and CrCoNiSi alloys. Detailed insights in the experimental manufacturing methods and thermomechanical treatments are essential for interpreting the observed microstructural and mechanical responses.

Three distinct sample geometries were produced for this study: cylindrical specimens, Charpy V-notch specimens, and tensile dog-bone-shaped specimens. Each geometry, with its specific dimensions, required specific heat-treatment parameters in terms of time and temperature. Alongside dimension considerations, the chemical composition of the alloys significantly influenced the selection of heat-treatment conditions, as the aim was to ensure a single-phase FCC solid solution across all compositions.

5.1.1 Manufacturing observations

As described in the experimental methods, cobalt, chromium, nickel, and silicon raw materials were prepared in desired quantities for processing through Arc-melting (using the Arc50 or Arc200 furnaces) and Induction casting (using the Ind500 furnace). For compositions containing silicon, two Ni-Si master alloys were designed to ensure the formation of FCC microstructure and avoid forming brittle intermetallic phases during alloying. We chose two compositions, Ni96Si4 and Ni92Si8 (at.%), to add small and large amounts of silicon, to further obtain the precise mass for the desired CrCoNiSi compositions. The design of these master alloys was guided by ThermoCalc phase predictions using the TCHEA5 database, which provides a well-assessed binary diagram for the Ni-Si system illustrated in *Figure 5.1*-a. The Ni-Si alloys were produced by Arc200, heat-treated in the fluidised-bed-furnace filled with Argon 4.7 at 1200°C for 12 hours to ensure chemical homogeneity, and water-quenched. They were subsequently cut to obtain smaller bulk pieces, as illustrated in *Figure 5.1-b*, for use in the casting of CrCoNiSi alloys.

The nominal compositions of the two Ni-Si master alloys, listed in *Table 4.1* were verified using GDOES. The measurements revealed negligible concentration of contaminating elements in the two ingots.

Thèse accessible à l'adresse : https://theses.insa-lyon.fr/publication/2025ISAL0036/these.pdf © [T. Langlois], [2025], INSA Lyon, tous droits réservés

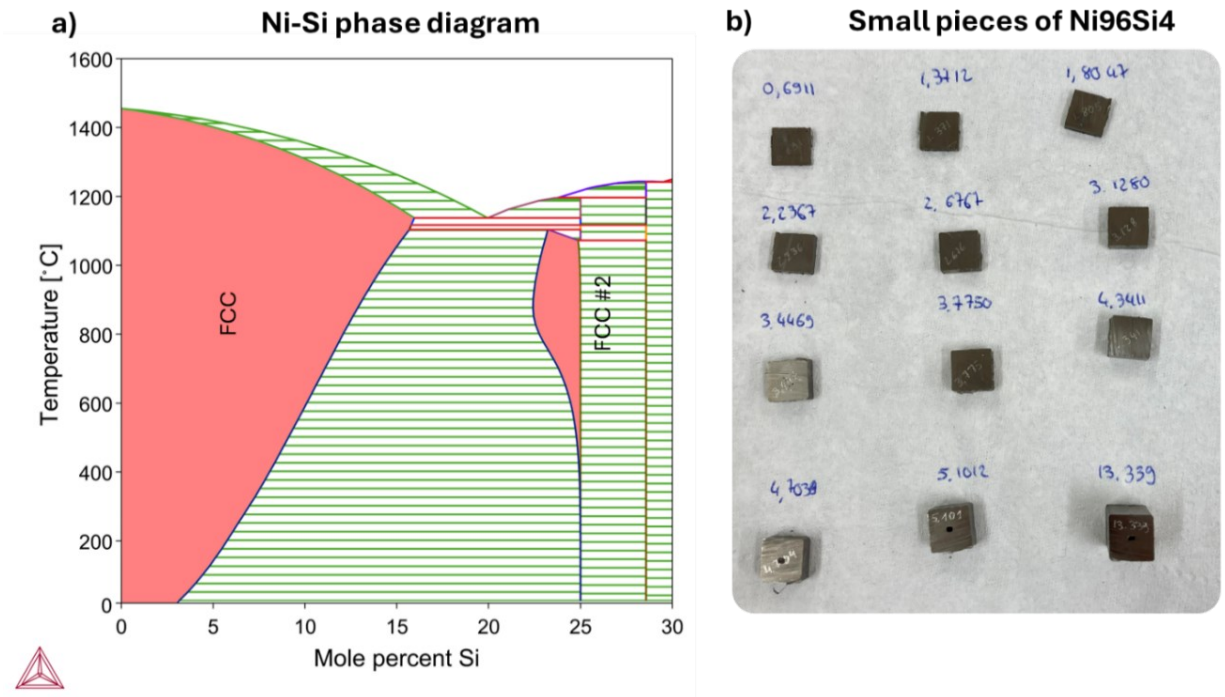


Figure 5.1. (a) Binary phase diagram for Ni-Si systems; (b) Smaller pieces of Ni94Si6 prepared for arc-casting of CrCoNiSi alloys (masses in grams are indicated above each piece).

Table 5.1. Bulk composition of NiSi master alloys casted by Arc200.

Alloy name	sample name	composition (at%)		
		Ni	Si	
$Ni_{96}Si_4$	NiSi4	*96.00*	*4.00*	*intended*
		94.09	5.12	measured
$Ni_{92}Si_8$	NiSi8	*92.00*	*8.00*	*intended*
		90.61	8.57	measured

Unlike the Arc50 furnace, which enables the use of a titanium getter to trap oxygen gas released in the vacuum chamber during melting, the Arc200 and Ind500 furnaces do not support the use of such getters. As a results, the oxygen mitigations can be less effective.

In the Ind500 furnace, molten materials were cast in rectangular moulds made of steels. In the following sections, chemical analyses indicate that iron was detected near the ingot's surface. This is likely due to the diffusion of iron from the steel mould into the alloy during casting, further exacerbated at very high temperatures. The presence of iron gradient can alter the material's microstructure, with local chemical gradient and the potential formation of unintended phases, and can alter the mechanical responses such as local hardness.

Thèse accessible à l'adresse : https://theses.insa-lyon.fr/publication/2025ISAL0036/these.pdf © [T. Langlois], [2025], INSA Lyon, tous droits réservés

5.1.2 Thermomechanical treatments

Several thermomechanical treatments were carried out to tailor the chemical homogeneity and mechanical properties of the alloys. The acceptable temperature ranges for thermal treatments were predicted with ThermoCalc and the TCHEA5 database. The solid solution span, delimited by the onset of liquid phases at high temperature and secondary phases at lower temperature, vary significantly depending on the cobalt and silicon content of the alloys (*Figure 4.7* and *Figure 4.8*). Subsequently, different heat-treatments were applied with respect to the experimental alloy compositions.

Ater casting, every ingot underwent a homogenisation treatment designed to mitigate chemical homogeneity and potential segregation arising from various cooling rate during solidification across different regions of the ingots. The temperatures and durations of homogenisation were tailored to compositions and geometries of the samples, as reported in *Table 5.2.* and *Table 5.3* for CrCoNi and CrCoNiSi alloys, respectively. XRD analysis was conducted to confirm the phases present in the alloys after heat-treatments.

Table 5.2. Homogenisation parameters in the fluidised-bed furnace for CrCoNi alloys (Small, medium, and large ingots have different homogenisation time because of their dimensions – phases identified using XRD).

sample name	**sample name**	**temperature (°C)**	**homogenisation time (h)**			**Phases**
			Arc50 samples	**Arc200 samples**	**Ind500 samples**	
$Cr_{25}Co_{50}Ni_{25}$	Co50	1000	0.5	-	-	FCC
$Cr_{30}Co_{40}Ni_{30}$	Co40	1000	0.5	-	-	FCC
$Cr_{33}Co_{33}Ni_{33}$	Co33	1000	0.5	1.5	3.0	FCC
$Cr_{40}Co_{20}Ni_{40}$	Co20	1000	0.5	-	3.0	FCC
$Cr_{45}Co_{10}Ni_{45}$	Co10	1200	0.5	1.5	3.0	FCC

Thèse accessible à l'adresse : https://theses.insa-lyon.fr/publication/2025ISAL0036/these.pdf © [T. Langlois], [2025], INSA Lyon, tous droits réservés

Table 5.3. Homogenisation parameters in the fluidised-bed furnace for CrCoNiSi alloys (Phases identified using XRD).

sample name	sample name	temperature (°C)	homogenisation time (h)			Phases
			Arc50 samples	Arc200 samples	Ind500 samples	
$Cr_{33}Co_{33}Ni_{33}$	Co33	1000	0.5	1.5	3.0	FCC
$(Cr_{33}Co_{33}Ni_{33})Si_6$	Co33Si6	1000	0.5	1.5	-	FCC
$Cr_{40}Co_{20}Ni_{40}$	Co20	1000	0.5	-	3.0	FCC
$(Cr_{40}Co_{20}Ni_{40})Si_1$	Co20Si1	1000	0.5	-	-	FCC
$(Cr_{40}Co_{20}Ni_{40})Si_2$	Co20Si2	1000	0.5	-	-	FCC
$(Cr_{40}Co_{20}Ni_{40})Si_3$	Co20Si3	1000	0.5	-	-	FCC
$(Cr_{40}Co_{20}Ni_{40})Si_6$	Co20Si6	1000	0.5	-	-	FCC
$(Cr_{40}Co_{20}Ni_{40})Si_9$	Co20Si9	1000	0.5	-	-	FCC
$Cr_{45}Co_{10}Ni_{45}$	Co10	1200	0.5	1.5	3.0	FCC
$(Cr_{45}Co_{10}Ni_{45})Si_1$	Co10Si1	1200	0.5	-	-	FCC
$(Cr_{45}Co_{10}Ni_{45})Si_2$	Co10Si2	1200	0.5	-	-	FCC
$(Cr_{45}Co_{10}Ni_{45})Si_3$	Co10Si3	1200	0.5	-	3.0	FCC
$(Cr_{45}Co_{10}Ni_{45})Si_6$	Co10Si6	1200	0.5	1.5	3.0	FCC
$(Cr_{45}Co_{10}Ni_{45})Si_9$	Co10Si9	1200	0.5	-	-	FCC

Subsequently, as detailed in the methods, Arc200 ingots underwent a cold rolling treatment. The parameters applied during cold rolling and subsequent recrystallisation are summarised in *Table 5.4*. XRD analysis confirms the presence of FCC phase, and EBSD mapping showed no evidence of secondary phases too.

Thèse accessible à l'adresse : https://theses.insa-lyon.fr/publication/2025ISAL0036/these.pdf © [T. Langlois], [2025], INSA Lyon, tous droits réservés

Table 5.4. Cold rolling and recrystallisation parameters (phases identified using XRD).

Cold Rolling parameters		**Recrystallisation**		
sample name	**Pass: thickness and reduction %**	**temperature (°C)**	**time (min)**	**phase(s)**
Co33	#1: 8.0mm - 7% #2: 7.4mm - 5% #3: 7.0mm - 6% #4: 6.6mm - 9% #5: 6.0mm - 7% #6: 5.6mm - 7% #7: 5.2mm - 8% #8: 4.8mm - 4% 4.6 mm (intermediate annealing) #9: 4.6mm -13% #10: 4.0mm -10% #11: 3.6mm -16% #12: 3.0mm -13% #13: 2.6mm -18% 2.2mm	1000	5	FCC
Co10		1200	5	FCC
Co33Si6	#1: 8.0mm - 6% #2: 7.5mm - 5% #3: 7.1mm - 7% #4: 6.6mm - 5% #5: 6.3mm - 3% #6: 6.1mm - 3% #7: 5.9mm - 3% #8: 5.7mm - 5% #9: 5.4mm - 4% #10: 5.2mm - 4% #11: 5.0mm - 4% #12: 4.8mm - 4% 4.6 mm (intermediate annealing) #13: 4.6mm -13% #14: 4.0mm -10% #15: 3.6mm -14% #16: 3.1mm -10% #17: 2.8mm -11% #18: 2.5mm -8% #19: 2.3mm -9% 2.1mm	1000	5	FCC
Co10Si6		1200	5	FCC

Thèse accessible à l'adresse : https://theses.insa-lyon.fr/publication/2025ISAL0036/these.pdf © [T. Langlois], [2025], INSA Lyon, tous droits réservés

After homogenisation, Ind500 ingots underwent a hot rolling treatment. Details of the thickness reduction, heat-treatment durations and temperatures are provided in *Table 5.5*. Phase identification was also performed using XRD and EBSD.

Table 5.5. Hot rolling parameters for Co10 and Co10Si6 ingots produced by Ind500 (phases identified using XRD).

Hot Rolling parameters			
sample name	**set point oven(°C)**	**Phase(s)**	**Pass: thickness and reduction %**
Co33	1000	FCC	no1 : 28.5mm - 11% no2 : 26.0mm - 12% no3 : 22.9mm - 12% no4 : 19.9mm - 14% no5 : 16.2mm - 16% no6 : 14.6mm - 12% no7 : 12.7mm - 10% 11.3mm
Co20	1000	FCC	
Co10	1200	FCC	no1 : 28.5mm - 11% no2 : 26.2mm - 11% no3 : 23.1mm - 11% no4 : 20.3mm - 12% no5 : 16.9mm - 13% no6 : 15.6mm - 12% no7 : 13.8mm - 10% 12.5mm
Co10Si6	1200	FCC+BCC	
Co10Si9	1200	FCC+σ	

The presence of BCC/B2 phase in Co10Si6 and sigma phase in Co10Si9 alloys is unintended. This issue is linked to the limitations of the ovens used for this treatment. The highest achievable temperature in these ovens is 1200°C, which is relatively low for the heat treatment of C-MPEAs. For the Co10 alloys with silicon addition, the phase diagram shows evidence of narrow temperature window, especially for higher silicon

Thèse accessible à l'adresse : https://theses.insa-lyon.fr/publication/2025ISAL0036/these.pdf © [T. Langlois], [2025], INSA Lyon, tous droits réservés

content (*Figure 4.7*). Precisely, CALPHAD calculations estimate the formation temperature of the sigma phase at 1155°C for the Co10Si9 alloy, which is close to the maximum working temperature of the oven.

Being near the oven limitation, the temperature in the oven decreased rapidly upon opening the door and rose slowly upon closing, preventing the optimal control of the microstructural evolution during hot rolling. Despite these challenges and the undesired secondary phases, the alloys were processed for impact testing. However, as will be discussed in the upcoming sections, the presence of the brittle sigma phase significantly impacted the toughness of these alloys.

5.2 Chemical analysis

5.2.1 Raw materials purity and oxides

The contamination levels of oxygen (O), carbon (C), nitrogen (N) and Sulphur (S) were analysed using the ONH-836 and CS-744 elemental analyser at Mateis. The purity levels provided by the suppliers for the raw materials used at Deakin is reminded in *Table 3.7*.

Table 5.6. Purity of the raw materials used at Deakin IFM.

Element	Type	Purity (wt.%)
Chromium	Bulk	99.1
Cobalt	Bulk	99.37
	Chip	99.99
Nickel	Bulk	99.8
	Chip	99.9
Silicon	Bulk	99.8

In line with the expected purity levels, the concentrations in trace elements for these raw materials are given in *Figure 5.2*. The results demonstrate high concentrations of oxygen and carbon in bulk chromium and cobalt, while their chip forms exhibit significantly lower contamination levels. The high value of carbon observed in pure

Thèse accessible à l'adresse : https://theses.insa-lyon.fr/publication/2025ISAL0036/these.pdf © [T. Langlois], [2025], INSA Lyon, tous droits réservés

silicon is unexpected. Further analysis on these raw materials (GDS, EDS/EDX, etc...) would be recommended for future projects.

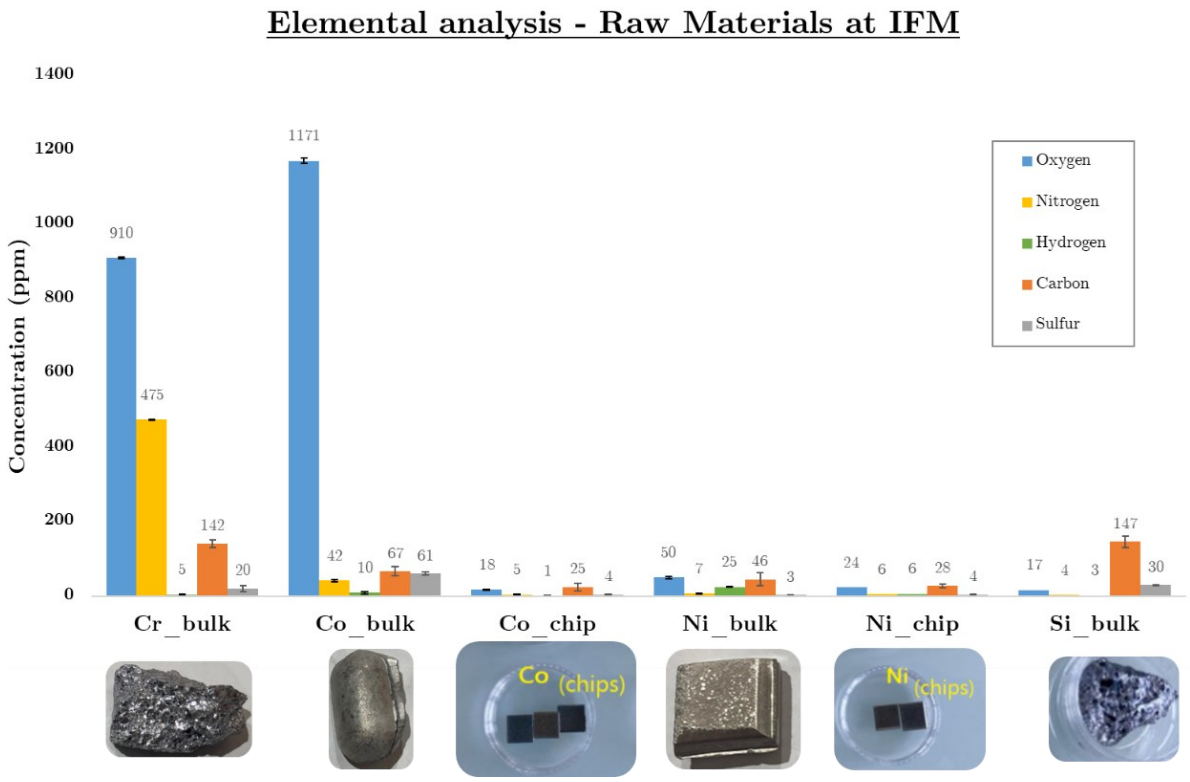


Figure 5.2. Elemental analysis for O/N/H and C/S concentrations (in wt. ppm) in raw materials at IFM.

The alloys produced in this study exhibit low contamination levels. After homogenisation, the highest oxygen content remains below 0.3 at.%. These low values can be attributed to the range of strategies employed to mitigate contamination at each stage of the manufacturing process. Materials were ground and cleaned with ethanol, then stored in low oxygen environments like desiccators. The casting equipment was cleaned, and very high vacuum was obtained, using inert Argon gas 4.7. Heat-treatments were also performed in very clean atmosphere and under inert Argon gas 4.7.

Despite these precautions, the presence of residual oxygen content can lead to the formation of oxides in the materials. These oxides often appear as black dots on the microstructural surface. EDS analysis reveals that these oxides primarily consist of Cr_2O_3 chromium oxides in both Co33 and Co10, as observed in *Figure 5.3-a*. Previous studies on other C-MPEA systems, such as CoCrFeNi and Cantor alloys [154], have

Thèse accessible à l'adresse : https://theses.insa-lyon.fr/publication/2025ISAL0036/these.pdf © [T. Langlois], [2025], INSA Lyon, tous droits réservés

reported the similar formation of chromium oxides. Instead of chromium oxides, silicon oxides are observed in CrCoNiSi alloys in *Figure 5.3-b*. This change of oxide is consistent with thermodynamic predictions made using evolved Ellingham diagrams: These diagrams, which compare the relative stability of oxides formed with various metals, are corrected to account for the activities of elements in the alloys, as opposed to their pure form [155]. To further understand the stability of these oxides in complex C-MPEA systems, ThermoCalc with the TCHEA5 database was employed to calculate the activities of metals in various compositions, including Co33, Co10 and Co10Si6. Using Gibbs free energy as a function of temperature for pure metals [156], and accounting for Co and Si, the Ellingham Diagram of the Co10Si6 alloy was drawn in *Figure 5.4*. Complementary calculations for the Co33, Co33Si6 and Co10 alloys are provided in *Figure 0.8* in the Appendix of Chapter 5, and are consistent with the observed microstructures.

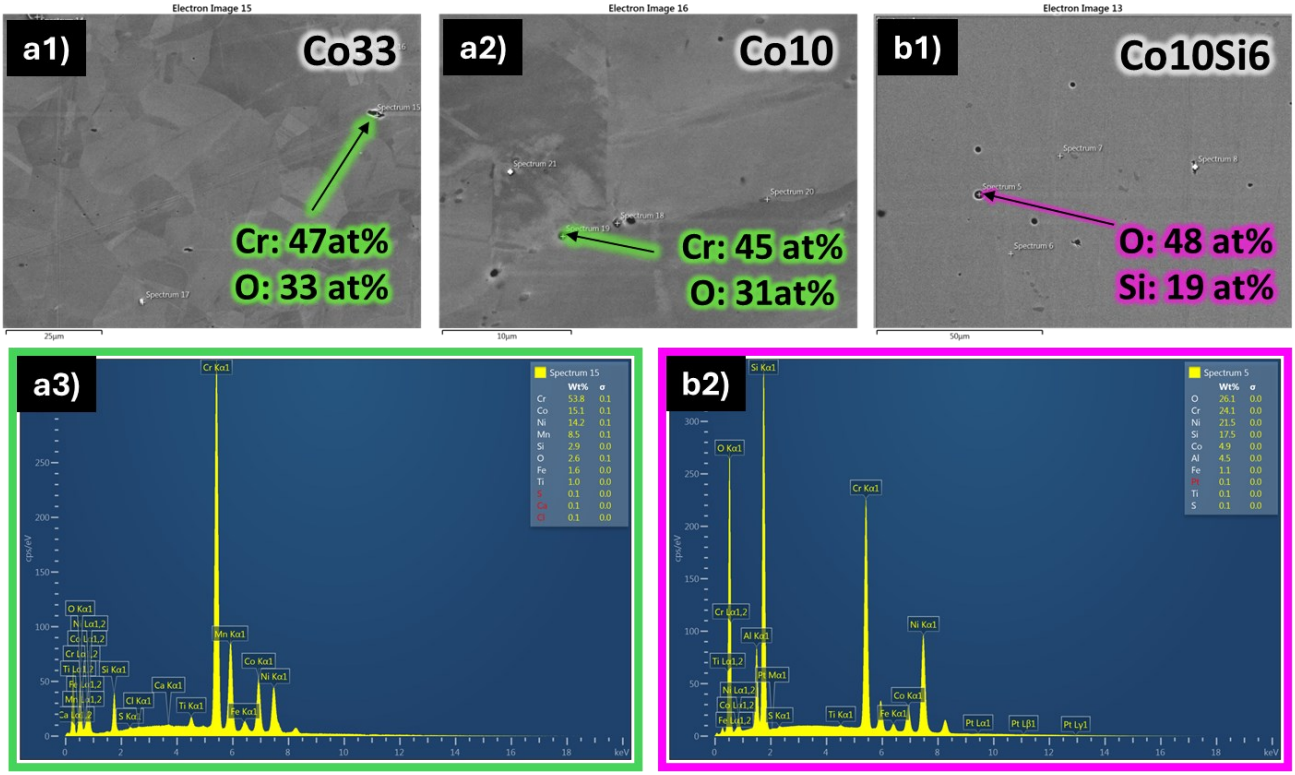


Figure 5.3. SEM imaging of metal oxides: (a1, a2) Cr oxide in CrCoNi alloys; (a3) corresponding EDS spectrum of the Cr oxide in a1; (b1, b2) SEM and corresponding EDS spectrum of a Si oxide in a CrCoNiSi alloy.

Thèse accessible à l'adresse : https://theses.insa-lyon.fr/publication/2025ISAL0036/these.pdf © [T. Langlois], [2025], INSA Lyon, tous droits réservés

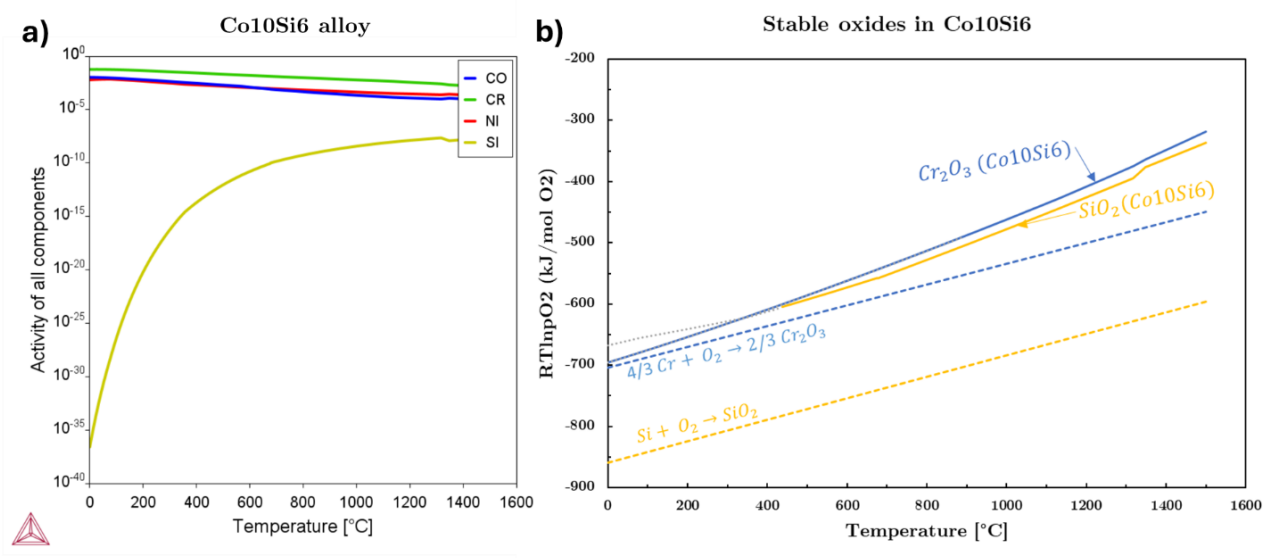


Figure 5.4. Thermodynamic consideration for the formation of oxides in CrCoNi and CrCoNiSi alloys: (a) Cr, Co, Ni and Si activities in the Co10Si6 alloy; (b) Relative stability of Cr2O3 and SiO2 oxides in the Co10Si6 alloy (solid line) compared to the oxides in equilibrium with the pure metals (dashed line), metastable domains of the oxides are represented in grey point lines [156].

Compared to the reference states for pure metal oxide formation, illustrated by the coloured dashed lines in *Figure 5.4*-b, the energy gap between these two oxides is narrower in Co10Si6. This change is related to the lowest activity of silicon in the Co10Si6 alloy in *Figure 5.4*-a.

To assess oxide concentration, graphic analysis using the ImageJ software was performed on a set of 20-25 images for Co33, Co10 and Co10Si6. The maximum spatial concentration of oxide was found to be 0.66%. The measured concentrations are relatively low, and no significant variation was detected across different casting methods. Given the limited concentration in oxides, it is unlikely that microstructural evolution or mechanical performance are significantly influenced by these oxides [154].

5.2.2 Experimental compositions

For large ingots produced using Arc200 and Ind500, bulk compositions were analysed with GDOES. Due to their short dimensions, Arc50 cylinders were analysed using EDS with the SEM JEOL JSM78000F. For all sample geometries, measurements were taken at multiple locations, as illustrated in *Figure 5.5*, to calculate average compositions and assess potential chemical gradients.

Thèse accessible à l'adresse : https://theses.insa-lyon.fr/publication/2025ISAL0036/these.pdf © [T. Langlois], [2025], INSA Lyon, tous droits réservés

Bulk measurements with GDOES were performed at a depth of 150 µm, with five measurement points and using our custom database for enhanced accuracy. Surface measurement with EDS were performed at a working distance between 10 and 15 mm with a 20kV and 37 µA. Both GDOES and EDS accuracy were verified using a reference AISI 304, whose results are given in *Table 5.7*.

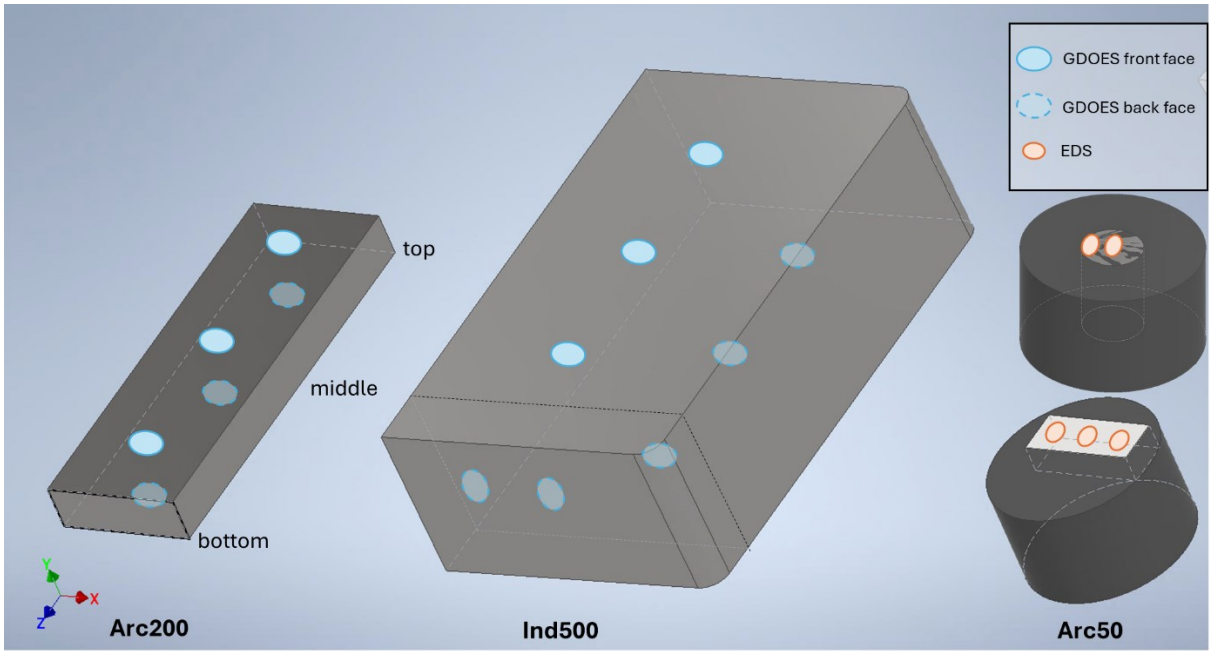


Figure 5.5. Descriptive schematics locating the position where chemical compositions are checked for all different samples.

Table 5.7. Chemical composition of the reference sample made of annealed AISI 304 measured using EDS and GDOES techniques.

Alloy name	composition	Mn	Si	P	S	Cr	Ni	Fe	N
AISI 304	*target (wt%)*	*0.0-2.0*	*0.0-1.0*	*0.0-0.05*	*0.0-0.03*	*17.50-19.50*	*8.00-10.50*	*Balance*	*0.0-0.11*
	nominal (wt%)	0.85	0.49	0.04	0.01	19.1	7.91	Balance	0

Both EDS and GDOES measurement techniques provide mass fraction values within the acceptable range for the reference material AISI304. Furthermore, both equipments showed good agreement.

Thèse accessible à l'adresse : https://theses.insa-lyon.fr/publication/2025ISAL0036/these.pdf © [T. Langlois], [2025], INSA Lyon, tous droits réservés

The bulk compositions of the Co-Cr-Ni-Si alloys produced in this study are summarised in *Table 5.8*. Results are presented after homogenisation treatments, mitigating the influence of potential segregation in the as-cast state. The bulk compositions of alloys produced using the Arc50 and Arc200 furnaces closely match the intended compositions, making them suitable for further analysis.

However, the alloys produced using the Ind500 furnace exhibit noticeable iron contamination, with iron content ranging from 1 to 5 at.%. This contamination will be considered in subsequent mechanical and microstructural analyses. To note the presence of this unintended iron, alloys produced by Ind500 are marked as Co33*, Co20*, Co10*, Co10Si3*, and Co10Si6* throughout the rest of the study.

Thèse accessible à l'adresse : https://theses.insa-lyon.fr/publication/2025ISAL0036/these.pdf © [T. Langlois], [2025], INSA Lyon, tous droits réservés

Table 5.8. Bulk compositions of CrCoNi and CrCoNiSi alloys after homogenisation.

Alloy name	sample name	composition (at%) Cr	Ni	Co	Si	Observations	Measurement method
$Cr_{25}Co_{50}Ni_{25}$	Co50	*25*	*25*	*50*	*0*		*(target value)*
		25.54	23.89	50.57	0.0		EDS (Arc50)
$Cr_{30}Co_{40}Ni_{30}$	Co40	*30*	*30*	*40*	*0*		*(target value)*
		30.18	29.55	40.28	0.0		EDS (Arc50)
$Cr_{33}Co_{33}Ni_{33}$	Co33	*33.33*	*33.33*	*33.33*	*0.0*		*(target value)*
		34.23	32.61	33.15	0.02		GDOES (Arc200)
		32.57	32.15	32.28	0.0	Fe: 3.00 at%	GDOES (Ind500)
		33.25	33.19	33.56	0.0		EDS (Arc50)
$(Cr_{33}Co_{33}Ni_{33})Si_6$	Co33Si6	*31.33*	*31.33*	*31.33*	*6.0*		*(target value)*
		31.85	31.13	30.71	6.15		GDOES (Arc200)
		32.27	30.47	31.17	6.08		EDS (Arc50)
$Cr_{40}Co_{20}Ni_{40}$	Co20	*40*	*40*	*20*	*0*		*(target value)*
		39.72	38.17	19.14	0.0	Fe: 2.59 at%	GDOES (Ind500)
		39.37	39.67	20.96	0.11		EDS (Arc50)
$(Cr_{40}Co_{20}Ni_{40})Si_1$	Co20Si1	*39.6*	*39.6*	*19.8*	*1.0*		*(target value)*
		39.89	37.85	20.60	1.19		EDS (Arc50)
$(Cr_{40}Co_{20}Ni_{40})Si_2$	Co20Si2	*39.2*	*39.2*	*19.6*	*2.0*		*(target value)*
		38.93	38.94	19.95	2.17		EDS (Arc50)
$(Cr_{40}Co_{20}Ni_{40})Si_3$	Co20Si3	*38.8*	*38.8*	*19.4*	*3.0*		*(target value)*
		36.74	40.19	20.11	2.96		EDS (Arc50)
$(Cr_{40}Co_{20}Ni_{40})Si_6$	Co20Si6	*37.6*	*37.6*	*18.8*	*6.0*		*(target value)*
		38.40	37.22	18.97	5.41		EDS (Arc50)
$(Cr_{40}Co_{20}Ni_{40})Si_9$	Co20Si9	*36.4*	*36.4*	*18.2*	*9.0*		*(target value)*
		36.45	36.41	18.59	8.55		EDS (Arc50)
$Cr_{45}Co_{10}Ni_{45}$	Co10	*45*	*45*	*10*	*0*		*(target value)*
		45.85	44.02	10.02	0.09		GDOES (Arc200)
		43.46	42.11	9.97	0.0	Fe: 4.46 at%	GDOES (Ind500)
		46.40	43.18	10.24	0.08		EDS (Arc50)
$(Cr_{45}Co_{10}Ni_{45})Si_1$	Co10Si1	*44.55*	*44.55*	*9.9*	*1.0*		*(target value)*
		45.46	43.08	10.02	1.44		EDS (Arc50)
$(Cr_{45}Co_{10}Ni_{45})Si_2$	Co10Si2	*44.1*	*44.1*	*9.8*	*2.0*		*(target value)*
		44.64	43.27	9.84	2.24		EDS (Arc50)
$(Cr_{45}Co_{10}Ni_{45})Si_3$	Co10Si3	*43.65*	*43.65*	*9.7*	*3.0*		*(target value)*
		44.15	42.93	9.66	3.17		EDS (Arc50)
$(Cr_{45}Co_{10}Ni_{45})Si_6$	Co10Si6	*42.3*	*42.3*	*9.4*	*6.0*		*(target value)*
		42.24	42.26	9.32	6.2		GDOES (Arc200)
		41.18	40.35	9.59	6.71	Fe: 2.17 at%	GDOES (Ind500)
		42.83	42.04	9.51	5.62		EDS (Arc50)
$(Cr_{45}Co_{10}Ni_{45})Si_9$	Co10Si9	*41.0*	*41.0*	*9.1*	*9.0*		*(target value)*
		41.50	40.67	9.55	9.08	Fe: 1.07 at%	GDOES (Ind500)
		40.75	41.16	9.52	8.57		EDS (Arc50)

Thèse accessible à l'adresse : https://theses.insa-lyon.fr/publication/2025ISAL0036/these.pdf © [T. Langlois], [2025], INSA Lyon, tous droits réservés

5.2.3 Chemical gradient and segregation

The local composition and the segregation of elements within a microstructure were analysed, because these are critical to understanding the macroscopic behaviour of CrCoNi and CrCoNiSi alloys. Homogenous microstructures are essential to accurately extrapolate microscopic observations to bulk properties of the material.

In this study, the evolution of chemical segregation from the as-cast state through to the homogenised reference state for mechanical testing was investigated using EDS mapping. *Figure 5.6* and *Figure 5.7* present EDS maps of Cr, Co, Ni and Si distributions in as-cast CrCoNi and CrCoNiSi alloys produced using the Arc50, Arc200, and Ind500 furnaces.

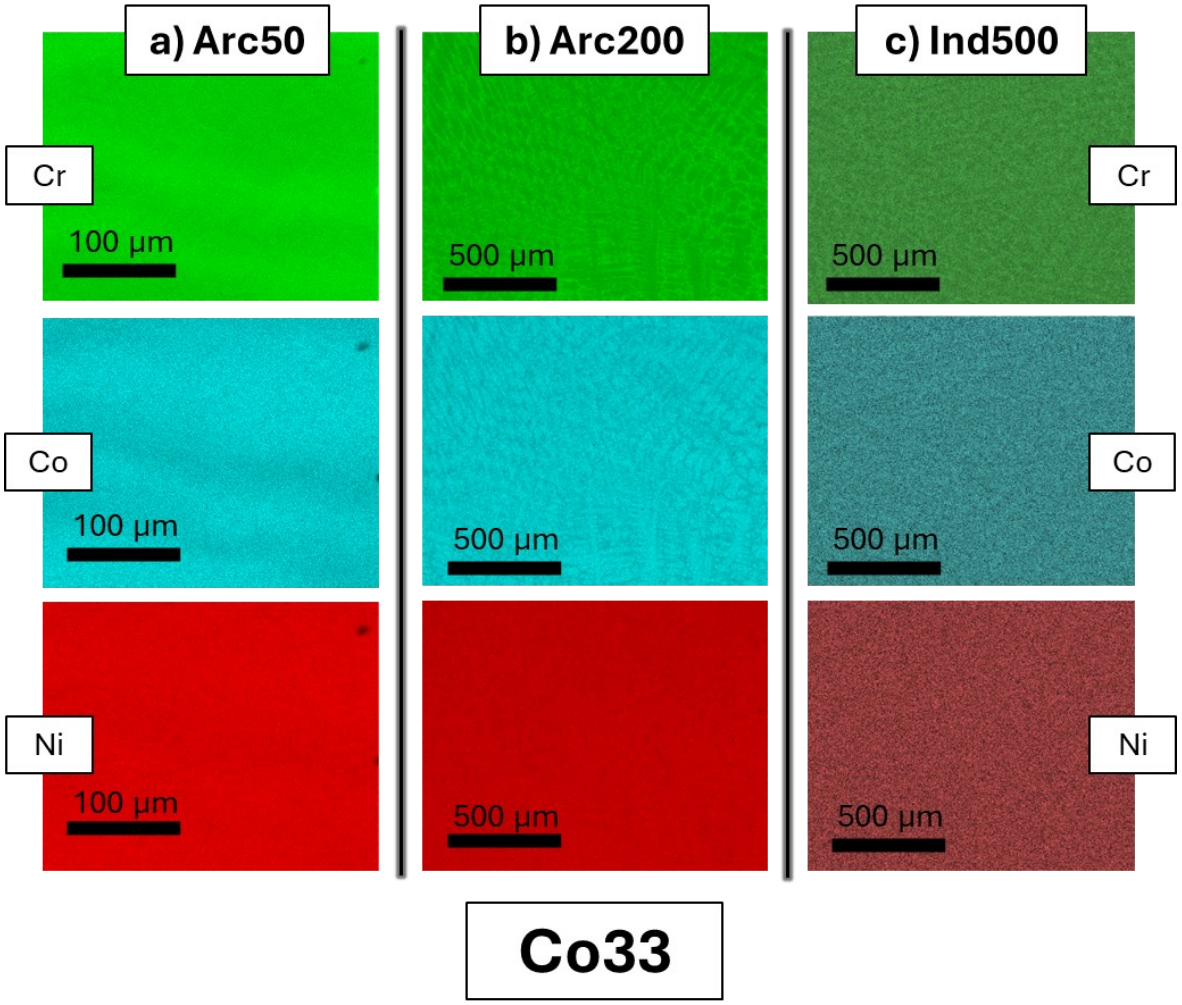


Figure 5.6. EDS maps for the Cr-Co-Ni K series in the Co33 alloys cast using (a) Arc50, (b) Arc200 and (c) Ind500.

Thèse accessible à l'adresse : https://theses.insa-lyon.fr/publication/2025ISAL0036/these.pdf © [T. Langlois], [2025], INSA Lyon, tous droits réservés

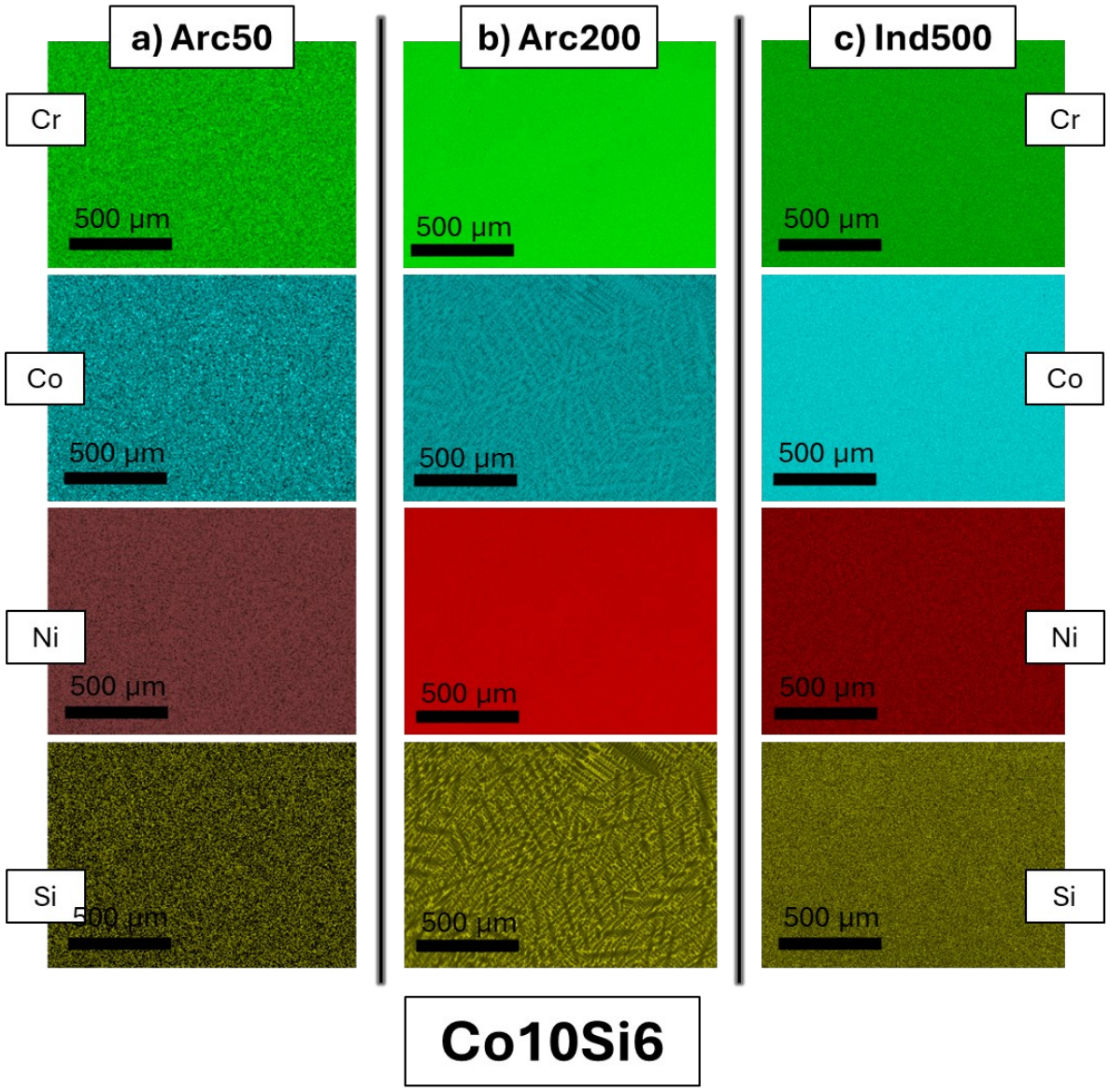


Figure 5.7. EDS maps for the Cr-Co-Ni-Si K series in the Co10Si6 alloys cast using (a) Arc50, (b) Arc200 and (c) Ind500.

These figures reveal different chemical segregation levels in as-cast samples for every casting technique. Alloys produced using the Arc200 furnace exhibit the most pronounced segregation, likely due to the slower cooling rates associated to its non-water-cooled copper mould. In CrCoNi alloys, there is significant partitioning of Cr and Co, while in CrCoNiSi alloys, partitioning shifts primarily to Co and Si. Previous studies demonstrated that Cr depletion is observed in areas around Ni and Co forming segregated clusters [157].

Thèse accessible à l'adresse : https://theses.insa-lyon.fr/publication/2025ISAL0036/these.pdf © [T. Langlois], [2025], INSA Lyon, tous droits réservés

In addition, EDS linescan were conducted on Co33 and Co10Si6 alloys to further quantify the segregation in as-cast sample, with results provided in *Figure 0.15* and *Figure 0.16* in the Appendix of Chapter 5.

Figure 5.8 and *Figure 5.9* illustrates the progressive reduction of chemical segregation during heat-treatment in CrCoNi and CrCoNiSi alloys produced with Arc200.

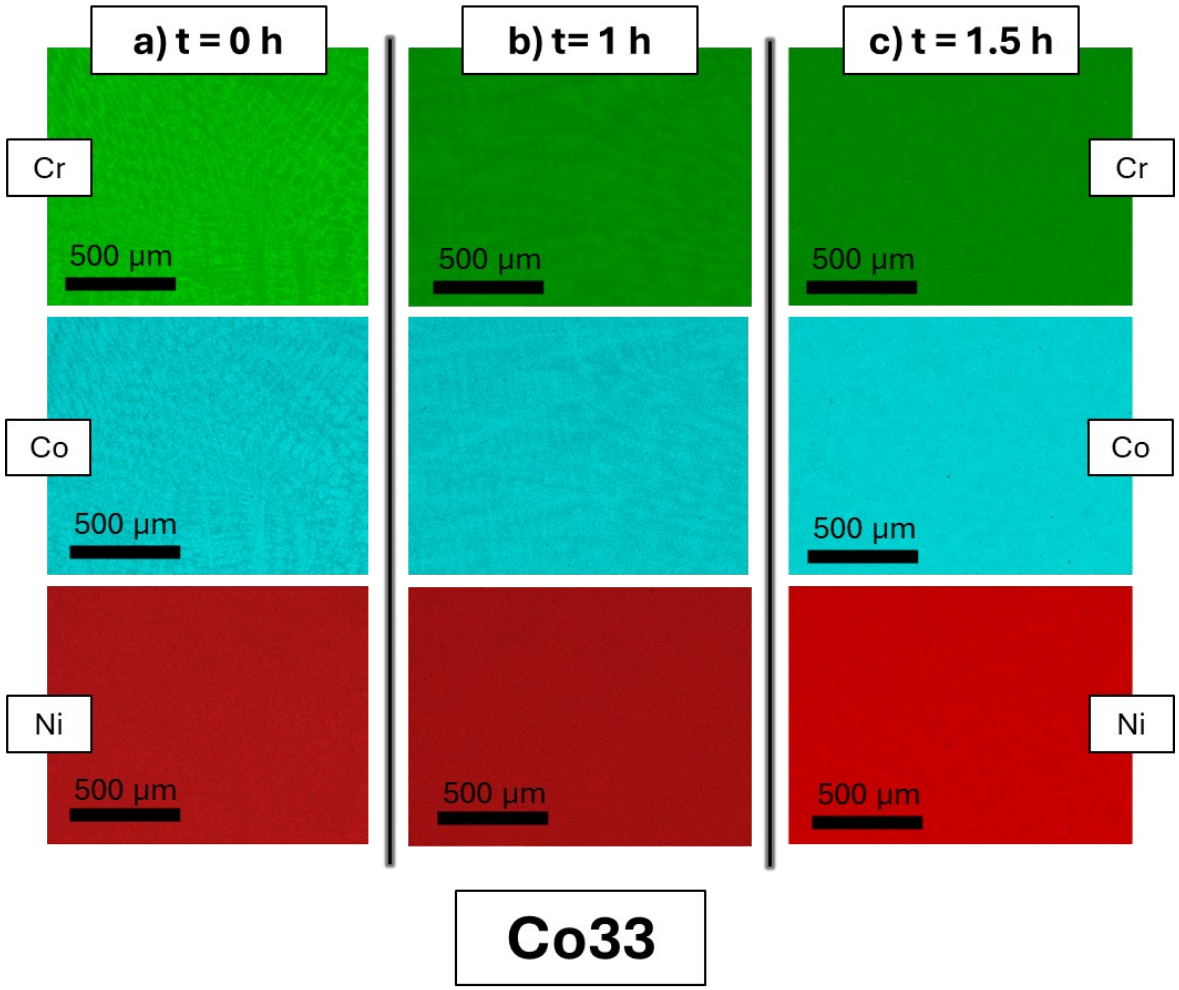


Figure 5.8. EDS maps for the Cr-Co-Ni K series in the Co33 alloys from Arc200 ingots in the following microstructures: (a) As-cast; (b) homogenised for 1 hour; (c) homogenised for 1.5 hours.

Thèse accessible à l'adresse : https://theses.insa-lyon.fr/publication/2025ISAL0036/these.pdf © [T. Langlois], [2025], INSA Lyon, tous droits réservés

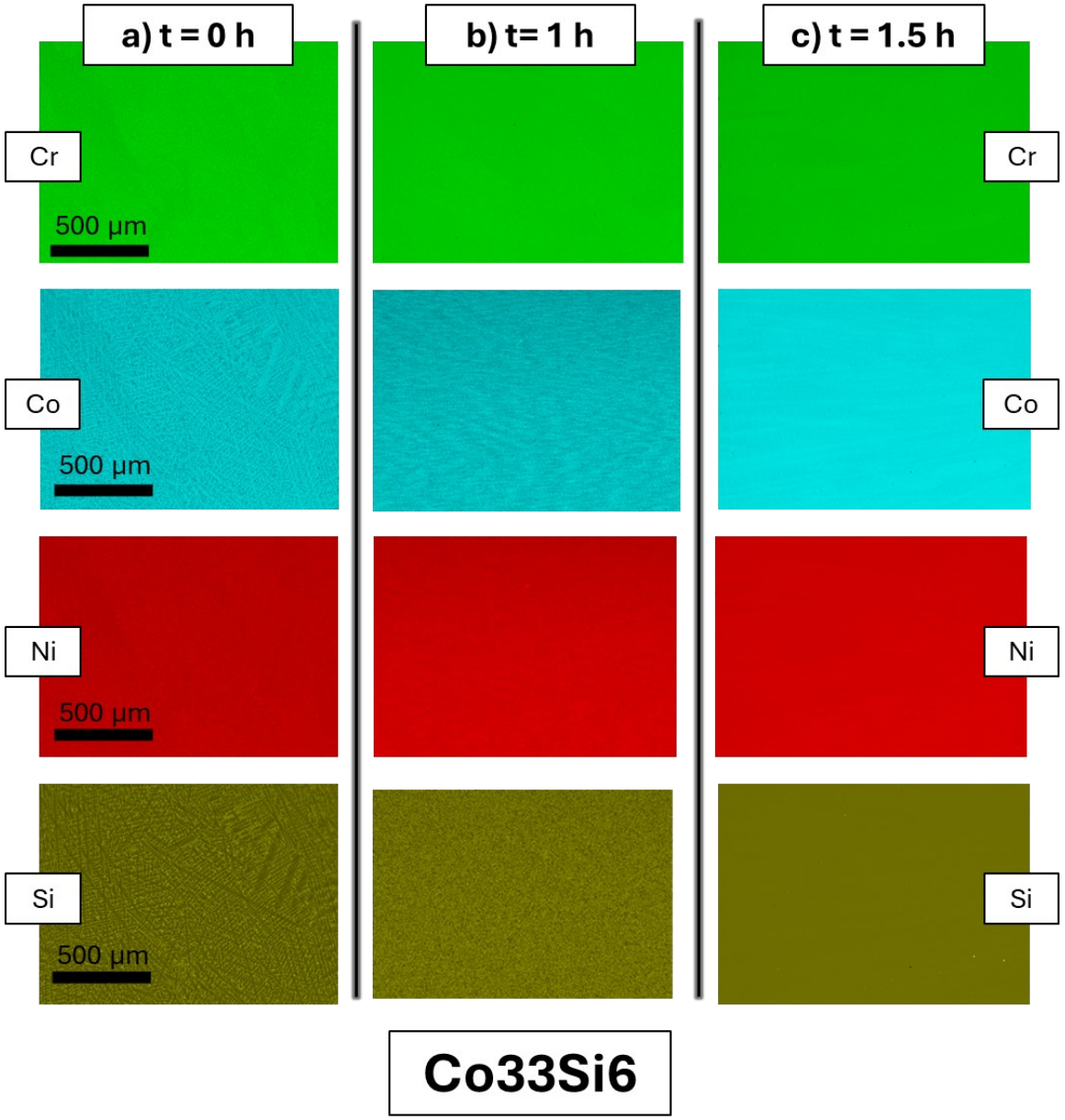


Figure 5.9. EDS maps for the Cr-Co-Ni-Si K series in the Co33Si6 alloys from Arc200 ingots in the following microstructures: (a) As-cast; (b) homogenised for 1 hour; (c) homogenised for 1.5 hours.

The observed near-uniform elemental distribution after 1.5 hours of homogenisation indicates that the microstructure is well-homogenised.

Post-homogenisation chemical gradients were analysed from core-to-shell and top-to-bottom of the Arc50, Arc200 and In500 ingots, as described in *Figure 5.5*. The bulk compositions across these region for Co33 and Co10Si6 are illustrated in *Figure 5.10*, *Figure 5.11* and *Figure 5.12* for Arc50, Arc200 and Ind500 geometries, respectively.

Thèse accessible à l'adresse : https://theses.insa-lyon.fr/publication/2025ISAL0036/these.pdf © [T. Langlois], [2025], INSA Lyon, tous droits réservés

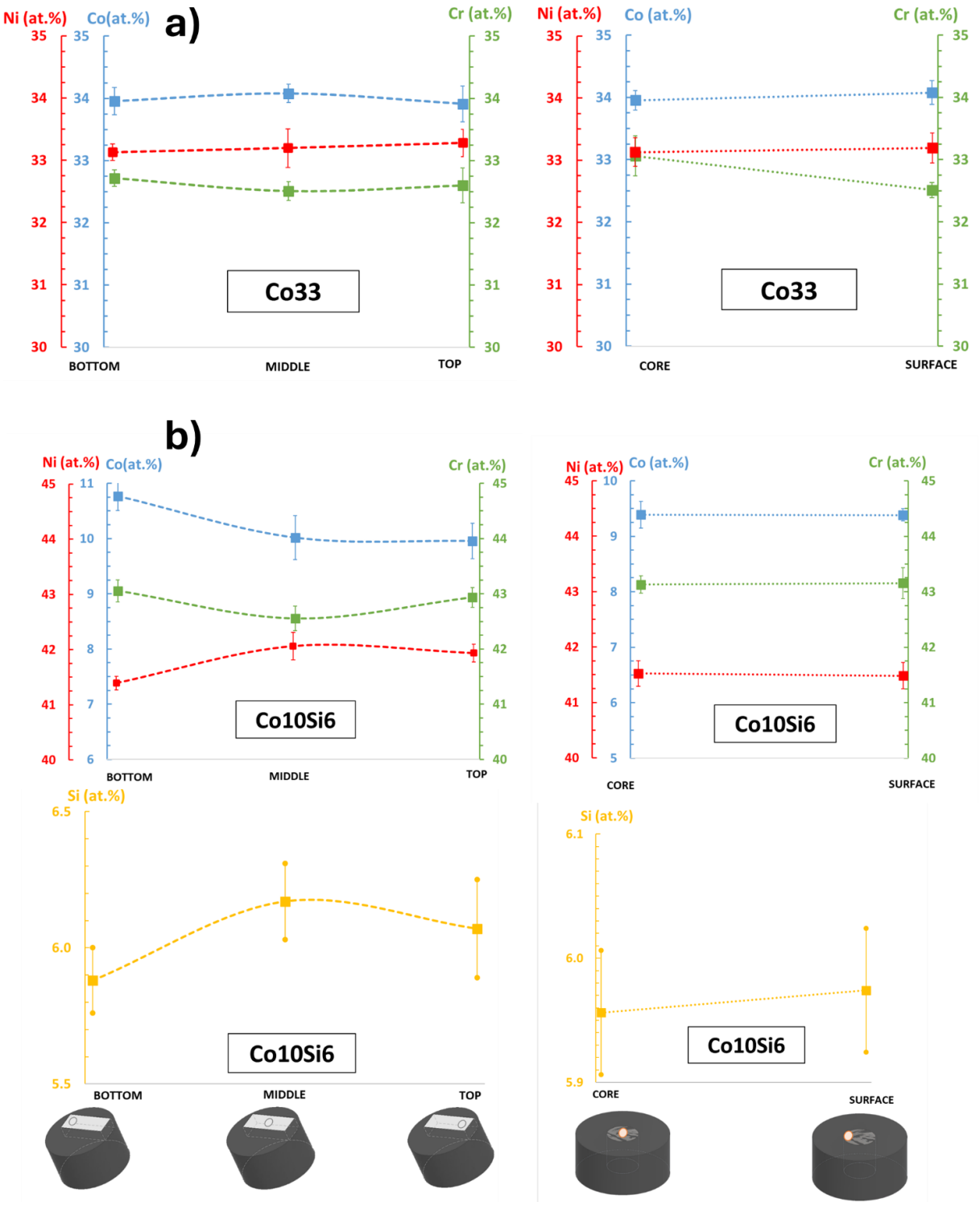


Figure 5.10. Bulk composition variation across various locations of Arc50 specimens: (a) As-homogenised Co33 alloy; (b) As-homogenised Co10Si6 alloy.

Thèse accessible à l'adresse : https://theses.insa-lyon.fr/publication/2025ISAL0036/these.pdf © [T. Langlois], [2025], INSA Lyon, tous droits réservés

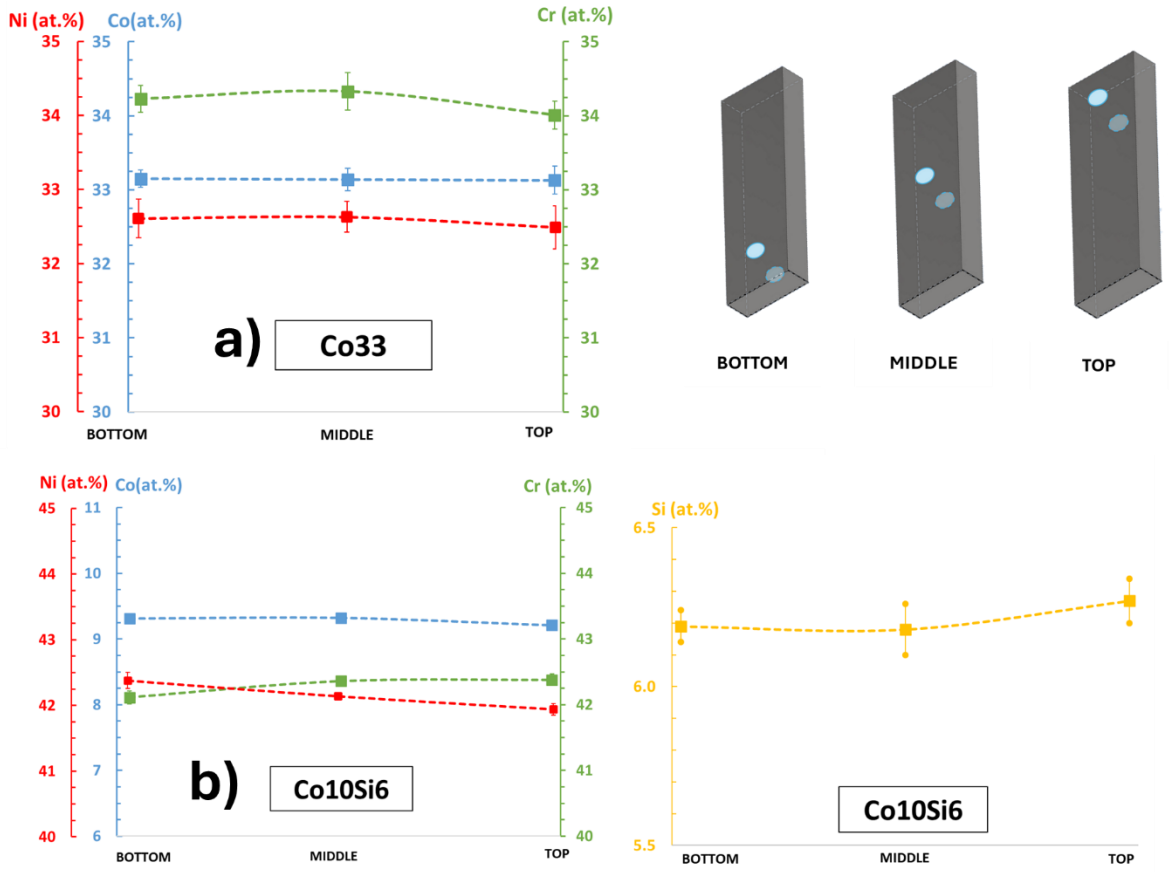


Figure 5.11. Bulk composition variation across various locations of Arc200 specimens: (a) As-homogenised Co33 alloy; (b) As-homogenised Co10Si6 alloy.

Thèse accessible à l'adresse : https://theses.insa-lyon.fr/publication/2025ISAL0036/these.pdf © [T. Langlois], [2025], INSA Lyon, tous droits réservés

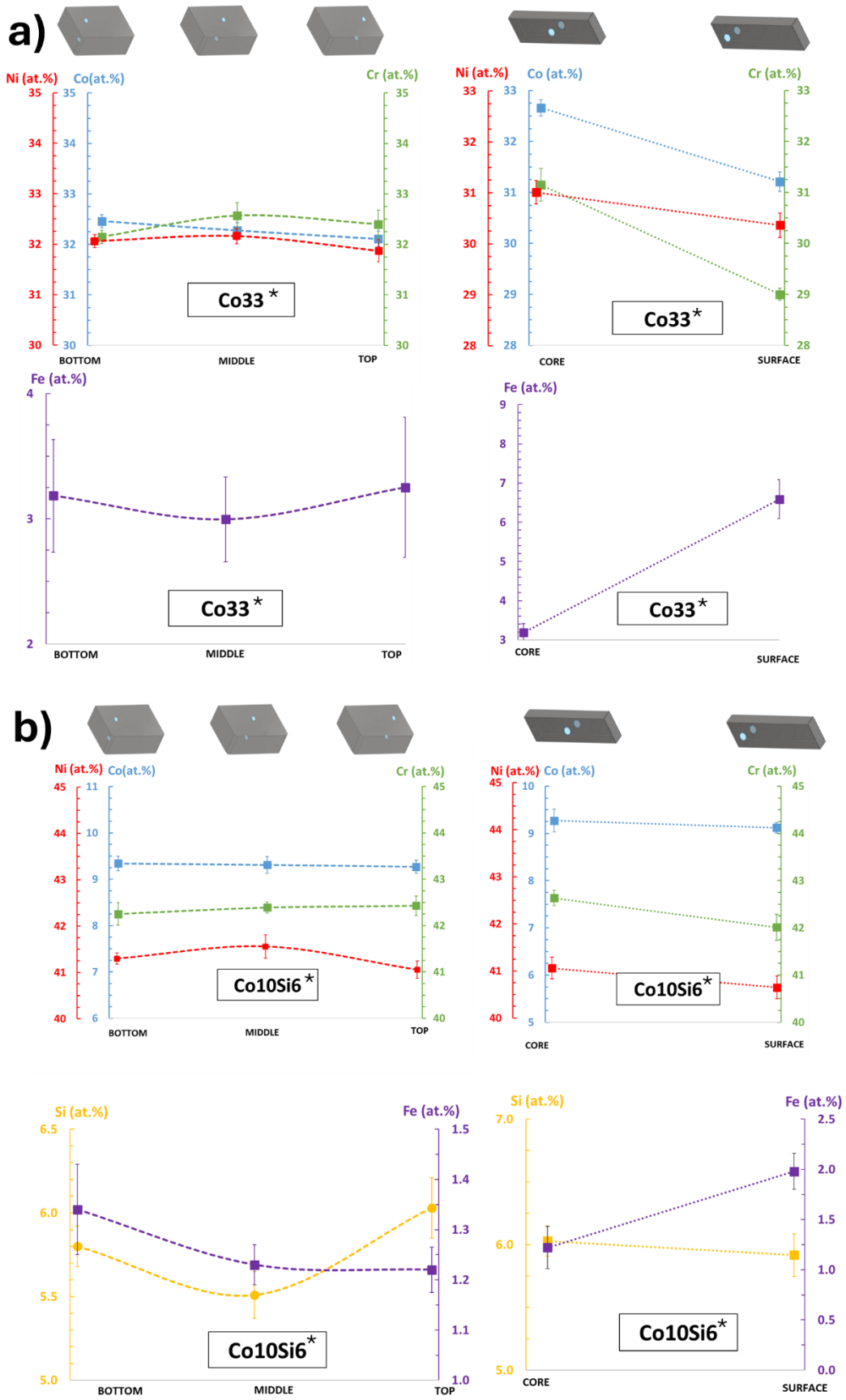


Figure 5.12. Bulk composition variation across various locations of Ind500 specimens: (a) As-homogenised Co33* alloy; (b) As-homogenised Co10Si6* alloy.

Thèse accessible à l'adresse : https://theses.insa-lyon.fr/publication/2025ISAL0036/these.pdf © [T. Langlois], [2025], INSA Lyon, tous droits réservés

All geometries exhibit a well-distributed composition near the surface. However, when analysing the gradient from surface to core, several effects are observed.

- In all geometries, an ever so slightly decreased homogeneity for CrCoNiSi alloys compared to CrCoNi and a depletion of Cr near the surface are observed. These phenomena can be associated to the large difference in melting temperature and surface energy of the elements in the alloys [20], and to the inherent complexity of the compositions.
- For Ind500 ingots, significant iron is detected near the sample surface, likely due to the diffusion from the mould to the sample, with a decreased content of 3 at.% in the core of the ingots. This percentage remains non-negligible.

To ensure clarity of the analyses, the remainder of this chapter is organised by processing method and intended mechanical testing, as detailed in *Table 5.9*. For each type of specimen – Compression, Charpy Impact and Tensile – the reference-state microstructures, mechanical responses and postmortem microstructures will be analysed systematically.

Table 5.9. Specimen characteristics for the three different casting methods.

Chapter section	Casting method	Specimen geometry	Mechanical test	Reference-state microstructure
5.3	Arc50	Cylinder	Compression test	As-Homogenised
5.4	Ind500	Charpy V-Notch	Impact test	As-Rolled (hot-rolling and waterquench)
5.5	Arc200	Dog-bone plate	Tensile test	As-Recrystallised (after cold-rolling)

Thèse accessible à l'adresse : https://theses.insa-lyon.fr/publication/2025ISAL0036/these.pdf © [T. Langlois], [2025], INSA Lyon, tous droits réservés

5.3 Compression specimens

5.3.1 Reference-state microstructure

Microstructural observations on the reference-state specimens, conducted before mechanical testing, are crucial for comparing the pre- and post-testing features in the microstructures, such as texture changes, defect density, and other characteristics. Quantifying pre-testing features such as grains size, residual stress (related to dislocation density) and crystallographic phases is also essential to understanding the mechanical response and compare the specimens.

Phase identification:

A systematic acquisition of diffraction patterns for the reference-state alloys was conducted using XRD measurements. This method allows for the identification of crystallographic information such as present phases, and lattice parameters. All the as-homogenised specimens produced by Arc50 exhibit a γ-FCC phase in solid solution (*Figure 5.13*), with the lattice parameter a_{FCC} shown in *Table 5.10*. The unit cell decreased with higher cobalt content and increased with silicon addition, consistent with previous observations from Chang [44].

Table 5.10. Lattice parameter of the FCC phase for the As-homogenised CrCoNi and CrCoNiSi alloys produced using the Arc50 furnace.

Alloy (at%)	Phase	a[nm] ± 0.005	lattice distorsion
Cr33Co33Ni33	γ	0.3558	2.69
Cr40Co20Ni40	γ	0.3570	2.65
Cr45Co10Ni45	γ	0.3577	2.75
(Cr40Co20Ni40)Si1	γ	0.3570	2.70
(Cr40Co20Ni40)Si2	γ	0.3572	2.74
(Cr40Co20Ni40)Si3	γ	0.3573	2.79
(Cr40Co20Ni40)Si6	γ	0.3573	2.91
(Cr40Co20Ni40)Si9	γ	0.3573	3.02
(Cr45Co10Ni45)Si1	γ	0.3578	2.79
(Cr45Co10Ni45)Si2	γ	0.3580	2.83
(Cr45Co10Ni45)Si3	γ	0.3581	2.87
(Cr45Co10Ni45)Si6	γ	0.3584	2.97
(Cr45Co10Ni45)Si9	γ	0.3583	3.07

Thèse accessible à l'adresse : https://theses.insa-lyon.fr/publication/2025ISAL0036/these.pdf © [T. Langlois], [2025], INSA Lyon, tous droits réservés

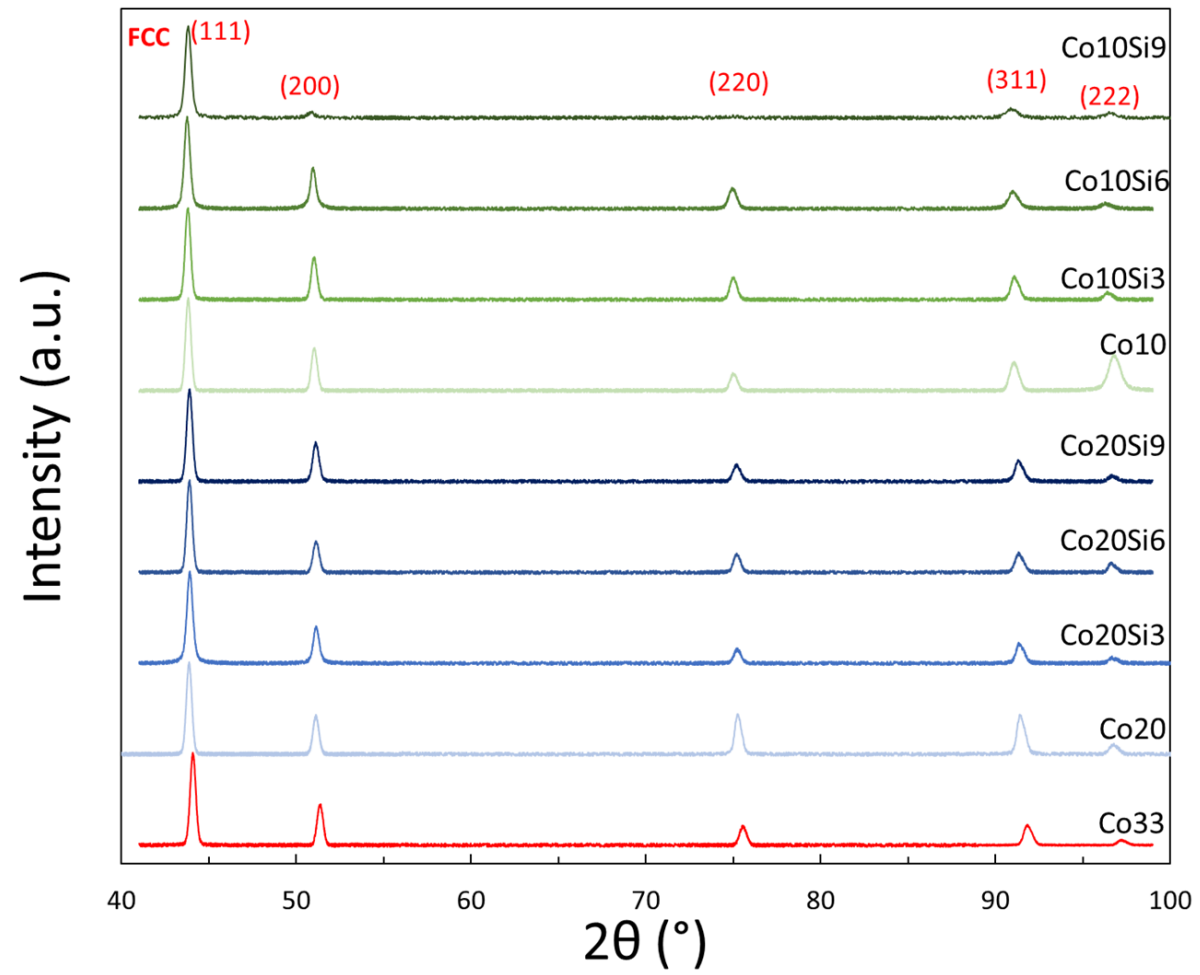


Figure 5.13. XRD Profiles of as-homogenised CrCoNi and CrCoNiSi alloys produced with the Arc50 furnace (unit of intensity normalised with respect to the highest (111) peak of the FCC profiles).

Microstructure characterisations:

To understand the mechanical responses of specimens and to accurately evaluate the effect of composition and temperature, the processing of material was intended for obtaining similar microstructural morphology withing a specimen geometry. In other words, grain size, shape and grain orientation, as well as residual stress, and twinning are tracked. This analysis is conducted using EBSD measurements. Inverse Pole Figure (IPF) maps for homogenised Arc50 specimens are illustrated in *Figure 5.14.* Every composition exhibits elongated grain morphology described with rather small variation of the average grain size $\overline{D}$ varying with the chemical composition, and with very low average aspect ratio $\overline{AR}$.

Thèse accessible à l'adresse : https://theses.insa-lyon.fr/publication/2025ISAL0036/these.pdf © [T. Langlois], [2025], INSA Lyon, tous droits réservés

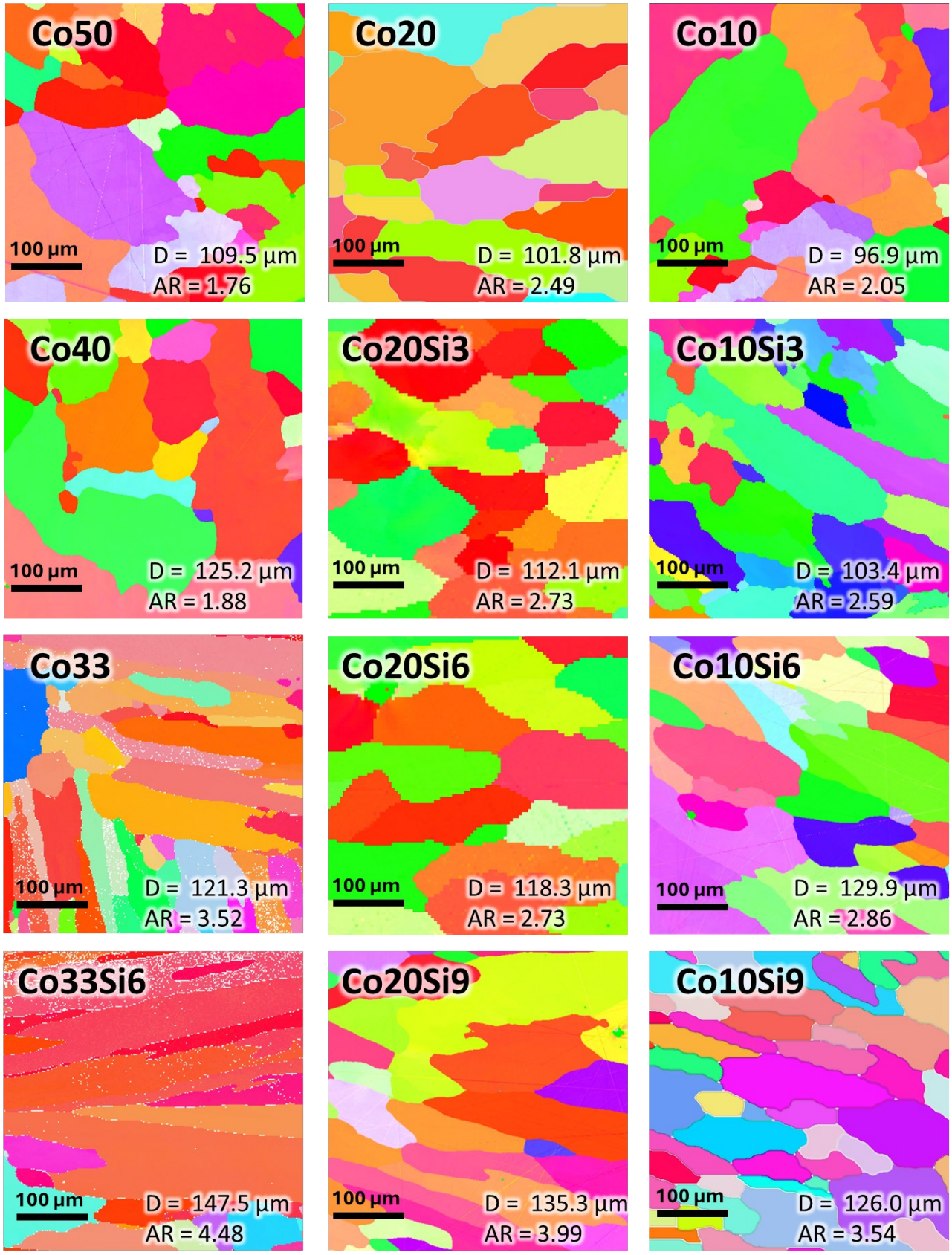


Figure 5.14. IPF maps of as-homogenised Arc50 microstructure acquired in the middle section of the specimens, the average grain size obtained by linear intercept method is given (change the last part of the sentence).

Thèse accessible à l'adresse : https://theses.insa-lyon.fr/publication/2025ISAL0036/these.pdf © [T. Langlois], [2025], INSA Lyon, tous droits réservés

Even if EBSD maps were not taken at the exact same location for every cylinder, silicon addition seems to promote elongated grains and the presence of texture, possibly through its effect on solidification dynamics and grain boundary energy [44]. Overall, texturing index do not indicate a pronounced preferential orientation of grains, but only few orientated in the <111>//x, where x is the drop casting direction. This orientation slightly increases in cobalt-lean compositions and with silicon addition.

Kernel Average Misorientation (KAM) maps in *Figure 5.15* show low degrees of misorientation after homogenisation at high temperature, indicating a microstructure with low dislocation density and minimal residual stress. This suggests that the alloy underwent a recovery process that minimises stored strain energy. This heat-treatment did not allow for recrystallisation, typically visible through annealing twins. This can be attributed to the large initial grain size after casting and the absence of pre-existing dislocations necessary to introduce stored energy for recrystallisation.

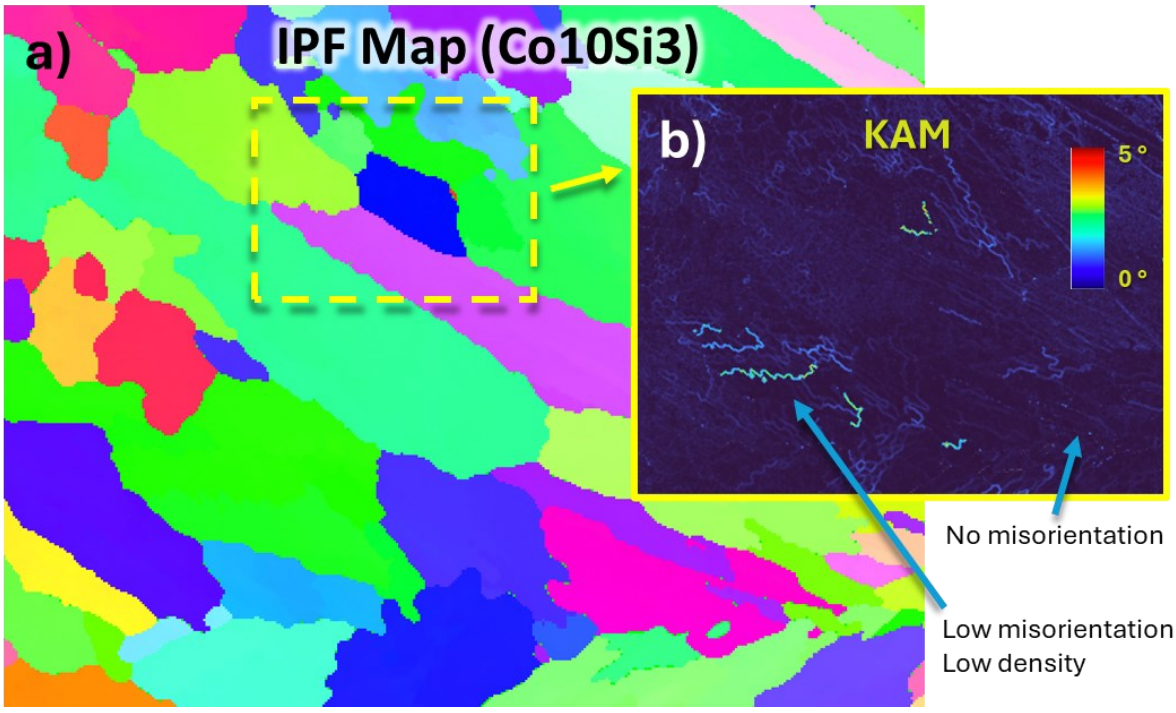


Figure 5.15. (a) Full IPF map of As-homogenised Co10Si3; (b) level of stress in subgrains highlighted with Kernel Misorientation Map (KAM).

Stacking Fault Energy

Thèse accessible à l'adresse : https://theses.insa-lyon.fr/publication/2025ISAL0036/these.pdf © [T. Langlois], [2025], INSA Lyon, tous droits réservés

With the powders filled from Arc50 ingots, the Stacking Fault Energy (SFE) was calculated by comparing XRD profiles of deformed and annealed powders for each composition, as described in the powder-filling method. XRD profiles of cold-worked powders collected at IFM and at Ansto are provided in *Figure 0.19* in the Appendix of Chapter 5. Additionally, partial Shockley dislocations were investigated using TEM for Co33, Co33Si6, Co10 and Co10Si6 (bulk form) with the help of our colleague Ziyu Ma at IFM (*Figure 0.20* in the Appendix of Chapter 5).

Figure 5.16 display the lattice parameter (a_{FCC}), Stacking Fault Probability (α), and microstrain ($\langle \varepsilon_{50}^2 \rangle_{111}$) from powder-XRD. SFE values from powder-XRD, TEM and thermodynamic predictions [44] are shown in *Figure 5.16-d*.

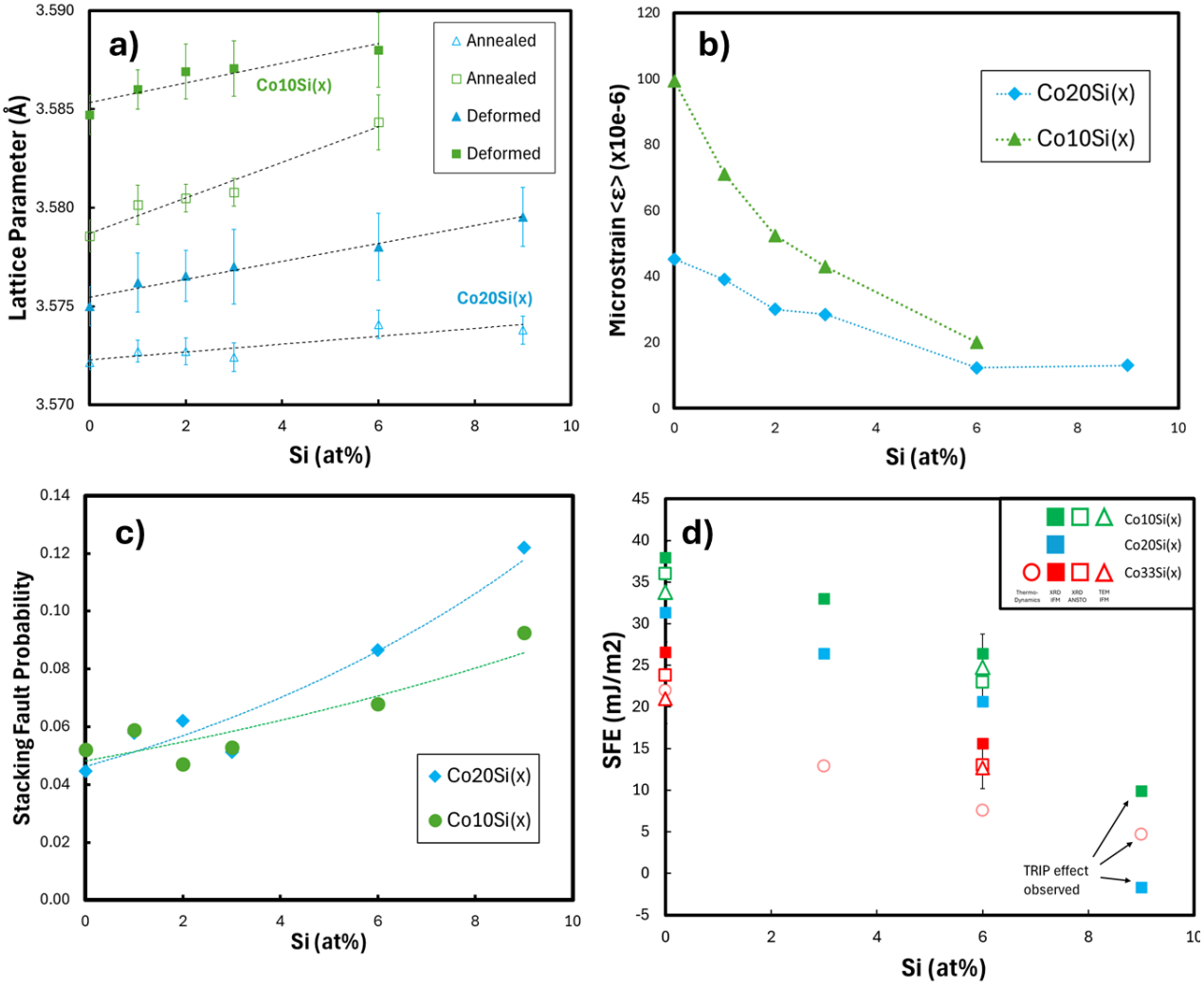


Figure 5.16. Powder XRD measurements: (a) Lattice parameter; (b) Microstrain; (c) Stacking Fault Probability; (d) Stacking Fault Energy (plain squares for powder-XRD at IFM, empty squares for PD-beamline at Ansto; empty triangles for TEM results and empty circle for thermodynamic predictions [44]).

Thèse accessible à l'adresse : https://theses.insa-lyon.fr/publication/2025ISAL0036/these.pdf © [T. Langlois], [2025], INSA Lyon, tous droits réservés

- The lattice parameter (a_{FCC}) increases with addition of silicon and decreases with higher cobalt content.
- Silicon has a pronounced effect on the stacking fault probability and microstrain, both of which depend strongly on the level of cold working. But their ratio $\alpha/\langle\varepsilon_{50}^2\rangle_{111}$ becomes constant at a specific level of deformation [41], indicating a consistent interplay between stacking faults and strain.
- The $\gamma \rightarrow \varepsilon$ martensitic transformation observed at 9 at.% of silicon (confirmed by EBSD measurement) affects peak broadening and strain relaxation in the XRD profiles, because the ε-HCP phase has a smaller unit cell volume than the γ-FCC phase [158].

It is important to note that SFE results obtained from different experimental methods vary significantly. First, thermodynamic predictions and powder-XRD measurement with Mathematica are given without standard error [159]. Second, factor such as ε-HCP precipitation may affect measurements for composition with higher silicon content.

Despite these variations, a consistent trend of decreasing SFE with increasing silicon content has been observed across literature, powder-XRD measurements, and TEM analysis. This trend highlights the significant role of silicon in altering the stacking fault energy and associated deformation mechanisms.

5.3.2 Mechanical properties

Hardness measurements have been performed on the rectangular cross-section of Arc50 cylinders. The hardness evolution as a function of cobalt and silicon content is shown in *Figure 5.17*. While the changes in hardness are small, they are significant because observed on many measurements.

- For the CrCoNi alloys, the average hardness is measured at 182 HV for Co33 and decrease to 170 HV for Co10.
- The addition of silicon consistently increased material hardness.

Thèse accessible à l'adresse : https://theses.insa-lyon.fr/publication/2025ISAL0036/these.pdf © [T. Langlois], [2025], INSA Lyon, tous droits réservés

Characterisation of the reference-state microstructures showed no evidence of secondary phases. Moreover, the average grain size was large, with no significant size gradient between compositions. Consequently, the observed change in hardness can be attributed to the solid solution hardening. The hardening effect of silicon addition on CrCoNi aligns with findings in previous studies [32].

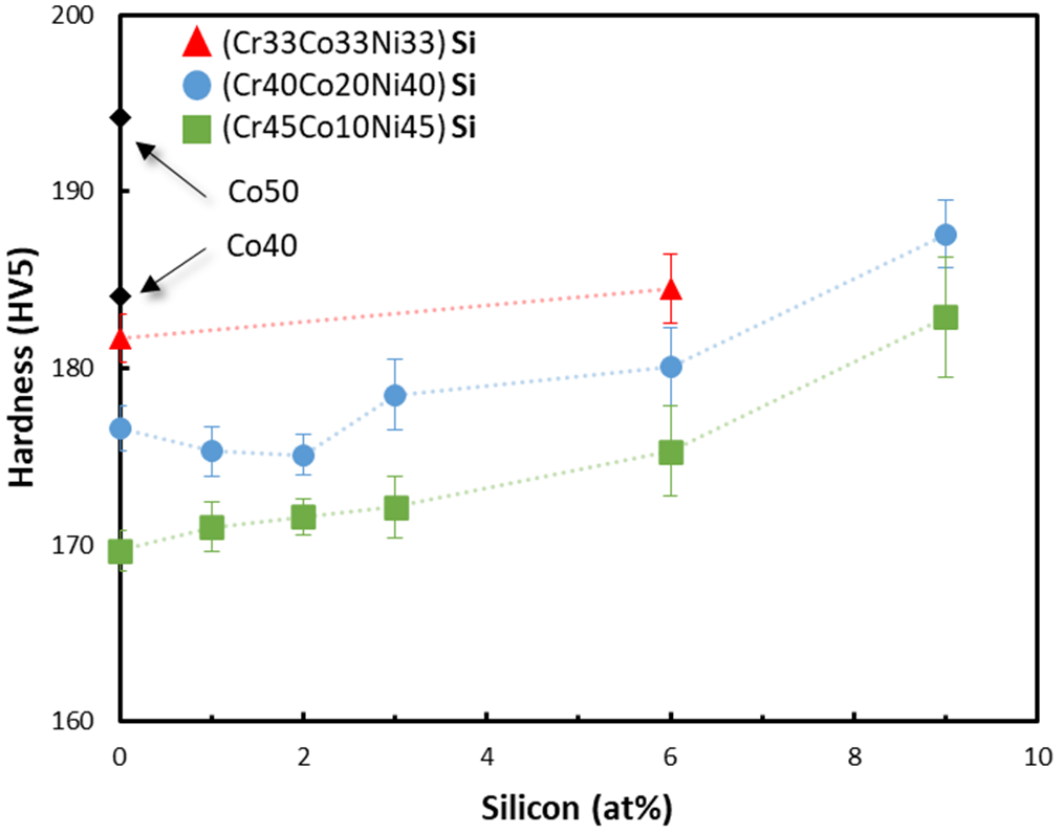


Figure 5.17. Vickers-Hardness measurements (HV5) for as-homogenised Arc50 specimens.

Profilometry-based Indentation Plastometry (PIP) was conducted on Arc50 specimens, with at least 5 valid measurements for each composition. Some indentations exhibited significant variation in the x and y profiles due to the high compositional anisotropy of the alloys, leading to invalid measurements. In such cases, additional grinding was necessary to remove unsatisfactory indents and ensure accurate subsequent measurements.

Thèse accessible à l'adresse : https://theses.insa-lyon.fr/publication/2025ISAL0036/these.pdf © [T. Langlois], [2025], INSA Lyon, tous droits réservés

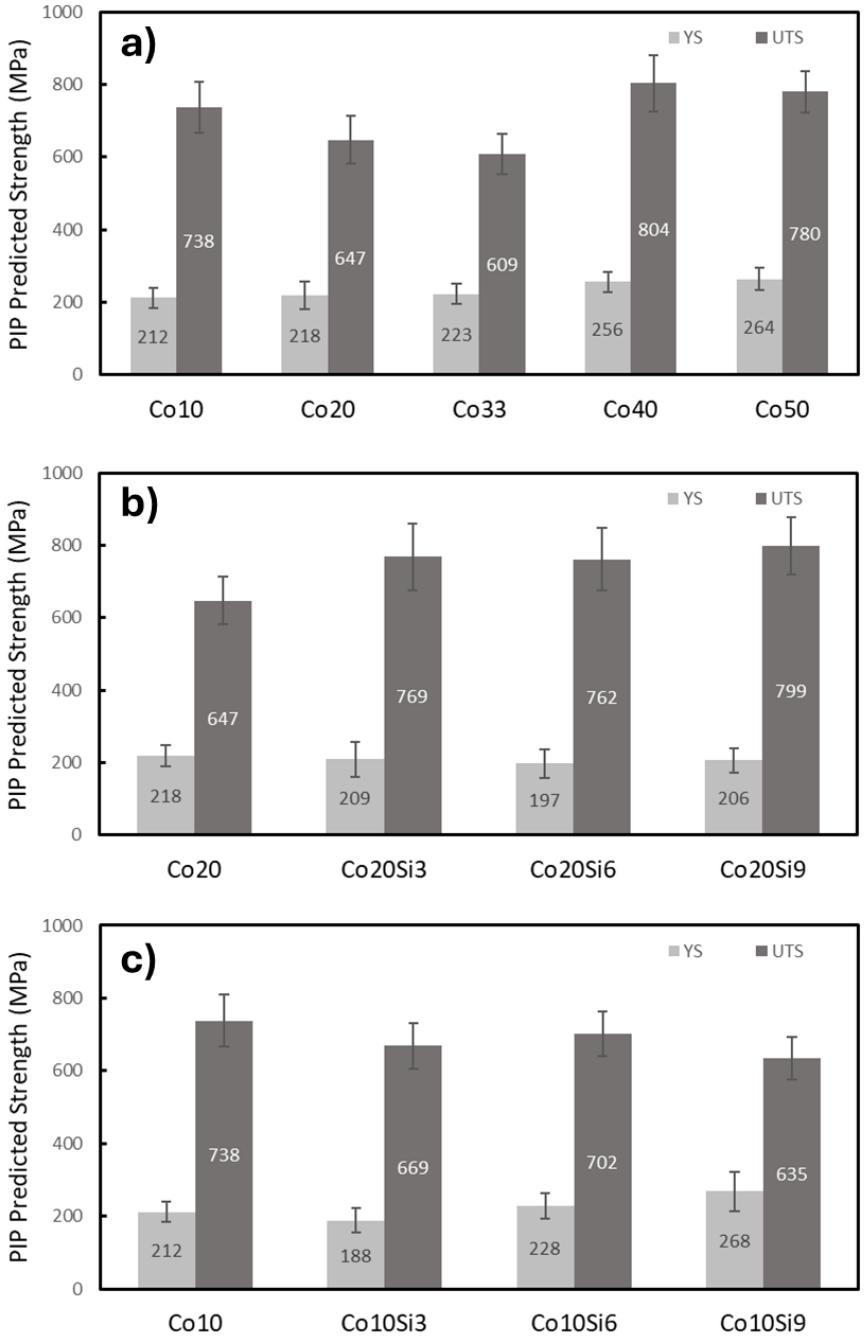


Figure 5.18. Strength predictions from PIP measurements for as-homogenised Arc50 specimens: engineering Yield strength (YS) and engineering Ultimate Tensile Strength (UTS). (a) CrCoNi compositions with various cobalt content; (b) Co20-based compositions with silicon additions; (c) Co10-based compositions with silicon additions.

The predicted Yield Strength (YS) and Ultimate Tensile Strength (UTS) values for the as-homogenised cylinders are shown in *Figure 5.18*.

- YS predictions align closely with the observed trend in hardness measurements.

Thèse accessible à l'adresse : https://theses.insa-lyon.fr/publication/2025ISAL0036/these.pdf © [T. Langlois], [2025], INSA Lyon, tous droits réservés

- However, UTS predictions showed significant discrepancies and error margins, highlighting the limitations of PIP methods for materials like MPEAs with significant anisotropy.

While this technique provides complementary estimates of tensile properties of materials, the observed uncertainties indicates that these results must be interpreted with caution.

The results of room-temperature compression testing for as-homogenised Arc50 specimens are shown in *Figure 5.19*, observing stress-strain and Strain-Hardening Rate (SHR) curves for the different compositions. The effect of cobalt and silicon on these properties is analysed in *Figure 5.19-a-b* and *Figure 5.19-c-d*, respectively.

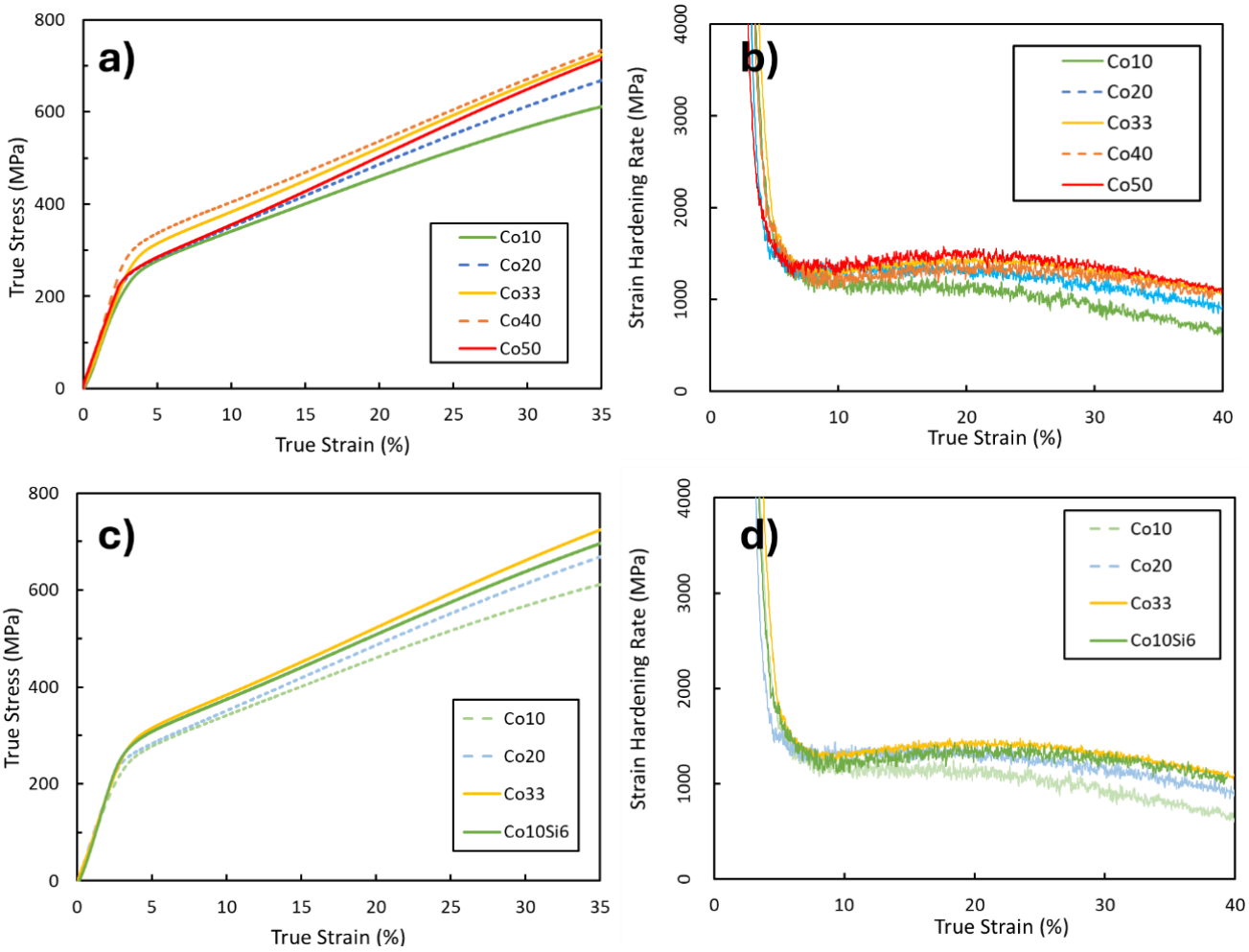


Figure 5.19. Compressive test results: (a) Effect of cobalt content on True Stress-Strain curves; (b) Corresponding Strain-Hardening Rate;
(c, d) Comparison of Co10Si6 with other compositions.

Thèse accessible à l'adresse : https://theses.insa-lyon.fr/publication/2025ISAL0036/these.pdf © [T. Langlois], [2025], INSA Lyon, tous droits réservés

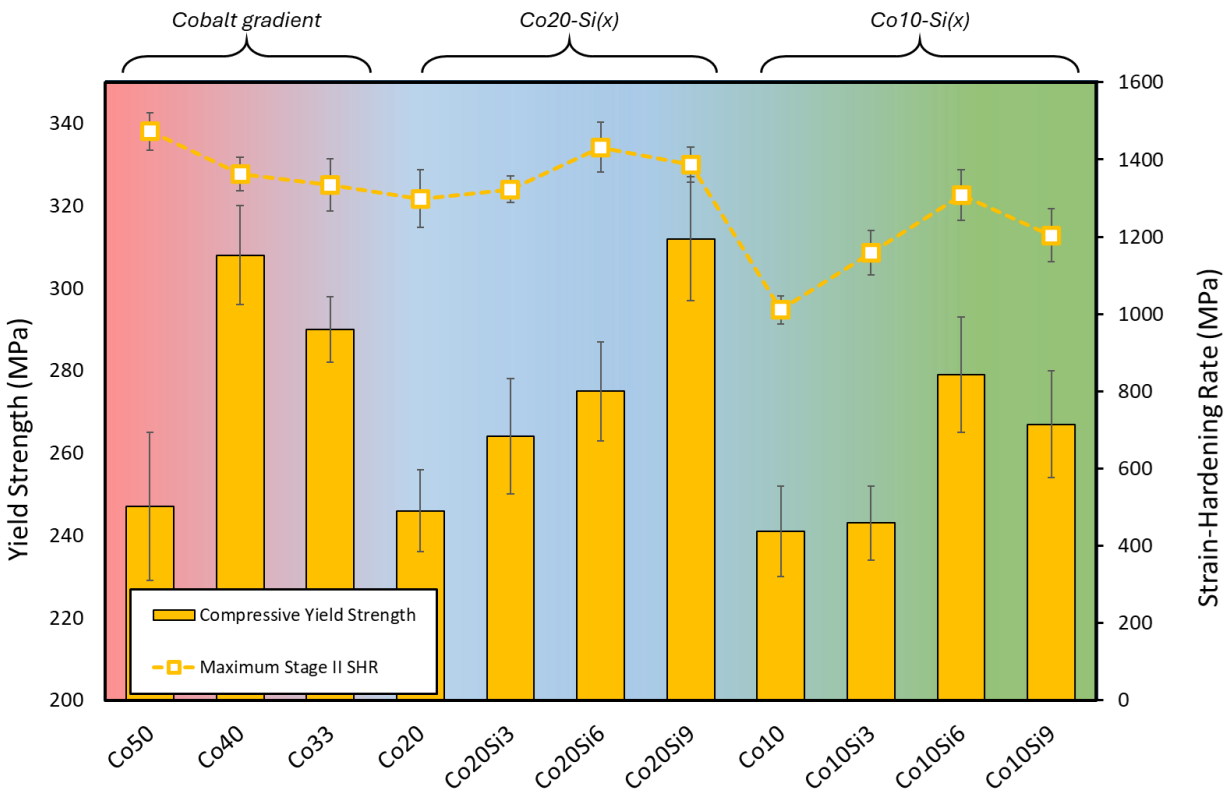


Figure 5.20. Compressive test statistics over 3 replicates values: average compressive Yield Stress and average strain-hardening rate at stage II of deformations.

Average values for Yield Strength (YS) and SHR values during the prolonged deformation stage are summarised in *Figure 5.20*. Compressive test results for the remaining compositions are provided in *Figure 0.21* in the Appendix of Chapter 5.

There is a clear influence of cobalt content on the compressive behaviour of CrCoNi alloys (illustrated in *Figure 5.19-a* and the red region in *Figure 5.22*).

- YS increases from 241 MPa (Co10) up to 308 MPa (Co40).
- Interestingly, YS drops sharply to 248 MPa in Co50.
- During plastic deformation, SHR values are raising significantly from 10 to 20 at.% cobalt, then moderately between 20 and 40 at.% cobalt, and further improves for 50 at.% cobalt, indicating different deformation behaviours. This trend is consistent with previous studies [56].

The effect of silicon is also visible (highlighted in blue and green regions in *Figure 5.22*).

Thèse accessible à l'adresse : https://theses.insa-lyon.fr/publication/2025ISAL0036/these.pdf © [T. Langlois], [2025], INSA Lyon, tous droits réservés

- Co20Si(x) alloys exhibits a monotonous increase in YS with higher silicon content, while SHR values remain relatively similar.
- For Co10Si(x) alloys, both YS and SHR values increases for compositions containing up to 6 at.% of silicon, but both properties drop sharply for 9 at.% of silicon.

These observations are consistent with studies suggesting that silicon addition lowers SFE, promoting different deformation mechanisms, such as TWIN and TRIP effects. The difference in compressive deformation behaviours across compositions are worth analysing the deformed microstructures to confirm or refute the activation of specific deformation mechanisms (dislocation slips, twinning or phase transformation) under the influence of composition.

5.3.3 Postmortem microstructural observations

To further investigate the impact of silicon and cobalt on the mechanical properties of CrCoNi and CrCoNiSi alloys, post-deformation microstructural analyses were conducted using EBSD on several compositions: Co50, Co33, Co10, Co10Si3, Co10Si6 and Co10Si9.

The Band Contrast (BC) and Kernal Avergage Misorientation (KAM) maps in *Figure 5.21* allow for the visualisation of dislocation density and the grain structure evolution after compression, among other strain-induced modifications. Twin boundaries are indicated by red lines on BC maps, and areas with high misorientation are revealed with KAM maps, which correlate with high dislocation density.

Thèse accessible à l'adresse : https://theses.insa-lyon.fr/publication/2025ISAL0036/these.pdf © [T. Langlois], [2025], INSA Lyon, tous droits réservés

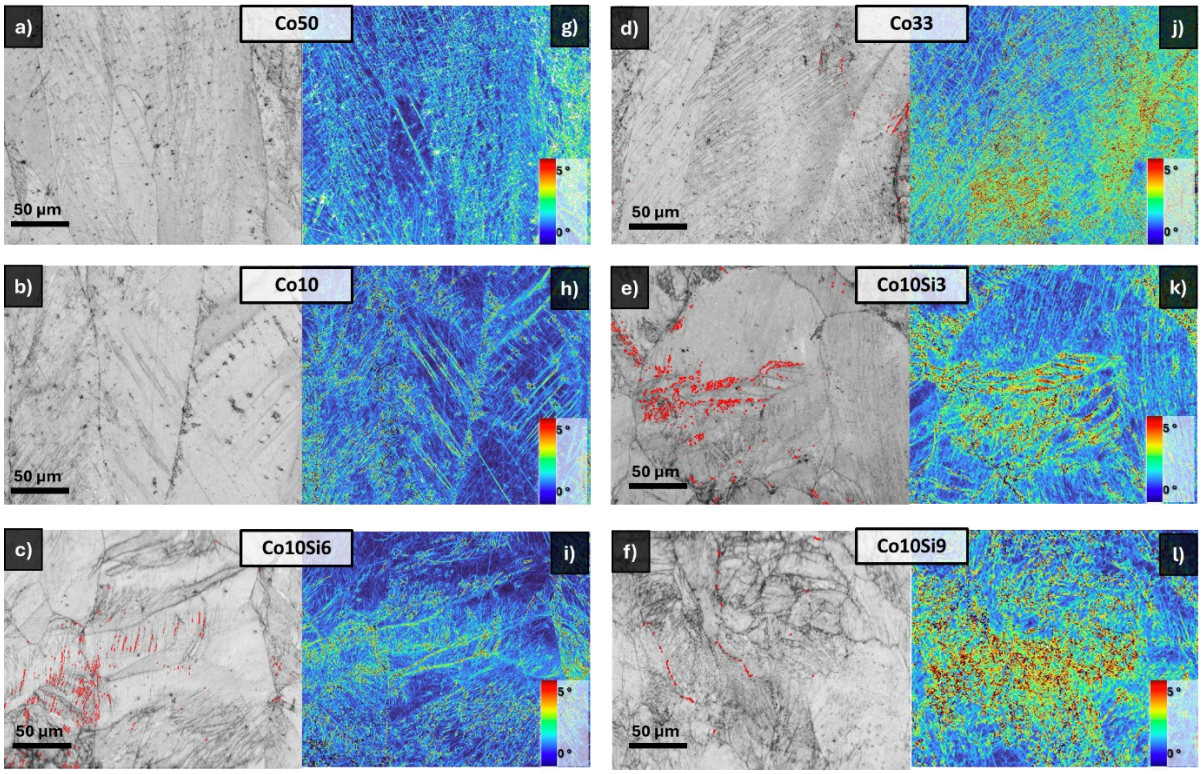


Figure 5.21. Arc50 microstructures after compression at around ε = 0.4 (a-f) Band Contrast maps with twin boundaries marked in red; (g-l) KAM maps.

- The deformed microstructures showed only few twin dislocations, and no secondary phases were detected. This observation suggests that the primary deformation mechanism in compression test was dislocation slip, rather than twinning or phase transformation.
- However, the distinct stress-strain evolutions observed among Co50, Co33 and Co10Si6 alloys are not consistent with this observation, indicating that additional mechanisms may be at play. For such high level of deformation, some grain orientations were poorly indexed due to the severity of the plastic deformation in compression.

Thus, to better understand the deformation mechanisms involved in CrCoNi and CrCoNiSi alloys, Charpy Impact tests and tensile tests are conducted.

Thèse accessible à l'adresse : https://theses.insa-lyon.fr/publication/2025ISAL0036/these.pdf © [T. Langlois], [2025], INSA Lyon, tous droits réservés

5.4 Impact loading specimens

5.4.1 Reference-state microstructure

Phase identification:

XRD profiles of the Ind500 ingots after hot rolling are provided in *Figure 5.22.* In addition to the γ-FCC matrix, a BCC phase was detected in the Co10Si6* alloy after hot rolling treatment. Weak diffraction peaks, appearing alongside those of the FCC matrix, were identified as belonging to an ordered BCC/B2 phase.

For the Co10Si9* alloy, an unknown phase was observed. The XRD profile for this alloy revealed additional minority peaks alongside the characteristic FCC peaks. These peaks were identified as belonging to a tetragonal structure of the $P4_2/mnm$ space group [127], with lattice parameters $a_\sigma = 8.76$ Å and $c_\sigma = 4.58$ Å. Detailed peak indexing for this latter phase is provided in *Figure 0.18* in the Appendix of Chapter 5, supported by data from [64]. The observed phases align with the thermodynamic predictions presented in Chapter 4 (*Figure 4.7*), reinforcing the challenges described regarding the heat-treatment for the Ind500 ingots.

Thèse accessible à l'adresse : https://theses.insa-lyon.fr/publication/2025ISAL0036/these.pdf © [T. Langlois], [2025], INSA Lyon, tous droits réservés

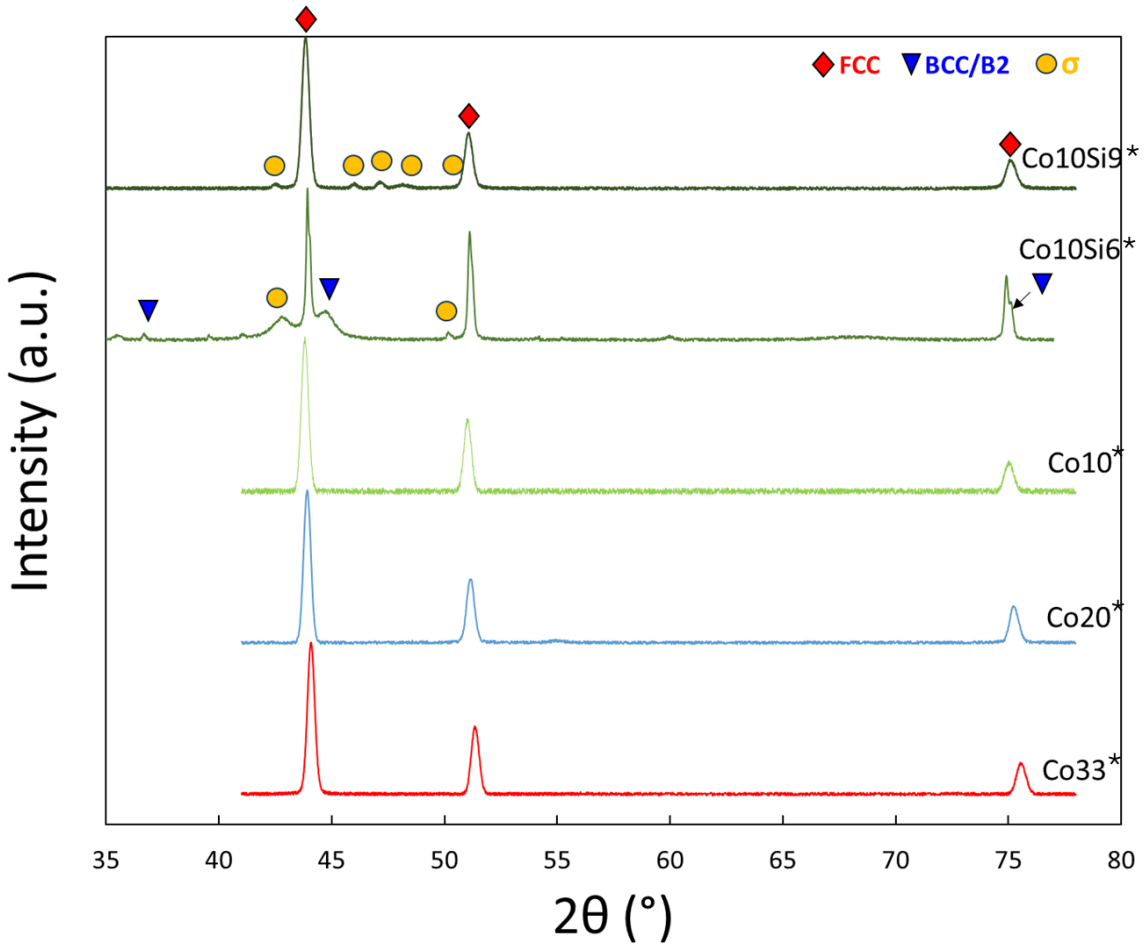


Figure 5.22. XRD Profile of CrCoNi and CrCoNiSi alloys produced by Ind500 and after hot rolling, showing FCC and BCC/B2 phases (latter phase indexed from [160]).

The formation of BCC and sigma phase was further confirmed using EDS and EBSD analyses, illustrated in *Figure 5.23* and *Figure 5.24*, respectively. These figures include BC maps, phase maps and corresponding EDS maps for the Co10Si6* and Co10Si9* alloys, respectively.

- in Co10Si6*, the B2 phase appears in intragranular regions, with dot shapes, consistent with findings from Chang [160].
- in Co10Si9*, sigma phase formation was mainly observed at grain boundaries, in agreement with Liu [64].

The chemical composition of the sigma phase and the fcc/σ interface in Co10Si9* alloys were investigated by EDS linescan [127], provided in *Figure 0.16* in the Appendix of Chapter 5. An approximate estimation of the volume fraction of the sigma phase in the Co10Si9* alloy is around 19%, as determined from EBSD data. The presence of BCC and sigma phase is expected to significantly influence the mechanical properties

Thèse accessible à l'adresse : https://theses.insa-lyon.fr/publication/2025ISAL0036/these.pdf © [T. Langlois], [2025], INSA Lyon, tous droits réservés

of these alloys. While these two phases can increase the yield strength of the material by precipitation hardening, they also contribute to brittleness, potentially limiting the ductility of these materials.

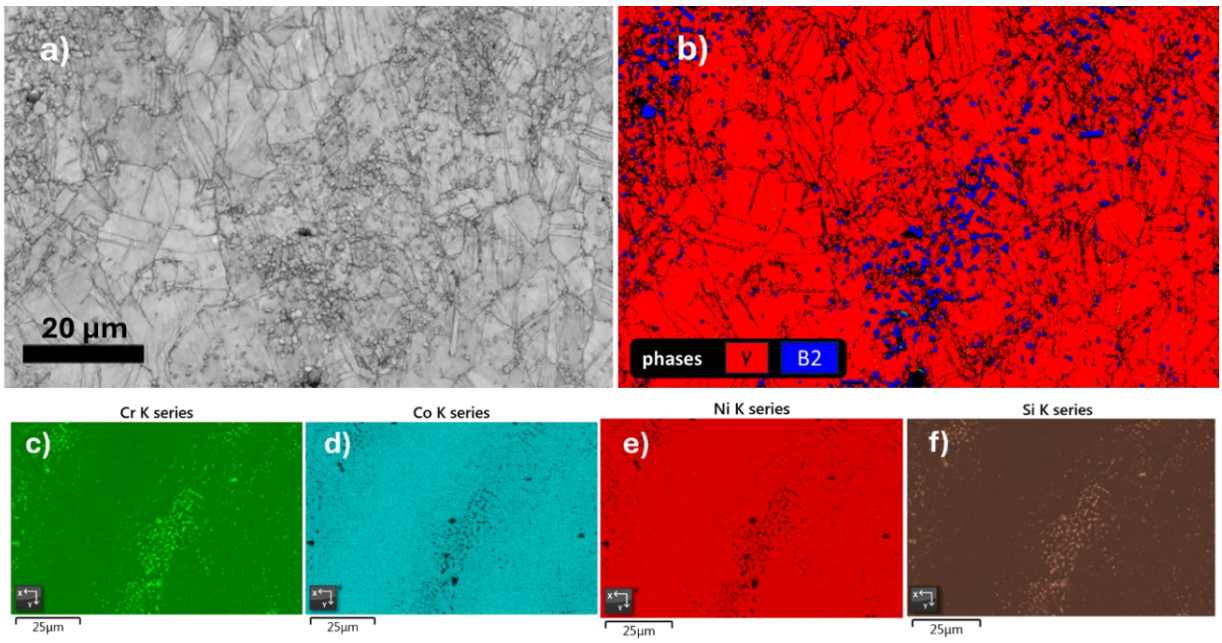


Figure 5.23. EBSD analysis of BCC/B2 phase in Co10Si6* alloy: (a) BC map; (b) phase map; (c-f) corresponding EDS maps.

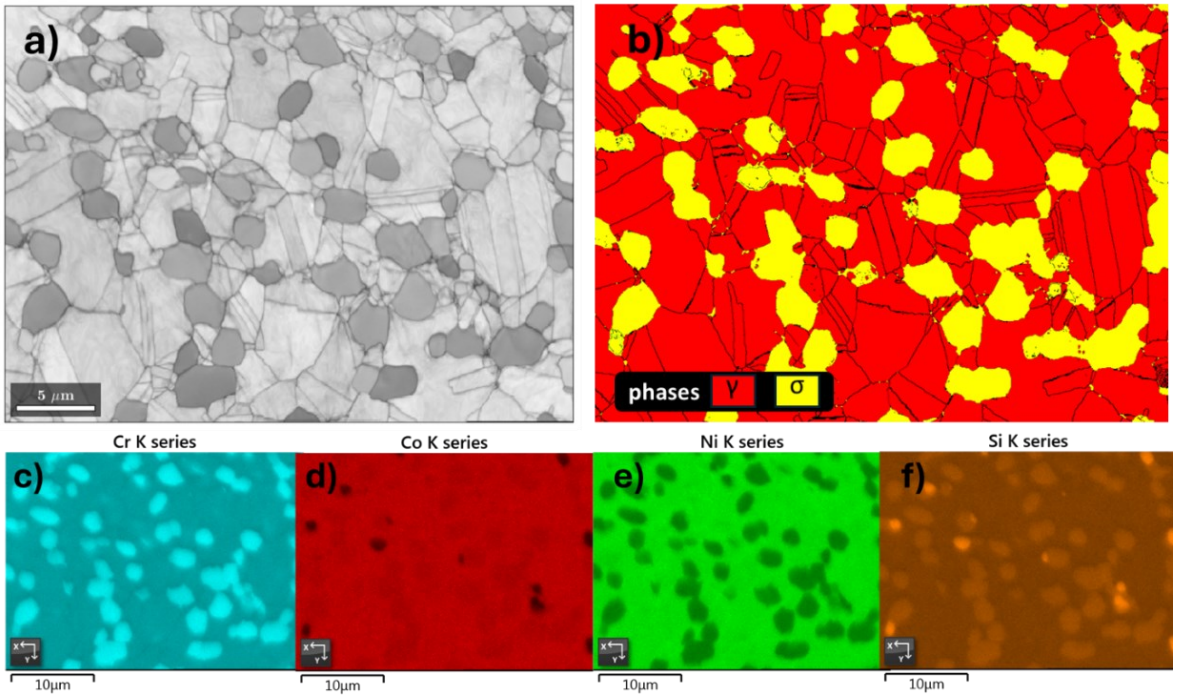


Figure 5.24. EBSD analysis of sigma phase in Co10Si9* alloy: (a) BC map; (b) phase map; (c-f) corresponding EDS maps.

Thèse accessible à l'adresse : https://theses.insa-lyon.fr/publication/2025ISAL0036/these.pdf © [T. Langlois], [2025], INSA Lyon, tous droits réservés

Microstructure morphology:

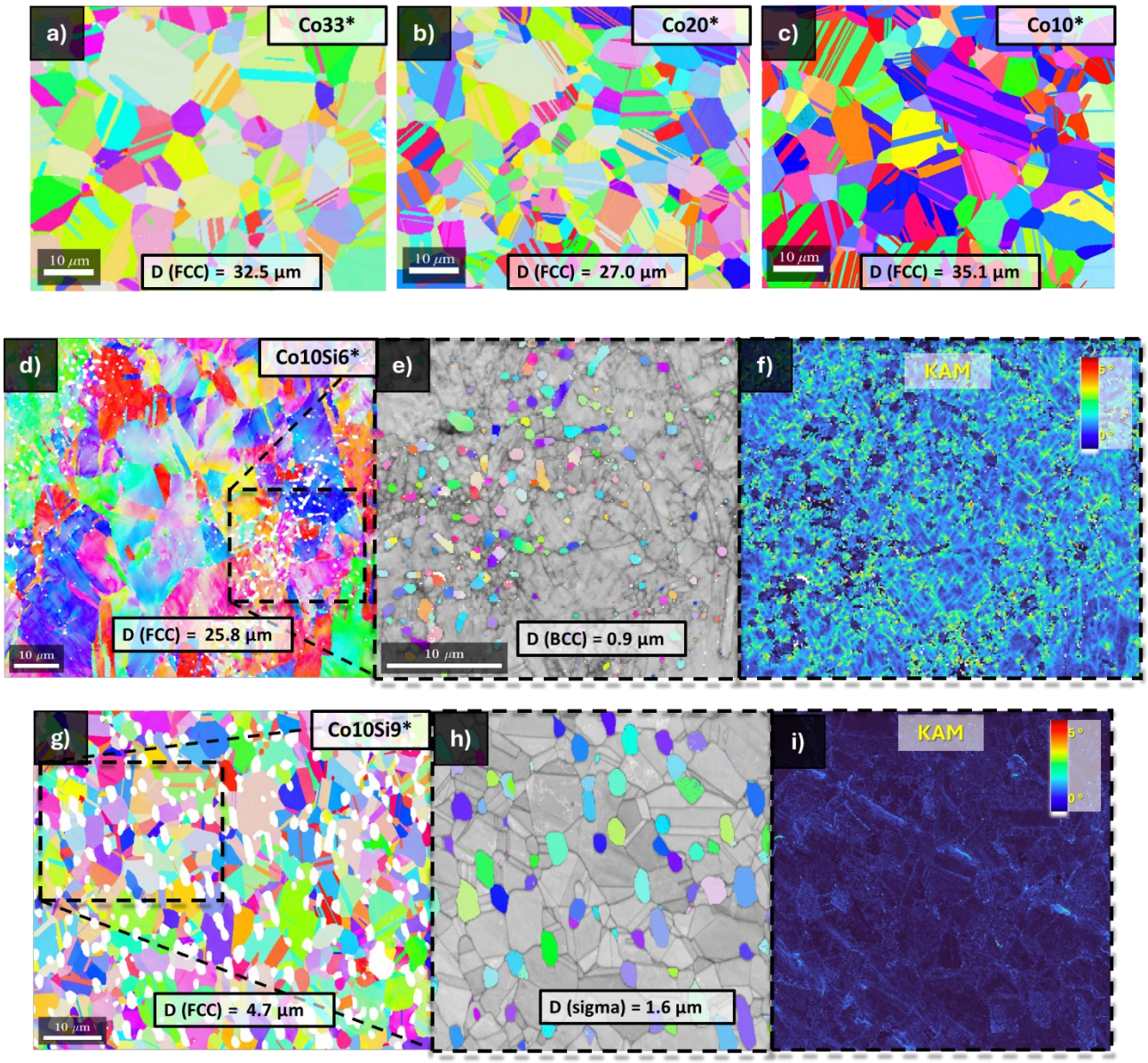


Figure 5.25. (a-c, d and g) IPF maps of the FCC phase in Ind500 specimens; (e) IPF grains of the BCC phase in Co10Si6* alloy and (f) corresponding KAM map; (h) IPF map of the sigma phase in Co10Si9* alloy and (i) corresponding KAM map.

Figure 5.25 illustrates the microstructures of Ind500 specimens after hot rolling treatment.

Thèse accessible à l'adresse : https://theses.insa-lyon.fr/publication/2025ISAL0036/these.pdf © [T. Langlois], [2025], INSA Lyon, tous droits réservés

- The FCC grains in all compositions exhibit a random orientation and equiaxed morphology, with comparable grain size across all compositions except for Co10Si9*.
- For Co10Si9*, sigma phase precipitates at the triple junctions of FCC grains, seemingly impeding the coarsening of the FCC grains.
- A BCC/B2 secondary phase was also observed in the Co10Si6* alloy. These precipitates are smaller than sigma ones and did not appear to significantly influence the coarsening of FCC grains.

In addition, secondary phases have a notable effect on residual stress, as observed in KAM maps.

- For compositions without secondary phases, the microstructure appeared fully recrystallised with minimal evidence of deformation.
- Despite the presence of sigma phase in Co10Si9*, the residual stress was effectively relieved, as indicated by the low KAM values in *Figure 5.25-i*. Annealing twins are also visible in the IPF map of the FCC grains of Co10Si9*. This suggests that the sigma phase, while limiting grain coarsening, did not act as an obstacle for recrystallisation and stress relaxation.
- For Co10Si6*, the BCC/B2 phase acts like an obstacle to residual stress removal: *Figure 5.25-f* shows intergranular deformation in the FCC phase, particularly near the BCC/B2 precipitates. This behaviour is likely due to an interaction between dislocations and the BCC/B2 phase, impeding complete stress relaxation and recrystallisation.

These observations highlight the roles of secondary phases like BCC and sigma. While sigma primarily affects grain coarsening, BCC/B2 phase introduces localised deformation, suggesting distinct mechanical behaviour attributed to the presence of each secondary phase.

Thèse accessible à l'adresse : https://theses.insa-lyon.fr/publication/2025ISAL0036/these.pdf © [T. Langlois], [2025], INSA Lyon, tous droits réservés

5.4.2 Mechanical properties

The formation of BCC/B2 and sigma phases in Co10Si6* and Co10Si9* indicates a shift from ductile behaviour typical of FCC solid solutions to a more brittle behaviour [44, 160]. To assess the impact of thermomechanical treatments in Ind500 ingots, various mechanical tests were performed.

Hardness measurements were conducted for all compositions in both homogenised and hot rolled states. The results are summarised in *Table 5.11*.

- For the Co33*, Co20* and Co10* alloys, hardness increases from 30 to 40 HV after hot rolling compared to the homogenised state. This increase is similar for the three compositions and is typical of work-hardening in refined microstructures after hot rolling.
- In contrast, both Co10Si6* and Co10Si9* alloys exhibit significant hardening after thermomechanical treatment, with hardness increments of 88 HV and 178 HV, respectively.

Table 5.11. Hardness (HV5) for Ind500 ingots after homogenisation and hot rolling.

Alloy	State	Hardness (HV5)
Co33*	As-homogenised	187 ± 3
	Hot-rolled	210 ± 4
Co20*	As-homogenised	190 ± 5
	Hot-rolled	236 ± 5
Co10*	As-homogenised	180 ± 2
	Hot-rolled	224 ± 10
Co10Si6*	As-homogenised	194 ± 3
	Hot-rolled	286 ± 8
Co10Si9*	As-homogenised	191 ± 5
	Hot-rolled	369 ± 8

This significant change in hardness can be attributed to the presence of BCC/B2 and sigma phases, which contribute to material hardening by hindering dislocation motion. Both secondary phases also limit the material's ability to accommodate plastic deformation, resulting in a more brittle behaviour under mechanical loading. These

Thèse accessible à l'adresse : https://theses.insa-lyon.fr/publication/2025ISAL0036/these.pdf © [T. Langlois], [2025], INSA Lyon, tous droits réservés

observations suggest much stronger materials, but with a trade-off in ductility, as further confirmed through toughness measurements conducted in impact loading testing.

Impact loading tests were conducted on all Charpy V-Notch (CVN) compositions, at both room temperature (293 K) and cryogenic temperature (77 K). The results for impact fracture toughness (A_k), measured as the total absorbed energy upon impact in Joule, are shown in *Figure 5.26* and compared to values for equimolar CrCoNi reported by Wu et al [161]. Additionally, lateral expansion measurements for the CVN surfaces are provided in *Figure 0.7* in the Appendix of Chapter 5.

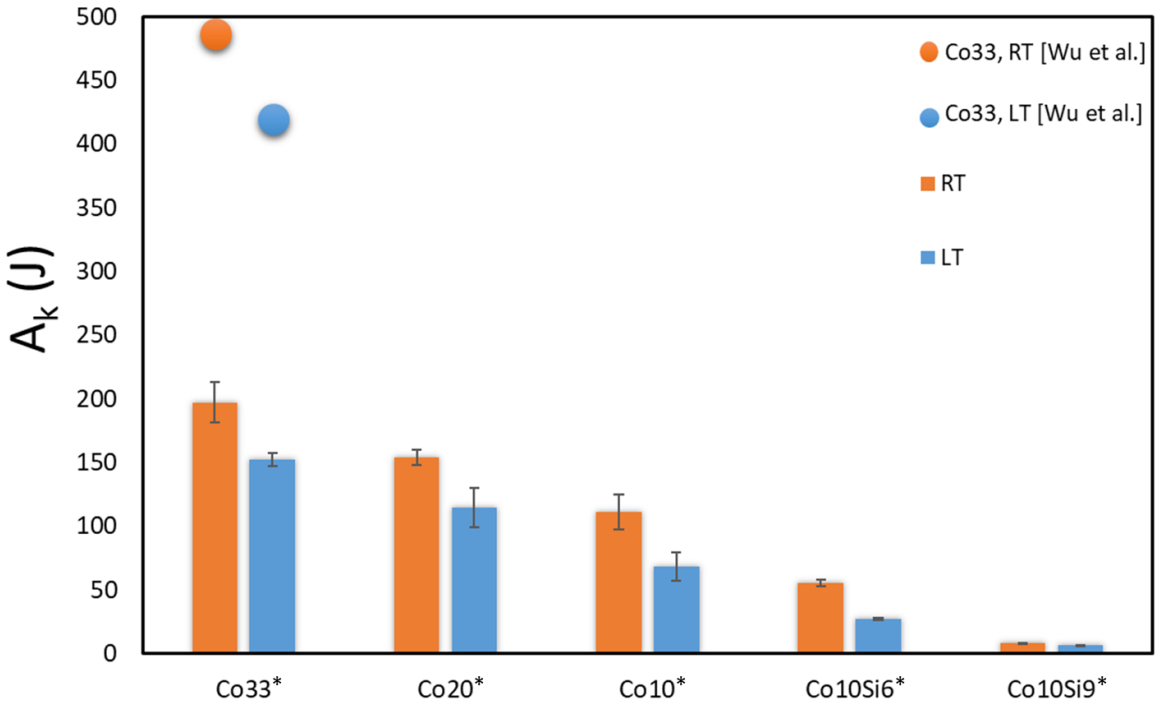


Figure 5.26. CVN Impact Energy (A_k) for the different Ind500 specimens, obtained from three replicates at 293 K (RT) and 77 K (LT), compared with literature values for equimolar CrCoNi from Wu et al. [161].

- The obtained impact energy values are much lower those reported in the literature. This discrepancy is likely due to the challenges encountered during the processing of Ind500 ingots. The unintended presence of iron in the ingots coupled with lower temperature and prolonged times during heat-treatment may have negatively influence the mechanical response of all compositions.

Thèse accessible à l'adresse : https://theses.insa-lyon.fr/publication/2025ISAL0036/these.pdf © [T. Langlois], [2025], INSA Lyon, tous droits réservés

- As anticipated, silicon-added compositions containing secondary phases (BCC/B2 and sigma) exhibit very low toughness values. This confirms their inherent brittle nature.
- Nevertheless, at cryogenic temperature, the reduction in toughness for Co33*, Co20* and Co10* aligns with literature values [161], demonstrating interesting properties compared to other alloys [162].

Further microstructural analysis is essential to fully understand the mechanisms influence the toughness of these materials, including the role of composition, secondary phases and residual stresses.

5.4.3 Postmortem microstructural observations

To better understand the mechanical properties observed during impact testing, fracture surfaces and cross-sectional microstructures near the tip of the deformed CVN specimens were analysed. These observations were performed on specimens tested at both room temperature (293 K) and cryogenic temperature (77 K).

Fracture surface analysis was conducted using SE2 imaging. The fractographic morphology after impact loading at both temperatures is illustrated in *Figure 5.27*. Dimples, marked with yellow arrows, are characteristic of ductile fracture, sign of plastic deformation formed after breaking in sub-grains [162]. Conversely, cleavage feature marked with red arrows, are indicative of brittle fracture mechanisms, where cracks propagate along crystallographic planes.

- Co33*, Co20* and Co10* alloys tested at room temperature show primarily ductile dimples. At lower temperature (77 K), the fracture morphology changes, showing an increased presence of cleavage. This transition correlates with the observed reduction in toughness from 293 K to 77 K in *Figure 5.26*.
- Conversely, the fracture morphologies of the Co10Si6* and Co10Si9* alloys appear very brittle, exhibiting a predominant cleavage features.

Thèse accessible à l'adresse : https://theses.insa-lyon.fr/publication/2025ISAL0036/these.pdf © [T. Langlois], [2025], INSA Lyon, tous droits réservés

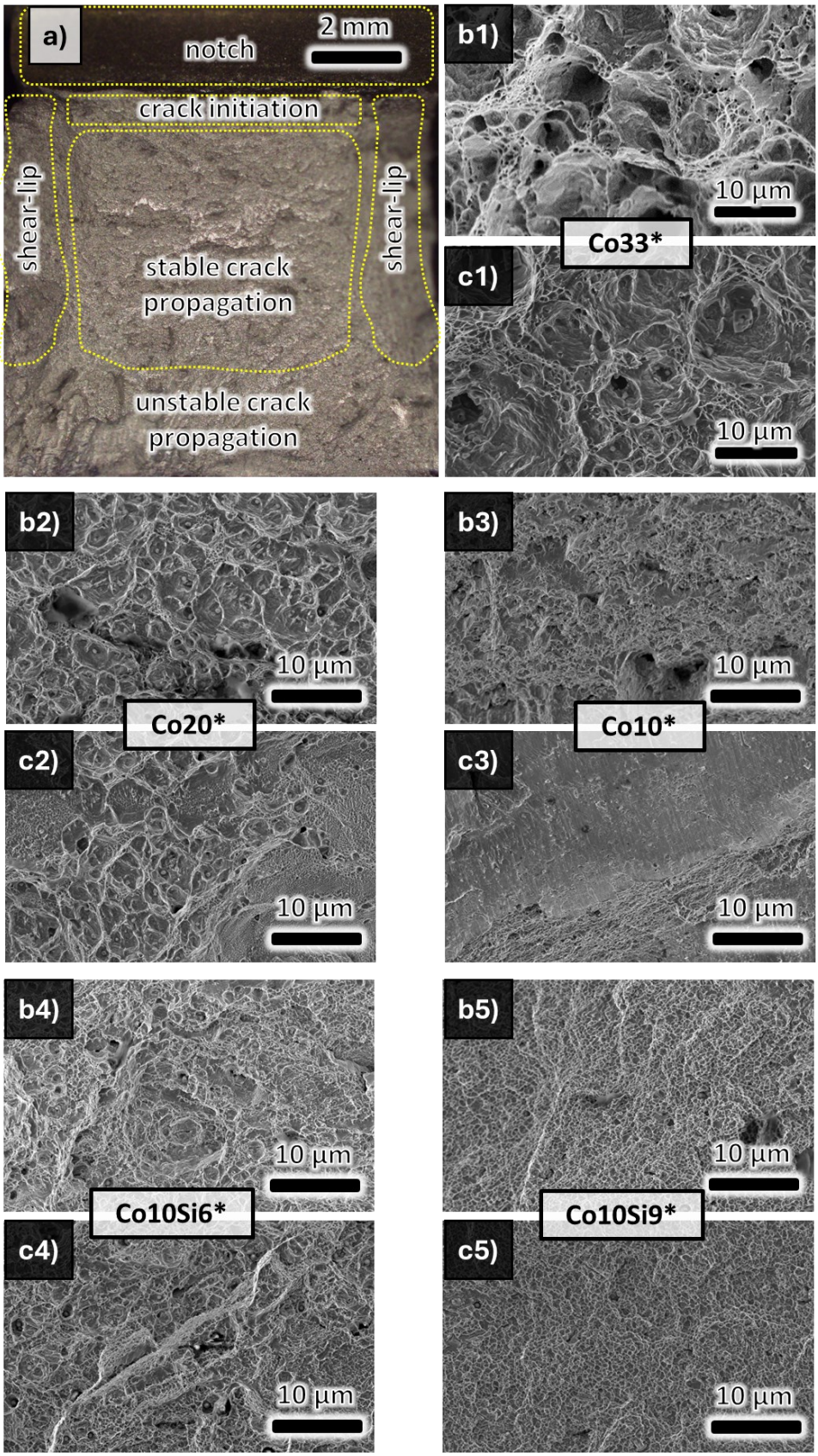


Figure 5.27. Fractographs after impact test of CVN specimens. (a) Fracture surface of Co33*. (b1-b5) Close-up views of crack propagation at 293 K. (c1-c5) Close-up views of crack propagation at 77 K.

Thèse accessible à l'adresse : https://theses.insa-lyon.fr/publication/2025ISAL0036/these.pdf © [T. Langlois], [2025], INSA Lyon, tous droits réservés

The analysis of grain microstructures was conducted using EBSD, with results illustrated in *Figure 5.28*. Band Contrast (BC), phase and KAM maps were acquired from cross-sectional regions approximately 100 μm behind the tip of the fracture surface after impact loading at 293 K and 77 K.

- Twin boundaries, marked in red in BC maps, are present in all analysed microstructures. They are mostly annealing twins, as deformation twins of nanometric scale are rarely captured at this resolution.

- Phase maps reveal a strain-induced $\gamma \rightarrow \varepsilon$ phase transformation in Co10Si9*. This observation suggests a low SFE for this alloy. Interestingly, the presence of sigma phase does not appear to hinder the TRIP effect, in agreement with previous studies [163].

KAM maps reveal the intergranular deformation level in the microstructure after impact loading. It is worth noting that deformation levels near the tip can vary significantly with composition and test temperature, as indicated by HV distributions in various literatures [164, 165].

- Compared to reference-state microstructures, the deformed states present increasing density of dislocations for the Co33*, Co20* and Co10* alloys, indicative of higher levels of plastic deformation.

- For Co10Si6*, the residual stress detected near the BCC/B2 precipitate inhibited further dislocation formation, affecting its low fracture toughness.

- For Co10Si9*, despite the formation of ε-HCP martensite, the KAM map shows very low levels of deformation. This suggests that the sigma phase is so brittle that no dislocation storage was permitted, contributing to its catastrophic failure behaviour during impact loading.

While Ind500 specimens provided interesting insights of the influence of secondary phases on hardness and toughness properties, the limitations of their thermomechanical treatment and resulting microstructures did not provide satisfying mechanical responses. To address these challenges, the last processing method focuses on Arc200 specimens. These materials underwent a more controlled thermomechanical treatment and were prepared for tensile testing, to provide a more comprehensive understanding of deformations mechanisms and mechanical performance of CrCoNiSi-based alloys.

Thèse accessible à l'adresse : https://theses.insa-lyon.fr/publication/2025ISAL0036/these.pdf © [T. Langlois], [2025], INSA Lyon, tous droits réservés

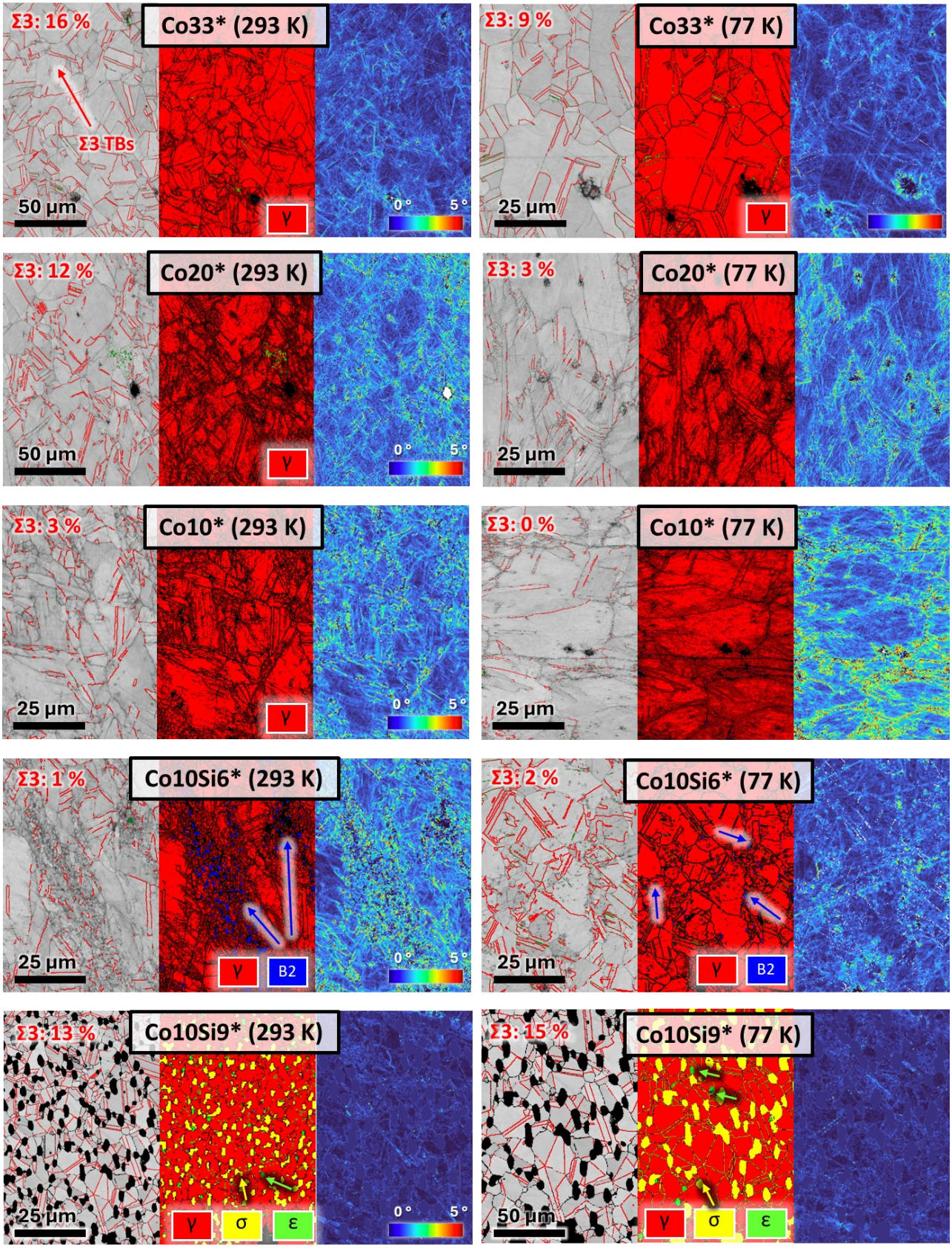


Figure 5.28. Microstructural analysis after impact test at 293 K (left) and 77 K (right), with a set of EBSD maps: BC (red lines indicate twin boundaries), Phase, and KAM.

Thèse accessible à l'adresse : https://theses.insa-lyon.fr/publication/2025ISAL0036/these.pdf © [T. Langlois], [2025], INSA Lyon, tous droits réservés

5.5 Tensile specimens

5.5.1 Reference-state microstructure

The reference-state microstructure of the Arc200 specimens was carefully examined to assess the effects of cold rolling and heat treatment on the grain morphology and potential secondary phase formation.

Phase identification:

Phase analysis was performed using XRD, as shown in *Figure 5.29* and EBSD phase maps (*Figure 0.23* in the Appendix of Chapter 5). XRD results reveal that all four compositions exhibit FCC solid solution microstructures. No evidence of secondary phase precipitation was observed.

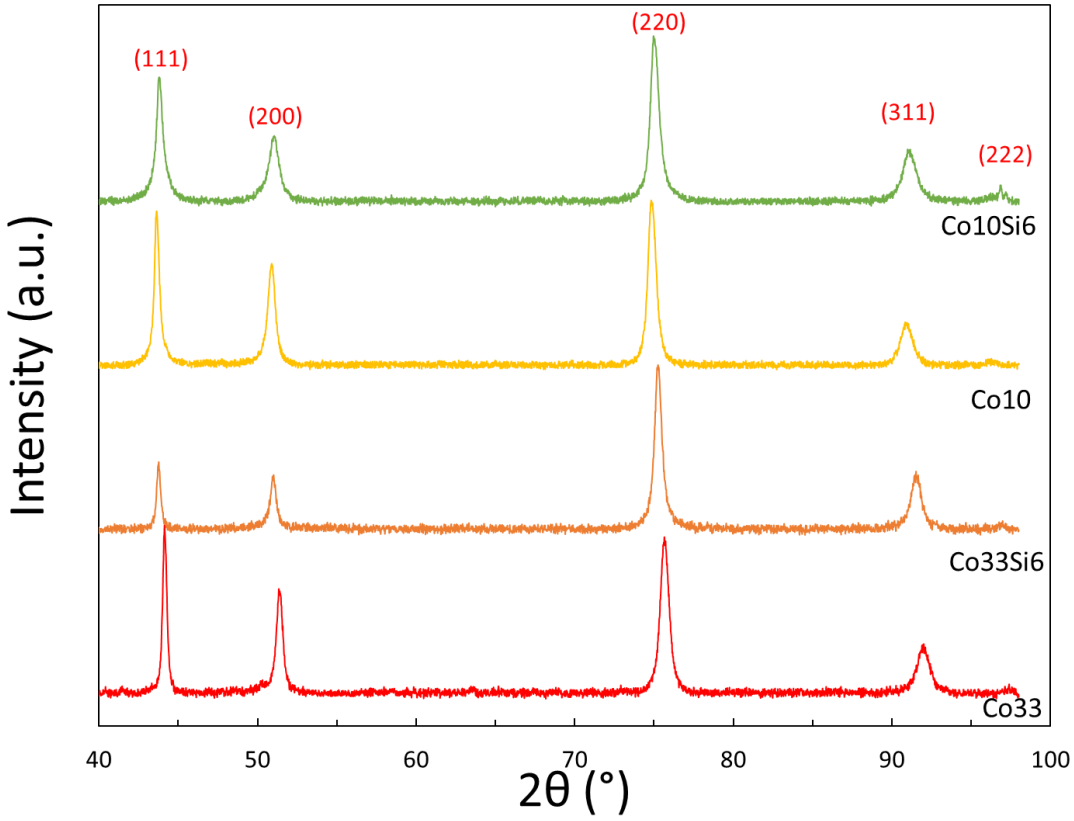


Figure 5.29. XRD profile of the four Arc200 samples after recrystallisation.

Thèse accessible à l'adresse : https://theses.insa-lyon.fr/publication/2025ISAL0036/these.pdf © [T. Langlois], [2025], INSA Lyon, tous droits réservés

Microstructure morphology:

The grain morphologies after cold rolling and subsequent recrystallisation are shown in *Figure 5.30*. The IPF maps, which illustrate grain orientation along the X axis (parallel to the Rolling Direction, RD), allows for the identification of different diffraction domains. With MATLAB, parent grains were reconstructed to measure grain size both with and without considering twin boundaries.

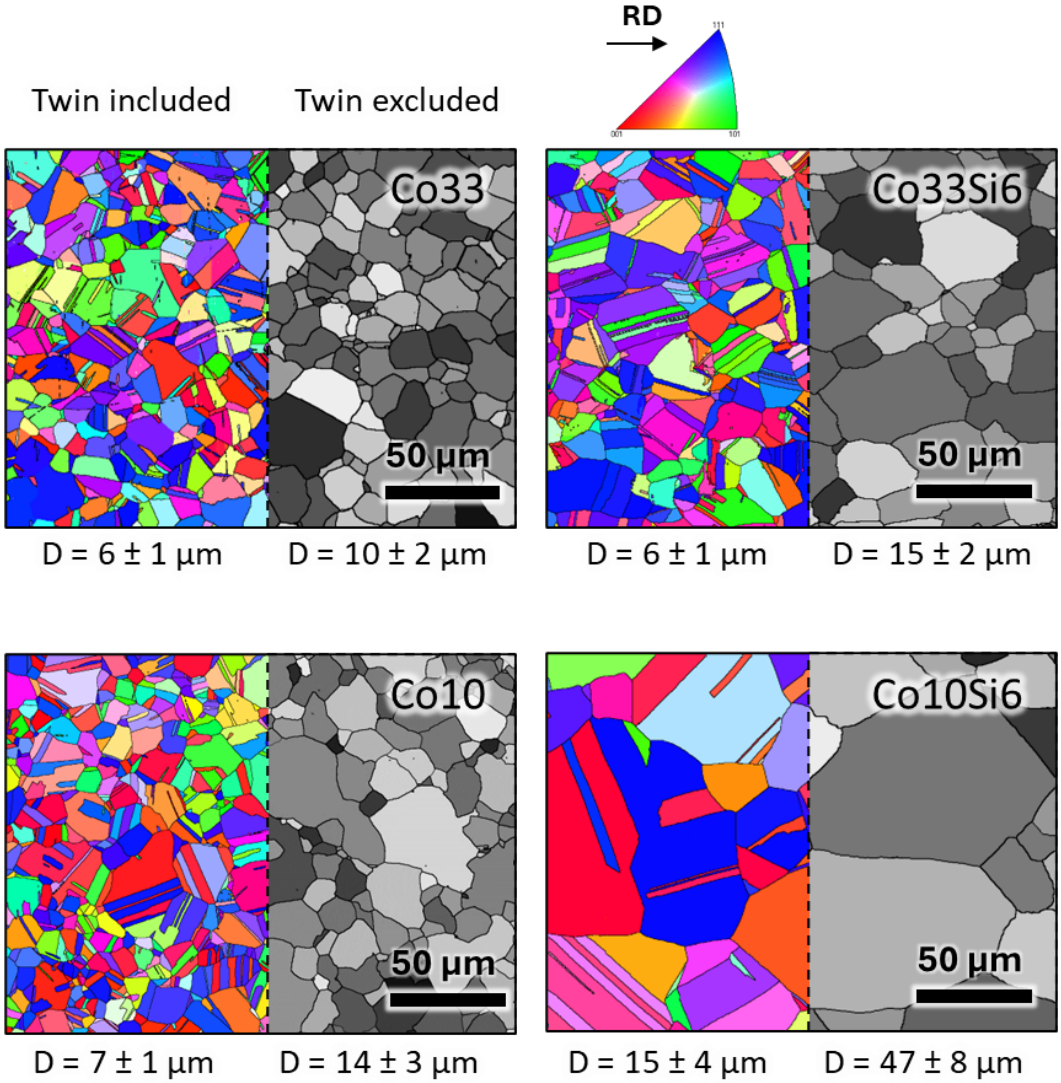


Figure 5.30. IPF X maps of the recrystallised Arc200 specimens (acquisition on the surface of the tensile specimens, with RD: rolling direction).

- Co33, Co33Si6 and Co10 have similar grain size, with and without considering twins. However, a noticeable increase in grain size is observed in the Co10Si6 alloy. This discrepancy suggests that silicon addition may affect

Thèse accessible à l'adresse : https://theses.insa-lyon.fr/publication/2025ISAL0036/these.pdf © [T. Langlois], [2025], INSA Lyon, tous droits réservés

the recrystallisation process and grain growth, promoting larger grains in this composition. This must be considered in mechanical analyses, especially from grain-boundary contributions to strengthening.

- Additionally, moderate grain size variations were observed within the same recrystallised ingots, with bigger grains near the edges. Unfortunately, the precise location of each machined specimen was not provided by the company responsible for machining.

Additionally, the KAM maps shown in *Figure 0.23* in Appendix of Chapter 5 reveal microstructures with complete recrystallisation and very low residual stress. These observations indicate that the alloys have undergone a thorough recovery during the heat-treatment process. The obtained microstructures, featuring small grains, low residual stress and the presence of annealing twins, are promising for achieving favourable tensile properties, as discussed in the following section.

5.5.2 Mechanical properties

Hardness measurement have been performed on both as-cast and recrystallised states to track the hardness evolution resulting from thermomechanical processing, as illustrated in *Figure 5.31*.

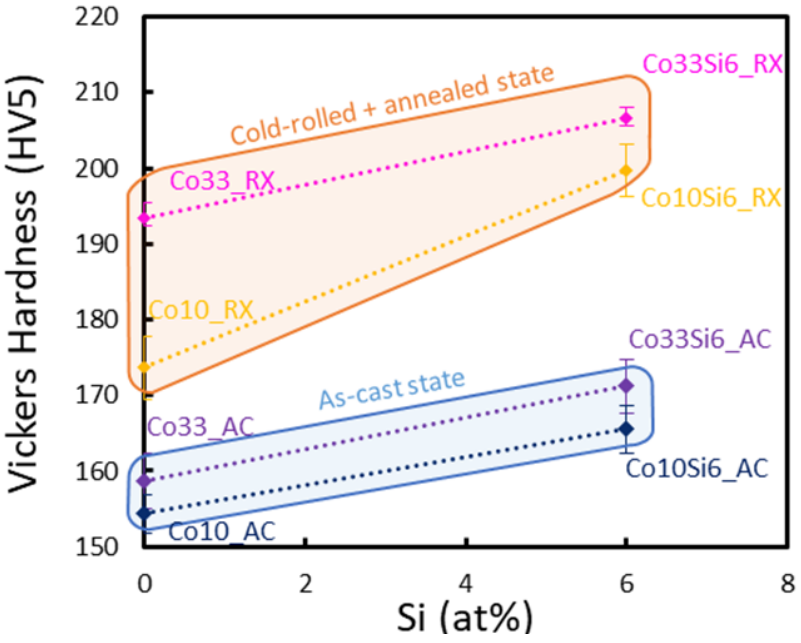


Figure 5.31. Vickers Hardness measurement for as-cast and recrystallised samples produced with the Arc200 furnace.

Thèse accessible à l'adresse : https://theses.insa-lyon.fr/publication/2025ISAL0036/these.pdf © [T. Langlois], [2025], INSA Lyon, tous droits réservés

Based on hardness results, following observations can be made:

- Like the as-homogenised Arc50 samples, hardness increases modestly with increasing silicon and cobalt contents in the as-cast Arc200 samples. This suggests that both elements contribute to solid solution hardening.
- After the thermomechanical treatment, the specimens show a more pronounced increase in hardness, with greater variability observed between Co10 and Co33, as well as between Co10 and Co10Si6.

These observations suggest that silicon and cobalt contents contribute significantly to the solid solution hardening.

Tensile tests were conducted at both room temperature (293 K) and low temperature (110 K). The validity of the tensile tests results was confirmed by comparing the stress-strain curves for the reference SS304 in this experiment and values reported in the literature at 293 K [166] and 77 K [167] (*Figure 0.24* in the Appendix of Chapter 5).

Thèse accessible à l'adresse : https://theses.insa-lyon.fr/publication/2025ISAL0036/these.pdf © [T. Langlois], [2025], INSA Lyon, tous droits réservés

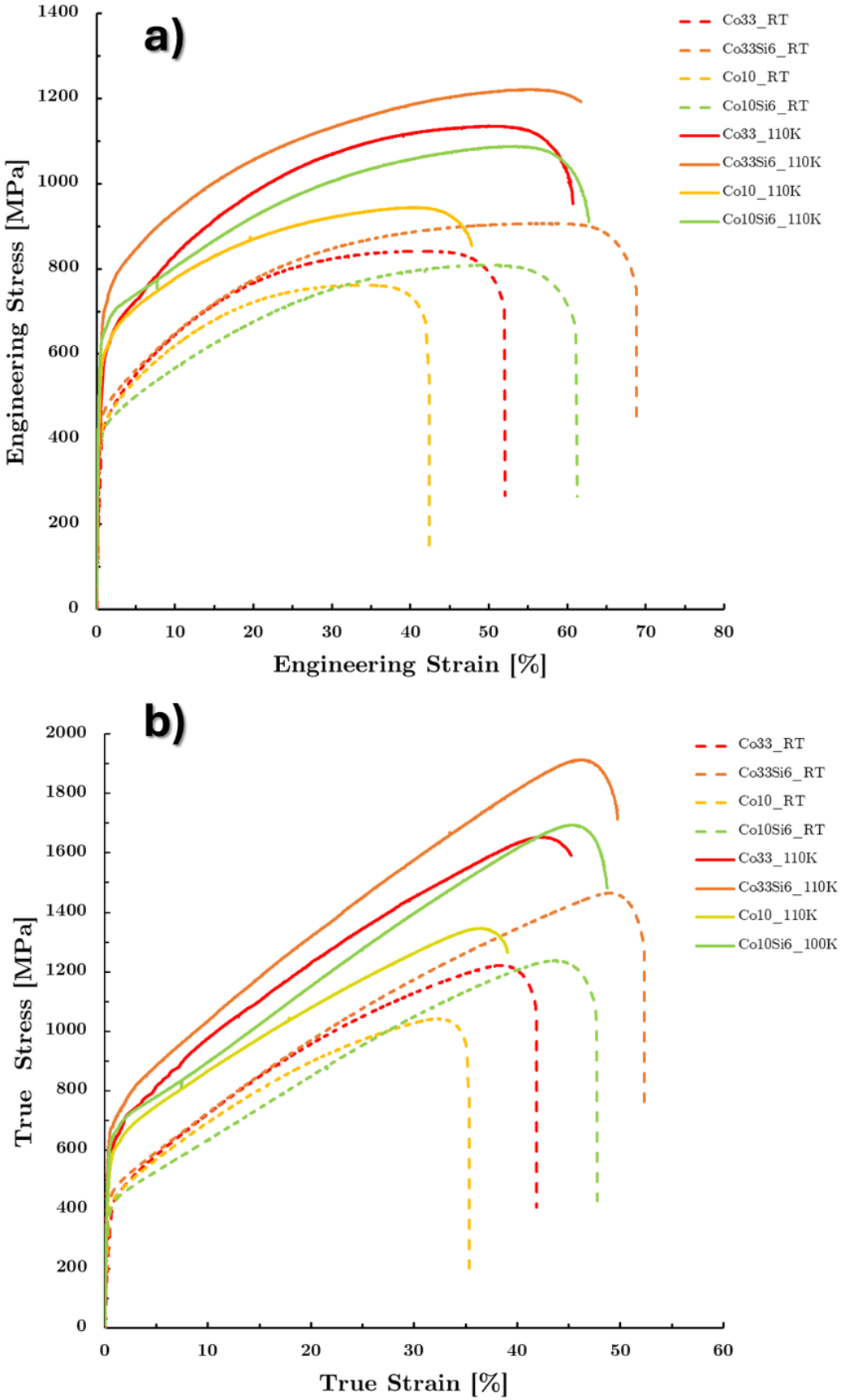


Figure 5.32. Tensile responses of Arc200 TDB specimens: (a) Engineering stress-strain curves; (b) True stress-strain curves.

Thèse accessible à l'adresse : https://theses.insa-lyon.fr/publication/2025ISAL0036/these.pdf © [T. Langlois], [2025], INSA Lyon, tous droits réservés

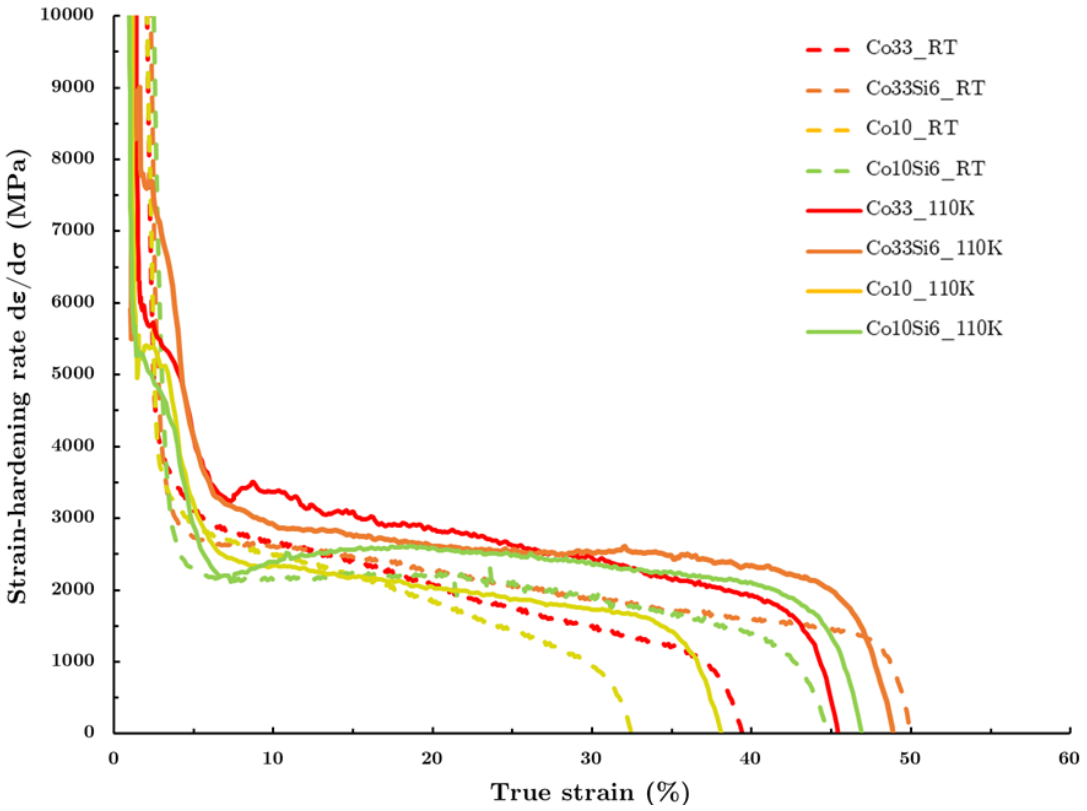


Figure 5.33. Tensile response of Arc200 TDB specimens: Strain-Hardening Rate curves.

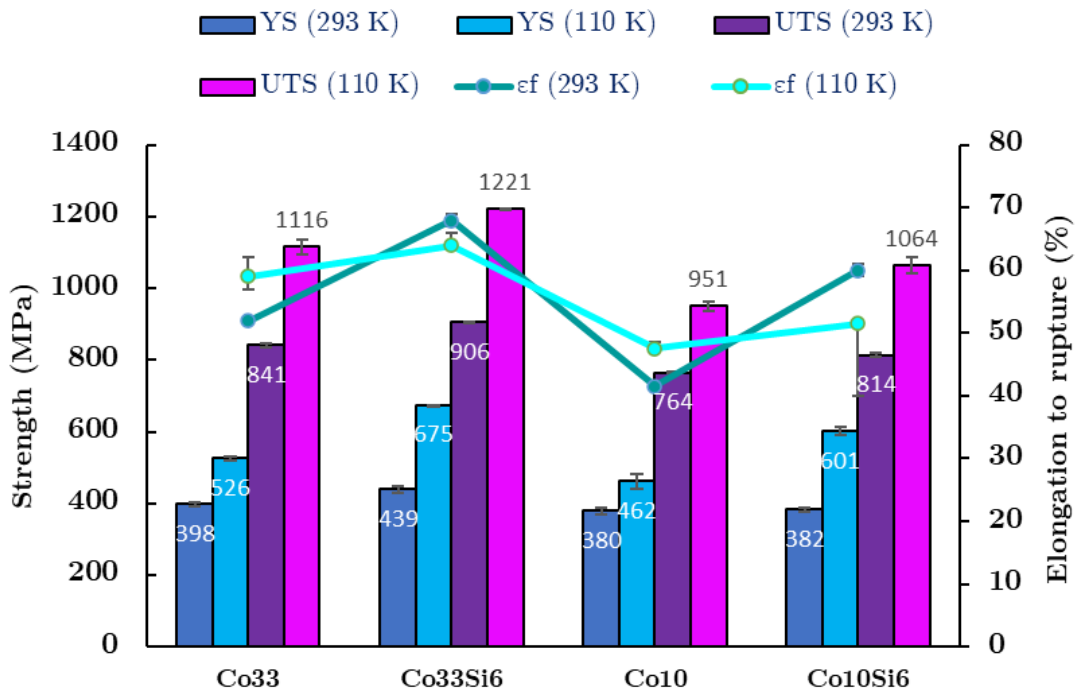


Figure 5.34. Comparison diagram of tensile properties of the different compositions at 293 K and 110 K.

Thèse accessible à l'adresse : https://theses.insa-lyon.fr/publication/2025ISAL0036/these.pdf © [T. Langlois], [2025], INSA Lyon, tous droits réservés

Tensile results are presented with engineering stress-strain curves (*Figure 5.32-a*), true stress-strain curves (*Figure 5.32-b*) and SHR curves (*Figure 5.33*). The evolution of tensile properties with respect to composition and temperature is summarised in *Figure 5.34*.

From the tensile test results, several key observations can be made:

- Increasing cobalt content in CrCoNi alloys results in enhanced tensile properties at both room and low temperatures. Specifically, Co33 exhibits superior tensile performance compared to Co10, with increased YS, UTS and elongation to rupture (ε_f), as illustrated in *Figure 5.34*.

- Silicon addition further improves tensile properties. When comparing Co33 with Co33Si6 and Co10 to Co10Si6, the increased YS, UTS and ε_f demonstrated the positive impact of silicon. These observations are consistent with similar studied at room temperature [44].

- Despite the lower cobalt content in Co1oSi6, the tensile properties of this material are rejuvenated and approach those of Co33 at both temperatures. This suggests that the addition of silicon compensates for the reduced cobalt content.

- The analysis of SHR curves in *Figure 5.33* show that silicon-added composition (Co33Si6 and Co10Si6) exhibits prolonged plastic deformation, with SHR values around 2000 MPa at room temperature, consistent with the literature [62]. At 110 K, an increase of SHR around 2700 MPa at $\varepsilon = 0.19$ is observed for Co10Si6, while SHR of Co33Si6 reaches an extremum around 3000 MPa at $\varepsilon = 0.32$, reflecting the decrease of SFE.

- At lower temperatures, a significant improvement in YS and UTS is observed across all compositions, while maintaining great elongation to rupture. With ε_f of 52% in Co10Si6 and 60% in Co33Si6 at 110 K, the addition of silicon allows for enhancing both strength and ductility at low temperatures.

The obtained tensile properties are in agreement with those from other CrCoNiSi studies [20, 62, 44, 64, 168], as illustrated in *Figure 5.35*. Given that Co10Si6 specimens exhibits the larger grain size, we can expect a more pronounced strengthening in samples with smaller grains.

Thèse accessible à l'adresse : https://theses.insa-lyon.fr/publication/2025ISAL0036/these.pdf © [T. Langlois], [2025], INSA Lyon, tous droits réservés

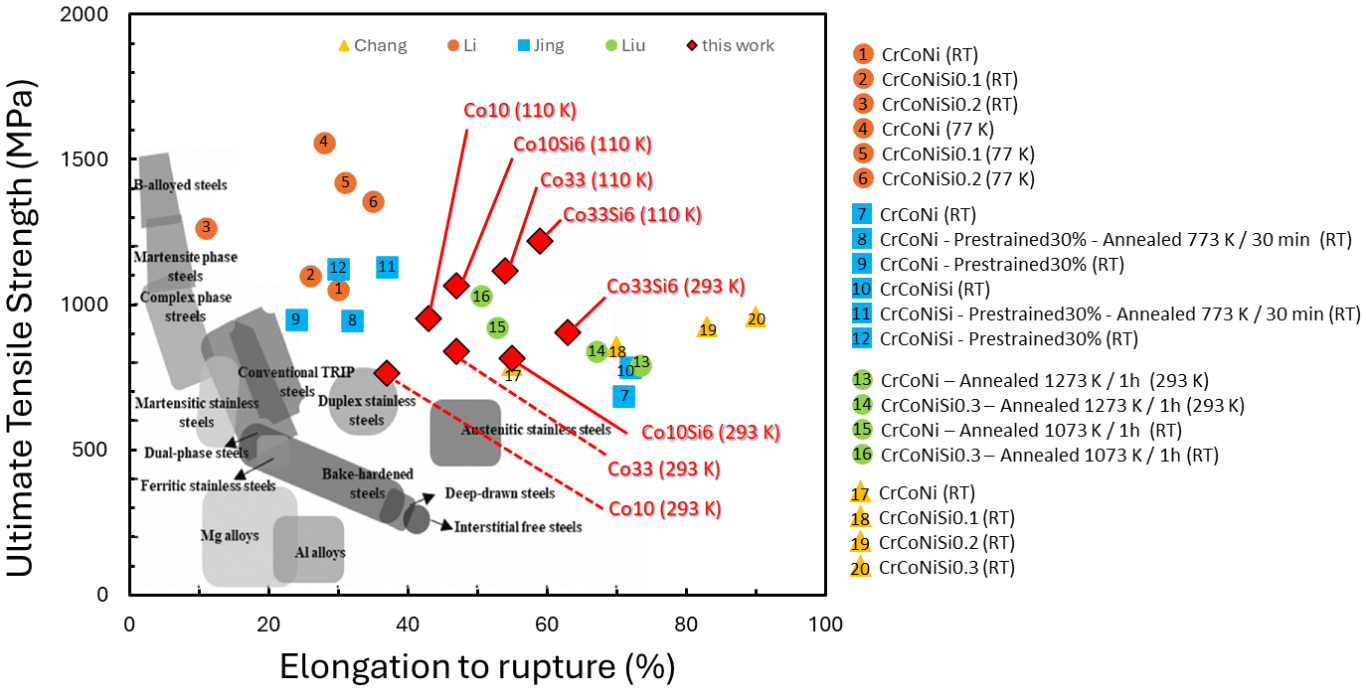


Figure 5.35. UTS vs elongation to rupture diagram. Comparison between different CrCoNiSi experimentally produced (Chang [44], Jing [62], Liu [64], Li [168]) and other classes of metals.

As previously reported in the literature, the addition of silicon to a CrCoNi base appears to break the typical stress-ductility trade-off [20, 44, 32, 64]. The synergy between strength and ductility is further enhanced at cryogenic temperatures, where CrCoNiSi compositions exhibit remarkable SHR values. When the true strain is 33%, the SHR of Co33Si6 (110 K) reaches a maximum of 2620 MPa, corresponding to approximately $\mu/30$ (the shear modulus (μ) is measured to be 78 MPa [64]). This value is close to those of TWIP steels ($\mu/20$ to $\mu/40$) and much higher than that of other FCC metals ($\mu/200$) at room temperature [63]. In contrast, other materials such as high carbon steels or martensitic steels often experience catastrophic loss of properties at cryogenic temperatures due to embrittlement effects [169].

These promising mechanical performances of CrCoNi and CrCoNiSi compositions at 293 K and 110 K highlight the importance of further investigating their microstructural evolution with respect to composition and temperature.

Thèse accessible à l'adresse : https://theses.insa-lyon.fr/publication/2025ISAL0036/these.pdf © [T. Langlois], [2025], INSA Lyon, tous droits réservés

5.5.3 Postmortem microstructural observations

The fracture surface of tensile specimens after rupture was analysed with SE2 imaging. The fractographic results are illustrated in *Figure 5.36*.

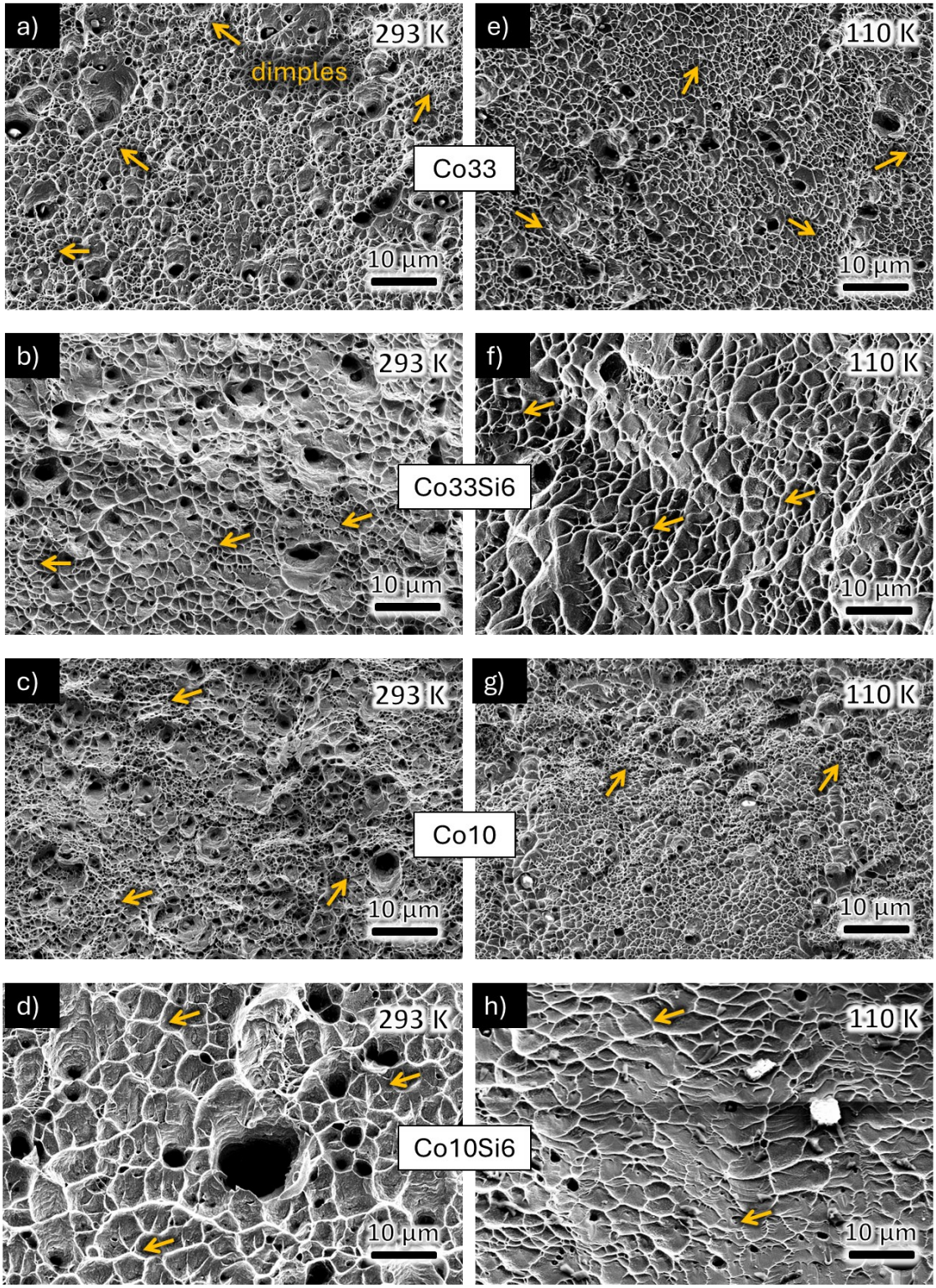


Figure 5.36. Fractographs of tensile specimens after rupture. (a-d) Tensile tests at 293 K; (e-h) Tensile tests at 110 K.

Thèse accessible à l'adresse : https://theses.insa-lyon.fr/publication/2025ISAL0036/these.pdf © [T. Langlois], [2025], INSA Lyon, tous droits réservés

- The fracture surfaces exhibit dimples, marked with yellow arrows. These features are characteristic of ductile fracture mechanisms. No significant cleavage plans were observed, suggesting that all the microstructures exhibit ductile rather than brittle behaviours.
- Silicon addition (Co33 vs Co33Si6; Co10 vs Co10Si6) appears to enlarge the microstructures, leading to larger dimples. This observation correlates with an increased ductility in other alloys [26].
- At 110 K, the dimples remain visible across all compositions, confirming that ductile fracture mechanisms remains at cryogenic temperatures.

To further investigate the influence of composition and temperature on the mechanical properties of CrCoNi and CrCoNiSi alloys, a detailed study of the microstructure at different strain levels in the tensile specimens was conducted using BSE and EBSD imaging, as explained in the materials and methods (*Figure 3.41*).

BSE imaging was particularly useful for observing contrasts in microstructure across the Head-Should-Rupture (HSR) regions of the sample, highlighting key features at high magnification. Interesting features where observed, such as those seen in Co33 in *Figure 5.37*. These BSE images enabled the identification of significant deformation features such as annealing twins, deformation twins and slip bands.

Thèse accessible à l'adresse : https://theses.insa-lyon.fr/publication/2025ISAL0036/these.pdf © [T. Langlois], [2025], INSA Lyon, tous droits réservés

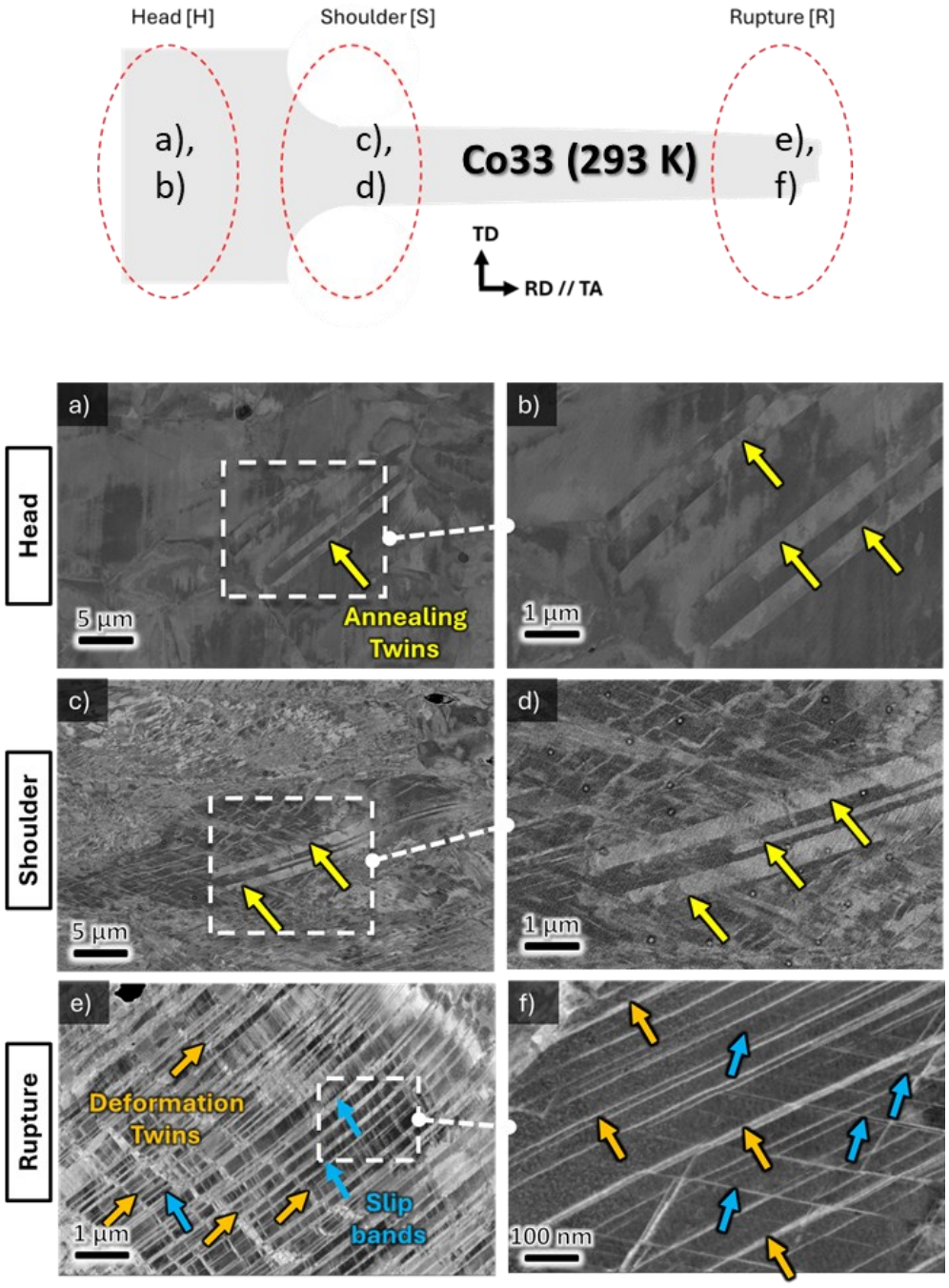


Figure 5.37. BSE images of Co33 after tensile test at 293 K, showing head, shoulder and rupture regions with different strain levels.

Further analysis using EBSD at low magnification allowed to track changes in grain size, texture, and the evolution of twins as a function of composition, temperature, and the degree of deformation across the HSR regions. The IPF X maps shown in *Figure 5.38*, represent the crystallographic orientations relative to the applied loading direction (Tensile Axis, TA) in the HSR regions for different alloys. These maps provide valuable insights into the evolution of grain orientation during tensile deformation.

Thèse accessible à l'adresse : https://theses.insa-lyon.fr/publication/2025ISAL0036/these.pdf © [T. Langlois], [2025], INSA Lyon, tous droits réservés

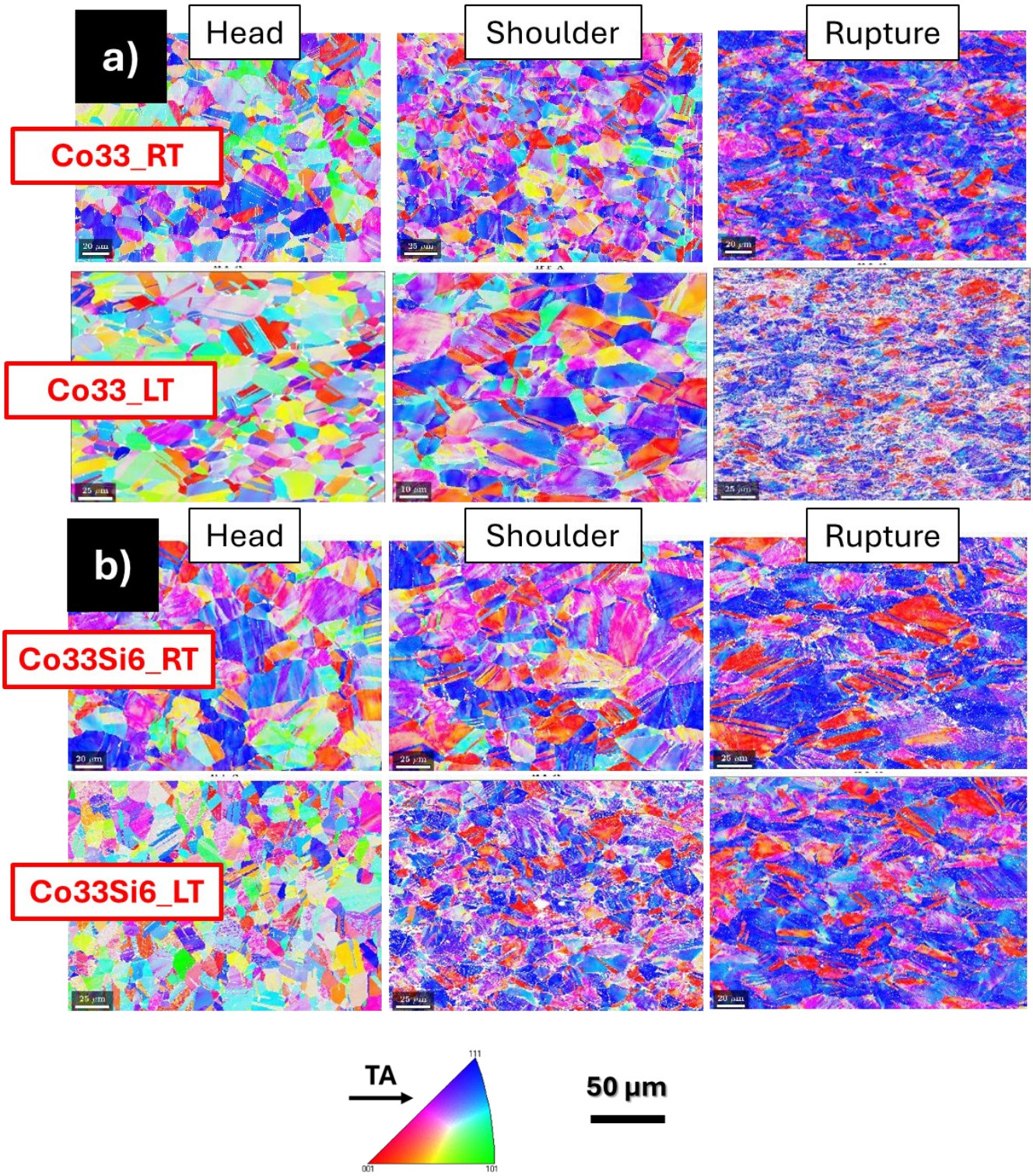


Figure 5.38. IPF map at low magnification in HSR regions for a) Co33; b) Co33Si6; c) Co10; d) Co10Si6 alloys.

Thèse accessible à l'adresse : https://theses.insa-lyon.fr/publication/2025ISAL0036/these.pdf © [T. Langlois], [2025], INSA Lyon, tous droits réservés

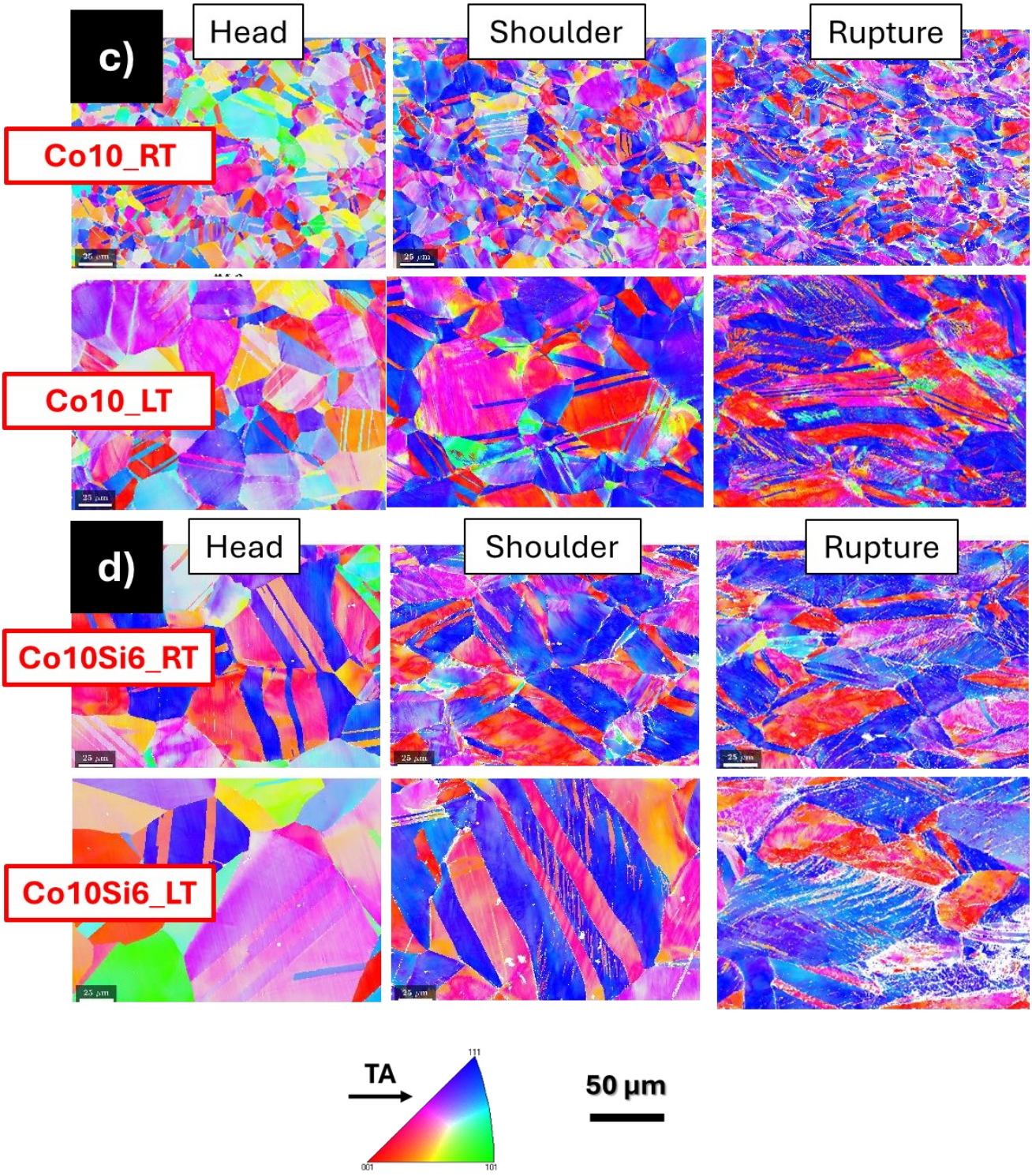


Figure 5.38 (continued). IPF maps at low magnification in HSR regions for a) Co33; b) Co33Si6; c) Co10; d) Co10Si6 alloys.

Thèse accessible à l'adresse : https://theses.insa-lyon.fr/publication/2025ISAL0036/these.pdf © [T. Langlois], [2025], INSA Lyon, tous droits réservés

The IPF maps reveal randomly equiaxed microstructures in the undeformed region of the specimens, with significantly larger grain size observed in Co10 and Co10Si6 alloys. At higher deformation levels, the grains are deformed along TA , and the grains begin to exhibit slight misorientation, indicated by a gradient of colour. This suggests an increase in plastic deformation in these regions.

Texturing was evaluated using low-magnification maps for all compositions at both room temperature and cryogenic temperature.

- In the undeformed regions, the microstructure is randomly equiaxed across all composition.
- At increased strain, a clear reorientation is observed towards the (111) orientation (represented by the blue colour in IPF maps) and (100) orientation (red colour).

To better quantify the degree of texturing, the Texturing Index (TI) was used. TI is defined as the difference between the intensity of the maximum peak in the pole figure and the average intensity. In the measurement, we account for plastic deformation and reorientation gradient within a map. The evolution of pole figures with strain, composition, and temperature is illustrated in *Figure 5.39*. These figures show the evolution of texturing as strain increases in different regions (Head, Shoulder, and Rupture) and for different compositions. The distributions in the pole figures are normalised with respect to the highest texturing coefficient observed in the HSR regions (TI max = 13 in Co10Si6 near the rupture, after tensile test at 110 K).

Thèse accessible à l'adresse : https://theses.insa-lyon.fr/publication/2025ISAL0036/these.pdf © [T. Langlois], [2025], INSA Lyon, tous droits réservés

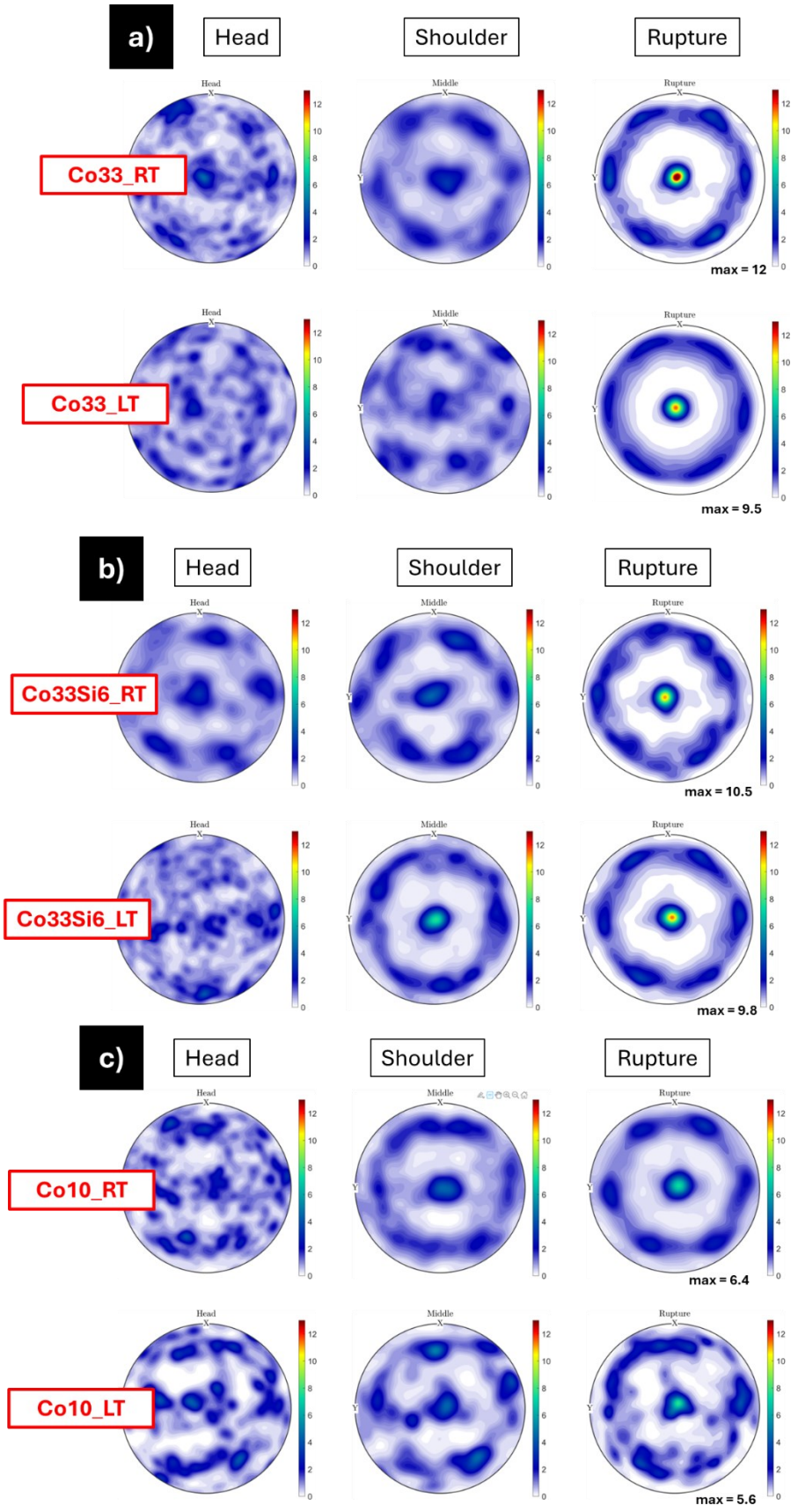


Figure 5.39. Pole Figures evolution with strain, composition and temperature (a) Co33, (b) Co33Si6, (c) Co10, (d) Co10Si6.

Thèse accessible à l'adresse : https://theses.insa-lyon.fr/publication/2025ISAL0036/these.pdf © [T. Langlois], [2025], INSA Lyon, tous droits réservés

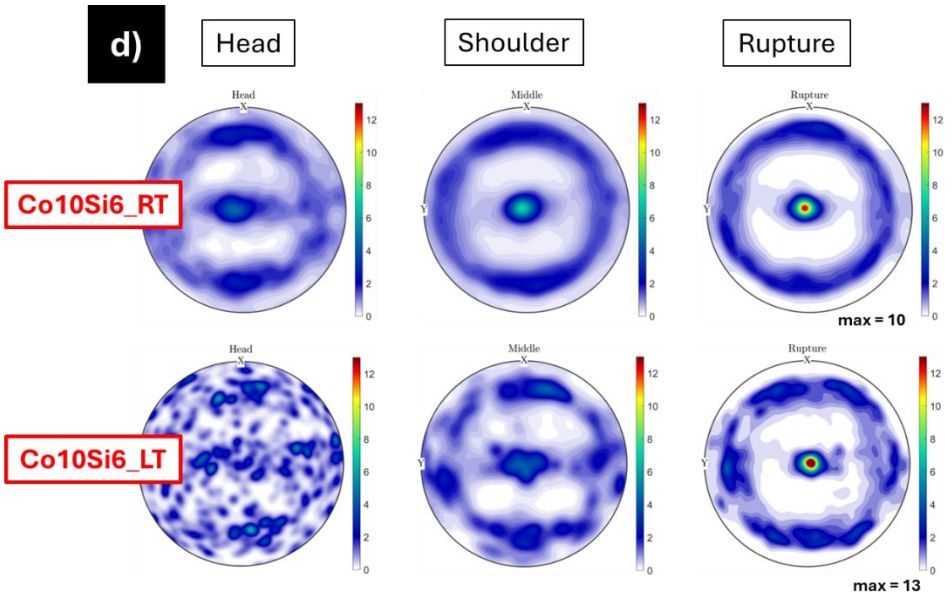


Figure 5.39 (continued). Pole Figures evolution with strain, composition and temperature (a) Co33, (b) Co33Si6, (c) Co10, (d) Co10Si6.

- A double-fibre texture is revealed across all compositions, especially in EBSD map near rupture. This corresponds to the (111) and (100) preferential orientation observed in blue and red in the IPF maps.
- Compositions with lower cobalt content exhibit less pronounced texturing, while silicon addition enhances the texturing effect, resulting in a more significant reorientation of the grains. This effect is especially visible in the Co33Si6 and Co10Si6 alloys. The Co10 alloy shows the least pronounced texturing.
- No significant effect of the test temperature on texturing was observed.

Annealing Twins (AT) were identified using our MATLAB scripts, with the corresponding statistics reported in *Figure 0.25* in the Appendix of Chapter 5. The following observations on AT were made:

- All specimens exhibit AT thicknesses of the same order of magnitude ranging from 1 µm to 50 µm.

Thèse accessible à l'adresse : https://theses.insa-lyon.fr/publication/2025ISAL0036/these.pdf © [T. Langlois], [2025], INSA Lyon, tous droits réservés

- Due to grain reorientation during tensile deformation, the ATs also align towards the (001) orientation of the FCC crystal system, to maintain the exhibit 60°/<111> misorientation with parent grains. This reorientation of ATs explains the strong double-fibre texture observed in the pole figures.

- Finally, the proportion of AT area per grain decreases as the deformation level increases across all composition. Experimental observations reveal that some ATs reorient toward the (111) orientation rather than the expected (001) orientation, as demonstrated in *Figure 5.40*. This reorientation makes them undetectable as twin for our script.

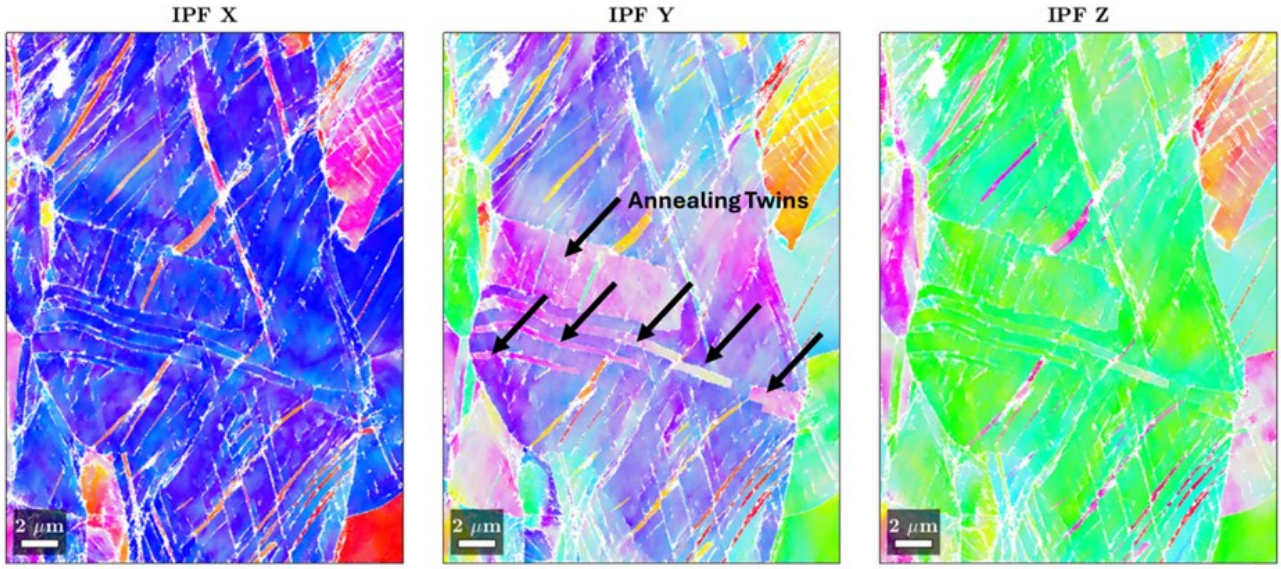


Figure 5.40. IPF maps. Annealing twin reoriented towards (111) in Co33_RT alloy.

EBSD maps captured at higher magnification allow for detecting deformations twins (DT), as illustrated in *Figure 5.41*. No DTs were observed in the head region of the tensile specimens. The shoulder regions provide intermediate deformation state, but the exact strain levels are not precisely defined in this area and some compositions did not show any DT nucleation in shoulder. Therefore, DT statistics were primarily collected from regions near the rupture. By capturing a significant number of twins in the rupture regions across different specimens, DT statistics are provided in *Figure 5.42*. Detailed distributions of DT thickness and DT surface area are provided in *Figure 0.26* and *Figure 0.27* in the Appendix of Chapter 5.

Thèse accessible à l'adresse : https://theses.insa-lyon.fr/publication/2025ISAL0036/these.pdf © [T. Langlois], [2025], INSA Lyon, tous droits réservés

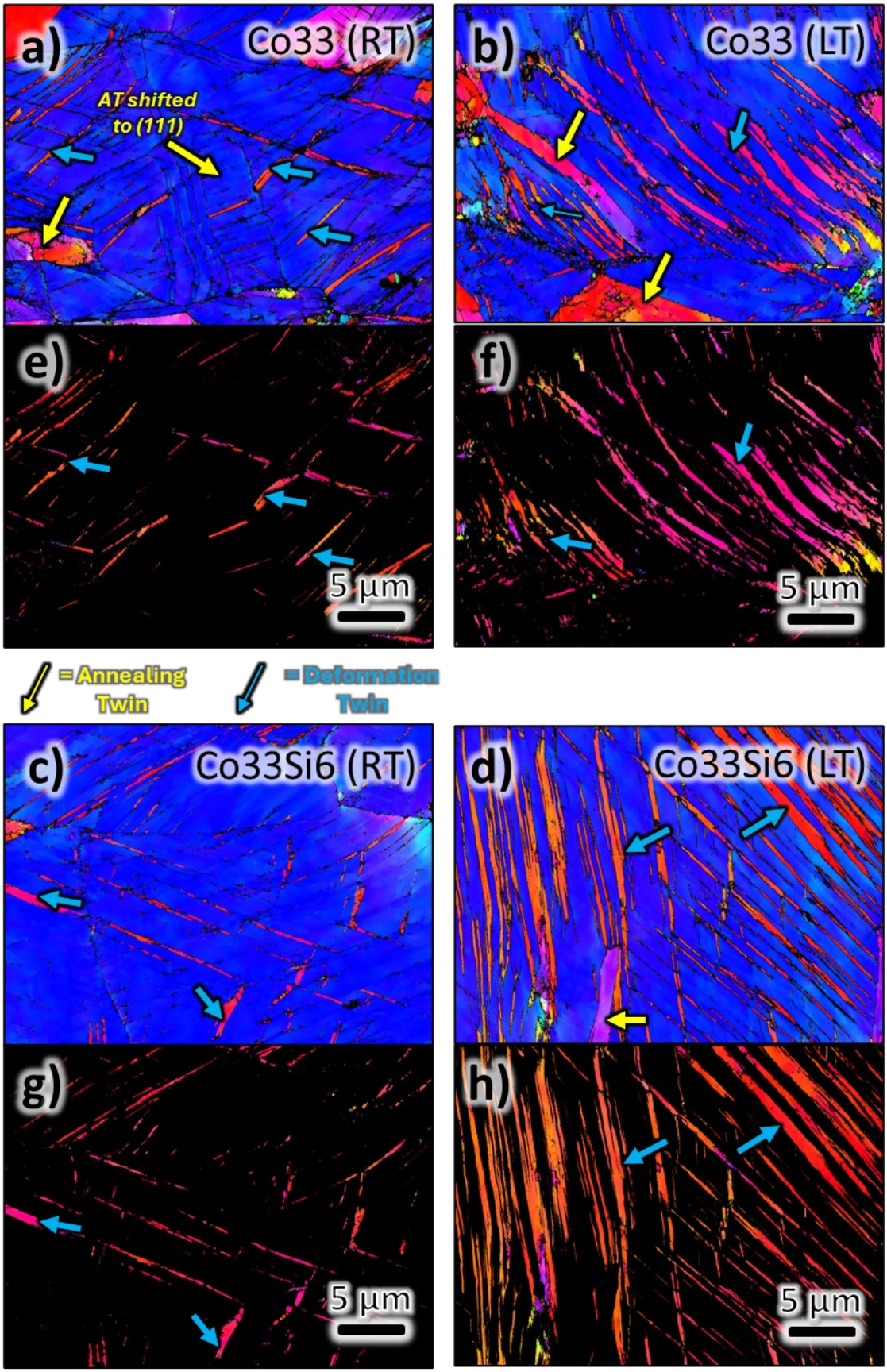


Figure 5.41. (a-d) IPF X maps at high magnification near the rupture of the specimens, (e-h) Corresponding deformation twin detection with MATLAB.

Thèse accessible à l'adresse : https://theses.insa-lyon.fr/publication/2025ISAL0036/these.pdf © [T. Langlois], [2025], INSA Lyon, tous droits réservés

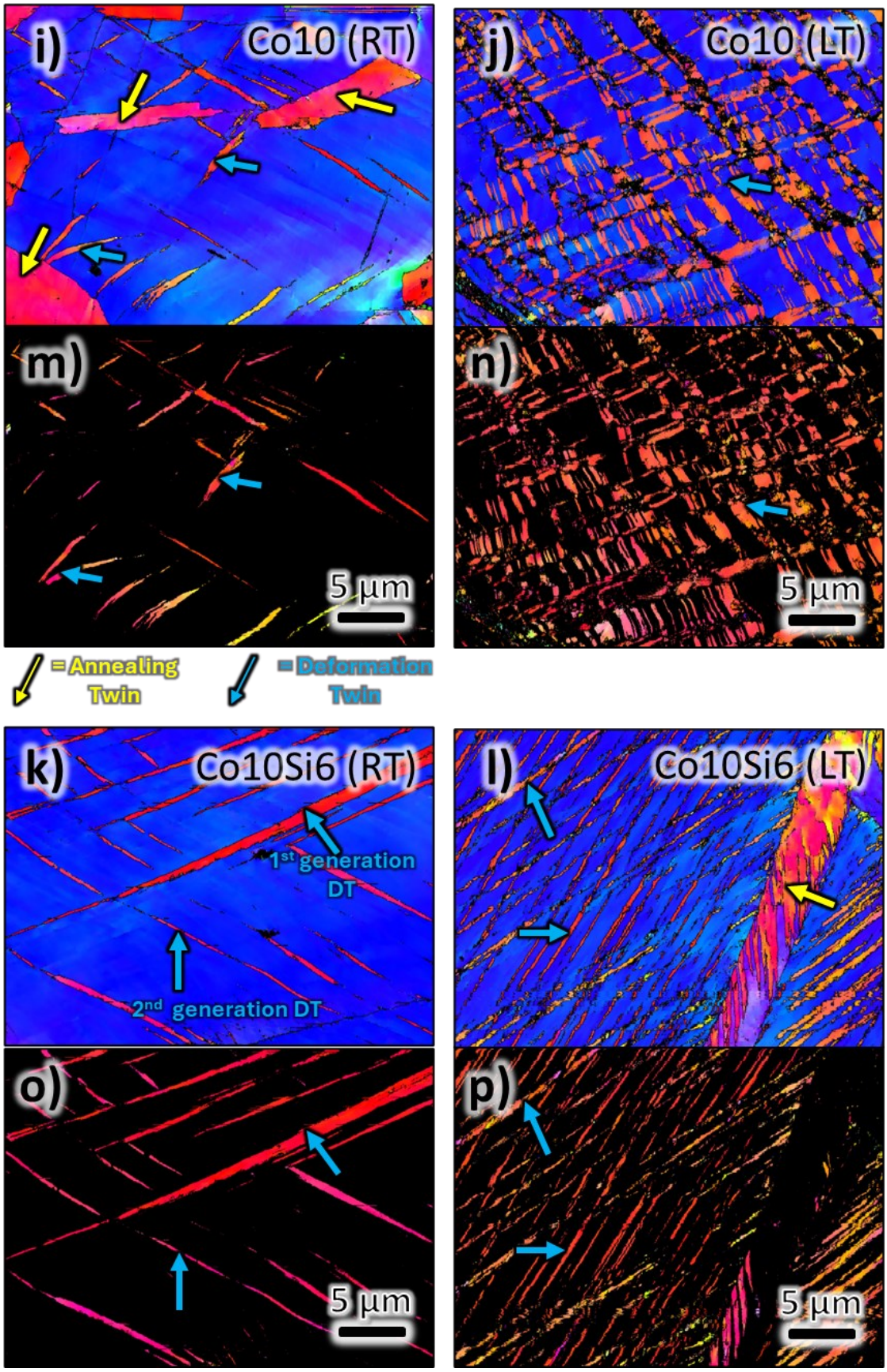


Figure 5.41 (continued) (a-d) IPF X maps at high magnification near the rupture of the specimens, (e-h) Corresponding deformation twin detection.

Thèse accessible à l'adresse : https://theses.insa-lyon.fr/publication/2025ISAL0036/these.pdf © [T. Langlois], [2025], INSA Lyon, tous droits réservés

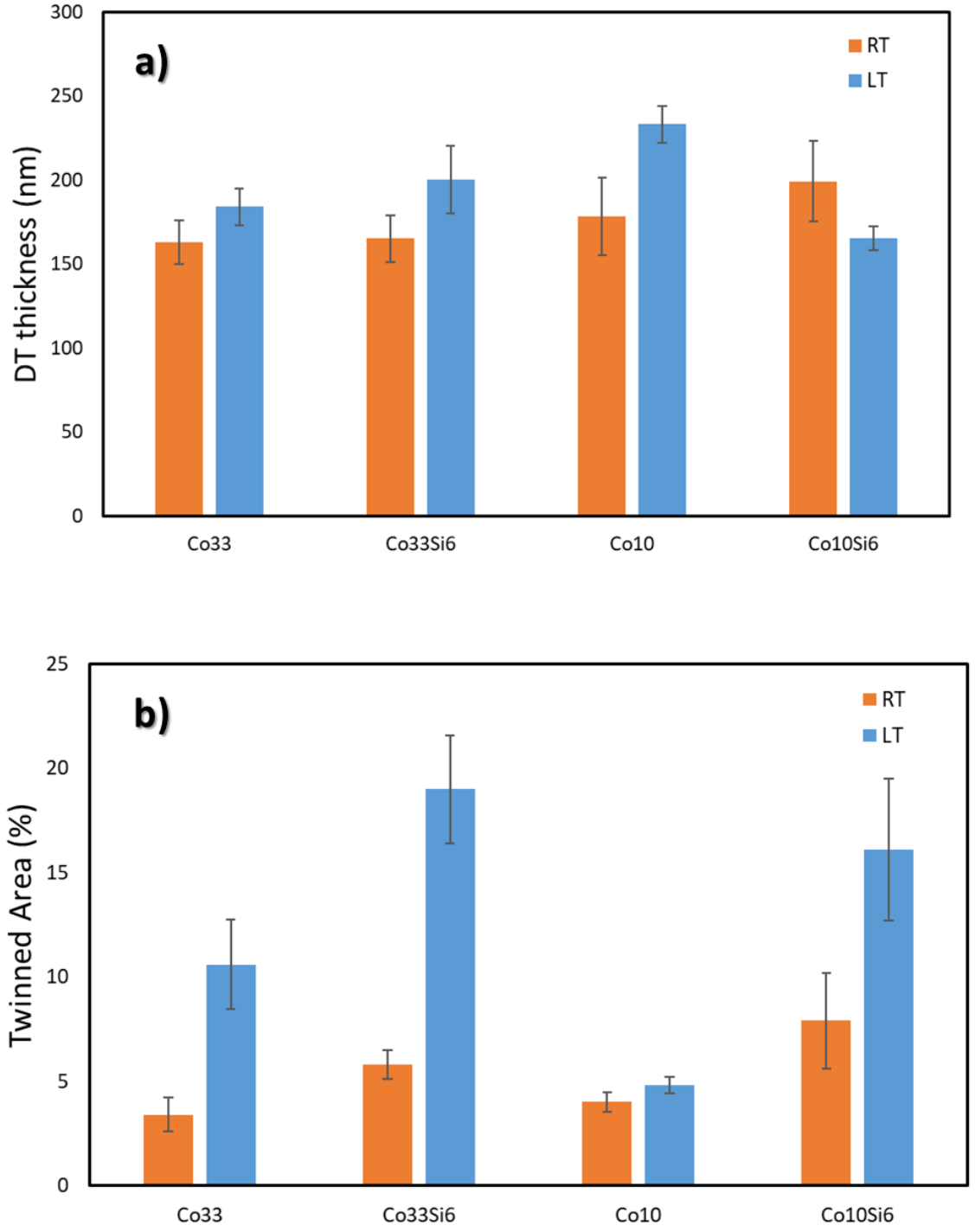


Figure 5.42. Deformation twins (DT): (a) average thickness; (b) average twinned area per map.

Thèse accessible à l'adresse : https://theses.insa-lyon.fr/publication/2025ISAL0036/these.pdf © [T. Langlois], [2025], INSA Lyon, tous droits réservés

The following key observations were made regarding deformation twins:

- DTs predominantly nucleate and grow in grains in the (111) orientation, as shown in the high-magnification maps. This is in agreement with Schmidt's factor that reflects the preferential deformation mechanism between slips systems and twinning systems [171].
- At lower temperatures, the DT thickness increases significantly for the CrCoNi alloys.
- However, with the addition of silicon, the growth in DT thickness at cryogenic temperature is less pronounced. This could be explained by the nucleation of second-generation DTs, illustrated by a double thickness distribution for Co10Si6 (*Figure 0.26* in the Appendix of Chapter 5). Evidence of second-generation DT is demonstrated in IPF map of Co10Si6 (*Figure 5.41-k*) [171].
- Compositions with silicon (Co10Si6 and Co33Si6) show the occurrence of DTs already in the shoulder region, indicating the critical stress for twinning is lower compared to CrCoNi alloys. These two alloys are the one showing increased stage II SHR in the stress-strain curves.
- Temperature also seems to lower the twinning threshold value, as seen by comparing Co10(RT) and Co10(LT). The later specimen exhibits both larger and more numerous DTs.
- Co10 is the alloy with the lowest YS, UTS and ε_f at room and cryogenic temperatures and it also exhibits the lowest DT occurrence of DTs. This observation underlines the key role of DTs in enhancing a material ability to accommodate plastic deformation.

The statistics for DTs are very interesting but must be interpreted with caution. Despite capturing microstructure in several locations near the rupture for all compositions, a large variation of local DT statistics was observed. Robust statistics could only be obtained with a larger number of significant maps. Moreover, stepwise or in-situ testing would have been highly beneficial for tracking the reorientation process and the initial appearance of DTs. In-situ testing was not carried out, whit certain limitations in cryogenic tests.

Thèse accessible à l'adresse : https://theses.insa-lyon.fr/publication/2025ISAL0036/these.pdf © [T. Langlois], [2025], INSA Lyon, tous droits réservés

5.6 Effect of composition and temperature

In this chapter, we have analysed various reference microstructures and deformed microstructures including those from as-homogenised Arc50, hot rolled Ind500, and cold rolled-annealed Arc200 specimens. These microstructures were studied alongside extensive mechanical testing methods, including hardness tests, powder-filling, compression testing, Charpy impact loading, and tensile loading.

From the results presented in the previous sections, we identified the following effects of cobalt, silicon, and temperature on the mechanical properties and microstructural evolution of CrCoNi and CrCoNiSi alloys.

Effect of Cobalt on microstructural features

- Cobalt significantly lowers the SFE of the materials, thereby enabling deformation mechanisms like TWIP and TRIP, improving ductility and strength, respectively.
- The addition of cobalt refines the grain size (Co33 vs Co10), reflecting change in measured hardness values.
- In deformed microstructures, Co-rich compositions exhibit ductile fracture morphologies, both in impact and tensile specimens, as compared to more brittle morphologies observed in cobalt-lean compositions.
- Finally, cobalt plays a key role in twinning activation in tensile specimens with much higher concentration of deformation twins in Co33 compared to Co10.

Effect of Cobalt on mechanical properties

- Hardness values increase moderately with cobalt content.
- Both compressive yield strength (YS) and strain hardening rate (SHR) values show a moderate increase with cobalt content (up to 40 at.%).
- Tensile strength, including YS, UTS, and elongation, are significantly higher in Co33 compared to Co10, further highlighting the importance of cobalt for mechanical enhancement.
- Fracture toughness of Co33 was significantly higher than that of Co10.

Thèse accessible à l'adresse : https://theses.insa-lyon.fr/publication/2025ISAL0036/these.pdf © [T. Langlois], [2025], INSA Lyon, tous droits réservés

Effect of Silicon on microstructural features

- Unlike cobalt, the addition of silicon increases the average grain size (e.g., Co33Si6 vs Co33 and Co10Si6 vs Co10).
- Silicon reduces SFE values like cobalt, which can further exacerbate microstructural evolution by promoting deformation twinning.
- Silicon addition results in an increased density of deformation twins and a more pronounced grain reorientation.
- The addition of silicon leads to reduced phase stability, as undesirable sigma and BCC/B2 phases were formed during thermomechanical treatments.

Effect of Silicon on mechanical properties

- In our choice of compositions, Silicon enhances both strength and ductility, either improving them (Co33Si6 vs. Co33) or rejuvenating them (Co10Si6 vs. Co10).
- The stress-strain curves for silicon-containing alloys show prolonged work-hardening during both compression and tensile testing, suggesting a change in the deformation mechanisms compared to other compositions.
- The precipitation of secondary phases in silicon-added composition led to catastrophic loss of mechanical properties. The measured fracture toughness in Co10Si6 and Co10Si9 indicated very brittle behaviour.

CVN impact loading and tensile tests have been carried out at both room temperature and cryogenic temperatures, allowing for evaluation of the temperature impact on mechanical and microstructural response of CrCoNi and CrCoNiSi alloys. At cryogenic temperatures, the microstructural and mechanical evolution of these alloys show significant changes:

Effect of temperature on microstructural features

- A moderate change in ductile to more brittle fracture morphologies is observed at lower temperature, but some dimples are persisting.
- The formation of deformation twins is accelerated at lower temperatures, as demonstrated in EBSD maps. This indicates the enhanced ability of materials to accommodate plastic deformation.

Thèse accessible à l'adresse : https://theses.insa-lyon.fr/publication/2025ISAL0036/these.pdf © [T. Langlois], [2025], INSA Lyon, tous droits réservés

- As reported in the literature, the SFE values are reduced at lower temperatures, which favours deformation mechanisms for enhanced ductility.

Effect of temperature on mechanical properties

- The tensile properties of all alloys improve significantly at 110 K compared to 293 K. Yield strength (YS), ultimate tensile strength (UTS), and elongation at rupture (ε_f) all show significant enhancement, with Co33 and Co33Si6 alloys demonstrating the most significant improvements.
- The fracture toughness at cryogenic temperatures remains well-maintained in CrCoNi alloys, with only moderate embrittlement observed.

5.7 Concluding remarks

In this chapter, the effects of cobalt and silicon on both mechanical and microstructural evolutions have been analysed. The impact of temperature was also investigated using various mechanical testing methods, providing a extensive understanding of how composition and temperature influence the performance of the alloys.

Moreover, the measurements in this chapter allowed us to evaluate the mechanical properties of the selected Co10Si6 alloy. This composition, optimised from sustainable footprints and mechanical predictions in Chapter 4, has demonstrated excellent mechanical performance. Co10Si6 closely matches the mechanical performance of the benchmark CrCoNi (Co33) alloy, both at room and cryogenic temperatures, showing its potential for meeting both our performance and sustainability objectives.

The findings from Chapters 4 and 5 placed Co10Si6 as a solid material candidate for good balance between sustainability and mechanical performance. The experimental mechanical results obtained in Chapter 5 serve to validate the predictions made in Chapter 4 regarding the mechanical properties. Additionally, the sustainability model developed for raw material footprints can be expanded to address factors such as processability, scalability, and energy consumption. These considerations are essential when evaluating the potential of Co10Si6 for industrial applications.

Thèse accessible à l'adresse : https://theses.insa-lyon.fr/publication/2025ISAL0036/these.pdf © [T. Langlois], [2025], INSA Lyon, tous droits réservés

6 Discussion and conclusion

Contents

6.1 Comprehensive discussion ---------- 222

6.1.1 Validation of the material's properties ---------- 223

6.1.2 Industrial-scale considerations ---------- 226

6.2 Conclusion ---------- 228

6.1 Comprehensive discussion

In this final chapter, we critically evaluate the methodology developed throughout this work to determine its reliability and practical relevance, with two primary considerations:

- **Accuracy of the predictive models**: By comparing the numerical estimates of mechanical properties with those obtained experimentally, we can evaluate how well our models capture the impact of composition on the mechanical performance and identify discrepancies or limitations. Limitations and improvements of the sustainability model are also discussed.
- **Industrial scale processability**: In this part, we focus on the feasibility of these alloys for large-scale manufacturing. This includes examining the robustness of their processing routes such as casting and thermomechanical treatments, as well as their potential industrial applications.

Thèse accessible à l'adresse : https://theses.insa-lyon.fr/publication/2025ISAL0036/these.pdf © [T. Langlois], [2025], INSA Lyon, tous droits réservés

6.1.1 Validation of the material's properties

The **solid solution strengthening (σ_{ss})** prediction model shown great accuracy across most C-MPEAs compositions from literature, as illustrated *Figure 4.10* and *Figure 4.11*. However, when the cobalt content is reduced in $Co_x(CrNi)_{100-x}$ alloys, the model tends to predict higher σ_{ss} values than those observed experimentally. Testing on Arc200 alloys revealed a moderate decrease in σ_{ss} as cobalt content decreased, suggesting that the model overestimates strengthening in these compositions. Several factors are likely to contribute to the observed discrepancy:

- The significant anisotropy in cobalt-lean alloys (illustrated in *Table 0.1* in the Appendix of Chapter 3) can destabilise the FCC phase, with isotropic assumptions less accurate in Varvenne model.
- The use of simplified elastic and isotropic assumptions is only accurate for isotropic materials and the current model neglects local size mismatch effect [121].
- Applying Vegard's rule for elastic constants assumes a linear change in properties with composition, even though non-linear evolution of materials properties in Co-Cr-Ni are modelled [150].

Overall, while this model effectively captures σ_{ss} in near-equiatomic compositions, it faces limitations in systems with lower phase stability, significant anisotropy and more complex chemistries.

Predicted and experimental results for the **Stacking Fault Energy (SFE)** of CrCoNi alloys are well aligned, providing a clear picture of how cobalt influences SFE. Experimental results for CrCoNiSi alloys allow identifying the effect of silicon too, as illustrated in *Table 6.1*.

Table 6.1. Predicted and experimental SFE in CrCoNi alloys, experimental evolution with Silicon content.

	Co-Cr-Ni systems		Co-Cr-Ni-Si systems
Base alloy	**Predicted SFE (mJ/m2)**	**Experimental SFE (mJ/m2)**	**Experimental SFE relation (mJ/m2)**
Cr33Co33Ni33	17.57	25.60	25.60 - 1.83 (at.% Si)
Cr40Co20Ni40	32.07	31.51	31.51 - 1.78 (at.% Si)
Cr45Co10Ni45	42.72	38.25	38.25 - 1.91 (at.% Si)

Thèse accessible à l'adresse : https://theses.insa-lyon.fr/publication/2025ISAL0036/these.pdf © [T. Langlois], [2025], INSA Lyon, tous droits réservés

- Both predictions and experimental results confirm that SFE decreases as cobalt content increases in CrCoNi alloys.
- The experimental results, obtained from powder XRD measurements are slightly overestimating SFE values compared to TEM measurements. Nevertheless, both measurement methods showed similar SFE evolution with silicon addition.
- In the Co-Cr-Ni-Si systems from this work, SFE decreases by approximately 1.84 $mJ.m^{-2}$ per 1 at.% Si added. This trend aligns with previous findings: Jeong et al. [172] reported a drop of 4 $mJ.m^{-2}$ per 1 wt.% Si (roughly 2 $mJ.m^{-2}$ per 1 at.% Si) for Fe-18Mn-0.6C TWIP steel, and Tian et al. [173] measured a reduction of 1.3 $mJ.m^{-2}$ per 1 at.% Si in Fe–Mn–C alloys.

These findings indicates that by carefully introducing silicon into cobalt-lean alloys, it is possible to tailor SFE of the material and therefore optimise TRIP and TWIP mechanisms for enhanced strength and ductility.

Regarding the developed **sustainability footprints** model, several limitations and potential improvements have been identified:

- The current model focuses only on primary resources. As more data on secondary resources become available, e.g. refined materials [174] or recycled waste to produce C-MPEAs [69], updating the model to incorporate new intrinsic properties (e.g., energy and carbon footprints) and account for the updated geographic origins of these secondary materials would result in a more comprehensive footprint assessment.
- The elemental footprints only account for extraction and transportation steps, rather than covering the entire life cycle. Energy and carbon footprints tied to manufacturing processes (casting, hot rolling, cold rolling annealing, etc) and end-of-life scenarios remain unexplored. Other studies place greater emphasis on processing footprints and potential mitigation strategies [175, 176].
- The decision to focus on elemental footprints was guided by the finding that share of raw material dominate the footprints in laboratories. Carbon

Thèse accessible à l'adresse : https://theses.insa-lyon.fr/publication/2025ISAL0036/these.pdf © [T. Langlois], [2025], INSA Lyon, tous droits réservés

emission database from the "CES 1point5 lab" [177] indicates that across hundreds of French laboratories, approximately 50% of total emissions originate from purchases, including raw materials and equipment, as illustrated in *Figure 6.1*. The shares of electricity and other categories in laboratory emissions are significantly lowers.

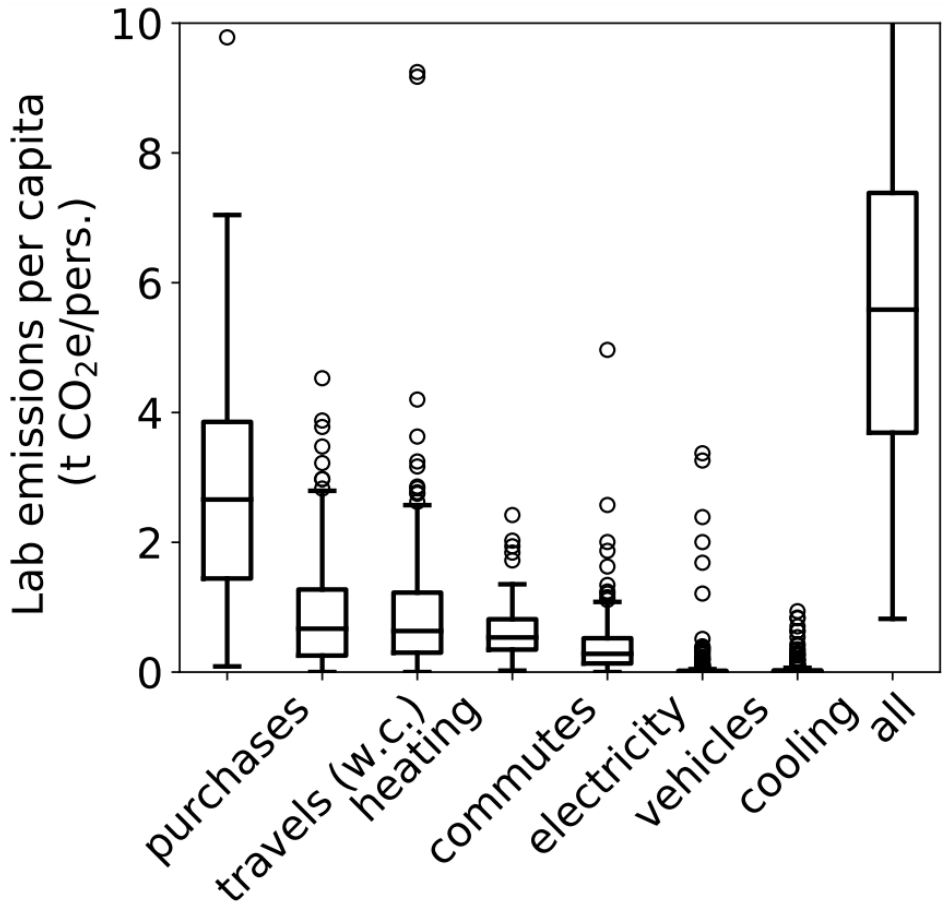


Figure 6.1. Comparison of French laboratory emissions per capita per emission type [177]. This study underlines the low emission of the electricity category in the database due to the French electricity system.

In summary, the predicted mechanical properties are sufficiently accurate, and the sustainability footprints model incorporates a large quantity of criteria, reinsuring the feasibility of a multi-scale optimisation that integrates mechanical and sustainability metrics.

Although the predictive mechanical models, sustainability footprints and experimental results provide solid insights for material selection, translating these findings into the real-world industry present some processability challenges.

Thèse accessible à l'adresse : https://theses.insa-lyon.fr/publication/2025ISAL0036/these.pdf © [T. Langlois], [2025], INSA Lyon, tous droits réservés

6.1.2 Industrial-scale considerations

Despite their promising mechanical properties demonstrated in laboratory experiments, some practical challenges emerge when considering industrial-scale production of CrCoNiSi alloys.

Achieving superior mechanical performance involved multiple **thermomechanical treatments**, such has homogenisation, rolling or annealing.

- These processes are time- and energy-intensive. For example, for one tonne of steel produced industrially in China in 2013, reheating, hot rolling and cold rolling were emitting 60.82 $kgCO_2$, 51.80 $kgCO_2$, 66.90 $kgCO_2$, respectively [175]. Some additive manufacturing methods (SLM: selective laser melting; EBM: electron beam melting; DED: direct energy deposition; WAAM: wire arc additive manufacturing; AFSD: additive friction stir deposition) are less energy intensive and do not require post-processing treatments [178]. A study of the processability of C-MPEAs using these methods could find a potential way to further reduce the sustainability footprints of these alloys [179].

- A further challenge in the processing of CrCoNiSi alloys is the narrow thermal window for maintaining a stable FCC structure. Being close to the technical limitation of the equipment, hot rolling heat-treatment in air furnaces led to BCC/B2 and sigma precipitation, respectively in compositions with 6 and 9 at.% Si. In comparison, heat-treatments in fluidised-bed furnace for the homogenisation of compression samples or the annealing of cold rolled tensile specimens did not produce any secondary phase.

- As industrial component sizes are typically larger than laboratory specimens, applying these processes in the correct temperature range and without thermal gradient can become significantly more challenging.

Nonetheless, the selected compositions have noticeable advantages compared to conventional materials, particularly in **cryogenic applications**:

- CrCoNi and CrCoNiSi alloys exhibits superior strength, ductility and toughness properties at low temperature, ideal for industrial applications in extreme environments.

Thèse accessible à l'adresse : https://theses.insa-lyon.fr/publication/2025ISAL0036/these.pdf © [T. Langlois], [2025], INSA Lyon, tous droits réservés

- Recent findings indicate that hydrogen can even strengthen C-MPEAs (*Figure 6.2 c and d* [12]), unlike the catastrophic hydrogen embrittlement (HE) observed in some steels where brittle BCC-α' martensite is formed under strain with a hydrogen environment. In the case of C-MPEAs, the formation of HCP-ε martensite under strain lowers hydrogen diffusivity rate [180].

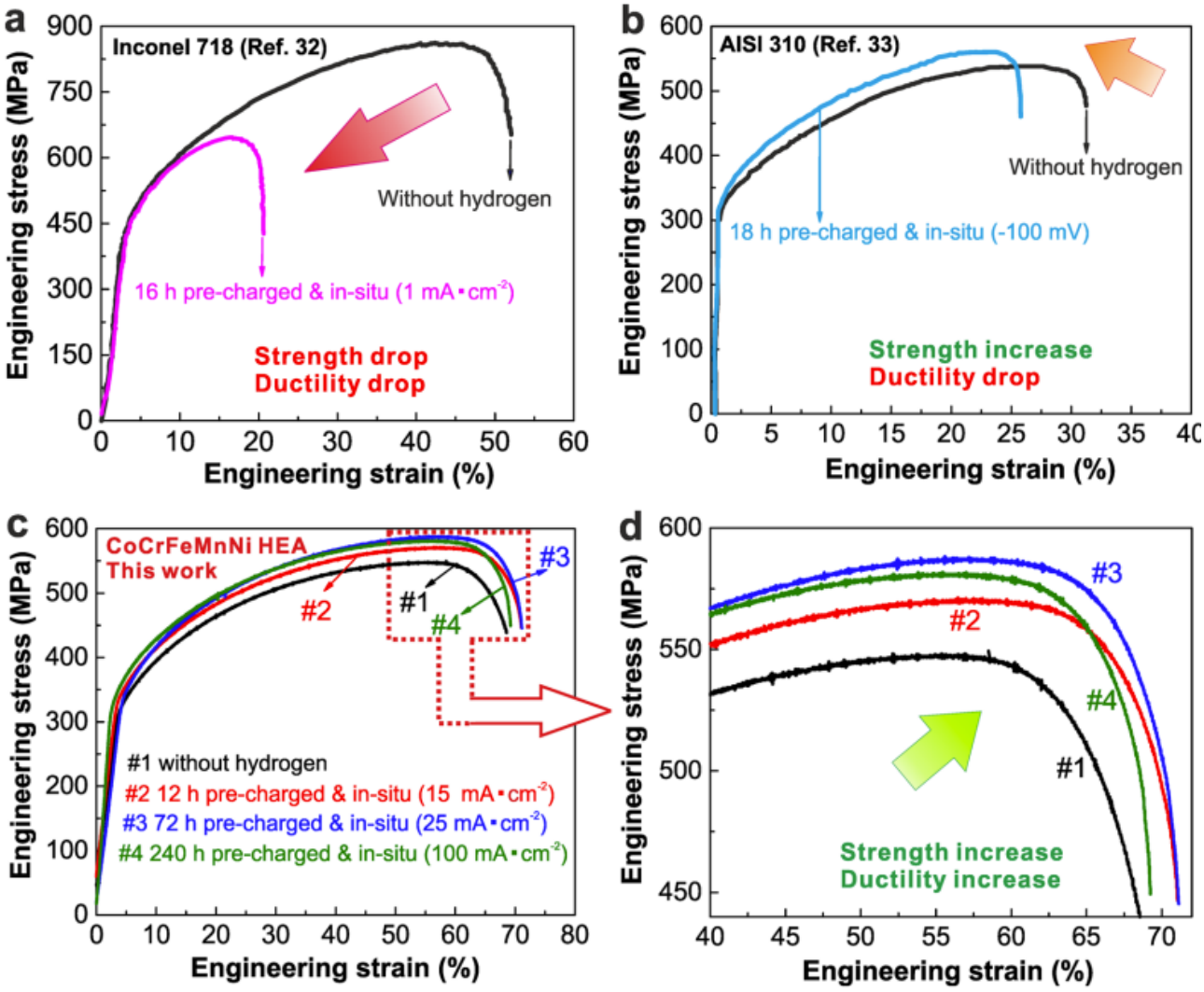


Figure 6.2. Engineering stress-strain curves under various in-situ hydrogen charging conditions of (a) Inconel 718; (b) AISI 310; (c, d) CoCrFeMnNi [12].

These aspects of C-MPEAs make them promising candidates for liquid hydrogen storage and transportation. By facilitating greener energy use, they may additionally contribute to broader sustainability objectives.

Thèse accessible à l'adresse : https://theses.insa-lyon.fr/publication/2025ISAL0036/these.pdf © [T. Langlois], [2025], INSA Lyon, tous droits réservés

6.2 Conclusion

This thesis introduced a novel approach to design multi-principal element alloys (MPEAs) that systematically integrates sustainability considerations. Investigating the Co–Cr–Ni system, well-known for its superior strength–ductility balance yet complicated by cobalt's environmental and societal challenges, our research objectives focused on:

- Evaluating the sustainability footprints of raw materials.
- Combining mechanical and sustainability metrics in alloy design.
- Assessing the mechanical properties of newly developed compositions.
- Investigating the effects of cobalt, silicon, and cryogenic temperatures on CrCoNi and CrCoNiSi alloys' microstructures and properties.

To address these objectives, both computational and experimental methodologies were employed:

- A sustainability footprint toolkit was developed to capture the ecological, economic, and ethical impacts of each raw materials and was adapted to alloys.
- CALPHAD, solid-solution strengthening and stacking-fault energy models were used to evaluate mechanical properties in the FCC domain of Co-Cr-Ni compositions.
- These models were incorporated in a multi-objective optimisation that balances mechanical and sustainability metrics.
- A fast-alloying process was introduced to rapidly evaluate multiple compositions with minimal material usage, while larger CrCoNi and CrCoNiSi specimens were tested for tensile and toughness properties at room and cryogenic temperatures.

Key results that address the research questions include:

Thèse accessible à l'adresse : https://theses.insa-lyon.fr/publication/2025ISAL0036/these.pdf © [T. Langlois], [2025], INSA Lyon, tous droits réservés

- Sustainability-wise, cobalt was identified as having more detrimental footprints than nickel and chromium, whereas Silicon showed one of the lowest sustainability impacts.
- Mechanically, reducing cobalt content lowered mechanical performance, but silicon addition recovered both strength and ductility. These elements, as well as temperature, play a significant role on SFE. TRIP and TWIP deformation mechanisms are promoted for low SFE, improving the overall strength–ductility balance.

By developing a sustainability footprint toolkit that goes beyond conventional environmental assessments to encompass economic and societal dimensions, this thesis offers a more holistic perspective on material impacts. Also contributing to **original findings**, the multi-objective design framework that equally integrates sustainability and mechanical metrics offers a new approach toward responsible alloy design.

From an experimental standpoint, some unknown areas were explored: The effect of silicon on non-equimolar, cobalt-lean CrCoNi compositions, as well as the effect of temperature on mechanical and microstructures features was investigated, showing the potential of these compositional regions for cryogenic applications using materials with lower sustainability impacts.

The computational and experimental challenges faced in this thesis, ranging from accuracy of the predictions to industrial-scale considerations, illustrate the study limitations. Nevertheless, several avenues for future research have been proposed, including the use of experimental data to enhance models' reliability and the use of other manufacturing processes to mitigate microstructural defects.

By showcasing a viable process that combine mechanical performance, and sustainability impacts, this thesis illustrates how sustainability can be elevated from a peripherical consideration to a central pillar in alloy design. It is an example and a call for holistic, multi-scale approaches in the selection of future high-performance and responsible materials.

Thèse accessible à l'adresse : https://theses.insa-lyon.fr/publication/2025ISAL0036/these.pdf © [T. Langlois], [2025], INSA Lyon, tous droits réservés

Appendix

Appendix of Chapter 3

Conversion table – Atomic/Mass fractions

Alloy Name	Composition														
	Cr	Co	Ni	Si	Fe	Mn		Al	Cu	C	O	Ti	Zn	Mg	total
	(at%)	(at%)	(at%)	(at%)	(at%)	(at%)		(at%)	(at%)	(at%)	(at%)	(at%)	(at%)	(at%)	
Molar mass (g/mol)	52.00	58.93	58.69	28.09	55.85	54.94		26.98	63.55	12.01	32.00	47.87	65.38	24.31	
Cr33Co33Ni33	33.33	33.33	33.33	0.00											100.00
Cr40Co20Ni40	40.00	20.00	40.00	0.00											100.00
Cr45Co10Ni45	45.00	10.00	45.00	0.00											100.00
Co20Si3	38.80	19.40	38.80	3.00											100.00
Co20Si6	37.60	18.80	37.60	6.00											100.00
Co20Si9	36.40	18.20	36.40	9.00											100.00
Co10Si3	43.65	9.70	43.65	3.00											100.00
Co10Si6	42.30	9.40	42.30	6.00											100.00
Co10Si9	40.95	9.10	40.95	9.00											100.00

Alloy Name	Composition														
	Cr	Co	Ni	Si	Fe	Mn		Al	Cu	C	O	Ti	Zn	Mg	total
	(w%)	(w%)	(w%)	(w%)	(w%)	(w%)		(w%)	(w%)	(w%)	(w%)	(w%)	(w%)	(w%)	
Cr33Co33Ni33	30.65	34.74	34.60	0.00	0.0	0.0	0.0	0.0	0.0	0.0	0.0	0.0	0.0	0.0	100.00
Cr40Co20Ni40	37.10	21.02	41.88	0.00	0.0	0.0	0.0	0.0	0.0	0.0	0.0	0.0	0.0	0.0	100.00
Cr45Co10Ni45	42.00	10.58	47.42	0.00	0.0	0.0	0.0	0.0	0.0	0.0	0.0	0.0	0.0	0.0	100.00
Co20Si3	36.53	20.70	41.24	1.53	0.0	0.0	0.0	0.0	0.0	0.0	0.0	0.0	0.0	0.0	100.00
Co20Si6	35.95	20.37	40.58	3.10	0.0	0.0	0.0	0.0	0.0	0.0	0.0	0.0	0.0	0.0	100.00
Co20Si9	35.35	20.03	39.90	4.72	0.0	0.0	0.0	0.0	0.0	0.0	0.0	0.0	0.0	0.0	100.00
Co10Si3	41.36	10.42	46.69	1.54	0.0	0.0	0.0	0.0	0.0	0.0	0.0	0.0	0.0	0.0	100.00
Co10Si6	40.70	10.25	45.94	3.12	0.0	0.0	0.0	0.0	0.0	0.0	0.0	0.0	0.0	0.0	100.00
Co10Si9	40.01	10.08	45.16	4.75	0.00	0.00	0.00	0.00	0.00	0.00	0.00	0.00	0.00	0.00	100.00

Figure 0.1. Conversion table from atomic fraction to mass fraction in Excel.

Thèse accessible à l'adresse : https://theses.insa-lyon.fr/publication/2025ISAL0036/these.pdf © [T. Langlois], [2025], INSA Lyon, tous droits réservés

Script for TC-Python

```python
from matplotlib import pyplot as plt
import numpy as np
import mpltern
from tc_python import *

database = "TCHEA5"
dependent_element = "Co"
composition = {"Co": 0.1, "Cr": 0.1, "Ni":0.1, "Si": 0.03}  # in mole fraction, starting point for calculation
temp = 1000 + 273.15
elements = list(composition.keys())
x_axis_element = "Cr"
xmin = 0
xmax = 1
y_axis_element = "Ni"
ymin = 0
ymax = 1

with TCPython() as session:
    session.set_cache_folder(".\cache")
    system = (session.
              select_database_and_elements(database, elements).
              get_system())

    calculator = system.with_phase_diagram_calculation()

    calculator.set_condition(ThermodynamicQuantity.temperature(), temp)

    for element in elements:
        if not "Co" in element:
            calculator.set_condition(ThermodynamicQuantity.mole_fraction_of_a_component(element), composition[element])

    xmax += -composition["Si"]
    ymax += -composition["Si"]
    zmin = xmin
    zmax = xmax
    phase_diagram = (calculator.
                     with_first_axis(CalculationAxis(ThermodynamicQuantity.mole_fraction_of_a_component(x_axis_element)).
                                     set_min(xmin).
                                     set_max(xmax)).
                     with_second_axis(CalculationAxis(ThermodynamicQuantity.mole_fraction_of_a_component(y_axis_element)).
                                      set_min(ymin).
                                      set_max(ymax)).
                     calculate())

    result_data = phase_diagram.get_values_grouped_by_stable_phases_of("M-P {}".format(x_axis_element),
                                                                       "M-P {}".format(y_axis_element))

    # these are result value groups, one for each phase. not sure what that really gives us...
    # from these groups we can unpack x, y and label
    groups = result_data.get_lines()
    invariants = result_data.get_invariants()

    ax = plt.subplot(projection='ternary', ternary_sum=97)

    # groups is now a dictionary with 5 keys, one for each phase that is present in this section.
    # but the content of every key is a result group, with the handles x, y and label.
    # label contains the phase name, x y contain the x y coordinates that we got into result_data
    # So we have to call them like this:
    for phase in groups.keys():
        x_coord = np.array(groups[phase].x)
        y_coord = np.array(groups[phase].y)
        z_coord = zmax*100 - x_coord - y_coord # The ternary plot requires also the z-coordinate for the dependent element
        # The ternary plots in the order of y, z, x
        plt.plot(y_coord, z_coord, x_coord, label=groups[phase].label)

    x_inv = np.array(invariants.x)
    y_inv = np.array(invariants.y)
    z_inv = zmax*100 - x_inv - y_inv
    plt.plot(y_inv, z_inv, x_inv, label=invariants.label, color='Red')

    # Ternary plot settings
    ax.set_ternary_lim(
        ymin*100, ymax*100,
        zmin*100, zmax*100,
        xmin*100, xmax*100
    )
    ax.set_tlabel(list(composition.keys())[2])
    ax.set_rlabel(list(composition.keys())[1])
    ax.set_llabel(list(composition.keys())[0])
    ax.grid()
    ax.set_title("CoCrNi-"+str(composition["Si"]*100)+"Si system")
    plt.legend()
    plt.show()
```

Figure 0.2. Python Script for pseudo-ternary diagrams using Visual Studio and TC-Python.

Thèse accessible à l'adresse : https://theses.insa-lyon.fr/publication/2025ISAL0036/these.pdf © [T. Langlois], [2025], INSA Lyon, tous droits réservés

```python
import numpy as np
from tc_python import *
import json
import multiprocessing as mp
import csv
folder = r'C:\Users\s222054963\JupyterLab\ThesisWorkflow\3-Mech\4-TCPython\Results'

def init_tc_python(e1:str,e2:str,e3:str,e4:str,e5:str, database:str, temperature:int):
    print('Init TC-Python')
    start_api_server()
    global start, eq_calculation
    start = SetUp()
    start.set_ges_version(5)
    start.set_cache_folder(os.path.basename(__file__) + "_cache")
    elements = [e1,e2,e3,e4,e5]

    eq_calculation = (
        start.select_database_and_elements(database, elements)
            .get_system()
            .with_single_equilibrium_calculation()
            .set_condition("T", temperature) #in Kelvin
    )


def clean_up_tc_python():
    print('Closes all TC-Python connections')
    PROCESSES = 4
    pool = mp.Pool(PROCESSES, initializer=init_tc_python)
    pool.map(clean_up_tc_python_single_instance, range(PROCESSES))


def clean_up_tc_python_single_instance(index):
    print('Closes TC-Python:{}'.format(index))
    stop_api_server()


def get_composition_conditions():
    lists_of_conditions = []
    min_composition = 1e-7
    delta = 0.25
    k = int(1 / delta + 1)

    list_of_x_1 = np.linspace(min_composition, 1, k)
    for x_1 in list_of_x_1:
        max_2 = 1 - x_1 + delta
        list_of_x_2 = np.arange(min_composition, max_2, delta)
        for x_2 in list_of_x_2:
            max_3 = 1 - x_1 - x_2 + delta
            list_of_x_3 = np.arange(min_composition, max_3, delta)
            for x_3 in list_of_x_3:
                max_Fe = 1 - x_1 - x_2 - x_3 + delta
                list_of_x_Fe = np.arange(min_composition, max_Fe, delta)
                for x_Fe in list_of_x_Fe:
                    conditions = {
                        "X(1)": x_1,
                        "X(2)": x_2,
                        "X(3)": x_3,
                        "X(Fe)": x_Fe}
                    lists_of_conditions.append(conditions)

    return lists_of_conditions
```

Figure 0.3. Python script for stable phase identifications in quinary subsystems with Visual Studio and TC-Python

Thèse accessible à l'adresse : https://theses.insa-lyon.fr/publication/2025ISAL0036/these.pdf © [T. Langlois], [2025], INSA Lyon, tous droits réservés

Bulk composition certificates

SPECTROMETER SERVICES PTY. LTD.
SPECTROGRAPHIC AND CHEMICAL ANALYSTS
A.B.N. 20 004 505 426
ACN 004 505 426
206 Newlands Road, Coburg 3058

Phone (03) 9350 1766
Fax (03) 9354 1052

DEAKIN UNIVERSITY - WAURN PONDS CAMPUS
INSTITUTE FOR FRONTIER MATERIALS
LOCKED BAG 20000
GEELONG VIC 3220

ATTENTION : Alireza Vahid

Report Number : 89194
Report Date : Tuesday, May 23, 2023
Job Number : C23/851
Cust. Order No.:

Interim report only

Samples	Cr %	Ni %	Co %	Fe %	Cu %	Si %	Mn %	Al %	Zn %	Ti %
1	28.1	65.9	5.05	0.26	0.02	0.24	<0.01	0.10	0.01	0.24
2	36.6	35.7	27.2	0.11	0.01	0.07	0.01	0.06	0.01	0.01
3	18.3	50.4	30.8	0.12	0.01	0.05	<0.01	0.06	0.02	0.01
4	54.4	29.6	15.5	0.14	0.02	0.08	<0.01	0.05	0.02	0.01
5	27.9	24.6	46.8	0.17	0.01	0.15	<0.01	0.07	0.02	0.02

Methods Used:
ICP-AES

Notes:
All elements reported as wt/wt %

Figure 0.4. Certified mass percentages of our GDOES-calibration samples (measured by ICP-AES at Spectrometer Services)

Temperature evolution in powder-annealing cycle

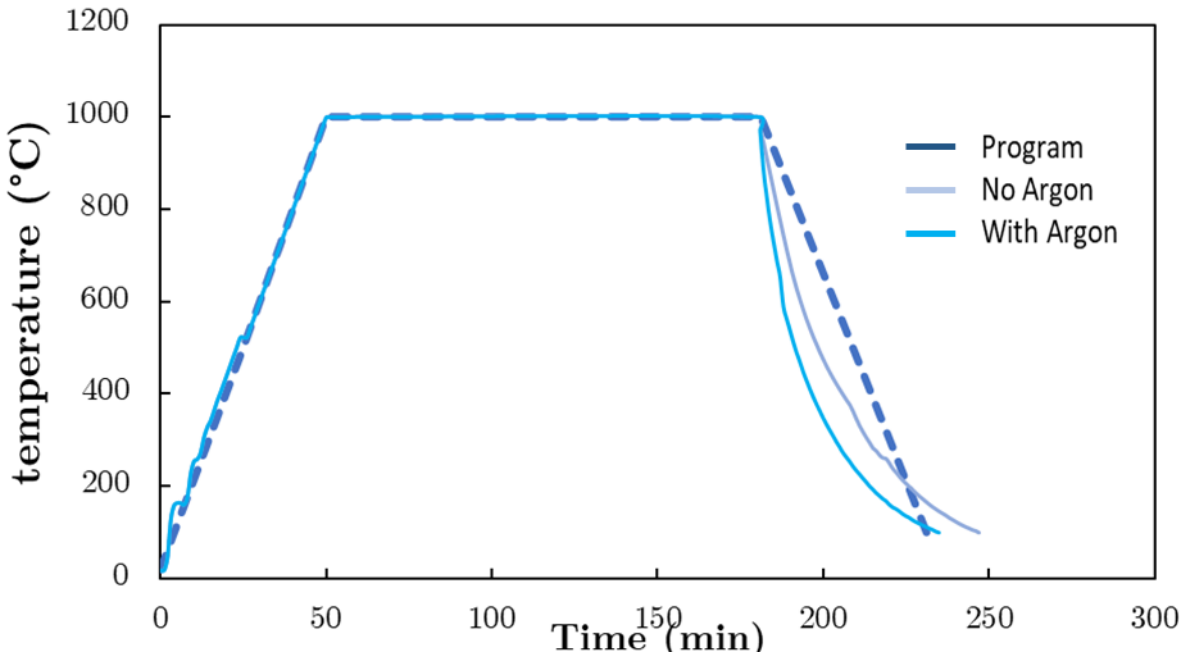


Figure 0.5. Temperature evolution in an annealing cycle of deformed powder.

Thèse accessible à l'adresse : https://theses.insa-lyon.fr/publication/2025ISAL0036/these.pdf © [T. Langlois], [2025], INSA Lyon, tous droits réservés

Temperature evolution with time for cryogenic impact tests

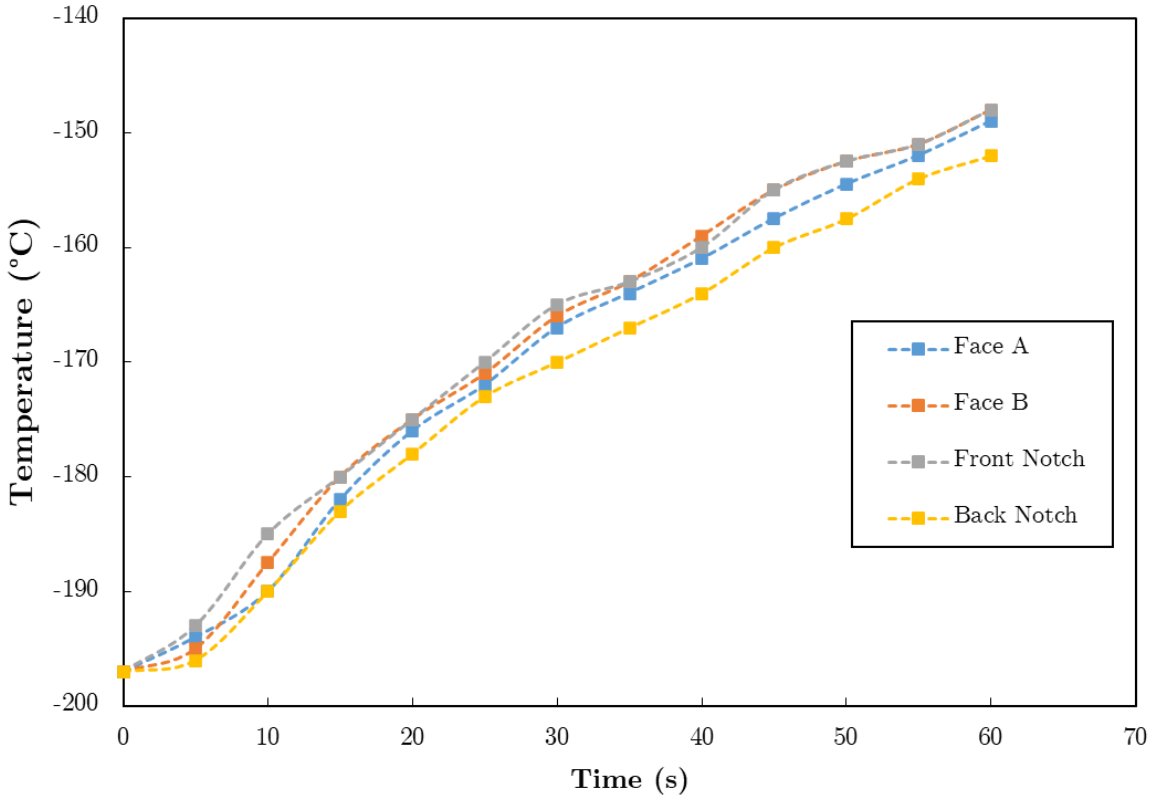


Figure 0.6. Temperature evolution of AISI 316L after removal from the nitrogen dewar.

Table 0.1. Atomistic calculation of elastic constants (cij). Shear modulus (μ), Poisson ratio (ν) and anistropy (A); obtained by Voigt average.

x (at% Co)	c_{11}	c_{12}	c_{44}	μ (GPa)	ν	A
5	239.97	208.14	108.22	71.3	0.353	6.80
10	251.72	204.54	113.94	77.8	0.342	4.83
15	259.35	202.53	120.73	83.8	0.332	4.25
20	267.63	199.93	126.27	89.3	0.323	3.73
25	272.61	197.77	131.72	94.0	0.315	3.52
30	276.64	193.23	136.37	98.5	0.306	3.27
33.3	276.96	190.31	137.78	100	0.302	3.18

Thèse accessible à l'adresse : https://theses.insa-lyon.fr/publication/2025ISAL0036/these.pdf © [T. Langlois], [2025], INSA Lyon, tous droits réservés

Appendix of Chapter 4

Python script for ternary maps

```python
from matplotlib import pyplot as plt
from tc_python import *
from Coloured_Ternary_diagram import *

# Define the ternary subsystems within Co-Cr-Fe-Mn-Ni space
# their position is important to have the correct neighbours

systems = [
    ("CrCoNi", {"Co": 0.1, "Cr": 0.1, "Ni": 0.1}, "Cr", "Ni"),
    ("CrCoFe", {"Co": 0.1, "Cr": 0.1, "Fe": 0.1}, "Cr", "Fe"),
    ("CrMnNi", {"Cr": 0.1, "Mn": 0.1, "Ni": 0.1}, "Cr", "Ni"),
    ("CrFeNi", {"Cr": 0.1, "Fe": 0.1, "Ni": 0.1}, "Cr", "Ni"),
    ("CoFeNi", {"Co": 0.1, "Fe": 0.1, "Ni": 0.1}, "Co", "Ni"),
    ("CoMnNi", {"Co": 0.1, "Mn": 0.1, "Ni": 0.1}, "Co", "Ni"),
    ("FeMnNi", {"Fe": 0.1, "Mn": 0.1, "Ni": 0.1}, "Fe", "Ni"),
    ("CrMnFe", {"Cr": 0.1, "Mn": 0.1, "Fe": 0.1}, "Cr", "Fe"),
    ("CoCrNi", {"Co": 0.1, "Cr": 0.1, "Ni": 0.1}, "Cr", "Ni"),
    ("CoFeMn", {"Co": 0.1, "Fe": 0.1, "Mn": 0.1}, "Co", "Mn"),
    ("CrNiMn", {"Cr": 0.1, "Ni": 0.1, "Mn": 0.1}, "Cr", "Ni"),
    ("CoCrMn", {"Co": 0.1, "Cr": 0.1, "Mn": 0.1}, "Co", "Mn"),
    ("FeNiMn", {"Fe": 0.1, "Ni": 0.1, "Mn": 0.1}, "Fe", "Ni"),
    ("CoCrFe", {"Co": 0.1, "Cr": 0.1, "Fe": 0.1}, "Co", "Fe"),
    ("MnFeNi", {"Mn": 0.1, "Fe": 0.1, "Ni": 0.1}, "Mn", "Ni"),
    ("CrFeMn", {"Cr": 0.1, "Fe": 0.1, "Mn": 0.1}, "Cr", "Mn")
]

fig, axes = plt.subplots(4, 4, figsize=(20, 20)) # create the main plot


for i, (system_name, composition, x_axis_element, y_axis_element) in enumerate(systems): % we loop the system
    ax = axes[i//4, i%4]

    with TCPython() as session:
        session.set_cache_folder(".\cache")
        system = (session.
                  select_database_and_elements("TCHEA5", list(composition.keys())).
                  get_system())

        calculator = system.with_phase_diagram_calculation()
        calculator.set_condition(ThermodynamicQuantity.temperature(), 1200 + 273.15)  # 1200°C
        for element in composition:
            calculator.set_condition(ThermodynamicQuantity.mole_fraction_of_a_component(element), composition[element])

        phase_diagram = (calculator.
                         with_first_axis(CalculationAxis(ThermodynamicQuantity.mole_fraction_of_a_component(x_axis_element)).
                                         set_min(0).set_max(1)).
                         with_second_axis(CalculationAxis(ThermodynamicQuantity.mole_fraction_of_a_component(y_axis_element)).
                                          set_min(0).set_max(1)).
                         calculate())

        result_data = phase_diagram.get_values_grouped_by_stable_phases_of("M-P {}".format(x_axis_element),
                                                                           "M-P {}".format(y_axis_element))

        groups = result_data.get_lines()
        invariants = result_data.get_invariants()
        coloured_data = get_coloured_diagram(result_data)

        ax.set_xlim(0, 1)
        ax.set_ylim(0, 1)
        if i % 2 == 0:  # Flip the correct triangle in systems list
            ax.set_ylim(1, 0)


plt.show()
```

Thèse accessible à l'adresse : https://theses.insa-lyon.fr/publication/2025ISAL0036/these.pdf © [T. Langlois], [2025], INSA Lyon, tous droits réservés

Figure 0.7. Script using TC-python to plot all the ternary diagrams within the Co-Cr-Fe-Mn-Ni space at 1200°C (right plot in *Figure 4.2*).

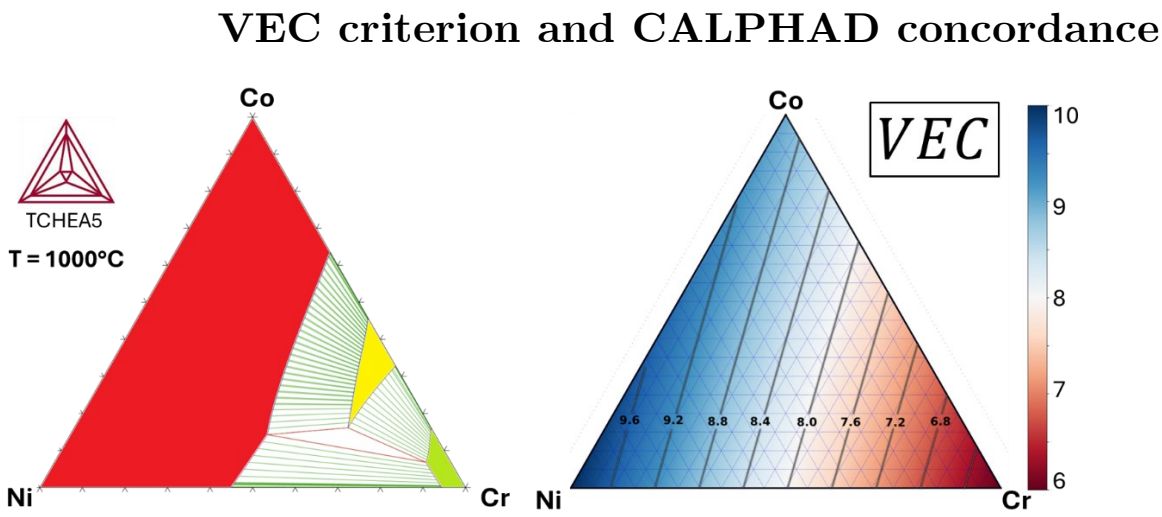


Figure 0.8. CALPHAD model (left) and VEC criterion (right; see Equation 1.3) provide similar phase predictions.

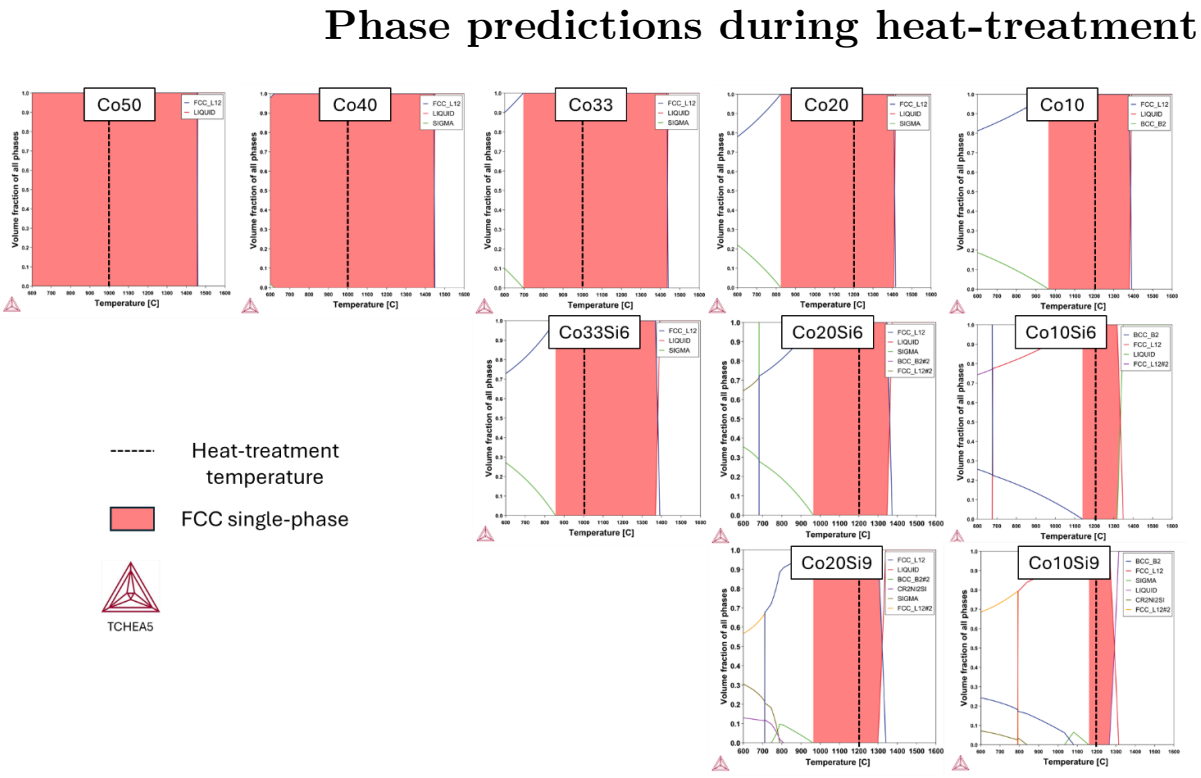


Figure 0.9. CALPHAD prediction of the stable phased at different heat-treatment temperatures for the experimental compositions.

Thèse accessible à l'adresse : https://theses.insa-lyon.fr/publication/2025ISAL0036/these.pdf © [T. Langlois], [2025], INSA Lyon, tous droits réservés

σ_{SS} maps after different heat-treatments temperatures

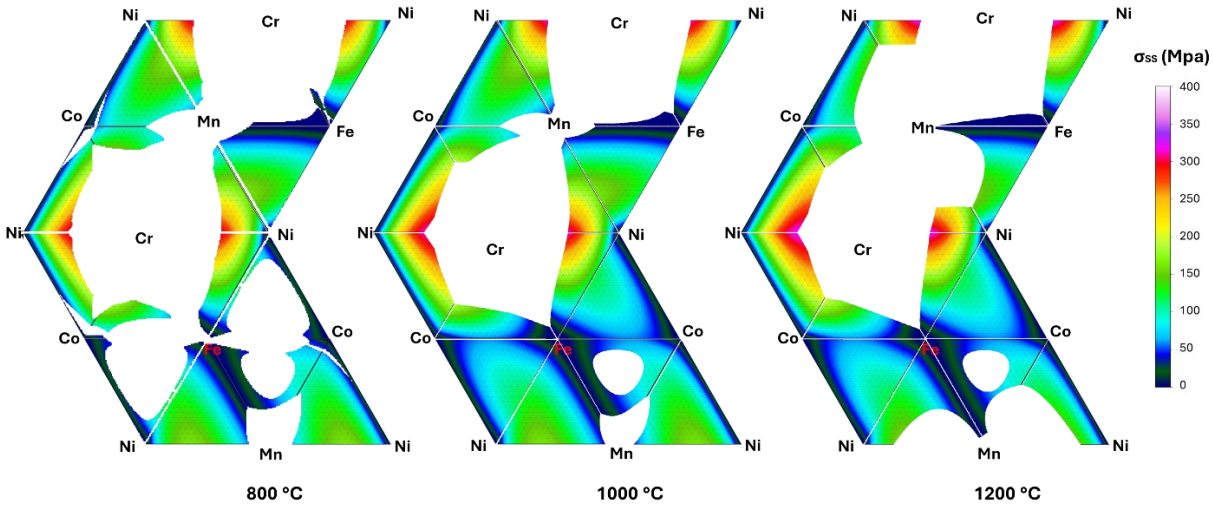


Figure 0.10. σ_{SS} maps at room temperature after heat-treatment at (left) 800°C, (middle) 1000°C and (right)1200°C.

Thèse accessible à l'adresse : https://theses.insa-lyon.fr/publication/2025ISAL0036/these.pdf © [T. Langlois], [2025], INSA Lyon, tous droits réservés

CrCoNi Mapping of the parameters in Varvenne et al. model

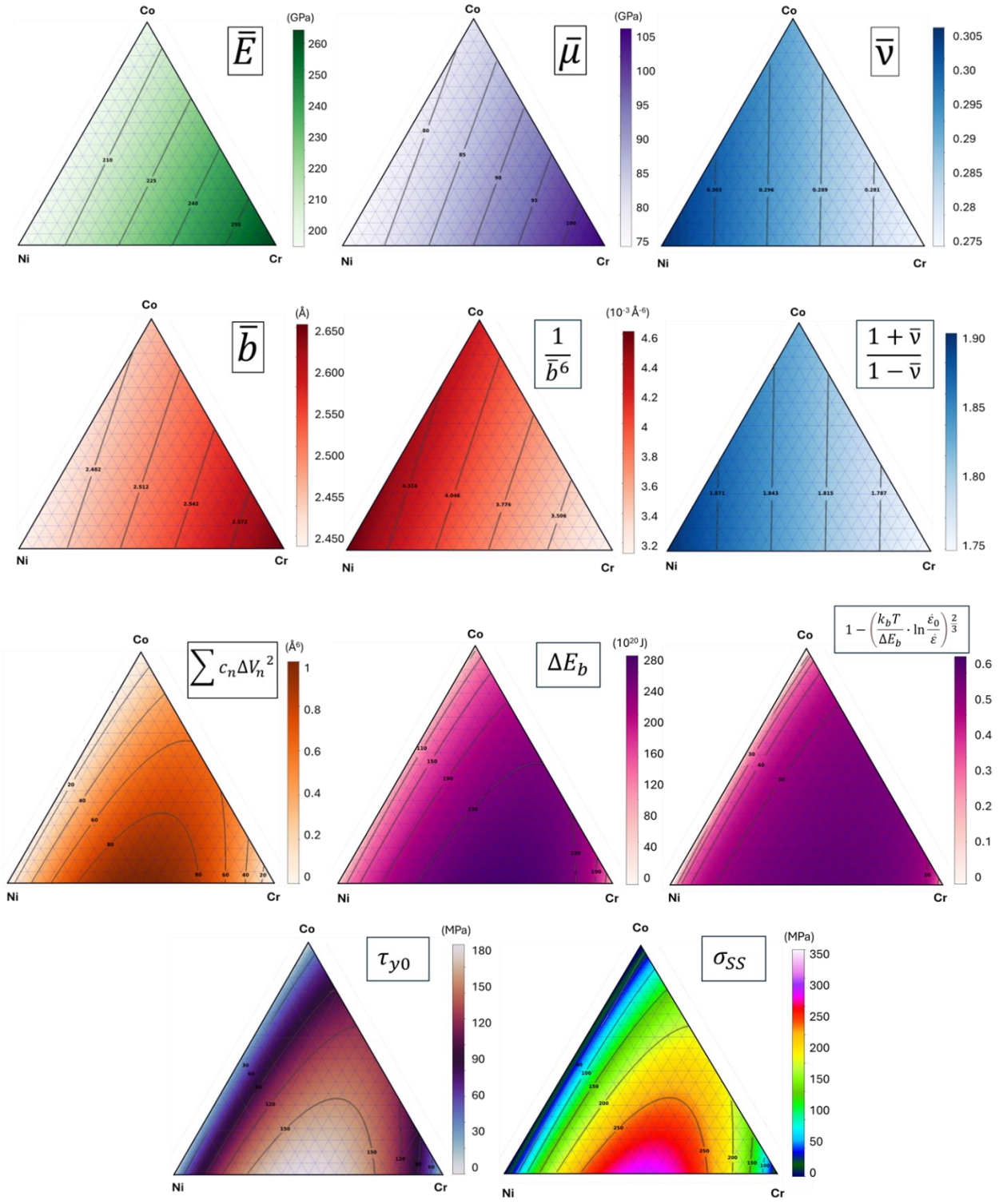


Figure 0.11. Evolution of the elastic and size parameters of the Varvenne model in the CrCoNi space (independently of the FCC limitation).

Thèse accessible à l'adresse : https://theses.insa-lyon.fr/publication/2025ISAL0036/these.pdf © [T. Langlois], [2025], INSA Lyon, tous droits réservés

Detailed sustainability performances for different alloy classes

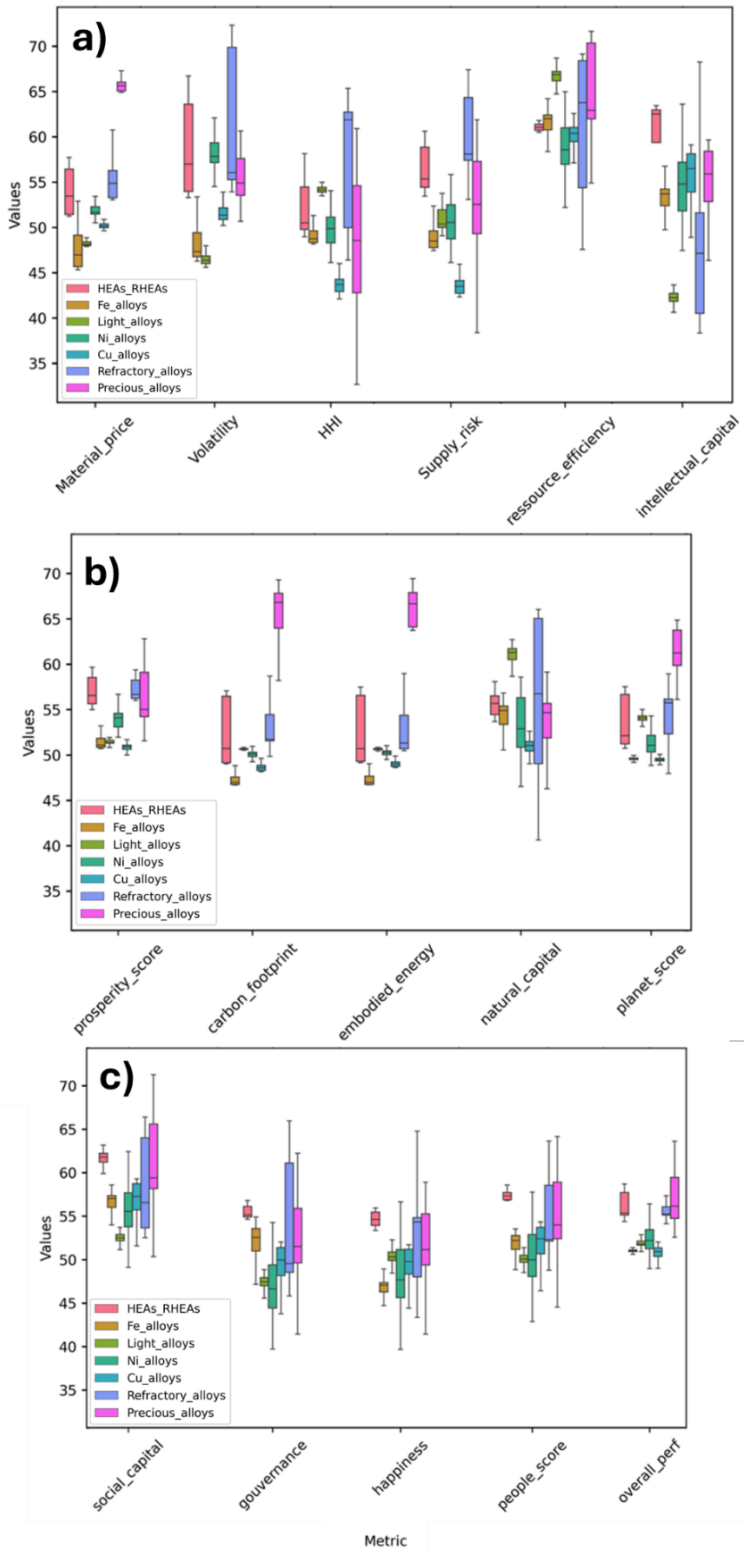


Figure 0.12. Several economic (a), environmental (b) and societal (c) indicators illustrating the sustainability performances of different alloy classes.

Thèse accessible à l'adresse : https://theses.insa-lyon.fr/publication/2025ISAL0036/these.pdf © [T. Langlois], [2025], INSA Lyon, tous droits réservés

Appendix of Chapter 5

CALPHAD calculation for Ellingham diagrams

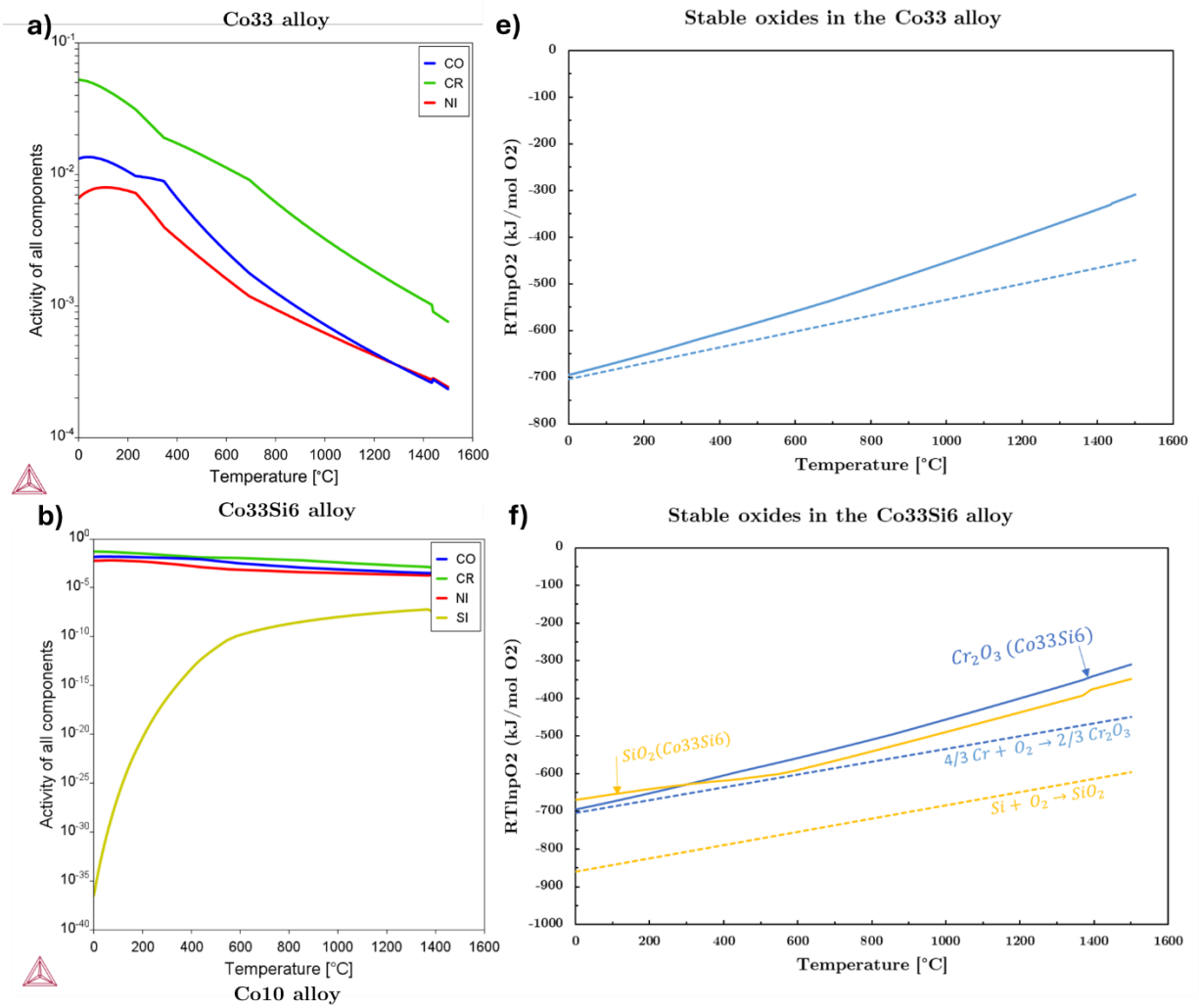


Figure 0.13. (a-d) Activities of elements in Co33, Co33Si6, Co10 and Co10Si6 (calculated with ThermoCalc2023 using the TCHEA5 database); (e-h) Corresponding energy of reaction in alloy for Cr_2O_3 and SiO_2 oxides.

Thèse accessible à l'adresse : https://theses.insa-lyon.fr/publication/2025ISAL0036/these.pdf © [T. Langlois], [2025], INSA Lyon, tous droits réservés

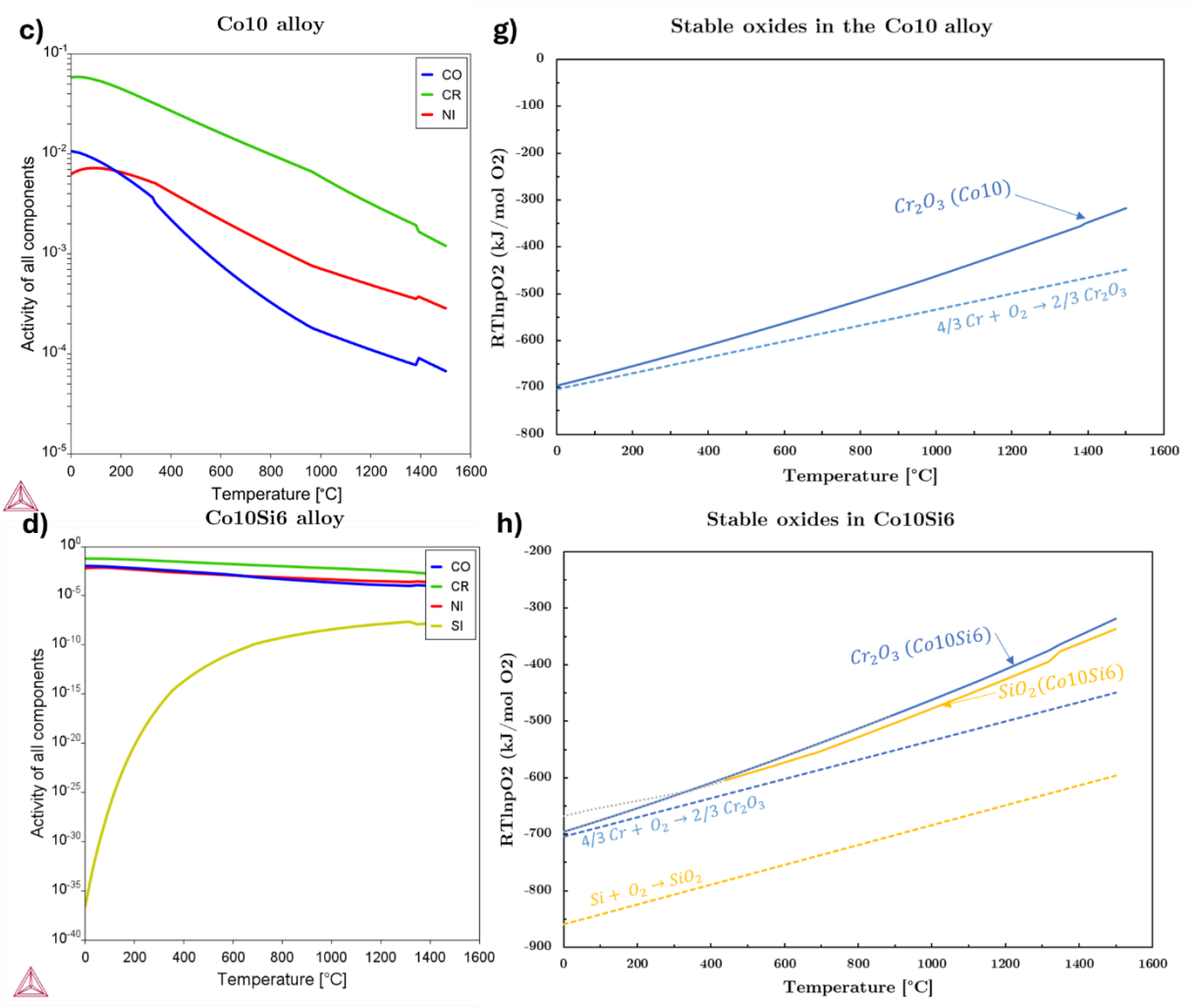


Figure 0.14. [Continued] (a-d) Activities of elements in Co33, Co33Si6, Co10 and Co10Si6 (calculated with ThermoCalc2023 using the TCHEA5 database); (e-h) Corresponding energy of reaction in alloy for Cr_2O_3 and SiO_2 oxides.

Thèse accessible à l'adresse : https://theses.insa-lyon.fr/publication/2025ISAL0036/these.pdf © [T. Langlois], [2025], INSA Lyon, tous droits réservés

Segregations in As-Cast alloys observed with EDS linescan

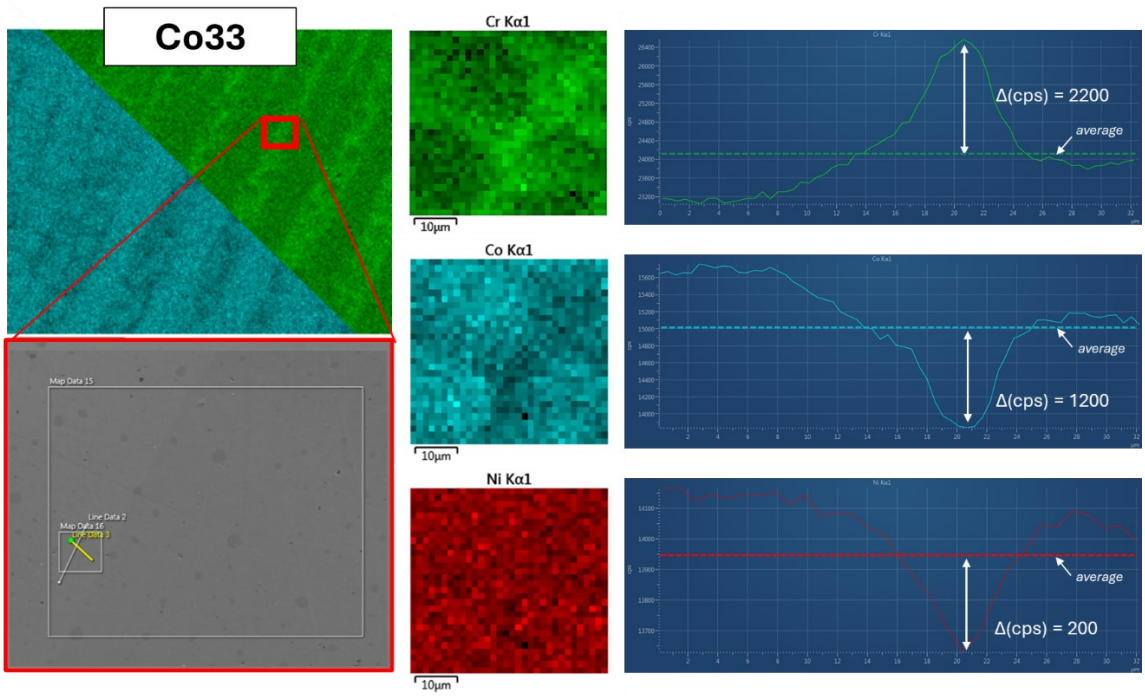


Figure 0.15. EDS linescans of the As-cast Co33 alloy with Cr (green), Co (blue) and Ni (red).

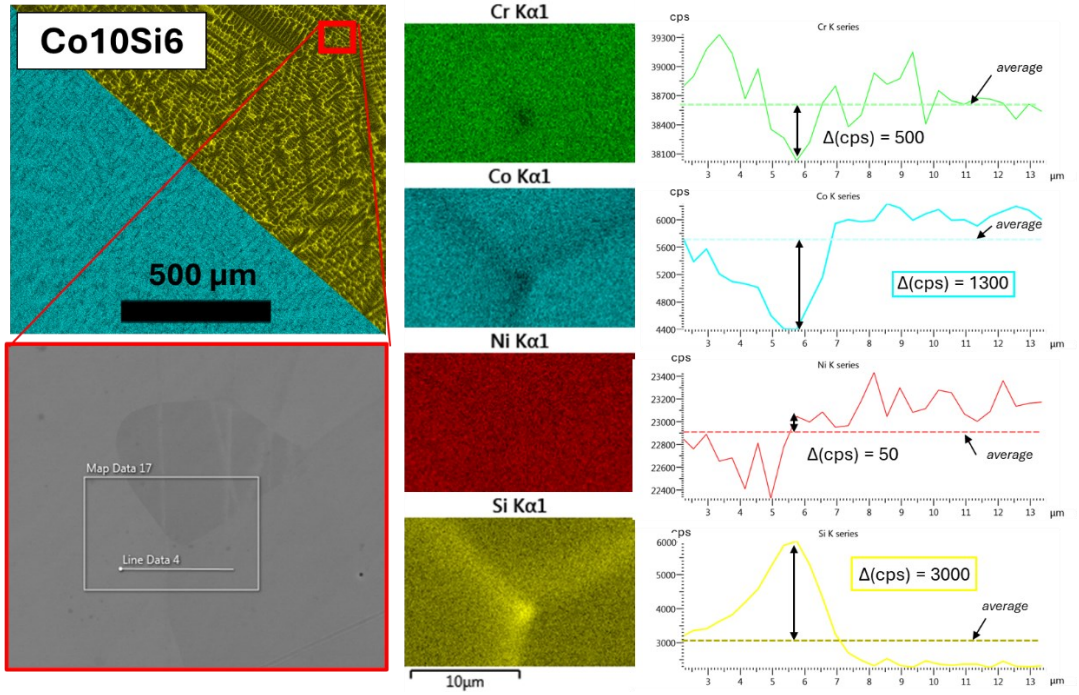


Figure 0.16. EDS linescans of the As-Cast Co10Si6 alloy with Cr (green), Co (blue), Ni (red) and Si (yellow).

Thèse accessible à l'adresse : https://theses.insa-lyon.fr/publication/2025ISAL0036/these.pdf © [T. Langlois], [2025], INSA Lyon, tous droits réservés

EDS linescan of the sigma phase in Co10Si9

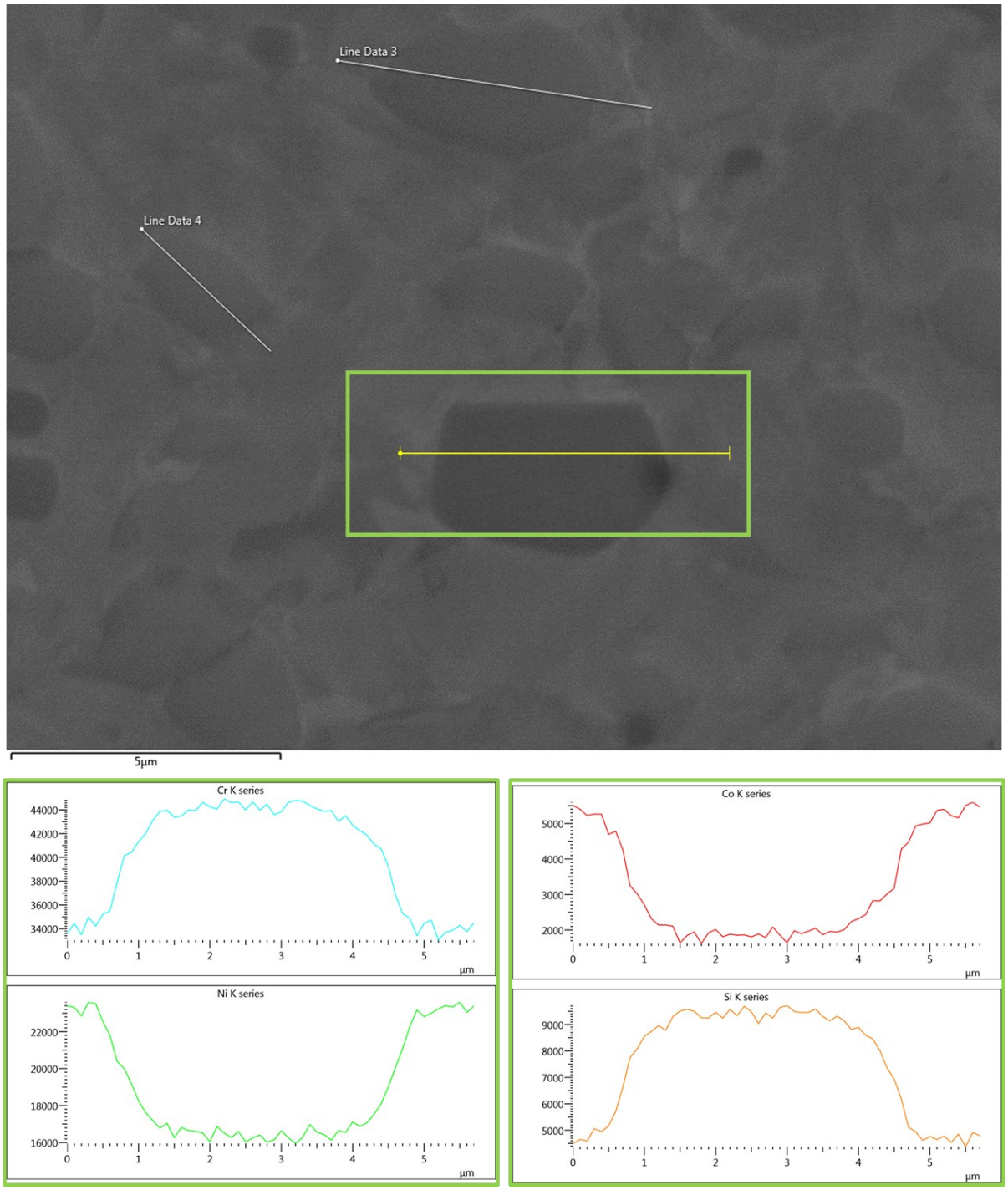


Figure 0.17. EDS linescan of the elemental distribution in the sigma phase of Co10Si6.

Thèse accessible à l'adresse : https://theses.insa-lyon.fr/publication/2025ISAL0036/these.pdf © [T. Langlois], [2025], INSA Lyon, tous droits réservés

XRD profile of Co10Si9 from Ind500

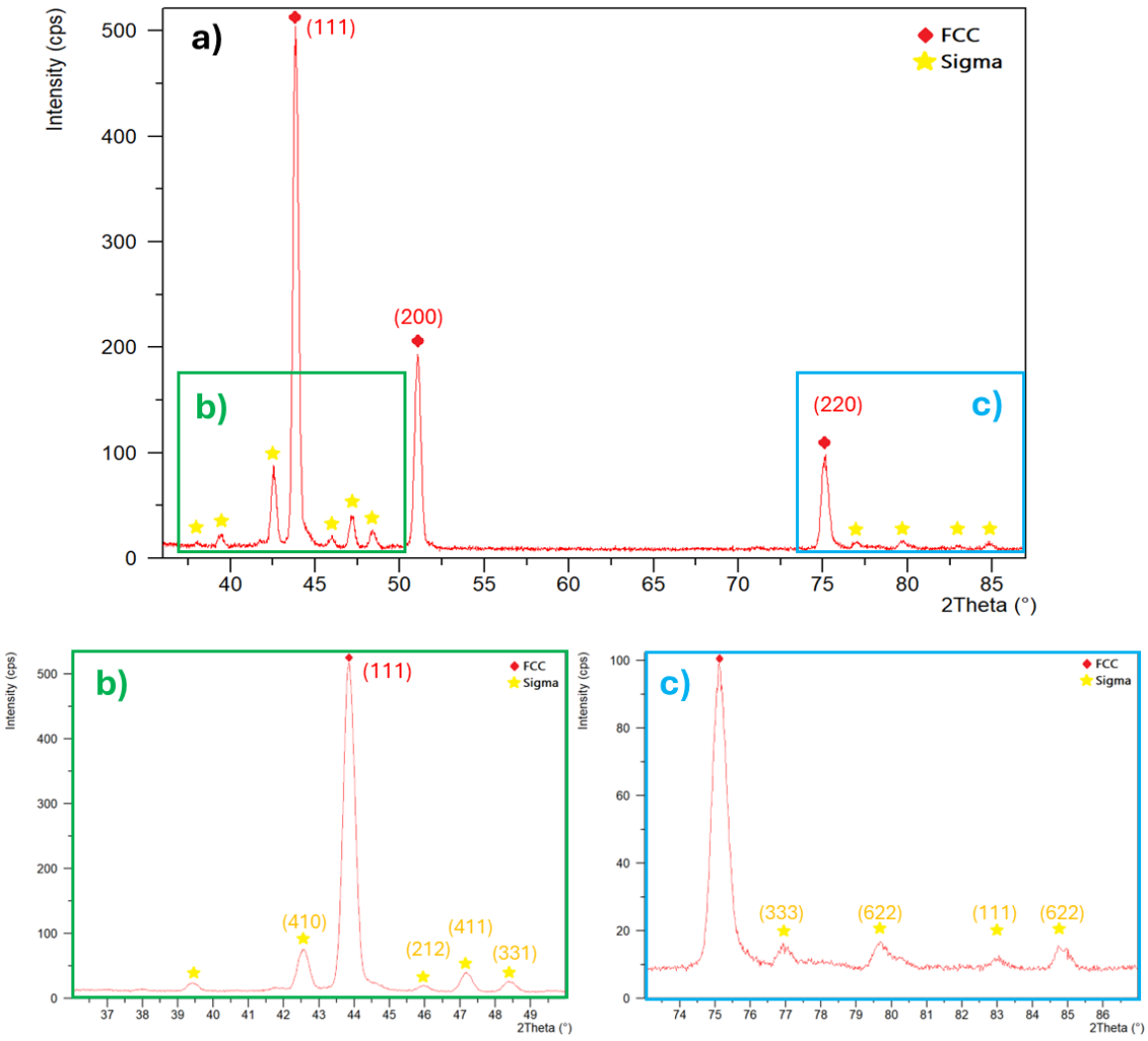


Figure 0.18. XRD Profile of a Co10Si9 alloy after hot rolling with the presence of FCC and sigma phases (peak indexation for the sigma phase from similar C-MPEA [127, 64]).

Thèse accessible à l'adresse : https://theses.insa-lyon.fr/publication/2025ISAL0036/these.pdf © [T. Langlois], [2025], INSA Lyon, tous droits réservés

Powder-XRD measurement at IFM and Ansto

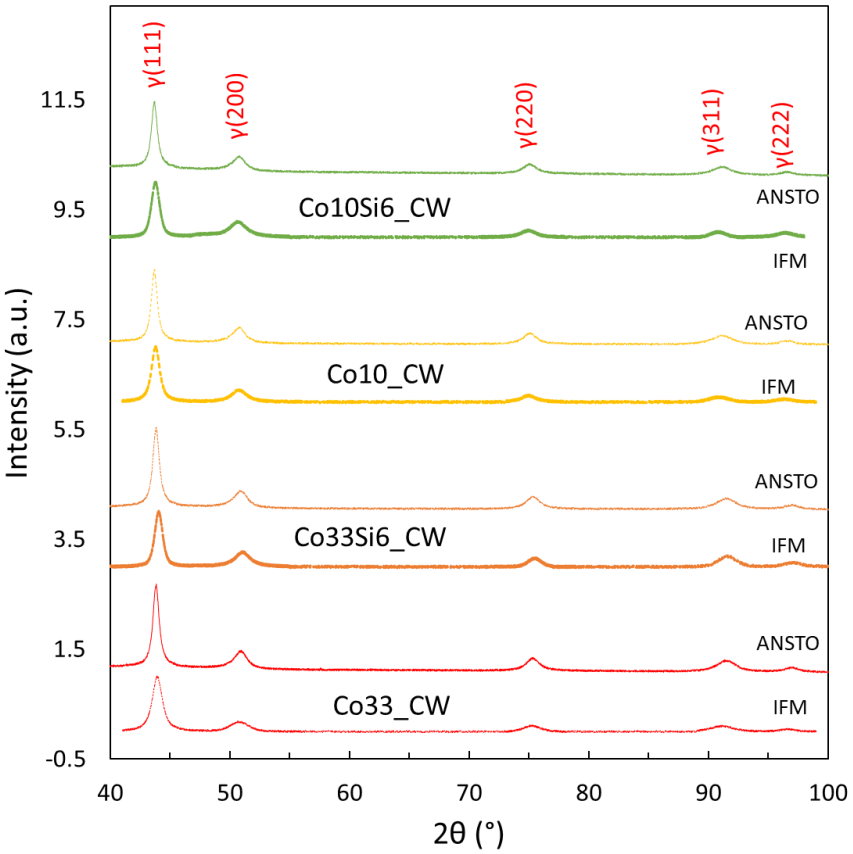


Figure 0.19. Comparison of Cold-worked powders acquired with X'Pert Pro MRD (IFM) and PD-Beamline (Ansto).

Thèse accessible à l'adresse : https://theses.insa-lyon.fr/publication/2025ISAL0036/these.pdf © [T. Langlois], [2025], INSA Lyon, tous droits réservés

Shockley Partial measured by TEM at IFM

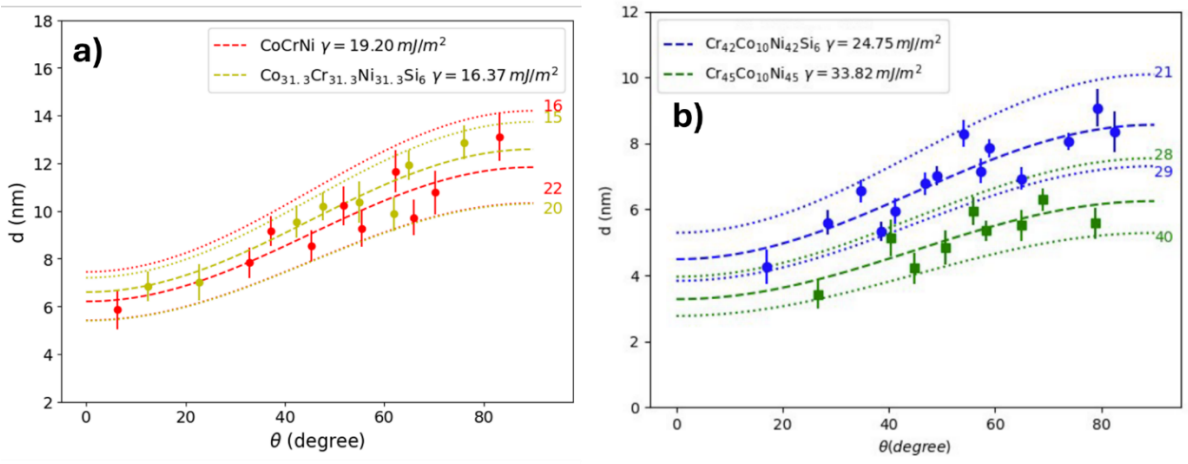


Figure 0.20. Dissociation withd d between two partial dislocation observed with TEM in (a) Co33 (red) and Co33Si6 (yellow); (b) Co10 (green) and Co10Si6 (blue). (Worked performed by Ziyu Ma at Deakin IFM)

Thèse accessible à l'adresse : https://theses.insa-lyon.fr/publication/2025ISAL0036/these.pdf © [T. Langlois], [2025], INSA Lyon, tous droits réservés

Compressive test results at room temperature

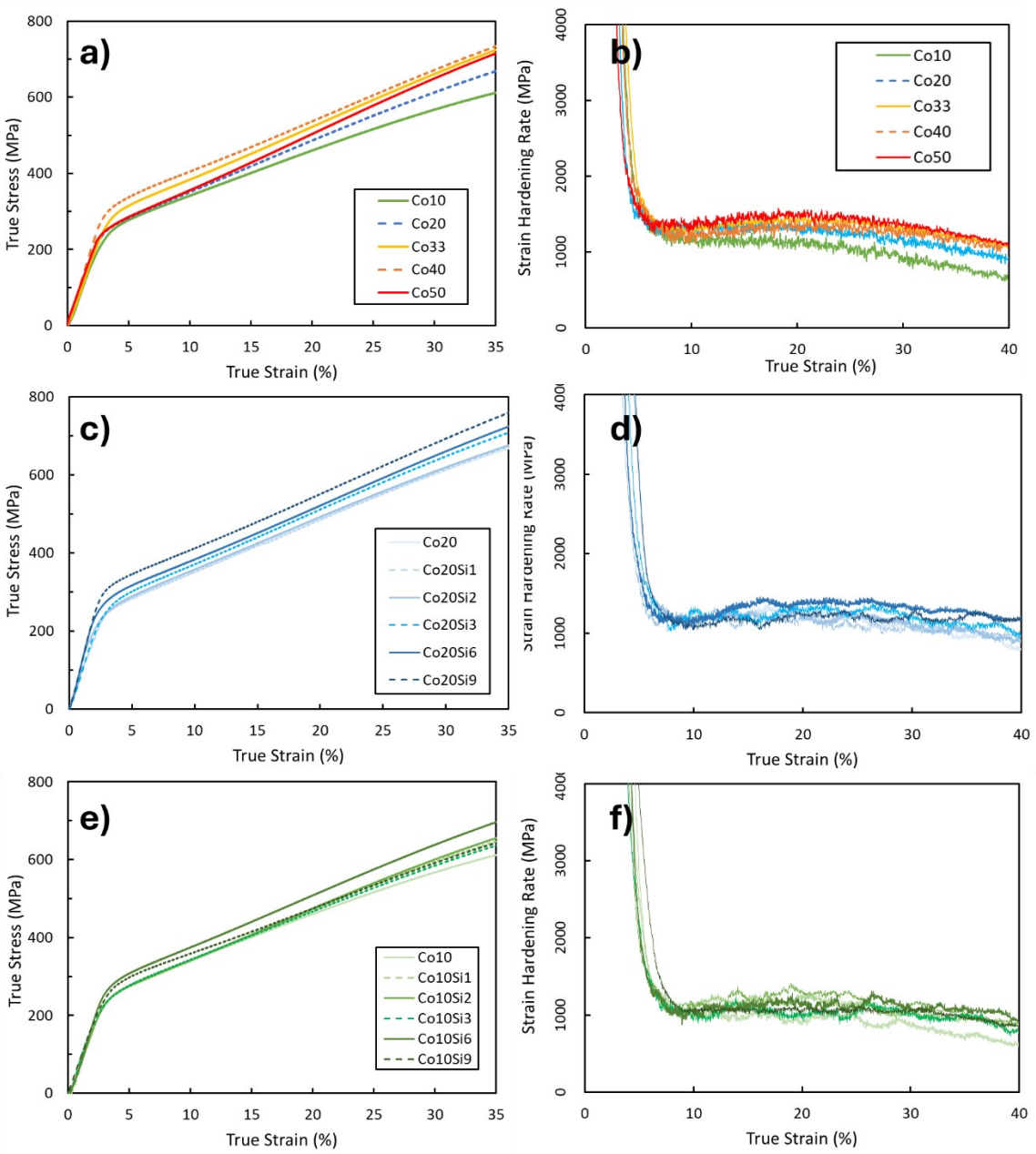


Figure 0.21. Stress-Strain and SHR curves of (a-b) Cobalt compositions; (c-d) Co20 with silicon addition; (e-f) Co10 with silicon addition.

Lateral expansion in CVN impact specimens

Thèse accessible à l'adresse : https://theses.insa-lyon.fr/publication/2025ISAL0036/these.pdf © [T. Langlois], [2025], INSA Lyon, tous droits réservés

Ingot name	alloy name	Specimen	dimensions (mm)				
			A1	**A3**	**A2**	**A4**	**Lateral expansion**
Ind_1	Co33(at%)	33_RT_1	0.52	0.74	1.00	0.75	**1.74**
		33_RT_2	0.48	0.68	0.92	0.69	**1.60**
		33_RT_3	0.50	0.54	0.96	0.96	**1.50**
		33_LT_4	0.78	0.72	0.50	0.77	**1.55**
		33_LT_5	0.40	0.56	0.76	0.57	**1.32**
		33_LT_6	not in the notch				X
Ind_2	Co20	20_RT_1	0.46	0.50	0.64	0.65	**1.15**
		20_RT_2	0.64	0.70	0.90	0.91	**1.61**
		20_RT_3	0.75	0.51	0.62	0.55	**1.37**
		20_LT_4	0.40	0.44	0.27	0.48	**0.92**
		20_LT_5	0.41	0.39	0.44	0.21	**0.84**
		20_LT_6	0.52	0.51	0.57	0.27	**1.09**
Ind_3	Co10	10_RT_1	0.68	0.50	0.65	0.49	**1.33**
		10_RT_2	0.60	0.55	0.80	0.46	**1.14**
		10_RT_3	0.58	0.44	0.48	0.53	**1.11**
		10_LT_4	0.13	0.16	0.13	0.20	**0.36**
		10_LT_5	0.41	0.37	0.31	0.37	**0.78**
		10_LT_6	0.20	0.23	0.28	0.22	**0.55**
		Spare					
Ind_4	Co10Si6	10.6_RT_1	0.24	0.30	0.26	0.27	**0.57**
		10.6_RT_2	0.26	0.32	0.29	0.32	**0.64**
		10.6_RT_3	0.21	0.26	0.24	0.24	**0.50**
		10.6_LT_4	0.12	0.07	0.11	0.11	**0.23**
		10.6_LT_5	0.11	0.08	0.10	0.11	**0.22**
		10.6_LT_6	0.10	0.09	0.09	0.10	**0.20**
		Spare					
Ind_5	Co10Si9	10.9_RT_1	0.05	0.03	0.04	0.03	**0.09**
		10.9_RT_2	0.04	0.05	0.03	0.02	**0.07**
		10.9_RT_3	0.01	0.03	0.06	0.02	**0.09**
		10.9_LT_4	0.01	0.03	0.02	0.03	**0.06**
		10.9_LT_5	0.00	0.00	0.04	0.00	**0.04**
		10.9_LT_6	calliper				**0.05**

Figure 0.22. Lateral expansion measurements in CVN specimens after impact loading, measured with a Vernier gage.

Thèse accessible à l'adresse : https://theses.insa-lyon.fr/publication/2025ISAL0036/these.pdf © [T. Langlois], [2025], INSA Lyon, tous droits réservés

Phase and KAM maps for tensile specimens

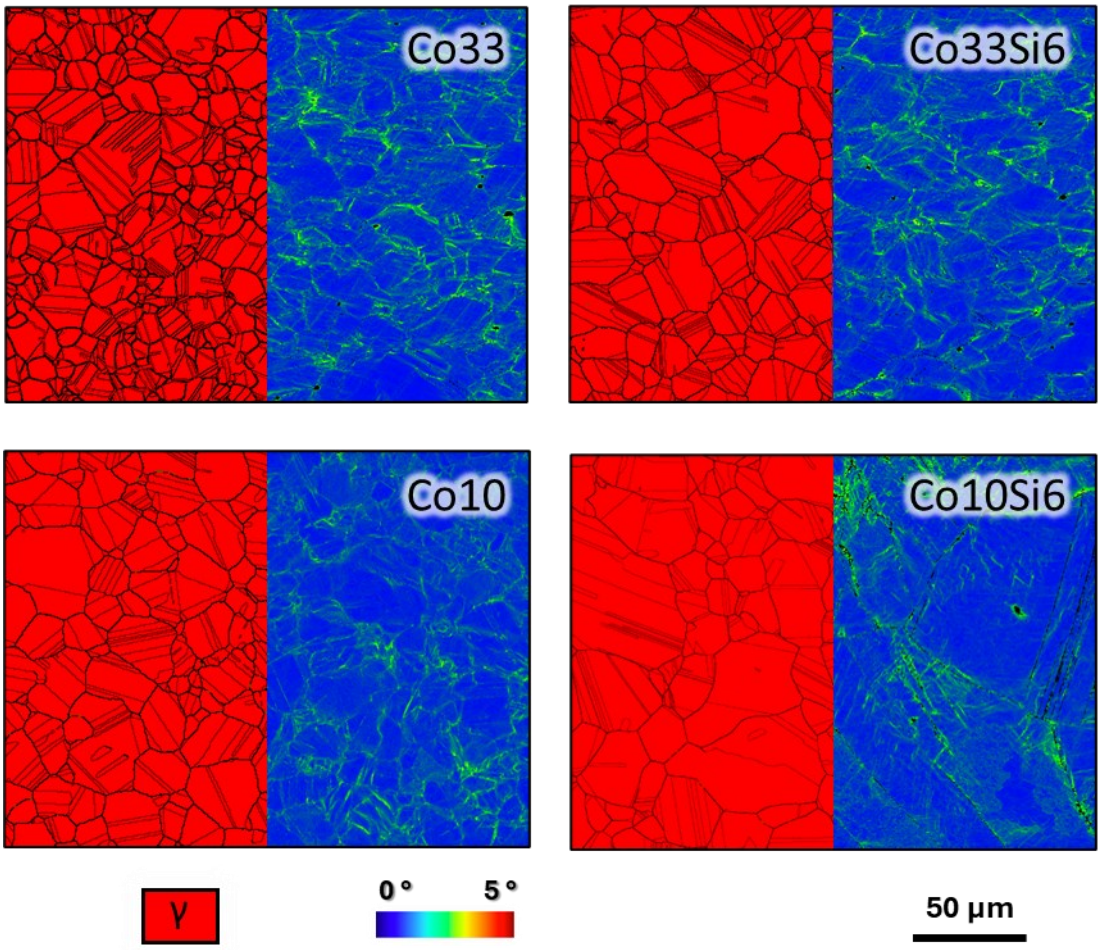


Figure 0.23. Phase map and KAM maps of recrystallised microstructures in tensile specimens.

Thèse accessible à l'adresse : https://theses.insa-lyon.fr/publication/2025ISAL0036/these.pdf © [T. Langlois], [2025], INSA Lyon, tous droits réservés

Reference stress-strain curves for SS304 at room temperature and cryogenic temperature

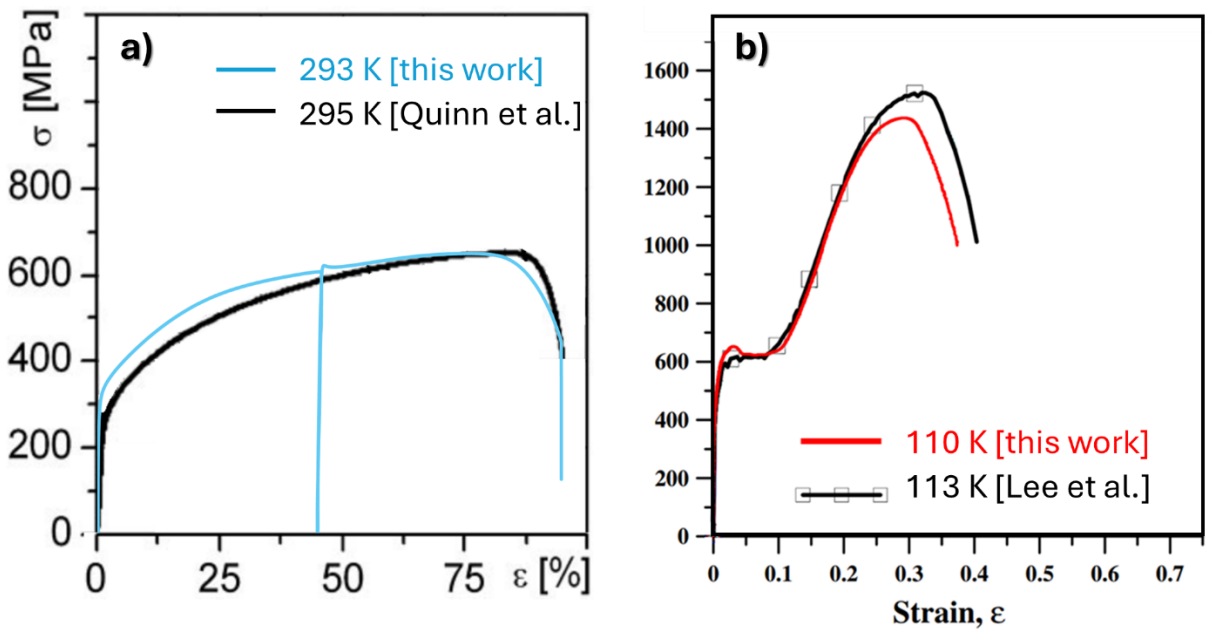


Figure 0.24. Engineering Stress-Strain curves of the reference material: SS304 Annealed (a) Tensile test at 293 K [166]; (b) Tensile test at 110 K [167].

Thèse accessible à l'adresse : https://theses.insa-lyon.fr/publication/2025ISAL0036/these.pdf © [T. Langlois], [2025], INSA Lyon, tous droits réservés

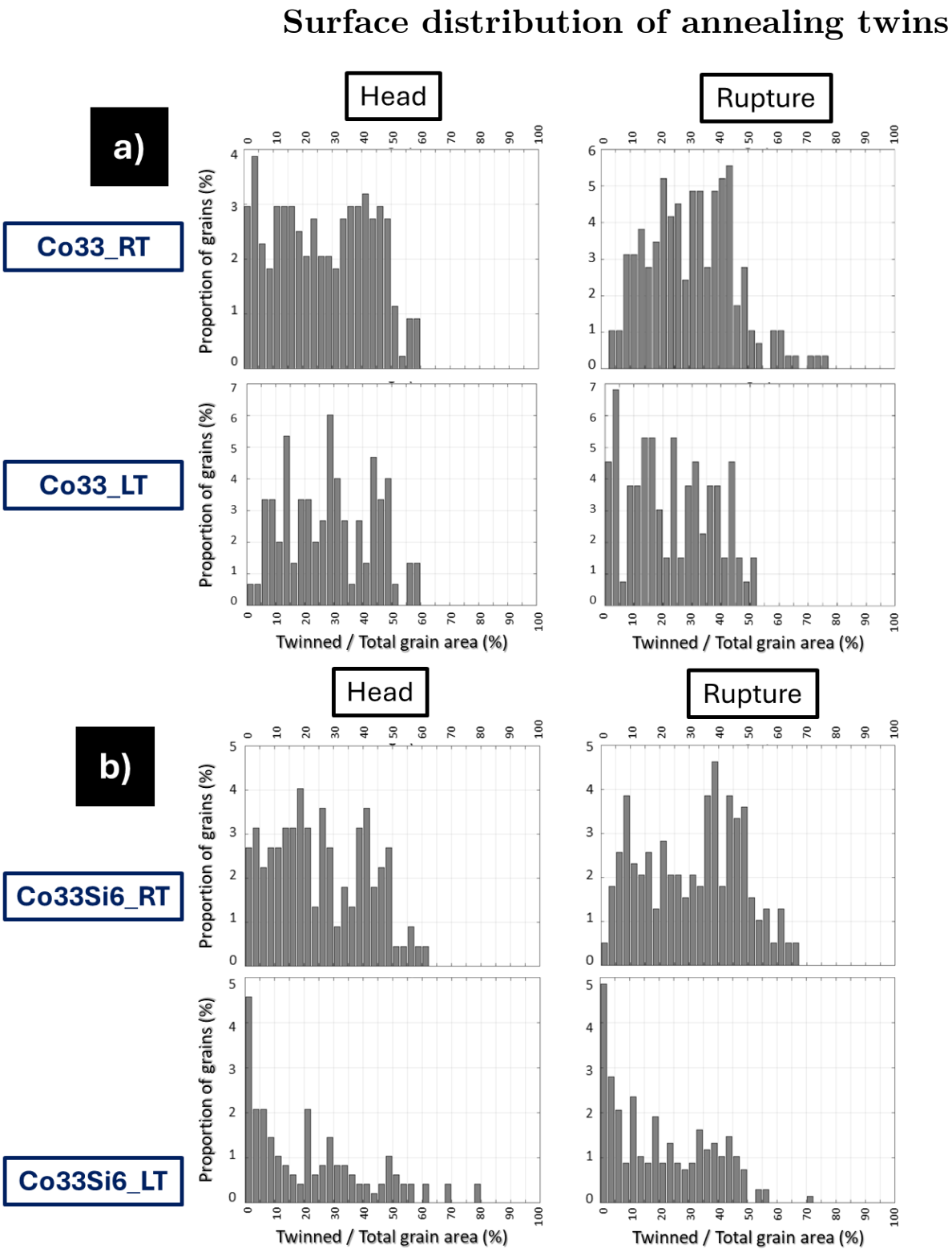


Figure 0.25. Twinned surface distribution of ATs from undeformed regions (left) to highly deformed regions (right) for (a) Co33, (b) Co33Si6, (c) Co10, (d) Co10Si6.

Thèse accessible à l'adresse : https://theses.insa-lyon.fr/publication/2025ISAL0036/these.pdf © [T. Langlois], [2025], INSA Lyon, tous droits réservés

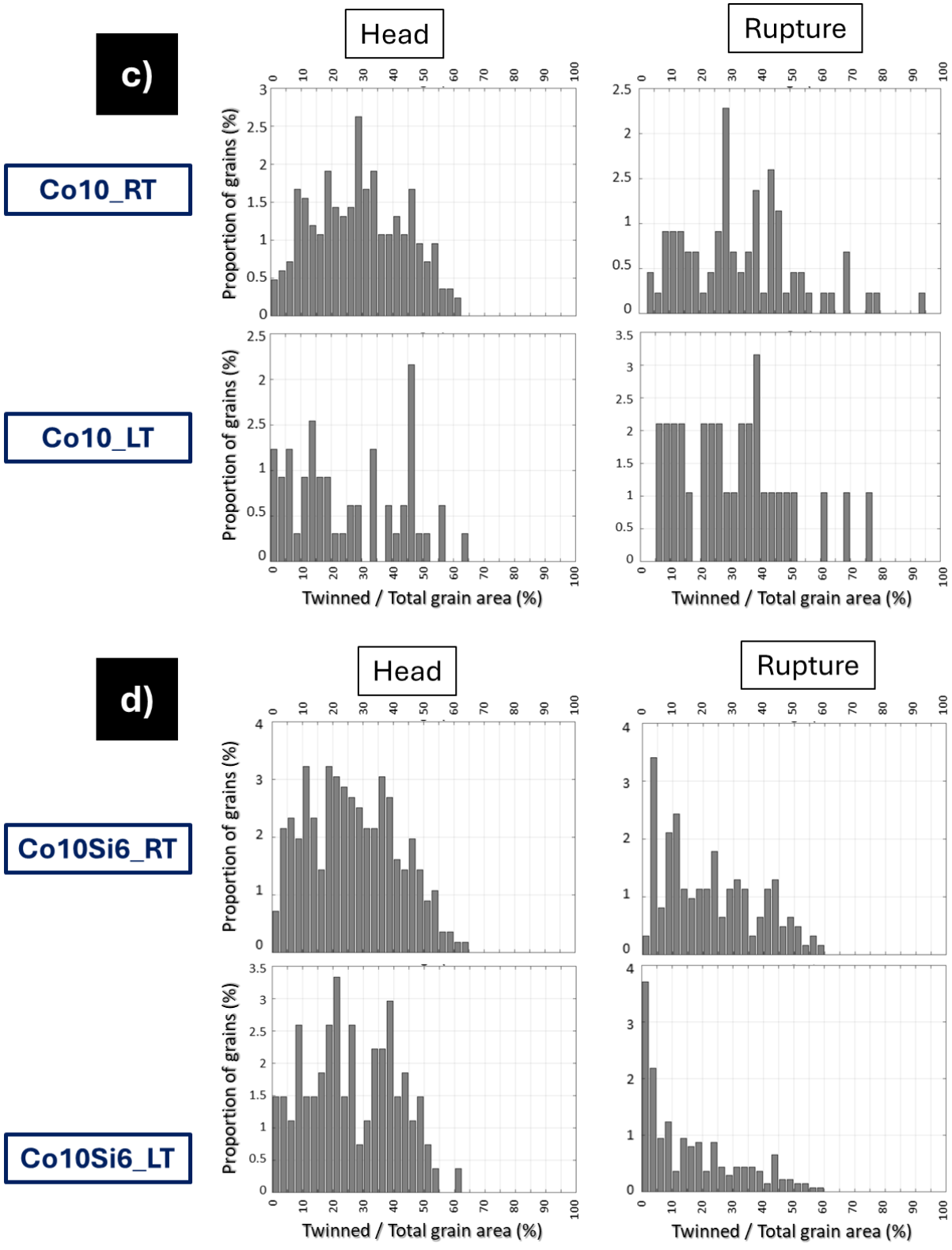


Figure 0.25 (continued) Twinned surface distribution of ATs from undeformed regions (left)to highly deformed regions (right) for (a) Co33, (b) Co33Si6, (c) Co10, (d) Co10Si6.

Thèse accessible à l'adresse : https://theses.insa-lyon.fr/publication/2025ISAL0036/these.pdf © [T. Langlois], [2025], INSA Lyon, tous droits réservés

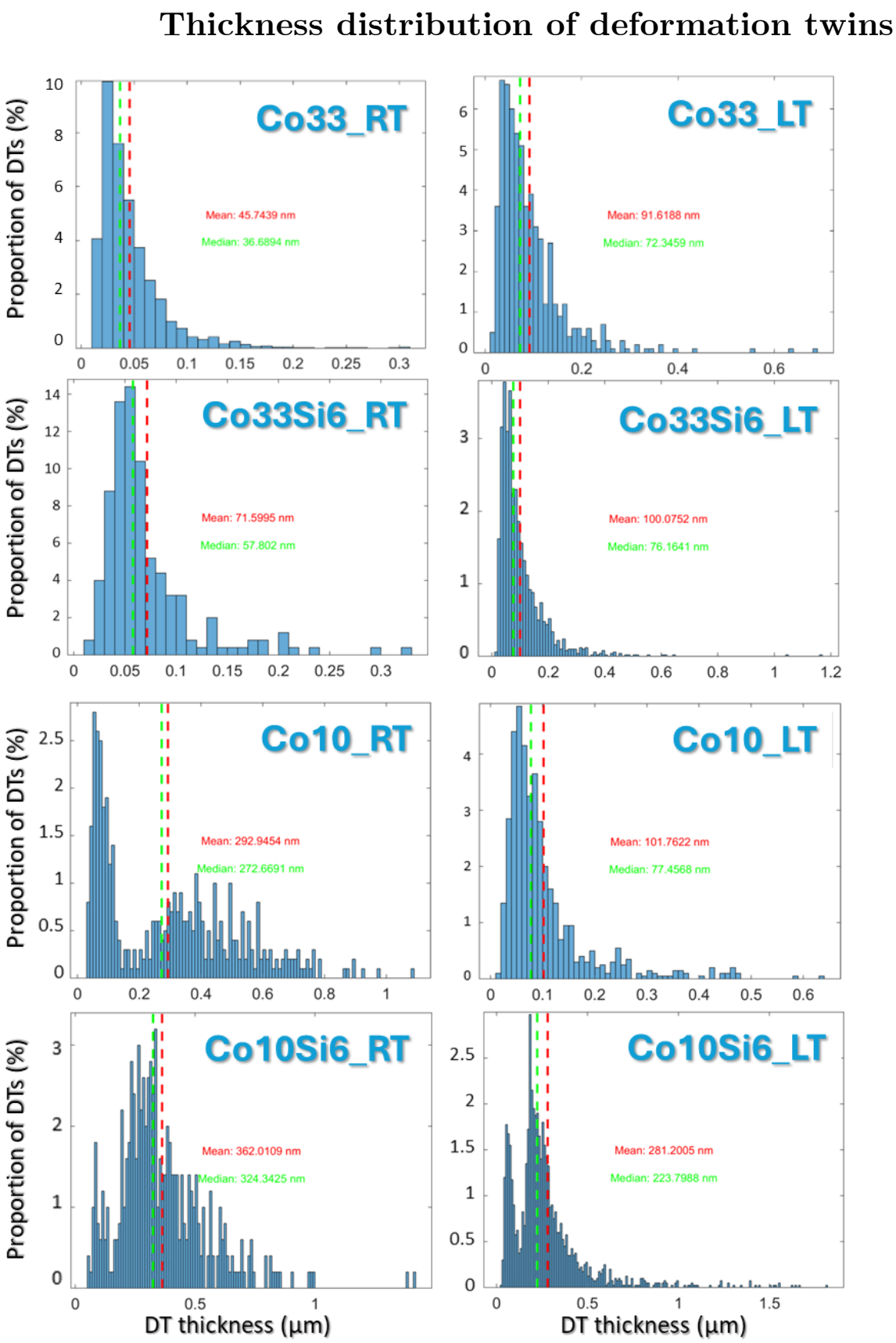


Figure 0.26. DT thickness near rupture regions of TDB specimens (left: 293 K, right: 110 K).

Thèse accessible à l'adresse : https://theses.insa-lyon.fr/publication/2025ISAL0036/these.pdf © [T. Langlois], [2025], INSA Lyon, tous droits réservés

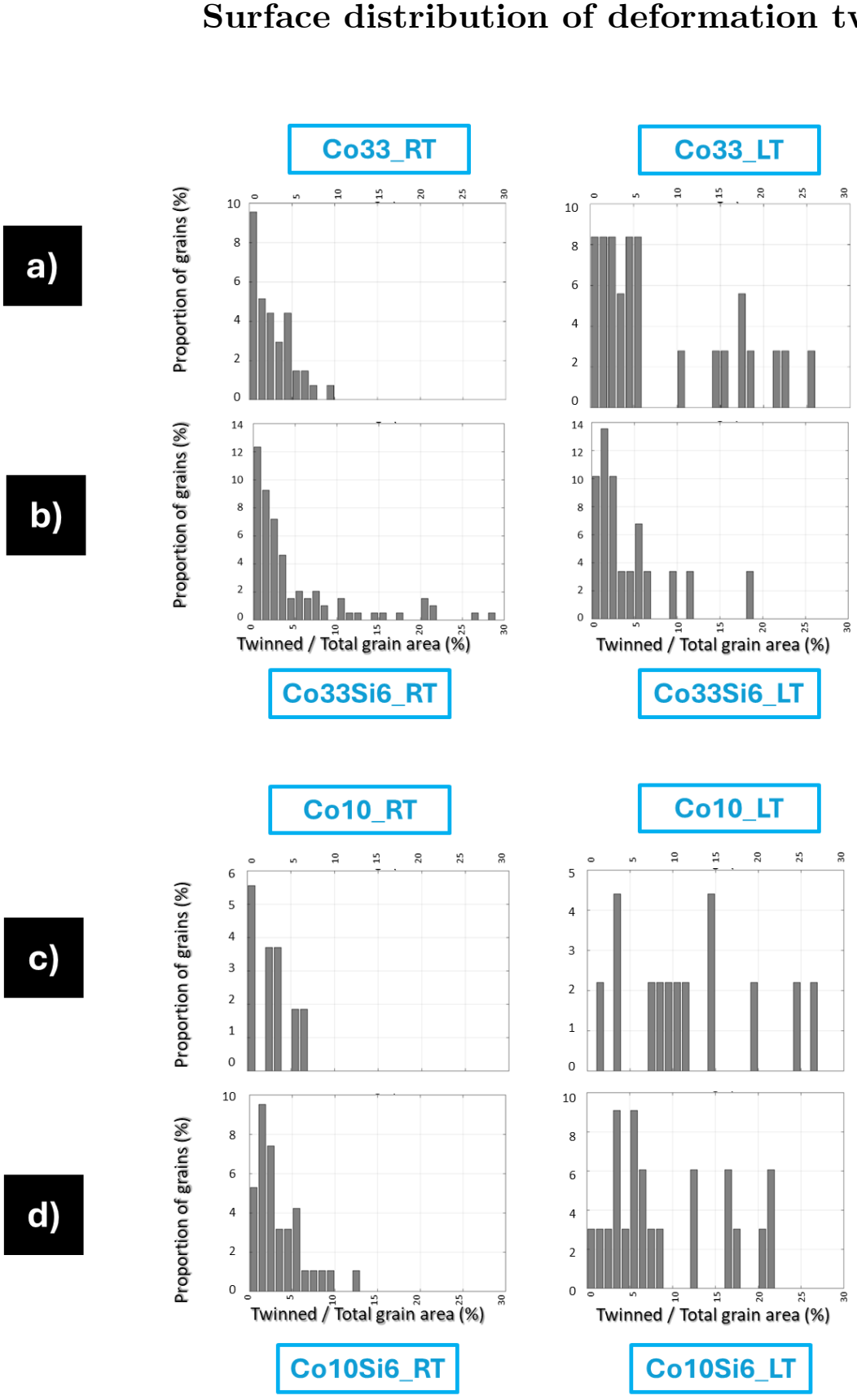


Figure 0.27. Twinned surface distribution of DTs near rupture regions for (a) Co33, (b) Co33Si6, (c) Co10, (d) Co10Si6 (left: 293 K, right: 110 K)

Thèse accessible à l'adresse : https://theses.insa-lyon.fr/publication/2025ISAL0036/these.pdf © [T. Langlois], [2025], INSA Lyon, tous droits réservés

Bibliography

[1] P. Ferro and F. Bonollo, "Materials selection in a critical raw materials perspective," *Materials and Design,* vol. 167, pp. 108-119, 2019.

[2] B. Gludovatz, A. Hohenwarter, K. Thurston, H. Bei, Z. Wu, E. P. George and R. O. Ritchie, "Exceptional damage tolerance of a CrCoNi MEA at cryogenic temperature," *Nature Communications,* vol. 7, no. 13183, 2016.

[3] M. Barnett, M. Senadeera, D. Fabijanic, K. Shamlaye, J. Joseph, S. Kada, S. Rana, S. Gupta and S. Venkatesh, "A scrap-tolerant alloying concept based on HEA," *Acta Materialia,* vol. 194, pp. 408-421, 2020.

[4] Y. Chen, J. Zhang and X. Wang, "Recent progress in high-entropy alloys: A review," *Materials Science and Engineering,* vol. 679, no. A, pp. 1-15, 2017.

[5] C. Varvenne, A. Luque and W. Curtin, "Theory of strengthening in fcc high entropy alloys," *Acta Materialia,* vol. 118, pp. 164-176, 2016.

[6] B. Cantor, I. Chang, P. Knight and A. Vincent, "Microstructural development in equiatomic multicomponent alloys," *Materials Science and Engineering,* Vols. 375-377, no. A, pp. 213-218, 2004.

[7] J.-W. Yeh, S.-K. Chen, S.-J. Lin, J.-Y. Gan, T.-S. Chin, T.-T. Shun, C.-H. Tsau and S.-Y. Chang, "Nanostructured High-Entropy Alloys with Multiple Principal Elements: Novel Alloy Design Concepts and Outcomes.," *Advanced Engineering Materials,* vol. 6, no. 5, pp. 299-303, 2004.

[8] F. Otto, Y. Yang, H. Bei and G. E.P, "Relative effects of enthalpy and entropy on the phase stabilityof equiatomic high-entropy alloys," *Acta Materialia,* vol. 61, pp. 5253-5260, 2013.

Thèse accessible à l'adresse : https://theses.insa-lyon.fr/publication/2025ISAL0036/these.pdf © [T. Langlois], [2025], INSA Lyon, tous droits réservés

[9] R. Kozak, A. Sologubenko and W. Steurer, "Single-phase high-entropy alloys - an overview," *Zeitschrift fiir Kristallographie,* vol. 229, pp. 515-528, 2014.

[10] A. Takeuchi, M. Gao, J. Qiao and M. Widom, "High-entropy alloys: Fundamentals and applications," *Materials Science and Engineering,* vol. 657, no. A, pp. 1-12, 2016.

[11] Z. Wu, H. Bei, F. Otto, G. Pharr and E. George, "Recovery, recrystallization, grain growth and phase stability of a family of FCC-structured multi-component equiatomic solid solution alloys," *Intermetallics,* vol. 52, pp. 32-41, 2014.

[12] H. Luo, Z. Li and D. Raabe, "Hydrogen enhances strength and," *Scientific Reports,* vol. 7, 2017.

[13] H. Luo, S. Sohn, W. Lu, L. Li, X. Li, C. Soundararajan, W. Krieger, Z. Li and D. Raabe, "A strong and ductile medium-entropy alloy resists," *naturecommunications,* vol. 11, 2020.

[14] X. Yang and Y. Zhang, "Prediction of high-entropy stabilized solid solution in multi-component alloys," *Materials Chemistry and Physics,* vol. 132, no. 2-3, pp. 233-238, 2012.

[15] I. Moravcik, H. Hadraba, L. Li, I. Dlouhy, D. Raabe and Z. Li, "Yield strength increase of a CoCrNi MEA by interstitial nitrogen doping," *Scripta Materialia,* vol. 190, pp. 72-75, 2020.

[16] S. Guo, C. Ng, J. Lu and C. T. Liu, "Effect of valence electron concentration on stability of fcc or bcc phase in high entropy alloys.," *Journal of Applied Physics,* vol. 110 (3), no. 034909, 2011.

[17] C. St John, "The brittle-to-ductile transition in pre-cleaved silicon single crystals," *Philosophical Magazine,* no. 32, pp. 1193-1212, 1975.

[18] E. Tarleton and S. Roberts, "Dislocation dynamic modelling of the brittle–ductile transition in tungsten," *Philosophical Magazine ,* vol. 89, 2009.

Thèse accessible à l'adresse : https://theses.insa-lyon.fr/publication/2025ISAL0036/these.pdf © [T. Langlois], [2025], INSA Lyon, tous droits réservés

[19] M. Bönisch, Y. Wu and H. Sehitoglu, "Twinning-induced strain hardening," *Scientific Reports,* vol. 8, 2018.

[20] M. Sohrabi, A. Khalor, H. Mirzadeh, K. Rodak and H. Kim, "Tailoring the strengthening mechanisms of high-entropy alloy stoward excellent strength-ductility synergy by metalloid silicon alloying: A review," *Progress in Materials Science ,* vol. 144, 2024.

[21] Z. Wu, H. Bei, G. Pharr and E. George, "Temperature dependence of the mechanical properties of equiatomic," *Acta Materialia,* vol. 81, pp. 428-441, 2014.

[22] P.-A. Geslin, "Modeling of solid solution strengthening in FCC alloys: Atomistic simulations, statistical models and elastic continuous approaches," *Computational Materials Science,* vol. 232, 2024.

[23] H. Zhang, D. Cai, X. Sun, H. Huang, S. Lu, Y. Wang, Q. Hu, L. Vitos and X. Ding, "Solid solution strengthening of high-entropy alloys from," *Journal of Materials Science & Technology,* no. 121, pp. 105-116, 2022.

[24] R. Labusch, "A statistical theory of solid solution hardening," *Physica Status Solidi,* vol. 41, no. 2, pp. 659-669, 1970.

[25] O. Senkov, J. Scott, S. Senkova, D. Miracle and C. Woodward, "Microstructure and room temperature properties of a high-entropy TaNbHfZrTi alloy," *Journal of Alloys and Compounds,* vol. 509, pp. 6043-6048, 2011.

[26] I. Toda-Caraballo and P. Rivera-Díaz-del-Castillo, "Modelling solid solution hardening in high entropy alloys," *Acta Materialia,* vol. 85, pp. 14-23, 2015.

[27] M. Walbrühl, D. Linder, J. Ågren and A. Borgenstam, "Modelling of solid solution strengthening in multicomponent alloys," *Materials Science & Engineering A,* vol. 700, pp. 301-311, 2017.

[28] F. Maresca and W. Curtin, "Theory of screw dislocation strengthening in random BCC alloys from," *Acta Materialia,* no. 182, pp. 144-162, 2019.

Thèse accessible à l'adresse : https://theses.insa-lyon.fr/publication/2025ISAL0036/these.pdf © [T. Langlois], [2025], INSA Lyon, tous droits réservés

[29] T. Manescau, "Etude d'alliages haute entropie du système Cr-Fe-Mn-Ni et développement d'alliages concentrés complexes par ajout de W-C pour applications tribologiques du secteur nucléaire," Lyon, 2022.

[30] F. Coury, K. Clarke, C. Kiminami, M. Kaufman and A. Clarke, "High Throughput Discovery and Design of Strong Multicomponent Metallic Solid Solutions," *ScientificReports,* vol. 8, 2018.

[31] G. Bracq, M. Laurent-Brocq, C. Varvenne, L. Perrière, W. J. Curtin, M. J and I. Guillot, "Combining experiments and modeling to explore the solid solution strengthening of high and medium entropy alloys," *Acta Materialia,* vol. 177, pp. 266-279, 2019.

[32] D. Wei, W. Gong, T. Tsuru, I. Lobzenko, X. Li, S. Harjo, T. Kawasaki, H.-S. Do, J. Bae, C. Wagner, G. Laplanche, Y. Koizumi, H. Adachi, K. Aoyagi, A. Chiba, B.-J. Lee, H. Kim and H. Kato, "Si-addition contributes to overcoming the strength-ductility trade-off in high-entropy alloys," *International Journal of Plasticity,* vol. 159, 2022.

[33] J. Wang and X. Zhang, "Twinning effects on strength and plasticity of metallic materials," *MRS Bulletin,* vol. 41, pp. 274-281, 2016.

[34] D. Wei, X. Li, W. Heng, Y. Koizumi, F. He, W.-M. Choi, B.-J. Lee, H. S. Kim, H. Kato and A. Chiba, "Novel Co-Rich High Entropy Alloys with Superior Tensile Properties," *Materials Research Letters,* vol. 7, no. 2, pp. 82-88, 2018.

[35] M. Koyama, T. Sawaguchi and K. Tsuzaki, "Premature Fracture Mechanism in an Fe-Mn-C Austenitic Steel," *Metallurgical and materials transactions A,* vol. 43, no. A, 2012.

[36] S. Yoshida, T. Ikeuchi, Y. Bai and N. Tsuji, "Effect of Cobalt-Content on Mechanical Properties of Non-Equiatomic CoCrNi Medium Entropy Alloys," *Materials Transactions,* vol. 61, no. 4, pp. 587-595, 2020.

Thèse accessible à l'adresse : https://theses.insa-lyon.fr/publication/2025ISAL0036/these.pdf © [T. Langlois], [2025], INSA Lyon, tous droits réservés

[37] M. Jabłońska, "Mechanical Properties and Fractographic Analysis of High Manganese Steels After Dynamic Deformation Tests," *Archives of Metallurgy and Materials,* vol. 59(3), pp. 671-679, 2014.

[38] J. Soler, ""First-principles study of stacking fault energies in FCC metals"," *Physical Review ,* vol. B, 2022.

[39] T. Khan, T. Kirk, G. Vazquez, P. Singh, A. Smirnov, D. Johnson, K. Youssef and R. Arroyave, "Towards stacking fault energy engineering in FCC high entropy alloys," *Acta Materialia,* vol. 224, pp. 121-128, 2022.

[40] L. Clarebrough, H. P. and H. Loretto, "Faulted defects and stacking-fault energy," *Canadian Journal of Physics,* vol. 45, 1967.

[41] P. Reed and R. Schramm, "Relationship between stackingfault energy and xray measurements of stackingfault probability and microstrain," *Journal of Applied Physics,* vol. 45, pp. 4705-4711, 1974.

[42] G. Olson and M. Cohen, "A general mechanism of martensitic nucleation: Part II. FCC → BCC and other martensitic transformations," *Metallurgical Transactions A ,* vol. 7, pp. 1905-1914, 1976.

[43] T. Achmad, W. Fu, H. Chen, C. Zhang and Z.-G. Yang, "Computational thermodynamic and first-principles calculation of stacking fault energy on ternary Co-based alloys," *Computational Materials Science,* vol. 143, pp. 112-117, 2018.

[44] H. Chang, T. Zhang, S. Ma, D. Zhao, R. Xiong, T. Wang, Z. Li and Z. Wang, "Novel Si-added CrCoNi medium entropy alloys achieving the breakthrough of strength-ductility trade-off," *Materials and Design,* vol. 197, 2021.

[45] G. O. L. Bertoli, A. Clarke, C. Kiminami and F. Coury, "Hall-Petch and grain growth kinetics of the low stacking fault energy TRIP Cr40Co40Ni20 multi-principal element alloy," *Applied Physics Letters,* vol. 119, 2021.

Thèse accessible à l'adresse : https://theses.insa-lyon.fr/publication/2025ISAL0036/these.pdf © [T. Langlois], [2025], INSA Lyon, tous droits réservés

[46] J. Lloyd, D. Field and K. Limmer, "A four parameter hardening model for TWIP and TRIP steels," *Materials and Design,* vol. 188, no. 108773, 2020.

[47] H. Bahmanpour, A. Kauffmann, M. Khoshkhoo, K. Youssef, S. Mula, J. Freudenberger, J. Eckert, R. Scattergood and C. Koch, "Effect of stacking fault energy on deformation behavior of cryo-rolled copper and copper alloys," *Materials Science and Engineering,* vol. 528(3), no. A, pp. 230-236, 2011.

[48] S. Kibey, J. Liu, D. Johnson and H. Sehitoglu, "Predicting twinning stress in fcc metals: Linking twin-energy," *Acta Materialia,* vol. 55(16), pp. 5429-5438, 2007.

[49] K. Vamsi, M. Charpagne and P. T.M, "High-throughput approach for estimation of intrinsic barriers in FCC structures for alloy design," *Scripta Materialia,* vol. 196, pp. 64-68, 2021.

[50] S. Martin, S. Wolf, M. U, L. Krüger and D. Rafaja, "Deformation Mechanisms in Austenitic TRIP/TWIP Steel as a Function of Temperature," *Metallurgical and Materials Transactions,* pp. 49-58, 2016.

[51] M. Schneider and G. Laplanche, "Effects of temperature on mechanical properties and deformation mechanisms of the equiatomic CrFeNi medium-entropy alloy," *Acta Materialia,* vol. 214, pp. 381-391, 2021.

[52] M. Traversier, P. Mestre-Rinn, N. Peillon, E. Rigal, X. Boulnat, F. Tancret, J. Dhers and A. Fraczkiewicz, Nitrogen-induced hardening in an austenitic CrFeMnNi high-entropy, Materials Science & Engineering, 2020.

[53] Z. Wang, I. Baker, Z. Cai, S. Chen, J. Poplawsky and W. Guo, "The effect of interstitial carbon on the mechanical properties and dislocation substructure evolution in Fe40.4Ni11.3Mn34.8Al7.5Cr6 high entropy alloy," *Acta Materiala,* vol. 120, pp. 228-239, 2016.

[54] J. Dabrowa and M. Danieleski, "State-of-the-Art Diffusion Studies in the High," *MDPI,* 2020.

Thèse accessible à l'adresse : https://theses.insa-lyon.fr/publication/2025ISAL0036/these.pdf © [T. Langlois], [2025], INSA Lyon, tous droits réservés

[55] A. Mehta and Y. Sohn, "Investigation of sluggish diffusion in FCC Al0.25CoCrFeNi high-entropy alloy," *Materials Research Letters,* vol. 9, pp. 239-246, 2021.

[56] H. Deng, M. Wang, Z. Xie, T. Zhang, X. Wang, Q. Fang and Y. Xiong, "Enhancement of strength and ductility in non-equiatomic CoCrNi medium-entropy alloy at room temperature via transformation-induced plasticity," *Materials Science & Engineering A ,* vol. 804, 2021.

[57] W. Fang, R. Chang, X. Zhang, P. Ji, X. Wang, B. Liu, J. Li, X. He, X. Qu and F. Yin, "Effects of Cobalt on the structure and mechanical behavior of non-equal molar CoxFe50−xCr25Ni25 high entropy alloys," *Materials Science & Engineering A,* vol. 723, pp. 221-228, 2018.

[58] F. Pan, P. Ding, S. Zhou, M. Kang and D. Edmonds, "Effects of silicon additions on the mechanical properties and microstructure of high speed steels," *Acta Materialia,* vol. 45, no. 11, pp. 4703-4712, 1997.

[59] C. Dinnis, J. Taylor and A. Dahle, "As-cast morphology of iron-intermetallics in Al–Si foundry alloys," *Scripta Materialia,* vol. 53, pp. 955-958, 2005.

[60] Z.-Y. Xiu, G.-Q. Chen, F.-X. Wang, G.-H. Wu, Y.-M. Liu and W.-S. Yang, "DOI: 10.1016/S1003-6326(09)60430-1," *Transactions of Nonferrous Metals Society of Chine,* vol. 20, no. 11, pp. 2134-2138, 2010.

[61] W. Li, D. Xie, D. Li, Zhang.Y., Y. Gao and P. Liaw, "Mechanical behavior of high-entropy alloys," *Progress in Materials Science ,* vol. 118, 2021.

[62] T. Jing, H. Zheng, Q. Liao, L. Song, Q. Guo, H. Peng and Y. Wen, "Breaking the trade-off between strength and ductility in nanostructured CrCoNi-based medium-entropy alloys by promoting twinning kinetics," *Journal of Alloys and Compounds,* vol. 922, 2022.

Thèse accessible à l'adresse : https://theses.insa-lyon.fr/publication/2025ISAL0036/these.pdf © [T. Langlois], [2025], INSA Lyon, tous droits réservés

[63] F. Yang, L. Dong, L. Cai, X. Hu and F. Fang, "Mechanical properties of FeMnCoCr high entropy alloy alloyed with C/Si at low temperatures," *Journal of Alloys and Compounds,* vol. 859, 2021.

[64] S. Liu, W. Lin, Y. Zhao, D. Chen, G. Yeli, F. He, S. Zhao and J.-J. Kai, "Effect of silicon addition on the microstructures, mechanical properties and helium irradiation resistance of NiCoCr-based medium-entropy alloys," *Journal of Alloys and Compounds,* vol. 844, 2020.

[65] A. Keith, C. Zlotea and P. Szilagy, "Perspective of interstitial hydrides of high-entropy alloys for vehicular hydrogen storage," *International Journal of Hydrogen Energy,* vol. 52, pp. 531-546, 2024.

[66] H. J. Hofstetter, H. A. Van der Voet and J. Guinée, Environmental Life Cycle Assessment of Products, Dordrecht: Kluwer Academic Publishers, 2004.

[67] M. Ashby, Materials and the Environment, Boston: MA: Butterworth-Heinemann, n.d..

[68] T. Graedel, E. Harper, N. Nassar, P. Nuss, B. Reck and B. Tuner, "Criticality of metals and metalloids," *Proceedings of the National Academy of Sciences of the United States of America,* vol. 112, pp. 4257-4262, 2015.

[69] J. Torralba, D. Iriarte and D. Tourret, "Using multicomponent recycled electronic waste alloys to produce high entropy alloys," *Intermetallics,* vol. 164, 2024.

[70] "Study on the review of the list of Critical Raw Materials: Critical Raw Materials Factsheets," European Commission, Brussel, 2020.

[71] E. Commission, "Raw Material Information System (RMIS)," Retrieved from, [Online]. Available: https://rmis.jrc.ec.europa.eu/.

Thèse accessible à l'adresse : https://theses.insa-lyon.fr/publication/2025ISAL0036/these.pdf © [T. Langlois], [2025], INSA Lyon, tous droits réservés

[72] Solability, "The Global Sustainable Competitiveness Index," 2021. [Online]. Available: https://solability.com/download/the-global-sustainable-competitiveness-index-2021/?tmstv=1666158435.

[73] E. Commission, "Critical Raw Materials Resilience: Charting a Path towards greater Security and Sustainability," 2020.

[74] WorldBank, "Cobalt in the Democratic Republic of Congo - Market Analysis," 2021.

[75] F. Calvao, C. Mcdonald and M. Bolay, "Cobalt mining and the corporate outsourcing of responsibility in the Democratic Republic of Congo," *The Extractive Industries and Society,* vol. 8, 2021.

[76] C. Nkulu, L. Casas, V. Hautfroid, T. De Putter, N. Saenen, T. Kayembe-Kitenge, P. Obadia, D. Mukoma, J.-M. Lunda Ilunga, T. Nawrot, O. Numbi, E. Smolders and B. Nemery, "Sustainability of artisanal mining of cobalt in DR Congo," *Nature Sustainability,* 2018.

[77] G. Bertoli, L. Otani, A. Clarke, C. Kiminami and F. Coury, "Hall–Petch and grain growth kinetics of the low stacking," *Applied Physics Letters,* vol. 119, 2021.

[78] A. Jain, S. P. Ong, G. Hautier, W. Chen, W. D. Richards, S. Dacek, S. Cholia, D. Gunter, D. Skinner, G. Ceder and K. Persson, "The Materials Project: A materials genome approach to accelerating materials innovation," *APL Materials,* vol. 1, no. 1, p. 011002, 2013.

[79] "Citrination," Citrination, [Online]. Available: https://citrination.com/.

[80] L. Ward, A. Dunn, A. Faghaninia, N. Zimmermann, S. Bajaj, Q. Wang, J. Montoya, J. Chen, F. Bystrom, M. Dylla, K. Chard, M. Asta, K. Persson, G. Snyder, I. Foster and A. Jain, "Matminer: An open source toolkit for materials data mining," *Computational Materials Science,* vol. 152, pp. 60-69, 2018.

[81] S. Ong, W. Richards, A. Jain, G. Hautier, M. Kocher, S. Cholia, D. Gunter, V. Chevrier, K. Persson and G. Ceder, "Python Materials Genomics (pymatgen):

Thèse accessible à l'adresse : https://theses.insa-lyon.fr/publication/2025ISAL0036/these.pdf © [T. Langlois], [2025], INSA Lyon, tous droits réservés

A robust, open-source python library for materials analysis," *Computational Materials Science,* vol. 68, pp. 314-319, 2013.

[82] F. Pedregosa, G. Varoquaux, G. A. V. Michel, B. Thirion and O. Grisel, "Scikit-learn: Machine learning in Python," *Journal of machine learning research,* 2011.

[83] H. Lucas, S. Fries and B. Sundman, Computational Thermodynamics "The CALPHAD Method"., Cambridge: University Press.

[84] O. Senkov, J. Miller, D. Miracle and C. Woodward, "Accelerated exploration of multi-principal element alloys for structural applications," *Calphad,* p. 50, 2015.

[85] H. Chen, H. Mao and Q. Chen, "Database development and Calphad calculations for high entropy alloys: Challenges, strategies, and tips," *Materials Chemistry and Physics,* vol. 210, pp. 279-290, 2018.

[86] G. Laplanche, P. Gadaud, C. Bärsch, K. Demtröder, C. Reinhart, J. Schreuer and E. George, "Elastic moduli and thermal expansion coefficients of medium-entropy subsystems of the CrMnFeCoNi high-entropy alloy," *Journal of Alloys and Compounds,* vol. 746, pp. 244-255, 2018.

[87] K. Kishore, C. A.V., P. Hung, S. kumar, M. Ranjan, M. Kawasaki and J. Gubicza, "Effect of Si on the evolution of plasticity mechanisms, grain refinement and hardness during high-pressure torsion of a non-equiatomic CoCrMnNi multi-principal element alloy," *International Journal of Plasticity ,* vol. 169, 2023.

[88] C. Borg, C. Frey, J. Moh, T. Pollock, S. Gorsse, D. Miracle, O. Senkov, B. Meredig and J. Saal, "Expanded dataset of mechanical properties and observed phases of multi-principal element alloys," *scientific data ,* vol. 7, 2020.

[89] D. Wen and M. Titus, "pySSpredict: A python-based solid solution strength prediction toolkit for complex concentrated alloys," *Computational Materials Science,* vol. 2020, 2023.

Thèse accessible à l'adresse : https://theses.insa-lyon.fr/publication/2025ISAL0036/these.pdf © [T. Langlois], [2025], INSA Lyon, tous droits réservés

[90] J. Hunter, "Matplotlib: A 2D Graphics Environment," *Computing in Science & Engineering,* vol. 9, no. 3, pp. 90-95, 2007.

[91] X. Wang and W. Xiong, "Stacking fault energy prediction for austenitic steels: thermodynamicmodeling vs. machine learning," *science and technology of advanced materials,* vol. 21, no. 1, pp. 626-634, 2020.

[92] "Producer price index - commodity data - chemical and allied products.," U.S. Bureau of Labor Statistics, 2021. [Online]. Available: https://www.bls.gov/ppi/commodity/chemical-and-allied-products.htm.

[93] "World Mining Data: Data Section," World Mining Data, [Online]. Available: http://www.world-mining-data.info/?World_Mining_Data___Data_Section.

[94] "Granta Design," Granta Edupack, Cambridge, UK, 2020.

[95] T. Graedel, E. Harper, N. Nassar, P. Nuss, B. Reck and B. Tuner, "Criticality of metals and metalloids," *Proceedings of the National Academy of Sciences of the United States of America,* vol. 112, pp. 4257-4262, 2015.

[96] "The Global Sustainable Competitiveness Index," Solability, 2021. [Online]. Available: https://solability.com/download/the-global-sustainable-competitiveness-index-2021/?tmstv=1666158435.

[97] "Study on the review of the list of Critical Raw Materials: Critical Raw Materials Factsheets," European Commission, Brussel, 2020.

[98] "Raw Material Information System (RMIS)," European Comission, [Online]. Available: https://rmis.jrc.ec.europa.eu/.

[99] "Study on the review of the list of Critical Raw Materials : Non-critical Raw Materials Factsheets," European Commission, Brussels, 2020.

Thèse accessible à l'adresse : https://theses.insa-lyon.fr/publication/2025ISAL0036/these.pdf © [T. Langlois], [2025], INSA Lyon, tous droits réservés

[100] S. Gorrse, T. Langlois and M. Barnett, "Considering sustainability when searching for new high entropy alloys," *Sustainable Materials and Technologies,* vol. 40, 2024.

[101] A. Rosen, "Periodic Trend Plotter : Python script to plot periodic trends as a heat map over the periodic table of elements," Github, 2017.

[102] S. Gorsse, N. Nguyen, O. Senkov and D. Miracle, "Database on the mechanical properties of high entropy alloys and complex concentrated alloys," *Data in brief,* vol. 21, pp. 2664-2678, 2018.

[103] S. Gorsse, M. Barnett and T. Langlois, Zenodo, April 2024. [Online]. Available: https://doi.org/10.5281/zenodo.10978935.

[104] S. Gorsse, T. Langlois and M. Barnett, "Commercial, Environmental and Societal Implications of High Entropy Alloys, Ni-Based Alloys, and Steels," *Scientific Data (Under Review).*

[105] M. Farsani and R. Gholamipour, "Silica-Free Zirconia-Based Primary Slurry for Titanium Investment Casting," *International Journal of Metalcasting,* vol. 14, pp. 92-97, 2019.

[106] Z. Lu, C. Zhang, N. Deng, H. Zhou, G. Wang, Y. Su, R. Fang and H. Zhang, "Evolution of grain boundary character distribution in near-surface regions of a cold rolled nickel-based superalloy during induction heating process," *Journal of Materials Research and Technology,* vol. 15, pp. 801-809, 2021.

[107] G. E. Dieter, Mechanical Metallurgy, New York Toronto London: McGraw-Hill Book Company, 1961.

[108] E. Orowan, "The Calculation of Roll Pressure in Hot and Cold Flat Rolling," *Proceedings of the Institution of Mechanical Engineers,* vol. 150, no. 1, pp. 140-167, 1943.

Thèse accessible à l'adresse : https://theses.insa-lyon.fr/publication/2025ISAL0036/these.pdf © [T. Langlois], [2025], INSA Lyon, tous droits réservés

[109] A. B947-14, *Standard Practice for Hot Rolling Mill Solution Heat Treatment for Aluminum Alloy Plate,* 2020.

[110] *Standard Specification for Steel, Sheet, Cold rolled, Carbon, Structural, High-Strength Low-Alloy, High-Strength Low-Alloy with Improved Formability, Required Hardness, Solution Hardened, and Bake Hardenable,* ASTM International, 2023.

[111] *ISO 6892-1:2019(en) Metallic materials - Tensile testing - Part 1: Method of test at room temperature,* 2019.

[112] *Standard Test Methods for Notched Bar Impact Testing of Metallic Materials,* ASTM International, 2024.

[113] B. A. B. Warren, "The Effect of ColdWork Distortion on XRay Patterns,," *Journal of Applied Physics,* vol. 21, pp. 595-599, 1950.

[114] R. R. R. Schramm, "Stacking fault energies of fcc fe-Ni alloys by x-ray diffraction line profile analysis.," *Metallic Transition A,* vol. 7, pp. 359-363, 1976.

[115] J. W. L. F. F. G. C. R. A. Unfried-Silgado, "Stacking fault energy measurements in solid solution strengthened Ni–Cr–Fe alloys using synchrotron radiation," *,Materials Science and Engineering A,* vol. 558, pp. 70-75, 2012.

[116] M. Walter, L. Mujica Roncery, S. Weber, L. Leich and W. Theisen, "XRD measurement of stacking fault energy of Cr–Ni," *Journal of Material Sciences,* vol. 55, p. 13424–13437, 2020.

[117] J. A. Castañeda, O. A. Zambrano, G. A. Alcázar, S. A. Rodríguez and J. J. Coronado, "Stacking Fault Energy Determination in Fe-Mn-Al-C Austenitic Steels by X-ray Diffraction," *MDPI Journal, Metals,* vol. 11, 2021.

[118] *Certificate Standard Reference Material® 660a,* National Institute of Standards & Technology, 2000.

Thèse accessible à l'adresse : https://theses.insa-lyon.fr/publication/2025ISAL0036/these.pdf © [T. Langlois], [2025], INSA Lyon, tous droits réservés

[119] G. Laplanche, M. Schneider, F. Scholz, J. Frenzel, G. Eggeler and J. Schreuer, "Processing of a single-crystalline CrCoNi medium-entropy alloy and evolution of its thermal expansion and elastic stiffness coefficients with temperature," *Scripta Materialia,* vol. 177, p. 44–48, 2020.

[120] G. Laplanche, A. Kostka, C. Reinhart, J. Hunfeld, G. Eggeler and E. George, "Reasons for the superior mechanical properties of medium-entropy CrCoNi compared to high-entropy CrMnFeCoNi," *Acta Materialia,* vol. 128, pp. 292-303, 2017.

[121] B. Sboui, D. Rodney and P. Geslin, "Elastic modelling of lattice distortions in concentrated random alloys," *Acta Materialia,* vol. 257, 2023.

[122] P. Yu, J.-P. Du, S. Shinzato, F.-S. Meng and S. Ogata, "Theory of history-dependent multi-layer generalized stacking fault energy— A modeling of the micro-substructure evolution kinetics in chemically ordered medium-entropy alloys," *Acta Materialia,* vol. 224, 2022.

[123] S. Kada, A. de Vaucorbeil, D. Fabijanic and M. Barnett, "Work hardening and the scratch resistance of Ni–Co alloys using a rapid prototyping approach," *Wear,* Vols. 510-511, 2022.

[124] G. Caglioti and F. R. A. Paoletti, "Choice of collimators for a crystal spectrometer," *Nuclear Instruments,* vol. 3, pp. 223-228, 1958.

[125] K. Buschow, P. van Engen and R. Jongebreur, "Magneto-optical properties of metallic ferromagnetic materials," *Journal of Magnetism and Magnetic Materials,* vol. 38, no. 1, pp. 1-22, 1983.

[126] J. S. Kasper, B. F. Decker and J. R. Belanger, "The Crystal Structure of the Sigma-Phase in the Co-Cr System," *Journal of Applied Physics,* vol. 22, no. 3, pp. 361-362, 1951.

Thèse accessible à l'adresse : https://theses.insa-lyon.fr/publication/2025ISAL0036/these.pdf © [T. Langlois], [2025], INSA Lyon, tous droits réservés

[127] G. Laplanche, S. Berglund, C. Reinhart, A. Kostka, F. Fox and E. George, "Phase stability and kinetics of σ-phase precipitation in CrMnFeCoNi high-entropy alloys," *Acta Materialia,* vol. 161, pp. 338-351;, 2018.

[128] *Standard Test Methods for Determining Average Grain Size Using Semiautomatic and Automatic Image Analysis,* ASTM International, 2023.

[129] O. Engler and V. Randle, Introduction to Texture Analysis: Macrotexture, Microtexture, and Orientation Mapping, Boca Raton: CRC Press, 2009.

[130] D. Savage, R. McCabe and M. Knezevic, "An automated procedure built on MTEX for reconstructing deformation twin hierarchies from electron backscattered diffraction datasets of heavily twinned microstructures," *Materials Characterization,* vol. 171, 2021.

[131] R. Hielscher, T. Nyyssönen, F. Niessen and A. A. Gazder, "The variant graph approach to improved parent grain reconstruction," *Materialia,* vol. 22, 2022.

[132] T. Langlois, "TwinStatistic_FCC," GitHub repository,, 2024. [Online]. Available: https://github.com/tlanglois17/TwinStatistic_FCC.

[133] *Standard Test Methods for Vickers Hardness and Knoop Hardness of Metallic Materials,* ASTM International, 2023.

[134] K. Sillapasa, Y. Mutoh, Y. Miyashita and N. Seo, "Fatigue Strength Estimation Based on Local Mechanical Properties for Aluminum Alloy FSW Joints," *Materials,* vol. 10, no. 2, p. 186, 2017.

[135] S. C. Krishna, N. Gangwar, A. Jha and B. Pant, "On the Prediction of Strength from Hardness for Copper Alloys," *Journal of Materials,* 2013.

[136] Y. Tian, L. Li, J. Li, b. Yang, S. Li and G. Qin, "Correlating Strength and Hardness of High-Entropy Alloys," *Advanced Engineering Materials,* vol. 23, 2021.

Thèse accessible à l'adresse : https://theses.insa-lyon.fr/publication/2025ISAL0036/these.pdf © [T. Langlois], [2025], INSA Lyon, tous droits réservés

[137] T. W. Clyne, J. E. Campbell, M. Burley and J. Dean, "Profilometry-Based Inverse Finite Element Method Indentation Plastometry," *Advanced Engineering Materials;,* 2021.

[138] S. T. M. o. C. T. o. M. M. a. R. Temperature, ASTM International.

[139] P. Chirstiansen, P. Martins and N. Bay, "Friction Compensation in the Compression Test," *Manufacturing Engineering Education,* pp. 85-104, 2019.

[140] A. Kumaraswamy and B. Sridhar Babu, "A novel method of evaluating flow curve for SS304 from low cost indentation experiments," *Journal of Engineering and Applied Sciences ,* vol. 5, 2010.

[141] "ISO 6892-3:2015(en) Metallic materials - Tensile testing - Part 3: Method of test at low temperature," 2015.

[142] F. Hahnenberger, M. Smaga and D. Eifler, "Influence of γ-α′-Phase Transformation in Metastable Austenitic Steels on the Mechanical Behavior During Tensile and Fatigue Loading at Ambient and Lower Temperatures," *Advanced Engineering Materials,* 2012.

[143] K. Lee, M. Chun, M. Kim and J. Lee, "A new constitutive model of austenitic stainless steel for cryogenic applications," *Computational Materials Science,* vol. 46, no. 4, pp. 1152-1162, 2009.

[144] D.-Y. Ryoo, N. Kang and C.-Y. Kang, "Effect of Ni content on the tensile properties and strain-induced martensite transformation for 304 stainless steel," *Materials Science and Engineering: A,* vol. 528, no. 6, pp. 2277-2281, 2011.

[145] L. Nguyen, J.-S. Hwang, M.-S. Kim, J.-H. Kim, S.-K. Kim and J.-M. Lee, "Charpy Impact Properties of Hydrogen-Exposed 316L Stainless Steel at Ambient and Cryogenic Temperatures," *Metals,* vol. 9, no. 6, 2019.

Thèse accessible à l'adresse : https://theses.insa-lyon.fr/publication/2025ISAL0036/these.pdf © [T. Langlois], [2025], INSA Lyon, tous droits réservés

[146] G. Laplanche, J. Bonneville, C. Varvenne, W. Curtin and E. George, "Thermal activation parameters of plastic flow reveal deformation mechanisms in the CrMnFeCoNi high-entropy alloy," *Acta Materialia,* vol. 143, pp. 257-264, 218.

[147] M. Traversier, E. Rigal, X. Boulnat, F. Tancret, J. Dhers and A. Fraczkiewicz, "Enhanced strain-hardening in newly designed Co-free austenitic high entropy alloys with an optimised nitrogen solubility," vol. 1010, 2025.

[148] S. Yoshida, T. Ikeuchi, T. Bhattacharjee, Y. Bai, A. Shibata and N. Tsuji, "Effect of elemental combination on friction stress and Hall-Petch relationship in face-centered cubic high / medium entropy alloys," *Acta Materialia,* vol. 171, pp. 201-215, 2019.

[149] N. L. Okamoto, K. Yuge, K. Tanaka, H. Inui and E. P. George, "Atomic displacement in the CrMnFeCoNi high-entropy alloy – A scaling factor to predict solid solution strengthening," *AIP Advances,* vol. 6, no. 12, 2016.

[150] A. Breidi, S. Fries, M. Palumbo and A. Ruban, "First-principles modeling of energetic and mechanical properties of Ni–Cr, Ni–Re and Cr–Re random alloys," *Computational Materials Science,* vol. 117, pp. 45-53, 2016.

[151] G. Meric de Bellefond, J. van Duysen and K. Sridharan, "Composition-dependence of stacking fault energy in austenitic stainless steels through linear regression with random intercepts," *Journal of Nuclear Materials,* vol. 492, pp. 227-230, 2017.

[152] E. Köster, A. Thölén and A. Howie, "Stacking fault energies of Ni–Co–Cr alloys," *Philosophical Magazine,* pp. 1093-1095, 1964.

[153] Solability, "The Global Sustainable Competitiveness Index," Solability, 2021. [Online]. Available: https://solability.com/download/the-global-sustainable-competitiveness-index-2021/?tmstv=1666158435.

[154] A. Gali and E. George, "Tensile properties of high- and medium-entropy alloys," *Intermetallics,* vol. 39, pp. 74-78, 2013.

Thèse accessible à l'adresse : https://theses.insa-lyon.fr/publication/2025ISAL0036/these.pdf © [T. Langlois], [2025], INSA Lyon, tous droits réservés

[155] E. Epifano and D. Monceau, "Ellingham diagram: A new look at an old tool," *Corrosion Science ,* vol. 217, 2023.

[156] "Ellingham Diagrams," University of Cambridge, 2006. [Online]. Available: https://www.doitpoms.ac.uk/tlplib/ellingham_diagrams/index.php.

[157] H. Hsiao, R. Feng, H. Ni, K. An, J. L. P. Poplawsky and J. Zuo, "Chemical Short-Range Ordering in a CrCoNi Medium-Entropy Alloy," *Condensed Matter,* 2022.

[158] X. Tian and Y. Zhang, "Effect of Si content on the stacking fault energy in -Fe–Mn–Si–C alloys: Part I. X-ray diffraction line profile analysis," *Materials Science and Engineering A,* vol. 516, pp. 73-77, 2009.

[159] S. Kada, A. de Vaucorbeil, D. Fabijanic and M. Barnett, "Work hardening and the scratch resistance of Ni–Co alloys using a rapid," *Wear,* pp. 510-511, 2022.

[160] H. Chang, T. Zhang, S. Ma, D. Zhao, T. Bai, K. Wang, Z. Li and Z. Wang, "Strengthening and strain hardening mechanisms in precipitationhardened CrCoNi medium entropy alloys," *Journal of Alloys and Compounds,* vol. 896, 2022.

[161] X. Wu, M. Yang, P. Jiang, C. Wang, L. Zhou, F. Yuan and E. Ma, "Deformation nanotwins suppress shear banding during impact test of CrCoNi medium-entropy alloy," *Scripta Materialia,* vol. 178, pp. 452-456, 2020.

[162] S.-K. Hwang, M. T. Tran, C. H. Dang, J.-M. Heo, H. W. Lee, K.-H. Jung and D.-K. Kim, "Exceptional cryogenic impact and fatigue properties of additively manufactured CrCoNi medium entropy alloy," *International Journal of Fatigue,* vol. 193, 2025.

[163] Q. Yang, D. Yan, Yong, Z., K. Gan and Z. Li, "Formation mechanisms of two types of sigma phases and the effects on mechanical behavior in a quaternary metastable high-entropy alloy," *Materials Science & Engineering A ,* vol. 894, 2024.

Thèse accessible à l'adresse : https://theses.insa-lyon.fr/publication/2025ISAL0036/these.pdf © [T. Langlois], [2025], INSA Lyon, tous droits réservés

[164] L. Z. C. W. P. J. F. Y. E. M. X. W. Muxin Yang, "High impact toughness of CrCoNi medium-entropy alloy at liquid-helium temperature," *Scripta Materialia,* vol. 172, pp. 66-71, 2019.

[165] X. Liu, H. Feng, J. Wang, X. Chen, P. Jiang, F. Yuan, H. Li, E. Ma and X. Wu, "Mechanical property comparisons between CrCoNi medium-entropy alloy and 316 stainless steels," *Journal of Materials Science & Technology,* vol. 108, pp. 256-269, 2022.

[166] S. Quinn, J. Dulieu-Barton, J. Eaton-Evans and P. Tatum, "Thermoelastic Investigation of Damage Evolution in Small Stainless Steel Pipework," in *Experimental Analysis of Nano and Engineering Materials and Structures*, Dordrecht, 2007.

[167] K. J. Lee, M. S. Chun, M. H. Kim and J. M. Lee, "A new constitutive model of austenitic stainless steel for cryogenic applications," *Computational Materials Science,* vol. 46, no. 4, pp. 1152-1162, 2009.

[168] Z. Li, L. Chen, P. Fu, H. Su, P. Dai and Q. Tang, "The effect of Si addition on the heterogeneous grain structure and mechanical properties of CrCoNi medium entropy alloy," *Materials Science & Engineering A ,* vol. 852, 2022.

[169] X. C. R. L. T. Gao, "High-entropy alloys: a review of mechanical properties and deformation mechanisms at cryogenic temperatures," *Journal of Materials Science ,* vol. 57, p. 6573–6606, 2022.

[170] R. Carney Luis and J. J. Mecholsky, "Relationship between Fracture Toughness and Fracture Surface Fractal Dimension in AISI 4340 Steel," *Materials Sciences and Applications,* vol. 4, 2013.

[171] Y. Deng, C. C. Tasan, K. G. Pradeep, H. Springer, A. Kostka and D. Raabe, "Design of a twinning-induced plasticity high entropy alloy," *Acta Materialia,* vol. 94, pp. 124-133, 2015.

Thèse accessible à l'adresse : https://theses.insa-lyon.fr/publication/2025ISAL0036/these.pdf © [T. Langlois], [2025], INSA Lyon, tous droits réservés

[172] K. Jeong, J.-E. Jin, Y.-S. Jung, S. Kang and Y.-K. Lee, "The effects of Si on the mechanical twinning and strain hardening of Fe–18Mn–0.6C twinning-induced plasticity steel," *Acta Materialia,* vol. 61, pp. 3399-3410, 2013.

[173] X. Tian and Y. Zhang, "Effect of Si content on the stacking fault energy in γ-Fe–Mn–Si–C alloys: Part I. X-ray diffraction line profile analysis," *Materials Science and Engineering: A,* vol. 516, no. 1-2, pp. 73-77, 2009.

[174] B. G. Survey, "World mineral statistics data," BGS, 5 May 2023. [Online]. Available: https://www.bgs.ac.uk/mineralsuk/statistics/world-mineral-statistics/world-mineral-statistics-archive/. [Accessed 2023].

[175] R. Hu and Q. Zhang, "Study of a low-carbon production strategy in the metallurgical industry in China," *Energy,* vol. 90, pp. 1456-1467, 2015.

[176] Q. Zhang, Z. Wei, J. Ma, Z. Qiu and T. Du, "How to minimise the carbon emission of steel building products from a cradle-to-site perspective: A systematic review of recent global research," *Journal of Cleaner Production,* vol. 368, 2022.

[177] M. De Paepe, L. Jeanneau, J. Mariette, O. Aumont and A. Estevez-Torres, "Purchases dominate the carbon footprint of," *PLOS Sustainability and Transformation,* vol. 3, no. 7, 2024.

[178] L. Jiang, R. Varma, M. Ramajayam, T. Dorin, M. R. Barnett and D. Fabijanic, "Effects of extreme deposition rate on the microstructure evolution of additive friction stir deposited AA6061 alloy," *Additive Manufacturing Letters,* vol. 13, 2025.

[179] C. Haase, F. Tang, M. Wilms, A. Weisheit and B. Hallstedt, "Combining thermodynamic modeling and 3D printing of elemental powder blends for high-throughput investigation of high-entropy alloys - Towards rapid alloy screening and design," *Material Science Engineering,* vol. A 688, pp. 180-189, 2017.

Thèse accessible à l'adresse : https://theses.insa-lyon.fr/publication/2025ISAL0036/these.pdf © [T. Langlois], [2025], INSA Lyon, tous droits réservés

[180] M. Koyama, T. Eguchi, K. Ichii, C. C. Tasan and K. Tsuzaki, "A new design concept for prevention of hydrogen-induced mechanical degradation: viewpoints of metastability and high entropy," *Procedia Structura Integrity,* 2018.

[181] S. Yan, X. He and Z. Zhu, "Hydrogen Embrittlement of CrCoNi Medium-Entropy Alloy with Millimeter-Scale Grain Size: An In Situ Hydrogen Charging Study," *Entropy, ,* vol. 25, no. 4, `2023.

[182] K. Ichii, M. Koyama, C. Tasan and K. Tsuzaki, "Comparative study of hydrogen embrittlement in stable and metastable," *Scripta Materialia,* vol. 150, pp. 74-77, 2018.

[183] W. Zhang, A. Chabok, B. Kooi and Y. Pei, "Additive manufactured high entropy alloys: A review of the microstructure and properties," *Materials & Design,* vol. 220, 2022.

[184] D. Kong, C. Dong, X. Ni, L. Zhang, C. Man, G. Zhu, J. Yao, L. Wang and X. Cheng, "Effect of TiC content on the mechanical and corrosion properties of Inconel 718 alloy fabricated by a high-throughput dual-feed laser metal deposition system," *Journal of Alloys and Compounds,* vol. 803, pp. 637-648, 2019.

[185] S. Liu, D. Wan, S. Guan, Y. Fu, Z. Zhang and J. HE, "A comparative study on nanoscale mechanical properties of CrMnFeCoNi high-entropy alloys fabricated by casting and additive manufacturing," *Journal of Materials Research and Technology,* vol. 33, pp. 1211-1219, 2024.

[186] B. Han, C. Zhang, K. Feng, Z. Li, X. Zhang, Y. Shen, X. Wang, X. Kokawa, R. Li, Z. Wang and P. Chu, "Additively manufactured high strength and ductility CrCoNi medium entropy alloy with hierarchical microstructure," *Materials Science & Engineering A ,* vol. 820, 2021.

[187] S. Yan, X. He and Z. Zhu, "Hydrogen Embrittlement of CrCoNi Medium-Entropy Alloy with Millimeter-Scale Grain Size: An In Situ Hydrogen Charging Study," *Entropy,,* vol. 25, no. 4, 2023.

Thèse accessible à l'adresse : https://theses.insa-lyon.fr/publication/2025ISAL0036/these.pdf © [T. Langlois], [2025], INSA Lyon, tous droits réservés

Thèse accessible à l'adresse : https://theses.insa-lyon.fr/publication/2025ISAL0036/these.pdf © [T. Langlois], [2025], INSA Lyon, tous droits réservés

FOLIO ADMINISTRATIF

THESE DE L'INSA LYON, MEMBRE DE L'UNIVERSITE DE LYON

NOM : LANGLOIS
(avec précision du nom de jeune fille, le cas échéant)

DATE de SOUTENANCE : 03.04.25

Prénoms : Théo, Rathana

TITRE : Sustainability footprints and mechanical performance in multi-principal element alloys

NATURE : Doctorat

Numéro d'ordre : 2025ISAL0036

Ecole doctorale : ED34

Spécialité : Matériaux

RESUME : Face aux défis environnementaux actuels, il est essentiel de développer des matériaux avec une plus faible empreinte sur notre société. Cette thèse se concentre sur de nouveaux alliages métalliques, avec plusieurs métaux en proportions similaires, offrant à la fois performance mécanique et faible empreinte. L'objectif principal est de réduire l'utilisation du cobalt, un métal qui pose des problèmes environnementaux et sociaux. Pour y parvenir, une méthode innovante et rapide a été mise en place, permettant de tester rapidement différentes compositions d'alliages. Les résultats montrent qu'en ajoutant du silicium, il est possible de créer des alliages performants avec moins de cobalt. Ces nouveaux matériaux sont particulièrement adaptés au stockage et au transport de l'hydrogène, soutenant ainsi la transition vers des énergies plus vertes et respectueuses de l'environnement. Cette recherche contribue à une production plus durable et à la réduction de l'impact écologique des matériaux utilisés dans l'industrie.

MOTS-CLÉS : Alliages haute entropie, Soutenabilité, Performance mécanique, Modélisation, Métallurgie, Optimisation multi-objective

Laboratoire (s) de recherche : MATEIS INSA Lyon

Directeur de thèse : BARNETT Matthew

Président de jury :

Composition du jury :

Mme. PEREZ PRADO, Maria Teresa	Professeur	IMDEA	Rapporteur
M. GODET, Stéphane	Professeur	ULB	Rapporteur
Mme. FRACZKIEWIECZ, Anna	Professeur	MINES Saint-Etienne	Examinatrice
M. TANCRET, Franck	Professeur	Univ Nantes	Président
M. BARNETT, Matthew	Professeur	Deakin University	Directeur de
M. FABIJANIC, Daniel	Associate Professor	Deakin University	thèse Encadrant
M. FABREGUE, Damien	Professeur	INSA Lyon	Co-directeur
M. BOULNAT, Xavier	Maître de conférences	INSA Lyon	Co-encadrant

Thèse accessible à l'adresse : https://theses.insa-lyon.fr/publication/2025ISAL0036/these.pdf © [T. Langlois], [2025], INSA Lyon, tous droits réservés

Thèse accessible à l'adresse : https://theses.insa-lyon.fr/publication/2025ISAL0036/these.pdf © [T. Langlois], [2025], INSA Lyon, tous droits réservés